Event-Scale Relationships Between Surface Velocity, Temperature and Chlorophyll in the Coastal Ocean, As Seen by Satellite

(NAGW-1251)

P. Ted Strub
College of Oceanography
Oregon State University
Corvallis, OR 97331-5503

Final Report
Covering 14 December 1987 to 15 December 1991

Introduction

The overall goal of this project was to increase our understanding of processes which determine the temporally varying distributions of surface chlorophyll pigment concentration and surface temperature in the California Current System (CCS) on the time-scale of 'events,' i.e., several days to several weeks. We also proposed to investigate seasonal and regional differences in these events. Additionally, we proposed to evaluate methods of estimating surface velocities and horizontal transport of pigment and heat from sequences of AVHRR and CZCS images. The four specific objectives stated in the original proposal were to:

1. Test surface current estimates made from sequences of both SST and color images using variations of the statistical method of Emery et al. (1986, JGR, **91**:12,865-12,878) and estimate the uncertainties in these satellite-derived surface currents;
2. Characterize the spatial and temporal relationships of chlorophyll and temperature in rapidly evolving features for which adequate imagery exist and evaluate the contribution of these events to monthly and seasonal averages;
3. Use the methods tested in (1) to determine the nature of the velocity fields in the CCS;
4. Compare the currents, temperature and currents in different seasons and in different geographic regions.

As proposed, we planned to obtain CZCS and AVHRR data from the West Coast Time Series (WCTS), wind data from operational atmospheric models and in situ data from CalCOFI and other programs. As carried out, AVHRR data were not available from the WCTS during the project. Previously collected AVHRR data from the 1981 CODE (Coastal Ocean Dynamics Experiment) period and from the 1987-88 CTZ (Coastal Transition Zone) period were used instead. CZCS data from the WCTS were used, as were LFM and FNOC wind fields and in situ data from the CODE, CalCOFI and CTZ projects.

Below and in the appendices, we describe the progress made on each of the objectives. Work continues on some of the objectives under other funding, extending this work in the CCS in comparison to other eastern boundary currents. In particular, work on the first objective has proceded beyond the stated goal, in that we have included the method of inverting the heat advection equation (with additional funding from ONR and TOPEX). The second and fourth objectives were accomplished with respect to chlorophyll fields in the CCS under this funding. This analysis is being extended to other eastern boundary currents under other NASA funding. The surface temperature analysis in the CCS will also be accomplished under that funding, now that the WCTS AVHRR data are available. The third objective (characterizing the nature of the surface velocity fields in the CCS) was partially accomplished using AVHRR, altimeter and field data from the 1987-88 CTZ project. That work continues under ONR and TOPEX funding, as described below.

Work supported wholly or partially by this grant resulted in 9 refereed papers, a

Masters thesis, and 14 presentations at professional conferences. (see Appendix A). The rest of this report consists of summaries of the major projects carried out with all or partial support from this grant. The appendices include a list of papers and professional presentations supported by the grant, as well as reprints of the papers.

Estimates of Surface Velocity from Sequences of AVHRR and CZCS Images (Objective 1)

Because AVHRR data were not available from the WCTS, AVHRR data from the CODE (1981) and CTZ (1987-88) projects were used. Coincident CZCS data were available for the 1981 period but not for 1987-88. Tokmakian et al (1990, [Appendix B]) reported results of comparisons of satellite-derived velocities to field data using sequences of AVHRR and CZCS images in 1981 and sequences of AVHRR images in 1987. The most innovative aspect of that study was the use of a quasi-geostrophic numerical model, initialized from a hydrographic survey in May 1987, to advect an AVHRR image from the same period, creating a 'synthetic' sequence of images with known surface velocities. Use of automated feature-tracking methods (the 'maximum cross-correlation' [MCC] method of Emery et al.) on the synthetic sequence resulted in an estimate of velocities which could be compared to the known velocities which created the sequence. The results of this study showed that: (1) for temporal separations of 12-hours or less, the RMS errors in the velocity fields were of order 0.2 ms^{-1}; (2) RMS errors in the fields increased rapidly for temporal separations greater than 12-hours; (3) fields generated from both AVHRR and CZCS images showed qualitative agreement with field measurements, but AVHRR images with 12-hour separations produced many more significant vectors than the CZCS images with 24-hour separation; (4) if several images are available for a short period, averaging the fields produces better results; and (5) the success of the method depends on the presence of sharp and distinct small-scale features, which are advected by the large-scale velocity field.

The importance of the last point became apparent during attempts to use other CZCS sequences from the WCTS to derive reasonable velocity fields, which were not as successful, since most of the images were more diffuse. This has led us to conclude that CZCS images can only rarely be used to estimate suface currents and pigment transports. Our present approach to satellite estimates of pigment or biomass transport is to combine the pigment concentrations from the CZCS (or future) sensor with velocity fields from other sources (AVHRR sequences and/or altimeters).

An even more thorough analysis of the ability to use AVHRR sequences to estimate surface currents was made in collaboration with Kathie Kelly (Kelly and Strub, 1992 [Appendix C]). An unusually clear sequence of 11 images over a 2.5 day period in July 1988 was used to derive velocity fields which were compared to surface drifters, ADCP velocities and altimeter velocities from the same period. Both the MCC and 'inverse' method (inversion of the heat advection equation) were tested. The conclusions of this study were: (1) for a sequence of several clear images with temporal separations of 4-12 hours, both methods can resolve the main circulation features (jets, eddies, etc.); (2)

RMS errors were again on the order of 0.2 ms^{-1}, which is also the order of magnitude of the difference between the ADCP fields and drifter velocities (the true surface velocity field is difficult to determine by any method!); (3) the satellite-derived fields generally underestimate the maximum velocities in the strongest jets; (4) in some cases, inclusion of altimeter data slightly improves the estimated velocity field. This last conclusion is based on only a small amount of altimeter data and it is still hoped that the combination of velocity fields from AVHRR sequences and several altimeters will provide an improved time series of surface velocity fields during the coming years.

The Nature of the Velocity Fields in the California Current System (Objectives 3 and 4)

Progress on this objective has been made using AVHRR, altimeter and field data from the CTZ project. Strub et al. (1991, [Appendix D]) used a wide variety of field and satellite data to conclude that: (1) there is a seasonal development of the flow field, with greater mesoscale variability in summer than winter; (2) the summer structure in both 1987 and 1988 consisted of a meandering jet that extended from north of Cape Blanco (43°N) to south of Point Conception (35°N); (3) the jet carries water with low temperatures and high salinity, nutrients and chlorophyll on its inshore flank, extending several hundred kilometers offshore on its meanders; (4) off Cape Mendocino (40°N) in February 1987, the stucture showed no similar jet, while in March 1987 a jet was only present over the shelf (20 kilometers from the coast).

These conclusions lead to the hypothesis that an alongshore jet forms in spring along a front created by upwelling, moving offshore and evolving into the meandering jet observed by the CODE, OPTOMA and CTZ projects. Use of the MCC method over the large-scale CCS during the exceptionally clear period in July 1988 produces velocities, which, when combined with cross-track altimeter velocities from the same period using objective analysis (OA) (Bretherton et al., 1976, DSR, **23**, 559-582), result in the picture of surface currents shown in Figure 1. A smoothing over scales of approximately 100 kilometers is inherent in the OA process. The structure consists of a meandering alongshore jet, as described above, and eddies of both sign inshore and offshore of the jet, although anticyclonic eddies predominate offshore of the jet. Drifters showed that the cyclonic eddy at the end of the meander at approximately 36.5°N, 126°W in Figure 1 persisted from June through August. Altimeter and AVHRR data suggest that the anticyclonic eddy at approximately 39.5°N, 130°W originated closer to the coast in February, on the offshore side of colder water, presumably caused by upwelling, which would be consistent with observed southward winds during most of February, 1988. This lends support to the argument that the initial development of the jet and eddy system is wind driven, regardless of season. The predominance of southward winds in spring and summer is the hypothesized reason for the regular appearance of the meandering jet in late spring and summer. This hypothesis will be tested using wind, AVHRR, altimeter and field data to be collected during the 1992-1994 period with ONR and TOPEX funding.

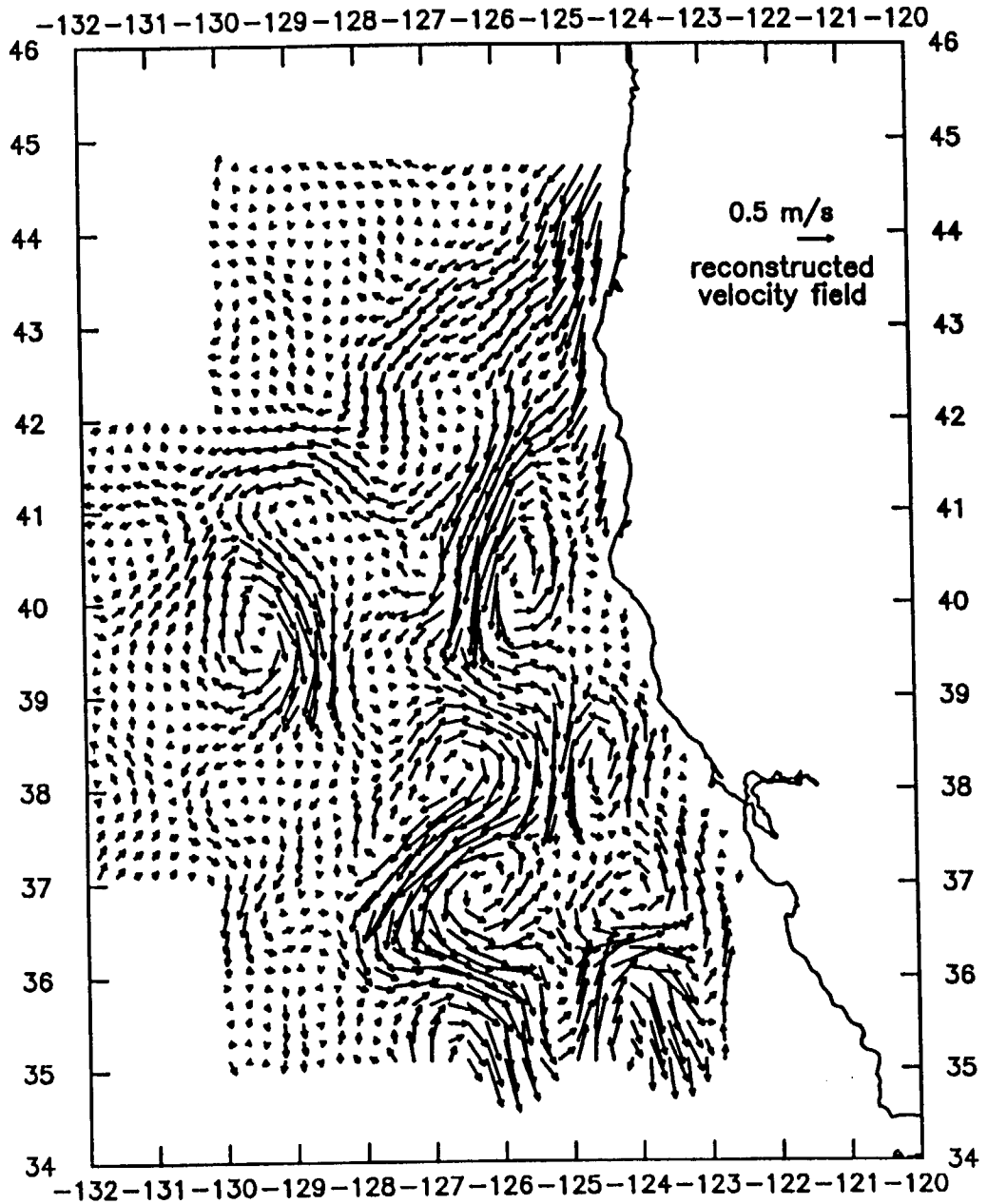

Figure 1

Automated feature-tracking of a sequence of 6 AVHRR images from 17-18 July 1988 was used to create a field of surface velocities. These and cross-track velocities from the Geosat altimeter from the same period were objectively analyzed using the method of Bretherton et al. (1976) to produce a streamfunction field, from which this velocity field was reconstructed. The jet flowing offshore at 37.5°N, 125-128°W was intensely sampled in the 1988 CTZ surveys.
P. Ted Strub, OSU

21-FEB-92

Seasonal and Regional Differences in Fields of Surface Chlorophyll Concentration (Objectives 2 and 4)

Three papers were written on this general topic. Thomas and Strub (1989 [Appendix E]) looked at the large-scale, short-term change in pigment concentrations at the time of the spring transition, when winds become strong and persistently southward, usually occuring in March or April. A 'spring bloom' extending several hundred kilometers offshore in a diffuse pattern (unlike the scalloped pattern in mid-summer) was observed in the CZCS data following the transition on some years, but was weak or absent on others. CalCOFI data were used to show the surface water to be nutrient limited in late winter off California, unlike the NE Pacific farther north or the North Atlantic. A 1-d numerical model was driven by winds from the NMC operational weather forecast model for each of the years with CZCS data. The results showed that: (1) during years when the winds that followed the transition were strongest and most persistent, the initial surface enrichment of the large-scale CCS after the transition is due to local vertical wind-mixing (nutrients mixed up from below the thermocline; (2) increasing surface radiation, combined with mixing, strengthen the thermocline, sealing off the mixed layer after several weeks to a month later, at which time coastal upwelling becomes the dominant factor, reducing the enriched region to a narrower alongshore band (presumably inshore of the jet which develops), which expands as the summer progresses. The timing and strength of wind forcing, in relation to radiation and other heating terms, is thus a critical source of interannual variability in phytoplankton productivity in spring. The ability of physical models to correctly parameterize this mixing will be important when biological processes are incorporated into the physical models to create ecosystem models.

In Thomas and Strub (1990, [Appendix F]), the seasonal development of the 'Ensenada Front' was investigated. In early summer, this front is seen as an east-to-west line at approximately 33°N, north of which are found higher concentrations of pigment concentration. By forming average transects running north-to-south across the front and east-to-west away from the coast at several latitudes, the results showed that: (1) many temporal and spatial characteristics of the pigment structure are repeated in different years; (2) the variations in the spatial structure of the front are controlled by changes north of the front, where concentrations reach maximum values in March through June, with persistently low values south of the front; (3) concentrations north of the front in the sampled region decrease in June through August, due to a seasonal shift in the cross-shelf distribution of pigment, which causes the region of greater pigment concentration to be confined closer to the coast in this region; (4) an increase in pigment concentration usually occurs again in fall before the winter decline; (5) superimposed on this general pattern is a great deal of interannual variability in the magnitude and location of the front, with the greatest difference found after the 1982-83 El Nino, when pigment concentrations were greatly reduced (spring-summer of 1993); and (6) little relation to wind forcing could be found for the interannual variations in anomalous

pigment concentrations.

The large-scale annual and interannual variability in the surface pigment concentrations were described in Strub et al. (1990, [Appendix G]). This paper also contained the details of the processing used to produce the initial version of the CZCS images in the WCTS, which used the single-scattering Rayleigh algorithm for the atmospheric correction. This produced an error (too large concentrations) in winter when sun-satellite angles are large. A method of reducing that error was presented in the paper. The March-October seasonal cycle was presented, using the corrected data, and compared to wind data. After removing the seasonal cycles from all data, the method of Canonical Correlation Analysis was used to investigate the extent to which wind-forcing could account for the monthly non-seasonal variability. The results showed that: (1) within the Southern California Bight (south of the Ensenada Front descibed above), seasonality is low, with a slight summer minimum; (2) elsewhere (from Baja California to Washington), there is a strong seasonal cycle, with a spring-summer maximum, a northward progression of high pigment concentration from California to Oregon, and a double maximum off Washington; (3) nonseasonal variability in pigment concentration over the large-scale CCS (out to 400 kilometers offshore) is most closely related to fields of wind-stress curl; (4) in the region limited to within 100 kilometers of the coast, the strongest relationships are found between the anomalous pigment concentrations and both alongshore wind stress and u_*^3; (5) the pigment-wind correlations explain only 25% of the pigment variability at most; (6) there is even lower correlations between the pigment anomalies and anomalous sea levels at the coast, which serves as a crude proxy for alongshore currents in the nearshore region; and (7) the largest interannual variability is associated with the 1982-83 El Nino, which caused low concentrations of pigment nearly everywhere, as noted previously. We should stress that the apparent weak connection between wind and pigment concentration applies to the anomalous (seasonal cycles removed) data. The latitudinal progression of the seasonal cycles of pigment concentration and wind variables show strong similarities, but cannot be quantified statistically, since all signals with a period of one year will be strongly correlated at some lag.

The fact that only 25% or less of the nonseasonal pigment variability could be related to wind variability confirmed our expectation that connections between biological variables and physical forcing is much more complex than the connections between physical forcing and physical responses. For instance, a similar analysis showed that 90% of the anomalous coastal sea level variability (from tide gauges) was related to alongshore wind stress. The weaker direct connection between physical forcing and biological variability may be partly due to greater noise in the CZCS data than in sea level data. It is also a reflection of the greater natural variability of biological variables and their episodic, non-linear response to forcing. A final conclusion, based on our experience in all of the above studies, is that temporal averaging, compositing or optimal interpolation (Chelton and Schlax, 1991, JGR **96**:14,669-14,692) is necessary to reduce

noise and obtain a coherent picture using CZCS color data. Whether this will be true of future color sensors with greater signal to noise characteristics remains to be seen, but for the CZCS data set, this fact limits the temporal resolution over short periods, i.e., 'events' with scales of less than 10 days.

Besides these papers, two additional papers were written by A. Thomas while funded by this grant, based on research completed as part of his PhD thesis, Thomas and Emery (1988, [Appendix H)] and Thomas (1992, [Appendix I]). Thomas was also co-author of another paper which compared environmental conditions to Dungeness crab larvae distributions (Hobbs, et al., 1992, [Appendix J]). Appendix A contains the references for all the papers and presentations which resulted from work partially or entirely funded by this grant.

APPENDIX A – Publications and Presentations

Refereed Journal Papers

Hobbs, R. C., L. W. Botsford and A. C. Thomas. The influence of hydrographic conditions and wind forcing on the distribution and abundance of Dungeness crab larvae. *Can. J. Fish. Aquat. Sci. (in press)*, 1992.

Kelly, K. A., and P. T. Strub. Comparison of Velocity Estimates from AVHRR in the Coastal Transition Zone. *J. Geophys. Res.*, (in press), 1992.

Strub, P. T., C. James, A. C. Thomas and M. R. Abbott. Seasonal and non-seasonal variability of satellite-derived surface pigment concentration in the California Current. *J. Geophys. Res.*, **95**, 11,501-11,530, 1990.

Strub, P. T., P. M. Kosro, A. Huyer, and CTZ Collaborators. The nature of the cold filaments in the California Current System. *J. Geophys. Res.*, **96**, 14,743-14,768, 1991.

Thomas, A. C., and W. J. Emery. Relationships between near-surface plankton concentrations, hydrography, and satellite-measured sea surface temperature. *J. Geophys. Res.*, **93**, 15,733-15,748, 1988.

Thomas, A. C., and P. T. Strub. Interannual variability in phytoplankton pigment distribution during the spring transition along the west coast of North America. *J. Geophys. Res.*, **94**, 18,095-18,117, 1989.

Thomas, A. C., and P. T. Strub. Seasonal and interannual variability of phytoplankton pigment concentrations across a California Current frontal zone. *J. Geophys. Res.*, **95**, 13,023-13,042, 1990.

Thomas, A. C.. Spatial patterns of zooplankton community composition and satellite measured surface temperature. *Cont. Shelf Res.*, (in press), 1992.

Tokmakian, R., P. Ted Strub, and J. McClean-Padman. Evaluation of the maximum cross-correlation method of estimating sea surface velocities from sequential satellite images. *J. Atmos. and Oceanic Tech.*, **7**, 852-865, 1990.

Presentations

Thomas, A. C. and P. T. Strub. Large-scale changes in patterns of chlorophyll concentration during the spring transition along the North American west coast. AGU Fall Meeting. San Francisco, California. December, 1988.

Tokmakian, R., P. T. Strub, and J. McClean-Padman. Computing coastal velocities

from CZCS and AVHRR satellite imagery. AGU Fall Meeting. San Francisco, California. December, 1988.

McClean-Padman, J., P. T. Strub, and R. Tokmakian. Translational and rotational motion objectively calculated from sequential infrared satellite images. AGU Fall Meeting. San Francisco, California. December, 1988.

Thomas, A. C. Large-scale changes in patterns of chlorophyll concentration during the spring transition along the North American west coast. University of Rhode Island, June, 1989.

Thomas, A. C. and P. T. Strub. Seasonal and interannual variability of phytoplankton pigment concentrations across a California Current System frontal zone. EPOC 1989. Monterey, California. October, 1989.

Strub, et al. The nature of the cold filaments in the California Current – squirts or meanders? AGU Ocean Sciences Meeting. New Orleans, Louisiana. February, 1990.

Strub, P. T., C. James, and A. C. Thomas. The seasonal cycle of CZCS- derived surface pigment concentration in the California Current. AGU Ocean Sciences Meeting. New Orleans, Louisiana. February, 1990.

Thomas, A. C. and P. T. Strub. Seasonal and interannual variability of phytoplankton pigment concentrations across a California Current System frontal zone. AGU Ocean Sciences Meeting. New Orleans, Louisiana. February, 1990.

Thomas, A. C. Large-scale changes in patterns of chlorophyll concentration during the spring transition along the North American west coast. Dalhousie University, March, 1990.

Strub, P. T., C. James, and A. C. Thomas. Interannual variability of satellite-derived surface pigment concentration in the California Current. Canadian Meteorology and Oceanographic Society; 24th Annual CMOS Congress, Victoria, B.C., Canada, May, 1990.

Thomas, A. C., Hobbs, R. C., and L. W. Botsford. The influence of hydrographic conditions and wind forcing on the distribution and abundance of Dungeness crab larvae. Canadian Meteorology and Oceanographic Society; 24th Annual CMOS Congress, Victoria, B.C., Canada, May, 1990.

Thomas, A. C. and P. T. Strub. Large-scale cross-shelf variability in pigment concentrations along the North American west coast. Brookhaven Symposia in Biology No. 37. Upton, New York. June, 1991.

Strub, P. T. Large-scale structure of the California Current in summer. AGU Ocean Sciences Meeting. New Orleans, Louisiana. February, 1992.

Thomas, A. C. and P. T. Strub. Large-scale cross-shelf variability in pigment concentrations along the North American west coast. AGU Ocean Sciences Meeting. New Orleans, Louisiana. February, 1992.

APPENDIX B

EVALUATION OF THE MAXIMUM CROSS-CORRELATION METHOD OF ESTIMATING SEA SURFACE VELOCITIES FROM SEQUENTIAL SATELLITE IMAGES

Robin Tokmakian, P. Ted Strub, and Julie McClean-Padman

Reprinted from JOURNAL OF ATMOSPHERIC AND OCEANIC TECHNOLOGY, Vol. 7, No. 6, December 1990
American Meteorological Society

Evaluation of the Maximum Cross-Correlation Method of Estimating Sea Surface Velocities from Sequential Satellite Images

ROBIN TOKMAKIAN

P. TED STRUB

JULIE MCCLEAN-PADMAN

Evaluation of the Maximum Cross-Correlation Method of Estimating Sea Surface Velocities from Sequential Satellite Images

ROBIN TOKMAKIAN

Institute of Oceanographic Sciences, Wormley, Godalming, Surrey, United Kingdom

P. TED STRUB

College of Oceanography, Oregon State University, Corvallis, Oregon

JULIE MCCLEAN-PADMAN

Department of Oceanography, Old Dominion University, Norfolk, Virginia

(Manuscript received 14 December 1989, in final form 29 June 1990)

ABSTRACT

We evaluate the method of estimating sea surface velocities from sequences of AVHRR and CZCS images using the maximum cross-correlation (MCC) technique. A set of synthetic images is created by advecting an AVHRR–SST field with a QG model velocity field. The MCC method of determining the sea surface velocities is then applied to the synthetic images. The rms differences and vector correlations between the model's velocity field and the field produced by the MCC method are presented. In addition, real AVHRR and CZCS images are used to find the rms difference between the satellite-derived velocity fields and in situ ADCP and hydrographic data. The tests show that AVHRR imagery yields the best results when images are separated by as short a period as possible. The rms errors at 6-h separation are on the order of 0.14 m s^{-1}, growing to $\geq$0.25 m s^{-1} at separations of more than 18 h. CZCS images are always separated by 24 h or more, but images with well-defined features may result in rms differences no larger than those produced by AVHRR images separated by 12 and 24 h. The method is most successful when several AVHRR image pairs separated by 12 h or less are available from a short (1–3 day) period and the velocity fields from the individual pairs are averaged to give a single synoptic picture of the current field. Specific examples show some of the reasons for incorrect vectors calculated by the method, and suggestions are made for improvements in the method.

1. Introduction

This study evaluates the maximum cross-correlation (MCC) method, objectively estimating sea surface velocities from sequences of satellite images. The method was originally developed for tracking clouds (Leese et al. 1971) and applied by Emery et al. (1986) to track oceanic features using sequences of infrared satellite images. Emery et al. compared the velocity field produced by the MCC method to surface drifter tracks and dynamic height fields and found qualitative agreement between the fields. Before the surface velocity fields calculated in this manner can be used in quantitative studies, the errors associated with the fields must be estimated. This is the goal of the present paper.

Some of the characteristics of the errors expected in velocity fields derived from sequential satellite images have been explored by Svejkovsky (1988) and Wahl and Simpson (1990). Svejkovsky used a subjective method of feature tracking, requiring an analyst to identify and track unique features from one image to the next. Using only the most identifiable features, Svejkovsky determined that subjective estimates of surface velocities differ from the velocities of surface drifters with an rms difference of 0.06 m s^{-1}. Svejkovsky used both Coastal Zone Color Scanner (CZCS) and Advanced Very High Resolution Radiometer (AVHRR) imagery to arrive at his conclusions. Wahl and Simpson used idealized models of uniform advection, horizontal diffusion, and surface heating to describe how the objective MCC method can be degraded by processes other than advection. The tests showed that nonadvective near-surface physical processes degrade the correlations between the image pairs over periods of less than 24 h. The greatest decrease in correlation was caused by spatially varying surface heating in the summer.

Two approaches are used to quantify the error in the sea surface velocity field estimated by the MCC method. In the first approach, a time series of synthetic

Corresponding author address: Dr. Ted Strub, College of Oceanography, Oregon State University, Oceanography Admin. Building 104, Corvallis, OR 97331-5503.

images is generated by advecting an initial AVHRR image with surface velocities from a high resolution quasi-geostrophic (QG) numerical model. The ability of the MCC method to recover the model velocities from the sequence of synthetic images is then quantified. In the second approach, velocity fields obtained from ship surveys are compared to the fields produced by applying the MCC method to nearly coincident CZCS and AVHRR images. Use of the synthetic images quantifies the error caused solely by rotation and distortion due to the geostrophic currents, without additional nonadvective processes. Use of the real sequences of images in comparison to field data quantifies the error caused by all sources. Comparison of the two approaches allows an estimate of the effect of nonuniform advection (rotation and distortion) and nonadvective processes (surface heating and mixing). One of the goals is to determine the relation between the temporal separation of the different types of images used in the MCC calculation and the rms error expected in the fields.

The differences between the AVHRR and CZCS images are: 1) what they see; 2) the depth to which they see into the water; and 3) the time separation between sequential images. The AVHRR sensor is an infrared instrument and thus sees the sea surface temperature (SST) in only the upper 15 μm of the ocean. In contrast, the visible channels used by the CZCS see differences in color caused mostly by phytoplankton pigment in the upper 5–15 m of the ocean. The CZCS sensor has the potential advantage of representing the upper ocean better than the AVHRR sensor. In practice, the SST seen by the AVHRR is found to be reasonably representative of the upper ocean when local winds blow between 5–10 m s^{-1}. Since neither temperature nor pigment concentrations are conservative in the upper ocean, it is best to keep the time separation between successive images short, in order to minimize the nonadvective processes. Here, the CZCS is at a disadvantage since it has a minimum separation of 24 h between images, while the minimum separation for the AVHRR images is 3–12 h depending on whether one or two satellites are operating. The differences between the two types of imagery provide the motivation to evaluate the rms errors of each.

2. Method and data description

a. MCC method

The MCC method has been described in detail by Emery et al. (1986), Garcia and Robinson (1989), and Wahl and Simpson (1990). A two dimensional space-lagged cross-correlation matrix (Press et al. 1986) is found for small regions in a pair of sequential images. The greatest positive correlation value is assumed to correspond to the location of the displacement of the first subimage in the second (larger) search subimage. The velocity vector at the center of the first subimage is calculated from this displacement and the time separation between the pair of images. The procedure is repeated for specified starting points over the image pair, either on a regular grid or at specific points for direct comparison to in situ data.

b. QG model and synthetic imagery description

To evaluate the velocity fields determined by the MCC method, a numerical model was used to produce synthetic SST fields. The Harvard Open Ocean Model (Robinson and Walstad 1987), a quasi-geostrophic model, was applied to an area off the northern California coast between 37°–40° N. Model resolution was 3 km with no bottom topography or surface forcing. CTD data from 18–26 May 1987, collected during the Coastal Transition Zone (CTZ) Experiment was used to initialize the model. The model velocity fields were used to advect an SST field from an AVHRR satellite image from 19 May 1987, producing synthetic images at regularly spaced times.

The advection equation is

$$\partial T/\partial t + u\frac{\partial T}{\partial x} + v\frac{\partial T}{\partial y} = 0, \qquad (1)$$

where T is the surface temperature and u, v are the velocity components provided by the model. A leapfrog time step and centered space derivatives were used, which introduced numerical dispersion, resulting in an artificial decrease in advective velocities (Mesinger and Arakawa 1976). For wavelengths longer than 11 km, attenuation of the true velocity is less than 10% (Tokmakian 1989). Since the subimage squares used in the MCC method have sides of 25–50 km, the numerical dispersion should not contribute significantly to errors in the displacements of these subimages, although it might distort the smaller features within the subimages reducing the correlations to some degree. The numerical dispersion is thus analogous to eddy diffusion in the real ocean, which is not included explicitly in the calculation of the synthetic images.

The domain of the model and synthetic images is limited to a region approximately 150 km × 340 km by the coverage of the hydrographic surveys used to initialize the model. Figure 1a shows this region, the locations where MCC velocities are calculated and the initial streamline field from the model. Velocities are to the southeast in the north of the domain and to the southwest in the southern half of the domain. Synthetic images for times 6, 12, 18, 24, and 30 h after the initial image were used in the analysis. Figures 1b–d show the synthetic images at 0, 12, and 24 h with lighter shades representing colder water. Advection of features to the southwest can be seen in the southern part of the sequence but the motion in the northern half is difficult to discern by eye.

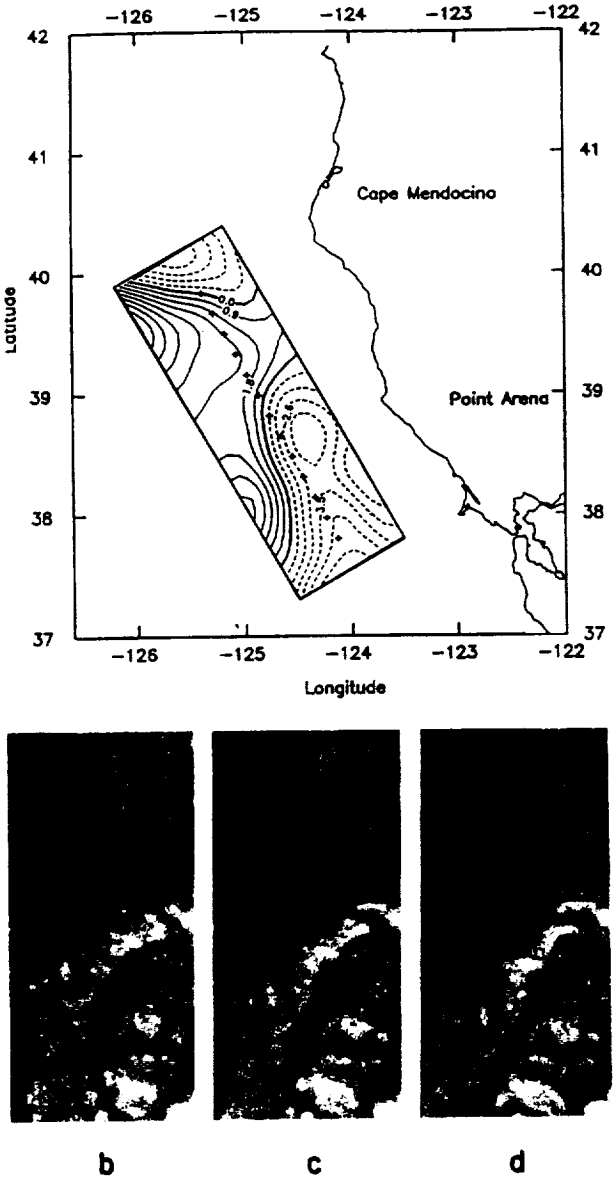

FIG. 1. (a) Streamlines of the QG model velocity field, showing the domain for the model and the synthetic images and the locations of the MCC grid points (crosses); (b) Synthetic SST field at 0 h (original AVHRR field); (c) at 12 h and (d) at 24 h.

c. CODE and CTZ data description

The satellite and field data available for comparison come from two experiments. The Coastal Ocean Dynamics Experiment (CODE) was located off northern California between approximately 37° and 39°N, extending offshore to about 125.5°W. The field data being used to evaluate the surface velocity field found by the MCC method is from the seventh leg of CODE-1, 4–10 July 1981 (Olivera et al. 1982). Two datasets are used for the comparison, the hydrographic dataset from which the dynamic heights (referenced to 500 db) and geostrophic velocities have been computed, and the acoustic Doppler current profiler (ADCP) dataset. Two sequential CZCS and four sequential AVHRR images were available from a cloud-free period 7–8 July 1981. The CZCS images occur at 1900 UTC with a separation of 24 h. The AVHRR images occur at 0300 and 1500 UTC, providing 12 (and 24) h separation times. The resolution of both sensors is approximately one kilometer. A 3 × 3 median filter was applied to the CZCS images to remove sensor noise (Denman and Abbot 1988).

The 1987 CTZ experiment was located off northern California between 39°–41°N. Field surveys from 18–26 May and 9–18 June provide fields of geostrophic velocities and dynamic heights relative to 500 db. The clearest AVHRR images come from the period between these surveys from 31 May–2 June 1987 (the CZCS sensor was no longer in operation at this time). ADCP data is available from a north–south transect from 3 June 1987, 30 hours after the last of the clear images, which provides the best comparison to the MCC velocities from the AVHRR images. This period between the two surveys is the same as that simulated by the QG model used to produce the synthetic images. Thus, although the lack of true synopticity makes the comparison more qualitative during the CTZ experiment, the comparison between the synthetic image results and the real image results is more direct at that time.

d. SST gradient and high-pass filter calculation

Tests of the method are made using raw SST fields from the images, horizontal gradients, and high-pass filtered SST fields. Gradients are formed with unweighted centered differences with spatial separations of four pixels (4.4 km) in each direction as used by Emery et al. (1986). The high-pass filter is accomplished in two steps; first, using a low-pass filter consisting of a centered 23 × 23 pixel average. The low-pass filtered image is then subtracted from the original image to produce the high-pass filtered image. The gradient images consist of very narrow lines which are found to decorrelate quickly in time. The high-pass filtered images retain more of the original structure of the SST field on scales of 25 km but eliminate larger-scale structure.

3. Results

a. Evaluation using synthetic images and model velocities

Initially the effect of different subimage sizes and the effect of using the high-pass filtered and gradients images rather than raw SST images was tested. The subimage size in the first image is varied from 25 to 50 km. The larger search areas in the second image are allowed to increase as the time separation between images increases, consistent with maximum velocities of

0.5 m s^{-1}. For separation periods of 30 h, this requires a search of 54 km in all directions covering the entire 150 km width of the synthetic image domain when the size of the initial subimage is added to the displacement. For this reason, 30 h is the maximum separation considered and the starting locations for the MCC calculation are limited to the 13 grid points along the center of the domain (Fig. 1a). Comparisons between the velocity fields are quantified in terms of the rms differences between the fields, calculated as:

$$\text{rms difference} = \left\{ \left[\sum_i (u_{1i} - u_{2i})^2 + (v_{1i} - v_{2i})^2 \right] \Big/ N \right\}^{1/2} \quad (2)$$

where N is the number of vectors used in the rms difference formation and the subscripts 1 and 2 refer to MCC-derived and model (or measured) velocities, respectively.

The initial tests result in lower rms differences using the 50 × 50 km subimage size and raw SST rather than gradients. Use of the high-pass filtered images produces results similar to the raw SST images, except all cross correlations are lower in value. Subimages of approximately 25 × 25 km produce unacceptably high rms differences (greater than 0.38 m s^{-1}) for all but the shortest separation time (rms difference = 0.12 m s^{-1} at 6-h separation). When gradient images are used, the rms difference increases to 0.20 m s^{-1} for the 6-h separation, and to 0.59 m s^{-1} for longer separations. The maximum correlation values associated with each vector average about 0.78 for raw SST fields separated by 6 h, while application of the gradient operator and high-pass filter cause the average correlations to drop to approximately 0.4. Based on these tests, a 50 × 50 km subimage size is used in all analyses discussed below and the gradient operator is not applied. The high-pass filter is used with one pair of images from the 1987 period, but the results are the same as those obtained using raw SST images.

Figure 2a shows both the rms differences and the average of the vectors' associated maximum correlations as a function of the separation time in hours. As the separation increases, the average of the maximum correlation coefficients associated with the vectors decreases while the rms difference increases. Differences in rms increase from 0.14 to 0.22 m s^{-1} as the separation times increase from 6 h to 18 h. For separation times of 24 h and greater, the rms differences are approximately 0.4 m s^{-1}.

Figure 2b shows the same information as Fig. 2a for the average of velocity fields (from pairs of synthetic images separated by the same time period over 3–4 days) compared to the model velocity field. This averaging causes the rms difference to drop from 0.14 to 0.11 m s^{-1} for 6-h separation (seven image pairs), from 0.22 to 0.11 m s^{-1} for 12-h separation (six image pairs), and from 0.36 to 0.30 m s^{-1} for 24-h separation (four image pairs). The rms difference for the 18-h separation average stays about the same at 0.22 m s^{-1} (five image pairs).

Another measure of the similarity of the two velocity fields is provided by the complex correlation of the velocity vector field from the model with the field produced by the MCC method. The calculation of complex correlations, written in polar coordinates as $\rho = \rho_v e^{i\theta}$, is described in Kundu (1976) and Bendat and Piersol (1986). For the purposes of this paper, the magnitude of the complex correlation, ρ_v, is called the field correlation to distinguish it from the scalar correlation values (correlating SST subimages) associated with individual vectors computed with the MCC method. Figure 3a shows the field correlation as a function of the separation time found by correlating the model fields and the MCC fields. The dashed line shows the approximate 95% significance level for 13 random vectors as determined by a repeated "bootstrap" randomization of the original data. The field correlations are high and significant for separation times less than 24 h, but not for separations of 24 h and greater. These field correlation values are plotted against the corresponding rms differences in Fig. 3b, and show that high vector field correlation values are associated with low rms values.

Once the velocity vector field is produced by the MCC method, a vector consistency check (VCC) can be applied to improve the estimate of the displacements (Collins and Emery 1988). This check determines whether the displacement associated with each vector lies within ±1 standard deviation of the mean x and y displacements of its neighbors. If it does not, a new vector is found which has the maximum correlation in a region around the mean displacement of the neighbors. For the one-dimensional line of points used with the synthetic images, the four nearest neighbors (two above and two below) are used. For the two-dimensional fields used in comparison to the in situ data below, the eight nearest surrounding points (two points in each direction) are used. If a vector fails the consistency test, a region 20 pixels by 20 pixels, centered on the mean displacement of the neighbors, is searched for the maximum correlation to define a new displacement. For the synthetic images, the consistency check did not change the results for the image pairs separated by the shorter time periods (6–18 h). It did reduce the rms values for the images separated by 24 h from 0.36 to 0.23 m s^{-1}, and from 0.42 to 0.29 m s^{-1} for the images separated by 30 h.

b. Evaluation using real imagery and field data

The comparison of model velocities to MCC velocities derived from the synthetic images is a "best case" test. The synthetic fields are only affected by the small amount of numerical diffusion and the degree or rotation and distortion contained in the QG model, in

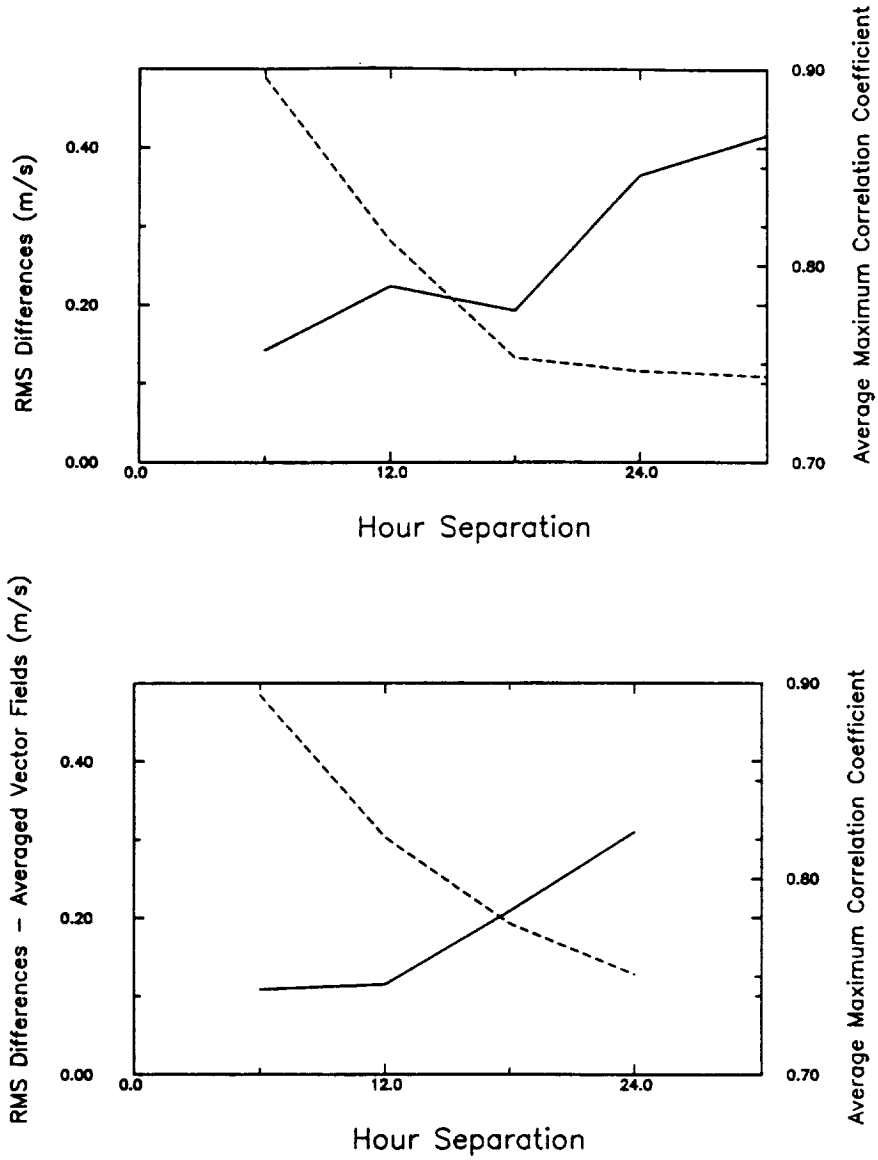

FIG. 2. (a) The effect of time separation on the rms difference (solid line) between model and MCC velocities and the average of the maximum cross-correlation values associated with the MCC vectors (dashed line); (b) As in Fig. 2a except using vector fields averaged over all pairs with the same time separations.

addition to the translation which the method attempts to retrieve. MCC velocities derived from real images are affected by additional nonadvective processes (surface heating, mixing, and ageostrophic motion), which cause the maximum correlations to be lower than those found from the synthetic images. To test whether the maximum correlation found for a given subimage region is greater than that expected for random correlations, an approximate 95 percent confidence limit is used. The value of this confidence limit is found by applying the MCC method to images separated by approximately one year, assuming all correlations between the images to be random. The 95 percentile value for all of the maximum correlations found between the images is used as the confidence limit. When raw SST images are used, the value is 0.80. When the high-pass filtered images are used the value is 0.40. Vectors associated with maximum correlations below this value are eliminated from the final velocity field. The final velocity fields produced with the high-pass filtered images and the lower 95 percent cutoff are similar to those produced with raw SST images and the higher cutoff. No further distinction between them are made.

Several AVHRR images are available from the same

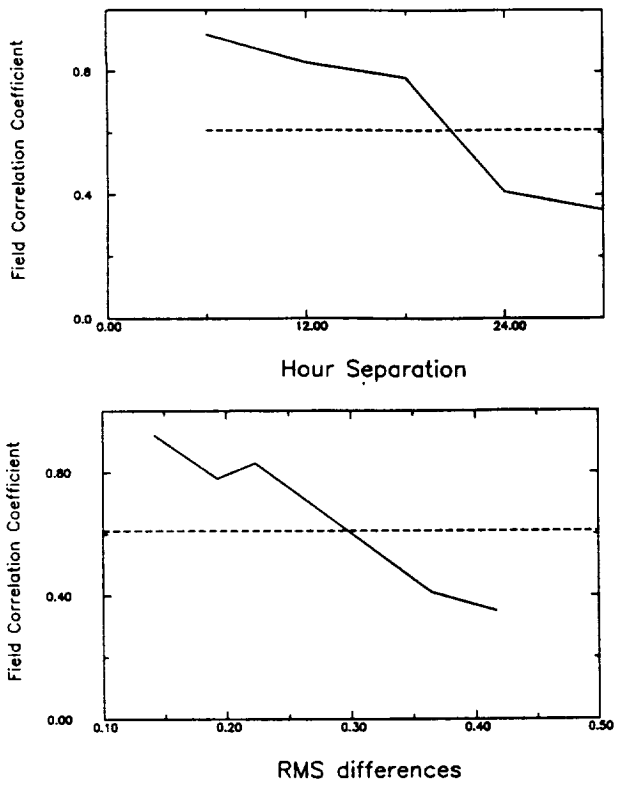

FIG. 3. (a) The effect of time separation on the magnitude of the complex correlation between MCC and model velocities (solid line). The dashed line shows an estimate of the 95 percent confidence limit. The magnitude of the complex correlation is called the field correlation, ρ_e; (b) The relation between the average vector field correlation, ρ_e, and the average associated rms difference, (m s^{-1}).

region and period as modeled to produce the synthetic images. Figure 4a shows the MCC velocities derived from a pair of high-pass images from 1–2 June 1987, separated by 14 h. The vectors are superimposed on the second high-pass filtered image of the pair. The velocity field shows the large-scale meander off Cape Mendocino and Point Arena, in general agreement with the southeastward flow south of Cape Mendocino and southwestward flow near Point Arena, seen in the streamlines derived from the 18–26 May 1987 cruise (Fig. 1a). The closest in situ data available for comparison come from a north–south ADCP transect from 3 June, approximately 30 h after the last image used in the MCC calculation. Figure 4b compares the ADCP and MCC velocities showing the general agreement in the change in direction from onshore to offshore flow at approximately 39.2°N. The rms difference between the ADCP and nearest MCC velocities (nine vectors) is approximately 0.15 m s^{-1}, similar to that obtained from the synthetic images under the same flow conditions. Figure 5 shows streamlines derived from the MCC field, in comparison to the dynamic height fields from surveys before and after the AVHRR image pair. Qualitative agreement with the meandering flow structure is good, although the difference in sampling times does not permit a more quantitative comparison.

The 1981 CODE dataset provides nearly coincident satellite and field (ADCP and geostrophic velocity) data which allows the best quantitative comparison of MCC and in situ velocity fields. In evaluating these comparisons, it is important to note that some of the variability comes from the sampling characteristics of the field data. In particular, the ADCP velocities are from a depth of 28 m while the MCC velocities are from the surface. Variability is also introduced by the time taken to complete the survey (approximately seven days), and by the interpolation of dynamic heights to a regular grid before calculation of geostrophic velocities. The variability in the field data can be quantified by finding the rms difference between the geostrophic and ADCP velocities, which is 0.25 m s^{-1}. This is probably a "worst case" comparison due to the very irregular sampling of the survey.

The gridded geostrophic velocity field (referenced to 500 db) is shown in Fig. 6a. Figure 6b shows the MCC velocity field from the CZCS image pair after eliminating vectors with associated correlation coefficients less than 0.8 and applying the vector consistency check. The rms difference between the geostrophic velocities and the MCC velocity field in Fig. 6b is 0.22 m s^{-1} and the field correlation is 0.58. Figure 6c shows the MCC velocity field derived from a pair of AVHRR images separated by 24 h on 7–8 July. The rms difference between the geostrophic velocities and this field is 0.22 m s^{-1} and the field correlation is 0.56. The best comparison is between the geostrophic velocities and the average of three MCC velocity fields derived from AVHRR images separated by 12 h shown in Fig. 6d. The rms difference is 0.18 m s^{-1} and the field correlation is 0.64. Statistics for all of the comparisons between geostrophic and MCC velocities are presented in Table 1. Application of the vector consistency check usually (not always) improves the comparison; averaging of several fields improves the comparison for the three AVHRR pairs separated by 12 h but not the two pairs separated by 24 h.

Figure 7a shows the velocity field at 28 m depth from the ADCP dataset. Figure 7b shows all the vectors derived from the CZCS image pair at the ADCP locations and Figs. 7c,d show the vectors derived from CZCS and AVHRR pairs of 7–8 July (24-h separation) after application of the consistency check and the correlation cutoff. Table 2 presents statistics comparing the ADCP velocities to the MCC velocities computed at the ADCP locations. Rms differences are approximately 0.3 m s^{-1}, larger than those comparing geostrophic and MCC velocities (Table 1). Applying the consistency check reduces the rms difference and increases the field correlation of the individual fields. Averaging the AVHRR fields does not improve the statistics of the 24-h fields, although it does reduce the rms differences for the 12-h fields (last two lines in

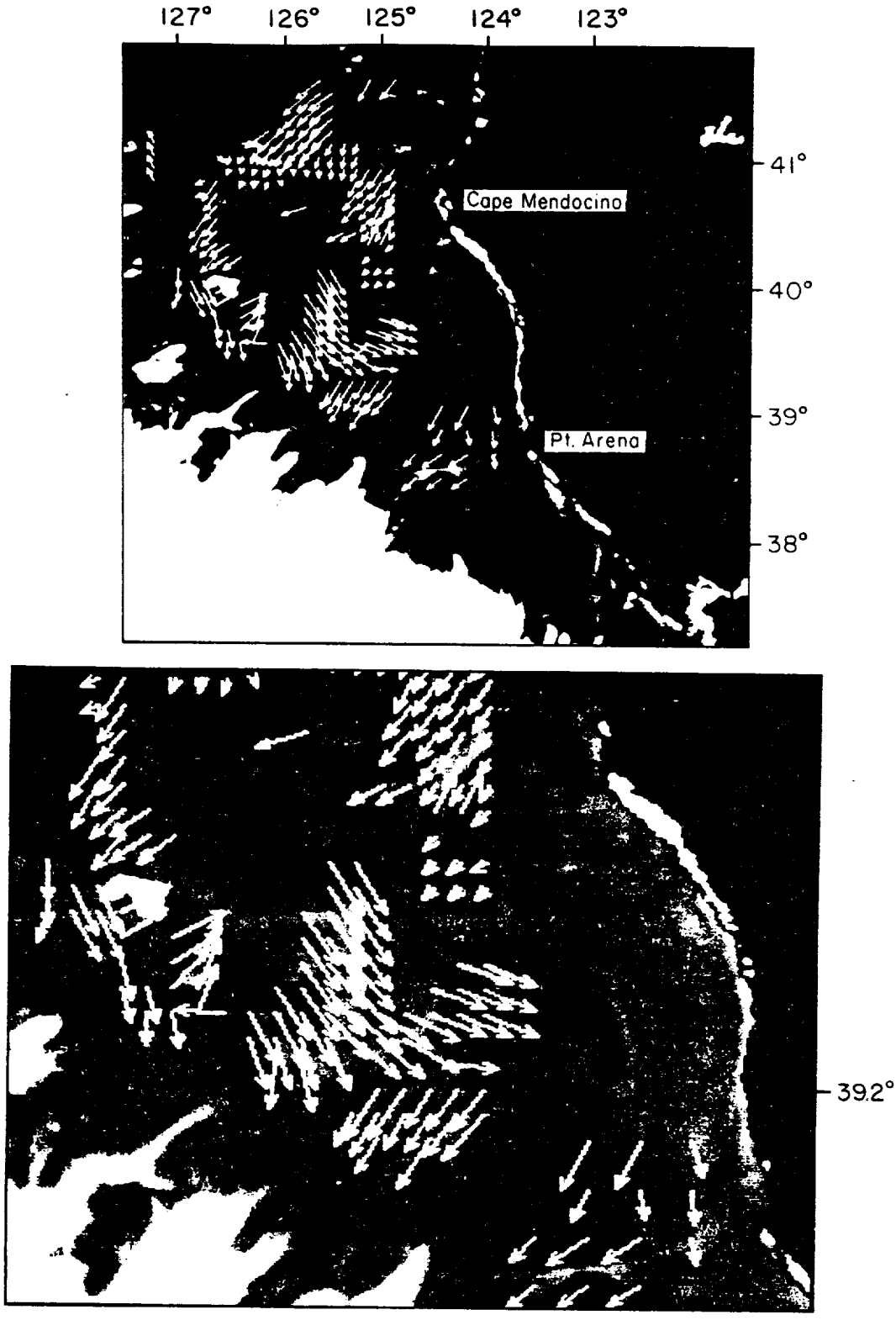

FIG. 4. (a) The displacement field obtained by applying the MCC technique to high-pass filtered AVHRR images collected at 2200 UTC 1 June and 1200 UTC 2 June 1987, overlaid on the high-pass filtered 2 June image; (b) An expanded view of Fig. 4a, showing ADCP velocities (black vectors) in comparison to the MCC velocities (white vectors).

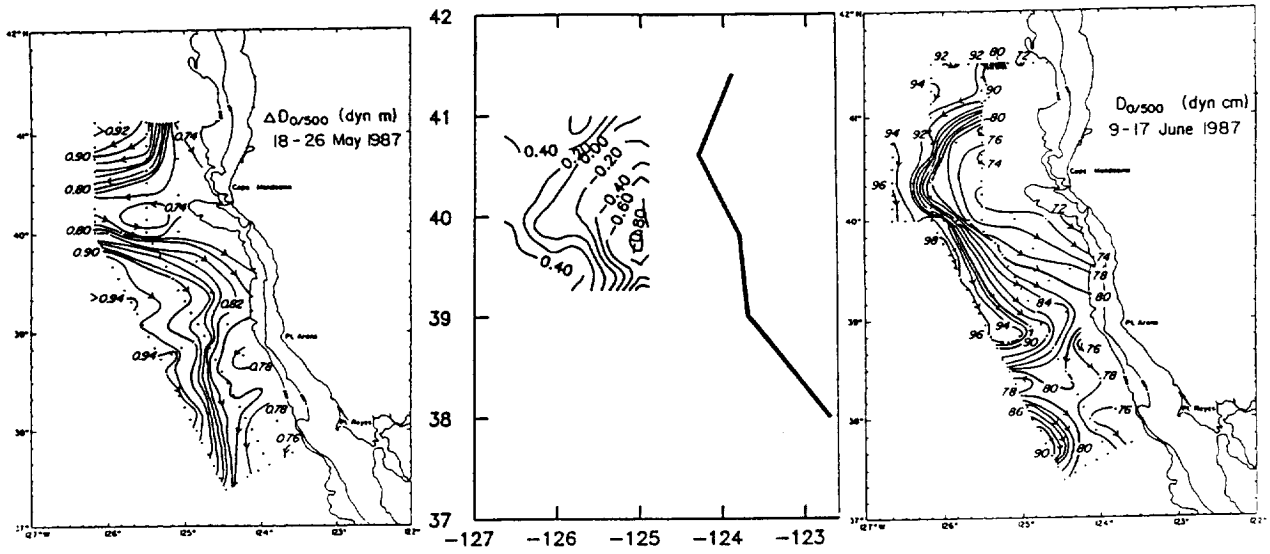

FIG. 5. Dynamic height fields from surveys on 16–26 May 1987 and 9–17 June 1987 in comparison to streamlines (center) derived from the MCC vectors shown in Fig. 4a.

Table 2). Field correlations are slightly higher for the CZCS-derived vectors in comparison to ADCP velocities than they were in comparison to geostrophic velocities. Field correlations are generally lower for the AVHRR-derived vectors, although the maximum value found for one AVHRR pair is higher ($\rho_v = 0.61$ for day 188/189–12 h, after the VCC check is applied).

Examining Figs. 6, 7 qualitatively shows that the MCC method resolves the westward flow at approximately 38.5°N, 124°–125°W. The averaged 12-h AVHRR velocity field (Fig. 6d) resolves the southeastward flow at 37.5°N, 124°–125°W better than the velocity field from the CZCS image pair (Fig. 6b). The southward flow from 38.5°N down to 38°N, 124°W is also resolved by the averaged field. In general, there are more significant vectors produced by the AVHRR images than by the CZCS images. The ADCP velocities are greater than the MCC and geostrophic velocities, there is also more small-scale structure in the ADCP velocities (Fig. 7a) than in the geostrophic velocities (Fig. 6a). Use of the 50 km subimage in the MCC calculation picks out only the large-scale flow structure and the MCC fields are more like the smoother geostrophic velocity field than the ADCP field, as reflected in the higher rms differences with the ADCP field.

4. Discussion

Physical and biological processes not included in the MCC method account for much of the difference between the MCC fields and either the model velocity fields or the in situ data. For the AVHRR images, these processes can be discussed by examining a simplified equation for the conservation of heat at the surface of the ocean:

$$\partial T/\partial t + \mathbf{V}_h \cdot \nabla_h T = S + K_h \nabla_h^2 T + K_z \frac{\partial^2 T}{\partial z^2} - w \frac{\partial T}{\partial z} \quad (3)$$

where the horizontal and vertical velocities have been shown separately, as have the horizontal and vertical eddy diffusivities (K_h, K_z), and S is the total surface heating by sensible, latent, and radiative heat flux. An equivalent equation can be formed for chlorophyll concentrations by replacing heating sources and sinks by biological sources and sinks. The MCC method assumes only horizontal translation of features in $\mathbf{V}_h$. Tests with the QG model quantify the error due to rotation and distortion caused purely by the large-scale geostrophic component of $\mathbf{V}_h$. Rotation and distortion caused by the ageostrophic part of $\mathbf{V}_h$ affect the real images but not the synthetic images. Other physical factors which affect the real images are represented by the terms on the right side of Eq. (3). These include vertical and horizontal mixing and advection. Surface heating and cooling affects the AVHRR images; biological growth, grazing, and sinking contribute to changes in the CZCS images.

Wahl and Simpson (1990) have used idealized models to estimate the effect of some of the processes on the right of Eq. (3). They find that horizontal diffusion has only a minor effect over time separations of 24 h and less, for values of K_h less than 100 $m^2 s^{-1}$. Spatially uniform surface heating and cooling has a greater effect, but is still only moderately important for time separations of 12 h and less. They find the most rapid decrease in correlation coefficients to be associated with spatially varying heating, caused by broken stratus clouds. This may limit the length of acceptable time separations between images to 6–9 h.

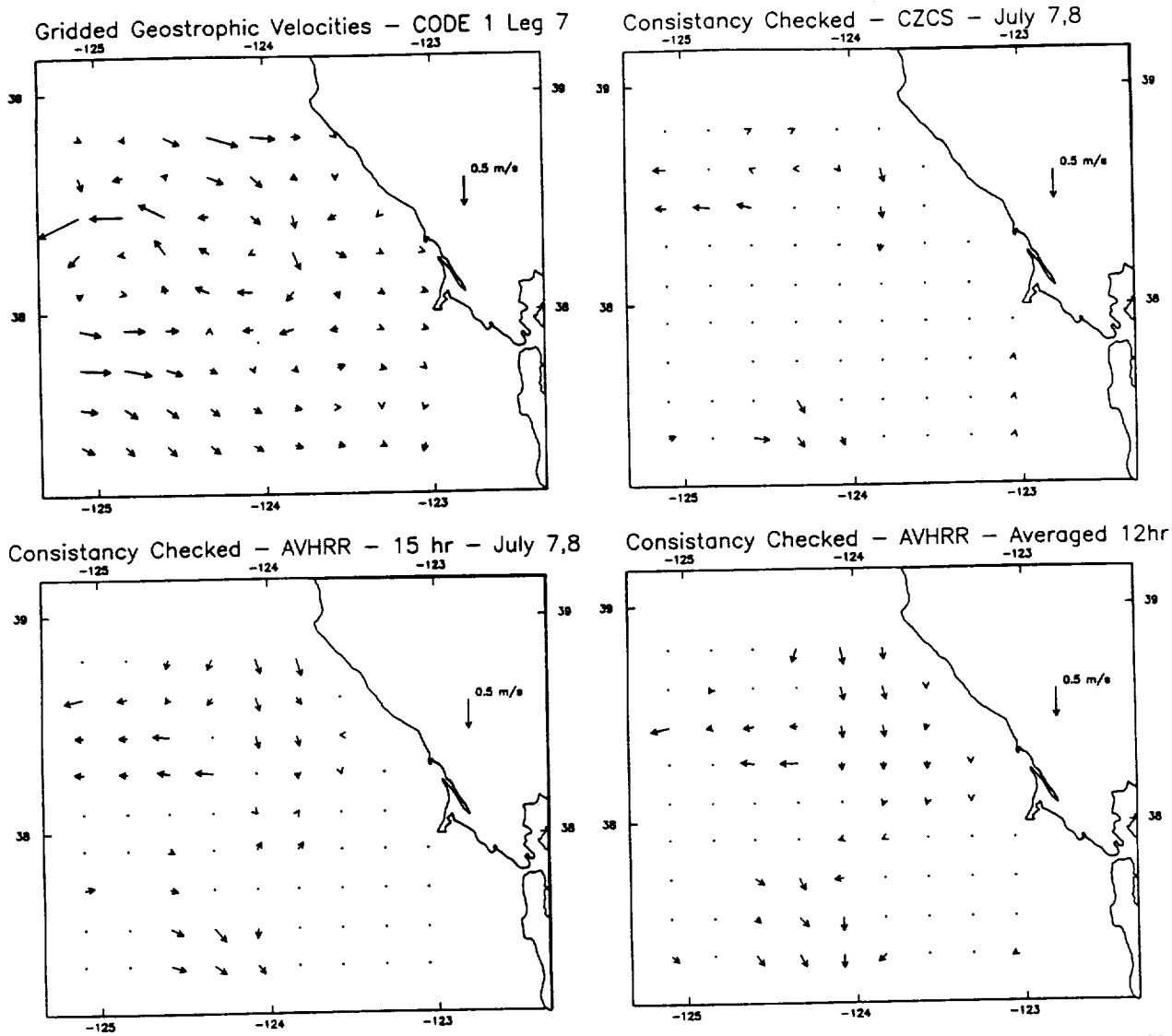

FIG. 6. (a) Velocity field from the gridded dynamic heights during CODE-1, 4–10 July, 1981; (b) Velocity field derived from CZCS images 7–8 July 1981 (24-h separation) after a vector consistency check and significance cutoff are applied; (c) Velocity field derived from AVHRR images 7–8 July 1981 (24-h separation) after a vector consistency check and significance cutoff are applied; (d) Average velocity field derived from 3 AVHRR image pairs, 7–8 July 1981 (24-h separations) after a vector consistency check and significance cutoff are applied.

They did not evaluate the effect of vertical mixing. The present results place geostrophic rotation and distortion intermediate between spatially uniform and spatially variable surface heating, degrading the cross correlations at separation times of 12 h and more. This result may be somewhat site specific, reflecting the relatively energetic nature of the meanders and jets in the California Current.

These nonadvective processes reduce the correlation coefficient in the region corresponding to the correct displacement of water parcels and allow the MCC method to find spurious incorrect displacements. When all of the MCC vectors derived from an image pair are plotted, as in Fig. 7b, a number of such clearly incorrect vectors are evident. Most of these are eliminated from the final field because of their low maximum correlation coefficient, resulting in a sparse velocity field, as in Fig. 7c. Examination of the details of these spurious correlations provides some insight into the circumstances under which the MCC method fails.

The large velocities represented by the two vectors marked A and B in Fig. 7b are different from the ADCP velocities from these locations in Fig. 7a, which were surveyed on 7–8 July, close to the time of the images. Thus, these incorrect velocities do not come simply from a lack of synopticity. The MCC velocities at these points are also different from the neighboring MCC velocities. Examination of one of the CZCS images

TABLE 1. Comparison to dynamic heights.

Correlation pair	Time	rms	ρ_v	θ
Day 188/189 CZCS—19 h	24	0.24	*0.52	−10.7
Day 188/189 CZCS—VCC	24	0.22	0.58	−10.9
Day 188/189 AVHRR—15 h	24	0.22	0.48	−26.1
Day 188/189 AVHRR—VCC	24	0.22	0.56	−27.3
Day 188/189 AVHRR—03 h	24	0.25	*0.39	−47.5
Day 188/189 AVHRR—VCC	24	0.23	0.44	−43.3
Day 188 AVHRR—03, 15 h	12	0.26	0.55	−39.6
Day 188 AVHRR—VCC	12	0.23	0.59	−40.7
Day 188/189 AVHRR—15, 03 h	12	0.20	0.49	−19.0
Day 188/189 AVHRR—VCC	12	0.21	0.33	−10.7
Day 189 AVHRR—03, 15 h	12	0.23	0.51	−21.0
Day 189 AVHRR—VCC	12	0.21	0.55	−22.0
Average AVHRR—24 h VCC fields	24	0.24	0.47	−29.5
Average AVHRR—12 h VCC fields	12	0.18	0.64	−23.1

* Not significant. VCC = vector consistency check.

from the pair (Fig. 8a) shows that these ADCP data points (located approximately at 123.5°W and 38.3°N) are in regions with weaker gradients in pigment concentration, rather than near the sharp fronts in the CZCS images. The displacements with the highest correlations correspond to displacements to areas which are clearly incorrect, although the pattern of pigment concentrations of the area in the second image is similar enough to that in the first image to cause high correlations (note that the correlation calculation removes the mean of each subimage). The field of correlations associated with the vector labeled A in Fig. 7b is shown in Fig. 8b. There are two distinctly different areas with high correlation values, a more distant region to the northwest and a closer region to the south. A similar pattern exists for the point labeled B. Figure 8c shows an expanded view of the image, with arrows drawn from points A and B to both maxima. The correlation with the distant region is slightly higher but the measured velocity field in Fig. 7a shows that the secondary closer peak is really the correct displacement of the parcel of water.

This discussion brings out a disadvantage of the use of large search areas, which increases the chance of spurious large correlations. Since the size of the search window in the second image is determined by the maximum velocity and the time separation between images, this provides another reason to minimize the time between images, allowing smaller search windows to be used. Figure 8b also suggests that more intelligent search strategies might be adopted, which locate the maxima by following gradients and preferentially choosing closer maxima unless distant maxima are significantly greater and the more reasonable choice.

One reason for the slightly lower correlation of the closer point in Fig. 8b may be rotation of the feature. To test this, the initial subimage was rotated by increments of 5° before repeating the calculation of the correlation matrix. At −20°, the maximum correlation is found in the closer secondary maximum of the contour plot to the southeast. This test provides support for the conclusions of Vesecky et al. (1987) who state that rotations of greater than 15° reduce the ability of the MCC method to track features between images. It also suggests the need to efficiently include rotation in the MCC search, in agreement with Kamachi (1989) and Emery (pers. comm.).

To examine whether the rms differences in velocity discussed above are caused equally by errors in magnitude and direction, rms differences were formed separately for direction and magnitude, comparing MCC vectors to velocities from the model generated synthetic fields and the measured ADCP and geostrophic velocities. Figure 9a shows the rms difference in direction as a function of time separation for the synthetic images (dashed line). This difference increases slowly with time (dotted line) for separations of 6–18 h and more rapidly for longer separations. The rms differences in direction of the vectors between the in situ data and the MCC vector fields from 12 and 24 h separations are also shown (crosses) and are much higher. The greater errors found with the real data suggest that the processes other than geostrophic rotation and distortion (shown on the right side of Eq. 3) have a major affect on the satellite-derived surface circulation over time periods of 12 h and more, implying that real images should be separated by less than this, if possible.

The rms differences in magnitude are shown similarly in Fig. 9b. There is not a consistent distribution pattern in the rms magnitude differences, although the lowest values occur for separations of 6 h and the highest occur for 24 h. Results from the synthetic images suggest that distortion and rotation of the features causes errors in direction of less than 30° for separations of 6–18 h increasing to 60° at 24 hours. Since the vector error is a function of the cosine of the angle, rms errors of 13% and 50% are associated with angles of 30° and 60°. Comparison to in situ data suggests that by time separations of 12 h, errors of 50 percent are caused by errors in angle, corresponding to rms errors of 0.15 m s^{-1} for typical velocities of 0.3 m s^{-1}. Errors in the magnitude of the velocities range from 0.1 to 0.2 m s^{-1}. Thus, both types of errors contribute equally in real images separated by 12 h and more. The results from the synthetic images suggest that both can be reduced by using shorter time separations.

The rms differences found in this paper are much higher than the value of 0.06 m s^{-1} reported by Svejkosky (1988) who restricted the in situ surface drifter velocities used for comparison to be within five hours of the satellite image and further restricted the points to those that could be tracked easily by eye. As noted above, some of the rms difference is due to the variability in the field data and its sampling patterns, but much is also due to the MCC method itself, which has several disadvantages in comparison to the subjective method. Subjectively selecting features to track from one image to the next results in the use of the most

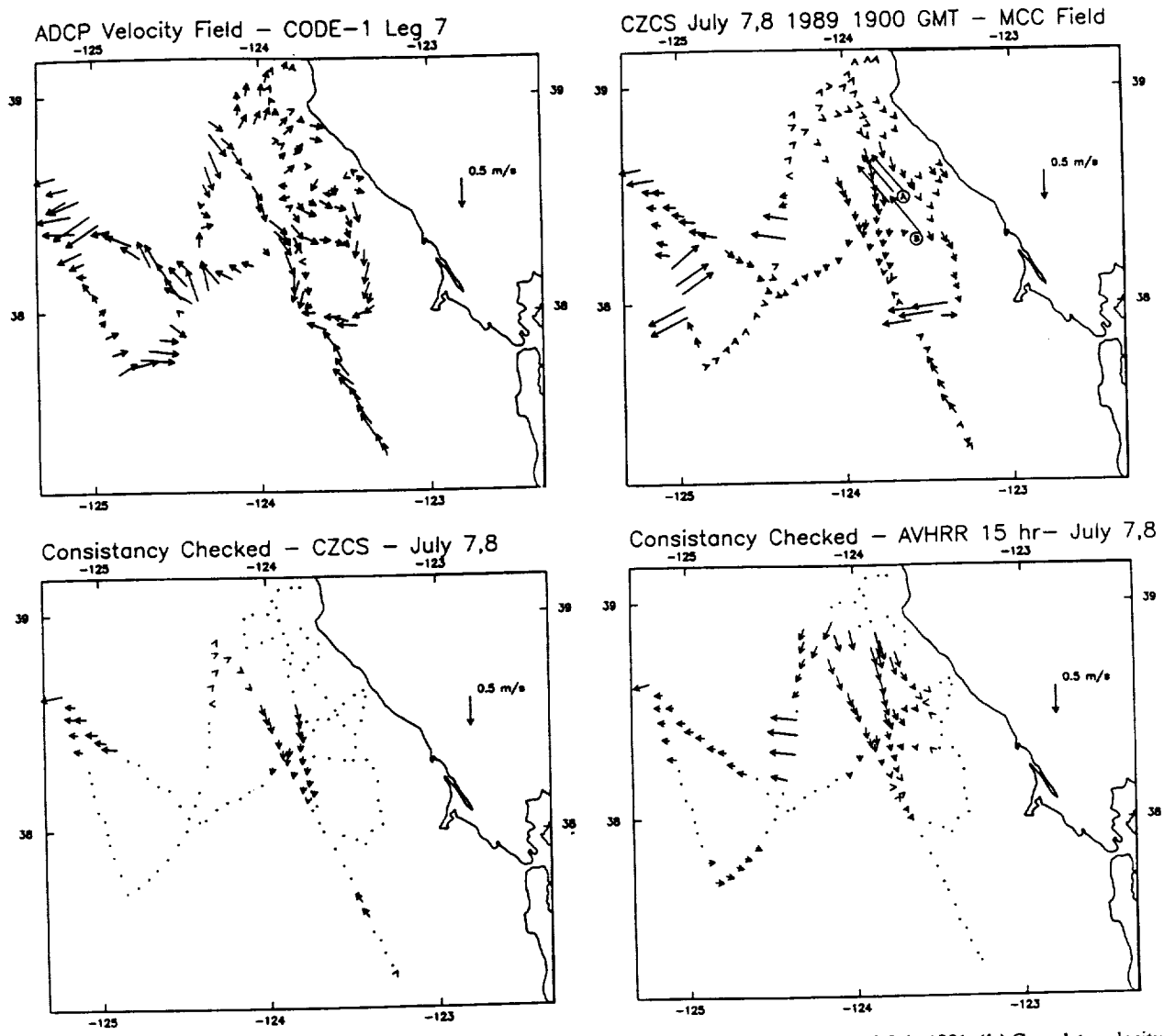

FIG. 7. (a) Velocity field from ADCP data during the same CODE-1 cruise as shown in Fig. 6a, 4–10 July 1981; (b) Complete velocity field derived from CZCS images 7–8 July 1981 (24-h separation). No significance cutoff or vector consistency check has been applied. Letters A and B denote starting locations for incorrect displacements discussed in section 4; (c) Velocity field derived from CZCS images 7–8 July 1981 (24-h separation) after the significance cutoff and vector consistency check are applied; (d) Velocity field derived from 2 AVHRR images 7–8 July 1981 (24-h separation) after the significance cutoff and vector consistency check and applied.

distinctive features, eliminating regions with low gradients. Rotation in features can also be followed more easily by eye. Visual inspection of the images results in an overall feeling for the pattern of changes in the image pairs, forcing the search to be restricted to only "reasonable" areas and reduces the chance of grossly incorrect displacements. The incorrect displacements shown in Fig. 7b would never have been found by visual tracking. In contrast to the subjective method, the objective MCC method, as used here, removes the guarantee that the feature being tracked is unique and easily identifiable. It allows searches of unreasonable areas which sometimes produce random, high correlations, and reduces the ability to follow rotating and distorting features. The lowest rms errors produced by the present MCC method applied to real images were obtained by averaging the three AVHRR fields with 12-h separation and was 0.18 m s^{-1}, three times the value found by Svejkosky. Tests with the synthetic images suggest that this might be reduced to around 0.10–0.15 m s^{-1} if images separated by 6 h were available.

It seems unlikely that the MCC method will ever yield rms errors as low as Svejkosky's 0.06 m s^{-1}. Even if this estimate is an overly optimistic assessment of the level of error that might be found for routine application of subjective feature tracking methods, the

TABLE 2. Comparison to ADCP.

Correlation pair	Time	rms	ρ_s	θ
Day 188/189 CZCS—19 h	24	0.27	0.64	−18.5
Day 188/189 CZCS—VCC	24	0.27	0.65	−19.7
Day 188/189 AVHRR—15 h	24	0.32	*0.18	−43.3
Day 188/189 AVHRR—VCC	24	0.28	0.38	−29.4
Day 188/189 AVHRR—03 h	24	0.31	*0.30	84.0
Day 188/189 AVHRR—VCC	24	0.24	*0.30	81.5
Day 188 AVHRR—03, 15 h	12	0.31	0.37	−42.2
Day 188 AVHRR—VCC	12	0.27	0.42	−42.8
Day 188/189 AVHRR—15, 03 h	12	0.27	0.49	−16.3
Day 188/189 AVHRR—VCC	12	0.23	0.61	−15.1
Day 189 AVHRR—03, 15 h	12	0.34	*0.29	−23.3
Day 189 AVHRR—VCC	12	0.29	0.37	−18.4
Average AVHRR—24 h VCC fields	24	0.28	*0.30	−67.7
Average AVHRR—12 h VCC fields	12	0.23	0.46	−29.7

* Not significant, VCC = vector consistency check.

discussion brings out a number of advantages of the subjective method. The advocates of objective methods emphasize the elimination of the human bias inherent in the subjective methods. This discussion makes it clear that the objective methods also eliminate the benefit of human insight, and substitute inferior computer-based pattern recognition for the more highly developed pattern recognition capabilities of human vision. The true advantages of the objective methods are: 1) the ability to automate and process large amounts of data; 2) uniform quality of the estimated fields; and 3) estimates of the uncertainties in the fields. The last point is important since fields of estimated uncertainties are necessary if the velocity fields are to be combined with other data in an optimal method. Based on the results presented here, an estimate of the spatially varying uncertainties in the surface velocities

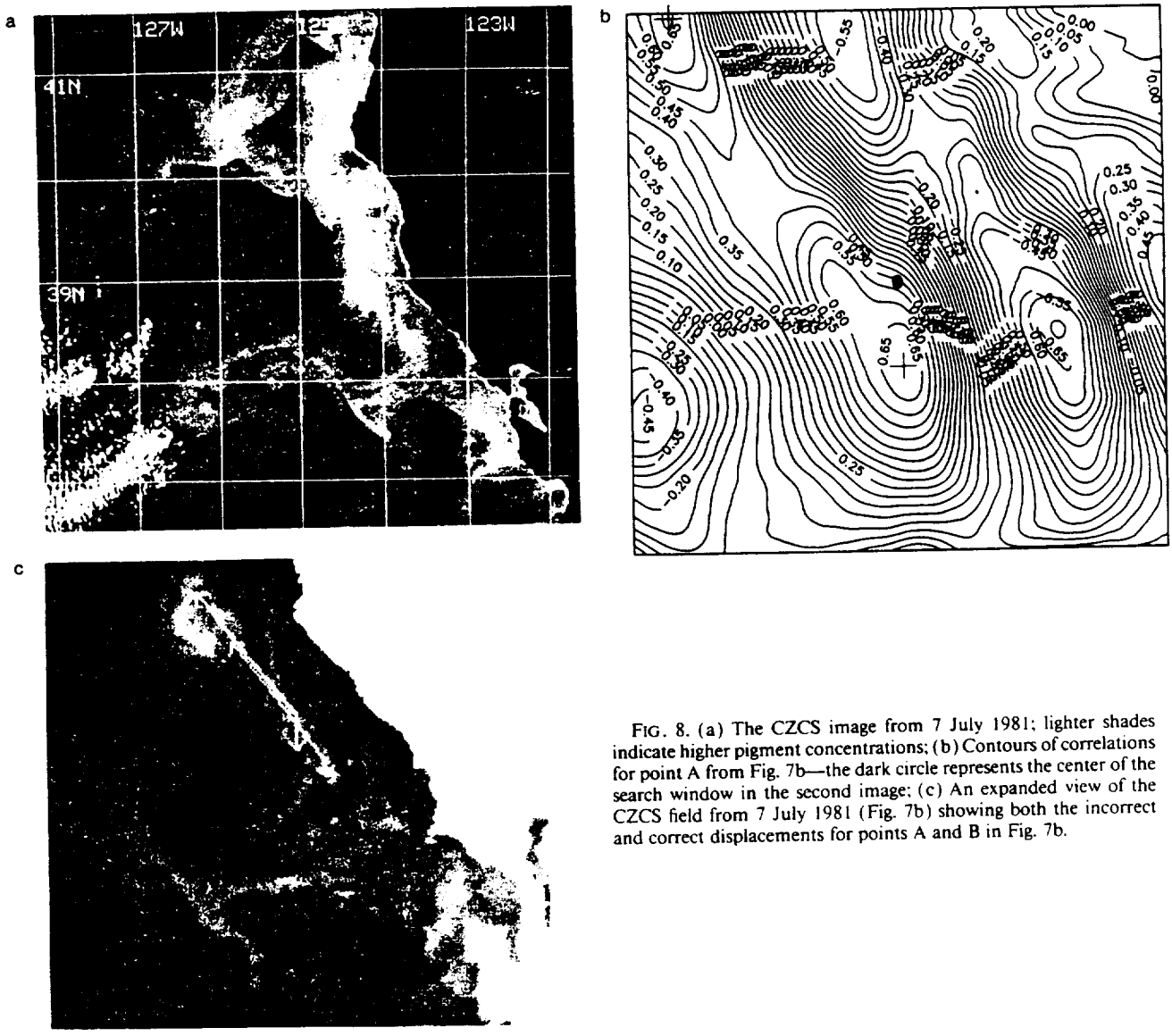

FIG. 8. (a) The CZCS image from 7 July 1981; lighter shades indicate higher pigment concentrations; (b) Contours of correlations for point A from Fig. 7b—the dark circle represents the center of the search window in the second image; (c) An expanded view of the CZCS field from 7 July 1981 (Fig. 7b) showing both the incorrect and correct displacements for points A and B in Fig. 7b.

might be based on the values of the maximum correlations associated with each vector. This would be an improvement over assigning a single value to the uncertainties of all vectors.

Another application of the MCC velocity fields is to include them in an extension of Kelly's (1989) inversion of the heat advection equation. Using a sequence of AVHRR images (identical to the sequence required in the MCC calculation), Kelly finds the velocity field that minimizes the misfit in the heat equation, subject to other constraints on divergence, vorticity, and kinetic energy. Additional constraints to minimize the difference between the final velocity field and a specified velocity field can be added, weighting the specified velocities according to their uncertainties. Use of the MCC velocities, weighted according to their maximum correlations, may provide an improvement in the along-isotherm component of the flow, which the inverse method has more difficulty in finding. Work is underway to evaluate this possibility.

5. Conclusions

Tests with both synthetic and real images suggest that the best results are found by using the vector consistency check and averaging several velocity fields obtained from images with separations of 6–12 hours. The lower limit on the rms errors in the California Current System is approximately 0.10–0.15 m s^{-1}, caused by rotation and distortion of the features by the large-scale currents, even when other nonadvective effects are minimized. Errors in magnitude and direction contribute equally in comparisons of field data and real images with separations of 12 h and more. Tests with the synthetic images suggest that errors can be reduced by using the shortest possible time separations (6 h), a conclusion in agreement with Emery et al. (1986).

The statistics of the real AVHRR and CZCS images, for this particular set of images, indicate that CZCS images separated by 24 h produce MCC velocity fields with rms errors as low as the AVHRR images separated by 12 h. The patterns in the pigment concentrations in the CZCS images used here exhibit stronger gradients which seem to persist longer than the corresponding SST fields in the AVHRR images. Although these tests furnish evidence supporting the argument that the MCC method can be applied to CZCS images with as much success as AVHRR imagery (Garcia and Robinson 1989), the method was applied to other CZCS imagery without strong fronts with less success. The key appears to be the strength of the features in the image. Even though the rms errors are similar to those from the AVHRR images, use of the CZCS images produce fewer significant vectors and a much sparser velocity field than that produced by an average of several AVHRR fields, which gives the most successful result.

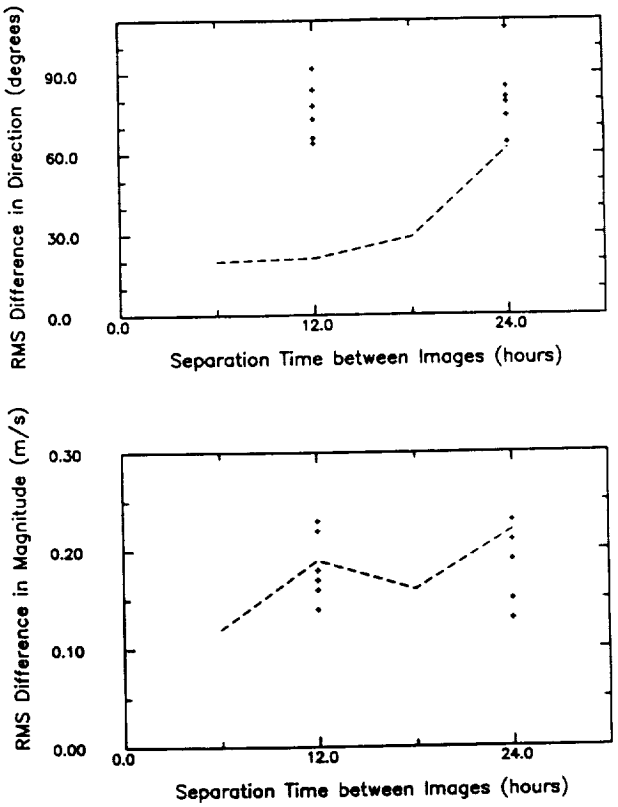

FIG. 9. Rms difference in (a) direction and (b) magnitude as a function of the time separation between images. Comparisons of model velocities to MCC velocities derived from the synthetic images is shown by the dashed line. Comparisons of the MCC velocities from each image pair to both ADCP and geostrophic velocities are shown by the crosses.

The results suggest that improvements that might be made in the MCC method include: 1) the inclusion of rotation in the search strategy; 2) improved search strategies that are more efficient and less easily fooled by distant regions with random high correlations; and 3) an automated scheme to adjust starting locations in the initial image to include regions with strong gradients in the subimage. The need for efficient and intelligent search strategies will become even more important when rotation is included in the search.

The results of the tests performed in this paper show that the MCC method successfully determines the surface velocity field in some instances and fails in others. The conditions under which the method is likely to be most successful are:

(1) Images have strong features.

(2) Several (3–5) image pairs, each separated by periods of 12 h or less, are available from a short (1–3 day) period.

(3) The resultant fields are coherent enough to allow use of a consistency check to eliminate outliers, after discarding those with correlation coefficients considered no different than random correlations.

(4) The resultant fields are then averaged.

In addition, better results are found when images come from periods when the wind has blown persistently for several days, reducing the effects of spatially varying surface heating and mixing. Even under these circumstances, absolute values of the velocity field will contain rms errors of 0.10–0.25 m s^{-1}. To put this in perspective, however, it is noted that rms differences between the ADCP and geostrophic velocities derived from data taken on the same cruise can be as large as 0.25 m s^{-1}.

These conclusions have policy implications for facilities which routinely capture and archive high resolution AVHRR data. Since the satellite-derived velocities are best for separations of 12 h and less, these operational centers should attempt to collect pairs of images with short time separations, rather than a single image on each day (a common policy). This will preserve as much of the information about surface motion as possible in the archived satellite data.

Acknowledgments. The authors benefitted from discussions with Bill Emery, Leonard Walstad, Jane Huyer, and Mike Kosro. Additional appreciation is extended to an anonymous reviewer for helpful comments. The model velocity fields were supplied by Leonard Walstad, the hydrographic data were supplied by Jane Huyer, the ADCP data were supplied by Mike Kosro, and the AVHRR and CZCS data were supplied by Mark Abbot. Support for this research came in part from NASA Grant NAGW-1251 and ONR Grant N-00014-87-K-0009.

REFERENCES

Bendat, J. S., and A. G. Piersol, 1986: *Random Data, Analysis and Measurement Procedures*, Wiley and Sons, 566 pp.

Collins, M. J., and W. J. Emery, 1988: A computational method for estimating sea ice motion in sequential Seasat synthetic aperture radar imagery by matched filtering. *J. Geophys. Res.*, **93**, 9241–9251.

Denman, K. L., and M. R. Abbott, 1986: Time evolution of surface chlorophyll patterns from cross-spectrum analysis of satellite color images. *J. Geophys. Res.*, **93**, 6789–6798.

Emery, W. J., A. C. Thomas, M. J. Collins, W. R. Crawford and D. L. Mackas, 1986: An objective method for computing advective surface velocities from sequential infrared satellite images. *J. Geophys. Res.*, **91**, 12 865–12 878.

Garcia, C. A. E., and I. S. Robinson, 1989: Sea surface velocities in shallow seas extracted from sequential Coastal Zone Color Scanner Satellite Data. *J. Geophys. Res.*, **94**, 12 681–12 691.

Kamachi, M., 1989: Advective surface velocities derived from sequential images for rotational flow field: limitations and applications of maximum cross-correlation method with rotational registration. *J. Geophys. Res.*, **94**, 18 227–18 233.

Kelly, K. A., 1989: An inverse model for near-surface velocity from infrared images. *J. Phys. Oceanogr.*, **19**, 1845–1864.

Kundu, P. K., 1976: Ekman veering observed near the ocean bottom, *J. Phys. Oceanogr.*, **6**, 238–242.

Leese, J. A., C. S. Novak and B. B. Clarke, 1971: An automated technique for obtaining cloud motion from geosynchronous satellite data using cross correlation. *J. Appl. Meteor.*, **10**, 110–132.

Mesinger, F., and A. Arakawa, 1976: *Numerical Methods Used in Atmospheric Models, Vol. 1*. Garp (Global Atmospheric Research Programme) Publications Series No. 17, 66 pp.

Olivera, M., W. E. Gilbert, J. Fleishbein, A. Huyer and R. Schramm, 1982: Hydrographic data from the first Coastal Ocean Dynamics experiment: R/V Wecoma, Leg 7, CODE Tech. Rep. 7, Data Rep. 95, Ref. 82-8, School of Oceanography, Oregon State Univ., Corvallis, 163 pp.

Press, W. H., B. P. Flannery, S. A. Teukolsky and W. T. Vetterling, 1986: *Numerical Recipes*. Cambridge University Press, 818 pp.

Robinson, A. R., and L. J. Walstad, 1987: The Harvard open ocean model: calibration and applications to dynamical process, forecasting, and data assimilation studies. *Appl. Num. Math.*, **3**, 89–131.

Svejkovsky, S., 1988: Sea surface flow estimation from Advanced Very High Resolution Radiometer and Coastal Zone Color Scanner Satellite Imagery: a verification study, *J. Geophys. Res.*, **93**, 6735–6743.

Tokmakian, R., 1989: Sea surface velocity determination using satellite imagery: validation and an application. M.S. thesis, College of Oceanography, Oregon State University, Corvallis, 105 pp.

Wahl, D. D., and J. J. Simpson, 1990: Physical processes affecting the objective determination of near-surface velocity from satellite data. *J. Geophys. Res.*, **95**, 13 511–13 528.

Vesecky, J. F., R. Samadani, J. M. Daida, M. P. Smith and R. N. Bracewell, 1987. Observing rotation and deformation of sea ice with synthetic aperture radar. *Proc. of the International Geoscience and Remote Sensing, Sensing Symposium*, IGARSS, Ann Arbor, 1137–1145.

APPENDIX C

COMPARISON OF VELOCITY ESTIMATES FROM AVHRR IN THE COASTAL TRANSITION ZONE

Kathryn A. Kelly and P. Ted Strub

Comparison of Velocity Estimates from AVHRR in the Coastal Transition Zone

KATHRYN A. KELLY

Woods Hole Oceanographic Institution, Woods Hole, Massachusetts

P. TED STRUB

College of Oceanography, Oregon State University
Corvallis, Oregon

Two methods of estimating surface velocity vectors from AVHRR data were applied to the same set of images and the results were compared with in situ and altimeter measurements. The first method used an automated feature-tracking algorithm and the second method used an inversion of the heat equation. The 11 images were from three days in July 1988 during the Coastal Transition Zone field program and the in situ data included ADCP vectors and velocities from near-surface drifters. The two methods were comparable in their degree of agreement with the in situ data, yielding velocity magnitudes that were 30–50% less than drifter and ADCP velocities measured at 15–20 m depth, with rms directional differences of about 60°. These differences compared favorably with a baseline difference estimate between ADCP vectors interpolated to drifter locations within a well-sampled region. High correlations between the AVHRR estimates and the coincident Geosat geostrophic velocity profiles suggested that the AVHRR methods adequately resolved the important flow features. The flow field was determined to consist primarily of a meandering southward-flowing current, interacting with several eddies, including a strong anticyclonic eddy to the north of the jet. Incorporation of sparse altimeter data into the AVHRR estimates gave a modest improvement in comparisons with in situ data.

1. Introduction

The prospect of obtaining time series of velocity maps of the ocean without having to make extensive field measurements has prompted numerous attempts to infer the surface velocity field from satellite image data. These fields represent nearly instantaneous estimates of the currents over a large area, avoiding the temporal aliasing inherent in ship surveys. Methods to infer the velocity field from images of sea surface temperature (SST) fall into two categories: those which follow features in the field without regard to the actual temperatures [for example, Vastano and Borders, 1984; Emery et al., 1986; Tokmakian et al., 1990] and those which use the heat equation and the measured SST [for example, Kelly, 1983; Wald, 1983; Kelly, 1989]. The advantage of the first type is that it does not require precise temperatures and therefore the results are less sensitive to errors in the data. Inversion of the data using the heat equation requires a correction for water vapor or viewing geometry. As a by-product, the analysis using the heat equation produces an estimate of the SST changes due to horizontal advection of heat in the upper ocean.

To evaluate and compare these two methods we have used them independently and in combination on a series of AVHRR images from the Coastal Transition Zone (CTZ) experiment [Brink and Cowles, 1991]. The images were from an unusually cloud-free period, spanning about three days in July 1988, and thus represent the best possible data conditions. There were also numerous field measurements with which to compare the estimates: primarily from the acoustic Doppler current profiler (ADCP) and surface drifters (drogued to 15 m) [Huyer et al., 1991; Brink et al., 1991]. In addition, the Geosat altimeter provided estimates of the anomalous geostrophic velocity, relative to the 2.5-year mean velocity. Although the altimeter gives only one component of the velocity, it has the advantage of sampling the field systematically along the tracks, unlike the drifters, which tend to be drawn into and oversample the most energetic jets. Although the primary focus of this analysis is the comparison of the two methods of using AVHRR sequences, we also looked at combining the two methods with each other and with other satellite or in situ data.

The two methods for estimating the velocities are the maximum cross-correlation (MCC) method of Emery et al. [1986] and a modified version of the Kelly [1989] inversion. The data used in the comparison are described in section 2, followed by a brief description of the methods in section 3, with emphasis on the modifications to the original methods. In section 4, we evaluate the velocity estimates by comparison with other data. Also in section 4 we describe the combination of AVHRR and other velocities using both objective analysis and the inversion of the heat equation. Section 5 contains a discussion of the interpretation of the velocity estimates and their usefulness. The last

section contains the summary and conclusions. The viewing angle correction for SST for the heat equation inversion is discussed in Appendix A and further details of the methods are presented in Appendices B and C.

2. Data Processing

The AVHRR images covered the region from 34.5°N to 39.5°N and from 122.3°W to 129.0°W during the period from July 16 through July 18 (year-days 198–200). Figure 1 shows one image from July 17 with velocities from surface drifters superimposed. The drifters and field surveys from this period showed a strong jet that flowed toward the southwest, from the northeast corner of the survey region (39.0°N, 124.3°W, 50 km from the coast) to approximately 36.5°N, 127.5°W (an offshore extent of approximately 300 km), where it turned cyclonically and flowed back onshore and to the south, forming a large meander [Huyer et al., 1991; Brink et al., 1991; Strub et al., 1991]. A closed cyclonic eddy (diameter less than 100 km) was found inshore of the cyclonic meander at 37°N and 126.5°W, and a larger (150 km diameter) anticyclonic eddy was traced by a surface drifter at approximately 35.5°N, 124°W [Strub et al., 1991]. ADCP velocity transects across the jet near 125°W revealed velocities as large as 0.8 ms^{-1} in the 20-40 km wide core of the jet [Dewey et al., 1991]. Surface drifters were apparently drawn by converging flow into an even narrower and more energetic core, where velocities as large as 1.2 ms^{-1} were encountered [Swenson et al., 1992]. The coldest water was often found in a narrow filament just inshore of the maximum velocities in the jet's core [Huyer et al., 1991; Chavez et al., 1991; Strub et al., 1991].

Images from the polar-orbiting NOAA 9 and NOAA 10 satellites were converted to brightness temperatures using only the channel 4 (10.3-11.3 μm) radiances. A total of 11 images from July 1988 were processed; the times of the images (year day and hour in UT) are given in Table 1. Images were registered to a common equirectangular projection, using the coordinates of known coastal features to correct the navigation to within approximately one pixel (1.08 km square). Although clouds in the data are a problem for either method of estimating the velocity, these images were relatively cloud free and no explicit cloud flagging was done. However, some cloud contamination was present and simple screening methods were used to discount the velocity estimates in these regions. The heat equation requires relatively accurate SST gradients. Following Kelly and Davis [1986], a simple viewing angle correction for water vapor was applied to the channel 4 data (see Appendix A). This correction removed trends in the mean and the variance of SST in the series of images (see Table A.1); however considerable scatter remained in the SST variance for the series of

images after the correction was applied.

Only two profiles (Figure 2) from the Geosat altimeter Exact Repeat Mission (ERM) were used for comparison with the velocity estimates, because the sampling interval (17 days) of the altimeter was so much larger than the interval over which velocity estimates were computed (2.5 days) and because only the ascending subtracks of the altimeter contained usable data. These profiles were separated spatially by approximately 100 km and three days in time; the dates for the profiles were days 200 and 203. Profiles for days 197 and 206 were available, but the low correlations between the velocity estimates and these profiles suggested that the temporal separation was too large for them to be useful.

Collinear height profiles for the 2.5-year ERM were processed using programs described in Caruso et al. [1990] to obtain a series of anomalous sea surface heights. Raw altimeter heights were adjusted for tides, water vapor, tropospheric and ionospheric delays, and surface pressure using correction factors provided on the National Oceanographic Data Center (NODC) distribution tapes [Cheney et al., 1987]. For each subtrack all of the profiles were interpolated to a common latitude-longitude grid with points separated by 0.98 s (approximately 7 km) alongtrack. Orbit errors over approximately 30° arcs were removed using a least-squares fit to a sine function, with period equal to the orbital period of the satellite. The mean of all the height profiles for each subtrack was removed and the anomalous sea surface height was low-pass filtered using a filter with a half-power point of 55 km to reduce instrument noise. Filtered anomalous sea surface height h was converted to anomalous crosstrack velocity u, assuming the geostrophic relationship

$$u = \frac{-g}{f}\frac{\partial h}{\partial y} \tag{1}$$

where y is the alongtrack coordinate, g is gravity and f is the Coriolis parameter. The anomalous geostrophic velocity profiles are shown in Figure 2, with positive (onshore) crosstrack velocities to the right. The maximum offshore jet velocity calculated in this manner was 0.67 ms^{-1}; this maximum is relatively low, probably because the half-power point for the spatial filter is larger than the jet width of 20–40 km.

The CTZ field program used Tristar Mark II drifters [Niiler et al., 1987] with 6-m radar reflector-shaped drogues at a central depth of 15 m. Positions of the drifters were determined 8 times each day using the ARGOS satellite system, with an accuracy of approximately 300 m for each position. The drifters are thought to follow horizontal currents with root-mean-square (rms) errors of only 0.01 ms^{-1} under normal conditions. The drifter positions over intervals of 4 days were fit to cubic splines to remove inertial and tidal signals. This procedure is equivalent to temporal smoothing

with a half power point of 0.45 cpd [Brink et al., 1991]. The final data set consisted of positions separated by 12 hours. Velocity vectors were calculated from pairs of these positions with nominal times at the midpoint of the time interval and locations at the midpoint of the two positions. The drifter velocities for the first three 12-hr periods used in the comparisons are shown in Figure 1.

ADCP data were collected by two ships using hull-mounted transducers: a 300 kHz transducer on the RV WECOMA and a 150 kHz transducer on the RV POINT SUR. Navigation data from LORAN-C receivers were used on each ship to convert the relative velocity from the ADCP to absolute current and ship velocities [Kosro et al., 1991]. The currents were filtered to remove signals with periods less than 30 minutes and averaged horizontally over 20-km bins. The top two bins used here were centered at 15.1 m and 19.1 m depth for the WECOMA and 16.7 m and 20.7 m for the POINT SUR. The ADCP data collected over the 2.5-day period at the nominal 20-m depth are shown in Figure 3. A comparison of the altimeter, drifter and ADCP velocities shows the more uniform spatial sampling of the altimeter and ADCP data, the relatively small region covered by the ADCP data, and the oversampling of the narrow jet by the drifters.

3. Analysis Methods

To compare the velocity estimates from the two different methods with each other and with the data, we defined five non-overlapping time intervals, each 12 hours long, beginning at noon UT on day 198. A best possible velocity estimate for each time interval was computed using each method; these estimates included multiple image pairs for each interval. Because the two methods have slightly different criteria for selecting the best pairs of images, the same pairs of images were not necessarily used for both the MCC and inverse solutions. Most of the estimates used three pairs of images. Each of the two methods is described briefly below with additional details included in the appendices.

MCC method

The MCC method [Emery et al., 1986] is an automated procedure for estimating the displacements of small regions of SST patterns between sequential AVHRR images. In this procedure a subregion of an initial image is cross-correlated with the same size subregion in a subsequent image, searching for the location in the second image which gives the maximum cross-correlation coefficient. The displacement of the water parcel corresponding to the first subregion is assumed to be the distance

between its initial location and the center of the subregion in the second image with the maximum cross-correlation. The size of the region searched in the second image (the search window) depends on the maximum displacement that could be caused by reasonable velocities at the ocean surface. The subregion used in the cross-correlation calculation (the correlation tile) should be large enough to contain a number of independent features in the SST field; the number of such features is related to the number of degrees of freedom in the cross-correlation calculation. High-pass filtering the SST field, retaining features smaller than 25 km, increased the number of degrees of freedom by eliminating larger-scale features. Appendix B describes the details of the MCC calculation. Additional details are contained in Emery et al. [1986], Garcia and Robinson [1989], and Emery et al. [1991]. The correlation tile used here was 25 pixels square and the search window was large enough to accommodate velocities of 1.0 ms^{-1} in any direction ($\pm$ 10–30 pixel displacements, depending on the time separations between images). Correlations were empirically determined to be significant with 90% confidence if values of the maximum cross-correlation coefficient r were greater than 0.4 for the 10-pixel search window or 0.6 for the 30-pixel search window.

Once a field of vectors had been produced by the MCC method (Figure 4a), a number of subsequent steps were performed to eliminate obviously erroneous vectors. Vectors associated with maximum cross-correlations less than 0.4 were eliminated, since these values were no greater than random correlations (Figure 4b). A nearest neighbor filter, using a 3 $\times$ 3 subgrid, was used to replace vectors which differed from the subgrid mean by more than three standard deviations. The new vector was calculated by searching a 20 $\times$ 20 pixel region around the mean displacement (Figure 4c). After this was done for each pair of images, a weighted average of 2 or 3 vector fields was performed, using r for the weighting factor, and excluding vectors with r below the cutoff. For the first three 12-hr periods, three fields were averaged using a cutoff of 0.4, in an attempt to eliminate clouds. Figure 4d shows an average vector field for day 199.75. For the last two 12-hr periods only two fields were used in the average with the cutoff reduced to 0.1 to keep as many vectors as possible, since there were no apparent clouds.

Inversion of SST Using the Heat Equation

The inversion of the heat equation for the surface velocity field was similar in concept, but differed in detail, from the method described in Kelly [1989]. The heat equation used here is given by

$$T_t + uT_x + vT_y = S(x,y) + m(x,y) \tag{2}$$

where u, v are the horizontal velocity components, T_x, T_y are the horizontal gradients of SST, and T_t is the temporal derivative of SST. The right-hand-side of (2) represents SST fluctuations which are due to residual measurement errors, surface heat fluxes, mixing and vertical advection. We explicitly removed the large spatial scale residual S, which is presumably not due to advection; the smaller scale residual m is an error term which was minimised in the inversion. Removing the large-scale term in the heat equation is analogous to high-pass filtering the images in the MCC method. Horizontal gradients of SST were computed for 16 × 16 pixel subsets (16 pixels is approximately 18 km) of the images. The temporal derivatives were computed by finite differences between images, using the average SST for each subset. There is an optimal temporal lag δt between images for the inversion: if δt is too large, the velocity field will change too much from one image to the next or a water parcel will move a distance larger than the subset over which the SST gradient is computed. If, on the other hand, δt is too small, measurement errors will dominate the temporal derivative of SST. The acceptable range of temporal lags was determined by examining the misfit of the best velocity solution to the the heat equation; only pairs of images separated by at least 6 hours and by no more than 18 hours were used in the inversions. The preferred value of δt for the inversion is approximately 12 hours, compared to preferred values of 4–6 hours for the MCC method.

The null space of the heat equation (2) contains velocity vectors which are parallel to isotherms as well as any velocity in a region of negligible SST gradients, because these velocity fields do not cause temporal changes in the SST. Kelly [1989] showed that in the absence of any constraint on the solutions, the inversion produced the cross-isotherm velocity component, smoothed by using a limited number of basis functions, but that the addition of a constraint on the solution, such as the minimization of horizontal divergence,

$$\alpha(u_x + v_y = 0) \tag{3}$$

gave plausible total velocity fields. The parameter α is a weighting factor which determines the importance of this constraint relative to the fit of the velocity solutions to the heat equation (2), which has weight 1.

Several specific changes from Kelly [1989] were made in the inversion method used here and they are discussed in more detail in Appendix C. Two-dimensional biharmonic splines [see, for example, Sandwell, 1987] were used as basis functions instead of the two-dimensional Fourier series. These splines have an adjustable knot density, so that the solutions behave better in regions of sparse data than functions with a fixed spatial grid. Another change that was made was in the computation of the large-scale temperature change term, which we have called S. To allow more than one pair

of images to be used in each inversion, we first removed the S term from each pair of images as a separate calculation, so that the actual form of (2) solved to obtain the velocity field was

$$uT_x + vT_y = -T_t' + m(x, y) \tag{4}$$

where $T_t' = T_t - S(x, y)$ is the residual temperature change after the large-scale contribution S is removed. This change was not incorporated into the inversions by Taggart [1991] on some of the same images because he used only one pair of images in each inversion. A comparison of his results with those obtained here suggested that the use of multiple images qualitatively improved the solutions, particularly in regions of small SST gradients or known cloud contamination.

By varying the weighting parameter α on the divergence, the inversion of the heat equation produces a whole family of solutions. Approximately seven solutions were computed for each time interval with α ranging from 0.005 to 0.32, resulting in solutions with rms speeds of about 0.15 – 0.60 ms^{-1} and divergences of $1 - 15 \times 10^{-6}\ s^{-1}$. The misfit of a solution is defined to be the ratio of the variance of $m(x, y)$, in (4) to the variance of the net temperature change, T_t', and values for all the computed solutions ranged from 30% to 85%. A consistent set of best solutions was chosen by requiring the solutions for each of the five time intervals to have similar rms speeds and divergence values; the optimal speed and divergence values were determined subjectively to give large jet speeds without large divergences or large vectors near the edges. Figure 5a shows the selected solution for day 199.75 with $\alpha = 0.04$. The solutions which were selected had rms speeds of about 0.23–0.31 ms^{-1} and divergences of $2.7–5.1 \times 10^{-6}\ s^{-1}$. Although these speeds were somewhat low, as discussed below, solutions with larger rms speeds did not have a better fit to the comparison data. The misfit to the heat equation varied considerably from one time interval to the next: the misfits of the selected solutions for the five time intervals were 77%, 35%, 34%, 54% and 76%, respectively.

4. Results

To assess the utility of the AVHRR velocity estimates, we compared them with measured velocities and with each other. All the vectors were measured or estimated at different locations; therefore one set of vectors had to be interpolated in each comparison to the grid of the other set of vectors. For the inverse solution, the spline coefficients define a continuous velocity field, so that the inverse solutions were always interpolated to the location of the data vectors. The MCC vectors, on the other hand, were computed independently at each grid point and thus they had to be interpolated to the location of the data vectors. All interpolation was done using overdetermined biharmonic splines with $nd = 2$ (see Appendix C), that is, the vectors were smoothed slightly in the interpolation.

For the vector comparisons we chose a measure of misfit which could distinguish between differences in magnitude and differences in direction: the rms ratio of the magnitude of the estimate relative to the data and the rms difference between the directions. To prevent a disproportionately large contribution to the directional difference from very small vectors, only those vectors with magnitudes larger than 0.05 ms^{-1} were used in the computation. As a baseline estimate for the effect of the interpolation, we interpolated an MCC estimate to its original grid, that is, we simply smoothed it: the the ratio of the smoothed magnitudes to the original magnitudes was 0.90 and the rms angular difference was 41°. These values can be used to evaluate the results below: a ratio near 0.90 and an angular difference near 40° are to be expected simply because of the necessary interpolation of vectors to make the comparison.

Comparisons of the AVHRR velocity estimates with data

While none of the more direct velocity measures can be considered the "true" velocity, because each of the measurements has its own sources of error, discrepancies between the AVHRR estimates and a variety of other measurements is suggestive of the nature and magnitude of the errors in the AVHRR estimates. ADCP, drifter and Geosat data were compared with the velocity estimates for each 12-hr interval. Because there were relatively few ADCP vectors, the vectors from two or three consecutive 12-hr intervals were combined in the comparisons.

To evaluate the differences between the AVHRR velocity estimates and the more direct velocity measurements, we computed a baseline comparison between the ADCP and drifter vectors for the same region. Because the direct measurements were sparse spatially and temporally compared with the AVHRR estimates, we combined direct measurements from the entire period (2.5 days) for the comparison. The ADCP measured in a more regular grid than the drifters; therefore we interpolated the ADCP vectors to the drifter locations which were within the region which was sampled well by the ADCP, as shown in Figure 3. Comparing the interpolated ADCP with the original drifter vectors gave a magnitude ratio (ADCP/drifter) of 0.58 and an rms directional difference of 59°. The small magnitude ratio, relative to the approximately 0.90 ratio expected from interpolation alone, demonstrates that the drifter speeds are systematically larger than those from the ADCP. There are a variety of reasons why these measurements might have systematic differences and a complete discussion of the differences is beyond the scope of this paper. The baseline comparison simply shows how much two independent measurements of the velocity might differ and still be useful measures.

The statistical comparisons of both the MCC and the inverse solutions with the drifter and ADCP

vectors are shown in Table 2. The number of drifter comparison vectors for each 12-hr period was about 35–40; the number of comparison vectors for ADCP is shown for each solution in Table 2. There are several clear trends in Table 2, of which the most apparent is the similarity between the statistics of the MCC and the inverse solutions. Based on the ADCP comparisons, on average the MCC estimates have slightly larger magnitudes, an rms ratio of 0.58 for all the estimates, compared with 0.51 for the inverse solutions, but at the expense of the directional disagreement, an rms difference of 74° compared with 66° for the inverse solutions. However, because the number of estimates is small and the scatter in the measures in Table 2 is large, these differences are not statistically significant. These differences between AVHRR and in situ data translate into rms differences in vector velocities of about 0.2–0.4 ms^{-1} in a region containing a jet with velocities of approximately 1.0 ms^{-1}.

Some other trends can be seen in Table 2 by comparing the differences in the statistics for ADCP with the differences for the drifters, recalling that the drifters preferentially sampled the jets. Using the rms ratio for all the AVHRR-derived velocity estimates in Table 2 (0.34 for drifters and 0.55 for ADCP) and taking into account the 10% reduction for interpolation, the AVHRR methods underestimate the drifter speeds by about 56%. This compares with an underestimate of the drifter speeds using ADCP of about 22%. The AVHRR methods underestimate speeds for the ADCP by about 35%. The rms directional difference relative to the drifters is about 60°, which is essentially the same as that for interpolated ADCP data (59°). The rms directional difference for all AVHRR-derived estimates for the ADCP is slightly larger (70°) than that for the drifters. This rms directional difference consists of both a mean difference and a standard deviation; the mean angular difference ranged from 0° to 29° for the estimates in Table 2. The MCC estimates had relatively small mean differences relative to the drifters (that is, in the jets) and larger mean differences relative to the ADCP; whereas the converse was true for the inverse solutions: the larger mean angular differences (9°–21°) were relative to the drifter data. For a baseline comparison, the mean angular difference between the drifter and ADCP vectors was 4°. There was no distinguishable pattern in the sign of the mean angular difference.

All five estimates from each method were compared with the Geosat cross-track velocity from day 200, which was the nearest measurement in time. This Geosat profile crossed the eastward flowing jet at nearly right angles, thus giving a reasonable estimate of the maximum jet speed. For these scalar comparisons the velocity vectors were interpolated to points along the Geosat subtrack, with a resolution of about 7 km, and the cross-track component at every point was computed. Then a linear regression was calculated between the velocity estimate $\hat{u}$ and the Geosat geostrophic velocity

u_g,

$$\hat{u} = a u_g + b \tag{5}$$

with all velocities given in units of ms^{-1}. The results are shown in Table 3, which includes the squared correlation coefficient, ρ^2. Again the results for the MCC and inverse solutions are similar, with magnitudes (rms value for a) of 0.56 and 0.44, respectively. Although the altimeter measures objectively, the jet represented a large part of the Geosat velocity variance in this particular profile. Thus the Geosat comparison data represent a sampling situation somewhere between that of the preferential jet sampling of the drifters and the more objective ADCP sampling. The resulting underestimates of 34% (MCC) or 46% (inverse) are therefore consistent with the vector data comparisons.

The correlation coefficients in these comparisons (Table 3) are relatively high (rms value for ρ^2 is 0.58), suggesting that, ignoring the low jet speeds, the flow fields from the AVHRR images are qualitatively accurate. This is illustrated in Figure 6, which shows the Geosat profile (solid line) on day 200 along with the profiles for the third and fourth estimates for both the MCC and inverse methods. Note that the resolution of flow features near the ends of the profiles is somewhat better using the inverse method than using the MCC method. Away from the edges of the images, multiple peaks of onshore and offshore flow are well resolved by both methods, which suggests that the underestimate of the jet speeds is not due to inadequate spatial resolution in the estimates. Correlation coefficients were substantially lower for regressions with the Geosat data from day 203, along a subtrack which is closer to the coast and which had a larger temporal separation. For the MCC estimates these correlations (ρ^2) were 0.34–0.56 and for the inverse solutions these correlations were much lower, 0.03–0.36. Correlations with the Geosat data for day 197 were even smaller, suggesting that the velocity field was changing too fast for these data to be useful for comparisons.

Comparison of AVHRR Estimates

To determine whether the AVHRR solutions agreed more with each other than with the data, we directly compared the two AVHRR-derived fields both quantitatively and qualitatively. The results using the vector statistical measures are shown in Table 4. The rms ratio of the magnitudes (inverse/MCC) has a mean of 0.66 over the 5 intervals; thus, the inverse solutions have magnitudes one-third less than the MCC estimates. This is apparently because the inverse solutions are smoother than the MCC estimates: after smoothing with the objective analysis procedure described in the next section, the MCC jet magnitudes were quite similar to those of the inverse solution (cf. Figures 4d,

5a and 7a). The difference in direction between the MCC and inverse solutions ranges from 60° to 75°, values comparable to the differences between either AVHRR solution and the ADCP vectors. Thus, although Table 2 suggests that the AVHRR solutions have similar directional differences with the data, they differ in direction as much from each other as either does from the data.

Nevertheless, a qualitative comparison of the solutions (Figures 4d and 5a) shows most of the same features in the circulation pattern. A jet flows toward the southwest from the northern edge (39°N, 125°W) to the western edge of the domain near 36.5°N, 128°W, then flows toward the southeast near 36°N, 126°W. A cyclonic eddy is found inshore of the jet near 37°N, 126.5°W. Anticyclonic eddies are found northwest of the jet near 38.5°N, 126.5°W and inshore of the jet near 35.5°N, 124°W. The MCC method results in a more continuous, meandering jet, whereas the inversion of the heat equation depicts the southern half of the jet as the inshore part of an anticyclonic eddy at 35.5°N, 126°W, that is shown only weakly, if at all, in the MCC solution. In general, the inverse solution is more eddy-like and the MCC estimate is more jet-like. The differences in character of the estimates is probably a function of the finer spatial grid of the inverse solution (18 km versus 27 km for the MCC), which allows for smaller features, and the minimization of horizontal divergence, which tends to produce closed circulation patterns.

The inverse solution shows an onshore and northward return flow southeast of the northern half of the jet, stretching from 36.5°N, 126°W to 38°N, 124°W. This coherent onshore flow is missing in the mean MCC estimate between 124°W and 126°W (Figure 4d), although it is present in a noisy fashion on some of the individual MCC fields (Figure 4c) and it appears in the subjective flow vectors shown in Figure 12 of Strub et al. [1991]. ADCP vectors at 37.5°N, 124.5°W (Figure 3) and dynamic height fields from the complete July 13–18 survey [Huyer et al., 1991] support the presence of a band of onshore flow more like the inverse solution than the MCC estimate. Just south of this region, at about 37.3°N, 124.5°W, along the cold filament extending southwest from Pt. Reyes, the estimates also disagree. The MCC estimate suggests offshore flow, whereas the inverse solution suggests onshore flow. A few days later (day 203), the Geosat profiles (Figure 2) suggest pronounced offshore flow just south of this region at about 36.8°N, 124.5°W.

Combining Information

To test whether either AVHRR method could be combined with other data to obtain better estimates we used two basic techniques. The first was the addition of a constraint on the heat equation inverse to require the solution to match other data. The second method was objective analysis to

combine MCC vectors with in situ data. The determination of whether the combined solutions were better than the original AVHRR solutions was limited by the accuracy of the comparison data, because the angular differences between the drifter and ADCP vectors were as large as that between the AVHRR and either in situ data set. Nevertheless an increase in the magnitudes of the AVHRR velocities with no degradation of the angular differences would clearly represent an improved solution.

Combined inversions .

The heat equation inversion is a least-squares procedure, which can be augmented with additional constraints by simply adding more equations (rows) to the system, with a weight which reflects the importance of the new information. To the system given by (3) and (4) we added the requirement that the velocity solutions (u, v) match the specificed vectors (u_s, v_s) at the locations x_i, that is,

$$\beta[u(\vec{x_i}) = u_s(\vec{x_i})] \tag{6}$$

$$\beta[v(\vec{x_i}) = v_s(\vec{x_i})] \tag{7}$$

where β is the weight given to this constraint relative to (4), analogous to α in (3). The specified vectors in this case were from the MCC estimates. Since the cross-correlation coefficient r from the MCC method reflects the accuracy of the velocity estimate at that point [Tokmakian et al., 1990], a multiple of the correlation value was used as the weight in (6) and (7), i.e., $\beta = r\beta_0$.

With the additional rows the matrices to be factored for the inverse were substantially larger; therefore the combined inversions were computed at a somewhat reduced resolution (54 km) compared with the original inversions (35 km), which corresponded to $nd = 3$ instead of $nd = 2$, as defined in Appendix C. A control solution at the lower resolution using only the AVHRR data for day 199.75 is shown in Figure 5b and its comparisons with vector data are shown as the "no data" solution in Table 5. This solution had the same input information as in Figure 5a, but the weight α was decreased slightly to maintain approximately the same speeds in the solution: a magnitude ratio of 0.57 for ADCP compared with 0.62 and a slight increase in the directional difference, 77° compared with 71°. Some features were lost in reducing the spatial resolution, the most notable of which is the breaking up of the continuous band of onshore flow south of the jet at 37.5°N, 125°W into two cyclonic eddies.

For the third time interval (day 199.75), the inverse solution was constrained to match the MCC estimates (Figure 5c); this solution differed from the ADCP data by as much as either of the estimates alone (solution CMB in Table 2), although there was a significant decrease in the directional

difference relative to the drifters (from 57° to 39°). The comparisons with Geosat data showed no significant improvement over either estimate alone, with $a = 0.63$ and $\rho^2 = 0.58$ (solution CMB in Table 3). Thus there was no obvious gain in information from the combination of the two methods.

We next tested whether the inversion of the heat equation could be improved by the addition of altimeter data. Because real velocity vectors are often approximately parallel to the isotherms and therefore produce little or no change in SST, the magnitude of the velocity could be largely underestimated in the heat equation inversion [Kelly, 1989]. The altimeter gives an estimate of the component of the geostrophic velocity perpendicular to the subtrack, so that except where the satellite subtrack is nearly parallel to the isotherms, the cross-track velocity component should improve the velocity estimate. The addition of altimeter data into the inversion was analogous to the MCC assimilation, except that only one velocity component could be matched to the altimeter data. The component of the solution vector (u, v) in the cross-track direction was required to match the geostrophic velocity from the altimeter u_g, that is,

$$\gamma(u \cos \Psi + v \sin \Psi = u_g) \tag{8}$$

where Ψ is the angle between the x-axis of the images (here, due east) and the perpendicular to the satellite subtrack. Again both sides of (8) were weighted relative to the heat equation, by the factor γ.

We assimilated a single altimeter profile for day 200 into the solution for day 199.75 and we assimilated profiles for both days 200 and 203, using $\gamma = 0.2$ in all cases. The solution using both profiles is shown in Figure 5d. The control case for the altimeter assimilations was the inversion at the lower spatial resolution (Figure 5b). The single profile assimilation did not significantly improve the solution (Table 5); however assimilation of both profiles (Figure 5d) gave increases in the ratios which were marginally significant, without increasing the directional differences. The assimilation degraded the fit to the heat equation from a misfit of about 64% for the control case, to misfits of 69% for one profile and 74% for two profiles. The assimilation of the Geosat data also changed the character of the velocity solution near the subtracks (cf. Figures 5b and 5d). It increased the strength of two anticyclonic eddies, one north of the jet at about 38°N, 126°W and one south of the jet at about 36°N, 124°W. It also created offshore flow near 36.5°N, 124.5°W, more like the MCC estimate (Figure 4d). The offshore flow was apparent in the original inversion (Figure 5a), but disappeared with the reduction in resolution (Figure 5b).

Objective Analysis.

To smooth the MCC vectors and combine them with altimeter data, we used objective analysis (OA, Bretherton et al. [1976]). We first fit a streamfunction to the MCC vectors using OA and then calculated a new vector field from this streamfunction, which had, by definition, zero divergence. We used the isotropic covariance function chosen by Walstad et al. [1991] for the streamfunction, based on an analysis of ADCP data in the CTZ region:

$$C_{\psi\psi} = (1 - \frac{s^2}{d^2})e^{-(s/c)^2} \tag{9}$$

where $C_{\psi\psi}$ is the covariance function of the streamfunction field, ψ is the streamfunction, s is the distance to data points and c and d are length scales with values $c = 100$ km and $d = 120$ km. Walstad et al. used smaller length scale values of $c = 50$ km and $d = 60$ km; the larger values used here were necessary to accommodate the larger spacing of the altimeter tracks. A rough estimate of the uncertainties in the MCC velocities, with units of ms^{-1} was taken to be $(1 - r)$, where r is the correlation coefficient. An estimate of 0.1 ms^{-1} was used for the uncertainty in the altimeter velocities.

Velocity estimates were reconstructed from the vectors shown in Figure 4d using OA without (Figure 7a) and with altimeter data (Figure 7b). Both the smoothing of the objective analysis and the incorporation of altimeter data affected the statistics of the velocity estimates relative to the in situ data. The smoothing alone reduced the rms angular differences (cf. Tables 2 and 5) from 55° to 48° for the drifters and from 65° to 55° for the ADCP vectors (a significant improvement). However, the magnitude ratios also decreased significantly, from 0.38 to 0.26 and from 0.54 and 0.48 for drifters and ADCP, respectively. The addition of the Geosat data had little effect on the magnitudes (Table 5), but it did increase the rms angular differences for the drifters from 48° to 67°, which was a significant degradation. Thus the assimilation of Geosat data into the MCC method did not improve the estimate statistics. Qualitatively, the velocity fields in Figure 7 contain the same features as previously seen, with the overall impression of a strong jet, meandering through a field of cyclonic and anticyclonic eddies. Inclusion of the altimeter data in the OA appears to have both increased the flow around the closed eddies and increased the continuity within the meandering jet.

5. Discussion

How good are the AVHRR methods for estimating velocity? Both methods produce nearly instantaneous pictures of the energetic flow features, which agree qualitatively with other velocities on scales greater than 50–100 km. Both methods systematically underestimate the magnitudes of the velocities as measured by drifters and ADCP at 20 m depth; however the directional differ-

ences are comparable with those obtained by comparing ADCP vectors with drifters for the same period. We suspect that the underestimate of the velocity, particularly in the jets, is inherent in the AVHRR data, rather than a limitation of the methods. We do not believe it is due to inadequate spatial resolution because a comparison with the Geosat velocity profiles (Figure 6) shows that all the small-scale features of the flow field are present in both AVHRR estimates. With comparable spatial resolution (the half-power point for the low-pass filter was 55 km) the Geosat profiles have jet velocities 1.5-2 times larger than the AVHRR estimates. Note that the average spline knot spacing for the inverse solution was about 35 km and the correlation tile for the MCC method was about 27 km. Varying the constraint weighting factors in the inversions did not produce more energetic jets in the solutions: the more energetic solutions had large vectors in a few regions near the edges of the images, with correspondingly large divergences, rather than larger jet speeds.

A detailed comparison of drifter displacements and SST feature motion in the region of the jet confirmed that the drifters are moving faster. For a small subsample of initial drifter locations, features were tracked subjectively and by the MCC method. The average ratio of subjectively determined velocity magnitudes to drifter magnitudes was approximately 0.6, while the MCC method yielded an average ratio of 0.4. Thus, subjectively tracking features produces somewhat greater velocities than the automated feature tracking (MCC) but does not produce the large velocities of the drifters. Some drifters moved across the cold filament, leaving SST features behind and moving into warmer water with relatively no features. In some regions, it was impossible to track features at all, even when strong velocities were indicated by the drifters (38.8°N, 123.9°W in Figure 1). This illustrates the fact that in some regions, processes other than horizontal advection dominate the heat budget and make the major contribution to changes in the SST field, violating the assumptions inherent in both AVHRR methods.

The similarity in the estimates from the two methods and in the nature of the errors suggests that the methods are equivalent, i.e., the small-scale features which are cross-correlated in the MCC method must be the same features which produce the SST differences used by the inversion to estimate velocities. The underestimate of the jet velocity suggests that either the small-scale SST features do not move at the speed of a water parcel in the jet or that the core of the jet is isothermal and therefore there is no SST difference resulting from advection in the jet core.

To some extent the problems of the AVHRR estimates may be corrected by assimilation of other data, although the preliminary attempts described here showed only modest improvements, and only for the heat equation inversion. The results here are somewhat in contradiction with the results of

Taggart [1991] who used this same method of assimilation with synthetic altimeter data. Using some of the same AVHRR images (A, C, E and G in Table 1) and profiles constructed from the ADCP vectors, Taggart showed that assimilating profiles at 25-km spacing gave little improvement in the velocity solutions over assimilation of a single profile. The analyses here suggested that two profiles, separated by about 100 km, gave better results than a single profile. Clearly the problem of combining AVHRR with other data needs a more careful examination.

What are the advantages and disadvantages of each AVHRR method? The inversion of the heat equation works better with slightly longer time separation between images (6-18 hours) and does not require the full spatial resolution of the images. Tests with these same images decimated by a factor of 4 produced similar statistics to the 1-km resolution images, suggesting that the inversion should work on the Global Area Coverage (GAC) 4-km data that is routinely archived, if adequate cloud flagging can be done. On the other hand, the MCC method gives larger jet velocities. The shorter optimal temporal separation of the MCC method would be an advantage when a region was clear only for a short period because of cloud cover. The MCC method may also be more successful when SST gradients are weak or when the SST gradients cannot be corrected properly.

To what extent is the divergence field of the AVHRR-derived estimates realistic and informative? The horizontal divergence was calculated from an average of the estimates for the last two 12-hr periods (days 199.75 and 200.25) for both the MCC and inverse methods, because divergence fields for individual estimates were quite noisy. The divergence field from the MCC method (not shown) had maximum magnitudes of 0.4–0.6 d^{-1} (5–7 $\times$ 10^{-6} s^{-1}); and these maxima occurred both within and outside of the region of strong offshore flow. Unlike the MCC estimate, the field of divergence from the inversion of the heat equation has its maximum values (about 0.4 d^{-1}) concentrated near the jet or near the coast. Much of the jet was convergent, with a maximum in the cyclonic eddy at its offshore edge (Figure 5a) and near where this eddy appears to be pinching off at 37.5°N, 125°W. This pattern of convergence was similar to the patterns of downwelling seen in the numerical simulation of a jet in Haidvogel et al. [1991, Plate 2]. An evaluation of the usefulness of the divergence field is limited by the lack of comparison data; the structure of the field from the inverse solution has plausible structure and magnitudes.

What information can be gained from the AVHRR-derived velocities? The qualitative agreement between the AVHRR estimates and the in situ data suggests that they can be useful in determining the appropriate conceptual model of the jets [see Strub et al., 1991]. In all AVHRR estimates the offshore-directed jet is fed by flow from the north; there is no evidence of flow from the south being

directed into the jet, except where the cyclonic eddy near its offshore edge recirculates water from the jet. In all AVHRR estimates the offshore-directed jet has a strong return flow; the return flow bifurcates into a cyclonic eddy and a southward flow similar to the mean 1988 flows calculated from the drifters [Brink et al., 1991, Figure 3d]. This asymmetry of the jet (inflow from the north and outflow to the south) suggests that the jets are primarily meanders of the southward flow, not simply an illusion created by the alignment of the nearby eddies.

Nevertheless, this meander is embedded in a strong eddy field and it is probably affected by interactions with these eddies. The anticyclonic eddy to the northwest of the jet is a feature that was observed only in the AVHRR-derived fields, despite the fact that it corresponds to a region of small SST gradients. An eddy has been found in this location during a number of summer surveys [Rienecker et al., 1987] and there has been speculation that this eddy was present during the 1988 surveys [Lagerloef, 1991], although none of the drifters entered this eddy. The field survey on July 13–18 [Huyer et al., 1991] shows what could be the eastern part of this eddy but did not sample far enough west to resolve more of it; the field survey on June 20-27 shows perhaps half of an eddy in the same approximate location but again did not sample far enough west to determine whether it was a closed eddy. Both AVHRR methods resolve this eddy and its existence is supported by an onshore flow north of the jet in the Geosat data on day 200 (Figure 2). This anticyclonic eddy and the cyclonic eddy to its south, which is the offshore end of the jet, have a dipole structure similar to that in the detached eddy in the numerical simulations of Haidvogel et al. [1991]; in fact, the narrowness of the jet and the onshore flow at 37.5°N, 125°W (cf. Figure 5a and Figure 3) suggest that the meander may be pinching off this pair of eddies.

6. Summary and Conclusions

A set of 11 relatively cloud free AVHRR images from a 3-day period and coincident drifter, ADCP and altimeter data were used to evaluate the performance of two methods of estimating horizontal velocities in the upper ocean from sequences of AVHRR images. The two methods are the MCC method [Emery et al., 1986] and the inversion of the heat equation [Kelly, 1989]. The comparisons of the estimates with the data were given in terms of the rms angular differences and the rms ratio of the magnitudes.

The most striking result is the similarity between the comparison statistics of the MCC and the inverse solutions and the qualitative agreement between the estimates. Both methods underestimate the magnitudes of the ADCP vectors by about 35% and the drifters by about 56%. Rms differences

in direction were from 60°–70°, which were only slightly larger than that from a baseline comparison (59°) established by interpolating ADCP vectors to the positions of velocity vectors from drifters. We suggest that the methods are equivalent, i.e., the small-scale features which are cross-correlated in the MCC method must be the same features which produce the SST differences used by the inversion to estimate velocities.

The underestimate of the velocity, particularly in the jets, is inherent in the assumptions used to derive the velocity from the AVHRR data, rather than a limitation of a particular method. The small-scale SST features near the jet move more slowly than a water parcel. In addition the core of the jet is nearly isothermal so that advection produces little SST difference between images. The underestimate of the jet speeds is not due to inadequate spatial resolution in the estimates. Both methods resolve the energetic flow features with horizontal scales of 50 km or more, although the inverse method appears to resolve flow features better near the edge of the images than the MCC method. Nevertheless the Geosat geostrophic jet velocities with comparable spatial resolution are 50–100% larger than the AVHRR estimates.

Despite their similar comparison statistics, the AVHRR-derived fields from the two different methods differed from each other in the statistical characterization nearly as much as they differed from the in situ data. The MCC estimates had larger magnitudes (by about one-third) than the inverse solutions, particularly in the jets, while the inversion produced smoother fields. The inversion uses slightly longer periods between images (12–18 hours compared to 4–12 hours for the MCC method) and perhaps lower spatial resolution (4 km compared to 1 km), making use of archived GAC data possible. It has the disadvantage of requiring an atmospheric correction for temperature gradients. Both methods require that as many images as possible be collected over periods of a few days. Both methods would also benefit from automated cloud screening techniques.

The AVHRR methods were combined with each other and with altimeter data to attempt to improve the estimates. The combination of the two methods did not significantly improve the statistical comparisons with the in situ data. Assimilation of the altimeter data into the inversion gave a modest improvement in the comparison statistics, when data from two subtracks were used. The large angular differences in the baseline comparison between the drifter and ADCP vectors and the small spatial region covered by the in situ data made it difficult to establish whether incorporating altimeter data significantly improved the solutions. Although the assimilation of altimeter data clearly needs to be investigated further, these results suggest that multiple altimeters (ERS-1 and TOPEX/Poseidon) or aircraft-deployed drifter data should be useful in constraining the

AVHRR-derived fields.

The qualitative accuracy of the flow fields suggested an interpretation of the velocity estimates in terms of proposed conceptual models of the California Current. The jets appear to be meanders of the southward flow and indicate a strong return flow south of the offshore-directed flow near Point Arena. These meanders are clearly interacting with a strong eddy field; an anticyclonic eddy to the northwest of the jet was a robust feature of all the AVHRR-derived fields and its existence was supported by an onshore flow north of the jet in the Geosat data. The divergence fields derived from the velocity estimates were noisy and therefore somewhat suspect; however the field computed from the inversion showed the jet to be predominantly convergent.

Appendix A – Path Length Correction for AVHRR Images

As discussed in Kelly and Davis [1986] (hereafter KD) an effective empirical correction for water vapor errors in the SST maps for northern California summer can be made by assuming that atmospheric water vapor is constant over several days. Therefore the correction can be parameterized simply in terms of the path length between the satellite and the sea surface, or alternatively, as a function of the zenith or nadir angle, θ (cf. KD). Zenith angles for the center of the images were estimated from maps of the orbital subtrack.

The relationship between the actual sea surface temperature T_s and the brightness temperature T_λ for a single channel of the AVHRR can be written (cf. KD)

$$T'_\lambda = T'_s - (\rho_o + \alpha U)(q_o + q_1 T'_s) + \alpha F(p_o + p_1 T'_s) \tag{A.1}$$

where $T'_\lambda = T_\lambda - T_o$, $T'_s = T_s - T_o$ and T_o is a reference temperature close to the mean SST in the maps. The factor ρ_o is the reflectance of the sea surface at zero zenith angle and α is the ratio of the actual path length to the path length at zero zenith angle, which for small angles can be approximated as $1/\cos\theta$. The terms U and F represent the absorption and emission, respectively, of infrared radiation by the atmosphere. The terms q and p come from a Taylor expansion of the inverse of the Planck function around the reference temperature T_o, $q = P/P'$ and $p = 1/P'$, where the Planck function relates the infrared radiance L_λ to the temperature of the radiator, $L_\lambda = P_\lambda(T)$, and $P' = \partial P/\partial T$. Here q_o and p_o are the functions q and p evaluated at T_o and q_1 and p_1 are the partial derivatives of q and p with respect to temperature, respectively, also evaluated at T_o.

An empirical correction for the channel 4 brightness temperatures was found by computing the linear regression coefficients between the spatial mean and standard deviation of the brightness temperature T_λ for each image and the path-length ratio α (see Table A.1). These relationships can

be seen by re-writing (A.1) as

$$T'_\lambda = T'_s(1 - \alpha A) - \alpha B - C \tag{A.2}$$

where

$$A = q_1 U - p_1 F \tag{A.3}$$

$$B = q_o U - p_o F \tag{A.4}$$

$$C = \rho_o q_o \tag{A.5}$$

The quantity ρ_o was assumed to be -0.01, based on KD (note that there was a sign error for this quantity in KD); its value does not affect the inversions because it is a constant for all the images and the SST maps are always differenced. The standard deviation of the brightness temperature σ_λ is then related to the standard deviation of the actual SST, σ_s, by

$$\sigma_\lambda = (1 - \alpha A)\sigma_s \tag{A.6}$$

The quantities σ_s and A were found from the linear regression between the standard deviation of the images and α and then this value of A was used to determine the value of B in the linear regression between the mean image temperature perturbation $< T'_\lambda >$ and α. These relationships can be seen most clearly by re-arranging the terms in (A.2) and averaging the temperatures spatially, to get

$$< T'_\lambda > = < T'_s > - C - \alpha(A < T'_s > + B) \tag{A.7}$$

The spatial average of T'_s, which was assumed constant for the series of images, was also found. The regressions were computed on a common 256 × 256 pixel subset of the original 512 × 512 images to eliminate possible contamination by unmasked land pixels, clouds and fog. The resulting values for $< T'_s >$ and σ_s were 2.13°C and 1.20°C, based on a reference temperature of 14°C. The values of A and B were then used along with (A.3) and (A.4) to estimate values of the parameters U and F, which were 0.0822 and 0.477×10^{-6}. There was considerable scatter in the regression of the standard deviation of temperature against path length, which reflects the inaccuracy of the assumption of constant water vapor. Nevertheless, the values of U and F compare favorably with those obtained by KD, which were 0.123 and 0.643×10^{-6} respectively, and suggest somewhat less atmospheric water vapor in July of 1988 than in July of 1981.

Appendix B – Details of the MCC Calculations

A number of tradeoffs affect the choice of the sizes for the correlation tile and the search window, as well as the use the high-pass filter. To resolve the motion in narrow jets, small correlation tiles are desired. However, larger correlation tiles contain more distinctive features and therefore give more

degrees of freedom in the correlations. If the search window is large, as required by long periods between images and large velocities, a greater number of cross-correlations must be calculated, increasing the chance of spurious cross-correlation coefficients and increasing the computation time. If the search window is kept artificially small, the ability to find realistic maximum velocities is lost. In the present study, the search window was large enough (10–30 pixels, depending on separation times) to find maximum velocities of slightly over 1.0 ms^{-1}. In retrospect, no coherent velocities over 0.8 ms^{-1} were found, implying that a smaller search window could have been used. The size of the correlation tile used was a 25-pixel square, small enough to marginally resolve jets of 20–40 km width, and large enough to contain a number of distinctive features with scales of 5-10 km.

The tendency for cross-correlation calculations to be dominated by larger-scale features in the fields can be reduced by high-pass (in wavenumber) filtering the images or by calculating SST gradients. Calculating gradients on the smallest possible grid (centered differences with 2 pixel spacing) allows very precise calculations of displacements in the absence of rotation or distortion. This method has been used with success in tracking ice motion [Collins and Emery, 1988]. The large degree of distortion or rotation in oceanic features between images, however, results in very low cross-correlations between gradient images. Therefore, we used a high-pass filter (two-dimensional cosine filter with a wavelength of 30 km) on the images, which retained features with scales less than 20–25 km.

An empirical estimate of the significance level of the maximum cross-correlation was determined by applying the MCC method to filtered images separated by 11 days, which should have produced only random cross-correlations. For a search window that allowed 10-pixel displacements in all directions, only approximately 10% of the maximum cross-correlations were above 0.4. For a search window that allowed 20 and 30-pixel displacements, approximately 10% of the maximum cross-correlations were above 0.55 and 0.60, respectively. These values are used as approximate 90% confidence limits for r. When no high-pass filter was applied to the images, these values were much higher (0.65, 0.79 and 0.85, respectively).

There are a variety of search strategies which can be employed in finding the location of the maximum value of r. The brute force method moves the correlation tile pixel-by-pixel through the search window, calculating r at each location and choosing the absolute maximum. Although this was the method employed in the present study, nearly identical results were obtained in much less time by first using a coarser grid to search for the approximate locations of all of the local maxima within the search window. The location of each local maximum was then used as the starting point

of a new calculation, using the full resolution data set, marching up the gradient in r until a new local maximum was found. The location of the largest value of r calculated within the search window was chosen as the location of the displacement. By skipping to every third pixel before calculating the initial cross-correlations and using only every other pixel in the initial cross-correlation calculations, the speed of the computation was increased by a factor of 8. Combined with the increased speed of modern workstations, this method produces velocity calculations with 20-km resolution (441 vectors) for a 512 x 512 pixel image pair in 6–10 minutes (on a VAXstation 3100), compared to the 18–24 hours required previously using the brute force method (on a microVAX II).

A final aspect of the search strategy involves the inclusion of rotation. Besides simply displacing the initial search tile and calculating r, the intial tile can be rotated through a reasonable range of angles to accommodate rotation of the features [Kamachi, 1989; Tokmakian et al., 1990]. Previously, the computation time for these additional calculations was prohibitive. Although it is now feasible, the additional searches increase the chance of erroneous high correlations. Our computations showed that with images close enough together in time, curving jets and eddies with diameters less than 100 km can be resolved with the basic method, that is, without rotation. Emery et al. [1991] in their investigation of an alternative method of following rotation in closed rings and eddies, also noted that the basic method, without rotation, produces similar results.

Appendix C – Details of the Inverse Calculations

Several specific changes from Kelly [1989] were made in the inversion method used here. The two-dimensional Fourier series used as basis functions were replaced by two-dimensional biharmonic splines [see, for example, Sandwell, 1987] The two-dimensional biharmonic spline Green's function $\phi(\vec{x})$ is $|\vec{x}|^2(\ln|\vec{x}|-1)$. The two horizontal velocity components are expanded in the Green's functions as

$$u(\vec{x}) = \sum_{j=1}^{M} A_j \phi(\vec{x} - \vec{x}_j) \tag{C.1}$$

$$v(\vec{x}) = \sum_{j=1}^{M} B_j \phi(\vec{x} - \vec{x}_j) \tag{C.2}$$

where the summation is over M valid subsets with centers x_j in the spatial domain of the image pairs. The spatial resolution of the splines depends on a parameter, called nd here, which sets the number of data per knot in the spline. The larger the value of nd, the smoother the velocity solution. The number M of coefficients A_j or B_j (which is the number of knots in the spline) is the total number of subsets in the images divided by the square of nd. In these calculations there were 29 subsets in the x-direction and 32 subsets in the y-direction, so that the number of coefficients was

$(29/nd) \times (32/nd)$ or 224 for $nd = 2$. We used a value of 2 or 3 for nd in all of the inversions, which gave a spatial resolution of about 35 or 53 km, respectively.

The use of biharmonic splines allowed us to use a simpler set of constraints on the velocity field. Test inversions on the images minimising divergence, kinetic energy and relative vorticity showed that minimising divergence was the most effective in producing solutions which resembled the in situ data. The global kinetic energy constraint used by Kelly [1989] was replaced here by a constraint applied only in regions of missing data. If only one image of a pair was cloud-free on a given subset, so that the horizontal SST gradients could be estimated, but T_t could not be estimated, the specification was that of no heat advection, that is, $uT_x + vT_y = 0$. If neither image was cloud-free on the subset, then the kinetic energy was minimized there, that is, $u = 0$ and $v = 0$.

Another change we made was in the computation of the large-scale temperature change term, S. In Kelly [1989] the S term was computed as part of the inversion, which allowed the SST changes to be distributed between the advective terms and S in a way which optimally minimized the residual m in (2). However, a different S term is required for each image pair, which if incorporated into the original method using multiple image pairs, would substantially increase the program complexity and the computation time. Therefore $S(x, y)$ was computed as the best fit to T_t, the temporal derivative of SST, for each image pair before doing the inversion. To allow more spatial structure, we changed the functional form of S from a linear gradient to biharmonic splines, but with $nd = 7$, which gave spatial scales for S of more than 120 km.

We also removed both the column weighting and the row weighting [Kelly, 1989] in these inversions. Column weighting was necessary in the original version to scale the size of S relative to the temperature gradients; however because S was computed separately here, the column weighting was unnecessary. The function of row weighting is to prevent large measured values of SST gradients from numerically dominating the solution to the inversion; in other words, the heat equation should be equally valid in regions of large and small gradients. In practice, however, small errors in T_t can produce unrealistically large velocities in regions with small SST gradients. For example, if the actual velocity is zero, then by (4), $T_t' = 0$. However, for an error in T_t' of ϵ, the inversion will attempt to find a solution which satisfies $uT_x + vT_y = \epsilon$; for regions of small horizontal SST gradients, the erroneous velocity will be large. This was not a problem in the original method [Kelly, 1989] because the column scaling factor for S was set large enough to prevent the row from being scaled by negligible SST gradients. Because S was not part of the inversion here, we eliminated row weighting and allowed the solution to be biased toward regions of large SST gradients, where we

expect heat advection to be greatest and where both the neglected terms in (4) and the SST errors are least likely to influence the solutions.

Acknowledgments. KAK gratefully acknowledges the support of the Office of Naval Research on contract N00014-90-J-1808 (Coastal Sciences Division) and contract N00014-86-K-0751 (University Research Initiative). Support for PTS was provided by NASA grant NAGW-1251, JPL contract 958128 and EOS grant NAF-5-30553. The field data were collected during the Coastal Transition Zone program, sponsored by the Office of Naval Research (ONR) through the Coastal Sciences Program (Code 1122CS). Peter Niiler and Ken Brink provided the drifter data and Steve Ramp and Mike Kosro provided the ADCP data for comparison with the AVHRR velocities. The AVHRR images were provided by the Scripps Satellite Oceanography Center. Altimeter data were provided to PTS by Lee Fu and Victor Zlotnicki at JPL and further processed by Donna Witter and Michael Schlax at Oregon State University. Corinne James processed the images and other data used at Oregon State University. We also thank Steve Lentz and the reviewers, whose suggestions made this manuscript clearer and more concise. This is Woods Hole Oceanographic Institution Contribution 7851.

References

Brink, K.H., and T.J. Cowles, 1991. The Coastal Transition Zone Program, *J. Geophys. Res.*, 96, 14,637–14,647.

Brink, K.H., R.C. Beardsley, P.P. Niiler, M. Abbott, et al., 1991. Statistical properties of near surface flow in the California coastal transition zone, *J. Geophys. Res.*, 96, 14,693–14,706.

Bretherton, F.P., R.E. Davis, and C.B. Fandry, 1976. A technique for objective analysis and design of oceanographic experiments applied to MODE-73, *Deep-Sea Res.*, 23, 559-582.

Caruso, M.J., Z. Sirkes and P.J. Flament, 1990. Altimeter processing tools for analyzing mesoscale ocean features, Woods Hole Oceanogr. Inst. Tech. Rept., WHOI-90-45.

Chavez, F.P., R.T. Barber, P.M. Kosro, A. Huyer, et al., 1991. Horizontal transport and the distribution of nutrients in the coastal transition zone off northern California: effects on primary production, phytoplankton biomass, and species composition. *J. Geophys. Res.*, 96, 14,833–14,848.

Cheney, R.E., B.C. Douglas, R.W. Agreen, L. Miller, D.L. Porter, N.S. Doyle, 1987. GEOSAT altimeter geophysical data record user handbook. NOAA Tech. Memorandum NOS NGS-46, 29 pp.

Collins, M.J., and W.J. Emery, 1988. A computational method for estimating sea ice motion in sequential Seasat synthetic aperture radar imagery by matched filtering. *J. Geophys. Res.*, 93, 9251-9251.

Dewey, R.K., J.N. Moum, C.A. Paulson, D.R. Caldwell, and Stephen D. Pierce, 1991. Structure and dynamics of a coastal filament, *J. Geophys. Res.*, 96, 14,885–14,907.

Emery, W. J., A. C. Thomas, M. J. Collins, W. R. Crawford and D. L. Mackas, 1986. An objective method for computing advective surface velocities from sequential infrared satellite images. *J. Geophys. Res.*, 91, 12,865–12,878.

Emery, W.J., C. Fowler, and C.A. Clayson, 1991. Satellite image derived Gulf Stream currents compared with numerical model results. *J. Atmos. and Oceanogr. Tech*, submitted.

Garcia, C.A.E., and I.S. Robinson, 1989. Sea surface velocities in shallow seas extracted from sequential Coastal Zone Color Scanner satellite data. *J. Geophys. Res.*, 94, 12,681-12,691.

Haidvogel, D.B., A. Beckmann, and K.S. Hedstrōm, 1991. Dynamical simulations of filament formation and evolution in the coastal transition zone. *J. Geophys. Res.*, 96, 15,017–15,040.

Huyer, A.J., P.M. Kosro, J. Fleischbein, S.R. Ramp et al., 1991. Currents and water masses of the coastal transition zone off Northern California, June to August, 1988. *J. Geophys. Res.*, 96, 14,809–14,831.

Kamachi, M., 1989. Advective surface velocities derived from sequential images for rotational flow field: limitations and applications of maximum cross correlation method with rotational registration, *J. Geophys. Res.*, 94, 18,227-18,233.

Kelly, K.A., 1983. Swirls and plumes or applications of statistical methods to satellite-derived sea surface temperatures. *Scripps Inst. Oceanogr., Ref. 83-15, CODE Tech. Rep. 18*, La Jolla, CA, 210 pp.

Kelly, K.A., and R.E. Davis, 1986. An analysis of errors in sea surface temperature in a series of infrared images from NOAA 6. *J. Geophys. Res.*, 91, 2633–2644.

Kelly, K.A., 1989. An inverse model for near-surface velocity from infrared images, *J. Phys. Oceanogr.* 19, 1845-1864.

Kosro, P.M., A. Huyer, S.R. Ramp, R.L. Smith, et al., 1991. The structure of the transition zone between coastal waters and the open ocean off northern California, winter and spring, 1987. *J. Geophys. Res.*, 96, 14,707–14,730.

Lagerloef, G.S.E., 1991. On the Point Arena Eddy; A recurring summer anticyclone in the California Current. submitted to *J. Geophys. Res.*

Niiler, P.P., R.E. Davis, and H.J. White, 1987. Water-following characteristics of a mixed layer drifter. *Deep-Sea Research*, 34, 1867-1881.

Rienecker, M.M., C.H. Reed, and C.N.K. Mooers, 1987. Mesoscale variability in the California Current System during 1982 to 1986: Maps of surface dynamic height, sea surface temperature, temperature at 50 m, mixed layer depth and depth of the 8C isotherm from observations during the OPTOMA program. INO Technical Report 87-01. 138 pp.

Sandwell, D.T., 1987. Biharmonic spline interpolation of GEOS-3 and Seasat altimeter data. *Geophys. Res. Let.*, 14, 139–142.

Strub, P.T., P.M. Kosro, A. Huyer and CTZ collaborators, 1991. The nature of the cold filaments in the California Current system. *J. Geophys. Res.*, 96, 14,743–14,768.

Swenson, M.S., P.P. Niiler, K.H. Brink, and M.R. Abbott, 1992. Drifter observations of a cold filament off Point Arena, California in July 1988, *J. Geophys. Res.*, in press.

Taggart, D.M., 1991. Determination of the near-surface velocity fields in the CTZ using combined altimetric and inverse modelling techniques, M.S. thesis, Naval Postgraduate School, Monterey, CA, 45 pp.

Tokmakian, R.T., P.T. Strub, and J. McClean-Padman, 1990. Evaluation of the maximum cross-correlation method of estimating sea surface velocities from sequential satellite images. *J. Atmos. and Oceanic Tech.*, 7, 852-865.

Vastano, A.C., and S.E. Borders, 1984. Sea surface motion over an anticyclonic eddy on the Oyashio Front. *Remote Sens. Environ.*, **16**, 87–90.

Wald, L., 1983. Predictability of the oceanic current field from routine satellite surveys of the sea-surface temperature field. Study made for the European Space Agency *CTAMN/83/R/05 - March, 1983*, 76 pp.

Walstad, L.J., J.S. Allen, P.M. Kosro, and A. Huyer, 1991. Dynamics of the coastal transition zone in 1987 through data assimilation studies, *J. Geophys. Res.*, **96**, 14,959–14,977.

Table 1: AVHRR images used in the velocity estimates

	year day in 1988 : hour UT
A	198:12
B	198:15
C	198:23
D	199:03
E	199:12
F	199:17
G	199:23
H	200:02
I	200:11
J	200:16
K	200:23

Table 2: Comparison of Solutions to Drifter and ADCP Vectors

Solution	Drifter		ADCP		
	$\delta\theta$	ratio	$\delta\theta$	ratio	no.
MCC 198.75	70°	0.27	81°	0.46	13
MCC 199.25	63°	0.26	63°	0.48	21
MCC 199.75	55°	0.38	65°	0.54	17
MCC 200.25	57°	0.41	86°	0.74	18
MCC 200.75	49°	0.46	72°	0.65	11
INV 198.75	49°	0.25	50°	0.48	11
INV 199.25	73°	0.25	53°	0.47	21
INV 199.75	68°	0.40	71°	0.62	17
INV 200.25	62°	0.33	53°	0.46	18
INV 200.75	52°	0.29	92°	0.48	13
CMB 199.75	39°	0.35	71°	0.55	16

Table 3: Comparison of Solutions to Geosat Cross-track Velocity

Solution	a	b	ρ^2
MCC 198.75	0.56	0.07	0.43
MCC 199.25	0.42	-0.03	0.53
MCC 199.75	0.64	-0.01	0.53
MCC 200.25	0.57	-0.07	0.69
MCC 200.75	0.58	-0.01	0.74
INV 198.75	0.39	-0.08	0.49
INV 199.25	0.49	-0.09	0.72
INV 199.75	0.48	-0.01	0.60
INV 200.25	0.49	-0.05	0.38
INV 200.75	0.33	-0.02	0.54
CMB 199.75	0.63	-0.05	0.58

Table 4: Comparison of MCC and Inverse Solutions

Time	$\delta\theta$	ratio
198.75	75°	0.63
199.25	68°	0.69
199.75	60°	0.76
200.25	61°	0.69
200.75	65°	0.58

Table 5: Geosat Assimilation Compared with Drifter and ADCP Vectors

Solution	Drifter		ADCP		
	$\delta\theta$	ratio	$\delta\theta$	ratio	no.
inverse:					
no data	57°	0.34	77°	0.57	18
day 200	58°	0.39	85°	0.59	18
both days	56°	0.38	69°	0.61	17
MCC:					
no data	48°	0.26	55°	0.48	18
both days	67°	0.27	58°	0.50	18

Table A.1: SST Before and After Path Length Corrections

Image		Before		After	
	zenith angle	mean T_λ	std. dev.	mean T_λ	std. dev.
B	46°	14.71	0.915	16.20	0.997
C	3°	15.23	1.166	16.06	1.260
D	26°	15.11	1.097	16.10	1.174
E*	45°	–	–	16.13	1.262
F	49°	14.59	1.336	16.20	1.513
G	18°	15.12	1.290	16.02	1.396
H	47°	14.48	1.042	15.98	1.102
I	52°	14.08	1.023	15.74	1.103
J	29°	14.91	1.129	15.94	1.242
K	30°	15.21	0.808	16.28	0.870

* Image E was not used to compute the empirical correction.

1 List of Figures

Fig. 1. SST from the AVHRR image on July 17, 17:07 UT (image F, Table 1), overlaid with drifter velocities from three of the five 12-hr periods used for comparison to the AVHRR-derived velocities. The scale arrow shows the length of a vector representing 0.5 ms^{-1}. Lighter gray shades correspond to cooler temperatures.

Fig. 2. Ascending subtracks of the Geosat altimeter. The cross-track component of geostrophic velocity, derived from the residual sea surface height profiles is plotted with positive (onshore) velocity towards the right. Only the three profiles from days 197, 200 and 203 were used in the comparisons with the velocity solutions. Maximum speed is about 0.67 ms^{-1}.

Fig. 3. The ADCP velocity vectors used in the comparison with the velocity solutions from AVHRR. All the individual vectors at a nominal depth of 20 m from the 2.5-day period are shown in the figure. Only those vectors within a 36-hr interval centered on the nominal solution time were used for the comparisons with each velocity solution in Table 2. The ADCP vectors were interpolated to the locations of the drifter vectors which were within the box (dashed line) to obtain baseline error statistics.

Fig. 4. (a) The full MCC field from the pair of images F and G (Table 1). The vector in the top right shows 0.5 ms^{-1}. (b) The same field as in a, after eliminating vectors with cross-correlation coefficient r less than 0.4. (c) As in b, after applying a nearest neighbor filter. (d) The weighted average of the fields from the three pairs of images for the third time interval (day 199.75), overlaid on the same AVHRR image as in Figure 1. Each velocity is weighted by r after eliminating individual velocities with r less than 0.4.

Fig. 5. The selected inverse solution for the third 12-hr period (day 199.75) (a) for the full spatial resolution with α =0.04, and (b) at a reduced spatial resolution with a weight of α =0.02. (c) As in b, except including the assimilation of the MCC field from day 199.75 with a weight of β =0.2. (d) As in b, except including assimilation of the Geosat data along subtracks on days 200 and 203 with weight γ =0.2. Solution is overlaid on the same AVHRR image as in Figure 1.

Fig. 6. The cross-track velocity profiles for Geosat and both types of AVHRR estimates. The Geosat geostrophic velocity profile for day 200 (solid line) and the MCC (dashed) and the heat equation (dotted) solutions for (a) day 199.75 and (b) day 200.25. Both solutions underestimate the magnitudes of the velocity, especially that of the offshore jet at about 37.5° N. However, both solutions resolve most features in the flow field as quantified by the relatively high correlations between the profiles (see Table 3).

Fig. 7. The velocity field reconstructed from the stream function using objective analysis of the field shown in Figure 4d (a) for the MCC vectors alone and (b) including the altimeter velocities along tracks for days 197, 200 and 203.

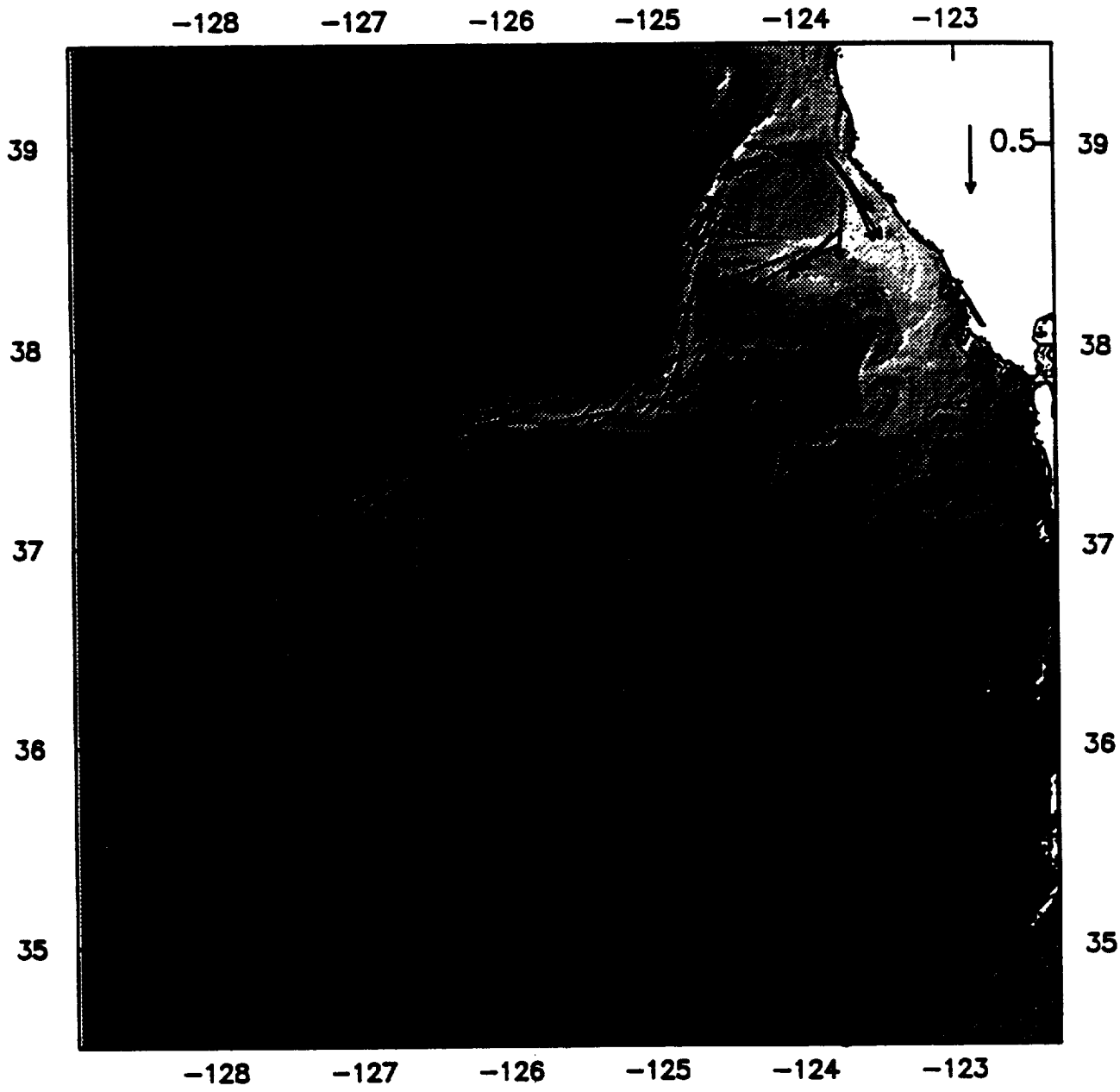

Fig. 1

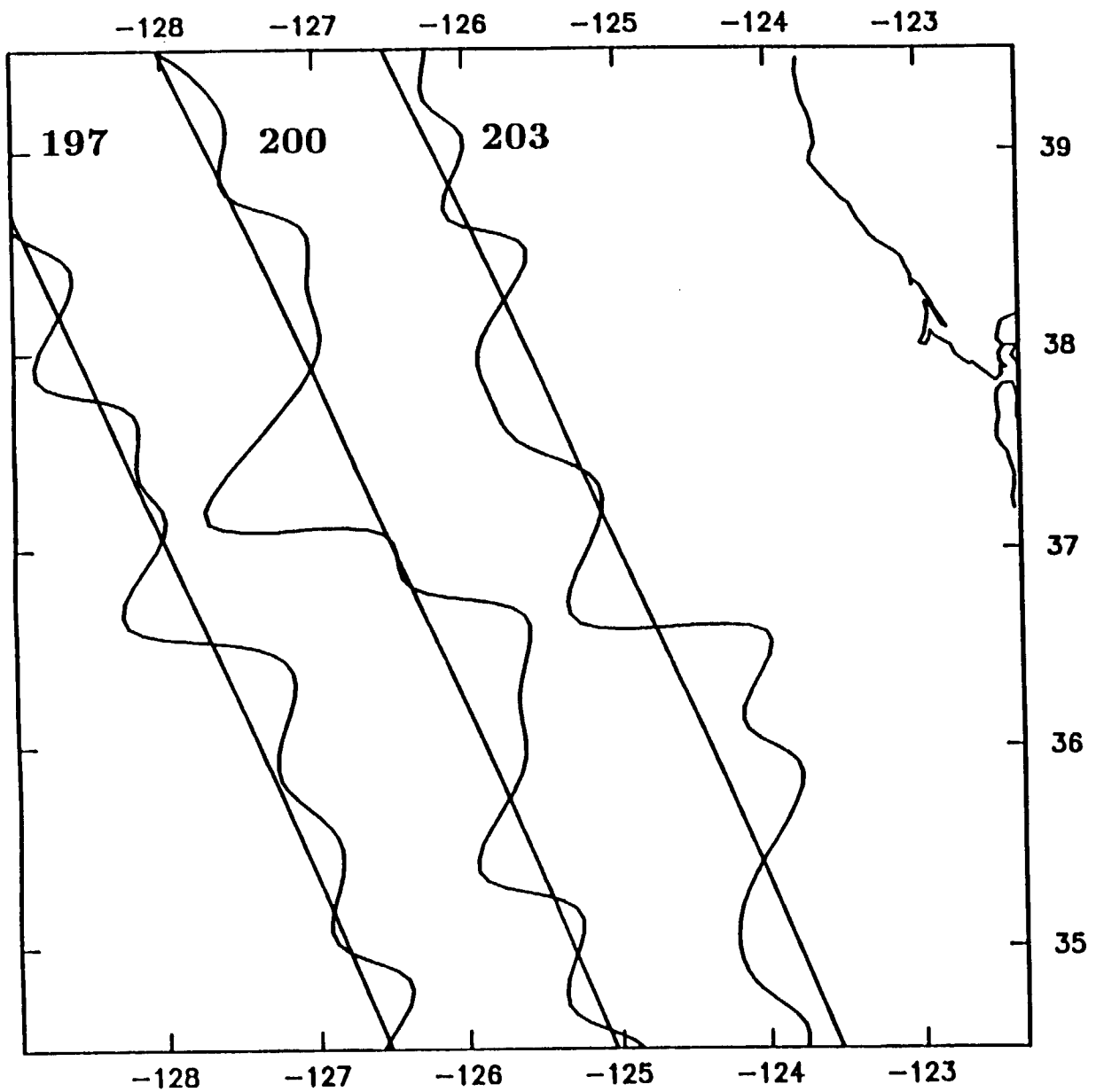

Fig. 2

VELPLTM 12-SEP-91

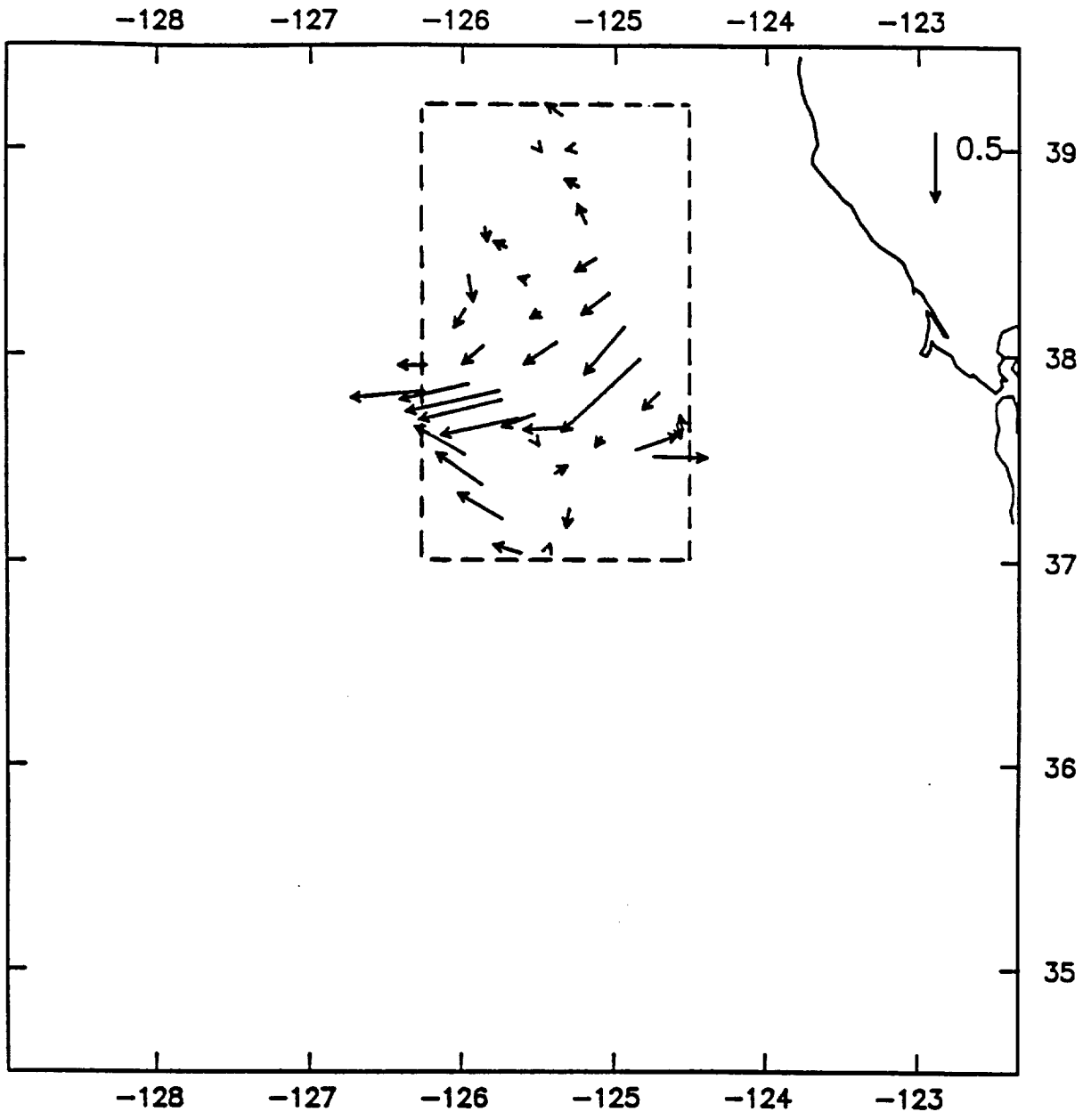

Fig. 3

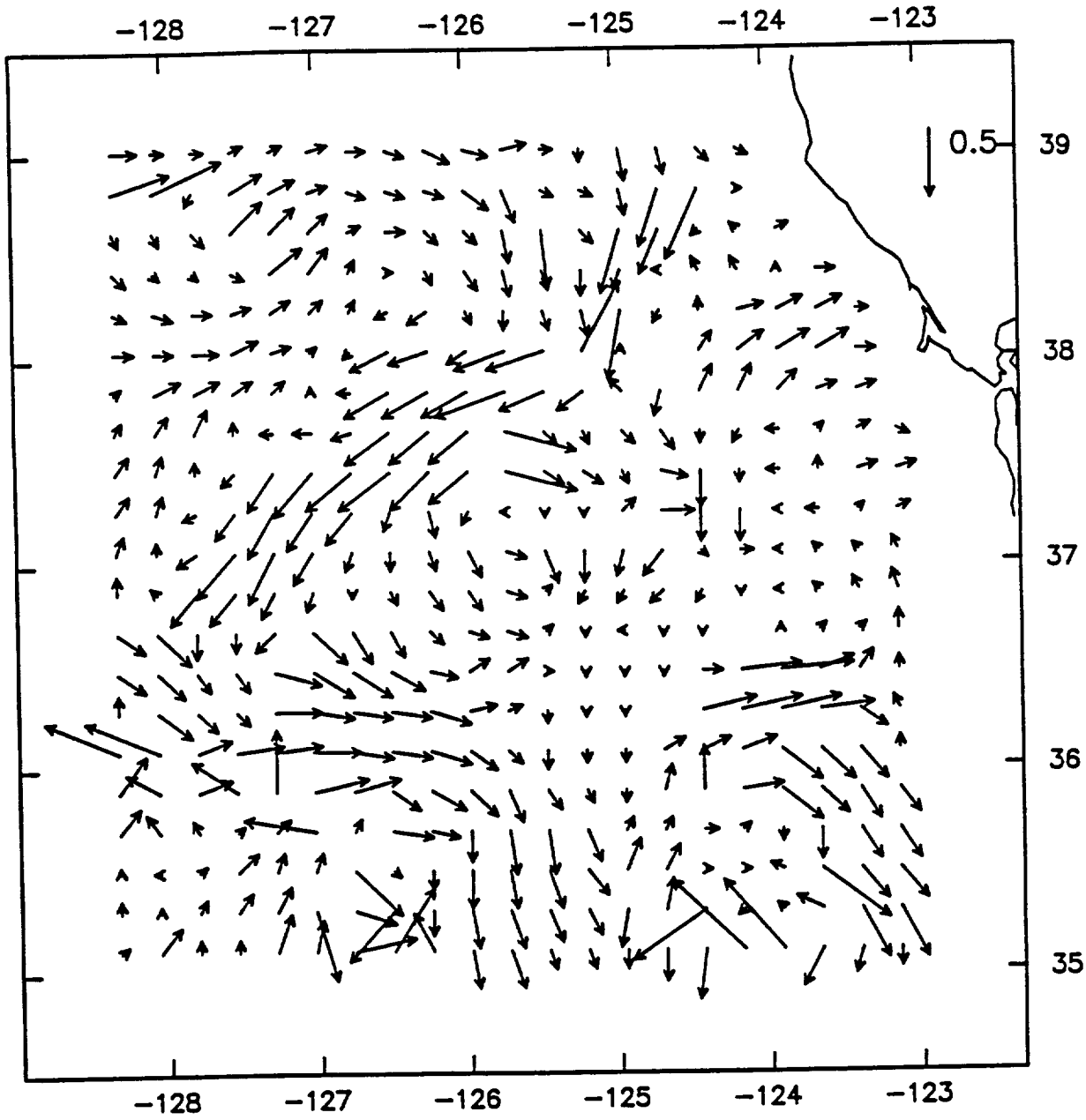

Fig. 4a

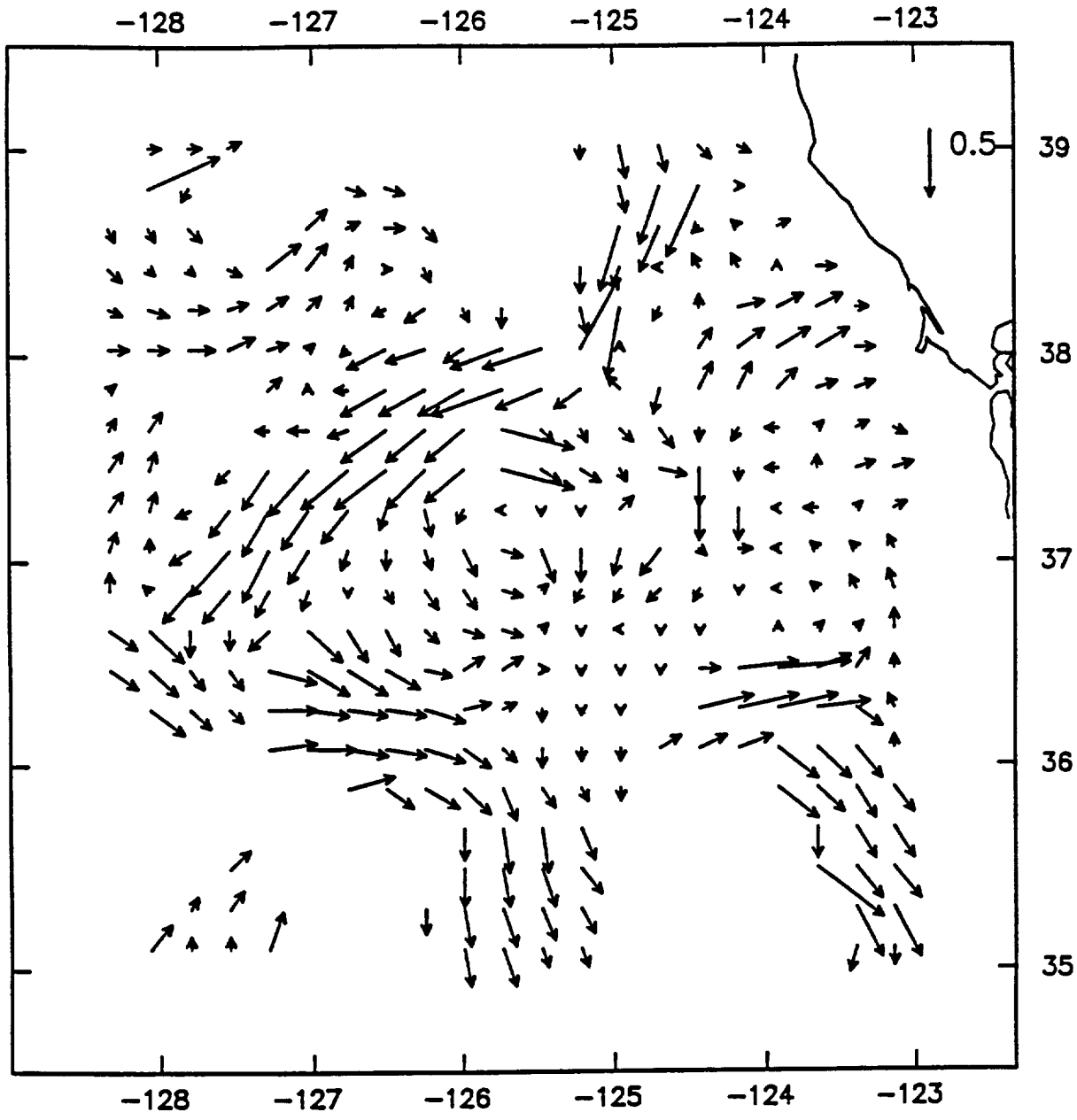

Fig. 4b

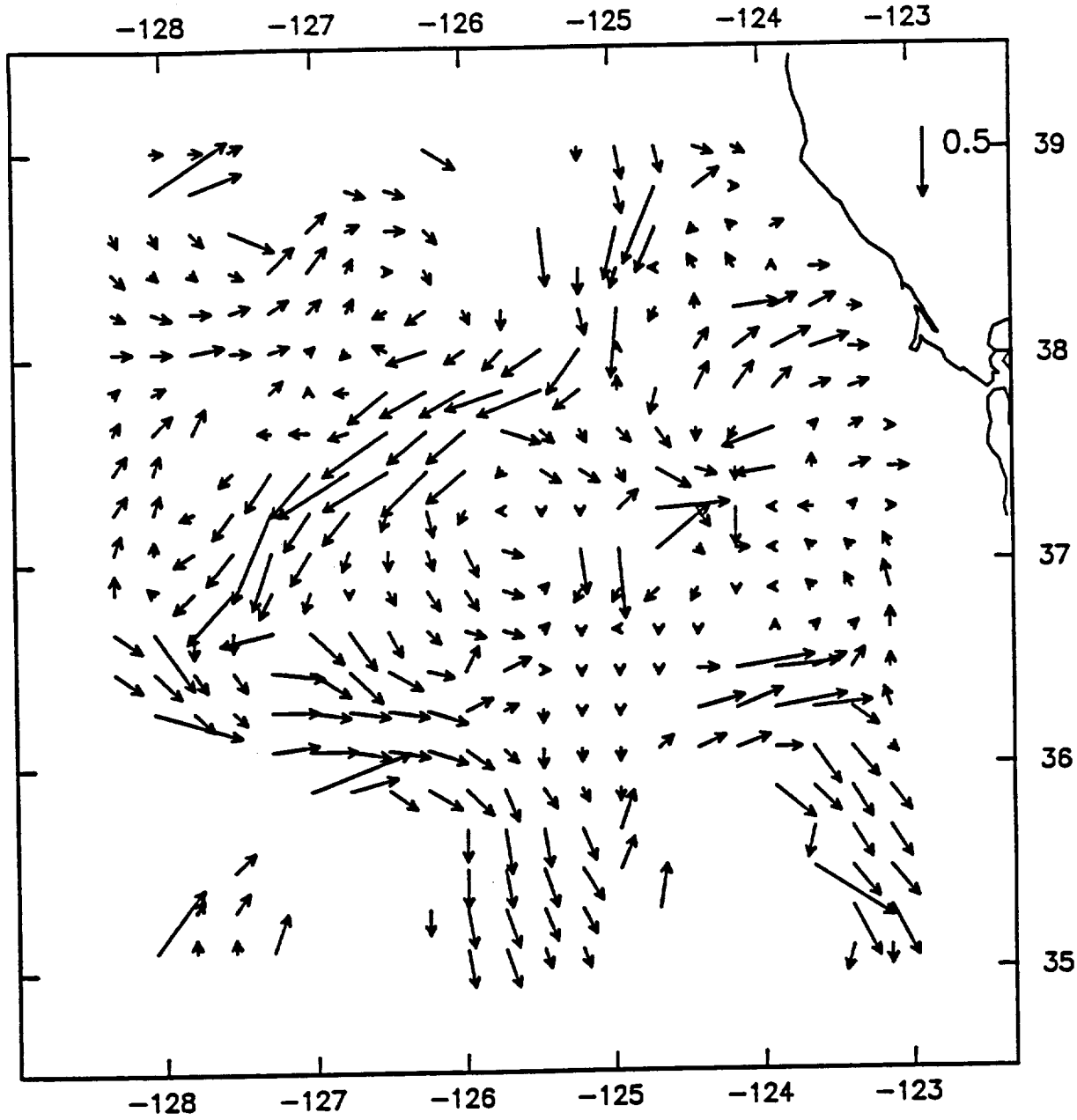

Fig. 4c

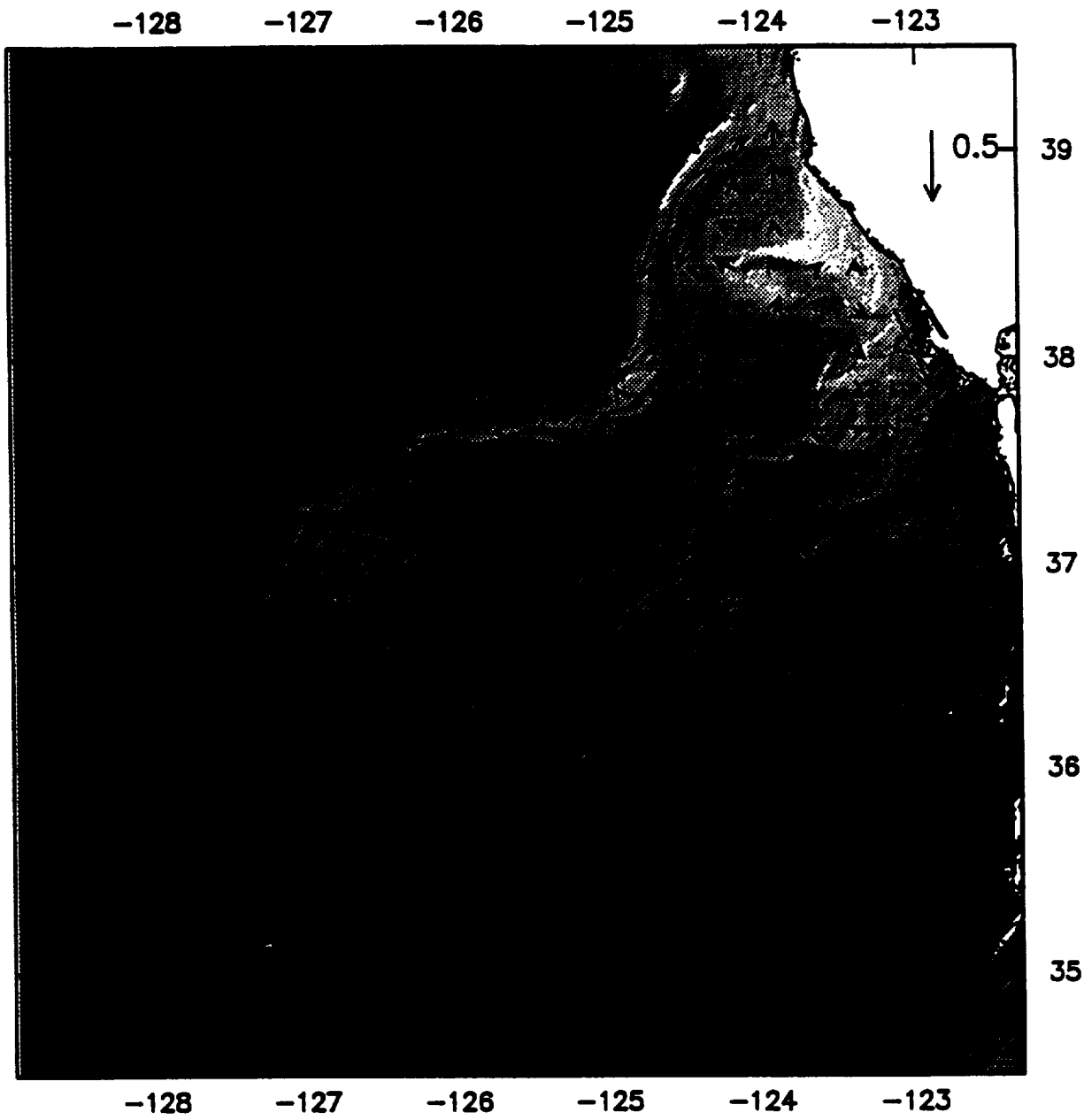

Fig. 4d

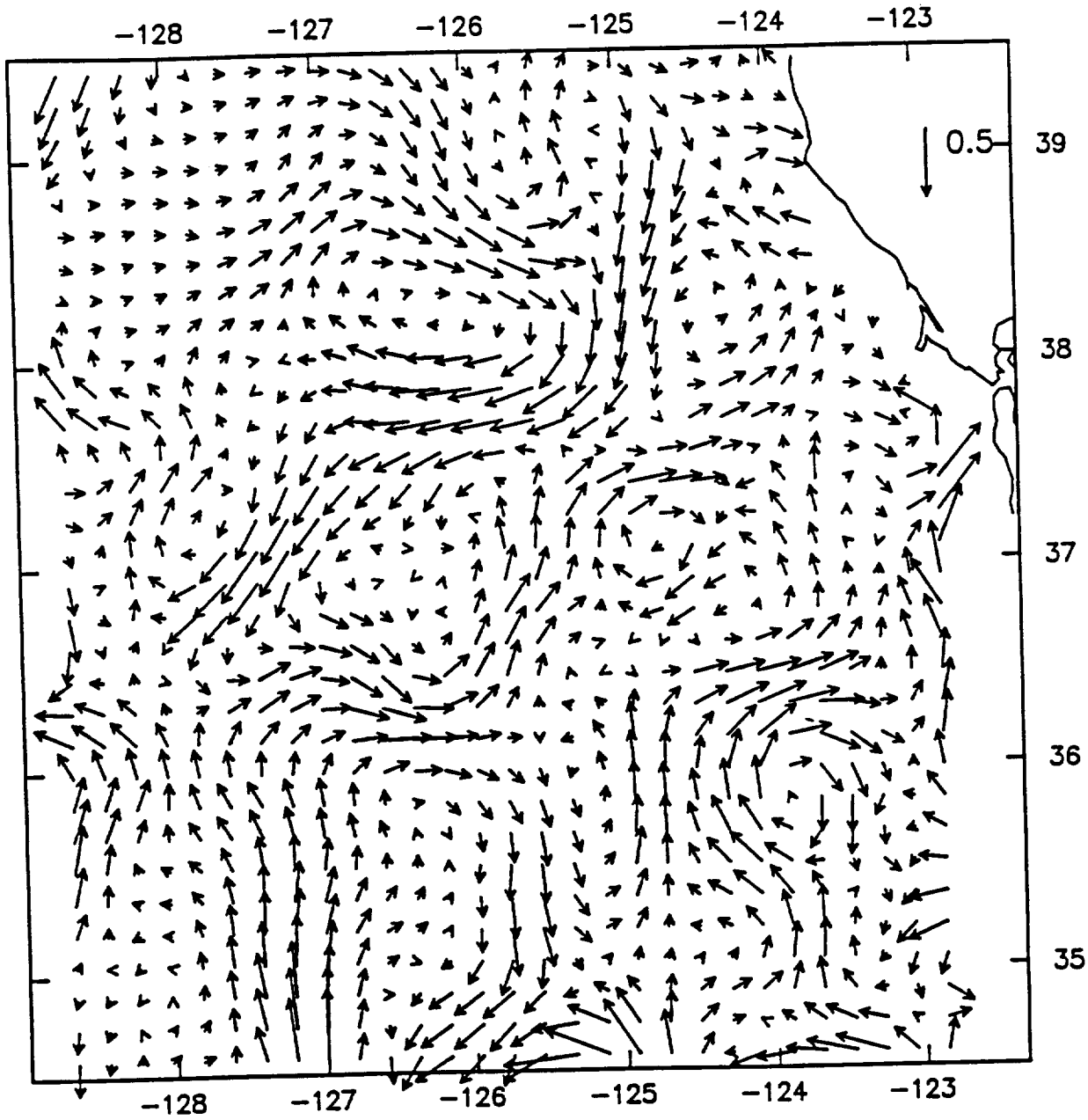

Fig 5a

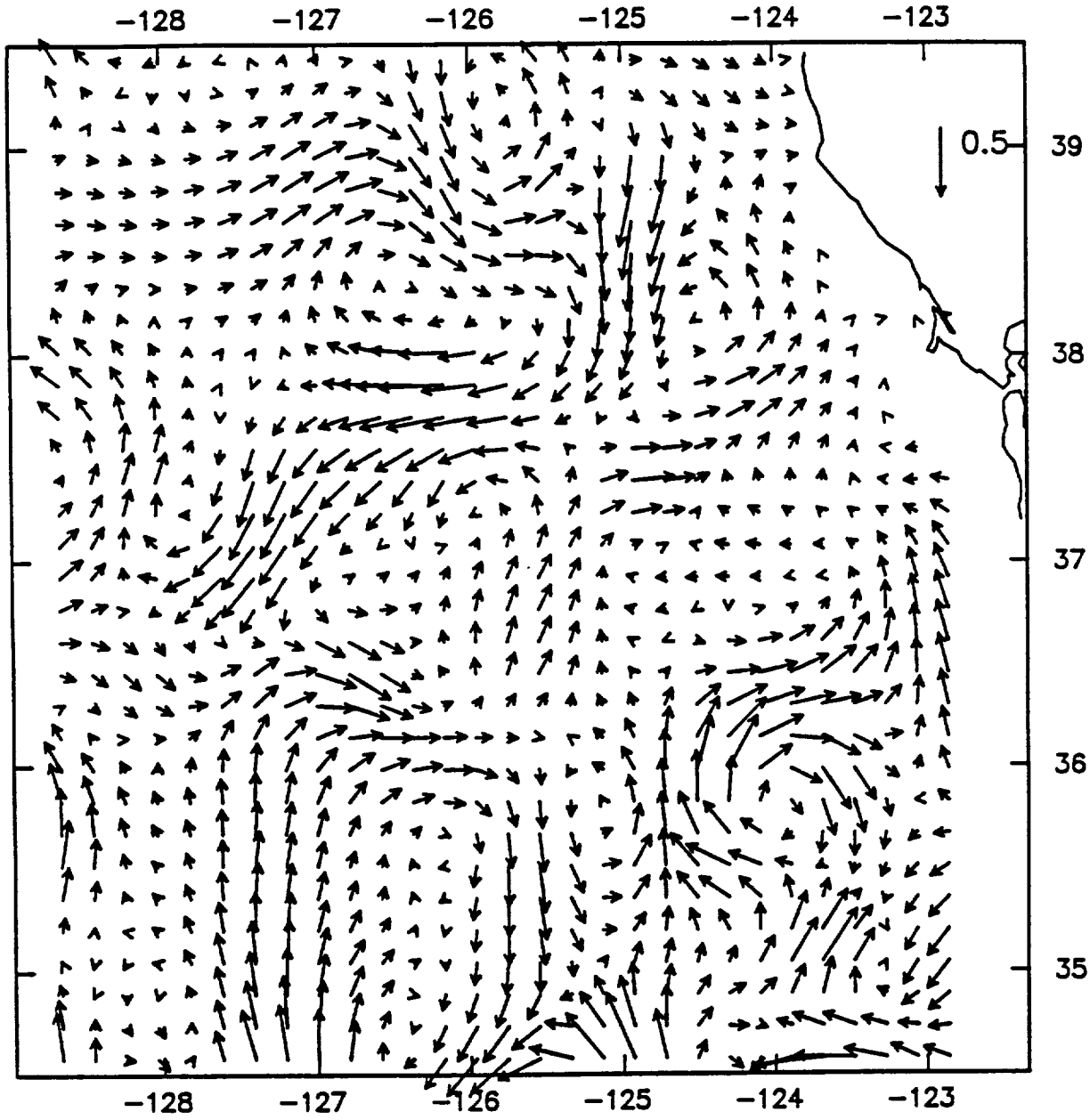

Fig 5b

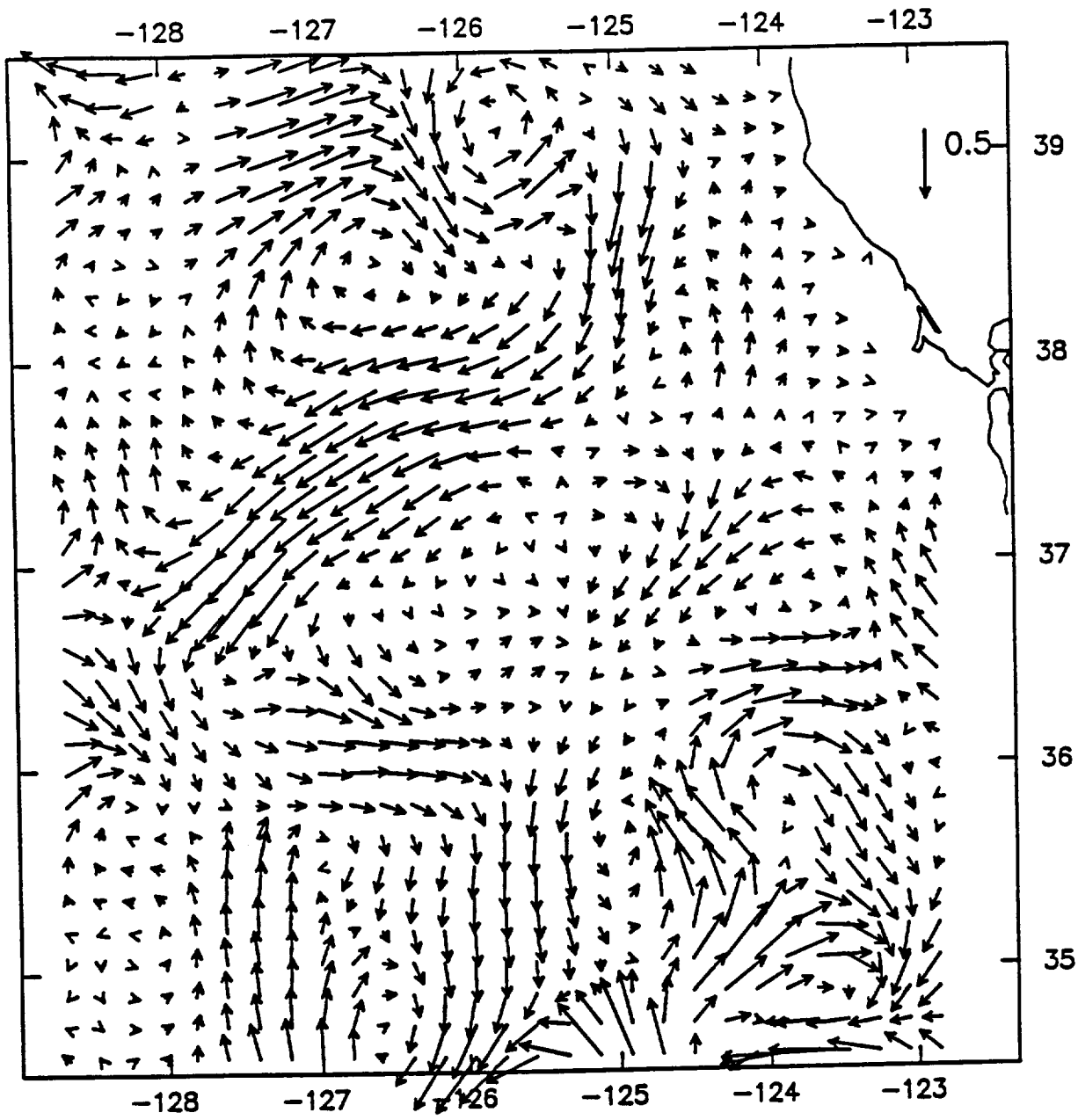

Fig 5c

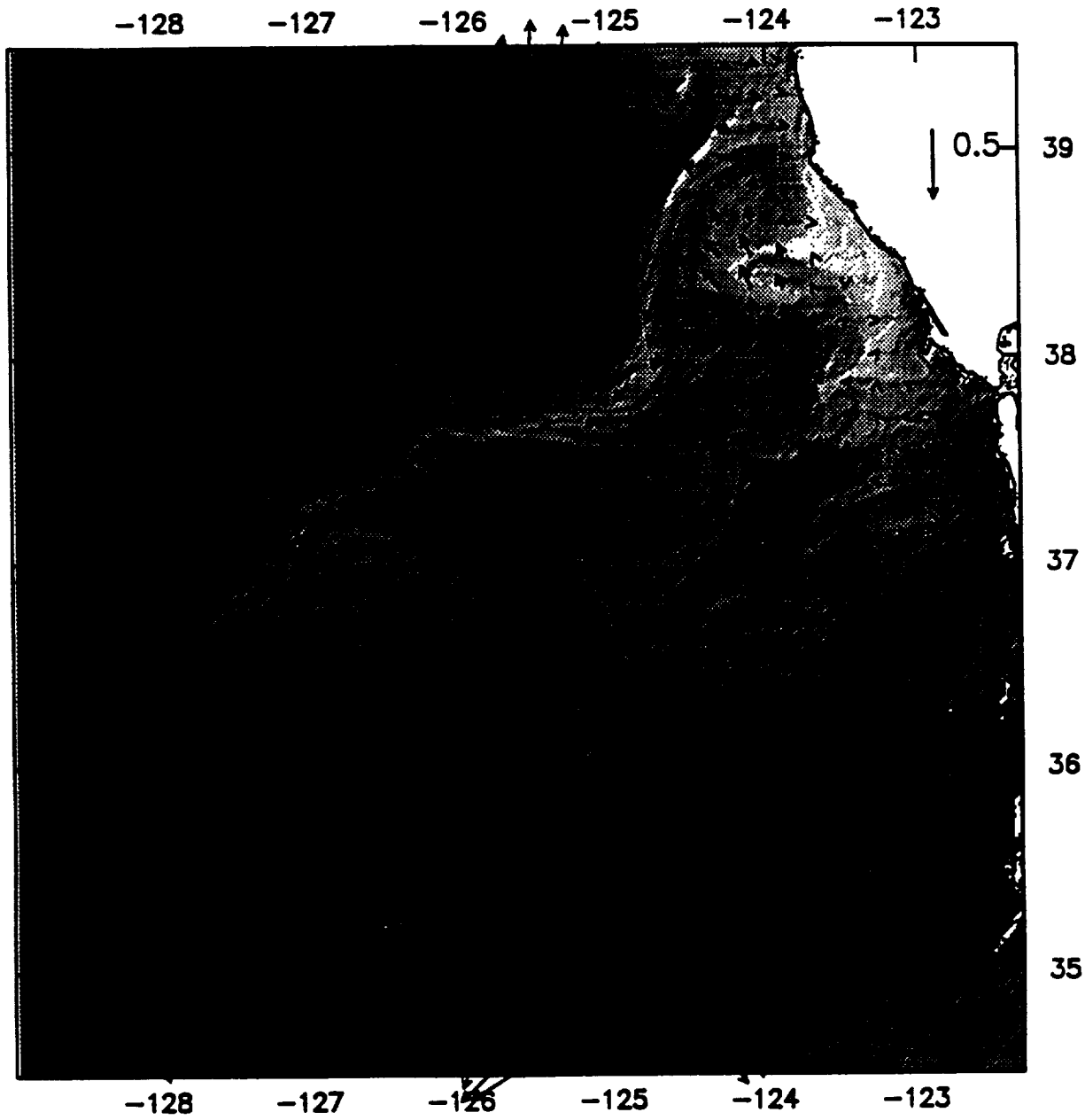

Fig 5d

(a) day 199.75

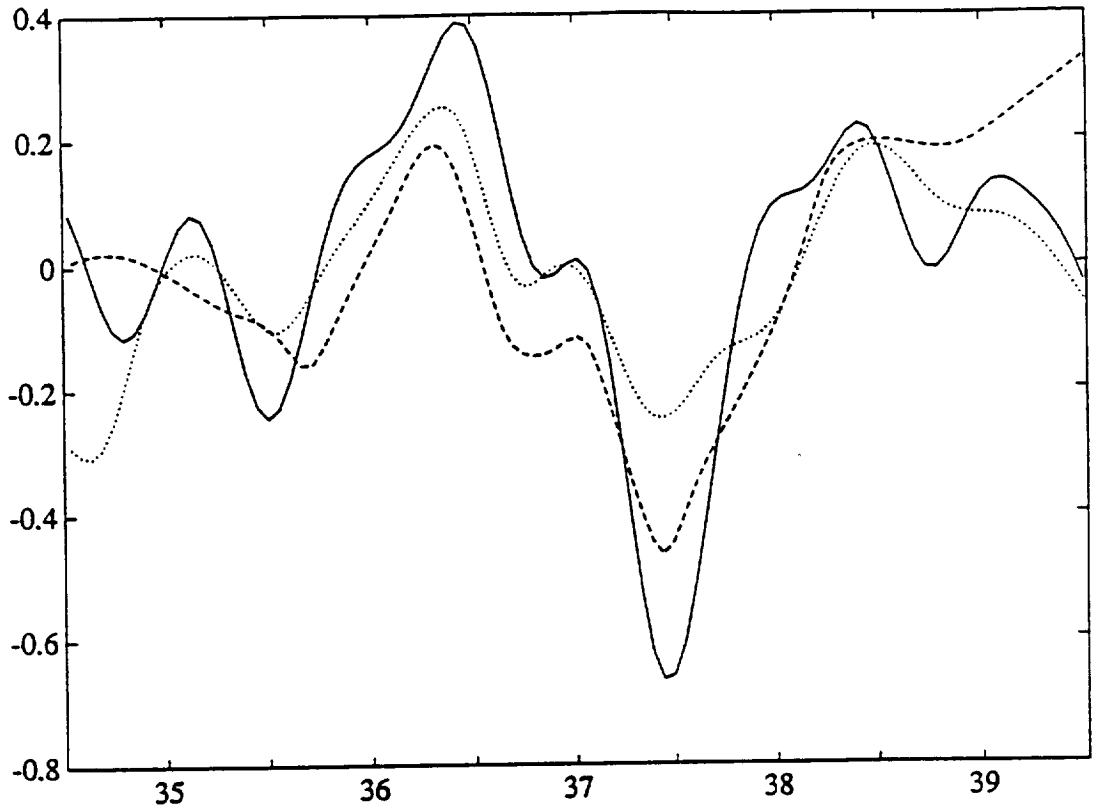

(b) day 200.25

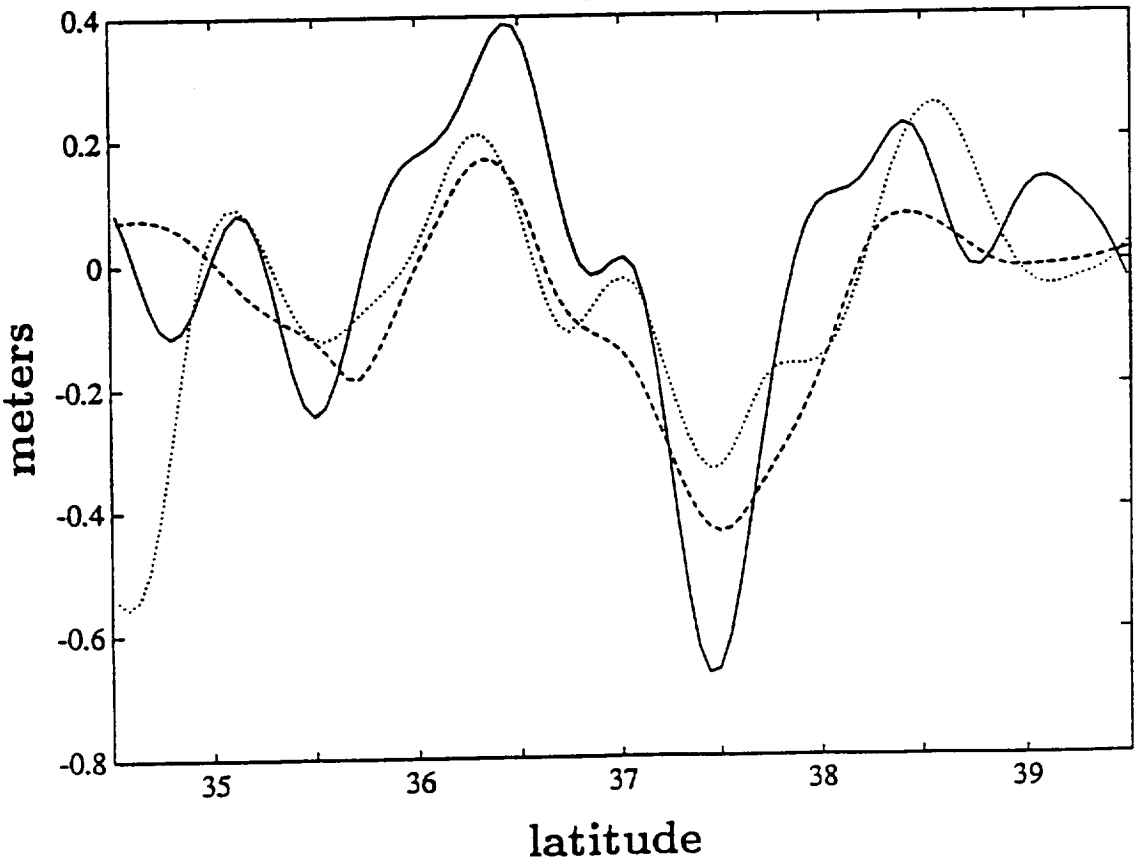

Fig. 6

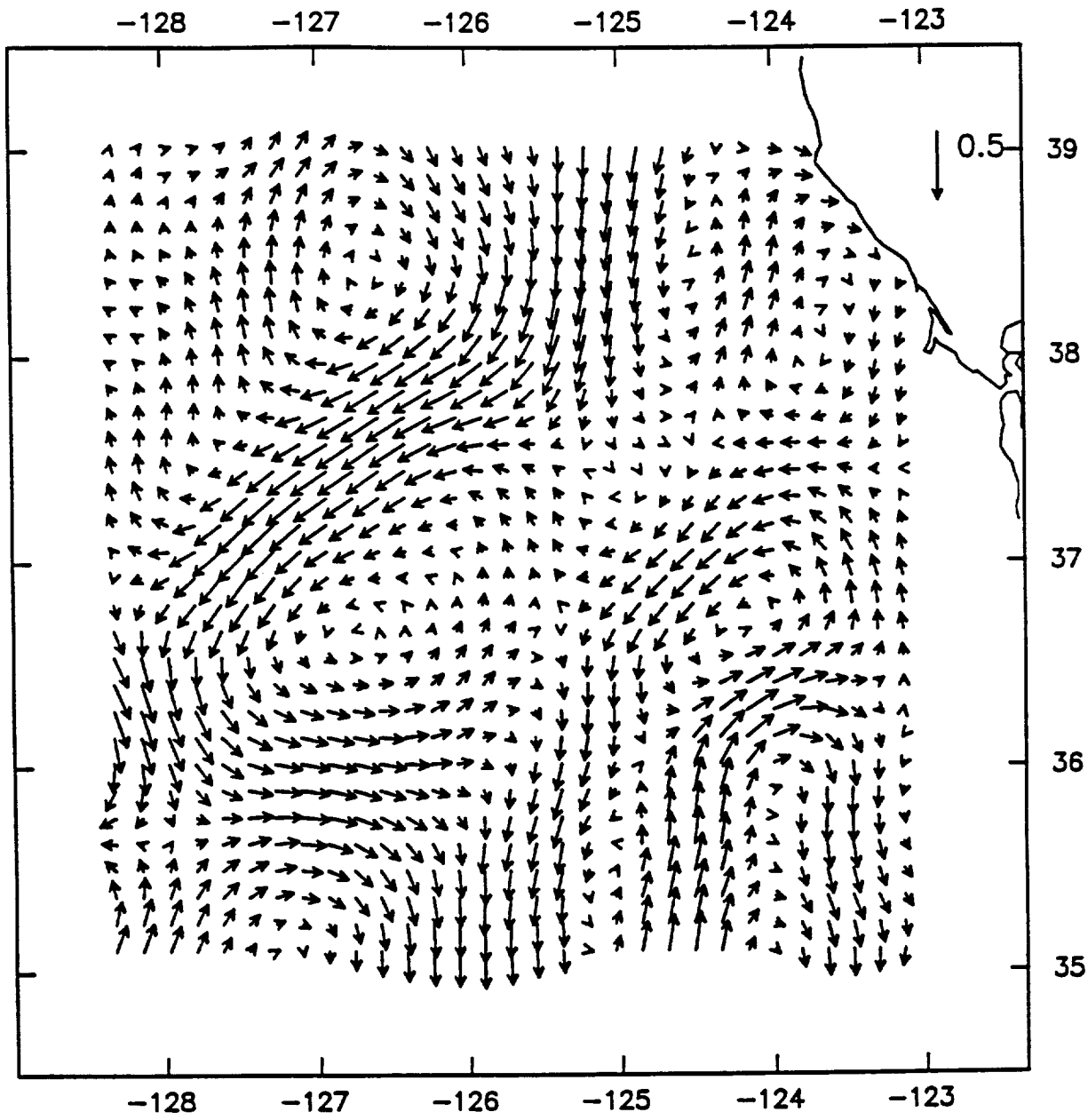

Fig 7a

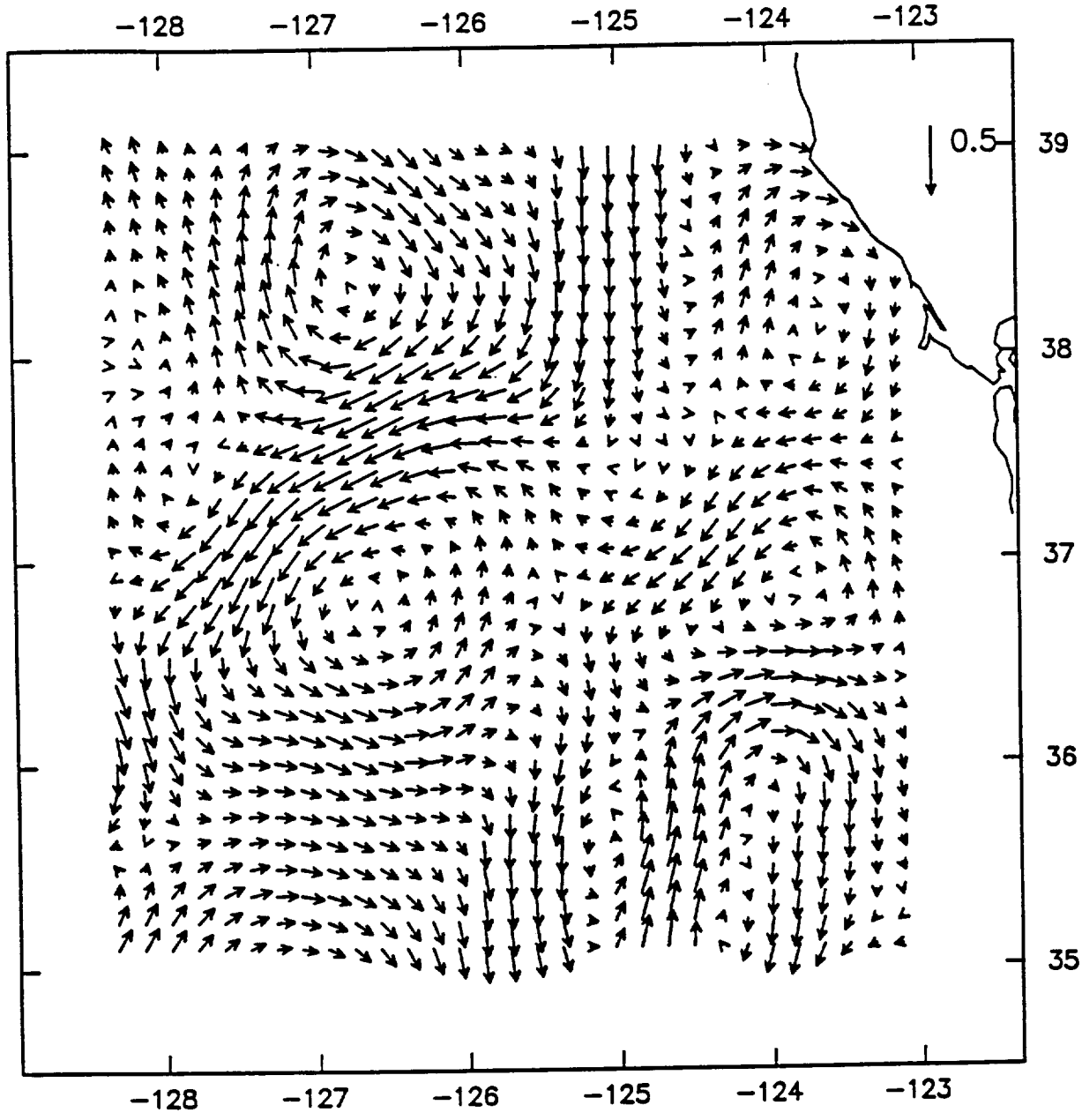

Fig 76

APPENDIX D

THE NATURE OF THE COLD FILAMENTS IN THE CALIFORNIA CURRENT SYSTEM

P. Ted Strub, P. Michael Kosro, and Adriana Huyer
and CTZ Collaborators

JOURNAL OF GEOPHYSICAL RESEARCH, VOL. 96, NO. C8, PAGES 14,743–14,768, AUGUST 15, 1991

The Nature of the Cold Filaments in the California Current System

P. TED STRUB, P. MICHAEL KOSRO, AND ADRIANA HUYER

College of Oceanography, Oregon State University, Corvallis

CTZ COLLABORATORS[1]

Data from the Coastal Transition Zone (CTZ) experiment are used to describe the velocity fields and water properties associated with cold filaments in the California Current. Combined with previous field surveys and satellite imagery, these show seasonal variability with maximum dynamic height ranges and velocities in summer and minimum values in late winter and early spring. North of Point Arena (between 39°N and 42°N) in spring–summer the flow field on the outer edge of the cold water has the character of a meandering jet, carrying fresh, nutrient-poor water from farther north on its offshore side and cold, salty, nutrient-rich water on its inshore side. At Point Arena in midsummer, the jet often flows offshore and continues south without meandering back onshore as strongly as it does farther north. The flow field south of Point Arena in summer takes on more of the character of a field of mesoscale eddies, although the meandering jet from the north continues to be identifiable. The conceptual model for the May–July period between 36°N and 42°N is thus of a surface jet that meanders through and interacts with a field of eddies; the eddies are more dominant south of 39°N, where the jet broadens and where multiple jets and filaments are often present. At the surface, the jet often separates biological communities and may appear as a barrier to cross-jet transport, especially north of Point Arena early in the season (March–May). However, phytoplankton pigment and nutrients are carried on the inshore flank of the jet, and pigment maxima are sometimes found in the core of the jet. The biological effect of the jet is to define a convoluted, 100 to 400-km-wide region next to the coast, within which much of the richer water is contained, and also to carry some of that richer water offshore in meanders along the outer edge of that region.

1. INTRODUCTION AND BACKGROUND

Several different velocity structures have been hypothesized to be associated with the cold filaments seen in satellite imagery from the California Current system and other eastern boundary currents [*Bernstein et al.*, 1977; *Traganza et al.*, 1983; *Flament et al.*, 1985; *Kelly*, 1985; *Shannon et al.*, 1985; *Johannessen et al.*, 1989]. The purpose of this paper is to summarize the evidence from the Coastal Transition Zone (CTZ) experiment and previous field studies with respect to the hypothesized velocity structures. The questions addressed are, (1) What is the spatial structure of the velocities and water properties associated with the filaments? (2) What is the temporal variability of that structure? (3) What are the biological implications of that structure and variability?

Three simplified conceptual models of the filaments are shown in Figure 1. "Squirts" are one-way jets, transporting coastally upwelled water to the deep ocean, perhaps terminating in a counterrotating vortex pair, with a shape in the sea surface temperature (SST) and pigment fields often referred to as "mushroom," "hammerhead," or "T" [*Ikeda and Emery*, 1984; *Davis*, 1985]. Onshore flow may occur in a broader and weaker return flow between the offshore squirts and/or in subsurface flow. The idealized squirt is generated by nearshore convergences, such as caused by local wind relaxations around capes [*Huyer and Kosro*, 1987; *Send et al.*, 1987] or other mechanisms [*Stern*, 1986]. The biological implication of this structure is that a large amount of enriched, salty, and cold coastally upwelled water (and biomass) is transported to the deep ocean.

An alternate conceptual model consists of a number of mesoscale eddies imbedded in a slow southward current [*Mooers and Robinson*, 1984; *Rienecker et al.*, 1987]. Where the eddies draw recently upwelled water away from the coast, they create a surface temperature structure similar to a squirt. The difference is that the pure squirt model envisions the generation by convergences in the nearshore region and the mesoscale eddy model envisions the offshore eddy field as the source of energy. The implication for nutrients and biomass is that offshore transport over long time periods should be accomplished by large-scale "eddy diffusion," i.e., quasi-random motions of parcels exchanged between eddies, parameterized by an eddy diffusivity that may vary with location and direction (alongshore versus offshore).

The third conceptual model consists of a continuous southward jet, meandering offshore and onshore. During

[1]C. James, L. J. Walstad, R. L. Smith, J. A. Barth, R. R. Hood, and M. R. Abbott, College of Oceanography, Oregon State University, Corvallis; K. H. Brink, Woods Hole Oceanographic Institution, Woods Hole, Massachusetts; T. L. Hayward, P. P. Niiler, and M. S. Swenson, Scripps Institution of Oceanography, La Jolla, California; R. K. Dewey, Science Applications International Corporation, Bellevue, Washington; F. Chavez, Monterey Bay Aquarium Research Institute, Pacific Grove, California; S. R. Ramp, M. L. Batteen, and R. L. Haney, Naval Postgraduate School, Monterey, California; D. L. Mackas, Institute of Ocean Sciences, Sidney, British Columbia; L. Washburn, University of California, Santa Barbara; D. C. Kadko, University of Miami, Miami, Florida; R. T. Barber, Duke University, Marine Laboratory, Beaufort, North Carolina; D. B. Haidvogel, Institute of Marine and Coastal Sciences, Rutgers University, New Brunswick, New Jersey.

Page number 91JC01024.
0148-0227/91/91JC-01024$05.00

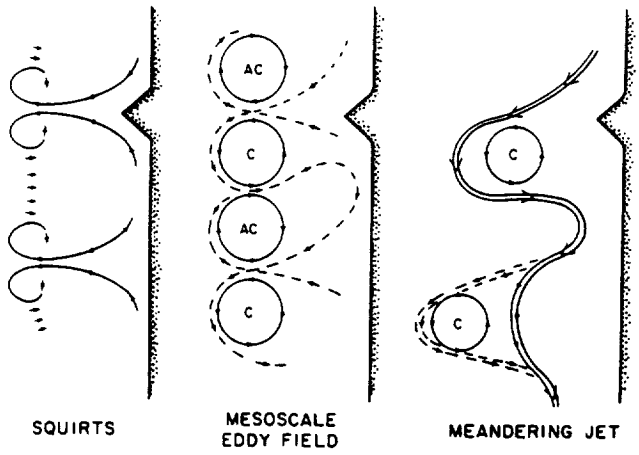

Fig. 1. The three simple conceptual models considered for the flow structure associated with the cold filaments.

its onshore excursions, it may entrain coastally upwelled water and create filaments of cold, rich water, which extend offshore on the next meander [*Coastal Transition Zone Group*, 1988]. Closed eddies may be created on either side of the jet by instabilities of the flow, but in the meandering jet model, the jet is the primary structure and source of energy. An important characteristic of the meandering jet is the presence of water in the core of the jet from far upstream, which would not be the case for squirts and would occur only haphazardly in a mesoscale eddy field. The biological implication of the meandering jet structure is that nutrients and biomass from the coastal ocean tend to remain on the inshore side of the jet.

The question is not whether the flow field associated with the cold filaments is always only a squirt, eddy, or meandering jet. We expect to find examples of each of these types of flow in a complex system such as the California Current. The question is whether there is a coherent pattern in the evolving mix of these regimes. The seasonal cycle is of special interest: if features in the velocity field appear for only part of the year, the primary structures may be indicated by the seasonal progression.

Previous observations have not resolved the large-scale synoptic structure of the currents well enough to differentiate between these models. The California Cooperative Oceanic Fisheries Investigations (CalCOFI) sampling was too coarse to define the filaments and seldom extended north of San Francisco. Long-term means based on the CalCOFI data off central California show a broad, meandering southward flow in summer [*Wyllie*, 1966; *Hickey*, 1979; *Lynn and Simpson*, 1987; *Chelton*, 1984], rather than the offshore-flowing jets that appear in more detailed surveys of the same area [*Chelton et al.*, 1988]. Off northern California, however, fields for April, July, and September [*Wyllie*, 1966; *Hickey*, 1979] show strong offshore flow near Point Arena (39°N) similar to features found in later studies. A finer-scale survey of the coastal ocean from 37°N to 43°N was made in May 1977 [*Freitag and Halpern*, 1981]. Although only the region within 100 km of the coast was surveyed, the dynamic height field shows a continuous jet, flowing from north of Cape Blanco to offshore-onshore jets south of Cape Mendocino, Point Arena, and Point Reyes.

More detailed measurements off northern California were made during the 1980s as part of the Coastal Ocean Dynamics Experiment (CODE) and the Ocean Prediction Through Observations, Modeling, and Analysis (OPTOMA) program. The CODE measurements in summer 1981–1982 were concentrated over the shelf, but two offshore surveys in July 1981 and July 1982 found strong offshore transports of cold water; the surveys did not cover a large enough area to determine whether a similar onshore flow occurred [*Flament et al.*, 1985; *Kosro and Huyer*, 1986]. During the OPTOMA program between 1982 and 1986, a large number of expendable bathythermograph (XBT) and conductivity-temperature-depth (CTD) surveys were made in a variable region extending 100–300 km offshore and alongshore off northern California with good seasonal coverage [*Rienecker and Mooers*, 1989*a*]. The surveys of the region farther offshore often have the appearance of a mesoscale eddy field, but midsummer fields from off Point Arena in 1984 and 1986 show a jet very much like that found in the July 1988 CTZ surveys [*Rienecker and Mooers*, 1989*a,b*]. South of the region sampled by the CTZ experiment, recurrent eddies have been documented by a number of studies [*Simpson et al.*, 1984, 1986; *Lynn and Simpson*, 1987].

2. The CTZ Experiment

The region of approximately 37.5°N–41.5°N was studied intensively in 1987 and 1988 [*Coastal Transition Zone Group*, 1988]. Hydrographic surveys of the region within 200 km of the coast were conducted in February, March, May, and June 1987 [*Kosro et al.*, this issue; *Hayward and Mantyla*, 1990; *Ramp et al.*, this issue; *Hood et al.*, 1990, this issue] and June–July 1988 [*Huyer et al.*, this issue; *Chavez et al.*, this issue; T.P. Stanton et al., Upper ocean response to a wind relaxation event in the coastal transition zone, submitted to Journal of Geophysical Research, 1990]. A fluorometer was mounted on the CTD to measure chlorophyll and related pigments on most cruises [*Schramm et al.*, 1988]. Repeated microstructure measurements were made on alongshore transects across filaments [*Dewey and Moum*, 1990; *Dewey et al.*, this issue]. Most of these surveys included continuous 300-kHz acoustic Doppler current profiler (ADCP) measurements, referenced using LORAN-C navigation data to produce absolute velocities in the upper 200 m [*Kosro et al.*, this issue]. Lagrangian measurements of the current structure were provided by surface drifters [*Paduan and Niiler*, 1990; *Brink et al.*, this issue; M.S. Swenson et al., Drifter observations of the dynamical and thermodynamical structures in a cold filament off Point Arena, California, in July 1988, submitted to Journal of Geophysical Research, 1990, hereinafter referred to as Swenson et al., submitted]. Sequences of satellite images were used to direct some of the field measurements and also to estimate surface currents by objective and subjective feature tracking [*Tokmakian et al.*, 1990]. Finally, numerical and laboratory models were used for process studies of coastal ocean circulation [*Haidvogel et al.*, this issue; *Allen et al.*, this issue; *Narimousa and Maxworthy*, 1989] and for hindcast studies using observations to provide the initial and boundary conditions for the model [*Walstad et al.*, this issue].

3. Results From the CTZ Experiments

3.1. *Large-Scale Seasonal Patterns in Wind and SST*

Wind forcing off northern California during 1987–1988 generally followed the normal seasonal cycle of mean

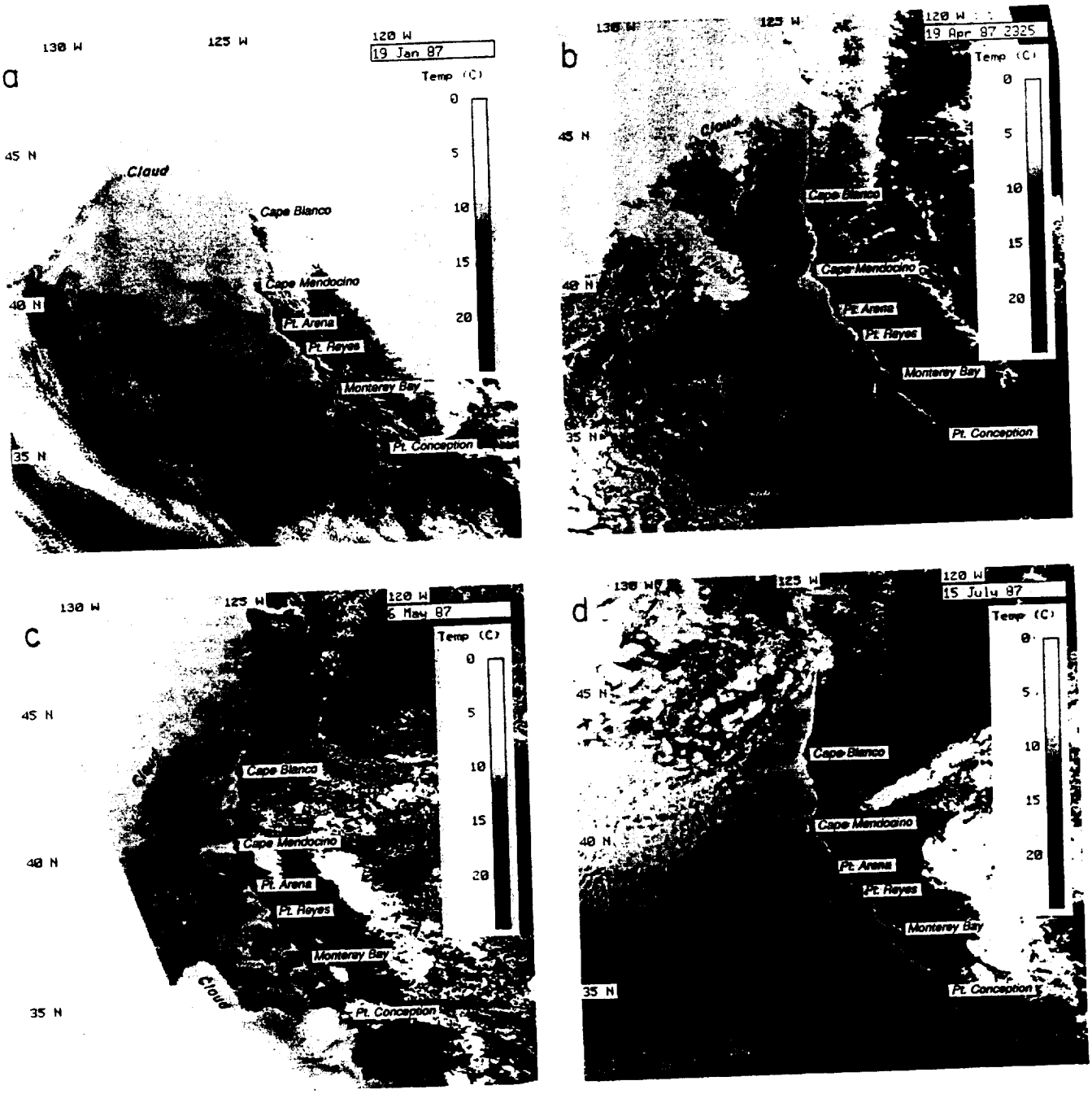

Fig. 2. Satellite SST images from the AVHRR sensor (note the changes in gray scale shading: (*a*) January 19, 1987; (*b*) April 19, 1987; (*c*) May 6, 1987; (*d*) July 15, 1987; (*e*) July 16, 1988; (*f*) October 18, 1987.

northward winds in winter and southward winds in spring–summer, with more variable winds in winter [*Hickey*, 1979; *Huyer*, 1983; *Strub et al.*, 1987*a*]. During the survey in February 1987, there was a period of strong southward winds for approximately 10 days, followed by a return to more northward winds, as is shown by *Kosro et al.* [this issue]. From mid-March to July 1987, winds were upwelling-favorable everywhere, with occasional relaxations and reversals. In 1988, winds were less upwelling-favorable north of Cape Mendocino until mid-June, after which winds were strongly upwelling-favorable everywhere, providing stronger and more persistent wind forcing off northern California from mid-June to mid-July 1988 than was experienced during the March–June 1987 field season.

An overview of the seasonal development of the cold filaments in 1987 and 1988 is provided by satellite SST fields over the large-scale California Current system (34°N–49°N). Six of these are shown in Figure 2. *Kosro et al.* [this issue] present a similar sequence with a greater number of images over a smaller region in 1987.

The image from January 19, 1987 (Figure 2*a*), is clear in the region south of 44°N and east of 128°W, where weak structure with large scales is evident in the offshore SST field. There are local regions of colder water near some capes, but no narrow filaments. Images from February 1987, shown by *Kosro et al.* [this issue], depict similar structure in early February, as well as a band of cold water next to the coast in late February (similar to the early

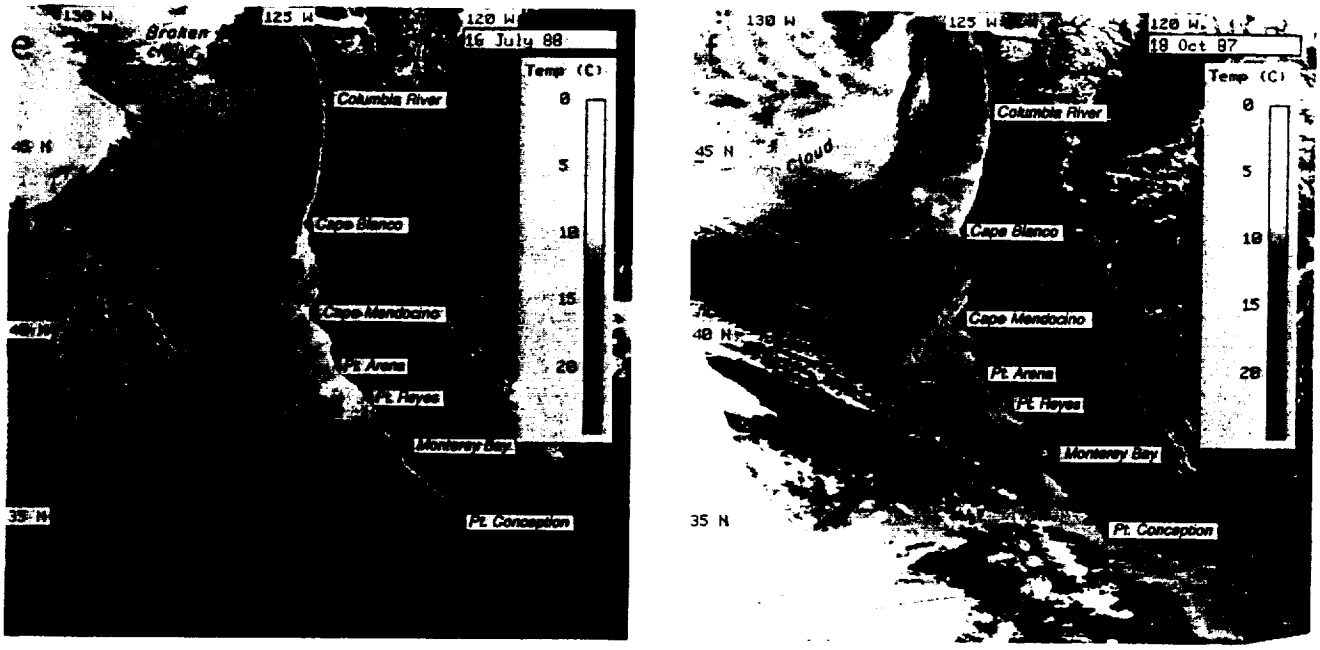

Fig. 2. (continued)

spring images in Figure 2*b*), which resulted from the period of strong southward winds in February. Images from March and April of both years are similar to the image from April 19, 1987 (Figure 2*b*), with colder water in a band within 100–150 km of the coast south of Cape Mendocino.

Images from May of both years are similar to that from May 6, 1987 (Figure 2*c*). Small (100 km), cyclonic filaments are found off Cape Blanco, Cape Mendocino, and Point Arena. These begin to develop in April (Figure 2*b*). Longer filaments extend from Point Reyes and from Point Sur (south of Monterey Bay). Features change fairly rapidly in May–June of these two years, both increasing and decreasing in length, as described in detail below.

By mid-July of both years (Figures 2*d* and 2*e*), filaments extend up to 300 km offshore from Cape Blanco, Cape Mendocino, and Point Arena. South of Point Arena in July 1988, there are several smaller filaments. North of Cape Blanco in May–July of both years, the region of colder temperatures narrows to the north and disappears near the mouth of the Columbia River (46.2°N), as in Figure 2*e*. Features north of Cape Blanco increase in size during the second half of summer and fall, as is demonstrated by the image from October 18, 1987 (Figure 2*f*), which shows longer filaments north and south of Cape Blanco. The scalloped edge of the region offshore of the cold water is suggestive of a line of anticyclonic eddies, as depicted by *Simpson et al.* [1986].

3.2. *Horizontal Fields of Velocity*

The relation between the horizontal velocity field and the filaments can be examined by comparing satellite images of SST with hydrographic fields and with tracks of surface drifters. Figure 3 shows the dynamic height anomaly fields relative to 500 dbar for four surveys in 1987, covering the period March–June 1987. These surveys are described in more detail by *Hayward and Mantyla* [1990] and by *Kosro et al.* [this issue], who show that results from a February survey are similar to those from the March survey. Satellite images (Figure 4) from the same region and period as the surveys show that filaments on the offshore edge of the cold water are associated with the inshore half of the jets, as was also noted by *Hood et al.* [1990] and *Kosro et al.* [this issue]. For example, in the May 18 image (Figure 4*b*), the coldest filament extends offshore at 40.3°N, 125°–126°W and is continuous with a wavy cool filament returning onshore between 40°N, 126°W and 39.5°N, 125°W. Figure 3*c* shows that the more northern filament lies within the southern half of an offshore-flowing jet centered at 40.6°N, 125.5°W, while the more southern filament is in the onshore-flowing jet centered at 39.8°N, 125.5°W. More detailed across-jet transects of surface velocity and temperature for this survey are presented by *Kosro et al.* [this issue].

If we interpret the cold filaments as showing the inshore side of a jet, the combination of satellite images and surveys shows the temporal development of a meandering jet in March–June 1987. The fields show a progression from a small dynamic height range (0.86–0.91 dyn m) in February–March to a large range (0.70–1.00 dyn m) and an alongshore jet with geostrophic velocities of 0.5–0.8 m s^{-1} in May and June. The alongshore jet was already present in mid-March, inshore of the CTZ survey, as was demonstrated by surface drifters which travelled from north of Cape Mendocino to near Point Arena at speeds of 0.1–0.6 m s^{-1} [*Magnell et al.*, 1990]. Interpretation of the April–May dynamic height field in Figure 3*b* is aided by ADCP surface velocities presented by *Hayward and Mantyla* [1990], which show a continuous jet flowing outside of closed eddies found southwest of Cape Mendocino and Point Arena. The May 5 SST field (Figure 4*a*) indicates that the jet meanders approximately 100–150 km offshore of Cape Mendocino.

By May 18, the meander off Cape Mendocino grows sharper and longer, extending 200–225 km offshore (Figure 4*b*). By June 1 (Figure 4*c*), the Cape Mendocino meander has smoothed out and extends only 150 km offshore, while the meander off Point Arena (39°N) has begun to grow. The increasing offshore transport in the cool feature at 39°N (Figure 4*c*) was documented by ADCP data along

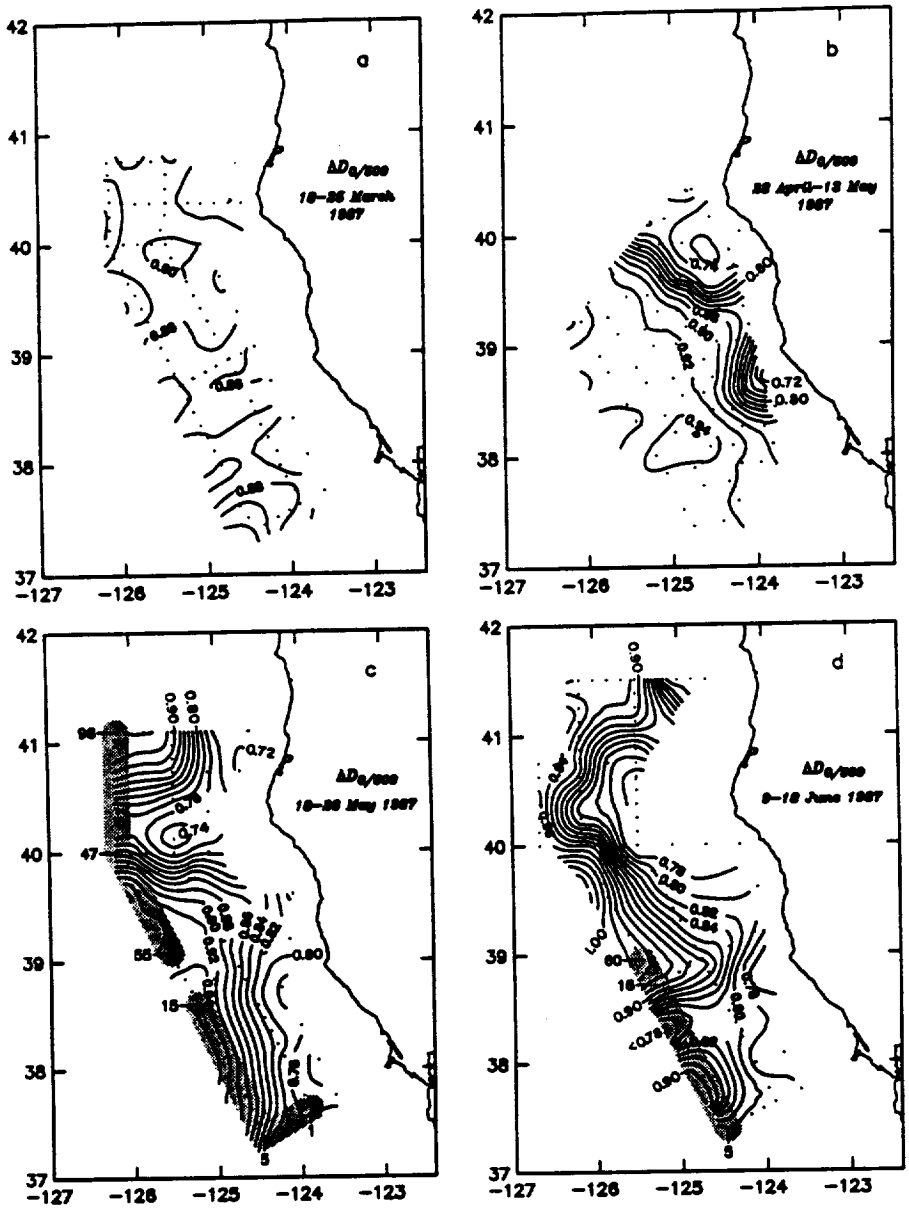

Fig. 3. Fields of dynamic height anomaly relative to 500 dbar from four cruises in 1987 (negative longitudes denote west longitude; contour interval is 0.02 dyn m): (*a*) March 18–25; (*b*) April 28 to May 13; (*c*) May 18–26; (*d*) June 9–18. The shading in Figures 3c and 3*d* indicates the location of transects shown in Figure 8.

north-south transects along 125°W (white line in Figure 4*c* [*Dewey and Moum*, 1990]); these show that westward transport in the upper 150 m increased from 2.1 Sv to 3.6 Sv during June 2–5. This could be interpreted as (1) a growing squirt, (2) the northern side of a growing meander, directing more flow into the component normal to the transect, or (3) an eddy that is spinning up. A dynamical interpolation of the flow field between the late May and mid-June surveys, using a quasi-geostrophic (QG) model [*Walstad et al.*, this issue], supports the interpretation of the growing meander. By June 10 (Figure 4*d*) the cool feature off Point Arena extends 200 km offshore to 126°W. The June 10 and 16 (Figure 4*e*) images show cold water being carried offshore and onshore in meanders off Cape Mendocino (39.5°–41°N) and Point Arena (38°–39°N) and offshore to the southwest again south of 38°N, as confirmed by the June 9–18 survey (Figure 3*d*).

Another aspect of the surface flow field is revealed by the tracks of surface drifters drogued at 15 m. Six drifters, released between May 18 and 20, 1987, near 38.1°N, 123.8°W, went north around a small cyclonic eddy off Point Arena that was not resolved by the dynamic height field in Figure 3*c*, and three others went southwest (Figure 5*a*, see also *Paduan and Niiler* [1990, Figure 2*c*]). This closed eddy was resolved in the ADCP data presented by *Kosro et al.* [this issue] (see also Figure 16*a* below). Tracks of similar drifters released on June 17–27 near 38.5°N, 124°W (Figure 5*b*), indicate that the offshore end of the meander between 38°N and 38.5°N (partially resolved by the survey in Figure 3*d*) is near 126°W. These also show that the offshore flow southwest of Point Reyes at 37.5°N, 124.6°W (Figure 3*d*), is the northern side of another meander that extends southwest to 36°N, 126°W. A comparison of Figures 5*a* and 5*b* shows the increase of the offshore extent of the meanders in the jet from 125°W to 126°W during the month between drifter surveys. In Figure 5*b* the drifters from the earlier deployment are seen south of 37°N, circulating slowly inshore of the jet.

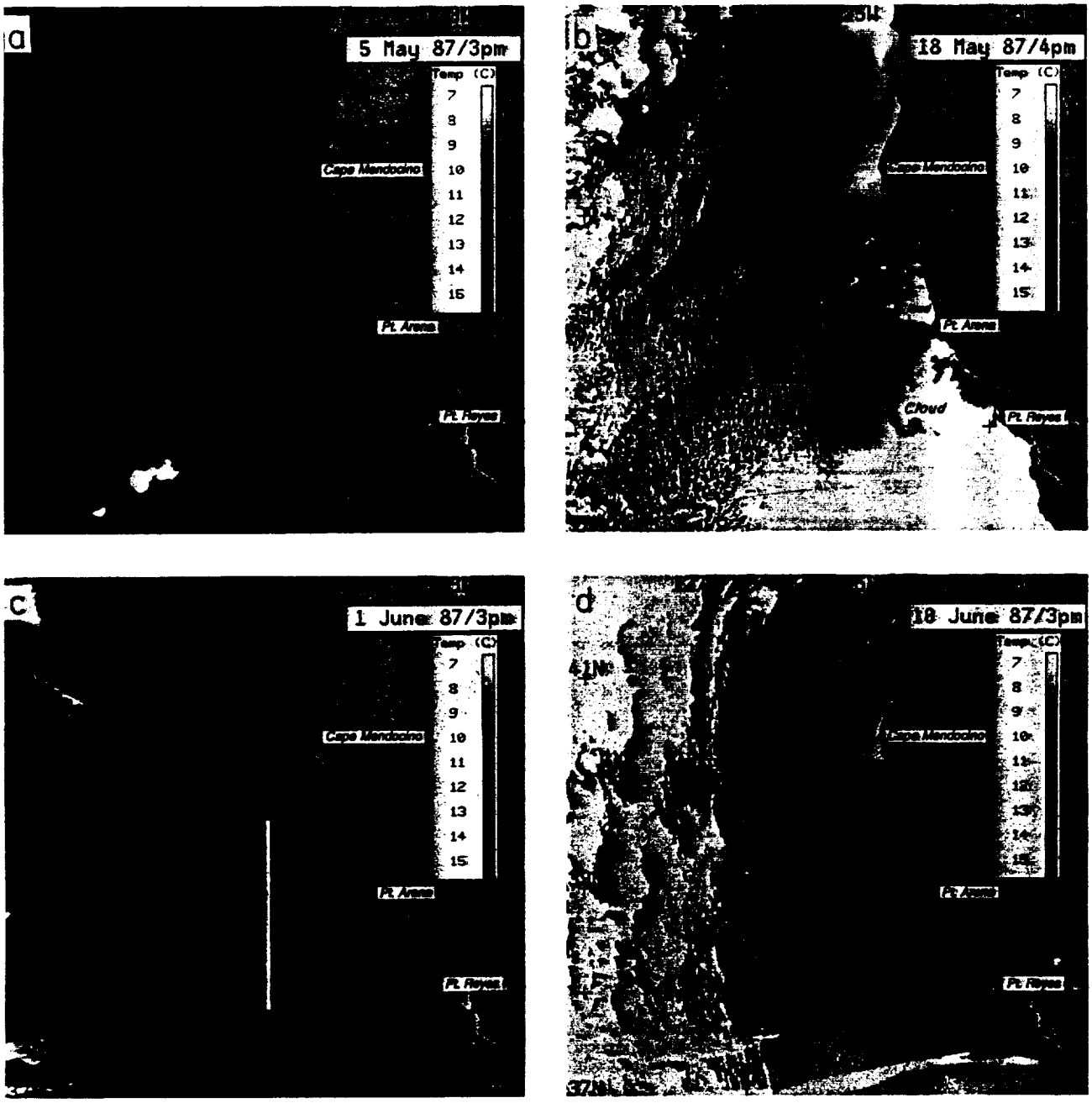

Fig. 4. Satellite SST images: (*a*) May 5, 1987; (*b*) May 18, 1987; (*c*) June 1, 1987 (the white line shows the transect sampled on June 2–5, 1987); (*d*) June 10, 1987; (*e*) June 16, 1987.

The surveys in 1987 did not extend past June, but the July 15, 1987, satellite image (Figure 2*d*) indicates that by mid-July the meander around Cape Mendocino extends again to approximately 40°N, 127°W, and curves back onshore south of Cape Mendocino and then offshore in a large filament extending southwest from Point Arena to approximately 38°N, 127°W. This long, offshore cold filament at 38°N presumably shows the cold water on the inside of the meander at 38°N, which has grown since it was sampled by the drifters in mid-June (Figure 5*b*). It is similar to the feature sampled from June 20 to August 4, 1988 (Figure 2*e*). It is also similar to features seen in July images from most other years and sampled by hydrography in 1981, 1982, 1984, and 1986 (discussed below). Thus we take the 1988 surveys (of a smaller area southwest of Point Arena) to represent a continuation of the general seasonal progression seen in the 1987 surveys.

Figure 6 shows fields of the dynamic height anomaly relative to 500 dbar from three cruises in 1988. The field from July 6–12 in Figure 6*a* is similar to the fields from surveys on June 20–27 and July 13–18, 1988 (see [*Huyer et al.*, this issue] for all five surveys). The primary feature during this month-long period was a fairly stationary jet flowing to the southwest from nearshore just north of Point Arena. *Huyer et al.* [this issue] show that the colder water of the filament lies on the southern half of the offshore jet. Smaller eddies of both signs are present in the slow moving water to the southeast of the jet, and there is an indication of return onshore flow south of the jet. The orientation of the jet in the survey region became

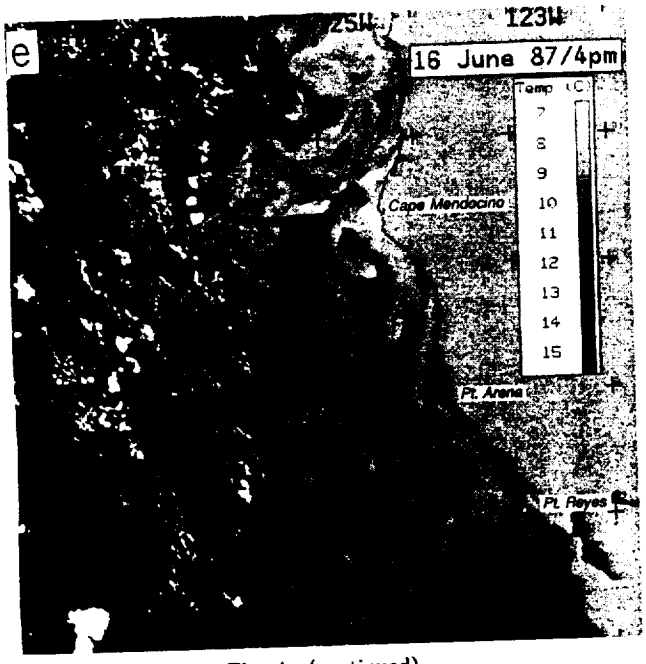

Fig. 4. (continued)

more nearly southward after July 21 (Figure 6*b*), and the jet broadened and weakened by the time of the last survey at the beginning of August (Figure 6*c*).

Surface drifters [*Brink et al.*, this issue; Swenson et al., submitted] from selected periods in June–August 1988 are shown superimposed on satellite images from the same periods in Figure 7. A drifter (labeled R), placed in a filament off Point Reyes at the end of June (Figure 7*a*), followed the filament offshore, circled cyclonically, and then proceeded southward, where it was entrained into a large anticyclonic eddy centered near 124.0°W and 35.7°N, which appears as warm water in the satellite images; it remained in this eddy throughout the end of July (Figure 7*c*). The rest of the drifters (labeled A) were released in the filament off Point Arena (Figure 7*a*). At the end of this filament, most of the drifters turned cyclonically around a "terminal eddy" (labeled E in Figure 7*b*). Some then were carried south in a continuation of the Point Arena jet (labeled A), some became entrained in the terminal eddy, and some leaked off to the northwest (labeled W). Some of the drifters never reached the terminal eddy, but left the jet on its southern side and returned onshore (labeled O). These circled cyclonically off Point Arena (Figure 7*c*) and rejoined the offshore jet.

Near the end of July (Figure 7*c*), the terminal eddy became somewhat cut off from the now more southward jet; some drifters (labeled S) continued south without ever passing around the terminal eddy and meandered back onshore on the north side of the anticyclonic eddy identified by the Point Reyes drifter (R). A month later (Figure 7*d*), the drifter paths show that the terminal eddy had moved to 36.7°N, 127.5°W, approximately 70 km west of its position in late July. Although partially covered by clouds, the drifters show that the anticyclonic eddy at 35.5°N, 123.7°W is near its original location, and they suggest another anticyclonic eddy near 34.5°N, 127.5°W. Southward flow is still found south of the terminal eddy, i.e., south of 36°N between 125°W and 127°W.

Several drifters from the 1988 deployment left the jet and travelled westward as far as 134°W at latitudes between 30°N and 39°N, without encountering another southward jet. Thus the observed jet off Point Arena at 39°N was not one of several similar offshore branches; it was the only such jet at that location and time, although there may have been other jets farther inshore over the shelf and slope. South of Point Arena, multiple cool filaments and drifter

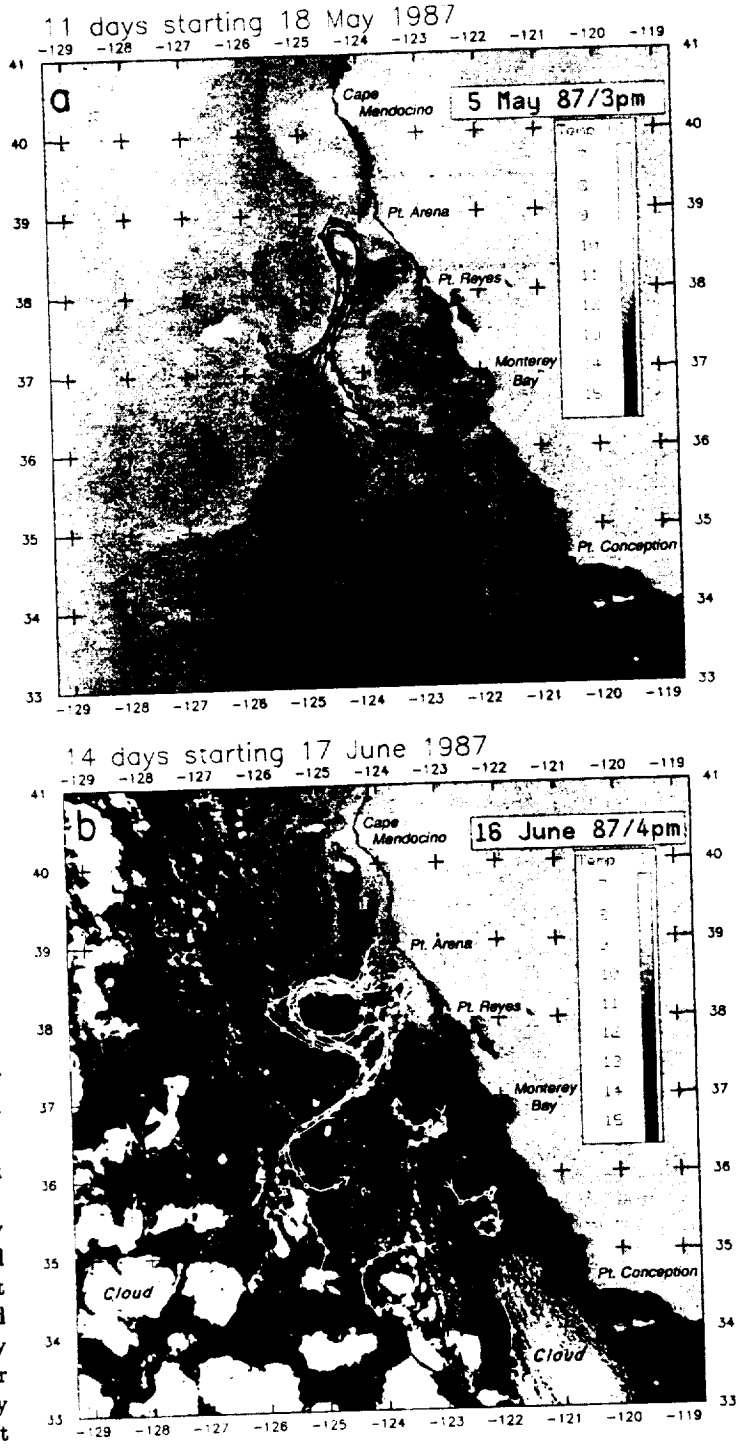

Fig. 5. Surface (15 m) drifter tracks (circles denote 24-hour positions): (*a*) 11-day tracks for drifters released during May 18–20, 1987, overlaid on the satellite SST image from May 5, 1987 (the closest image that was clear over a large area) (circles denote 24-hour positions); and (*b*) 14-day drifter tracks for surface drifters released during June 17–27, 1987, as well as the earlier drifters still in the area, overlaid on the satellite SST image from June 16, 1987.

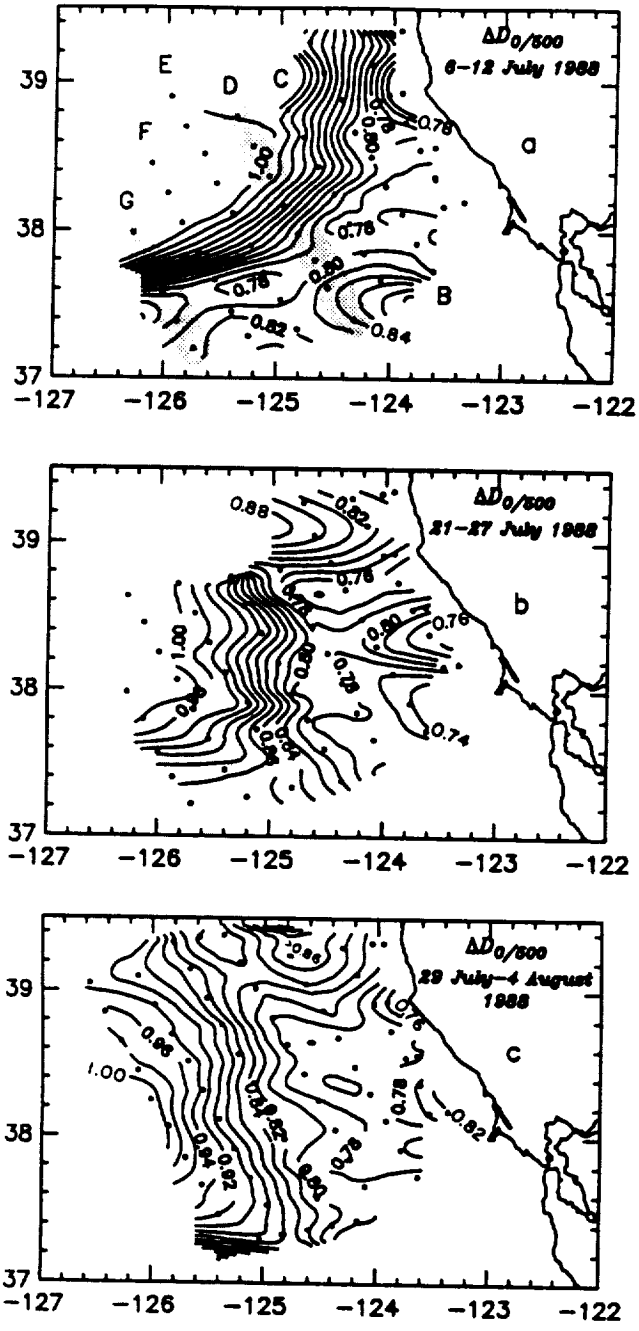

Fig. 6. Fields of dynamic height anomaly relative to 500 dbar from three surveys in 1988 (contour interval is 0.02 dyn m): (*a*) July 6–12; (*b*) July 21–27; (*c*) July 29 to August 4. The shading and letters indicate sections shown in Figure 9.

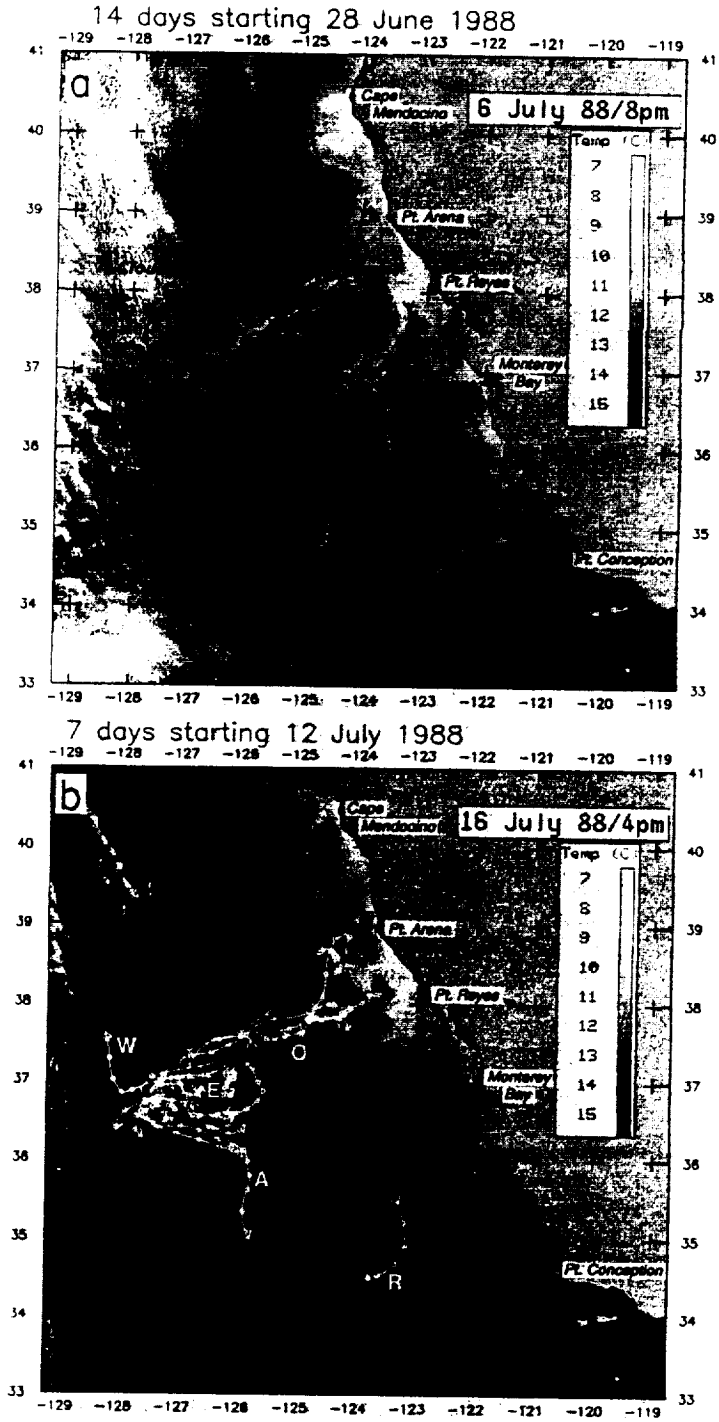

Fig. 7. Surface (15 m) drifter tracks (circles denote 24-hour positions): (*a*) 14-day tracks of drifters starting June 28, 1988, overlaid on the satellite SST image from July 6, 1988; (*b*) 7-day tracks of drifters starting July 12, overlaid on the satellite SST image from July 16; (*c*) 7-day tracks of drifters starting July 25, overlaid on the satellite SST image from July 28; (*d*) 7-day tracks of surface drifters starting August 27, overlaid on the satellite SST image from August 30.

paths inshore of the jet indicate that the transport is not contained in a single jet. Statistical analysis of the drifter motion suggests that the flow south of Point Arena can be characterized by an approximately equal combination of mean southward flow (0.5 m s^{-1}) and an eddy diffusivity that is stronger in the offshore direction (5–8 x 10^3 m^2 s^{-1}) than in the alongshore direction (2–5 x 10^3 m^2 s^{-1}) [*Brink et al.*, this issue].

3.3. *Relation of Velocities to Water Properties*

Examination of the spatial relation between the velocities and the water properties (temperature T, salinity S, nutrients, and biomass) allows us to address two questions:

(1) What is being transported alongshore and offshore at a given location; i.e., are the jets conveyers or barriers for offshore transport?; (2) What are the upstream sources of the water in the jet, as compared with those inshore and offshore of the jet; i.e., are the jets continuous over extensive alongshore distances?

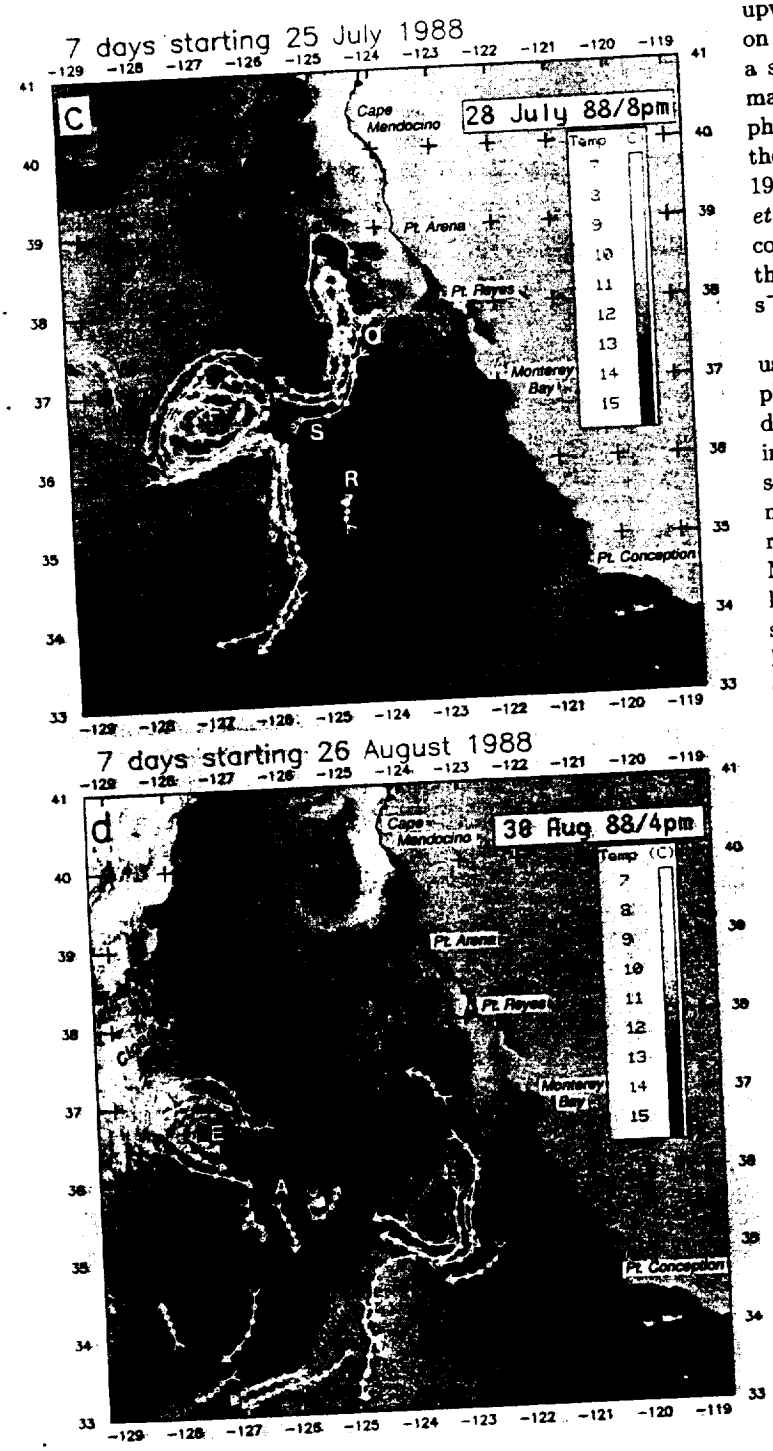

Fig. 7. (continued)

3.3.1. *Surface properties and across-jet sections.* The view that the jets associated with the filaments act as barriers, trapping the colder and richer upwelled water on their inshore side, is most consistent with the surface fields. In early May 1987 (Figure 3*b*), *Hayward and Mantyla* [1990] found a minimum of salinity in a fresh tongue of surface water on the offshore side of the jet. The same pattern was found in a patchy manner in the later 1987 cruises [*Kosro et al.*, this issue] and was consistently found in the jet off Point Arena in June–July 1988 [*Huyer et al.*, this issue]. Thus the outer part of the jets found off Cape Mendocino and Point Arena does not consist of recently upwelled water. A temperature minimum was often found on the inshore half of the jet, sometimes coincident with a salinity maximum and sometimes closer to the velocity maximum than the salinity maximum. Surface nitrate and phytoplankton pigment were highest on the inshore side of the maximum velocities in the jet [*Hayward and Mantyla*, 1990; *Kosro et al.*, this issue; *Hood et al.*, this issue; *Chavez et al.*, this issue], although relatively high values of pigment concentrations (1.0–8.0 mg m^{-3}) occurred in regions on the inshore side of the jet where velocities were 0.2–0.5 m s^{-1} [*Hayward and Mantyla*, 1990; *Hood et al.*, 1990].

Like the surface fields, vertical sections across the jet usually show the highest concentrations of nitrate and phytoplankton pigment inshore of the jet, but they also demonstrate that moderately high values of pigment extend into the inshore flank of the jet and that pigment maxima sometimes appear directly in, or even offshore of, the maximum velocities in the jet. Examples of these different relationships can be seen in vertical sections from the late May 1987 cruise (Figures 8*a* and 8*b*). The sections are located along the southern and offshore boundaries of the survey (Figure 3*c*). In Figure 8*a*, stations 1–5 form a line extending offshore (roughly east-west) and stations 6–15 extend roughly north-south, along the southern part of the farthest offshore line (approximately 150 km from the coast). The vertical line in Figure 8*a* divides the offshore and alongshore sections. The viewer is effectively looking offshore toward the southwest corner of the survey. Figure 8*b* shows the northern part of the same offshore boundary, where it cuts across the sharp meander off Cape Mendocino (Figure 3*c*). The viewer is looking offshore. The ADCP velocities at the top of the figures are the components normal to the sections, defined positive poleward and shoreward.

Along the southern boundary (Figure 8*a*, sampled on May 18–19), water flows out of the survey region to the southwest along a strong salinity gradient, with coldest temperatures (<12°C) and highest pigment concentrations (>1.5 mg m^{-3}) directly in the core of the jet (we note again that the pigment concentrations used in the present paper are derived from fluorometer measurements, as described by *Schramm et al.* [1988]). Station 5 is near 37.4°N, 124.5°W, where a cold filament can be seen in the June 1 satellite image of Figure 4*c*. On the northern half of the meander off Cape Mendocino (Figure 8*b*, sampled on May 23–26), the strongest offshore velocity (0.5 m s^{-1} at station 91) is in a strong gradient of salinity (32.75–33.25 psu) and in the coldest water (<12°C) on the northern side of the domed structure. The onshore jet is on the southern side of the domed structure in water where surface salinity is less than 33.0 psu (with patches less than 32.75 psu) and the temperature has a strong horizontal gradient. The narrow temperature minimum at station 88 is near 40°N, 126°W, where the wavy cold filament in Figures 4*b* and 4*c* flows back onshore toward the southeast, after curving cyclonically around the end of the meander. A phytoplankton pigment maximum (>2.0 mg m^{-3}) straddles the offshore velocity maximum in the upper 50 m, with local maxima north (offshore) of the offshore-flowing jet (station 93) and on the inshore sides of the velocity maxima (stations 88 and 90). The pigment maxima are between 20 and 30 m deep. Thus regions of maximum biomass (1.5–3.0 mg m^{-3}) appear inshore, within and offshore of the jet 150

km from the coast (Figure 8*b*) in a meander that extends approximately 225 km offshore of Cape Mendocino, before continuing within the jet out of the southwest corner of the survey region off Point Reyes (Figure 8*a*).

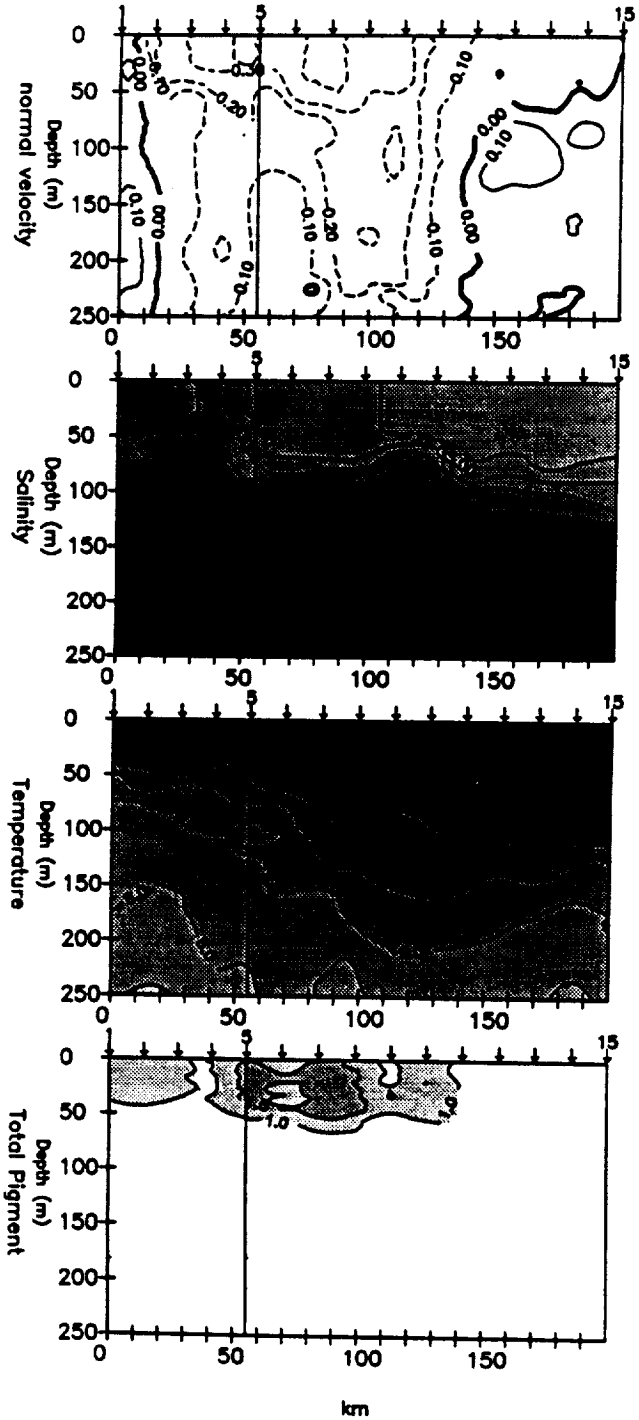

Fig. 8*a*. Sections of (top to bottom) ADCP velocity, salinity, temperature and total pigment concentration (derived from the fluorometer) along the southwest border of the survey on May 18-19, 1987. Stations 1–5 form a cross-shelf transect, and stations 5–15 form an alongshore transect, with the viewer looking toward the south and offshore (see Figure 3 for transect locations). The velocity is the component normal to the transects, defined to be positive poleward and shoreward. Contour intervals are 0.1 m s^{-1}, 0.25 psu, 1.0°C, and 0.5 mg m^{-3} for velocity, salinity, temperature, and pigment concentration, respectively. Pigment concentrations below 1.0 mg m^{-3} appear light with no contours, and pigment concentrations above 4.5 mg m^{-3} appear black with no contours.

Figure 8*c* presents a similar north-south section along the southern half of the offshore boundary during the June 1987 survey. These data were collected mostly on June 10 and can be compared closely with the satellite image in Figure 4*d*. The more northern offshore flow (0.6 m s^{-1} at station 15) is near 38.6°N, 125.25°W, and the onshore flow of 0.3 m s^{-1} in the middle of the section (station 11) is near 38.1°N, 124.9°W. There is a narrow temperature minimum in the left flank of the offshore flow and generally cold water between the offshore and onshore velocity maxima, adding strength to the interpretation of a meandering jet along the outer edge of the cold water in the satellite image. The drifter tracks in Figure 5*b* begin a week later and show this offshore-onshore meander to have moved slightly

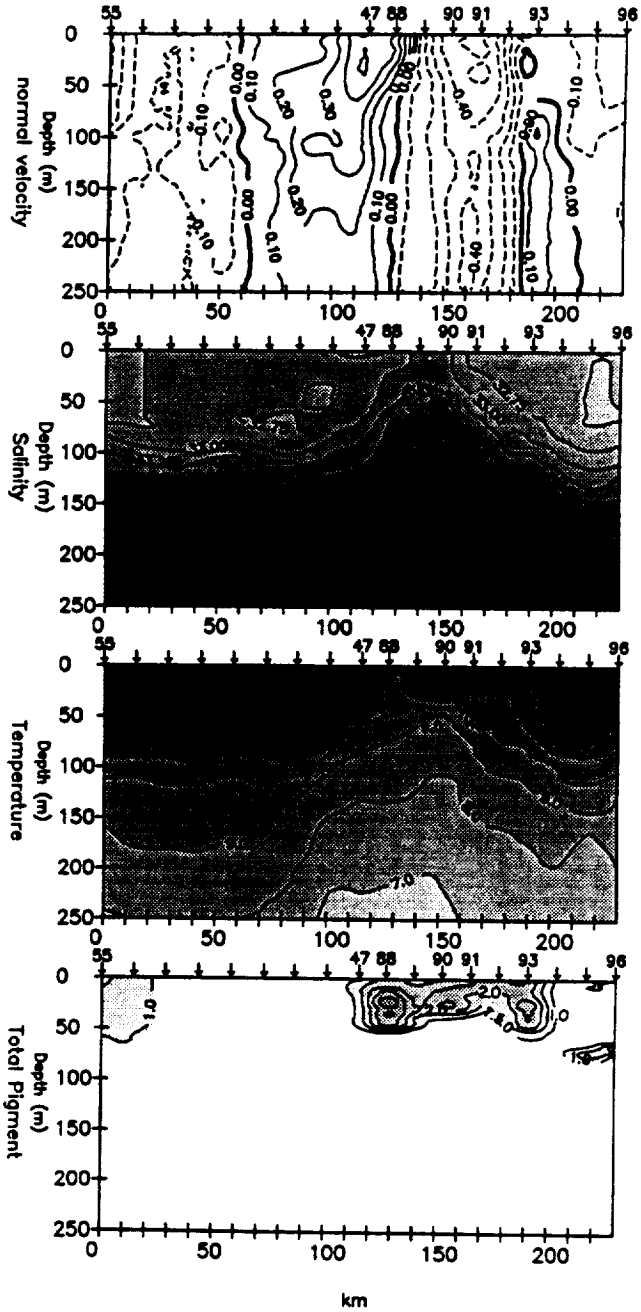

Fig. 8*b*. As in Figure 8*a* for a section along the northwest border of the survey on May 23–26, 1987. Stations 55–96 form an alongshore transect along the line farthest from shore (see Fig. 3), with the viewer looking offshore. The velocity is the component normal to the transects, defined to be positive shoreward.

south in that time. The northern half of this meander corresponds to the feature that grew off Point Arena in early June [*Dewey and Moum*, 1990]. Temperature and salinity show a domed structure similar to that found in the center of the meander off Cape Mendocino in May. Higher phytoplankton pigment concentrations (>1.5 mg m^{-3}) occur inshore of the velocity maxima in regions where the water is moving offshore at up to 0.5 m^{-1} and onshore at up to 0.3 m s^{-1}. The highest pigment concentrations (>4.0 mg m^{-3}) occur south of the more

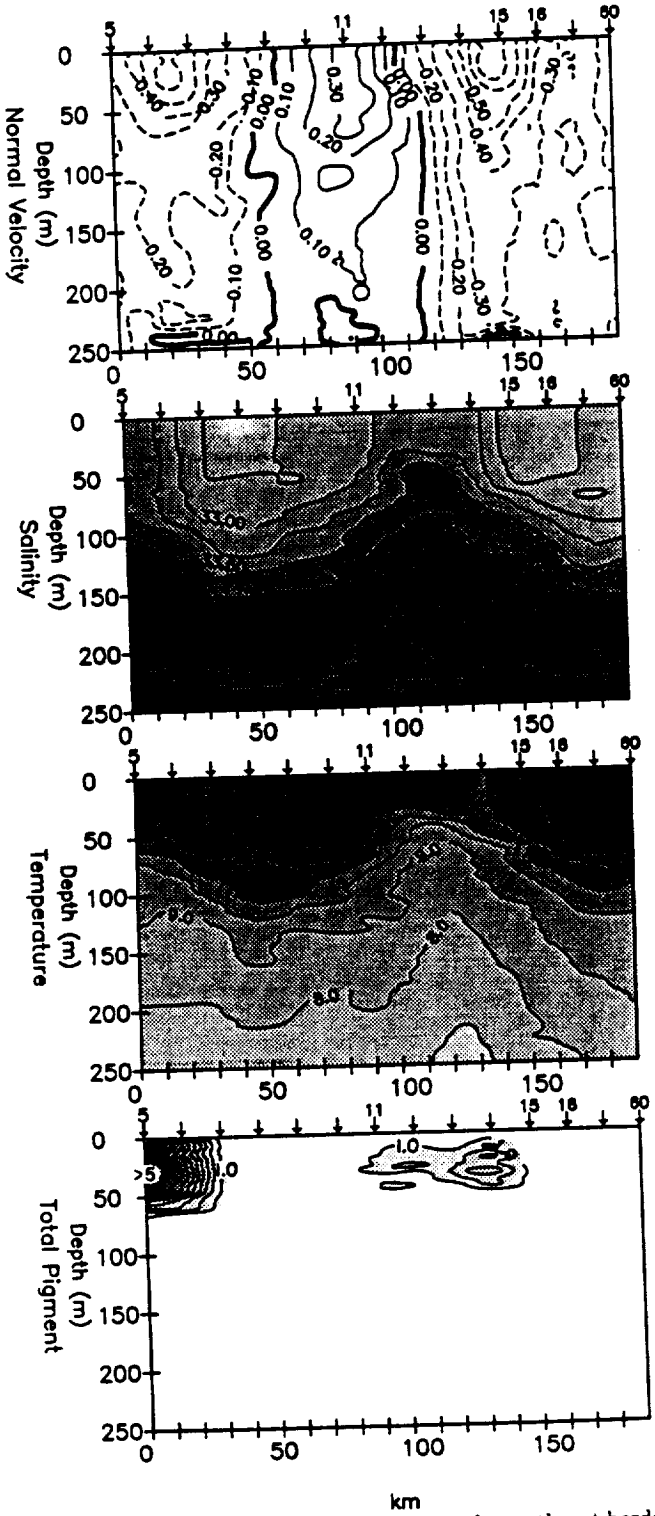

Fig. 8c. As in Figure 8a for a section along the southwest border of the survey on June 10, 1987 (see Figure 3).

southern offshore-flowing jet (stations 5–6, near 37.3°N, 124.5°W), in a region where velocities are greater than 0.3 m s^{-1}. Drifter paths show this to be the inshore region of another meander (Figure 5*b*).

During the repeated surveys of the jet flowing southwest from Point Arena in June–July 1988, the surface fields have features similar to those found in the offshore-flowing northern half of the meanders off Cape Mendocino and Point Arena in the 1987 surveys. A tongue of fresh water is found on the jet's offshore (northern) side, while cold, salty water is found inshore (south) of the jet [*Huyer et al.*, this issue] and the jet lies on the offshore (northern) side of the surface pigment and nitrate gradients [*Chavez et al.*, this issue]. Two across-jet (roughly north-south) transects of onshore velocity, temperature, salinity, nitrate, and total pigment from the July 6–12 survey are presented in Figures 9*a* and 9*b* (see Figure 6*a* for transect locations). As in Figure 8, the viewer is looking offshore and the ADCP velocity is the component normal to the transect, defined positive onshore. These illustrate the distribution of the variables across the jet at distances of approximately 150 km (Figure 9*a*, line D) and 275 km (Figure 9*b*, line G) from the coast, during a period when the jet's position was fairly stationary.

The transects show an irregular domed structure in T, S, and nitrate between the offshore-flowing jet in the north and the weak onshore flow in the south of the transects. The structures are not symmetric about the jet; the velocities and horizontal gradients are weaker to the south. Fresh surface water (<32.75 psu) is found in the northern half of the offshore-flowing jet. Along line D (Figure 9*a*), there is a narrow temperature minimum and nitrate maximum at station 133 (38.0°N, 124.8°W) on the southern side of the offshore jet, where velocities normal to the transect are 0.3–0.4 m s^{-1}. This is also the location of maximum pigment concentrations and the location of a cold filament in the satellite images from July 12 and 16 and drifter tracks in Figures 7*a* and 7*b*. The dome of high salinity appears displaced to the south of the narrow temperature minimum, at the location of zero velocity. Patterns similar to line D were found as far offshore as line F (two transects farther offshore). Farther offshore along line G, the salinity maximum is on the southern side of the offshore-flowing jet, more like the temperature minimum at line D. The minimum of temperature and the maxima of nitrate and pigment are broader, stretching from the southern side of the offshore flow into the northern side of the onshore flow. A shallow salinity minimum is found in the onshore flow at line G. These same patterns were generally found on transects from the June 20–27 and July 13–18 surveys, with the exception that during the July 13–18 survey, minimum surface temperatures increased and maximum pigment concentrations decreased, even though nitrate values remained high.

Repeated sampling (approximately 15 transects) along line D from July 2 to July 16 confirm the picture presented above, with respect to surface variables, with much greater (1 km) spatial resolution [*Dewey et al.*, this issue]. After aligning all 15 of the transects on the density front and averaging over all of the transects, one finds the following qualitative picture, proceeding from south to north: (1) a wide local maximum in salinity where the shallowest (15 m) offshore ADCP velocity is zero, 25 km south of the front; (2) a narrower minimum in temperature north of

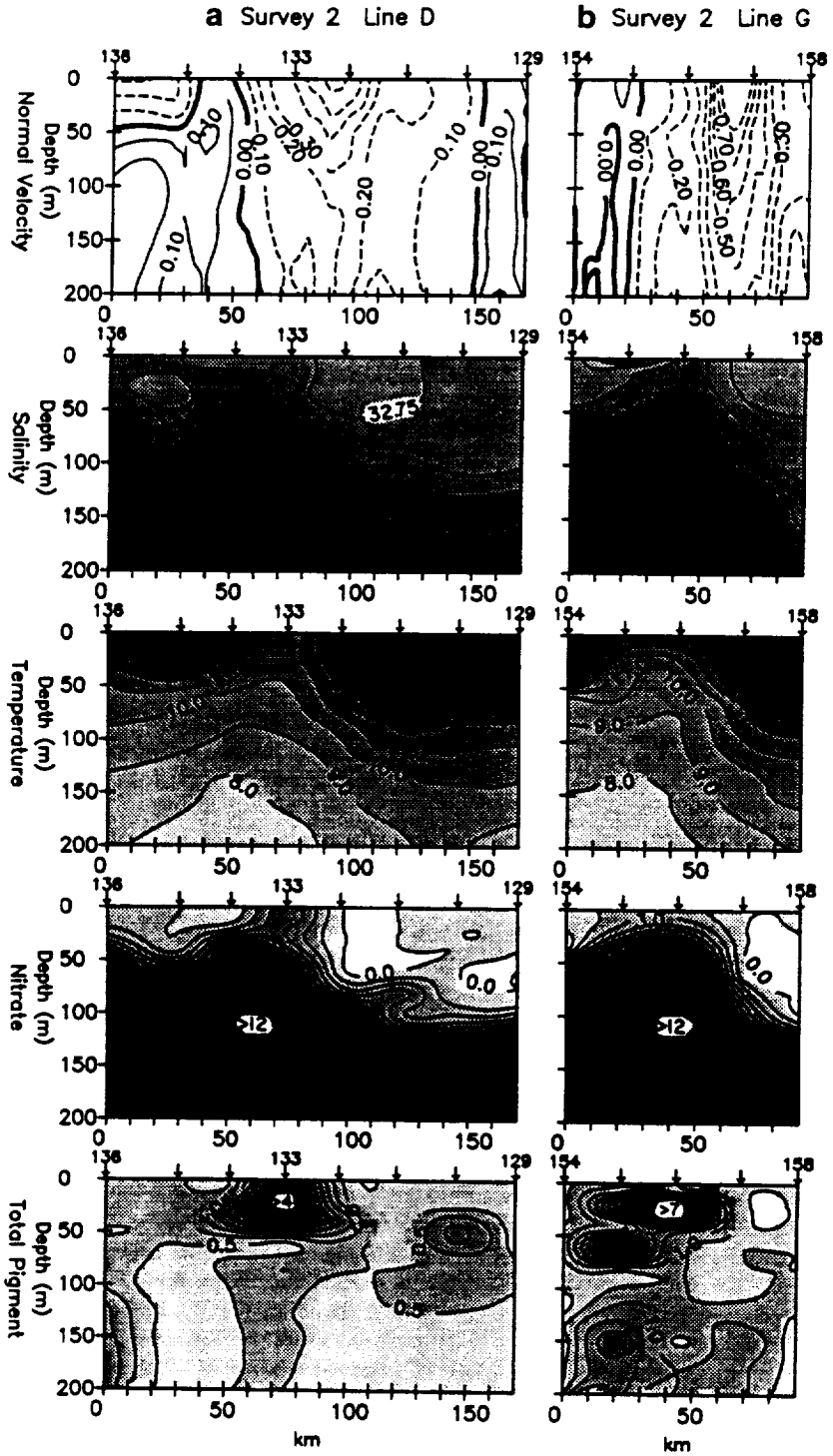

Fig. 9. Sections of ADCP velocity, temperature, salinity, nitrate, and total pigment (derived from the fluorometer) concentration during the July 6–12, 1988 survey. The velocity is the component normal to the transects, defined to be positive shoreward. Contours are as in Figure 8, except that the 0.5 mg m^{-3} contour is shown for pigment, and pigment concentrations above 4.0 mg m^{-3} appear black with no contours. Nitrate is contoured with a 1.5-μM interval and concentrations of nitrate above 12.0 μM appear black with no contours. (*a*) Cross-jet transect along line D on July 9–10; (*b*) Cross-jet transect along line G on July 12. (See Figure 6 for transect locations).

the salinity maximum in water moving offshore at 0.3 m s^{-1}, 10 km south of the front; (3) the maximum offshore velocity (0.6 m s^{-1} in this average) centered 5 km north of the front; and (4) a wide salinity minimum centered 20 km north of the front, in water moving offshore with velocities of 0.3 m s^{-1}. Surface values for velocity, temperature, and salinity during one transect on July 8–9 are presented in the inset of Figure 10*b*, and show some of the same characteristics as the ensemble average.

Although the orientation of the jet in the survey region became more southward during the surveys on July 21–27 and July 29 to August 4 (Figures 6*b* and 6*c*), there continued to be warm, fresh, nitrate-deficient water on the offshore side of the southward jet and cold water with

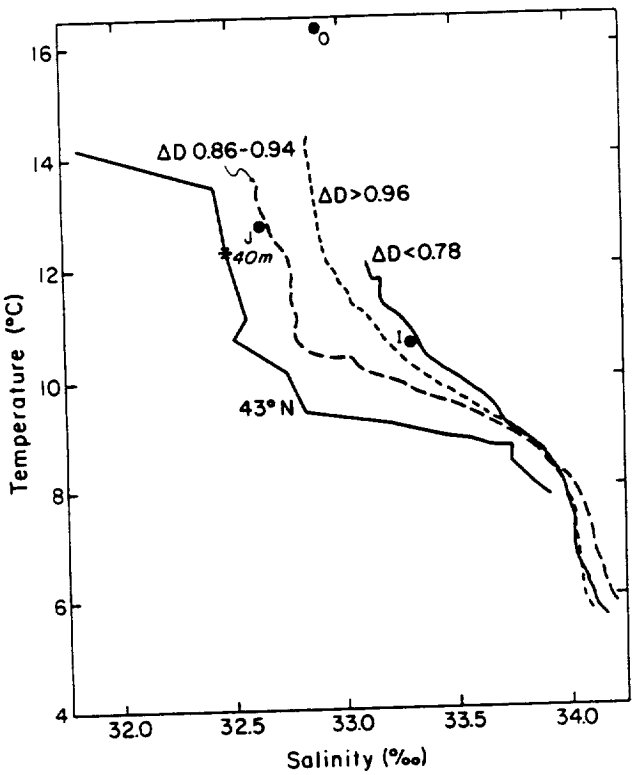

Fig. 10a. Mean T-S diagrams from the July 6-12, 1988, survey, after *Huyer et al.* [this issue], with profiles averaged according to the surface dynamic height, composited to show profiles judged to be "in the jet" ($0.86 < \Delta D < 0.94$ dyn m); "offshore" of the jet ($\Delta D > 0.96$ dyn m); and "inshore" of the jet ($\Delta D < 0.78$ dyn m). The most offshore profile from north of Cape Blanco (43°N) in June 1987 is also included, and the value at 40 m is indicated by an asterisk. Point T-S values used to define the source waters in Table 1 are shown as solid circles (I=inshore, O=offshore, J=jet).

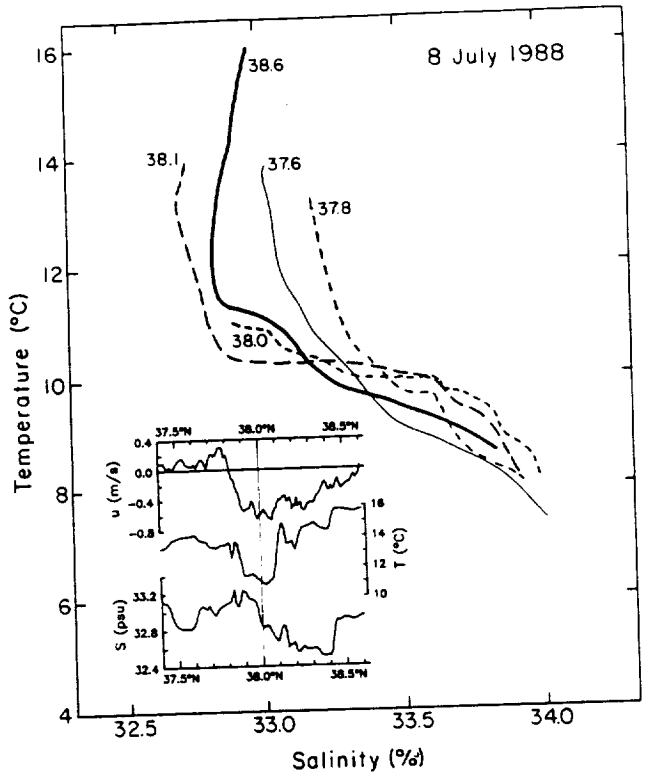

Fig. 10b. T-S diagrams from July 8-9, 1988, averaged over selected 0.1° latitude bands along line D (see Figure 6a). The profiles are labeled with the latitude of the southern boundary of the 0.1° band. The cross-track ADCP velocity at 25 m, the surface temperature, and the surface salinity along the transect are plotted against latitude in the inset.

high nitrate on the inshore side. Pigment values continued to decline to maximum values of only 0.5–1.0 mg m^{-3} during the last survey despite high concentrations of nitrate inshore of the jet, and warmer and fresher water appeared closer to the coast. *Chavez et al.* [this issue] discuss the nutrient and pigment fields in more detail.

3.3.2. *T-S relationships.* One of the most robust results of the 1987–1988 CTZ surveys is the description of a jet that carries along a surface salinity minimum while it separates water of low salinity and nitrate on its offshore side from water of high nitrate and salinity on its inshore side [*Hayward and Mantyla*, 1990; *Hood et al.*, 1990, this issue; *Huyer et al.*, this issue; *Kosro et al.*, this issue; *Chavez et al.*, this issue]. High values of pigment are associated with the inshore characteristics but may also appear directly in the jet or even offshore of the jet in a patchy manner. In trying to relate this structure to the larger-scale California Current, the question arises as to the source of the water masses directly in and separated by the jet. The cold, salty, and nutrient-rich water is presumably of an upwelled origin, either next to the coast or in situ. The fresh water in the salinity minimum must come from farther upstream.

Huyer et al. [this issue] separate the T-S profiles for CTD stations from the 1988 CTZ surveys, based on the surface dynamic height, into offshore ($\Delta D > 0.96$ dyn m), jet ($0.86 < \Delta D < 0.94$ dyn m) and inshore ($\Delta D < 0.78$ dyn m) water. Their results from the July 6–12 survey are shown in Figure 10a. The jet water is freshest, followed by the offshore water; both are fresher than the inshore water. Measurements made north of Cape Blanco (43°N) at the end of the June 1987 CTZ survey are plotted in the same figure and show water with salinities near 32.5 psu and temperatures of 10.3°–13.3°C between 30 and 70 m at the station farthest offshore (43.2°N, 125.0°W). These values of salinity are in agreement with historical summer values of salinity north of Cape Blanco [*Huyer*, 1983] and with a survey off Cape Blanco in August 1986, which found salinities of <32.0 psu north of Cape Blanco and < 32.5 psu south of Cape Blanco [*Mourn et al.*, 1988]. Mixing of this water from north of Cape Blanco with offshore water similar to that found in the CTZ region would produce water with the T-S properties found in the jet.

The most detailed sampling of the water characteristics across the jet during the 1988 surveys is provided by the 15 repeated transects of microstructure profiles every 1 km along line D during July 2–16 [*Dewey et al.*, this issue]. T-S profiles (averaged over 0.1° latitude bands) from the microstructure transect on July 8 (similar to the July 9–10 transect in Figure 9a) are presented in Figure 10b. The alongtrack values of velocity (normal to the transect) at 25 m depth, surface temperature, and salinity for the same microstructure transect are shown inset in the figure. In the region of onshore flow to the south of the jet (37.6°–37.7°N), the T-S profile shows intermediate characteristics, similar to those previously attributed to "southern" water by *Rienecker and Mooers* [1989b] and *Paduan and Niiler* [1990]. Moving north, in the region where cross-shelf velocities switch from onshore to offshore

(37.8°–37.9°N), salinities are greatest and temperatures decrease (the "inshore" water of *Huyer et al.* [this issue], and "upwelled source" water of *Paduan and Niiler* [1990]). In the region near the maximum offshore velocity (38.0°–38.1°N), the *T-S* profile shows a cold, nearly isothermal layer in which salinity increases with depth. This is in the narrow temperature minimum at station 133 in Figure 9*a* and the narrow cold filament along the drifter track in the July 12 satellite image (Figure 7*b* at 38.0°N, 124.8°W). At the surface it is fresher than the "upwelled source" water of *Paduan and Niiler* [1990] and fresher than the water found over the shelf (> 33.5 psu) in this region and farther north in August 1988 by *Magnell et al.* [1989*a*]. North of the offshore velocity maximum, but still within the offshore-flowing jet (38.1°–38.2°N), the surface water is warmer and fresher and the *T-S* profile looks like the fresh "jet" water described by *Huyer et al.* [this issue] and the "northern" water described by *Paduan and Niiler* [1990]. The isothermal surface water between 38.0°N and 38.1°N is very similar to the deeper water in the pycnocline at 38.1°–38.2°N. The salinity minimum extends to 38.4°N. North of this, (38.6°–38.7°N) along line D in 1988, the water is saltier and warmer, like the "offshore" water of *Huyer et al.* [this issue].

The identification of phytoplankton and zooplankton species adds further evidence for the upstream source of the jet and the role of the jet in separating water masses. Sampling along line D in July 1988 found different zooplankton species at locations offshore of the jet, within the core of the jet and inshore of the jet [*Mackas et al.*, this issue]. The jet thus carries within its center zooplankton species not found locally inshore or offshore in July 1988, supporting the presence of water from a more distant upstream source. Likewise, *Hood et al.* [1990] find different phytoplanktonic species on either side of the jet in June 1987. Further identification of the species in specific patches by *Hood et al.* [this issue] shows that a deep patch of pigment directly in the jet at 70–100 m depth at 41.5°N in June 1987 is similar to the species found inshore of the jet, in upwelled water, and not the species found in the deep pigment maximum offshore of the jet. Since this patch is below the euphotic zone, they conclude that it has been entrained into the jet and subducted from somewhere inshore and farther upstream. Evidence for subduction within the offshore-flowing jet sampled in 1988 is also provided by *Kadko et al.* [this issue] and *Washburn et al.* [this issue].

3.3.3. ***Weighted least squares water mass analysis.*** In an attempt to quantify the distribution of source water in the CTZ surveys, the weighted least squares (WLS) water mass analysis of *Mackas et al.* [1987] is used. In this analysis, one specifies values of parameters (temperature, salinity, tracer concentrations) for a number of source water masses. The method determines the best fit of each water parcel to the source characteristics. Each parcel is described as the sum of fractions of the source water types. The sum of the fractions is forced to equal 1.0, and no fraction is allowed to be less than zero. The method weights the parameters by a combination of the variability caused by the measurement error and by uncertainties in the source definitions. A measure of the reliability of the fit is provided by a chi-square test. The method works best with conservative, independent parameters and requires that the number of parameters be as large as the number of source water types (preferably larger). During the 1988 cruises, five variables were used: temperature, salinity, nitrate, silicate, and phosphate, all measured at discrete depths [*Chavez et al.*, this issue].

We are interested in the upper 100 m of the water column, where none of these parameters are strictly conservative (salt may be more conservative at this time of year in this region). Rather than trying to identify distant sources in this nonconservative region, the WLS method was applied with the goal of determining the extent to which the different water masses remained coherent over the month and a half period of surveys. The source definitions used values measured during the July 6–12, 1988, survey at a depth of 40 m (where temperature is somewhat more conservative than at the surface) at three different stations that were judged to be "in" the jet, "offshore" of the jet and "inshore" of the jet. The values are shown in Table 1, and the *T-S* values are plotted in Figure 10*a* (solid circles). Considering only *T-S*, the "inshore," "jet," and "offshore" water are similar to the values defined by *Huyer et al.* [this issue].

TABLE 1. Water Mass Source Definitions

	Station Sources					
	Station	T, °C	S, psu	NO_3, μM	PO_4, μM	SiO_4, μM
Inshore	117	10.3	33.3	12.00	1.40	8.93
Jet	115	12.5	32.6	0.01	0.50	2.15
Offshore	143	16.1	32.9	0.11	0.44	2.57

Figure 11*a* shows the fraction of each of the water types found at 40 m depth over the domain of the July 6–12, 1988 survey. Overlaying the surface dynamic height fields shows that "jet" water stays mostly within the jet, with "offshore" and "inshore" water found appropriately offshore and inshore. There is a fairly large amount of patchiness. Examination of the chi-square statistics show these distributions to be significant at the 90% level in regions where jet or "offshore" water represents more than 50% of the water. The regions where inshore water represents the majority of the water are less significant. Application of the WLS analysis to the other surveys at 40 m depth, using the source definitions from the July 6–12 survey, yields similar results. The fields from the June 20–27 and July 13–18 surveys, when the jet was oriented like the July 6–12 survey, are not shown but look like Figure 11*a*. The fields from the July 21–27 and July 29 to August 4 surveys, after the jet has become more north-south, are shown in Figures 11*b* and 11*c*. Even though the jet has shifted position, the water identified as "jet" coincides with the 0.8–0.9 dyn m contours in Figure 6, with a similar amount of patchiness.

The primary result of the WLS analysis is to show the presence of water within the jet during all five surveys that can be distinguished in an objective way from water farther inshore and offshore. Although the properties of the jet water are patchy in space, they do not change much over the month and a half period of surveys. This supports the interpretation of the biological data and the

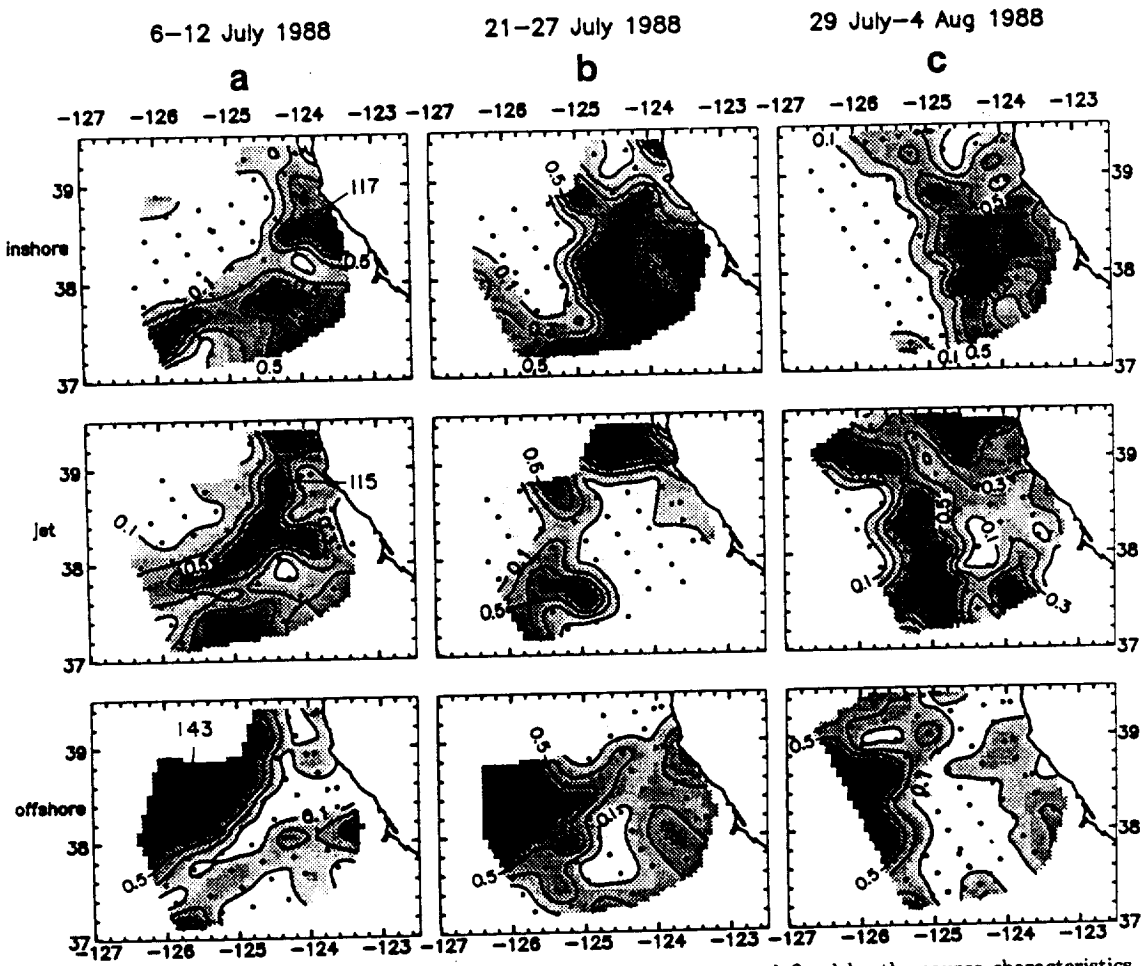

Fig. 11. Horizontal distributions at 40 m depth of the three water types defined by the source characteristics in Table 1 for the three surveys shown in Figure 6. Units are fractions of the water contributed by each source. The locations of the stations (117, 115, 143) used to define the three water types during the July 6–12 survey are shown. The first contour shown is 0.1 and the contour interval is 0.2. (*a*) July 6–12, (*b*) July 21–27, (*c*) July 29 to August 4.

simpler T-S analysis. It also demonstrates graphically the degree of patchiness, indicating intermingling of water types upstream of the survey. These results are similar to the isopycnal analysis by *Huyer et al.* [this issue].

3.4. *Satellite-Derived Flow Field*

A final tool in the analysis of the surface velocity field is the use of sequential advanced very high resolution radiometer (AHVRR) images to infer patterns of motion [*Vastano and Borders*, 1984; *Emery et al.*, 1986; *Kelly*, 1989; *Tokmakian et al.*, 1990]. To determine whether a continuous flow can be traced from Cape Blanco to the Point Arena jet and beyond, a set of 11 clear images from July 16–18, 1988, has been animated, displayed in sequence. This period came at the end of a month of persistently strong upwelling-favorable winds, at the beginning of a week-long wind relaxation [*Huyer et al.*, this issue]. The animation allows us to map the patterns of motion over the 3-day period in a qualitative sense, rather than quantifying the velocities. The advantage of the qualitative interpretation of the animation is that the human eye is adapted to detect motion, even when features are rotating and distorting rapidly. The results of the subjective evaluation of the flow field over this 3-day period are shown in Figure 12. Arrows depicting the qualitative direction of the flow field (not the magnitude of the velocities) are overlaid on the image from July 16, covering the region from 34°N to 46°N. There are no arrows in regions where the direction of flow could not be clearly determined.

Starting in the north at 44°N, the cold coastal features appear to move southward and offshore. The cold water north of Cape Blanco (43°N) flows offshore and separates to form a rapidly rotating cyclonic eddy that moves southward over the 3 days. The colder coastal water south of Cape Blanco also flows to the southwest and eventually extends off Cape Mendocino at 40°N, 126°W. Inshore of this flow is a more complex region that shows northward motion of the warm water and southwestward motion of the cold water north of Cape Mendocino, which eventually merges with the outer flow from Cape Blanco. There is a divergent pattern at 40°N, 126°W, where some of the flow "leaks" offshore and the rest returns onshore. The onshore flow at 40°N turns both north and south, the southward branch flowing into the jet off Point Arena. A mass of cold water emerges south of Cape Mendocino near 39.8°N. This has the appearance of a squirt, as defined at the beginning of the paper, and may be related to the observed wind relaxation. It carries cold water offshore and terminates in opposing vortices, cyclonic to the south and anticyclonic to the north. The cyclonic eddy moves to the south and hits the outer side of the jet near 39.0°N, 124.5°W, where *Huyer et al.* [this issue] suggest it may have influenced the

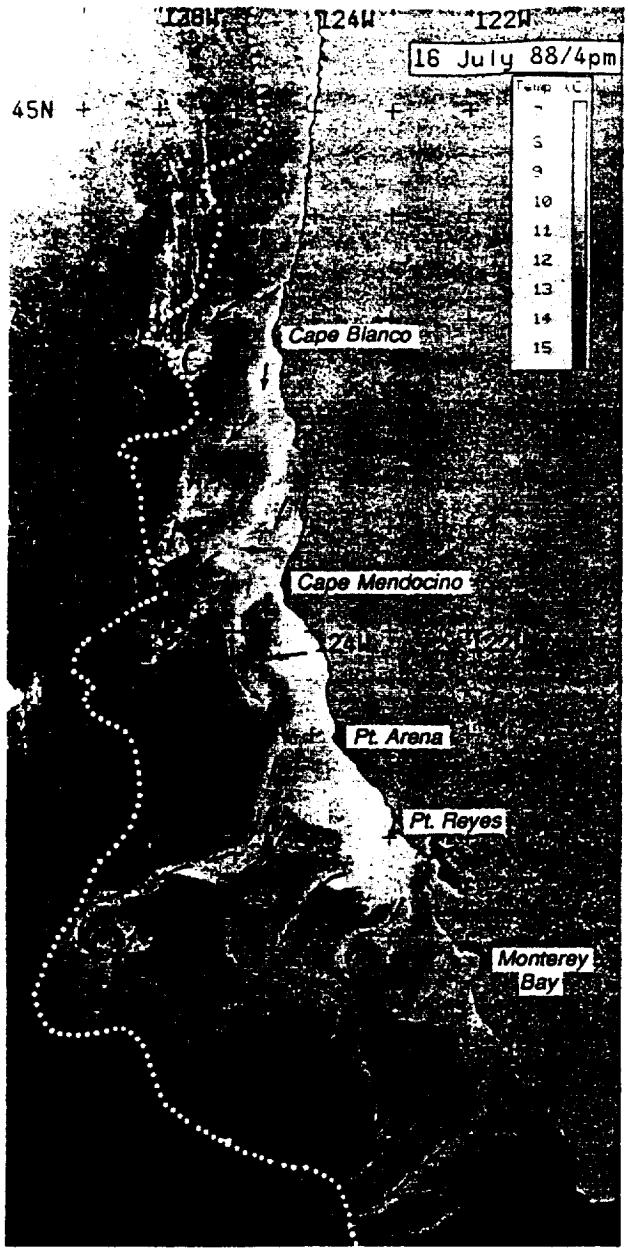

Fig. 12. The subjectively determined (by PTS) July 1988 flow field, from an animation of 11 images on July 16–18, 1988, superimposed on the satellite SST field from July 16. The black arrows depict the direction of the flow, not the magnitude of the velocities. The white dotted line traces the path taken by a surface drifter in September–October 1984 [*Thomson and Papadakis*, 1987]. Although the drifter was from a different year and month than the July 1988 satellite images, it traces out a path similar to the outer edge of the region of cold filaments in the July images.

reorientation of the jet, which occurred at about this time. Offshore of the squirt, the animation shows southward flow that connects the Cape Mendocino meander to the Point Arena jet. Thus a continuous flow can be traced from Cape Blanco to the Point Arena jet, along the outer margin of a much more complex flow field. Water leaves and enters the jet along the path of the jet, suggesting mixing and intermingling of the jet with surrounding water, which would contribute to the observed patchiness of the downstream water mass characteristics.

Starting at the base of the Point Arena filament, the flow is largely as depicted earlier by the 1988 drifter study (Figure 7), with extra details where there were no drifters. The jet terminates in an eddy with moderately rapid rotation. There is some leakage off the northwest corner of the eddy and motion around the eddy and then to the south. Some onshore flow to the south of the jet can be seen, as can offshore flow in several other filaments along the coast to the south. Anticyclonic rotation is evident in the large eddy sampled by the Point Reyes drifter (Figure 7) at 35°N–36°N, 123°W–125°W. For comparison, the path of a satellite-tracked surface drifter which travelled from Vancouver Island (49°N) southward along the coast in September–October 1984 is included in Figure 12 to show that drifters at other times have followed a continuous north-to-south path along the outer edge of this same general region ([*Thomson and Papadakis*, 1987], discussed in more detail below).

4. Discussion

4.1. *Comparison With Previous Results*

4.1.1. *Seasonal evolution.* Observations from the CTZ surveys and satellite (AVHRR) data favor the picture of a strong (0.5–1.0 m s^{-1}), narrow jet that appears sometime between March and May and connects the region from north of Cape Mendocino to that south of Point Arena, at least through July. The seasonal increase in the strength of mesoscale meanders and eddies is in agreement with a late-summer maximum in rms sea surface topography found from analysis of a year-long record of Geosat altimeter data in two independent studies [*Flament et al.*, 1989; *White et al.*, 1990].

To verify this seasonal pattern over a longer time period, dynamic height fields were examined from the CODE (1981–1982), OPTOMA (1982–1986), and CTZ (1987–1988) surveys, located within the region 37°N–42°N and offshore to 128°W. The approximate range of dynamic heights (relative to 500 dbar) within each survey has been tabulated and used to form a mean monthly dynamic height range. Most of the CODE cruises were confined to a narrow coastal region and were not used; the OPTOMA cruises that covered small regions were also not used. If more than one cruise was conducted in the same year-month, the largest range was used for that year-month. The mean monthly progression of the dynamic height range is shown in Figure 13 as the solid line, along with the values from the individual surveys. Given the low number of samples available and the differences in the regions sampled by different surveys, only the general trend of a summer-fall maximum and a winter-spring minimum should be considered significant. Thus there is an agreement of the seasonal progression from this longer (8 year) time series with the results from the altimeter data in 1987 and the interpretation of the satellite SST fields in 1987–1988.

Magnell et al. [1989a,1990] present nearshore CTD surveys and drifter deployments around Cape Mendocino from the Northern California Coastal Current Study (NCCCS) in 1987 and 1988. The nearshore hydrography off Cape Mendocino from March 17–19, 1987 (prior to the CTZ survey in Figure 3*a*) shows a jet located approximately 20 km from the coast at 40.4°N, 124.6°W, with a small anticyclonic eddy inshore of the jet. NCCCS drifters released in March of both 1987 and 1988 travelled nearly uniformly south with little meandering, approximately 20–30 km from shore, from north of Cape Mendocino past Point Arena and sometimes as far as Point Reyes, with velocities of up

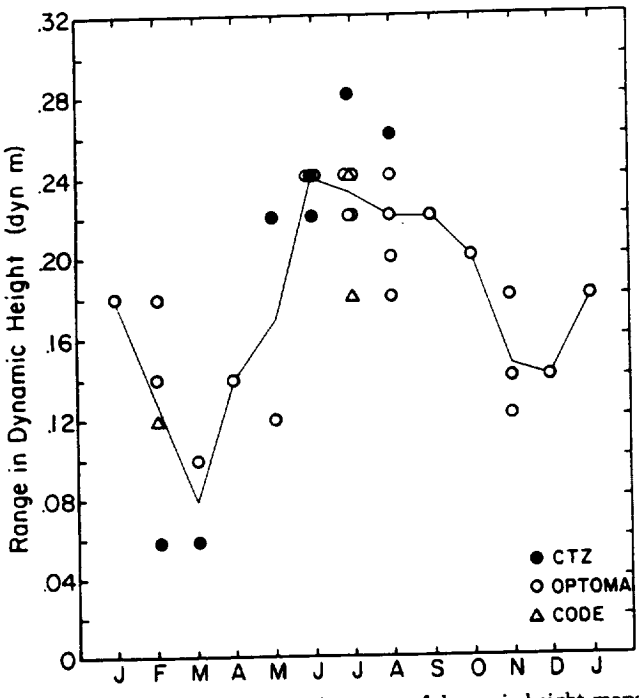

Fig. 13. Seasonal variation in the range of dynamic height maps from the CODE, OPTOMA, and CTZ surveys (1981–1988). The maximum ranges of dynamic heights off 37°–42°N are shown as individual symbols, and the means for each calendar month are connected by the continuous line. Identical values found in different years are indicated by slightly offset symbols.

to 0.6 m s^{-1}. This suggests the presence of a nearshore jet in March of both years.

These observations lead to the hypothesis that the seasonal evolution of the velocity field off Cape Mendocino and Point Arena begins in March or earlier with a jet close to the coast, perhaps along an upwelling front. Offshore movement of a jet associated with an upwelling front is indicated by the CODE data south of Point Arena (near 38.6°N) at the time of the spring transition (March–April) in 1981 and 1982. Current moorings over the shelf [*Strub et al.*, 1987*b*] and CTD cruises [*Huyer and Kosro*, 1987] revealed uniformly southward velocities in an initial response to southward winds. As the wind forcing continued, however, the southward jet moved offshore, and the velocity field over the shelf became more variable. We hypothesize that as the jet moves farther offshore, it separates the more variable region inshore, where upwelled water is found, from the offshore environment. Other jets and eddies may appear inshore of the seaward jet. For example, moored current measurements over the shelf south of Point Arena [*Magnell et al.*, 1989*b*] indicate an inshore jet over the shelf simultaneous with the seaward jet observed offshore in early July 1988 [*Huyer et al.*, this issue]. Similarly, hydrographic sections from the NCCCS survey in August 1988 [*Magnell et al.*, 1989*a*] indicate a southward jet over the shelf and slope at most locations from north of Cape Mendocino to south of Point Arena. These jets can presumably separate from the coast and create multiple jets (each with an associated filament) inshore of the seaward jet, similar to those seen in the drifter tracks and satellite images south of Point Arena (Figure 7). We stress that this hypothesized seasonal progression applies only to the Cape Mendocino and Point Arena region and that further observations are needed to verify it. Farther south, where upwelling-favorable winds are present during most of the year, the temporal evolution of the jet and eddy field remains to be determined.

4.1.2. *Continuity with regions farther north.* Several pieces of evidence suggest continuity of the jet off Cape Mendocino and Point Arena with flow north of Cape Blanco. The satellite image from 6 May 1987 (Figure 2*c*) shows a cyclonic filament off Cape Blanco similar to those off Cape Mendocino and Point Arena, which were observed to be associated with a meandering jet and inshore cyclonic eddies. ADCP data collected after the 9–18 June 1987 survey north of Cape Mendocino show offshore flow north of Cape Blanco, onshore flow south of Cape Blanco, and flow to the southwest between Capes Blanco and Mendocino, leading into the survey region of Figure 3*d* [R. L. Smith, Coastal upwelling in the modern ocean, submitted to Evolution of Upwelling Systems: Miocene to Present, edited by C. P. Summerhayes, W. Prell, and K. C. Emeis, Burlington House Publishers, Bath, 1991]. This flow was along the edge of cold features similar to those in Figure 2*d* and is consistent with the very fresh water (< 32.0 psu) found at the surface on the offshore side of the jet at the northern entrance to the 9–18 June 1987 survey (see Figures 5 and 14 of *Kosro et al.* [this issue]). Animation of the satellite sequence from 16–18 July 1988 (Figure 12) also suggests a continuous flow from Cape Blanco to south of Point Arena. This is consistent with the surface salinity minimum observed in the offshore half of the jet in 1988 and with T-S characteristics in the jet (Figure 10*a*).

Three previous studies provide evidence that the surface currents off Cape Blanco in May, August and September are similar to, and may be continuous with, the meandering jet found off Cape Mendocino. In May 1977, *Freitag and Halpern* [1981] found a jet flowing continuously from north of Cape Blanco to Cape Mendocino, where offshore and onshore flow was seen, similar to the meander found in late May 1987 except displaced slightly to the south. Minimum salinities in the offshore portion of the jet increased from north to south from less than 32.4 psu north of Cape Blanco to 32.6 psu off Point Arena. In August 1986, *Moum et al.* [1988] found a symmetric offshore and onshore current west of Cape Blanco, similar to that found off Cape Mendocino in late May 1987 (Figure 3*c*). Cold water was contained inshore of the jet, which transported fresh water (32.0–32.5 psu) on its outer edge around the cape to the south. Finally, the continuity of the southward flow along the offshore edge of the filament region is supported by the track of a drifter which travelled southward along the coast from Vancouver Island (49°N) in September–October 1984 [*Thomson and Papadakis*, 1987]). The drifter track is shown in Figure 12, superimposed on the July 1988 flow pattern. Starting north of Cape Blanco within 100 km of the coast, the drifter experienced offshore-onshore meanders of 50–100 km amplitude at Cape Blanco, between Cape Blanco and Cape Mendocino, southwest of Cape Mendocino, and southwest of Point Arena. It took approximately a month to travel from Cape Blanco to Point Arena and outlined the system of cold filaments that existed at that time (see *Thomson and Papadakis* [1987] for overlays of the drifter tracks and coincident satellite SST images).

4.1.3. *Across-jet structure and in situ upwelling.* Close examination of the spatial distribution of *T-S* properties along line D in July 1988 (Figure 10*b*) reveals that the

coldest water in the filament (38.0°–38.1°N) is much fresher than coastally upwelled water found inshore of the jet, but is similar to the deeper water found slightly farther offshore in the jet (38.1°–38.2°N). Profiles with a similar isothermal upper region were found to occur in the jet along the path of a drifter moving offshore in the jet [*Kadko et al.*, this issue], although warming at the surface was evident from stations farther offshore than line D. These profiles are very much like those shown by *Rienecker and Mooers* [1989*b*, Figure 8] from the "cold core" of a jet off Point Arena in July 1986. The structure of transects from across the 1986 jet [*Reinecker and Mooers*, 1989*b*, Figure 5*a*] is nearly identical to that found at line D in July 1988 (Figure 9*a*). These *T-S* profiles suggest that upwelling occurs locally within the jet and that the cold water in the narrowest filaments seen in the satellite images may just be the fresher, northern water found in the offshore half of the jet, without the upper part of the water column.

Several mechanisms have been suggested which would cause upwelling locally within the jet. Model studies by *Haidvogel et al.* [this issue] and *Allen et al.* [this issue] suggest an alternating pattern of downwelling and upwelling on the offshore-flowing and onshore-flowing branches of the jet, respectively. However, the observations along line D come from the offshore-flowing water, where the model predicts downwelling and where *Kadko et al.* [this issue] and *Washburn et al.* [this issue] interpret the observations to indicate subsidence. Whether the narrow region with the isothermal *T-S* relation in the upper water (Figure 10*b*) could be the remnant of upwelling which occurred during the onshore-flowing branch of the meander remains to be determined.

An alternate mechanism for in situ upwelling is proposed by *Paduan and Niiler* [1990], who use conservation of vorticity to argue that in situ upwelling will take place in a jet which flows downwind, preferentially to the right of the jet (the side of the jet with negative relative vorticity). This would cause upwelling in the fresher water on the offshore side of the jet, consistent with the *T-S* profiles found in Figure 10*b*. However, the observations along line D do not conform to the theoretical situation, since the wind direction was more cross-jet than along-jet and the observed surface temperature minimum with the isothermal upper layer was found on the inshore side of the velocity maximum. *Paduan and Niiler* [1990] stress that the exact location of the upwelling maximum is sensitive to the distribution of relative vorticity, which is more complicated in the observed jet than in their Gaussian jet. We note that the model studies quoted above have no wind forcing and that the theoretical argument of *Paduan and Niiler* [1990] lacks the three-dimensional dynamics which cause the upwelling and downwelling in the numerical models. Thus although the water properties suggest in situ upwelling of the fresher water as the source of the water in the coldest narrow filament, the mechanisms that might cause that upwelling are not yet known.

4.1.4. *Similarity to other July fields.* The Point Arena jet sampled in June–July 1988 (Figure 6*a*) and the satellite SST fields associated with the jet (Figure 2*e*) are very similar to jets sampled by surveys in 1981 [*Kosro and Huyer*, 1986], 1982, 1984, and 1986 (Figure 14) and July images from 1981–1986 (Figure 15) and 1987 (Figure 2*d*). The dynamic height fields (Figure 14) from July 1982 [*Flament et al.*, 1985], July 1984 [*Rienecker et al.*, 1987], and July 1986 [*Rienecker and Mooers*, 1989*b*] all show a strong offshore-flowing jet extending west or southwest from Point Arena, as sampled in 1988. The satellite images from other July (Figure 15) often show cold water off Cape Mendocino, warm water southwest of Cape Mendocino between 39°N and 40°N, and one or more filaments

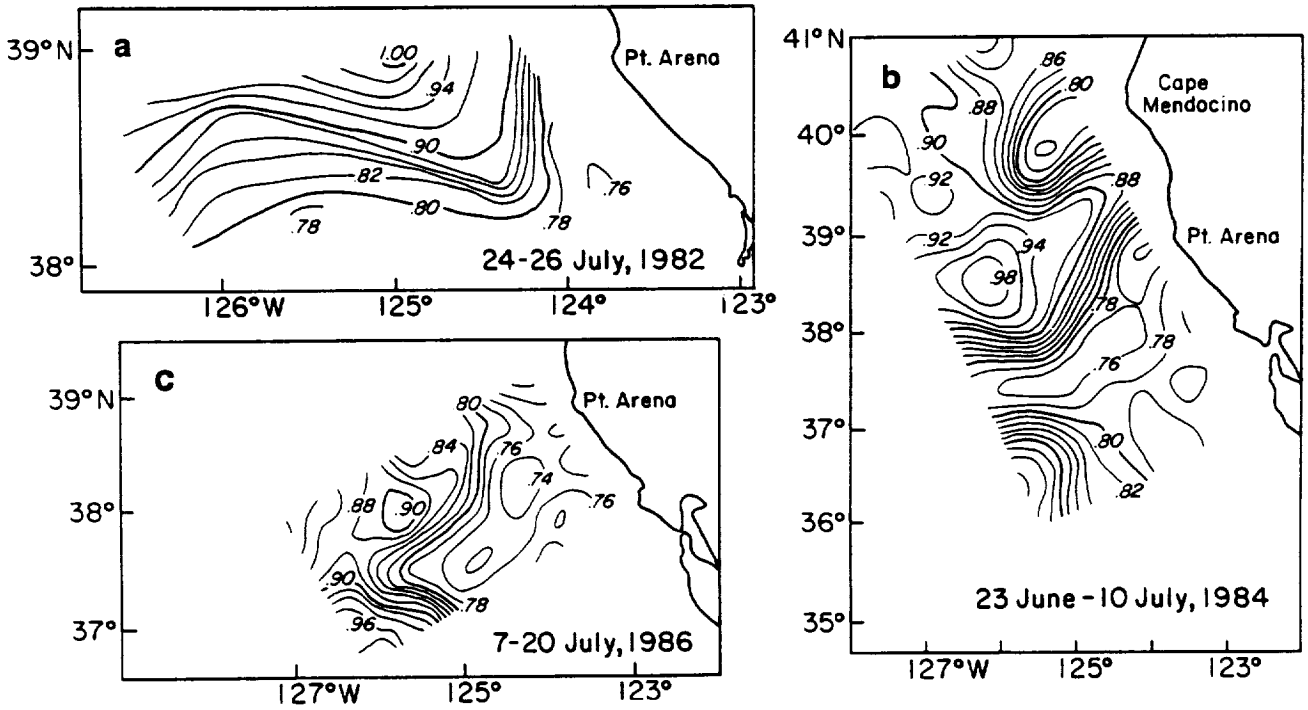

Fig. 14. Fields of dynamic height anomaly from July surveys in (*a*) 1982 (relative to 500 dbar, after *Flament et al.* [1985]), (*b*) 1984 (relative to 450 dbar, after *Rienecker et al.* [1987]), and (*c*) 1986 (relative to 450 dbar after *Rienecker and Mooers* [1989*b*]). The contour interval is 0.02 dyn m.

extending offshore from the region between Point Arena and Point Reyes (38°–39°N). This pattern is consistent with a meander off Cape Mendocino, onshore flow south of the cape, and offshore-flowing jets between Point Arena and Point Reyes. The images also show the degree of interannual variability in the position of the offshore filaments, which may leave the coast anywhere from north of Point Arena (1984) to Point Reyes (1981; see *Kosro and Huyer* [1986] for the 1981 dynamic height field). The 1984 dynamic height field (Figure 14*b*) and satellite image (Figure 15*d*) support the image of a jet that connects the meander off Cape Mendocino to an offshore-flowing jet at Point Arena, which meanders back onshore at 37°N but does not approach as close to the coast as it did between 39°N and 40°N, a pattern similar to that inferred from the drifters and the sequence of satellite images in July 1988 (Figures 7 and 12). The 1986 dynamic height field (Figure 14*c*) covers the jet off Point Arena out beyond the meander's turn to the southeast at 37°N, as is also evident in the satellite image (Figure 15*f*). The OPTOMA surveys in 1984 and 1986 show anticyclonic eddies to the north and west of the jet off Point Arena but also demonstrate that the surface transport in the closed eddies is less than the transport in the continuous jet.

Although the fields from 1984 and 1986 support the model of the meandering jet at the surface, they make it clear that most of the flow that continues south after passing around the cyclonic eddy at the end of the jet off Point Arena does not immediately return close to the coast but continues south, 200–300 km from shore, in contrast to the meander off Cape Mendocino. For the July 1984 jet (Figure 14*b*), this is confirmed by a July 1984 CalCOFI

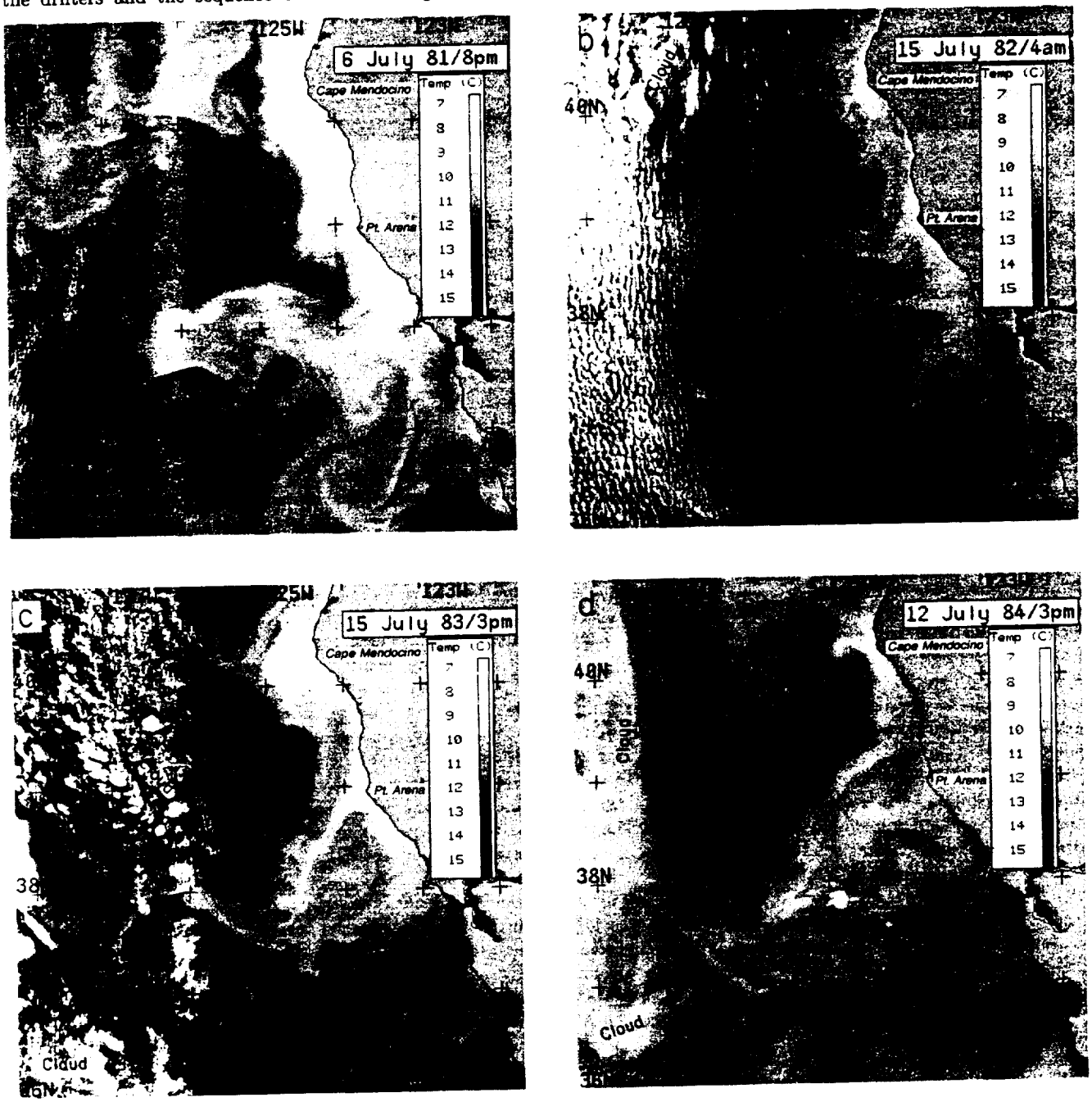

Fig. 15. Satellite SST images from July in other years: (*a*) 1981, (*b*) 1982, (*c*) 1983, (*d*) 1984, (*e*) 1985, (*f*) 1986.

C-2

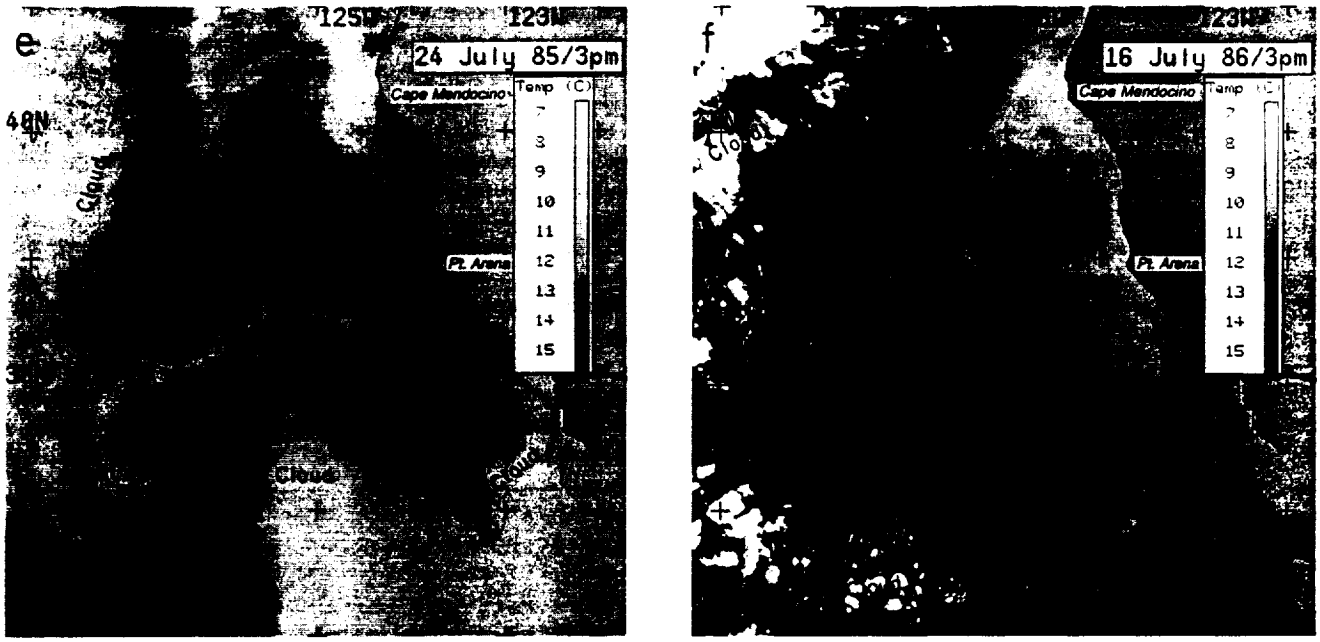

Fig. 15. (continued)

cruise, which showed the main jet extending south of 35°N, 200 km offshore, between anticyclonic (offshore) and cyclonic (inshore) eddies [*Chelton et al.*, 1988]. This pattern is similar to the path taken by drifters in 1988, which continue to the south from 35°N to 33°N between 125°W and 127°W (Figures 7*c* and 7*d*). This is also the path taken by the surface drifter that passed through this region in October 1984 [*Thomson and Papadakis*, 1987] (Figure 12).

4.2. *Comparison With Model Studies*

Although a number of modeling studies have addressed the three-dimensional structure and variability in eastern boundary currents, each study has included only a few of the processes which may influence the circulation patterns in those systems (such as surface buoyancy flux, surface wind stress, wind stress curl, bottom bathymetric features, variable coastline, realistic three-dimensional density and velocity structure, etc.). These "process studies" show the range of responses to isolated processes and often produce velocity fields with meanders and eddies similar to the observations, but they cannot evaluate the relative importance of all the different processes.

For example, *Philander and Yoon* [1982] demonstrate that the response of an eastern boundary current to annual periodic southward wind forcing (with no curl) is a banded structure of currents, associated with westward propagating Rossby waves. These may contribute to the offshore eddy field, as supported by Geosat altimeter data [*White et al.*, 1990]. An alternate explanation of the eddy field is simply the evolution of an initial, alongshore, baroclinic jet (equatorward surface jet over a poleward undercurrent, typical of summer and fall) [*Ikeda and Emery*, 1984; *Haidvogel et al.*, this issue]. These models suggest the importance of coastal topographic features, such as capes, in perturbing the jet. *Pierce et al.* [this issue] and *Allen et al.* [this issue] show that the spatial scale of the most unstable perturbations of jets similar to those observed in the 1987 CTZ surveys is approximately 250 km, a scale which is roughly similar to the separation between capes along the coast of southern Oregon and California. Other models, spun-up from rest by a spatially uniform and steady wind stress, produce a jet which becomes unstable and forms meanders and eddies, without coastal capes or bathymetric features [*Batteen et al.*, 1989; *McCreary et al.*, 1991].

An interesting result is found when *McCreary et al.* [1991] force their model with an annually oscillating (spatially uniform) wind stress. The result is an upwelling front and jet, which develops seasonally and eventually becomes unstable in spring–summer, producing meanders and eddies on both the inshore and offshore side of the jet. In winter, the system decays to weaker, large-scale eddies. Thus seasonal wind forcing alone, with no curl and no coastal or topographic features, can cause the development of an unstable jet, which moves offshore and develops into a jet and eddy field. The scales of the features in the model are sensitive to model parameterizations, especially those involved with horizontal and vertical mixing, which is a point of concern, since these processes are not well represented in numerical models.

Another type of numerical model study uses initial and boundary conditions derived from hydrographic and ADCP surveys to hindcast ("dynamically interpolate") the developing current structure between surveys [*Robinson et al.*, 1986; *Rienecker et al.*, 1987; *Walstad et al.*, this issue]. Such studies provide details of the evolving current structure which extend the observations (within the assumptions incorporated in the models). For example, *Walstad et al.* [this issue] initialize a QG model with the density field and ADCP velocities from a rectangular subregion of the May 18–26, 1987, CTZ survey (Figure 3*c*) and interpolate boundary conditions between that survey and the June 9–18 survey. Figure 16 shows the stream functions from the model at the start, middle and end of the simulation. The initial field shows why some of the

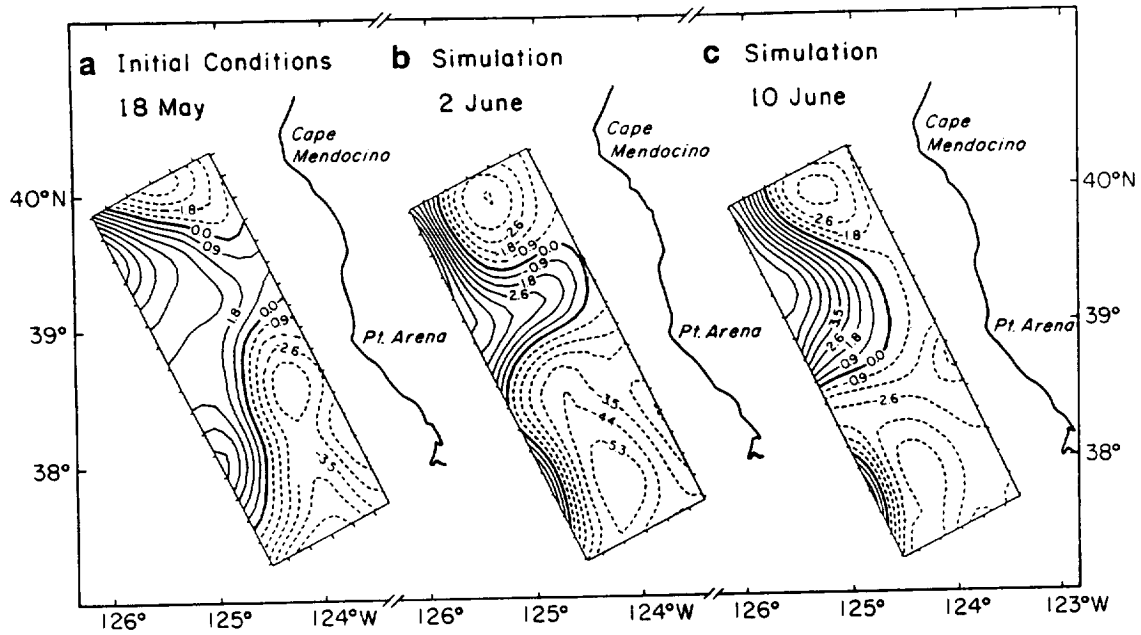

Fig. 16. Streamline fields from the QG model hindcast study of *Walstad et al.* [this issue]. (*a*) Initial conditions, May 22,1987; (*b*) June 2 simulation; (*c*) June 10 simulation.

drifters released at 38.1°N, 123.8°W, went north around the closed eddy of Point Arena and some flowed to the southwest (Figure 5*a*). During the simulation, the onshore flow south of Cape Mendocino becomes a sharper onshore meander between the two capes, while the streamlines off Point Arena begin to bow outward, creating the sharp offshore meander off Point Arena observed in the June 1987 cruise. The growth of the meander off Point Arena around June 2 was observed as the growing cold feature in the AVHRR images (Figure 4*c*) and in the ADCP measurements of increasing offshore transport on June 2–5, 1987, at 39°N, 125°W [*Dewey and Moum*, 1990]. The model demonstrates how the growth of a meander may look like a squirt in satellite images and even in a field survey of a limited domain.

Rotating laboratory tank experiments represent a final type of model. *Narimousa and Maxworthy* [1989] present results from a series of two-layer experiments in a tank that include rotation, surface stress (with and without curl), idealized capes and bottom ridges. Their results suggest that (1) bathymetric ridges produce an offshore-onshore meander coincident with the feature, while capes do not, (2) both ridges and capes produce meanders approximately 100–150 km downstream of the feature, and (3) a positive offshore maximum of wind stress curl produces offshore eddies which draw the coastal water offshore. Although it is tempting to use these conclusions to explain the strong onshore flow south of Cape Mendocino as due to the ridge offshore of the cape, the primitive equation numerical model results of *Haidvogel et al.* [this issue] produces a narrow meander directly offshore of the cape without a ridge in the model bathymetry, contradicting the first conclusion from the laboratory model.

These studies show that depending on the choice of model parameters and forcing, a number of models can produce features that are similar to certain aspects of the observations. At this point, however, none of the model results have demonstrated conclusively which physical processes are responsible for generating the different features observed in the California Current system.

4.3. *Biological Implications*

The CTZ surveys provide evidence that off Cape Mendocino and Point Arena in May–July, the observed jet separates water masses and biological assemblages at the surface and carries nutrients and biomass along on its inshore flank and sometimes within its core. Thus one important implication of the observed structure is that the gradient in biological properties between the richer nearshore and oligotrophic offshore regimes is often concentrated in a narrow frontal region across the jet. Processes which produce cross-jet transport will move biomass and nutrients from the inshore to the offshore environment, where they may be left by meanders and cutoff eddies.

A phytoplankton pigment maximum is often found on the inshore half of the jet as it flows both offshore and onshore (Figures 8 and 9). The net effect of the meanders on offshore transport of biomass depends on the biological processes and vertical motions which occur during the meanders. In a drifter-following experiment during July 1988, which extended beyond the normal CTZ survey region, *Kadko et al.* [this issue] and *Washburn et al.* [this issue] document the subsidence of patches of high pigment concentrations as the drifter moved offshore, at subsidence rates of up to 25 m day^{-1}. Before the drifter reached the end of the filament, pigment concentrations near the drifter were vastly reduced from inshore values and nitrate values were undetectable down to 100 m. It is not clear, however, whether this was true everywhere at this distance from shore or whether the drifter simply missed a patch of pigment such as seen along line G in July 1988, 275 km from shore (Figure 9*b*).

One of the more detailed examinations of the evolution of biological processes within a jet meander is presented by *Abbott et al.* [1990], who discuss fluorometer measurements and water samples collected on a drifting buoy which

sampled the offshore-onshore meander at 38°N in June 1987, shown in Figure 5*b*. During the first 2 days of offshore motion, phytoplankton pigment concentrations (as inferred from strobe-stimulated fluorescence) increased, and nitrate plus nitrite concentrations decreased, indicating phytoplankton growth. At the same time, the initially large concentration of nonfluorescent material decreased substantially. This material covaried with the pigment concentrations, implying that a large proportion of it was biological detritus, which sank out of the upper water column in the first few days of offshore transport. Pigment concentrations then decreased during the rest of the offshore motion, reflecting zooplankton grazing and/or subsidence. By the time the drifter reached the offshore terminus of the meander, there was a strong diurnal cycle of fluorescence around a steady mean value, indicating a balance between daytime growth and nighttime grazing. These results apply to the surface and do not take into account the subsidence described by *Kadko et al.* [this issue] and *Washburn et al.* [this issue].

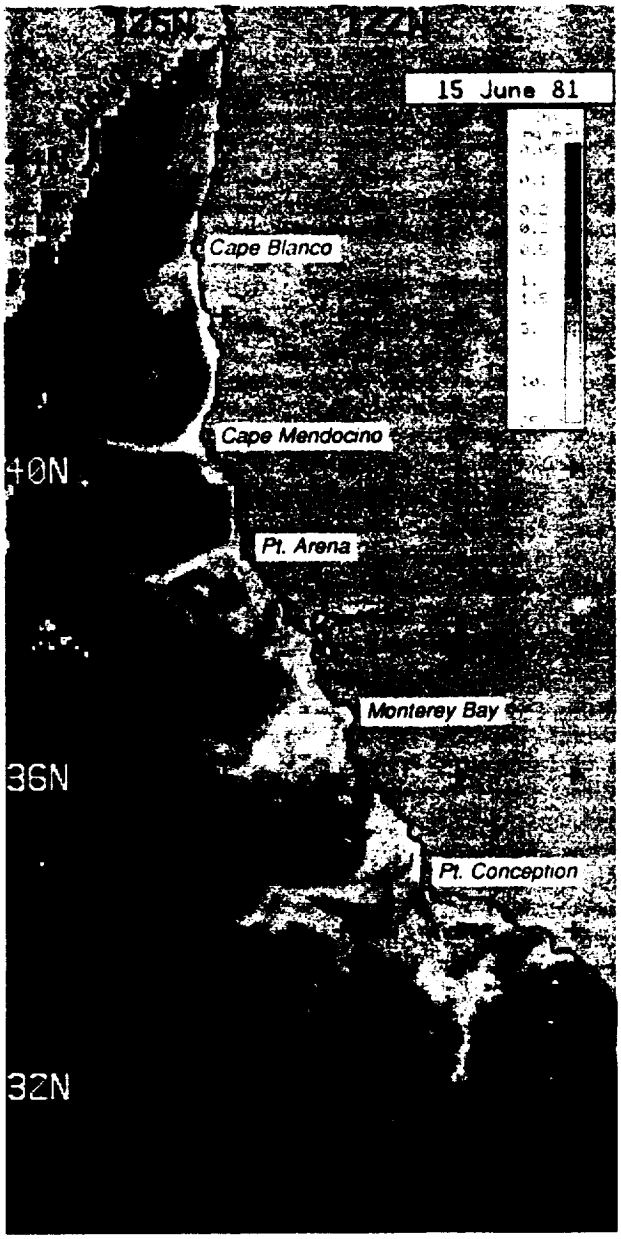

Fig. 17. Surface pigment concentration derived from the CZCS satellite data from June 15, 1981.

To examine the relative magnitudes of offshore and onshore pigment flux, the velocity and pigment concentrations in Figure 8 have been used to calculate the horizontal flux of pigment (the product of normal velocity and pigment concentration) through the upper 100 m of these vertical sections. Although the interpretation of these flux calculations is complicated by the spatially patchy nature of pigment, they provide a more quantitative approach than arguments based simply on the relative positions of pigment and velocity maxima using the same data [*Hood et al.*, 1990; *Chavez et al.*, this issue; *Kosro et al.*, this issue]. The results are that approximately equal amounts of phytoplankton pigment ($1.1–1.3 \times 10^5$ kg day^{-1}) are being transported by the offshore and onshore branches of the meander off Cape Mendocino during the May 18–26 survey (Figure 8*b*). In the meander which appears between stations 9 and 60 in Figure 8*c* during the June 9–18 survey, more pigment (1.3×10^5 kg day^{-1}) is being transported in the offshore branch than is returning (0.3×10^5 kg day^{-1}) in the onshore branch. This is the meander sampled by the drifter described by *Abbott et al.* [1990]. In both May and June 1987 surveys, approximately 2.5×10^5 kg day^{-1} is being transported offshore by the jet at the southwest corner of the surveys. To the extent that the surface drifters in Figure 5 represent the motion of this pigment, most of the biomass and nutrients leaving the survey at its southwest corner remains in meanders and eddies 100–300 km from the coast over the next 10–30 days. During this time, processes such as described by *Abbott et al.* [1990] are likely to transform this pigment into other biological products and detritus, which eventually fall out of the water column. These calculations indicate that at some times the onshore-flowing branch of meanders may carry as much pigment as the offshore-flowing branch, while at other times more is carried offshore than returns. They also indicate that a large amount of biological material is carried offshore to the southwest of Point Arena and Point Reyes, which enriches the ocean in the region 100–400 km from shore.

In some sense, the net biological impact of this system of meanders and eddies can be seen directly in satellite color imagery [*Abbott and Zion*, 1985; *Abbott and Barksdale*, this issue] such as the coastal zone color scanner (CZCS) image from June 15, 1981 in Figure 17, processed as described by *Strub et al.* [1990]. On the basis of the CTZ surveys, we interpret the edge of the region with high pigment concentrations to represent the center of an alongshore jet that flows from north of Cape Blanco to south of Point Arena. There is a detached patch of pigment between capes Blanco and Mendocino, similar to the cold eddy off Cape Blanco in Figure 12, a large meander off Cape Mendocino, similar to Figure 4*b*, which returns near shore north of Point Arena, and an offshore-flowing filament at Point Arena that marks the northern edge of a wider and more convoluted region of high pigment concentrations. At the southern edge of the image, the region of high productivity is interrupted in the Southern California Bight by the "Ensenada Front," where oligotrophic water from the deep ocean flows onshore into the bight [*Peláez and McGowan*, 1986; *Thomas and Strub*,

1990]. Thus although it is likely that processes (squirts and eddies) other than the jet augment productivity inshore of the jet [*Hayward and Mantyla*, 1990; *Chavez et al.*, this issue], the jet is seen to carry nutrients and biomass offshore, along the edge of a region 100–400 km in width, within which the deep ocean is more productive than it is offshore of the jet.

5. Summary and Conclusions

The CTZ and NCCCS surveys in 1987–1988, along with past surveys from the CODE and OPTOMA programs (1981–1986) provide 8 years of evidence with which we can partially answer the questions posed in the introduction. These results apply primarily to the region between approximately 36°N and 42°N during February–July.

5.1. The Spatial Structure of Horizontal and Vertical Transports

5.1.1. *Meandering jet.* Between 39°N and 42°N, the data strongly support the model of a meandering jet, flowing along the offshore border of the region of cold water seen in the satellite images during March–July. We refer to this jet as the seaward jet to distinguish it from other jets that may be present farther inshore. The fact that the jet was closer to the coast in March and stronger than the eddy inshore of the jet [*Magnell et al.*, 1990] suggests a seasonal development that supports the seaward jet as the primary structure in this region and period. The OPTOMA data show the presence of eddies but also support the greater transport in the jet, favoring the meandering jet model. The largest "synoptic" survey in this region, obtained by combining the July 1984 OPTOMA (Figure 14*b*) and CalCOFI data [*Chelton et al.*, 1988], shows a continuous flow from north of Cape Mendocino to south of Point Conception, with eddies inshore and offshore of the jet. Drifters that left the jet in July 1988 and traveled as far west as 134°W did not encounter another southward jet, supporting the contention that the jet which flowed offshore from Point Arena carried most of the surface transport of the California Current at that time and location. We stress that these conclusions apply only to the February–July period; the full seasonal evolution of the system remains to be determined.

A number of features have been found repeatedly, although not universally, in the seaward jet. A tongue of fresh water is often found in the upper 30–50 m of the jet's offshore flank, and a narrow temperature minimum is sometimes found just inshore of the jet's maximum velocity (Figure 8 and 9). This narrow temperature minimum is seen as a cold narrow filament in the satellite images, embedded in the larger region of cool water inshore of the jet. T-S diagrams (Figure 10*b*) show this filament to be nearly isothermal in the upper ocean, resembling the water in the pycnocline beneath the fresh water found just offshore of the maximum velocity, suggesting in situ upwelling within the jet. The mechanism causing this upwelling has yet to be determined, as does its relation to the subsidence described by others. We stress that these conclusions apply to the seaward jet. Other jets and filaments inshore of the seaward jet may have different structures and T-S characteristics.

The presence of the band of fresher water in the upper 20–50 m on the offshore side of the jet at Point Arena supports its continuity with water north of Cape Mendocino and Cape Blanco. The presence of different plankton species offshore, within and inshore of the jet [*Mackas et al.*, this issue; *Hood et al.*, 1990, this issue] also supports the origin of the jet in a water mass farther upstream. The large-scale field of horizontal motion inferred from a sequence of satellite SST images (Figure 12) shows continuity from Cape Blanco to Point Arena during a 3-day period in July 1988, although it also shows that water both leaves and enters the jet along the way, which may contribute to the observed patchiness off Point Arena. The continuous flow from north of Cape Blanco to Point Conception is similar to the path taken by a surface drifter in September–October 1984 [*Thomson and Papadakis*, 1987]. A jet flowing from north of Cape Blanco to south of Cape Mendocino was previously observed in May 1977 by *Freitag and Halpern* [1981]. South of 39°N, the drifters (Figure 7) and satellite-derived field shows that the seaward jet travels through a field of eddies with multiple filaments inshore of the jet, which may be different than the seaward jet and its associated filaments.

5.1.2. *Mesoscale eddy field.* The data show that closed eddies are present in the California Current system. Between 39°N and 42°N, the nearshore hydrography from the March 1987 NCCCS survey and the CTZ surveys show cyclonic eddies located southwest of the capes, inshore of the jet. The eddy surveyed in March is weaker than the jet, as is indicated by the dynamic topography and by the fact that drifters followed the jet but did not become entrained in the eddy [*Magnell et al.*, 1990]. South of 39°N in June–August, the CTZ drifters and hydrography show the presence of both cyclonic and anticyclonic eddies inshore of the jet. Analysis of drifter data by *Brink et al.* [this issue] suggests that eddy and jet transports are roughly equal in this region.

The CTZ and CODE hydrographic data do not extend far enough offshore to determine whether anticyclonic eddies exist offshore of the jet, as has been proposed by others [*Simpson et al.*, 1986; *Mooers and Robinson*, 1984; *Rienecker et al.*, 1987; *Ramp et al.*, this issue]. The OPTOMA data provide most of the hydrographic evidence for the presence of an anticyclonic eddy offshore of the jet between Cape Mendocino and Point Arena, but CTZ drifters in May–June 1987 and June–July 1988, and NCCCS drifters in March of 1987 and 1988 did not map out an eddy in that location. In August 1988, a large anticyclonic eddy offshore of the jet around 35°N was mapped by several CTZ drifters, and a small anticyclonic eddy was found between Cape Mendocino and Point Arena by an NCCCS drifter (although inshore of the cold water boundary), indicating that the drifters are not excluded from mapping such eddies.

Thus the data support the existence of smaller, cyclonic eddies inshore of the jet north of 39°N in March–June and numerous eddies inshore and offshore of the jet south of 39°N in June–August. The long meander that grows off Point Arena in June–July of 1987 and 1988 has a cyclonic eddy within the offshore terminus of the meander, which appears to be cut off and left offshore of the jet in late July 1988, remaining vigorous over at least the next month and moving offshore at approximately 70 km per month (0.03 m s^{-1}), the approximate speed of Rossby wave propagation [*White et al.*, 1990]. Whether these eddies are

present at other times of the year is not known, especially south of 39°N, but the February 1987 cruise, the historical hydrographic data and the altimeter data suggest that eddies between 39°N and 42°N are weaker in winter than summer.

5.1.3. *Squirts.* Most of the evidence does not support the interpretation that the larger filaments in the SST images are squirts, as defined in the introduction. The seaward jet which borders the larger regions of cold water, the band of fresh water found in the outer half of the jet, and the *T-S* characteristics of the narrow cold core of the filaments all argue strongly against a coastal origin of that water. The measurements from current moorings over the shelf north and south of Cape Mendocino show mean southward flow north of the cape and mean northward flow south of the cape during 1987–1988, which has been interpreted as evidence for the nearshore convergence associated with squirts [*Magnell et al.*, 1990]. However, these measurements are also consistent with the confluent flow field created by the meandering jet north of the cape and cyclonic eddy southwest of the cape as determined by the hydrographic data (Figure 3), which provides a more complete picture of the field.

Something looking like a squirt of cold water appears in the sequence of AVHRR images animated to produce the flow depiction shown in Figure 12, emerging between Cape Mendocino and Point Arena over a 3-day period. Whether this is truly a squirt (caused by a nearshore convergence) or cold water pulled from the coast by a pair of previously existing eddies cannot be determined from the images, although its occurrence at the time of a wind relaxation favors the squirt hypothesis. It seems likely that nearshore convergences do produce squirts at times and that they are shorter (100 km) than the long filaments and occur inshore of the observed jet, with time scales of days, contributing to the richness and patchiness of the water properties in that region.

5.2. *Temporal Variability*

Hydrographic data from the CODE, OPTOMA, and CTZ programs between 37°N and 42°N show a seasonal increase in the range of dynamic height fields from winter–spring to summer–fall (Figure 13). This agrees with the interpretation of satellite SST images (Figure 2) and with 1 year of Geosat altimeter data. NCCCS drifters and hydrographic data in March 1987 suggest that the flow field may appear as a jet closer to the coast in early spring, moving farther offshore in April–May. There is some suggestion of a similar behavior in previous analyses of the CODE data, where a southward jet developed initially over the shelf at the time of the spring transition and moved offshore as winds remained upwelling-favorable. This seasonal progression is similar to the wind-driven jet and eddy field modeled by *McCreary et al.* [1991], which suggests that the eddy field could arise from instabilities in a wind-driven jet, making the jet the primary structure.

Hydrographic data and satellite images (Figures 3, 4, 6, and 7) suggest that individual features can grow from a meander 100–150 km from the coast to one 200–225 km from the coast in a period of 2 weeks or less (May 5 to May 18, 1987) and retreat back to the original offshore extent in a similar period (May 18 to June 1, 1987); the jet may leave cutoff eddies in the process (July 16 to July 28, 1988). Features such as the offshore jet at Point Arena may persist for a month in one position (June 20 to July 18, 1988), then reorient in a period of a week or two. Animation of a sequence of satellite images from July 16–18 shows a great deal of structure in currents and SST features with spatial scales of 100 km or less and time scales of several days (Figure 12).

5.3. *Biological Implications*

The jet that flows from north of Cape Mendocino to Point Arena transports nutrient-poor water along its offshore half and nutrient-rich water on its inshore half and appears to separate assemblages of plankton species [*Hood et al.*, 1990, this issue; *Mackas et al.*, this issue]. Although phytoplankton biomass, as represented by phytoplankton pigment concentrations, is generally patchy, it is usually greater inshore and lower offshore of the jet (surface values below 0.5 mg m^{-3} offshore of the jet's center). Moderate pigment concentrations (1–4 mg m^{-3}) may appear in the jet, more often on the inshore or deeper part, where velocities are 0.2–0.5 m s^{-1}. Thus biomass and nutrients are carried along on the inshore half of the jet on its offshore meanders, as is evident in images from the CZCS, which show filaments extending as far offshore as they do in SST images (Figure 17). If meanders create cutoff eddies, the biological material in the eddies remains offshore, as is also evident in CZCS images. Subsidence in the offshore-flowing branch of the meanders may move phytoplankton and nutrients below the euphotic zone and biological processes may transform it during the long meanders. Although the quantitative details of the horizontal and vertical fluxes of nutrients and biomass in these filaments have yet to be determined, the CZCS satellite images suggest that the meandering jet and eddy field creates a region of high productivity that remains mostly inshore of the seaward jet. This region is narrower, on average, north of Point Arena than it is between Point Arena and Point Conception. It is terminated in the Southern California Bight by the onshore advection of oligotrophic water from the deep ocean.

Acknowledgments. The CTZ program was funded by the Coastal Sciences Program of the Office of Naval Research (Code 1122CS). Support for PTS was provided by ONR grants N00014-87K0009 and N00014-90J1115, with additional support provided by NASA grants NAGW-869 and NAGW-1251. Many people contributed to the CTZ data gathering and to the analysis of the data presented here. We especially thank Tim Cowles, John Allen, Steve Pierce, Curt Davis, Burt Jones, Eileen Hofmann, Tim Stanton, Bill Emery, Michele Rienecker, and several anonymous reviewers for their comments. Melinda Stewart and Barbara McVicar helped with the word processing and formatted the final text.

REFERENCES

Abbott, M.R., and B. Barksdale, Phytoplankton pigment patterns and wind forcing off central California, *J. Geophys. Res.*, this issue.

Abbott, M.R., and P.M. Zion, Satellite observations of phytoplankton variability during an upwelling event, *Cont. Shelf Res.*, *4*, 661–680, 1985.

Abbott, M.R., K.H. Brink, C.R. Booth, D. Blasco, L.A. Codispoti, P.P. Niiler, and S.R. Ramp, Observations of phytoplankton and nutrients from a Lagrangian drifter off northern California, *J. Geophys. Res.*, *95*, 9393–9409, 1990.

Allen, J.S., L.J. Walstad, and P.A. Newberger, Dynamics of the coastal transition zone jet, 2, Nonlinear finite amplitude behavior, *J. Geophys. Res.*, this issue.

Batteen, M.L., R.L. Haney, T.A. Tielking, and P.G. Renaud, A numerical study of wind forcing of eddies and jets in the California Current system, *J. Mar. Res.*, *47*, 493–523, 1989.

Bernstein, R.L., L. Breaker, and R. Whritner, California Current eddy formation: Ship, air and satellite results, *Science*, *195*, 353–359, 1977.

Brink, K.H., R.C. Beardsley, P.P. Niiler, M. Abbott, A. Huyer, S. Ramp, T. Stanton, and D. Stuart, Statistical properties of near-surface flow in the California coastal transition zone, *J. Geophys. Res.*, this issue.

Chavez, F., R.T. Barber, A. Huyer, P.M. Kosro, S.R. Ramp, T.P. Stanton, and B. Rojas de Mendiola, Horizontal transport and the distribution of nutrients in the coastal transition zone off northern California: Effects on primary production, phytoplankton, biomass, and species composition, *J. Geophys. Res.*, this issue.

Chelton, D.B., Seasonal variability of alongshore geostrophic velocity off central California, *J. Geophys. Res.*, *89*, 3473–3486, 1984.

Chelton, D.B., A.W. Bratkovich, R.L. Bernstein, and P.M. Kosro, Poleward flow off central California during the spring and summer of 1981 and 1984, *J. Geophys. Res.*, *93*, 10,604–10,620, 1988.

Coastal Transition Zone Group, The Coastal Transition Zone Program, *Eos Trans. AGU*, *69*(27), 697–707, 1988.

Davis, R.E., Drifter observations of coastal surface currents during CODE: The method and descriptive view, *J. Geophys. Res.*, *90*, 4741-4755, 1985.

Dewey, R.K., and J.N. Moum, Enhancement of fronts by vertical mixing, *J. Geophys. Res.*, *95*, 9433–9445, 1990.

Dewey, R.K., J.N. Moum, C.A. Paulson, D.R. Caldwell, and S.D. Pierce, Structure and dynamics of a coastal filament, *J. Geophys. Res.*, this issue.

Emery, W.J., A.C. Thomas, M.J. Collins, W.R. Crawford, and D.L. Mackas, An objective method for computing advective surface velocities from sequential infrared satellite images, *J. Geophys. Res.*, *91*, 12,865-12,878, 1986.

Flament, P., L. Armi, and L. Washburn, The evolving structure of an upwelling element, *J. Geophys. Res.*, *90*, 11,765–11,778, 1985.

Flament, P., P.M. Kosro, and A. Huyer, Mesoscale variability off California as seen by the Geosat altimeter, Proceedings of IGARSS '89, 12th Canadian Symposium on Remote Sensing, *IEEE Publ. 89CH2768-0*, vol. 2, 1063–1068, Inst. of Electr. and Electron. Eng., New York, 1989.

Freitag, H.P., and D. Halpern, Hydrographic observations off northern California during May 1977, *J. Geophys. Res.*, *86*, 4248–4252, 1981.

Haidvogel, D.B., A. Beckmann, and K.S. Hedström, Dynamical simulations of filament formation and evolution in the coastal transition zone, *J. Geophys. Res.*, this issue.

Hayward, T.L., and A.W. Mantyla, Physical, chemical and biological structure of a coastal eddy near Cape Mendocino, *J. Mar. Res.*, *4*, 825–850, 1990.

Hickey, B.M., The California Current system—Hypotheses and facts, *Prog. Oceanogr.*, *8*, 191–279, 1979.

Hood, R.R., M.R. Abbott, A. Huyer, and P.M. Kosro, Surface patterns in temperature, flow, phytoplankton biomass, and species composition in the coastal transition zone of northern California, *J. Geophys. Res.*, *95*, 18,081–18,094. 1990.

Hood, R.R., M.R. Abbott, and A. Huyer, Phytoplankton and photosynthetic light response in the coastal transition zone off northern California in June 1987, *J. Geophys. Res.*, this issue.

Huyer, A.E., Coastal upwelling in the California Current system, *Prog. Oceanogr.*, *12*, 259–284, 1983.

Huyer, A.E., and P.M. Kosro, Mesoscale surveys over the shelf and slope in the upwelling region near Point Arena, California, *J. Geophys. Res.*, *92*, 1655–1682, 1987.

Huyer, A., P.M. Kosro, J. Fleischbein, S.R. Ramp, T. Stanton, L. Washburn, F.P. Chavez, T.J. Cowles, S.D. Pierce, and R.L. Smith, Currents and water masses of the coastal transition zone off northern California, June to August 1988, *J. Geophys. Res.*, this issue.

Ikeda, M., and W.J. Emery, Satellite observations and modeling of meanders in the California Current system off Oregon and northern California, *J. Phys. Oceanogr.*, *14*, 1434–1450, 1984.

Johannessen, J.A., E. Svendsen, S. Sandven, O.M. Johannessen, and K. Lygre, Three-dimensional structure of mesoscale eddies in the Norwegian coastal current, *J. Phys. Oceanogr.*, *19*, 3–19, 1989.

Kadko, D.C., L. Washburn, and B.H. Jones, Evidence of subduction within cold filaments of the northern California coastal transition zone, *J. Geophys. Res.*, this issue.

Kelly, K.A., The influence of winds and topography on the sea surface temperature patterns over the northern California slope, *J. Geophys. Res.*, *90*, 11,783–11,798, 1985.

Kelly, K.A., An inverse model for near-surface velocity from infrared images, *J. Phys. Oceanogr.*, *12*, 1845–1864, 1989.

Kosro, P.M., and A. Huyer, CTD and velocity surveys of seaward jets off northern California, July 1981 and 1982, *J. Geophys. Res.*, *91*, 7680–7690, 1986.

Kosro, P.M., A. Huyer, S. Ramp, R.L. Smith, F. Chavez, T.J. Cowles, M. Abbott, P.T. Strub, R.T. Barber, P.F. Jessen, and L.F. Small, The structure of the transition zone between coastal waters and the open ocean off northern California, spring 1987, *J. Geophys. Res.*, this issue.

Lynn, R.J., and J.J. Simpson, The California Current system: The seasonal variability of its physical characteristics, *J. Geophys. Res.*, *92*, 12,947–12,966, 1987.

McCreary, J.P., Y. Fukamachi, and P.K. Kundu, A numerical investigation of jets and eddies near an eastern ocean boundary, *J. Geophys. Res.*, *96*, 2515–2534, 1991.

Mackas, D.L., K.L. Denman, and A.F. Bennett, Least squares multiple tracer analysis of water mass composition, *J. Geophys. Res.*, *92*, 2907–2918, 1987.

Mackas, D.L., L. Washburn, and S.L. Smith, Zooplankton community patterns associated with a California Current cold filament, *J. Geophys. Res.*, this issue.

Magnell, B.A., J.F. Borchardt, C.L. Greengrove, J.M. Federiuk, and N.A. Bray, Northern California Coastal Circulation Study, data report 2, Main measurement program, March–August 1988, vol. 1, Lagrangian and hydrographic observation, EG&G Washington Anal. Serv. Cent., Inc., Waltham, Mass., 1989*a*.

Magnell, B.A., J.F. Borchardt, C.L. Greengrove, J.M. Federiuk, and N.A. Bray, Northern California Coastal Circulation Study, data report 2, Main measurement program, March–August 1988, vol. 2, Moored instrument, meteorological, and sea level measurements, EG&G Washington Anal. Serv. Cent., Inc., Waltham, Mass., 1989*b*.

Magnell, B.A., N.A. Bray, C.D. Winant, C.L. Greengrove, J. Largier, J.F. Borchardt, R.L. Bernstein, and C.E. Dorman, Convergent shelf flow at Cape Mendocino, *Oceanography*, *3*(1), 4–11, 1990.

Mooers, C.N.K., and A.R. Robinson, Turbulent jets and eddies in the California Current and inferred cross-shore transports, *Science*, *223*, 51–53, 1984.

Moum, J.N., D.R. Caldwell, and P.J. Stabeno, Mixing and intrusions in a rotating cold-core feature off Cape Blanco, Oregon, *J. Phys. Oceanogr.*, *18*, 823–833, 1988.

Narimousa, S., and T. Maxworthy, Application of a laboratory model to the interpretation of satellite and field observations of coastal upwelling, *Dyn. Atmos. Oceans*, *13*, 1–46, 1989.

Paduan, J.D., and P.P. Niiler, A Lagrangian description of motion in northern California coastal transition filaments, *J. Geophys. Res.*, 18,095–18,109, 1990.

Peláez, J., and J.A. McGowan, Phytoplankton pigment patterns in the California Current as determined by satellite, *Limnol. Oceanogr.*, *31*, 927–950, 1986.

Philander, S.G.H., and J.-H. Yoon, Eastern boundary current upwelling, *J. Phys. Oceanogr.*, *12*, 862–879, 1982.

Pierce, S.D., J.S. Allen, and L.J. Walstad, Dynamics of the coastal transition zone jet, 1, Linear stability analysis, *J. Geophys. Res.*, this issue.

Ramp, S.R., P.F. Jessen, K.H. Brink, P.P. Niiler, F.L. Daggett, and J.S. Best, The physical structure of cold filaments near Point Arena, California, during June 1987, *J. Geophys. Res.*, this issue.

Rienecker, M.M., and C.N.K. Mooers, A summary of the OPTOMA program's mesoscale ocean prediction studies in the California Current System, in *Mesoscale/Synoptic Coherent Structures in Geophysical Turbulence*, edited by J.C.J. Nihoul, and B.M. Jamart, pp. 519–548, Elsevier, Amsterdam, 1989*a*.

Rienecker, M.M., and C.N.K. Mooers, Mesoscale eddies, jets, and fronts off Point Arena, California, July 1986, *J. Geophys. Res.*, *94*, 12,555–12,569, 1989*b*.

Rienecker, M.M., C.N.K. Mooers, D.E. Hagan, and A.R. Robinson, A cool anomaly off northern California: An investigation using IR imagery and in situ data, *J. Geophys. Res.*, *90*, 4807–4818, 1985.

Rienecker, M.M., C.N.K. Mooers, and A.R. Robinson, Dynamical interpolation and forecast of the evolution of mesoscale features off northern California, *J. Phys. Oceanogr.*, *17*, 1189–1213, 1987.

Robinson, A.R., J.A. Carton, N. Pinardi, and C.N.K. Mooers, Dynamical forecasting and dynamical interpolation: An experiment in the California Current, *J. Phys. Oceanogr.*, *16*, 1561–1579, 1986.

Schramm, R.E., J. Fleischbein, R. March, A. Huyer, P.M. Kosro, T. Cowles, and N. Dudek, CTD observations in the coastal transition zone off northern California 18–27 May, 1987, *Data Rep. 141, Ref. 88-3*, 191 pp., Coll. of Oceanogr., Oreg. State Univ., Corvallis, 1988.

Send, U., R.C. Beardsley, and C.D. Winant, Relaxation from upwelling in the Coastal Ocean Dynamics Experiment, *J. Geophys. Res.*, *92*, 1683–1699, 1987.

Shannon, L.V., N.M. Walters, and S.A. Mostert, Satellite observations of surface temperature and near surface chlorophyll in the southern Benguela region, in *South African Ocean Color and Upwelling Experiment*, edited by L.V. Shannon, pp. 183–210, Sea Fisheries Research Institute, Cape Town, South Africa, 1985.

Simpson, J.J., T.D. Dickey, and C.J. Koblinsky, An offshore eddy in the California Current system, I, Interior dynamics, *Prog. Oceanogr.*, *13*, 5–49, 1984.

Simpson, J.J., C.J. Koblinsky, J. Peláez, L.R. Haury, and D. Wiesenhahn, Temperature–plant pigment–optical relations in a recurrent offshore mesoscale eddy near Point Conception, California, *J. Geophys. Res.*, *91*, 12,919–12,936, 1986.

Stern, M.E., On the amplification of convergences in coastal currents and the formation of "squirts," *J. Mar. Res.*, *44*, 403–421, 1986.

Strub, P.T., J.S. Allen, A. Huyer, R.L. Smith, and R.C. Beardsley, Seasonal cycles of currents, temperatures, winds, and sea level over the northeast Pacific continental shelf: 35°N to 48°N, *J. Geophys. Res.*, *92*, 1507–1526, 1987*a*.

Strub, P.T., J.S. Allen, A. Huyer, and R.L. Smith, Large-scale structure of the spring transition in the coastal ocean off western North America, *J. Geophys. Res.*, *92*, 1527–1544, 1987*b*.

Strub, P.T., C. James, A.C. Thomas, and M.R. Abbott, Seasonal and nonseasonal variability of satellite-derived surface pigment concentrations in the California Current, *J. Geophys. Res.*, *95*, 11,501–11,530, 1990.

Thomas, A.C., and P.T. Strub, Seasonal and interannual variability of phytoplankton pigment concentrations across a California Current system frontal zone, *J. Geophys. Res.*, *95*, 13,023–13,042, 1990.

Thomson, R.E., and J.E. Papadakis, Upwelling filaments and motion of a satellite-tracked drifter along the west coast of North America, *J. Geophys. Res.*, *92*, 6445–6461, 1987.

Tokmakian, R.T., P.T. Strub, and J. McClean-Padman, Evaluation of the maximum cross-correlation method of estimating sea surface velocities from sequential satellite images, *J. Atmos. Oceanic Technol.*, *7*, 852–865, 1990.

Traganza, E.D., V.M. Silva, D.M. Austin, W.E. Hanson, and S.H. Bronsink, Nutrient mapping and recurrence of coastal upwelling centers by satellite remote sensing: Its implication to primary production and the sediment record, in *Coastal Upwelling: Its Sediment Record*, edited by E. Suess and J. Thiede, pp. 61–83, Plenum, New York, 1983.

Vastano, A.C., and S. Borders, Sea surface motion over an anticyclonic eddy on the Oyashio Front, *Remote Sens. Environ.*, *16*, 87–90, 1984.

Walstad, L.J., J.S. Allen, P.M. Kosro, and A. Huyer, Dynamics of the coastal transition zone in 1987 through data assimilation studies, *J. Geophys. Res.*, this issue.

Washburn, L., D.C. Kadko, B.H. Jones, T.L. Hayward, P.M. Kosro, T.P. Stanton, A. Huyer, S.R. Ramp, and T.J. Cowles, Water mass subduction and the transport of phytoplankton in a coastal upwelling system, *J. Geophys. Res.*, this issue.

White, W.B., C.-K. Tai, and J. DiMento, Annual Rossby waves characteristics in the California Current region from the Geosat exact repeat mission, *J. Phys. Oceanogr.*, *20*, 1297–1310, 1990.

Wyllie, J.G., Geostrophic flow of the California Current at the surface and at 200 m, *CalCOFI Atlas 4*, 12 pp. and 280 charts, State of Calif. Mar. Res. Comm., La Jolla, 1966.

M. R. Abbott, J. A. Barth, R. R. Hood, A. Huyer, C. James, P. M. Kosro, R. L. Smith, P. T. Strub, and L. J. Walstad, College of Oceanography, Oregon State University, Corvallis, OR 97331.

R. T. Barber, Duke University Marine Laboratory, Beaufort, NC 28516.

M. L. Batteen, R. L. Haney, and S. R. Ramp, Naval Postgraduate School, Monterey, CA 93943.

K. H. Brink, Woods Hole, Oceanographic Institution, Woods Hole, MA 02543.

F. P. Chavez, Monterey Bay Aquarium Research Institute, 160 Central Avenue, Pacific Grove, CA 93950.

R. K. Dewey, Science Applications International Corporation, 13400 Northup Way, Suite 36, Bellevue, WA 98005.

D. B. Haidvogel, Institute of Marine and Coastal Sciences, Rutgers University, P.O. Box 231, New Brunswick, NJ 08903.

T. L. Hayward, P. P. Niiler, and M. S. Swenson, Scripps Institution of Oceanography, University of California, San Diego, La Jolla, CA 92093.

D. C. Kadko, Rosenstiel School of Marine and Atmospheric Science, University of Miami, 4600 Rickenbacker Causeway, Miami, FL 33149.

D. L. Mackas, Institute of Ocean Sciences, Sidney, British Columbia, Canada V8L 4B2.

L. Washburn, Department of Geography, University of California, Santa Barbara, CA 93106.

(Received July 16, 1990;
accepted October 26, 1990.)

APPENDIX E

INTERANNUAL VARIABILITY IN PHYTOPLANKTON PIGMENT DISTRIBUTION DURING THE SPRING TRANSITION ALONG THE WEST COAST OF NORTH AMERICA

A. C. Thomas and P. Ted Strub

JOURNAL OF GEOPHYSICAL RESEARCH, VOL. 94, NO. C12, PAGES 18,095–18,117, DECEMBER 15, 1989

Interannual Variability in Phytoplankton Pigment Distribution During the Spring Transition Along the West Coast of North America

A. C. THOMAS AND P. T. STRUB

College of Oceanography, Oregon State University, Corvallis

A 5-year time series of coastal zone color scanner imagery (1980–1983, 1986) is used to examine changes in the large-scale pattern of chlorophyll pigment concentration coincident with the spring transition in winds and currents along the west coast of North America. The data show strong interannual variability in the timing and spatial patterns of pigment concentration at the time of the transition event. In both 1980 and 1981 a large increase in pigment concentration occurs (from 0.5 mg m^{-3} to >3.0 mg m^{-3} in 1980 and from 0.3 mg m^{-3} to >1.5 mg m^{-3} in 1981). In these years, as well as in 1982, the increase takes place between ≈33°N and ≈41°N, but it occurs in a region centered 300 km offshore in 1980 and within 300 km of the coast in 1981 and 1982. These changes are in contrast to 1983 and 1986, when virtually no change in pattern or concentration is associated with the transition. Calculations of light availability and in situ data suggest this region is nutrient limited even in the mid to late winter. Time series of pigment concentration and wind forcing for extended periods before and after the transition date show that increases in concentration are associated with strong wind mixing events prior to the transition and with the onset of southward wind stress (upwelling) at the time of the transition. Interannual variability in the response of pigment concentration to the spring transition appears to be a function of spatial and temporal variability in vertical nutrient flux induced by wind mixing and/or the upwelling initiated at the time of the transition. Interannual differences in the mixing regime are illustrated with a one-dimensional mixing model.

1. INTRODUCTION

A spring transition in wind and current structure off the west coast of North America marks the end of the winter regime of northward mean flow within the California Current System (CCS) and the beginning of the summer regime characterized by upwelling and southward flow [*Hickey*, 1979]. This transition usually occurs quite rapidly, often over the course of a few days [*Huyer et al.*, 1979; *Breaker and Mooers*, 1986], with large alongshore length scales of 500 to 2000 km [*Strub et al.*, 1987*a*].

Biological responses to this physical transition and the sudden switch to a mean upwelling-favorable wind have not been investigated. The short time and large spatial scales over which the transition occurs preclude the possibility of adequately mapping chlorophyll distributions during the event with data from ship cruises. The availability of satellite estimates of surface pigment concentration from the coastal zone color scanner (CZCS) on Nimbus 7, however, allows a synoptic representation of these patterns at the time of the transition with the necessary space and time scales.

We analyze CZCS data from 5 years (1980–1983 and 1986) to determine if large-scale changes in near-surface pigment distribution take place in association with the spring transition event. We present the major differences and similarities between years and relate our observations to large-scale forcing mechanisms in an attempt to explain the observed patterns of concentration and interannual variability. In section 2 we provide a brief description of the physical spring transition event and a synopsis of the biological and physical regimes within the CCS during winter and summer. A description of the satellite data and their treatment and of other data sets used in the study is given in section 3. In section 4, spatial patterns of pigment concentration from the spring transition period are presented together with temporal patterns of concentration over periods extending before and after the transition. These patterns are discussed in relation to large-scale forcing in section 5, using wind data, calculations of incident solar radiation, and available in situ profiles of density, chlorophyll, and nutrient concentrations. Section 6 contains a summary and conclusions of these results.

Paper number 89JC01398.
0148-0227/89/89JC-01398$05.00

2. BACKGROUND

The physical spring transition is a response to large-scale wind forcing [*Huyer et al.*, 1979; *Strub et al.*, 1987*a*; *Strub and James*, 1988]. As the winter Aleutian low-pressure system weakens and moves northwestward, the North Pacific high-pressure system and a low-pressure system over the southwestern United States strengthen, changing the dominant winds from northward to southward over the continental margin. This southward wind stress results in an offshore Ekman transport and the onset of the well-documented summer upwelling regime along the west coast, with lower coastal sea levels, southward surface currents and a strong cross-shelf density gradient [*Huyer*, 1983]. The strength of this oceanic response is greatest north of approximately 35°–37°N [*Strub et al.*, 1987*a*]. South of this latitude, the event is weak or not present; here the monthly mean wind stress is southward all year and the seasonal change in sea level is small [*Strub et al.*, 1987*b*]. The physical spring transition typically takes place between mid-March and the end of April and can usually be identified as a rapid drop in coastal sea level over a few days, with levels remaining low thereafter.

Winter chlorophyll distributions within the full extent of the CCS are not well documented. Available data provide a broad-scale picture of pretransition conditions. Early winter (November–December) surface concentrations in the northward flowing Davidson Current off the southern British Columbia coast are <0.2 mg m^{-3} [*Thomas and Emery*, 1986,

1988]. *Landry et al.* [1989] show that the long-term mean (1954–1984) surface chlorophyll concentration off the Washington and Oregon coasts in late winter is ≈1.0 mg m^{-3}. Midwinter (January) surface concentrations from the southern portion of the study area (≈34°N) decrease from ≈1.0 mg m^{-3} nearshore to less than 0.2 mg m^{-3} in regions greater than 300 km offshore [*Haury et al.*, 1986]. This gradient is also observed in satellite images of the same area [*Smith et al.*, 1988]. In winter, the vertical distribution of chlorophyll is often uniform with depth, and the thermocline is relatively deep (≈75 m) [*Michaelsen et al.*, 1988] in the central and southern California region. These authors show that in spring, the water column stratifies and a subsurface chlorophyll maximum develops. *Eppley et al.* [1985] point out that ship data show that total water column production in the Southern California Bight does not show a seasonal cycle but that chlorophyll concentration in the upper attenuation depth of the euphotic zone (that region sampled by the CZCS) has a winter maximum and summer minimum. A portion of this seasonality observed in CZCS data is a result of much of the summer production and biomass occurring as a subsurface chlorophyll maximum, below the depth sampled by the satellite sensor (as discussed by *Campbell and O'Reilly* [1988]), and shown by *Michaelsen et al.* [1988]. These authors show that the amplitude of this annual cycle is largest in offshore regions and relatively small within 100 km of the coast in the central California region. A winter maximum is not evident in ship data off the Oregon and Washington coasts [*Landry et al.*, 1989].

Summer distributions of chlorophyll in the CCS have been more fully documented and illustrate the characteristics of the region after the transition. Using comparisons of critical depth and the depth of mixing, *Parsons et al.* [1966] show the onset of the spring bloom in the North Pacific can start at latitudes less than ≈45°N in February and move northwestward. Summer coastal distributions are characterized by strong temporal and spatial variability closely related to wind stress and resultant upwelling [*Small and Menzies*, 1981; *Abbott and Zion*, 1985] and along-shelf and cross-shelf advection [*Abbott and Zion*, 1987]. These studies show a general trend of high biomass near the coast in the upwelling zones, decreasing offshore to the oligotrophic conditions of central Pacific water. Mean summer surface concentrations of greater than 2.5 mg m^{-3} are found in coastal regions off central California, with concentrations less than 0.5 mg m^{-3} in regions farther than ≈250 km from shore [*Smith et al.*, 1988]. These authors state that spatial patterns offshore are dominated by larger-scale variability than those nearshore, and biomass is consistently lower. Variability in both concentration and spatial patterns is maximum in the early summer [*Barale and Fay*, 1986]. *Chelton et al.* [1982] and *Chelton* [1982] argue that the large-scale biological variability in offshore regions within the CCS is coupled more closely to changes in southward advection and wind stress curl than to coastal upwelling.

3. DATA PREPARATION

The CZCS images utilized in this study are part of the West Coast Time Series. They were recorded at the Scripps Satellite Oceanography Facility (La Jolla, California) and processed at the Jet Propulsion Laboratory (Pasadena, California) with software developed by O. Brown and R. Evans (University of Miami). Atmospheric correction was done with coefficients found by *Gordon et al.* [1983*a*, *b*]. The images were initially navigated into square 512 × 512 pixel images with spatial resolutions of 100 pixels per degree. Each of these original images from a single satellite pass over the west coast of North America was then subsampled and combined to form a 512 × 512 pixel image of the entire west coast (≈22°N to 55°N) with a spatial resolution of ≈14.3 pixels per degree. Radiance measured by the CZCS was processed to yield values of pigment concentration. The accuracy of the CZCS pigment measurements is estimated to be log [Chlorophyll] ± 0.5 [*Gordon et al.*, 1980]. Tests by *Smith et al.* [1988] showed the accuracy of the CZCS data when compared with ship data from the southern California coast was ≈ ±40% for pigment values ranging from 0.05 to 10.0 mg m^{-3}. *Abbott and Zion* [1987] reported a regression of log-transformed satellite pigment on ship chlorophyll to have an r^2 of 0.8 and a slope of 1.0 in the coastal region of the CCS off northern California.

TABLE 1. The Spring Transition Date

Year	Date
1980	March 22
1981	March 26
1982	April 18
1983	April 4
1986	March 17

The transition date in each year is defined here as the spring date when sea levels at 41.8°N (Crescent City tide gauge data) drop rapidly in a period of a few days and stay low. The alongshore coherence of this date for each year was confirmed with sea level data from tidal stations north and south of this station. *Strub et al.* [1987*a*] show that this location and procedure are a reasonable signature of the event over the study area and that the date of the transition varied between March 22 and April 18 for the 9 years of data which they examined. The date of the spring transition in each of the years studied here is given in Table 1.

Visual inspection of the available images from the spring transition period in each year indicates that cloud cover is too widespread for single images to depict pigment distributions before or after the actual event. In addition, very few images were recorded during 1984 and 1985 owing to problems on the satellite, so descriptive and statistical analysis of the spring transition is restricted to the 5-year time series 1980–1983 and 1986. Cloud cover even in these years results in large spatial gaps in the data (see also *Kelly* [1985], *Abbott and Zion* [1987], and *Michaelsen et al.* [1988]). To fill these gaps, we have formed composite images over periods centered about the spring transition date. Following the procedure of *Strub et al.* [1987*a*], we identify the date of the physical transition in each year from time series of coastal sea level data and then form temporal composites over both 10- and 15-day periods before and after this date. Pigment concentrations for each pixel in these composites are calculated by averaging over all available images within the time period without including cloud-contaminated pixels. To reduce the effect of single images and outlying pixel values, a concentration is assigned to pixels only if there were at least two representations within the time period. Pixels failing this criterion are flagged as cloud. The 10- and 15-day periods

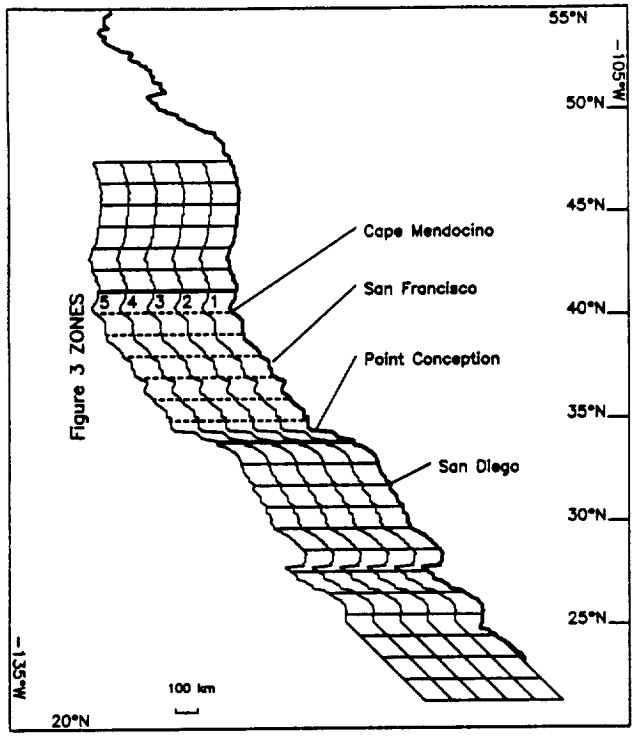

Fig. 1. A coastal outline of the study area showing major geographic points. The 100 × 100 km regions over which pigment from each 15-day composite was averaged to produce the spatial points for input into the EOF calculation are shown. Also shown are the northern and southern boundaries (bold lines) of the five 100-km-wide zones in the northern–central California region over which pigment concentrations in the 10-day composites were averaged to produce a time series in each year for Figure 3.

were chosen as a compromise between filling the spatial gaps by temporal averaging and retaining temporal resolution about the transition event. The 15-day composites are used to illustrate spatial patterns of pigment concentration, and a time series of 10-day composites is used to show temporal changes in concentration in selected regions.

The algorithm used to correct these images for atmospheric (Rayleigh) scattering is known to produce artificially high values of pigment concentration in regions of large solar zenith angle. Thus pigment concentrations estimated by the CZCS at high latitudes during winter cannot be trusted. Although reduction of this problem is now possible in the raw data processing [*Gordon et al.*, 1988], the West Coast Time Series were processed with a previous algorithm. For this reason, patterns of pigment off northern Oregon, Washington, and British Columbia for this spring period will not be interpreted or described. In this study we concentrate on patterns between approximately 23°N and 43°N.

Three other archived data sets are used for comparison with the satellite images. The central and southern portions of our study area (Figure 1) coincide with vertical profiles of temperature, salinity, chlorophyll, and nitrate obtained during California Cooperative Oceanic Fisheries Investigations, (CalCOFI) cruises [*Scripps Institution of Oceanography* (*SIO*), 1985]. Daily wind velocities are available for grid points over the study area as part of the limited-area fine mesh (LFM) wind product of the National Meteorological Center, Washington, D. C. Daily observations of cloud cover collected by ships of opportunity are available in the Comprehensive Ocean Atmosphere Data Set (COADS) [*Woodruff et al.*, 1987]. These are used to estimate solar radiation.

4. RESULTS

4.1. *Spatial Patterns Before and After the Transition*

CZCS image composites formed from the 15-day periods before and after the spring transition date in each year are shown in Plate 1. These 5 years show strong interannual variability in the response of pigment patterns to the transition event.

Two spatial patterns are common to all years. First, pigment concentrations are relatively high (>1.0 mg m^{-3}) within 50 km of the coast throughout the study area both before and after the transition event. In general, this shelf-slope region does not show any large-scale response to the transition event. *Barale and Fay* [1986] also show that high pigment values in regions nearest the coast are maintained throughout the year and show relatively little seasonal and interannual variability. High pigment values after the transition are an expected product of an upwelling regime [*Abbott and Zion*, 1985]. The higher pigment values prior to the transition adjacent to the coast are most likely supported by both episodic upwelling events which can occur even in winter [*Huyer*, 1983] and by interactions of bathymetry with tidal and other currents, all of which can lead to trophic enrichment of the shelf region [*Barale and Fay*, 1986]. Turbidity in the upper water column probably also contributes to the continually high satellite pigment estimates in this region closest to the coast. The effects of case 2 water are discussed further at the end of section 4.2. The second pattern common to each of the years is a negligible change in pigment patterns at the time of the transition in the southern portion of the study area. South of ≈33°N, the region of higher pigment concentrations (>1.0 mg m^{-3}) remains within ≈100 km of the coast both before and after the transition with no offshore expansion after the transition date. This is coincident with the region where the spring transition in physical processes is small or nonexistent [*Strub et al.*, 1987*a*].

The 15-day composites for 1980 (Figure 2*a*) show that large changes in pigment concentration occur at the time of the transition in the region between ≈43°N and ≈33°N. Pretransition pigment concentrations above 1.0 mg m^{-3} are generally restricted to within 150 km of the coast. After the transition, concentrations exceeding 3.0 mg m^{-3} occupy regions up to 500 km from the coast with the tongues extending 750 km offshore. The alongshore extent of this increase is difficult to estimate owing to cloud cover in the north, but a strong front perpendicular to the shore at approximately 33°N separates these high concentrations from concentrations of less than 0.5 mg m^{-3} to the south. Maximum change in pigment concentration at the time of the transition is within a broad region centered ≈300 km from shore with an alongshore length scale greater than 600 km. In this region of maximum change, pigment concentrations increase from ≈0.5 mg m^{-3} to greater than 3.0 mg m^{-3} in an average of 15 days over an area of ≈300,000 km^2.

Pigment patterns during the 1981 transition (Plate 1*b*) show an increase in concentration of similar alongshore

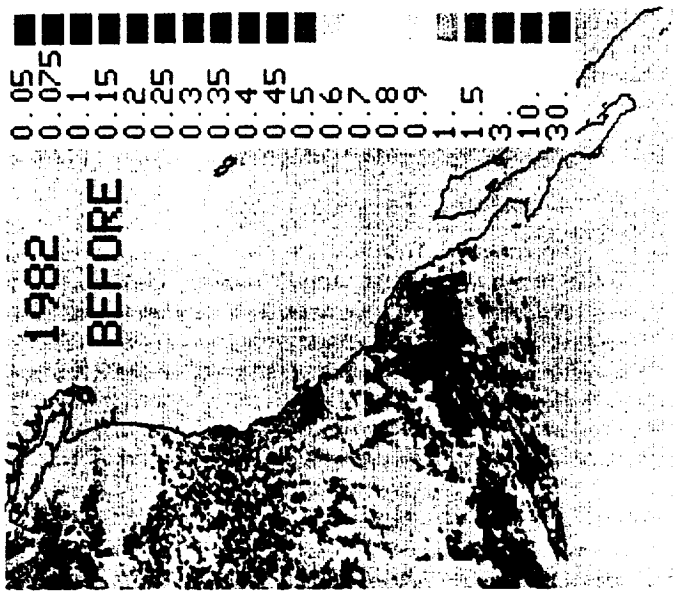

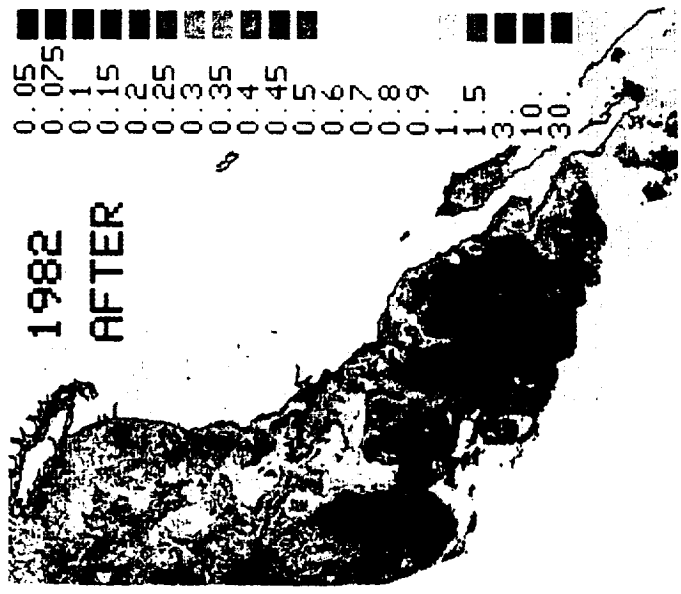

Plate 1c

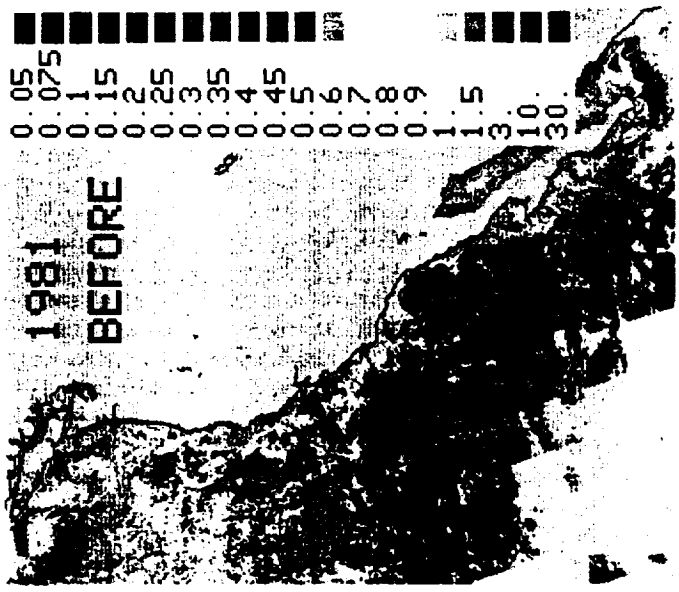

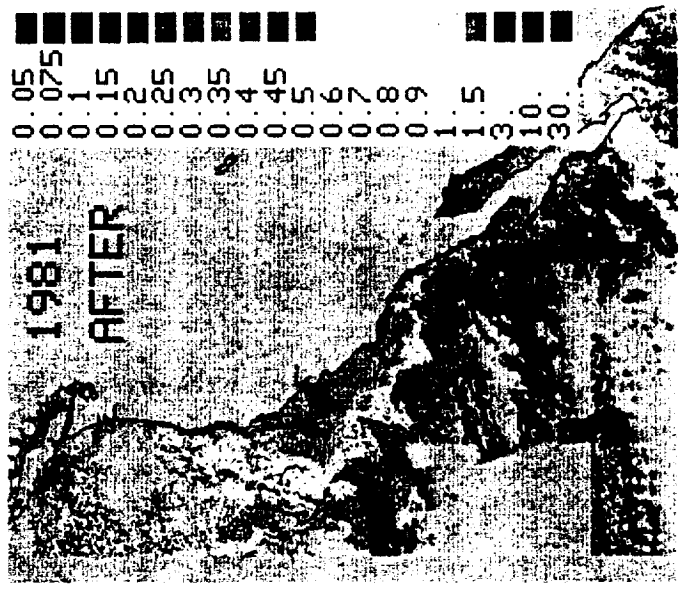

Plate 1b

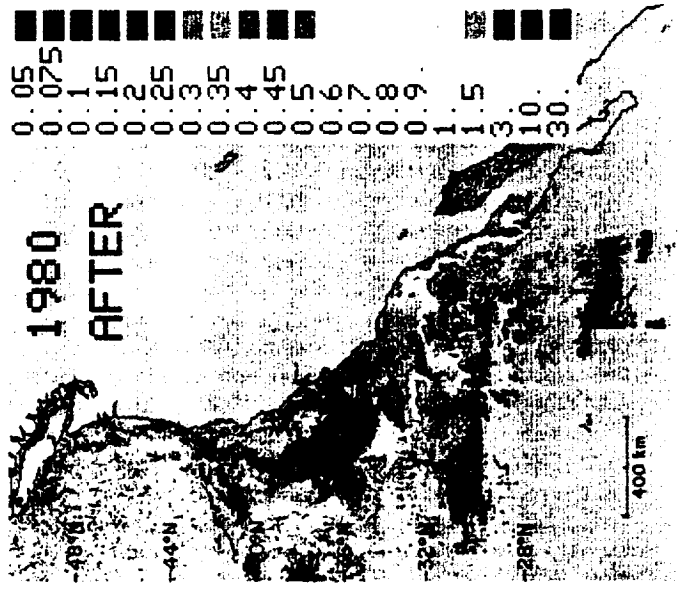

Plate 1a

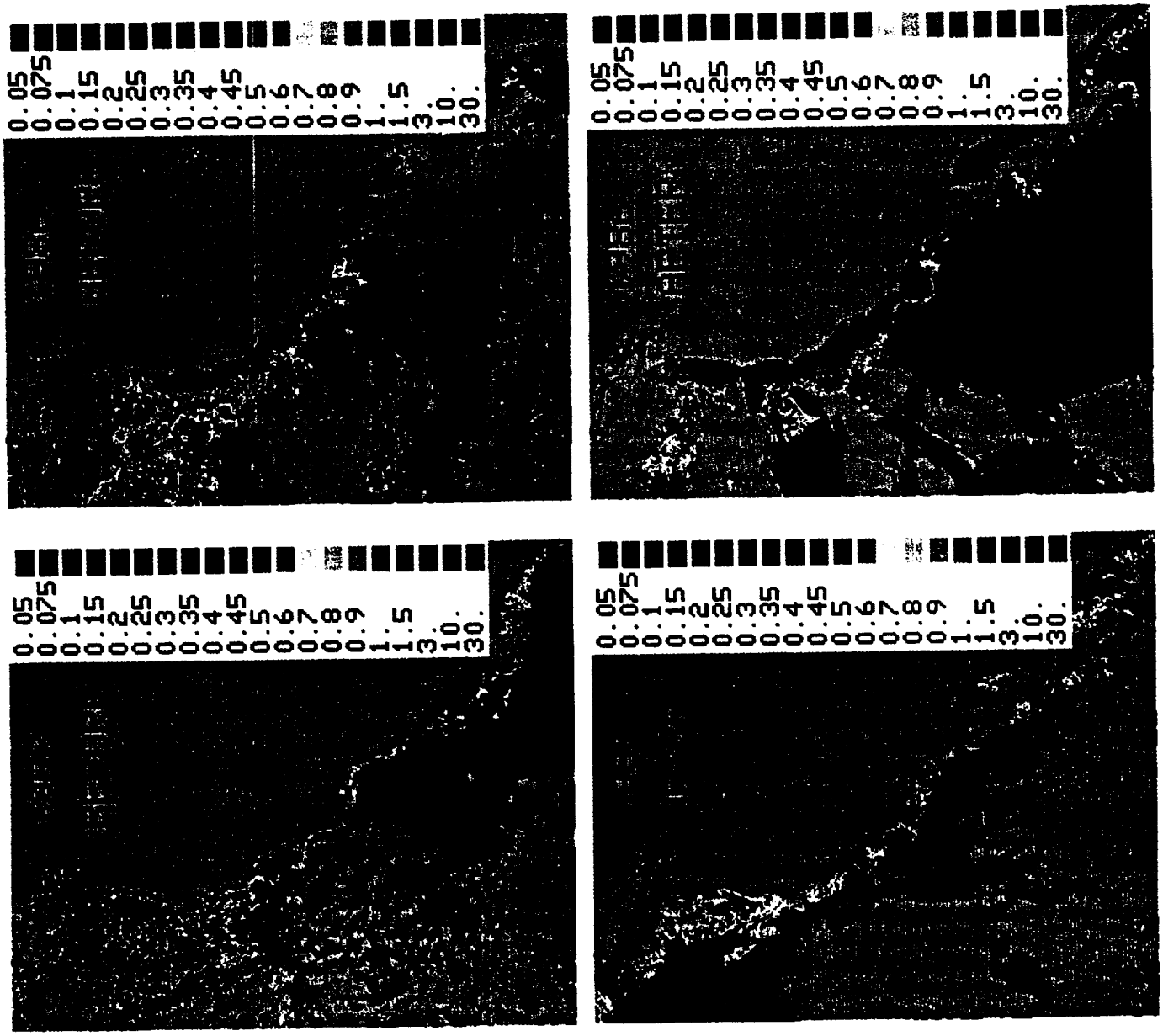

Plate 1. Image composites of coastal zone color scanner data of the California Current System in spring. Patterns of mean pigment concentration over 15-day periods (top) before and (bottom) after the physical spring transition dates (see Table 1) in each year are shown; years and the transition date in each are (*a*) 1980, March 22; (*b*) 1981, March 26; (*c*) 1982, April 18; (*d*) 1983, April 4; and (*e*) 1986, March 17. Regions north of ≈42°N are strongly influenced by the failure of the atmospheric correction algorithm and are not interpreted in this study.

length scales as the 1980 event. The maximum change in concentration, however, is more closely associated with the coast, in a region from ≈50 km to ≈300 km offshore. The large-scale change in concentration during the 1981 event is from ≈0.3 mg m^{-3} to ≈1.5 mg m^{-3} over a region of ≈180,000 km^2.

Changes in pigment patterns associated with the 1982 transition (Plate 1*c*) are of a different character than those previously seen. Prior to the transition (as well as can be visualized through the clouds), distributions in 1982 appear similar to 1980 and 1981. After the transition, however, the offshore increase in concentration shows considerably more spatial variability than was present in previous years and does not extend south of ≈35°N. Offshore concentrations greater than 1.0 mg m^{-3} are developed into eddy and jetlike features more closely resembling those previously described in association with summer upwelling periods for this region [*Abbott and Zion*, 1985, 1987; *Pelaez and McGowan*, 1986] than the broad-scale, diffuse increases seen after the 1980 and 1981 transitions.

There is virtually no change in pigment pattern associated with the physical spring transition in 1983 (Plate 1*d*). Concentrations of ≈1.0 mg m^{-3} within 100 km of the coast are present both before and after the transition. This concentration does not increase, and an offshore expansion of the region of higher concentrations occurs only in the relatively restricted region within 100 km of the shore between San Francisco Bay and Cape Mendocino. This lack of response to the spring transition is repeated in 1986 (Plate 1*e*). Pigment concentrations before and after the event are higher than those in 1983 within the coastal region (≈1.5 mg m^{-3}), and they extend farther from shore (≈250 km). However, there are no large-scale changes in this pattern in association with the physical transition.

We have simplified this strong interannual variability in the large-scale changes of pigment patterns at the time of the spring transition by decomposing the image composites into empirical orthogonal functions (EOFs). Each of the 15-day composites shown in Plate 1 was spatially averaged into 1° × 1° blocks (Figure 1) using only cloud-free pixels. This spatial averaging assigned a pigment concentration to more than 97% of the total number of blocks, with the remainder filled by spatial averaging of the blocks immediately to the north and south. The pigment pattern represented by the blocks (now 125 spatial points per field) were treated as a 10-point time series (the 15-day composites before and after the transition event in each of the 5 years) for calculation of the EOFs. Each mode of an EOF decomposition is composed of a spatial pattern whose amplitude in time is described by a time series. Actual pigment concentration associated with the mode for any spatial point at a particular time can be reconstructed by multiplication of the spatial value and the amplitude in the time series.

The spatial patterns and amplitude time series of the dominant modes of the EOFs of pigment patterns during the spring transition are shown in Figure 2. The first mode explains 60.1% of the total variance with a spatial pattern describing an offshore region of maximum change associated with the transition event (Figure 2*a*). The time series shows the strength of this pattern during the 15-day periods before and after the transition in each of the 5 years. This mode is dominated by the strong increase in offshore chlorophyll in 1980 (the time series indicates a positive change), with weaker offshore increases in 1981 and 1982. No similar change is seen during the 1983 and 1986 transition. The second EOF mode, accounting for 10.3% of the total variance, primarily represents variance north of ≈43°N where the CZCS algorithm is not reliable. This mode is not interpreted further. The third EOF mode (Figure 2*b*) explains 8.3% of the variance and although of questionable statistical significance, agrees well with, and helps quantify, the visual interpretation. This mode shows a region of maximum variance next to the coast between ≈36°N and 41°N. The time series shows both 1981 and 1982 to have positive changes (increases in pigment concentration) associated with this pattern, with 1981 having the largest response. This pattern did not change during the transition in 1980 and actually decreased in 1983 and 1986.

4.2. *Temporal Changes in Pigment Concentration*

To characterize the temporal development of changes in pigment concentration at the time of the spring transition, a time series of fourteen 10-day composites of the CZCS data was formed of the six 10-day periods before and eight 10-day periods after the event in each year. Each of these composites was spatially averaged into five 1° wide zones between 34°N and 41°N (see Figure 1) to provide an indication of cross-shelf variability in the temporal changes. This latitudinal range was where maximum interannual variability and maximum changes in pigment concentration were seen in the 15-day composites (Plate 1).

The time series of concentrations in each of the five zones in each year are shown in Figure 3, together with alongshore wind stress and the strength of the wind mixing for the same period. Wind forcing will be discussed in section 5. These pigment time series include images from the early portions of each year when the CZCS algorithm is known to produce artificially high values at higher latitudes. We have attempted to reduce this error by subtracting a correction function from the original images prior to the formation of the temporal and spatial averages. This function is latitudinally dependent (increasing from south to north) with a period of 1 year, maximum in winter and minimum in summer. We assume that the true chlorophyll levels are low some distance from the coast for most of the year. The function is obtained from an EOF analysis of 5 years of monthly averaged CZCS data images subsampled to form a 2.5° wide strip beginning 2.5° offshore, extending from 25°N to 50°N. Our assumption is that a latitudinally dependent function with an annual cycle and a peak at high latitudes in the winter months is primarily due to algorithm failure (dominated by Rayleigh scattering error) and not in situ biological processes in this offshore region. The first EOF mode (70.5% of the variance in this offshore strip) shows this latitudinal pattern and seasonal cycle. Interpolated values of this function, depending on latitude and date, were subtracted from the images used to form the time series presented in Figure 3. This correction function reduces pigment concentrations in the early parts of the times series (average reduction of 1.3 mg m^{-3} in February) but has little effect at the time of the transition and later into the year. In addition to the algorithm errors, any true annual cycle in offshore pigment with a winter maximum is also removed by the correction function. As this study is an analysis of relatively

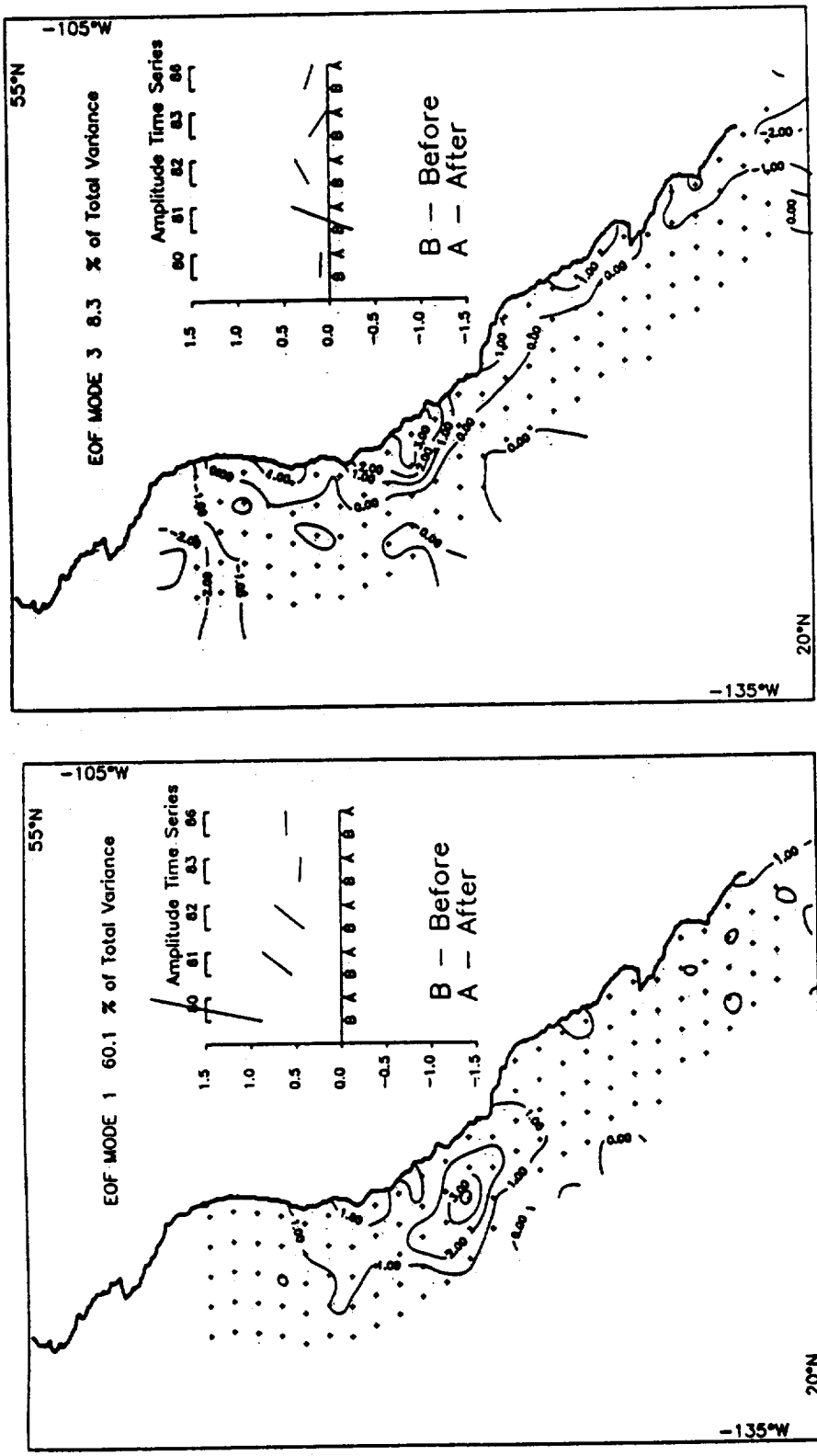

Fig. 2. Spatial patterns and amplitude time series of the (*a*) first and (*b*) third most dominant EOF modes of pigment patterns at the time of the spring transition. The time series shows the strength of the corresponding spatial pattern before and after the transition date in each of the years analyzed. The second mode (10.3% of the total variance) represented primarily variance north of ≈43°N where the CZCS algorithm is most suspect (see text).

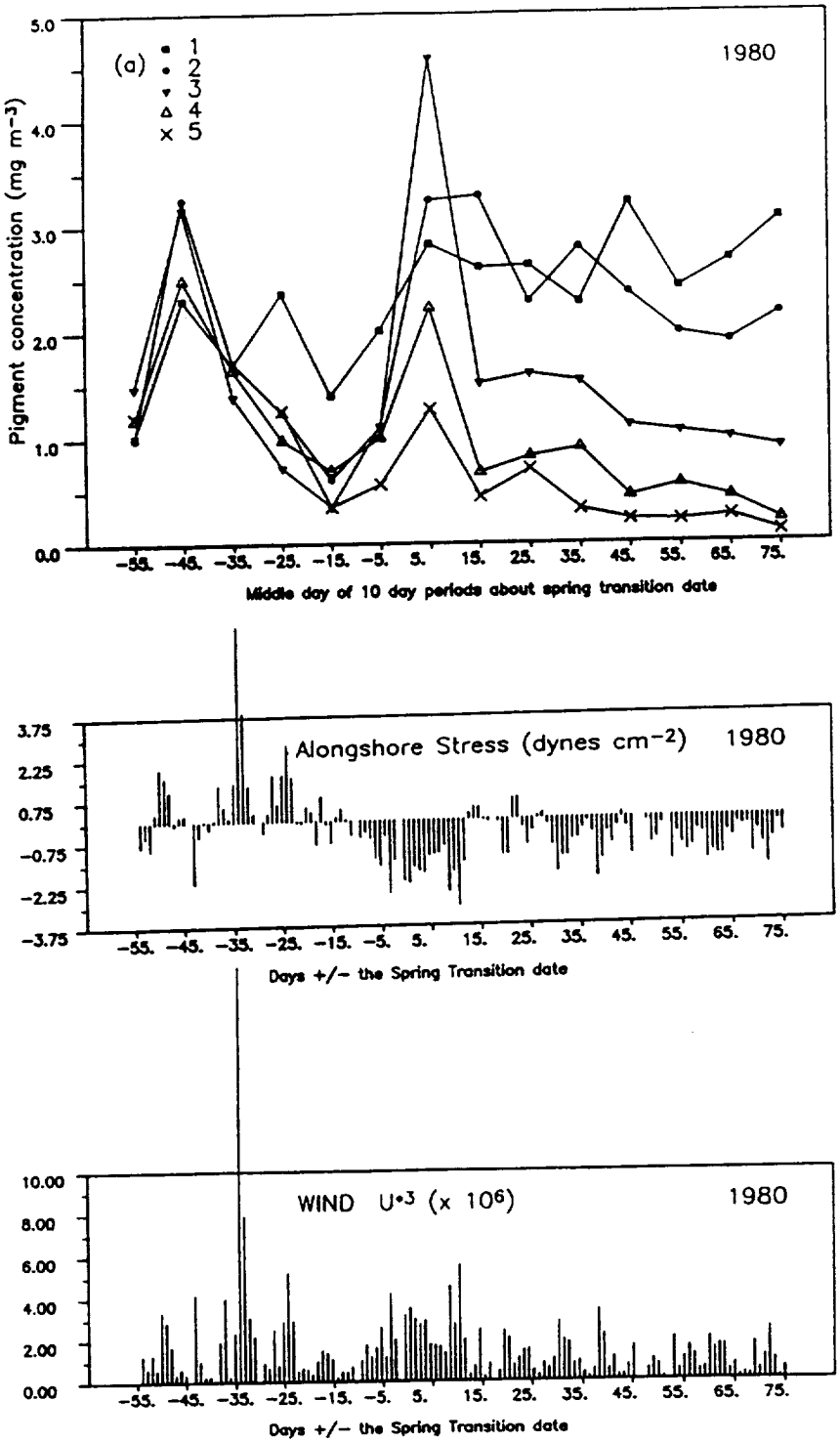

Fig. 3. Time series of pigment concentrations formed from 10-day composites spatially averaged over each of five 100-km-wide zones progressing offshore (zones 1–5 shown in Figure 1) for (*a*) 1980, (*b*) 1981, (*c*) 1982, (*d*) 1983, and (*e*) 1986. The spring transition date forms the starting point for six 10-day periods before and eight 10-day periods after the spring transition date for each year. Each time point represents a 10-day mean concentration and is plotted as the middle day of that period. Missing time points indicate that no satellite pigment estimates were available in the zone over the 10-day time period. Also shown for the same time period are daily values of alongshore wind stress and wind mixing strength (U_*^3) calculated from LFM wind data and averaged over all grid points within the five-zone region shown in Figure 1.

short time scale events superimposed on the annual cycle, the removal of any such annual cycle was not considered a problem.

The time series of pigment concentrations in each of the five zones during 1980 is shown in Figure 3*a*. These data show that the zone nearest the coast (zone 1) maintains a relatively high concentration (2.0–3.0 mg m^{-3}) both before and after the transition event. In the four zones farther from

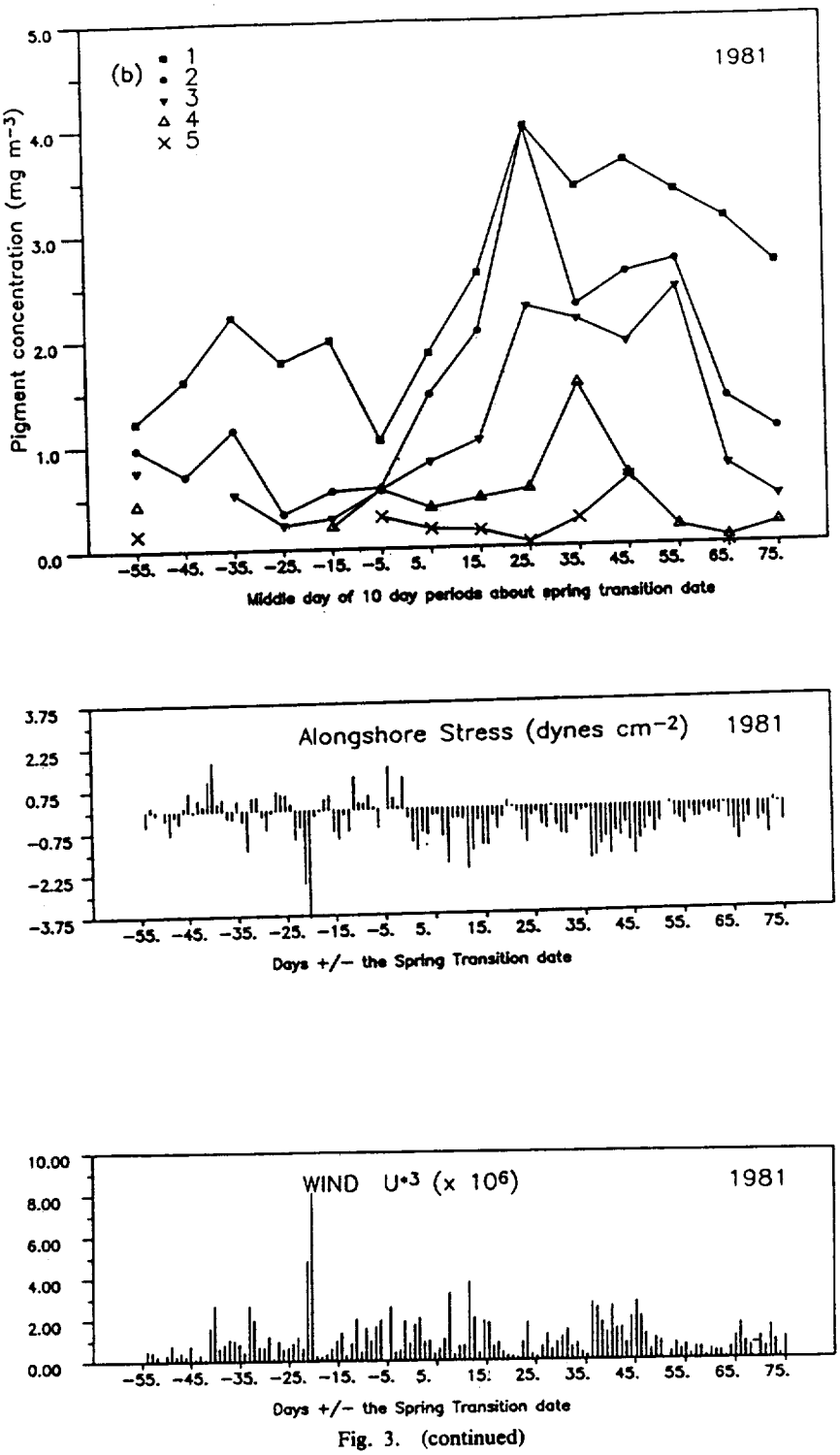

Fig. 3. (continued)

shore (zones 2–5), however, pigment concentrations increase sharply in the 10-day period (plotted as day 5) after the transition, to values 2–4 times higher than those immediately prior to the transition. These concentrations decrease after the first 10-day period, initially very rapidly but then return slowly to pre-transition concentrations after ≈50–60 days. The magnitude of the increase and the mean pigment concentration associated with this increase are greatest 200–400 km offshore.

The 1981 time series (Figure 3*b*) support the observation that the primary response of pigment concentrations to the transition in this year is in regions closest to the coast. Increases in mean pigment concentration begin at the time of the transition but increase more gradually than those in 1980. Increases are maximum within 200 km of the coast (zones 1 and 2) (from ≈1.0 mg m^{-3} to 4.0 mg m^{-3}), decreasing in magnitude in zones farther seaward. High concentrations are maintained over a month-long time period. Thereafter, con-

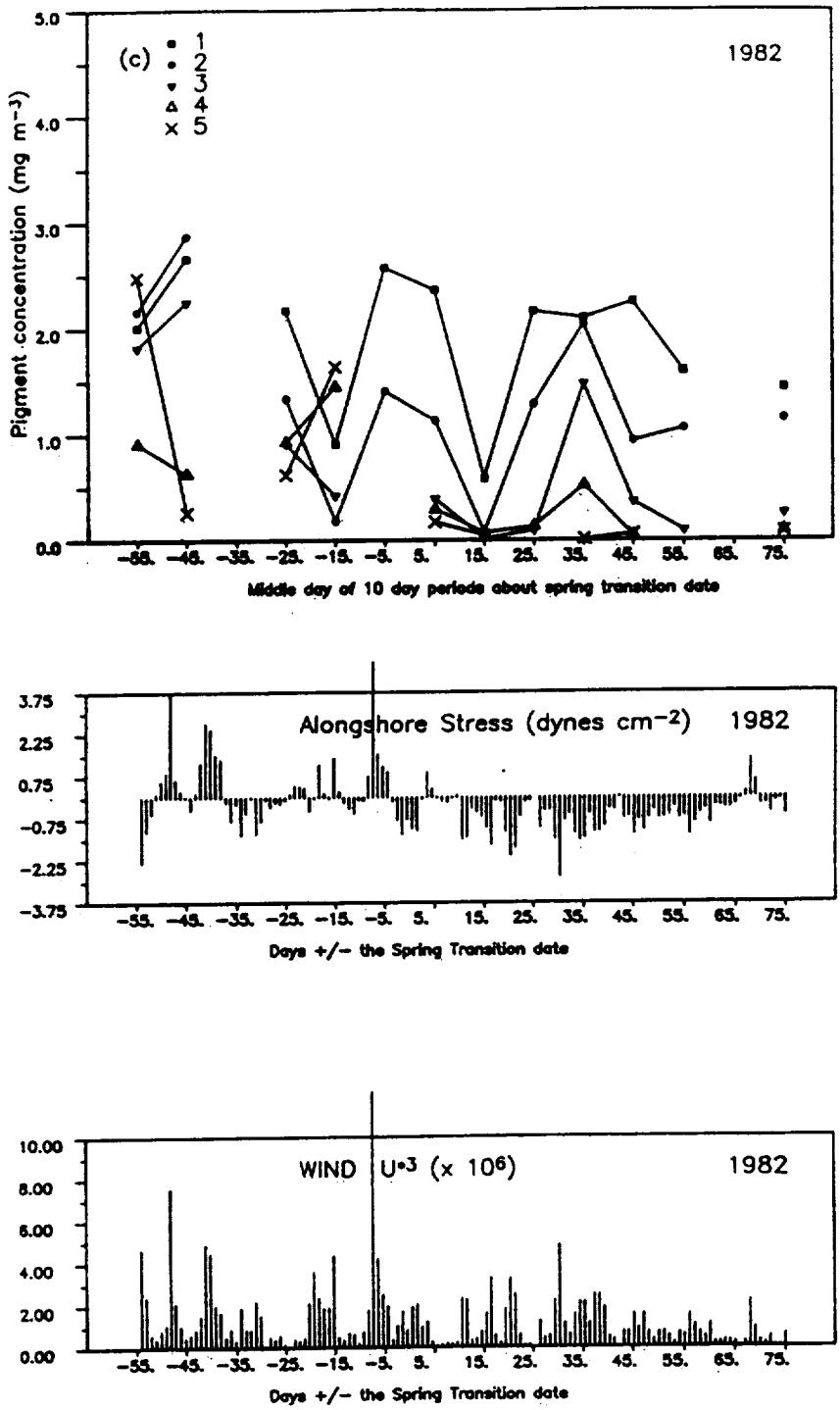

Fig. 3. (continued)

centrations appear to decrease. Concentrations in the three zones nearest the coast are higher after the transition than at any time prior to the event.

The pigment concentration time series in 1982 (Figure 3*c*) indicates a series of episodic events with largest amplitudes in zone 1 and decreasing amplitudes in zones farther from the coast. A short time scale increase (≈20 days) is initiated in the 10-day period immediately prior to the transition in the two zones closest to the coast, followed by a decrease to pretransition values and then another increase in the 30- to 40-day period after the transition. These data are difficult to interpret due to the gaps caused by clouds; however, changes in concentration in regions nearer the coast do appear more episodic in 1982 than in previous years.

In 1983 (Figure 3*d*) the largest increase in pigment concentration is dissociated from the date of the physical transition. There is a minor increase in concentration (0.5 mg m^{-3}) at the time of the physical transition that is restricted to the two zones nearest the coast (1 and 2) and of short (≈10 days) duration. The time series shows a relatively large concentration increase in the period 40–20 days before the transition (peaks of 4.5 and 3.2 mg m^{-3} in zones 1 and 2,

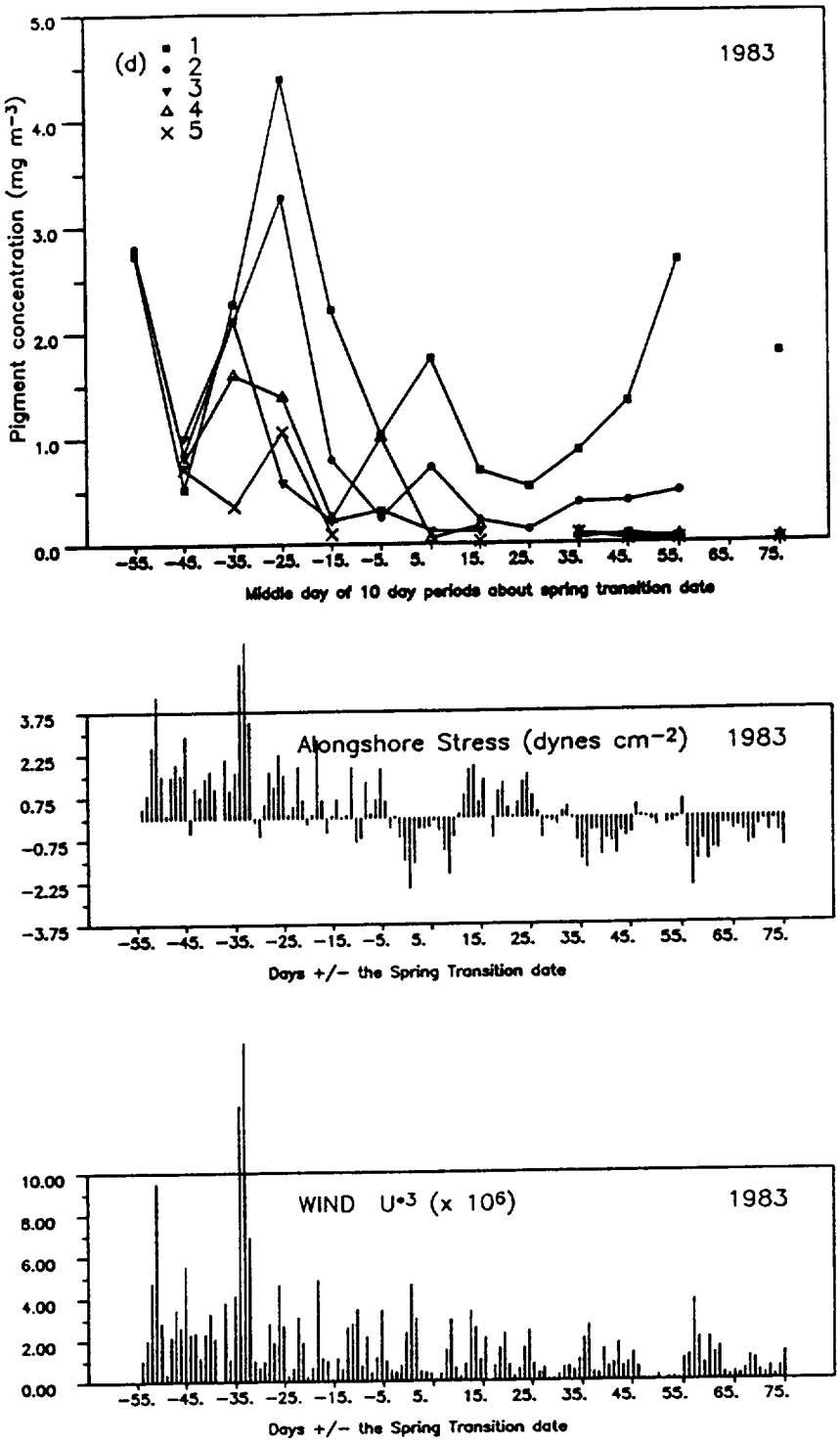

Fig. 3. (continued)

respectively) followed by a sharp decrease immediately prior to the transition (days 10–0). After the transition, fluctuations in concentration occur only within 100 km of the coast, and concentrations in all four zones to seaward remain low (<0.4 mg m^{-3}) in comparison to previous years.

Pigment concentrations in 1986 (Figure 3*e*) increase in the period 30–20 days prior to the transition date but exhibit relatively little variability after this. No major change occurs at the time of the physical transition. Increases associated with the transition event occur only in the two zones nearest the coast and are of short duration (≈10 days) and small magnitude (≈0.5 mg m^{-3}). A relatively stable cross-shelf concentration gradient is maintained throughout the study period with the three zones farthest seaward exhibiting only small changes in concentration.

The algorithms used to estimate pigment concentration from the satellite data assume that color in the water is derived from chlorophyll and related degradation products (case 1 water). Regions where significant amounts of color are contributed from other sources (case 2 water) will appear

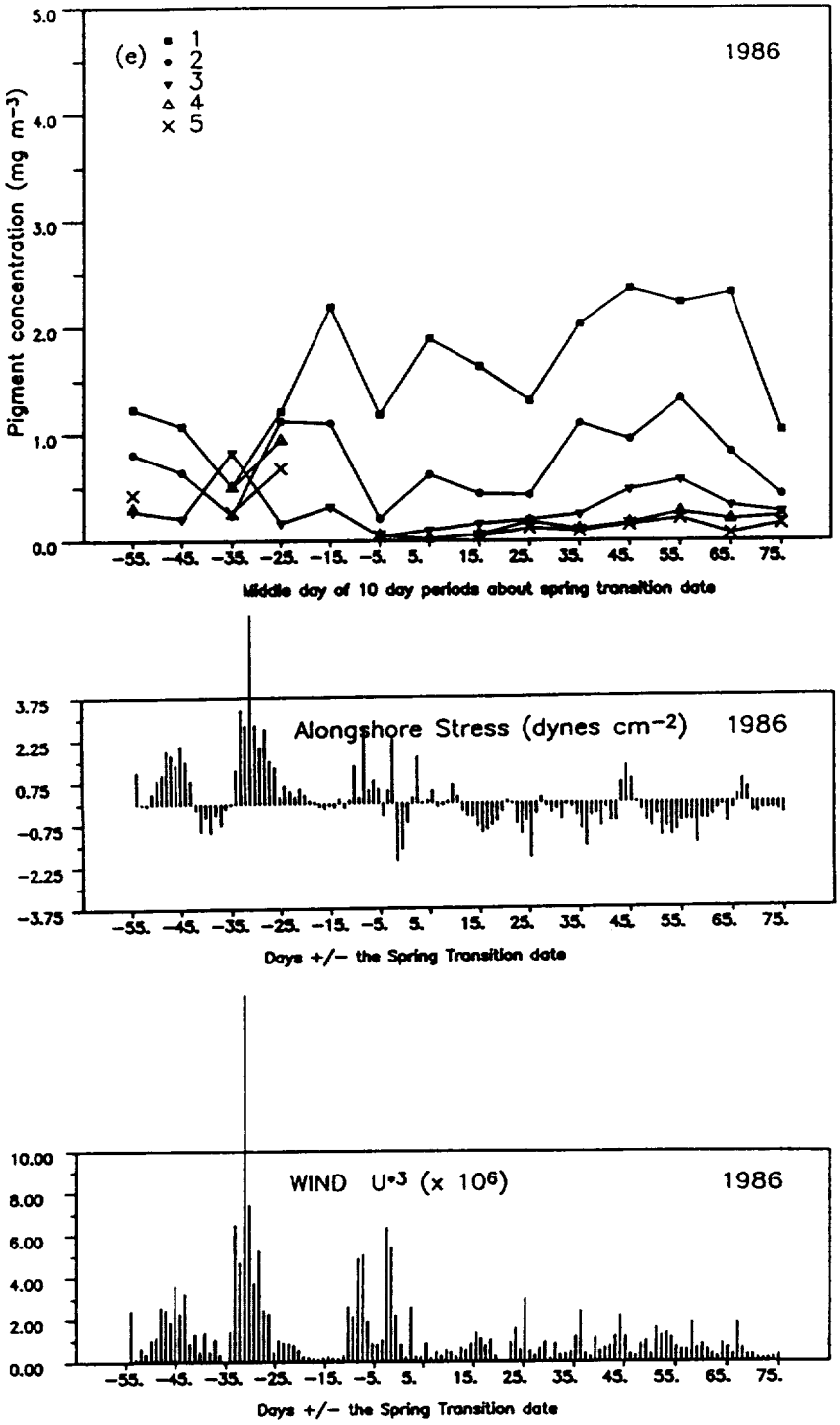

Fig. 3. (continued)

as regions of high pigment concentration in the imagery. This problem will be greatest near the coast over the shelf and probably contributes to the consistently high values observed closest to the coast where turbulence and runoff introduce sediment into the upper water column. In the study region, however, the shelf is usually of the order 20–30 km wide, and regions farther offshore are less likely to be turbid owing to suspended sediment. The fact that the zone closest to the coast in Figure 3 (zone 1) is an average over a 1° wide band reduces the potential bias introduced by shelf turbidity. Furthermore, the strong temporal correlation of pigment concentration between this zone and those further to seaward argues that concentrations averaged over zone 1 are not unduly contaminated by case 2 water.

5. Discussion

We have posed the question, What is the response of pigment concentration to the onset of upwelling favorable winds at the time of the spring transition? The results

presented in the preceding section demonstrate a large degree of interannual variability in the spatial pattern and temporal development of pigment concentrations at the time of the physical spring transition. The large increase in concentration in 1980 occurs offshore as a diffuse pattern over a large spatial area and does not appear to have been connected to coastal upwelling. The large increase in 1981 is more closely confined to the region near the coast, spreading offshore after the transition in a manner consistent with previous descriptions of a wind-driven coastal upwelling event. The response in 1982 is concentrated near the coast but is weaker and more variable in both space and time than that in previous years. In 1983 there is actually a decrease in pigment concentration at the time of the physical transition, but a major increase takes place 20–30 days prior to the transition. Concentrations in 1986 are higher than those in 1983, both before and after the transition, and extend farther from shore. However, there is little change in either concentration or pattern at the time of the physical transition. Instead, concentrations within 200 km of the coast increase in the period 20–30 days before the physical transition. The interannual variability of these responses does not appear to be directly related to the actual date of the physical transition per se (see Table 1). Neither the spatial patterns nor the time series of pigment concentrations show a consistent relationship to the Julian day of the event. Our discussion, then, is directed at identifying forcing mechanisms that can account for the interannual variability in the spatial pattern of pigment increase in those years when concentrations do show a response to the physical transition, and that can account for those years in which concentration increases were dissociated from the physical event.

Three possible mechanisms might account for the increases in pigment concentration in the spring. First, increases in concentration could be due to a localized increase in the rate of primary production. In a nutrient-limited regime, increases in production are dependant on a vertical and/or horizontal flux of nutrients. In a light-limited regime, a reduction in the depth of mixing (increased vertical stratification) and/or increases in solar radiation can lead to increases in rates of production. Second, offshore increases in chlorophyll biomass observed in the images after the transition might be a result of advection due to offshore Ekman transport and/or to coastal jets from nearshore zones of high productivity. The third possibility is that there is no increase in total water column pigment concentration but simply a vertical redistribution of existing phytoplankton within the water column. The CZCS integrates pigment concentration over one attenuation depth. An apparent increase in concentration will occur if vertical mixing brings an increased proportion of the total water column biomass within the upper attenuation depth. This depth-sampling bias of the CZCS also contributes (along with the atmospheric algorithm failure) to the apparently inverted seasonal cycle in chlorophyll biomass often observed in the satellite data [*Campbell and O'Reilly*, 1988; *Michaelson et al.*, 1988].

5.1. *Water Column Conditions in the Late Winter*

Unfortunately, there are virtually no in situ biological data during the time periods of interest describing the properties of the water column in the region where maximum interannual variability in pigment patterns occurs. Vertical profiles of hydrographic and biological properties from two CalCOFI line 60 stations (≈300 and 400 km off San Francisco) in February 1984 [*SIO*, 1984] are shown in Figure 4. These indicate a well-mixed surface layer extending to 75 m depth. Within this mixed layer, nitrate levels are low and uniform (0.2 μM) and chlorophyll levels are low (0.1–0.2 mg m^{-3}). The offshore profile indicates a deep chlorophyll maximum of ≈0.3 mg m^{-3}. Beneath the mixed layer is a strong pycnocline, coincident with the nutricline. CalCOFI data from regions closer to shore during the same survey show a somewhat shallower mixed layer (50 m); offshore data from farther south (line 77 at 33.4°N) during this survey show similar mixed layer depths and a coincident nutricline with higher temperatures, lower nitrate, and similar chlorophyll concentrations. Data from February 1985 [*SIO*, 1985] from line 80 (32.8°N) show similar conditions for this offshore region. Thus the profiles shown in Figure 4 are taken to represent upper ocean conditions prior to the transition in the offshore region of interest (zones 3–5 in Figure 1). Conditions closer to shore, where pigment concentrations generally remained relatively high, indicate a shallower mixed layer depth and nutricline. Most CalCOFI data during these cruises are from south of Point Conception where the satellite data show little response to the physical transition (Plate 1). The in situ data indicate that in these regions the nutricline is often below the pycnocline and probably remains relatively isolated from surface physical forcing. This may explain why the region of pigment increase seen at the time of the transition in 1980–1982 is not observed south of ≈33°N.

These CalCOFI data suggest that the water column sampling bias of the CZCS is not responsible for large-scale increases in pigment concentration observed in the image composites. The possibility that increases in concentration are due to a vertical redistribution of existing phytoplankton biomass presupposes the existence of a deep chlorophyll maximum of biomass sufficient to account for the ≈4 and 2 mg m^{-3} increases in concentration observed in 1980 and 1981 image composites, respectively, when integrated over the upper attenuation depth. While the vertical profiles shown in Figure 4 do indicate the presence of a deep chlorophyll maximum, the magnitude of this maximum would be insufficient to account for the observed increases if it were mixed vertically into the upper attenuation depth observed by the CZCS.

5.2. *Advection*

It is possible that advection of biomass from coastal upwelling regions contributes to the observed interannual variability in pigment pattern at the time of the transition. Water properties associated with an upwelling front can be carried into offshore regions by advection and eddy diffusion in areas of strong and persistent upwelling [*de Szoeke and Richman*, 1984]. Offshore Ekman transport is dependant on southward wind stress, which is linked to the forcing of the transition itself, becoming strong only after the spring transition date [see *Strub et al.*, 1987*a*]. Time series of daily alongshore wind stress (spatially averaged over all five zones shown in Figure 1) are presented in Figure 3 and show that the transition date in each year is associated with a southward wind event. This event is strongest in 1980 and most

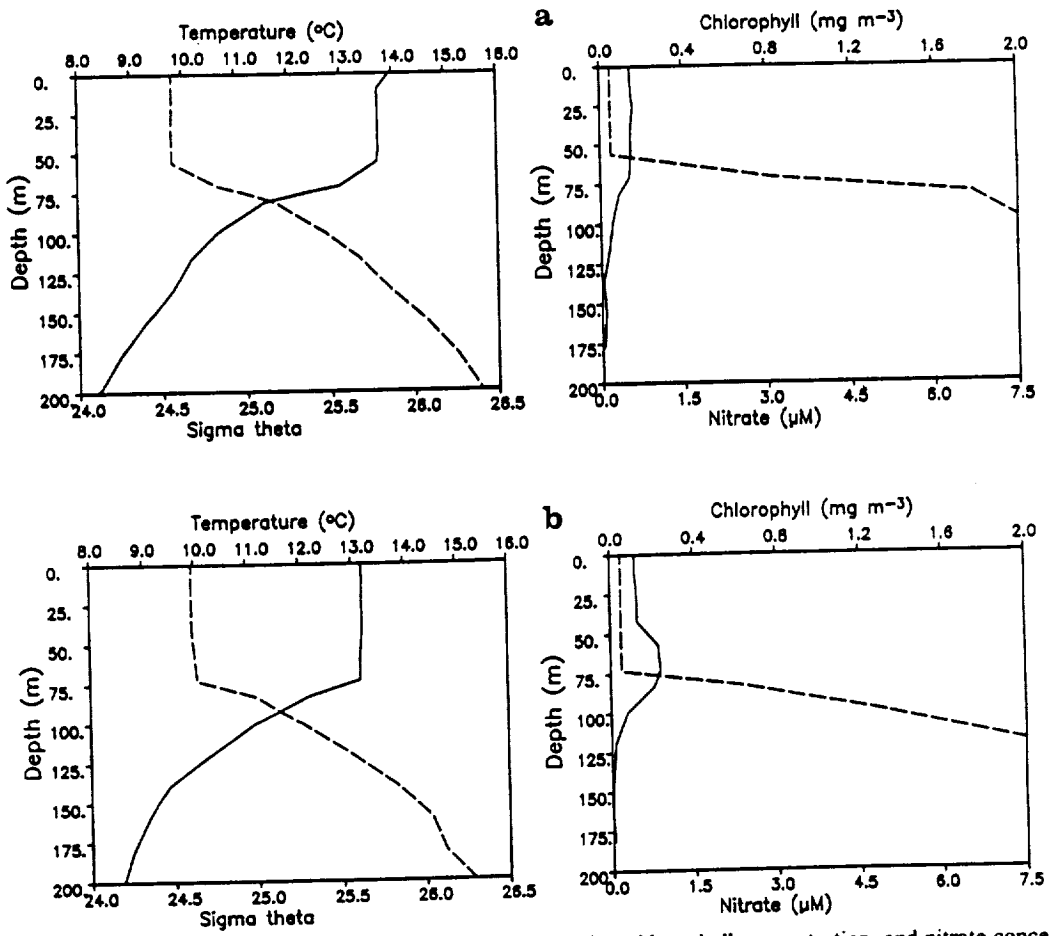

Fig. 4. Representative vertical profiles of temperature, density, chlorophyll concentration, and nitrate concentration in the pretransition period for the offshore region of maximum pigment concentration variability (see Plate 1): (*a*) CalCOFI station 60/90 (36°36.2'N, 125°47.7'W) and (*b*) CalCOFI station 60/100 (36°16.5'N, 126°29.4'W), in February 1984. The stations are approximately 305 km and 380 km offshore, respectively. Density and nitrate concentration are shown by the dashed profiles in the right and left plots, respectively.

persistent in 1981. It is least persistent in 1982 and 1986, when periods of northward wind stress (relaxation of upwelling) occur within 5 days after the transition date. Ekman transport velocities in the surface layer measured by *Kosro* [1987] during an upwelling event off northern California were of the order of 5.0 cm s^{-1}. At this velocity, phytoplankton supported by coastal upwelling would take ≈70 days to be advected 300 km offshore. Advection from upwelling zones is thus unable to explain the sudden offshore increase within 10 days of the transition date in 1980 (Figure 3*a*); nor does it explain increases in concentration that occur prior to the transition date during periods of northward wind stress in other years. The temporal trend in 1981 (Figure 3*b*), however, is more consistent with patterns expected during coastal upwelling and offshore advection. Major increases in concentration occur after the onset of southward wind stress and are more closely associated with the coast than those in 1980. Maximum concentrations do not occur until 20–30 days after the transition, occurring first in zones closer to shore and later in zones farther from shore.

Cross-shelf jets off the California coast [*Mooers and Robinson*, 1984; *Abbott and Zion*, 1987] have cross-shelf velocities exceeding 50 cm s^{-1} [*Mooers and Robinson*, 1984; *Kosro*, 1987] which could advect biomass 300 km offshore within a 7-day period. The spatial patterns of pigment in 1980 do not suggest such features. The large scale and diffuse pattern of increased concentration and the lack of any visual evidence of jets in individual images making up the composite suggest that jets were not responsible for high offshore pigment concentrations in 1980. This argument appears less valid in 1982, when surface pigment patterns after the transition resemble jets previously seen in satellite images [*Rienecker et al.*, 1985; *Abbott and Zion*, 1987].

Advection of biomass from coastal upwelling sites does not explain all of the observed interannual variability in either the magnitude of the pigment changes or the spatial pattern of observed increases. While advection may play a role in the observed pigment distributions, it does not explain the large and diffuse increase 300–500 km offshore in 1980, nor does it explain the pretransition increases in 1983 and 1982 following strong northward winds associated with downwelling and onshore Ekman transport. Furthermore, Figure 3*d* shows that upwelling-favorable (and offshore transporting) winds were present in 1983 when no changes in concentration took place at the time of the physical transition.

5.3. *Quantification of the Light Regime*

Low concentrations of nitrate (<0.2 μM) in the upper mixed layer and a subsurface chlorophyll maximum (Figure

TABLE 2. The Spring Light Regime

Year	Day When Solar Radiation Exceeded 157 W m^{-2}		15-Day Mean, W m^{-2} (34°N to 41°N)	
	Date	Days Relative to ST	Before ST	After ST
1980	March 14	−6	181	203
1981	March 25	−1	154	239
1982	March 20	−30	205	260
1983	March 31	−5	174	235
1986	March 16	−1	142	191

ST, spring transition.

4) suggest that light is not limiting in this region of the CCS in winter. This argues that observed pigment increases in the spring do not develop in response to the classical North Atlantic spring bloom situation parameterized by *Sverdrup* [1953]. We test this assumption using the quantification of *Riley* [1957], who shows that depth-averaged, vertically integrated solar radiation in the upper mixed layer must be greater than ≈43 Ly d^{-1} for the spring bloom to start in the North Atlantic (assuming nutrients are not limiting). Using an extinction coefficient of 0.1 m^{-1} and the mixed layer depth of 75 m indicated in Figure 4, we integrate and solve the light extinction equation $I_z = I_0 e^{-kz}$ for I_0. With this model, an I_0 of 157 W m^{-2} is necessary to initiate a spring bloom. Total incident clear sky solar radiation can be modeled as a harmonic function of latitude and Julian day [*Reed*, 1977]. Solar radiation values for 39°N were calculated and modified by the mean observed daily cloud cover obtained from the COADS data set and compared with this 157 W m^{-2} value. Details of the solar radiation model and modification for cloud cover are given in Appendix A.

Table 2 shows the dates in each year when the spatially averaged (over a region approximating zones 1 and 2 in Figure 1) solar radiation exceeds 157 W m^{-2} as well as the mean solar radiation for the 15-day periods before and after the spring transition date in each year. Except for 1982, the date when a North Atlantic type of spring bloom situation could develop is closely associated with the date of the transition and does not explain the large differences in pigment response in 1980 and 1981 compared with 1983 and 1986. The mean light intensity over the 15-day periods before and after the transition dates indicate that light is probably not limiting either before or after the transition, except in 1986. Again, these data cannot explain the large interannual differences in pigment response to the spring transition and substantiate the argument that light is not limiting during the late winter and spring in this region of the CCS. Note especially that the major increases in pigment concentration in 1983 and 1986 occur a month prior to the earliest physical transitions when light levels are low.

5.4. *Wind Forcing*

Vertical profiles of nitrate and chlorophyll from this region of the CCS in winter (Figure 4) suggest that the surface mixed layer is a nutrient limited regime. Differences in wind forcing and resulting vertical nutrient flux to the upper part of the water column might be responsible for the observed interannual variability in pigment concentrations during the physical spring transition. This forcing can be either vertical mixing by the wind or upwelling due to southward alongshore wind stress, both of which might introduce nutrients into the upper water column. Conversely, vertical transport of nutrients is affected by the water column density structure (mixed layer depth and stratification), its position relative to the nutricline, surface heating at the time of wind events, and the relative depth of previous mixing events. The vertical profiles shown in Figure 4 (and other data from this and 1985 CalCOFI cruises) indicate that for pretransition periods in 1984 and 1985, the areas of maximum pigment variability seen in Plate 1 (the offshore region north of ≈34°N) are regions where the nutricline is coincident with the pycnocline. In such regions, surface forcing can significantly affect the flux of nutrients into the upper water column.

Daily values of both wind mixing strength (as u_*^3) and alongshore wind stress are plotted in Figure 3 for the same time period as the pigment time series. These data show that increases in pigment concentration prior to the transition date occur following strong wind mixing events. After the transition dates, strong wind mixing events are also upwelling events, and it is not possible to separate their respective effects. We present daily values of the wind products rather than temporal means in order to show the peaks in wind forcing.

The short time scale pigment increase at the transition date in 1980 (Figure 3*a*) is associated with a sustained period of increased mixing which starts approximately 5 days prior to the transition date. This wind is also upwelling favorable and results in the largest pigment increase observed at the time of the transition in the image composites. Nutrient flux into the upper water column due to the combined effect of wind-driven vertical mixing and upwelling can explain the simultaneous increase in concentration in each of the zones as well as the large and diffuse pattern of these high concentrations seen in Plate 1*a*. The reason why the strong mixing event 35 days prior to the transition is not associated with an increase in pigment concentration is not evident in these data. The event, however, is of short duration (2 days) and occurs sufficiently early in the year (mid February) for light levels to be very low.

In general, no large wind mixing event takes place prior to the transition in 1981 (Figure 3*b*). The post-transition increase in pigment concentration occurs in association with the southward alongshore wind stress which begins at the transition date. Both the previously discussed spatial patterns and time series suggest that 1981 pigment concentrations are responding to a wind-driven coastal upwelling event and subsequent offshore advection. A moderate, short

TABLE 3. The Mean Wind Regime for 15-Day Periods Before and After the Spring Transition Averaged Over the Region 34°N to 41°N

	Alongshore Wind Stress, dyn cm^{-2}		Wind Mixing U_*^3, $\times 10^{-6}$	
Year	Before	After	Before	After
1980	−0.105	−0.120	1.8	2.2
1981	0.015	−0.100	1.3	1.4
1982	0.024	−0.040	2.1	0.9
1983	−0.002	−0.004	1.8	1.3
1986	0.026	−0.094	2.3	0.7

time scale mixing event which is also upwelling favorable takes place 20 days prior to the transition and might be associated with slight increases seen in the two zones nearest the coast in the period 10–20 days before the transition.

The increase in 1982 which begins in the 10-day time period just prior to the transition is associated with a strong mixing event during northward winds beginning at day −8 (Figure 3*c*). A second increase in the three zones closest to shore 20–40 days after the transition is associated with southward wind stress beginning at day 20.

The pigment time series in 1983 shows that the major increase in concentration 20–40 days prior to the transition is associated with large values of u_*^3 beginning at day −37 (the end of February) (Figure 3*d*). Although wind mixing remains relatively strong during the actual transition, an increase in concentration takes place only in the zone closest to the coast at this time. This increase is relatively minor and is associated with a 2-week period of southward wind stress. Concentrations in all four zones farther seaward remain low after the transition despite this southward wind stress. It is possible that the lack of pigment response to wind mixing and southward alongshore wind stress (upwelling) after March in 1983 is due to an anomalously deep pycnocline and nutricline associated with the 1982–1983 El Niño. A deeper pycnocline would increase the isolation of surface water from deeper, nutrient-rich water. *Rienecker and Mooers* [1986] show the surface mixed layer off northern California in February 1983 to be warmer, deeper, and more strongly stratified than the climatological mean. *Huyer and Smith* [1985] show the April 1983 pycnocline off Oregon to be ≈40 m deeper than a 6-year average, and McGowan [1985] shows the March nutricline off southern California to be at 80 m compared with the usual 50 m.

Pigment concentrations in 1986 in the two zones closest to the coast increase in the period 20–30 days prior to the transition in association with a strong wind-mixing event beginning at day −34 (Figure 3*e*). The data show that these winds would not induce upwelling. Concentrations remain relatively constant after this period, potentially supported by another strong mixing event and the onset of southward alongshore wind stress at the time of the transition. Increases in concentration in the second and third zones from the coast, beginning 30 and 40 days (respectively) after the onset of upwelling are consistent with offshore advection of pigment.

We have summarized the interannual variability of surface wind forcing by forming spatial averages of u_*^3 and alongshore wind stress over the entire five-zone region shown in Figure 1 for the 15-day periods before and after the transition event in each year. Table 3 shows that 1980 has the strongest upwelling favorable winds and is the only year in which they were present both before and after the transition. In addition, wind mixing is relatively strong both before and after the transition. In 1981, wind mixing is weaker, but southward wind stress becomes strong after the transition. It is interesting to note that 1980 and 1981, the only years with a strong increase in pigment concentration at the transition, are also the only years with stronger wind mixing after the transition than before. In both 1982 and 1986, wind mixing becomes weak after the transition. Strong mixing before the transition in 1986 is accompanied by relatively strong southward wind stress after the transition to maintain approximately constant concentrations over the transition period. The inability of relatively strong wind mixing at the time of the transition in 1983 to introduce nutrients into the upper water column might be due to the anomalously deep pycnocline.

For the late winter and early spring periods analyzed in this study, the curl of the wind stress does not appear to play a strong role in nutrient input to the upper water column. Previous work [*Chelton*, 1982] suggests that offshore regions of increased zooplankton biomass in the southern CCS during summer might be an indirect response to nutrient input by Ekman pumping associated with a zone of positive wind stress curl. Comparison of the contours of wind stress curl averaged over the 15-day periods before and after the transition date in each year show that the region of positive curl evident in climatological data [*Nelson*, 1977] expands offshore after the transition between ≈33° and 41°N. This response is strongest in 1980 and 1981 and weakest in 1986. However, maximum vertical velocities calculated from the wind stress curl are ≈0.3 m d^{-1}. Figure 4 shows the pycnocline (and nutricline) to be ≈75 m deep. These velocities are probably incapable of changing the nutrient regime in the upper attenuation depth of the water column sampled by the CZCS within the short (10–15 days) time period observed in Plate 1 and Figure 3. Furthermore, time series of wind stress curl over the same periods shown in Figure 3 show that the pretransition pigment concentration increases both in 1983 and 1986 are associated with time periods of generally negative curl.

5.5. *Model Evaluation of Interannual Variability in Vertical Mixing*

The preceding section discusses surface wind forcing as an index of offshore vertical mixing and coastal upwelling. Vertical mixing (in the absence of upwelling), however, is affected by a number of processes besides wind stirring (u_*^3). The effects of surface heating, penetrative radiation, and vertical shear of the horizontal currents at the base of the mixed layer are also important, as are the initial depth of the mixed layer and the strength of the stratification at the base of the mixed layer [*Niiler and Kraus*, 1977]. The lack of in situ density data from most years, however, prevents us from evaluating interannual differences in the density fields, except for the comments on the anomalously deep pycnocline during spring of 1983 noted above. Using a one-dimensional numerical model of vertical mixing, however, we can quantify the interannual variability in mixing caused

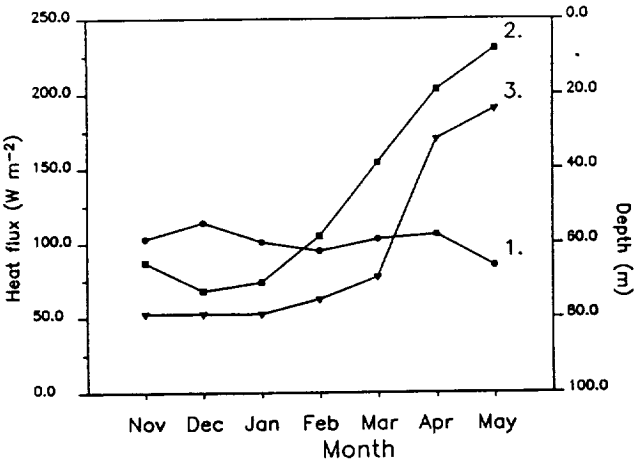

Fig. 5. Changes in the climatological mean surface heat budget terms in the winter and spring averaged over the region 34.5°–41.5°N and 121.5°–127.5°W showing cooling due to sensible heat flux + latent heat flux + net longwave radiation (plotted as circles, line 1) and heating due to solar radiation I_0 (squares, line 2). The depth of the mixed layer after 15 days of wind forcing by idealized wind stress under these conditions in each month is also shown (triangles, line 3).

by differences in wind stress and solar radiation. All of these processes are included in the model to some extent.

Components of the climatological monthly mean surface heat budget over the CCS are available from *Nelson and Husby* [1983]. These have been averaged over the region from 34.5°–41.5°N and 121.5°–127.5°W (excluding land) and are presented in Figure 5. They show the rapid increase in solar heating in March, while cooling due to all other terms remains nearly constant at $\approx$100 W m^{-2}. The degree to which surface winds can mix nutrients upward at the base of the mixed layer will depend on the timing of the wind events relative to this onset of net surface heating. Because a relatively cloud-free period of high radiation often occurs at the time of the transition, wind events associated with earlier winter storms should be more effective in mixing than the actual wind event associated with the transition and the onset of southward winds, Similarly, transitions that occur later in the season should be associated with less vertical mixing, owing to increased solar radiation.

Daily surface radiation estimated from COADS cloud cover and bulk radiation formulae (Appendix A) are used with twice-daily LFM winds to drive the one-dimensional second-order closure turbulence model of *Mellor and Yamada* [1982] for the period surrounding the spring transition in each of the 5 years considered above. Initial conditions for the model simulation of each year are identical and similar to those shown for the offshore profile of Figure 4 (75-m-deep mixed layer, started from rest). Details of the model are presented in Appendix B. The model is used as a measure of the relative differences in mixing power which result from the balance of wind and radiative forcing in each year, rather than as an absolute measure of mixed layer depths. Although less satisfying than actual in situ data, the model provides a mechanism for evaluating these competing influences on vertical mixing. Simpler scaling arguments for mixed layer depth based on daily or longer means of wind forcing, radiation, and heating [*Niiler and Kraus*, 1977; *Price et al.*, 1986] were evaluated and found to be less satisfactory, since these arguments apply to periods of constant forcing. The actual surface forcing in spring fluctuates between strong heating and cooling, as well as between stronger and weaker mixing, with diurnal and synoptic periodicity. The numerical model provides the means of quantifying the net effect of the competing, temporally varying, forces.

The model is first used as an alternate to simple scaling arguments to calculate the monthly mean mixed layer depths that might be expected from climatological forcing. Surface winds characteristic of typical winter storms are used in competition with climatological surface heating and solar radiation. These winds are typical of moderately strong mid-latitude storms with wind stress alternating between mildly southeastward (0.14 N m^{-2}) and strongly northeastward (0.32 N m^{-2}) with a 4-day period. Daily averaged solar radiation for each month is taken from *Nelson and Husby* [1983] and distributed over a cosine-shaped function with a 12-hour period followed by 12 hours of darkness to simulate the diurnal cycle. Surface cooling by processes other than solar radiation is held constant at 110 W m^{-2}. The model is run for 15-day period for each month and the maximum mixed layer depth (as defined by the density difference at the bottom of the mixed layer) over the last 4 days noted. This idealized seasonal progression of mean mixed layer depth and the surface forcing is presented in Figure 5. The results show that such winds would slightly deepen the initial 75-m mixed layer in November–January, maintain the mixed layer at 75 m depth in February, and result in mixed layer depths of 69, 32, and 24 m for the radiation typical of March, April, and May, respectively. This quantifies the notion that increasing solar radiation will inhibit vertical mixing as the season progresses.

Using the same initial conditions, the model is forced with the actual daily solar radiation and twice daily wind stress from each of the 5 years and constant net surface cooling (representing sensible and latent heat loss plus net infrared radiation). The solar radiation calculated from the harmonic bulk formula and cloud correction is greater than the climatological values presented by Nelson and Husby. To compensate for this, a greater net cooling of 130 W m^{-2} is used to avoid unrealistic heat buildup. Wind stress is increased by 50% to compensate for the known tendency of the Mellor-Yamada model to mix less than field measurements [*Martin*, 1985]. This is equivalent to increasing the drag coefficient used in the wind stress calculation from 1.3×10^{-3} to 2.0×10^{-3}. As the model results are interpreted in a relative rather than absolute sense, these modifications have no impact on our discussion of interannual differences.

Results of the model are shown in Figure 6 over the 15-day periods before and after the spring transition in each year. These results are presented as depth-time contours of the log (base 10) of the eddy diffusivity for heat, K_H, which also applies to other passive substances (including nutrients). In addition to eddy diffusivity, the model includes a constant background diffusivity of 10^{-5} m^2 s^{-1}. Thus, contours of -5 are taken to represent the bottom of the mixed layer, where the diffusivity begins to be governed by the background level of mixing rather than by turbulence. Regions of strong turbulent mixing ($K_H > 10^{-2}$ and $K_H > 10^{-1}$) are shown by hatching. In each year, there is an initial period of adjustment in the model usually lasting less than 2 days (several inertial periods). This is caused by using the same initial conditions in each year (the 1984 CalCOFI data) which are not in balance with the actual winds, radiation, heat flux and model dynamics of each year. Adjustment results in the

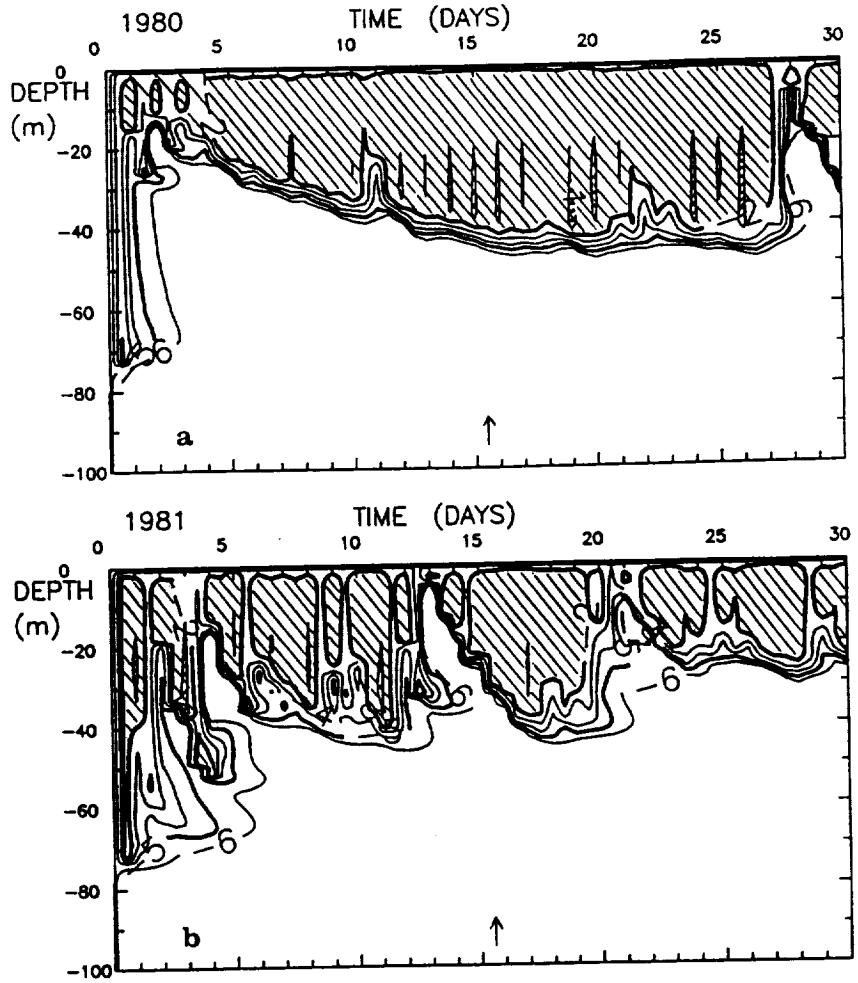

Fig. 6. Time-depth contours of $\log_{10}$ eddy diffusivity of heat, K_H, illustrating interannual differences in the mixing regime for the 30-day period starting 15 days before the spring transition date (shown as an arrow) in (*a*) 1980, (*b*) 1981, (*c*) 1982, (*d*) 1983, and (*e*) 1986. Diffusivity values were generated by a one-dimensional mixing model that balances daily wind stress and daily heat budget values. Periods of strong mixing ($K_H > -2$ and $K_H > -1$) are shown as hatched and cross hatched, respectively. The -5 contour, which equals the background diffusivity in the model, represents the extent of turbulence and is taken as the base of the mixed layer.

setup of stratification shallower than the initial 75 m in each year (mean conditions result in net heating of the water column prior to the transition in each year). It should be emphasized that the model is used to test the degree to which wind mixing, in the absence of upwelling, would bring nutrients into the upper water column.

Most years have a period of moderate to strong mixing prior to the transition due to winter storms (Figure 6). In 1982, 1983, and 1986, both the mixing intensity and mixed layer depth are strongly reduced after the transition. These are years with weak or nonexistent increases in offshore chlorophyll content at the time of the transition. In 1981 there is a 5-day period of mixing after the transition that equals the mixing prior to the transition. This year had the second largest posttransition increase in offshore chlorophyll concentration. In 1980, the feature that stands out as qualitatively different from the other years is the steady increase in mixed layer depth and mixing intensity. This is caused both by the increasing wind (Figure 3*a*) and by the lack of a strong increase in solar radiation at the time of the transition. These characteristics of the mixing regime would allow the steady erosion of the density gradient beneath the mixed layer and a continuous entrainment of nutrients over a period of 20 days or more. This steady increase in mixing intensity and entrainment over the 1980 transition period is not seen in other years and may explain the large increase in offshore pigment concentration evident in the satellite imagery shown in Plate 1*a*. In 1983 the pycnocline is known to have been deeper than the climatological mean, making the initial mixed layer used here too shallow and reducing the effect of mixing beyond that predicted by the model. The deepest and most intense mixing predicted by the model is seen 5–10 days prior to the transition in 1986 but does not appear coincident with any increase in pigment concentration. In this year, however, a stronger wind event occurs 25–35 days prior to the transition which is coincident with an increase in pigment concentration (Figure 3*e*). It is possible that the mixing event shown in the model either acts only to maintain the already elevated pigment concentrations by further vertical mixing or does not mix below the depth of the previous (and stronger) wind event, in which case, this mixing event does not introduce any new nutrients and need not be associated with an increase in pigment concentration. This is similar to the strong mixing and pigment response

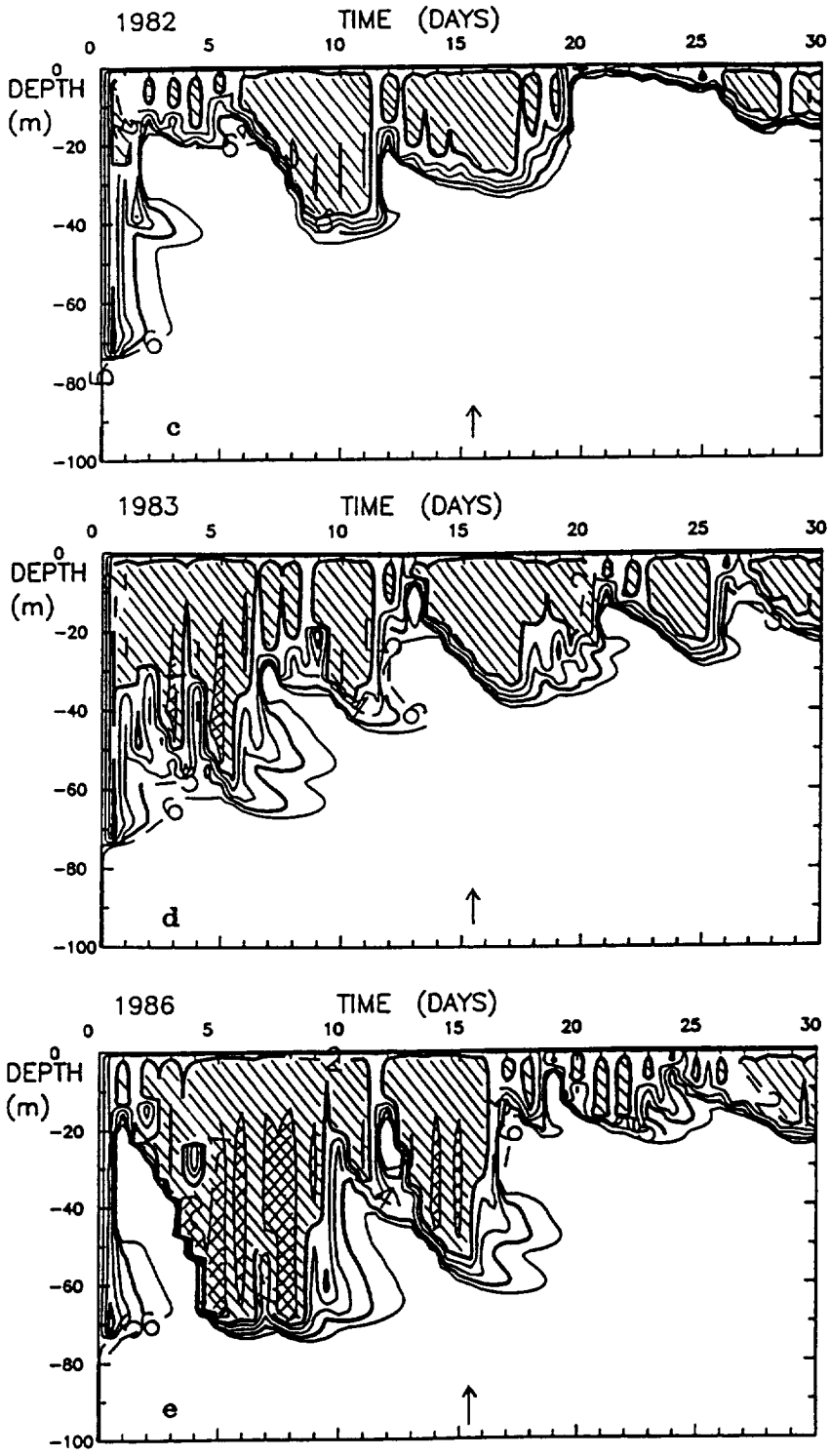

Fig. 6. (continued)

seen 35 days prior to, but not coincident with, the transition in 1983. These years illustrate the importance of the timing of the transition in relation to prior mixing events in late winter. Strong late winter wind events can reduce the role of wind mixing in the nutrient input at the actual time of the transition and make nutrient flux into surface layers a stronger function of alongshore wind stress and upwelling.

6. SUMMARY AND CONCLUSIONS

1. CZCS image composites reveal strong interannual variability in the changes in pigment pattern associated with the spring transition in current structure along the west coast of North America. In both 1980 and 1981, large increases in concentration take place between ≈33°N and ≈41°N. The

maximum increase in 1980 occurs in a region centered ≈300 km offshore, and in 1981 it occurs within 300 km of the shore. The magnitude of changes at the time of the transition is less in 1982, and spatial patterns of concentration more variable than those of other years. In both 1983 and 1986, virtually no change in pigment pattern or concentration takes place at the time of the transition.

2. South of ≈33°N, where the magnitude of the spring transition in wind and current structure is known to be small or nonexistent, changes in pigment concentration are also small in each of the years analyzed.

3. Pigment concentrations within 50 km of the coast over the entire study region (22°N to ≈41°N) remain approximately the same over the transition period, most likely owing to nutrient enrichment which occurs even in winter in shelf and coastal regions.

4. Time series of pigment concentration for extended periods before and after the transition show that the concentration increase in 1980 occurs within the 10-day period immediately after the transition date. In 1981 a more gradual increase over a 30-day period is initiated at the time of the transition. Temporal patterns in 1982 indicate episodic pigment increases in the zones within 200 km of the coast. Although no significant increase takes place at the time of the transition in either 1983 or 1986, relatively large increases do take place in the periods 20–40 days prior to the transition.

5. Available in situ data suggest that this region has a mixed layer ≈75 m deep and is strongly stratified and nutrient limited even in mid to late winter. Comparisons of CZCS measured pigment time series with wind forcing in each year show that increases both prior to and at the time of the transition are associated with strong wind mixing events. Beginning at the time of the physical transition, this wind mixing also represents southward alongshore wind stress (upwelling). Both of these processes support a vertical nutrient flux and potential increases in phytoplankton concentration. Interannual variability of this forcing in conjunction with variability in nutricline and pycnocline depths is most likely responsible for the observed interannual variability of pigment concentrations at the time of the transition.

6. Comparisons of the offshore wind-mixing regimes from each year are made with a one-dimensional mixing model. The model shows that strong vertical mixing in 1980 steadily entrains increasingly deeper water around the time of the transition. This might explain the large and diffuse offshore increase in pigment concentration in this year. Vertical mixing is also relatively strong in 1981 both before and after the transition date, with steady southward alongshore wind stress beginning at the transition date. The model shows that vertical mixing after the transition is relatively weak in each of the other years. Nutrient flux resulting from southward wind stress at the time of the transition in 1983 might also be reduced by the anomalously deep pycnocline (and nutricline) associated with the 1982–1983 El Niño.

7. These data suggest that surface pigment increases in the winter nutrient limited regime off central and northern California are strongly influenced by nutrient flux induced by wind forcing. In the early portion of the year, when solar heating is low, wind mixing is important. As the season progresses, the effect of wind mixing is reduced by stratification, and vertical nutrient flux is increasingly dependent on southward alongshore wind stress and resultant upwelling. This wind forcing is initiated at the time of the spring transition. Large increases in pigment concentration occur when both types of forcing occur together.

8. A large portion of the observed interannual variability in the response of pigment concentration to the spring transition (the onset of upwelling-favorable winds) appears to be due to the relative timing of this event with respect to prior wind mixing events and seasonal solar heating and stratification.

9. The results shown here demonstrate the danger of forming conclusions about spatial patterns based on just a few years of satellite data. It is obvious that our conclusions about the response of pigment concentration to the physical spring transition would have been very different had our analysis been restricted to the first 1–2 years.

APPENDIX A: SOLAR RADIATION FORMULAE

Incoming clear sky radiation was calculated from the harmonic formula of *Seckel and Beaudry* [1973]. This reproduces the values of the Smithsonian tables with an atmospheric transmissivity of 0.7. *Reed* [1977] found this formula to compare favorably with direct measurements over a range of latitudes extending from the Gulf of Alaska to the tropics. This formula is

$$I_c = A_0 + A_1 \cos(\phi) + B_1 \sin(\phi) + A_2 \cos(2\phi) + B_2 \sin(2\phi) \quad \text{(A1}a\text{)}$$

where I_c is the incident clear sky radiation, $\phi = 2\pi/365(t - 21)$, t is the Julian day number, and the other constants are functions of latitude λ, expressed in degrees:

$$A_0 = -32.65 + 674.76 \cos\left(\frac{2\pi}{360}\lambda\right) \quad \text{(A1}b\text{)}$$

$$A_1 = 19.88 + 397.26 \cos\left[\frac{2\pi}{360}(\lambda + 90)\right] \quad \text{(A1}c\text{)}$$

$$A_2 = -1.32 + 16.10 \sin 2\left[\frac{2\pi}{360}(\lambda - 45)\right] \quad \text{(A1}d\text{)}$$

$$B_1 = -6.75 + 224.38 \sin\left(\frac{2\pi}{360}\lambda\right) \quad \text{(A1}e\text{)}$$

$$B_2 = -1.04 + 29.76 \cos 2\left[\frac{2\pi}{360}(\lambda - 5)\right] \quad \text{(A1}f\text{)}$$

These values give I_c in units of langleys per day; values of watts per square meter are obtained by multiplying by 0.4846.

The correction for cloud cover is also that suggested by *Reed* [1977]:

$$I = I_c(1. - 0.62C + \alpha) \quad \text{(A2)}$$

where I is the incident solar radiation after the cloud correction (no correction for albedo) and α is the noon solar altitude given by

$$\sin\alpha = \sin\frac{2\pi}{360}(\lambda)\sin\frac{2\pi}{360}\left[23.45° \sin\frac{2\pi}{365}(t - 82)\right] + \cos\frac{2\pi}{360}(\lambda)\cos\frac{2\pi}{360}\left[23.45° \sin\frac{2\pi}{365}(t - 82)\right] \quad \text{(A3)}$$

The final correction is that for albedo, the radiation reflected from the surface. For this we used a constant value

of $A = 0.07$, approximating the mean value found by *Payne* [1972] in spring for the Atlantic Ocean at our latitude:

$$I_0 = (1 - A)I \tag{A4}$$

Although the specific parameterization of solar radiation used here may contain biases in terms of absolute accuracy, radiation is used in the numerical model of vertical mixing, in more of a relative than absolute sense, to determine the interannual differences in solar radiation at the time of the transition.

APPENDIX B: THE NUMERICAL MODEL

The numerical model of vertical mixing used in section 5.5 is that described in detail as the level 2.5 model by *Mellor and Yamada* [1982]. This model solves the equations for conservation of horizontal momentum, salt and heat:

$$\frac{\partial U}{\partial t} = fV + \frac{\partial}{\partial z}\left(K_M \frac{\partial U}{\partial z}\right) \tag{B1a}$$

$$\frac{\partial V}{\partial t} = -fU + \frac{\partial}{\partial z}\left(K_M \frac{\partial V}{\partial z}\right) \tag{B1b}$$

$$\frac{\partial S}{\partial t} = \frac{\partial}{\partial z}\left(K_H \frac{\partial S}{\partial z}\right) \tag{B1c}$$

$$\frac{\partial T}{\partial t} = \frac{\partial}{\partial z}\left(K_H \frac{\partial T}{\partial z}\right) - \frac{1}{\rho c}\frac{\partial I}{\partial z} \tag{B1d}$$

where U and V are the mean eastward and northward velocity, S is the mean salinity, T is the mean temperature, I is the penetrative radiation, ρ and c are water density and specific heat, and f is the Coriolis parameter. These mean quantities are functions of time and depth. Vertical and horizontal advection are neglected in this model, as are horizontal pressure gradients. The assumption implicit in the model is that the vertical turbulent fluxes of momentum, heat, and salt can be expressed as "eddy diffusions," with "eddy diffusivities" given by K_M for momentum and K_H for heat and salt. Other passive scalars can be included in a manner similar to salinity. Density is calculated from temperature and salinity after each time step using an equation of state.

In the above form, the model is a general "K" model. The aspect of the model that identifies it as the Mellor-Yamada level 2.5 model is the manner of specification of K_M and K_H, which are also functions of time and depth. These are given by

$$K_M = lqS_M \qquad K_H = lqS_H \tag{B2}$$

where l is the turbulent length scale and q is the turbulent velocity scale. These are calculated using the differential equations given below. S_M and S_H are functions of the stability of the water column, calculated as algebraic functions of the mean density and velocity fields of the water.

The value of q is calculated at each depth and time by a parameterization of the equation for conservation of turbulent kinetic energy (TKE), expressed as $q^2/2$:

$$\frac{\partial}{\partial t}\frac{q^2}{2} - \frac{\partial}{\partial z}\left[K_q \frac{\partial}{\partial z}\frac{q^2}{2}\right] = P_s + P_b - \varepsilon \tag{B3a}$$

where K_q is a diffusivity for TKE, related algebraically to K_M; P_s, P_b, and ε are shear production of TKE, buoyant production of TKE, and dissipation of TKE, given by

$$P_s = K_M \frac{\partial^2 U}{\partial z^2} + K_M \frac{\partial^2 V}{\partial z^2} \tag{B3b}$$

$$P_b = \frac{g}{\rho} K_H \frac{\partial \rho}{\partial z} \tag{B3c}$$

$$\varepsilon = \frac{q^3}{A_1 l} \tag{B3d}$$

where A_1 is an empirical constant and g is the acceleration of gravity.

To calculate the turbulent length scale l at each depth and time, an equation analogous to that for TKE is formed for the product of TKE and turbulent length scale,

$$\frac{\partial}{\partial t}(q^2 l) - \frac{\partial}{\partial z}\left[K_l \frac{\partial}{\partial z}(q^2 l)\right] = lE_1[P_s + P_b] - \frac{q^3}{B_1}\left\{1 + E_2\left(\frac{l}{kL}\right)^2\right\} \tag{B4}$$

where E_1, E_2, and B_2 are empirical constants and L is a measure of the distance from the nearest surface. See *Mellor and Yamada* [1982] for a complete derivation and discussion of these equations. The boundary conditions at the surface specify that the momentum fluxes are given by the wind stresses, the heat flux is given by the sum of the heat budget terms excluding penetrative radiation, and the salt flux is a function of ambient salinity, precipitation, and evaporation. The turbulent length scale l is assumed to go to zero at the surface; the turbulent velocity scale is found at the surface by setting the parameterizations for shear production and dissipation equal to each other. At the bottom of the domain, all fluxes are assumed to go to zero.

The incident surface visible radiation at the surface is calculated as described in Appendix A. Within the water column, this radiation is described as a double exponential, following *Paulson and Simpson* [1977]:

$$I(z) = [R \exp(z/\zeta_1) + (1 - R) \exp(\zeta_2)]I_0 \tag{B5}$$

where R is the fraction of visible radiation called "longwave," absorbed in a shallow layer with e-folding depth of ζ_1, and the rest is called "shortwave," absorbed with a deeper e-folding depth of ζ_2. Values used here are $R = 0.58$, $\zeta_1 = 0.5$ m and $\zeta_2 = 17.4$ m.

The numerical method of solution for the above equation set is implicit, allowing longer time steps than possible with an explicit method. The time step used here is 30 min. The variables are represented on a vertical grid with approximately 1 m resolution. This grid is compressed into a logarithmic distribution near the surface to increase the resolution near the surface forcing. The vertical domain of the model is 200 m, extending well below the region where the mean quantities are affected by the surface forcing.

Acknowledgments. We thank M. Abbott for access to the CZCS west coast time series, NCAR for the meteorological data, and those responsible for the collection of the CalCOFI data. C. James computed the EOF used as a latitudinal correction in the pigment time series. This work was supported by NASA grant NAGW-1251 and by a Killam Postdoctoral Fellowship (A.C.T.). Modeling was supported by NSF grant OCE-8614026.

REFERENCES

Abbott, M. R., and P. M. Zion, Satellite observations of phytoplankton variability during an upwelling event, *Cont. Shelf Res.*, *4*, 661–680, 1985.

Abbott, M. R., and P. M. Zion, Spatial and temporal variability of phytoplankton pigment off northern California during Coastal Ocean Dynamics Experiment 1, *J. Geophys. Res.*, *92*, 1745–1756, 1987.

Barale, V., and R. W. Fay, Variability of the ocean surface color field in central California near-coastal waters as observed in a seasonal analysis of CZCS imagery, *J. Mar. Res.*, *44*, 291–316, 1986.

Breaker, L. C., and C. N. K. Mooers, Oceanic variability off the central California coast, *Prog. Oceanogr.*, *17*, 61–135, 1986.

Campbell, J. W., and J. E. O'Reilly, Role of satellites in estimating primary productivity on the northwest Atlantic continental shelf, *Cont. Shelf Res.*, *8*, 179–204, 1988.

Chelton, D. B., Large-scale response of the California Current to forcing by wind stress curl, *CalCOFI Rep. 23*, pp. 130–148, Calif. Coop. Oceanic Fish. Invest., Univ. of Calif., San Diego, La Jolla, 1982.

Chelton, D. B., P. A. Bernal, and J. A. McGowan, Large-scale interannual physical and biological interaction in the California Current, *J. Mar. Res.*, *40*, 1095–1125, 1982.

de Szoeke, R. A., and J. G. Richman, On wind-driven mixed layers with strong horizontal gradients—A theory with application to coastal upwelling, *J. Phys. Oceanogr.*, *14*, 363–377, 1984.

Eppley, R. W., E. Stewart, M. R. Abbott, and U. Heyman, Estimating ocean primary production from satellite chlorophyll, Introduction to regional differences and statistics for the Southern California Bight, *J. Plankton Res.*, *7*, 57–70, 1985.

Gordon, H. R., D. K. Clark, J. L. Mueller, and W. A. Hovis, Phytoplankton pigments from the Nimbus-7 coastal zone color scanner: Comparisons with surface measurements, *Science*, *210*, 63–66, 1980.

Gordon, H. R., D. K. Clark, J. W. Brown, O. B. Brown, R. H. Evans, and W. W. Broenkow, Phytoplankton pigment concentrations in the Middle Atlantic Bight: Comparison of ship determinations and CZCS estimates, *Appl. Opt.*, *22*, 20–36, 1983*a*.

Gordon, H. R., J. W. Brown, O. B. Brown, R. H. Evans, and D. K. Clark, Nimbus 7 CZCS: Reduction of its radiometric sensitivity with time, *Appl. Opt.*, *22*, 3929–3931, 1983*b*.

Gordon, H. R., J. W. Brown, and R. H. Evans, Exact Rayleigh scattering calculations for use with the Nimbus-7 coastal zone color scanner, *Appl. Opt.*, *27*, 862–871, 1988.

Haury, L. R., J. J. Simpson, J. Pelaez, C. J. Koblinsky, and D. Wiesenhahn, Biological consequences of a recurrent eddy off Point Conception, California, *J. Geophys. Res.*, *91*, 12,937–12,956, 1986.

Hickey, B. M., The California Current System—Hypotheses and facts, *Prog. Oceanogr.*, *8*, 191–279, 1979.

Huyer, A. E., Coastal upwelling in the California Current System, *Prog. Oceanogr.*, *12*, 259–284, 1983.

Huyer, A. E., and R. L. Smith, The signature of El Niño off Oregon, 1982–1983, *J. Geophys. Res.*, *90*, 7133–7142, 1985.

Huyer, A. E., E. J. Sobey, and R. L. Smith, The spring transition in currents over the Oregon continental shelf, *J. Geophys. Res.*, *84*, 6995–7011, 1979.

Kelly, K. A., Separating clouds from ocean in infrared images, *Remote Sens. Environ.*, *17*, 67–83, 1985.

Kosro, P. M., Structure of the coastal current field off northern California during the Coastal Ocean Dynamics Experiment, *J. Geophys. Res.*, *92*, 1637–1654, 1987.

Landry, M. R., J. R. Postel, W. K. Peterson, and J. Newman, Broad-scale distributional patterns of hydrographic variables on the Washington/Oregon shelf, in *Coastal Oceanography of Washington and Oregon*, edited by M. R. Landry and B. M. Hickey, pp. 1–40, Elsevier, New York, 1989.

Lentz, S., A description of the 1981 and 1982 spring transitions over the northern California shelf, *J. Geophys. Res.*, *92*, 1545–1567, 1987.

Martin, P. J., Simulation of the mixed layer at OWS November and Papa with several models, *J. Geophys. Res.*, *90*, *903–916*, 1985.

McGowan, J. A., El Niño 1983 in the Southern California Bight, in *El Niño North*, edited by W. S. Wooster and D. L. Fluharty, pp. 166–184, Washington Sea Grant Program, University of Washington, Seattle, 1985.

Mellor, G. L., and T. Yamada, Development of a turbulence closure model for geophysical fluid problems, *Rev. Geophys.*, *20*, 851–875, 1982.

Michaelsen, J., X. Zhang, and R. C. Smith, Variability of pigment biomass in the California current system as determined by satellite imagery, 2, Temporal variability, *J. Geophys. Res.*, *93*, 10,883–10,896, 1988.

Mooers, C. N. K., and A. R. Robinson, Turbulent jets and eddies in the California Current and inferred cross-shore transports, *Science*, *223*, 51–53, 1984.

Nelson, C. S., Wind stress and wind stress curl over the California Current, *Rep. NMFS-SSRF-714*, 87 pp., Natl. Oceanic and Atmos. Admin., Monterey, Calif., 1977.

Nelson, C. S., and D. M. Husby, Climatology of surface heat fluxes over the California Current region, *Rep. NMFS-SSRF-763*, 155 pp., Natl. Oceanic and Atmos. Admin., Monterey, Calif., 1983.

Niiler, P. P., and E. B. Kraus, One-dimensional models of the upper ocean, in *Modelling and Prediction of the Upper Layers of the Ocean*, edited by E. B. Kraus, pp. 143–172, Pergamon, New York, 1977.

Parsons, T. R., L. F. Giovando, and R. J. LeBrasseur, The advent of the spring bloom in the eastern subarctic Pacific Ocean, *J. Fish. Res. Board Can.*, *23*, 539–546, 1966.

Paulson, C. A., and J. J. Simpson, Irradiance measurements in the upper ocean, *J. Phys. Oceanogr.*, *7*, 952–956, 1977.

Payne, R. E., Albedo of the sea surface, *J. Atmos. Sci.*, *29*, 959–970, 1972.

Pelaez, J., and J. A. McGowan, Phytoplankton pigment patterns in the California Current as determined by satellite, *Limnol. Oceanogr.*, *31*, 927–950, 1986.

Price, J. F., R. A. Weller, and R. Pinkel, Diurnal cycling: Observations and models of the upper ocean response to diurnal heating, cooling, and wind mixing, *J. Geophys. Res.*, *91*, 8411–8427, 1986.

Reed, R. K., On estimating insolation over the ocean, *J. Phys. Oceanogr.*, *7*, 482–485, 1977.

Rienecker, M. M., C. N. K. Mooers, D. E. Hagan, and A. R. Robinson, A cool anomaly off northern California: An investigation using IR imagery and in situ data, *J. Geophys. Res.*, *90*, 4807–4818, 1985.

Riley, G. A., Phytoplankton in the north central Sargasso Sea 1950–52, *Limnol. Oceanogr.*, *2*, 252–270, 1957.

Scripps Institution of Oceanography (SIO), Physical, chemical and biological data report, *SIO Ref. 84-23*, Univ. of Calif., La Jolla, 1984.

Scripps Institution of Oceanography (SIO), Physical, chemical and biological data report, *SIO Ref. 85-14*, Univ. of Calif., La Jolla, 1985.

Seckel, G. R., and F. H. Beaudry, The radiation from sun and sky over the North Pacific Ocean (abstract), *Eos Trans. AGU. 54*, 1114, 1973.

Small, L. F., and D. W. Menzies, Patterns of primary productivity and biomass in a coastal upwelling region, *Deep Sea Res.*, *28*, 123–149, 1981.

Smith, R. C., X. Zhang, and J. Michaelsen, Variability of pigment biomass in the California Current System as determined by satellite imagery, 1, Spatial variability, *J. Geophys. Res.*, *93*, 10,863–10,882, 1988.

Strub, P. T., and C. James, Atmospheric conditions during the spring and fall transitions in the coastal ocean off western United States, *J. Geophys. Res.*, *93*, 15,561–15,584, 1988.

Strub, P. T., J. S. Allen, A. Huyer, and R. L. Smith, Large-scale structure of the spring transition in the coastal ocean off western North America, *J. Geophys. Res.*, *92*, 1527–1544, 1987*a*.

Strub, P. T., J. S. Allen, A. Huyer, R. L. Smith, and R. C. Beardsley, Seasonal cycles of currents, temperatures, winds, and sea level over the northeast Pacific continental shelf: 35°N to 48°N, *J. Geophys. Res.*, *92*, 1507–1526, 1987*b*.

Sverdrup, H. U., On conditions for the vernal blooming of phytoplankton, *J. Cons. Int. Explor. Mer*, *18*, 287–295, 1953.

Thomas, A. C., and W. J. Emery, Winter hydrography and plankton distributions on the southern British Columbia shelf, *Can. J. Fish. Aquat. Sci.*, *43*, 1249–1258, 1986.

Thomas, A. C., and W. J. Emery, Relationships between near-surface plankton concentrations, hydrography, and satellite-measured sea surface temperature, *J. Geophys. Res.*, *93*, 15,733–15,748, 1988.

Woodruff, S. D., R. J. Slutz, R. L. Jenne, and P. M. Steurer, A comprehensive ocean-atmosphere data set, *Bull. Am. Meteorol. Soc.*, *68*, 1239–1250, 1987.

P. T. Strub and A. C. Thomas, College of Oceanography, Oregon State University, Corvallis, OR 97331.

(Received March 3, 1989;
revised June 13, 1989;
accepted June 16, 1989.)

APPENDIX F

SEASONAL AND INTERANNUAL VARIABILITY OF PIGMENT CONCENTRATIONS ACROSS A CALIFORNIA CURRENT FRONTAL ZONE

A. C. Thomas and P. Ted Strub

JOURNAL OF GEOPHYSICAL RESEARCH, VOL. 95, NO. C8, PAGES 13,023–13,042, AUGUST 15, 1990

Seasonal and Interannual Variability of Pigment Concentrations Across a California Current Frontal Zone

A. C. THOMAS AND P. T. STRUB

College of Oceanography, Oregon State University, Corvallis

Previously published physical and biological data document a zonally oriented frontal region within the California Current system separating colder and more eutrophic water north of ≈33°N from warmer, more stratified, and oligotrophic water farther to the south. Satellite images of phytoplankton pigment from the coastal zone color scanner from 1979–1983 and 1986 are used to examine the seasonal and interannual variability of both the latitudinal position of this front and the pigment concentrations associated with it. Many temporal and spatial characteristics of the pigment structure are repeated in different years, and a general seasonal cycle is described. Variations in the frontal structure are controlled primarily by changes in pigment concentration north of the front. Seasonality is minimum south of the front where concentrations remain low (<0.5 mg m^{-3}) throughout the spring, summer, and fall. The frontal gradient is typically strongest from late March until early June when higher concentrations (>2.0 mg m^{-3}) are present north of the front. Lower pigment concentrations within the sampled region (0.5–1.0 mg m^{-3}) north of the front in mid–late summer (June–August), resulting from a seasonal shift in the cross-shelf distribution of pigment, reduce and often eliminate the pigment gradient forming the front. Concentrations greater than 1.0 mg m^{-3} typically extend 150–250 km farther offshore in spring (April) than in summer (June–July). Superimposed on this general seasonality is strong interannual variability in the magnitude of the frontal gradient, its latitudinal position, and the seasonal development of higher biomass in regions north of the front. Pigment concentrations during the El Niño year of 1983 are distinctly lower than those of other years. The patterns evident in the satellite data are compared with available in situ measured hydrographic data and nutrient and phytoplankton concentrations. A comparison of the seasonal and interannual variability of these patterns to surface wind shows little direct relation between frontal strength or position and wind forcing.

1. INTRODUCTION

Characteristics of the flow within the California Current system (CCS) are highly variable in both space and time [*Hickey*, 1979]. Large-scale variability and forcing of this eastern boundary current is discussed by *Lynn and Simpson* [1987] and *Strub et al.* [1987*a*]. In general, the flow of the CCS in regions away from the shelf and shelf break is equatorward throughout the year. At a latitude of ≈32°N, however, this flow makes an eastward turn toward the coast. The core of the CCS occurs 300 to 400 km offshore north of this latitude but is found within 200 km of the coast off Baja California [*Lynn and Simpson*, 1987]. This shoreward flow forms the southern portion of the cyclonic flow in the Southern California Bight (SCB) and feeds the northward flow along the coast off central California described by *Chelton et al.*, 1988; *Strub et al.*, 1987*a*; and *Wickham et al.*, 1987. The rest of the CCS continues equatorward along the Baja coast [*Wyllie*, 1966]. This onshore flow is evident in hydrographic data [*Wyllie*, 1966; *Roesler and Chelton*, 1987; *Simpson et al.*, 1987] and in drifter data [*Reid et al.*, 1963]. More recently, *Niiler et al.* [1989] described the three-dimensional structure of this feature, presenting evidence for significant upwelling within its core. *Pares-Sierra and O'Brien* [1989] demonstrate that this flow pattern is a stable feature of a nonlinear, reduced gravity model forced by wind stress and wind stress curl. The absence of any topographic effects in their model indicates that this feature is not a result of bottom topography. The latitudinal variability in the position of this eastward flow produces a zonal maximum in the long-term (≈30 years) variability of dynamic height over southern portions of the CCS [*Lynn and Simpson*, 1987].

This eastward flow forms a zonally oriented frontal region within the CCS which separates warmer and more oligotrophic water from more eutrophic water found both to the north and farther south off Baja [*Peláez and McGowan*, 1986; *Strub et al.*, 1990]. The frontal zone is the southern boundary of the extensive offshore region of higher biomass associated with the upwelling and cross-shelf transport characteristic of northern and central California during the summer. North of the front, physical forcing within the CCS is dominated by strong seasonality in upwelling, offshore transport, and wind mixing. South of the front, seasonality is much weaker, and upwelling winds occur throughout the year [*Strub et al.*, 1987*a*]. The seasonal development of phytoplankton biomass to the north of the front can therefore be expected to contrast strongly with that south of the front.

The spatial and temporal characteristics of this frontal zone have biological implications at most trophic levels of the planktonic community of the CCS. *Peláez and Guan* [1982] show a strong, latitudinally oriented, frontal zone in coastal zone color scanner (CZCS) satellite images of phytoplankton pigment concentration of this region for the summer of 1981, with higher concentrations restricted to regions north of the frontal zone. *Peláez and McGowan* [1986] use a series of individual CZCS images from

Paper number 90JC01181.
0148-0227/90/90JC-01181$05.00

1981 and 1982 to illustrate a seasonal change in the position of the frontal zone. During these years the frontal zone in their images moves south in spring and summer and reaches its southernmost position in August or September. The cross-frontal pigment gradient weakens in late summer and then moves northward in fall and winter. *Peláez and McGowan* present coincident CZCS and hydrographic data that support the hypothesis that low pigment concentrations south of the front are due to the onshore flow of oligotrophic offshore water in this semipermanent meander of the CCS. *Haury* [1984] shows decreases in the concentration of zooplankton species commonly associated with CCS water in meridional transects from north to south across this region which are coincident with an increase in pycnocline and nutricline depth shown by *Simpson* [1984*a*]. Maps of euphausiid species distribution presented by *Brinton* [1967] indicate that this frontal region is an important faunal boundary. *Fiedler* [1984] shows that the northern and offshore extent of anchovy spawning in this region in 1980 is limited by a frontal region of colder water advected southward from the Point Conception area. Interannual variability of the albacore tuna catch in the SCB is also thought to be related to the strength and position of this frontal zone [*M. Laurs, personal communication*, 1989].

A systematic analysis of the mesoscale seasonal and interannual variability of phytoplankton distributions in this region has not been made. In this study we utilize CZCS imagery from 6 years to contrast temporal characteristics of the pigment concentration to the north of the front with those south of the front and to examine the latitudinal variability of the frontal zone. Processing of the satellite imagery is discussed in section 2. The data are presented in section 3 using both time series of pigment concentrations and specific examples of recurrent features identified as a seasonal pattern. In section 4, spatial patterns and seasonality evident in the imagery are discussed in relation to meridional transects of physical, chemical, and biological data available from California Cooperative Oceanic Fisheries Investigations (CalCOFI) cruises and time series of wind stress and mixing, contrasting the physical forcing in northern and southern portions of the study area. A summary and conclusions are presented in section 5.

2. DATA AND METHODS

The CZCS images used in this study were recorded at the Scripps Satellite Oceanography Facility and processed at the Jet Propulsion Laboratory to form the West Coast time series (WCTS) under the direction of M. Abbott (details of the processing are given by *Strub et al.* [1990]). Initial calculations made use of the entire WCTS, which covers the period from mid-1979 to mid-1986. A severe lack of data in 1984 and 1985, due to difficulties with the sensor, prevented the formation of a meaningful time series in these years, and they were not included in this analysis. The final time series presented here covers the period from mid-July 1979 to December 1983 and from January to mid-June 1986.

Accuracy of the CZCS pigment measurements is estimated to be log [Chlorophyll] ±0.5 by *Gordon et al.* [1980, 1983] for summer data. *Smith et al.* [1988] showed the similarity between the CZCS data and ship data from the southern California coast to be ±40% for pigment concentrations between 0.05 and 10.0 mg m^{-3}. Regression of log transformed WCTS satellite pigment on ship chlorophyll [*Abbott and Zion*, 1987] results in an r^2 of 0.8 and a slope of 1.0 for summer data off northern California. The atmospheric correction algorithm used to process the WCTS is known to overestimate pigment concentrations at the large solar zenith angles present during winter at higher latitudes. Examination of pigment time series (presented in section 3) identified winter periods of high pigment concentration (often >3.0 mg m^{-3}) in each year. These concentrations are more than 3 times higher than those found during winter CalCOFI cruises to the same region in 1984 and 1985 [*Scripps Institution of Oceanography (SIO)*, 1984*a*, *b*, 1985*b*]. The winter period over which the data are not valid could be subjectively identified within the time series in a manner consistent from year to year (discussed in section 4). In general terms, winter data in the WCTS from the months November, December, January, and February in each year appear to be affected by the image processing error and will not be discussed in this paper. A detailed discussion of known problems of the WCTS data set is presented by *Strub et al.* [1990].

The WCTS data used in this study consist of the mosaic images covering the west coast from ≈22°N to 55°N at a spatial resolution of ≈14.3 pixels per degree. Further temporal and spatial averaging is used to reduce gaps in the image time series. Although this averaging decreases both the spatial and temporal resolution of the satellite data, it produces a more uniform time series than that of individual images. The averaging is an effective compromise between the quantitative utilization of as much of the archived satellite data set as possible, estimating position and variability of the desired oceanographic features, and filling gaps caused by clouds and missing data. Ten-day composites of each pixel are formed using all images in the first 360 days of each year. Each of the composites formed in this study can be considered statistically independent, since the temporal separation of the data within them (average of 10 days), is considerably longer than previous estimates of the time scales of decorrelation of surface patterns in color and infrared satellite imagery. *Thomas and Emery* [1988] estimate a decorrelation time scale of 2–3 days for the continental shelf region off southern British Columbia, and *Kelly* [1983] estimates 4–5 days for the Coastal Ocean Dynamics Experiment (CODE) region off central California. *Denman and Abbott* [1988] show that features at length scales between 50 and 150 km become decorrelated at time scales of 7 to 10 days in the CCS off British Columbia and Washington.

The 10-day composite images are then subsampled by longitudinally averaging across a 100-km-wide, latitudinally oriented transect running from ≈38°N to ≈30°N (Figure 1). Latitudinal resolution along this meridional transect is equal to the pixel resolution of the mosaic images (≈8 km). This procedure results in 120 potential data points per transect for each of the 36 time periods in each year (except 1979 and 1986, for which only 6 months of data are available). A second subset of the data (a zonal transect, see Figure 1) is formed to allow a comparison of the spring and summer cross-shelf distribution of pigment concentration in the northern portion of the study area. The mean cross-shelf pigment distribution within the region shown in Figure 1 is calculated by latitudinally averaging pixels from south to north, (≈35°N to 38°N, 45 pixels) in

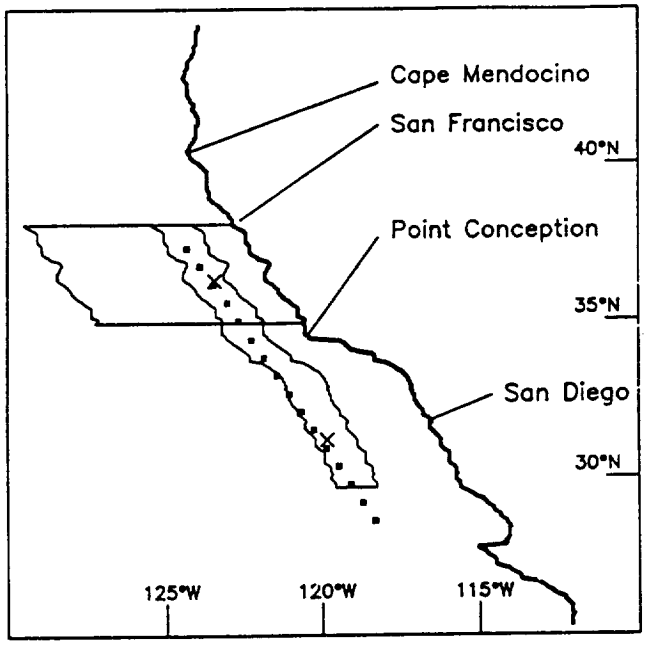

Fig. 1. A coastal outline of the study area showing major geographic points. The 100 km wide meridional transect within which data are zonally averaged from each of the 10-day composite images is shown, as are the locations of CalCOFI station 70 from each of the CalCOFI lines from which in situ data are reported. The latitudinal and offshore extent of the region over which an average cross-shelf transect is formed is also shown (extending offshore north of 35°N). The two grid points from which LFM wind values are used to characterize wind forcing over the northern and southern portions of the transect are shown by crosses.

three consecutive 10-day composites in spring (April–May) and summer (June–July) of each year (except 1979). These three mean transects are then averaged together to form an overall mean spring and summer cross-shelf pigment distribution. Each of these transects has 95 spatial points, extending ≈760 km offshore.

Despite the spatial and temporal averaging, gaps due to clouds and lack of data persist in the time series. At each spatial point, these gaps are filled by optimal interpolation in time. The gaps account for 25.1% of the total number of points making up the space and time series of the meridional transect (120 space points and 181 time points). The nature of these gaps is such that missing data tend to co-occur temporally at the spatial points, and gaps of more than three consecutive (10 day) periods are rare. Temporal averaging of the three cross-shelf transects in spring and summer of each year eliminated all missing data points in each period.

In situ measurements of density structure, nitracline depth, and nutrient and chlorophyll concentration are taken from available CalCOFI data reports. Daily wind velocities at grid points covering the study area are available from the limited-area fine mesh (LFM) data set from the National Meteorological Center.

3. Results

Image-derived pigment concentrations along the meridional transect are plotted as contours in time and latitude in Figure 2 for the periods of available data. These data show the seasonal development of pigment concentrations from 38.1°N to 29.7°N in each year, identifying times and latitudes when strong gradients develop and a frontal zone is present. In the following presentation we take concentrations less than 0.5 mg m^{-3} to be indicative of oligotrophic water of southern and/or offshore origin and the gradient between this and concentrations greater than 1.0 mg m^{-3} to be the primary signature of the frontal zone. An examination of contours less than 0.5 mg m^{-3} showed this to be a consistent representation of the frontal zone.

Concentrations appear relatively high (often >3.0 mg m^{-3}) in the winter months (≈ November–February) of each year, most consistently north of ≈32°N. The extent to which this winter seasonal maximum in the WCTS data represents actual pigment concentration within the water column is unknown. The atmospheric correction algorithm used to process the WCTS produces artificially high values at the large solar zenith angles present in winter. Both the late spring increase and the late fall decrease in pigment concentration, however, run counter to the trend imposed by algorithm error and are probably not an artifact of the data processing. This argues that although the actual concentrations within these features might be influenced by algorithm problems, the observed trends and associated patterns between the spring increase and the fall decrease are at least qualitatively correct. If the spring increase and the fall decrease in concentration are accepted as real, the periods of uniform low concentration immediately after and before the winter maxima can be believed. This is supported by the previously mentioned CalCOFI data from 1984 and 1985. In this paper, we accept as valid those data in each year between the spring and fall periods of uniform low pigment concentration within the transect evident in Figure 2. The winter data are presented in Figure 2 only for completeness; the time periods within which the data are considered valid are indicated on each time series.

3.1. *The Seasonal Cycle*

Interannual comparison of the data in Figure 2 indicates that a number of features of the seasonal development of pigment concentration along the transect recur in different years and a generalized seasonal cycle is evident. The principal features of this cycle are presented below and illustrated in Figure 3 as individual transects using specific (10-day average) periods from 1981 as an example.

1. Low pigment concentrations (often <0.5 mg m^{-3}) are present over the entire latitudinal range of the study area in the early spring (sometime in March or April).

2. Concentrations in the southern portion of the transect (south of ≈32°N) remain less than 0.5 mg m^{-3} from spring, throughout the summer and into the fall. There is, however, considerable seasonal and interannual variability in the location of the northern limit of this oligotrophic water.

3. North of ≈32°N, pigment concentrations during the year show a large degree of seasonal variability. In general, a sudden (often within 10 days) increase in concentration takes place in the late spring. This establishes a strong frontal gradient during the early portion of the summer separating oligotrophic water (<0.5 mg m^{-3}) from higher pigment concentrations to the north (>2.0 mg m^{-3}).

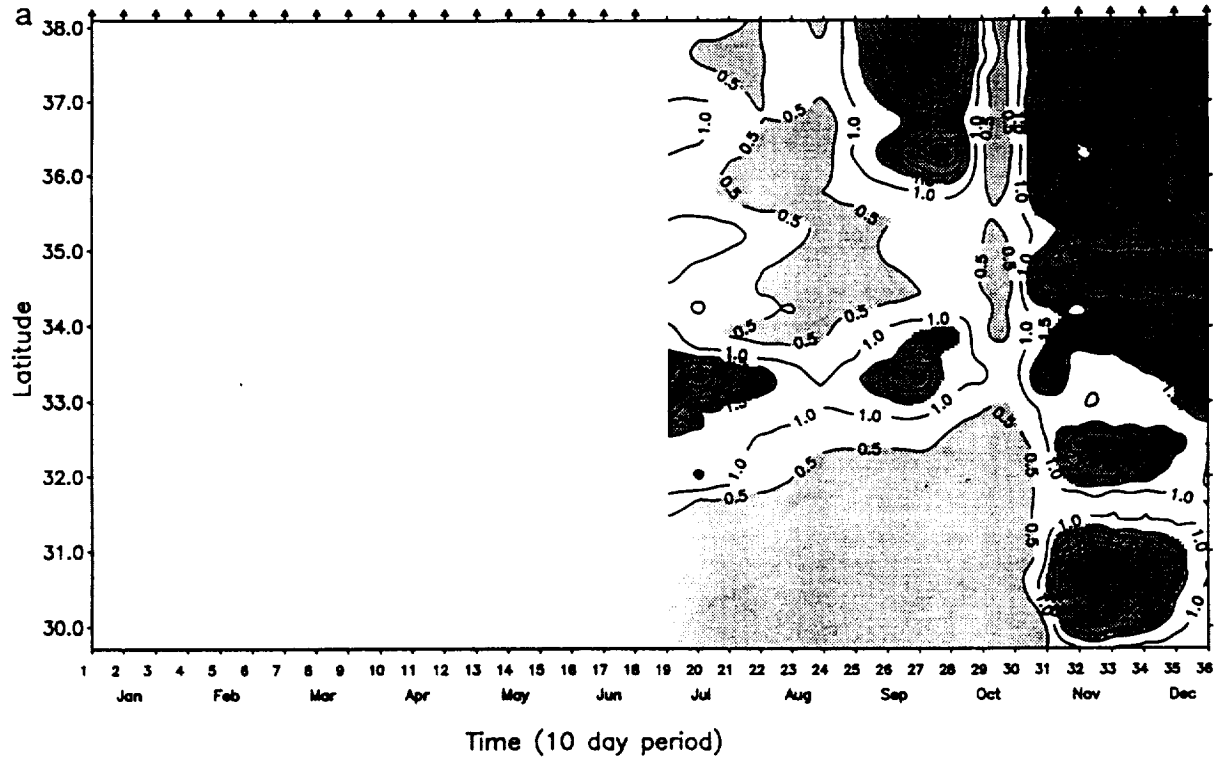

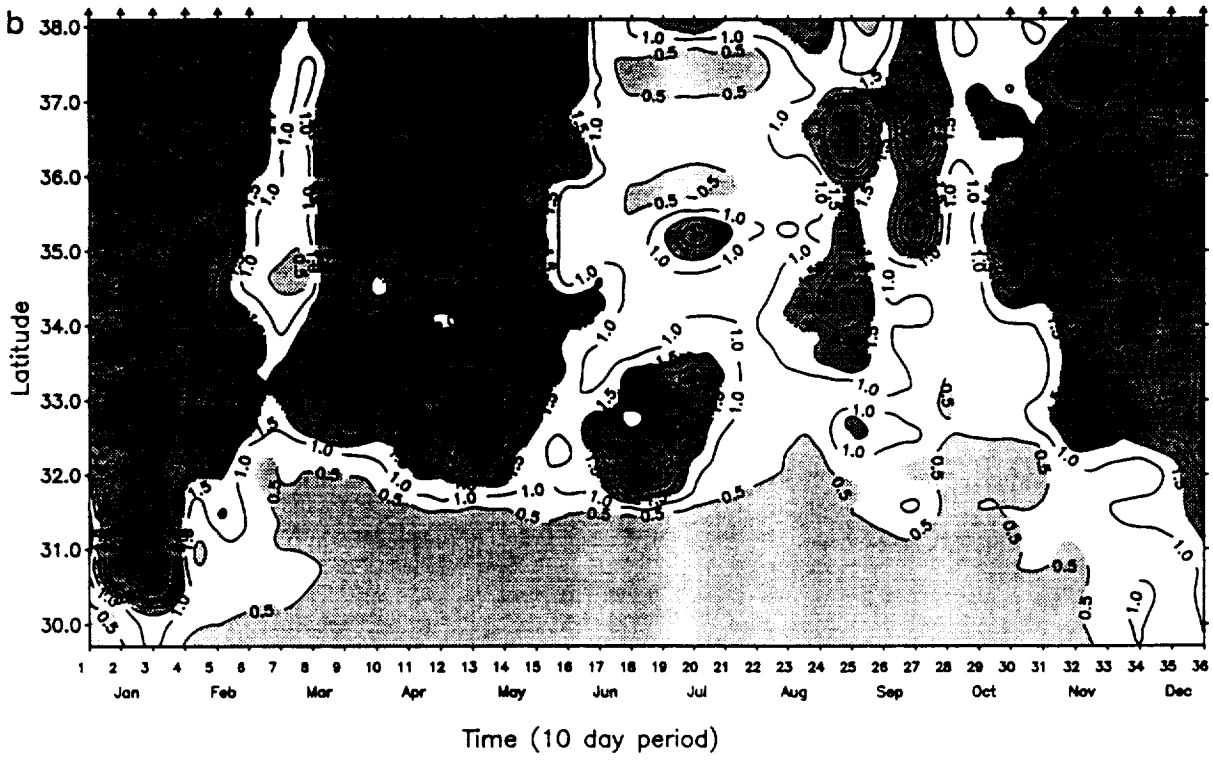

Fig. 2. Contours of phytoplankton pigment concentration in time and latitude from the meridional transect in Figure 1 for (*a*) 1979, (*b*) 1980, (*c*) 1981, (*d*) 1982, (*e*) 1983, and (*f*) 1986. Contours of concentrations greater than 3.0 mg m^{-3} are not shown for clarity. Each year (except 1979 and 1986; see text) comprises 36 meridional transects in time, each representing a 10-day image composite, and 120 alongshore measurements (≈8 km resolution) representing the mean concentration at each latitude over the width of the transect. Winter periods over which the data are suspect on account of algorithm error and periods in 1979 and 1986 of missing data are shown at the top of each plot as open triangles.

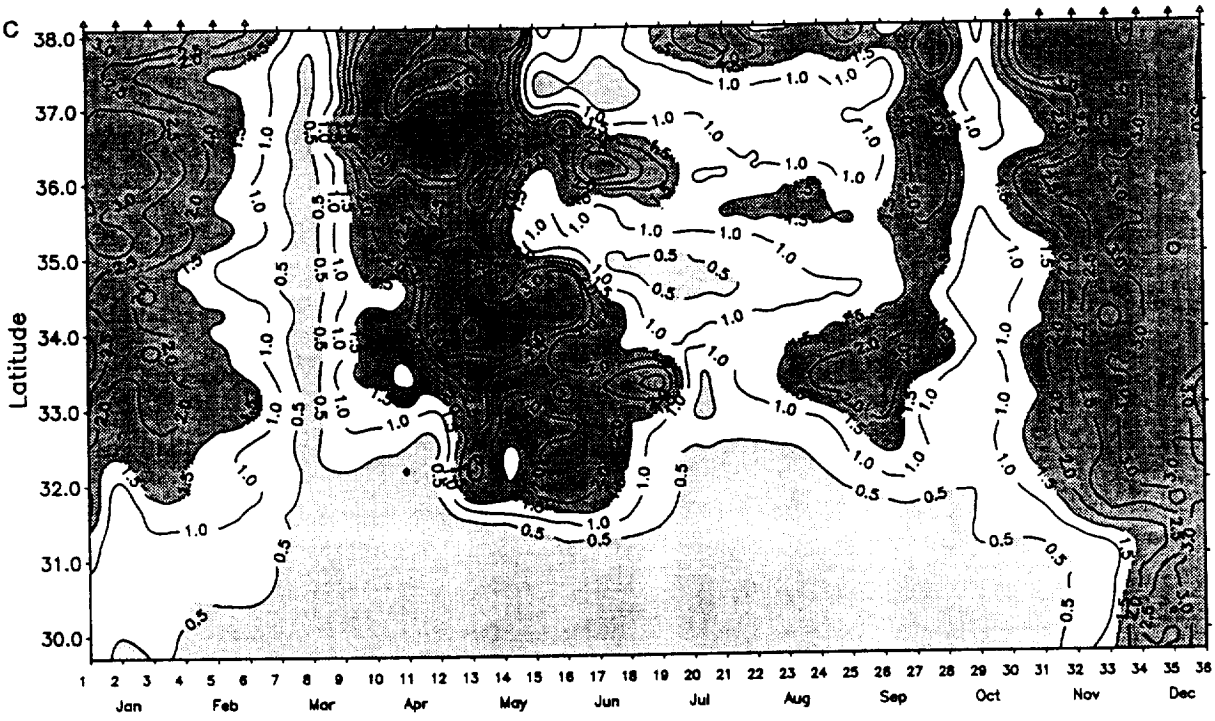

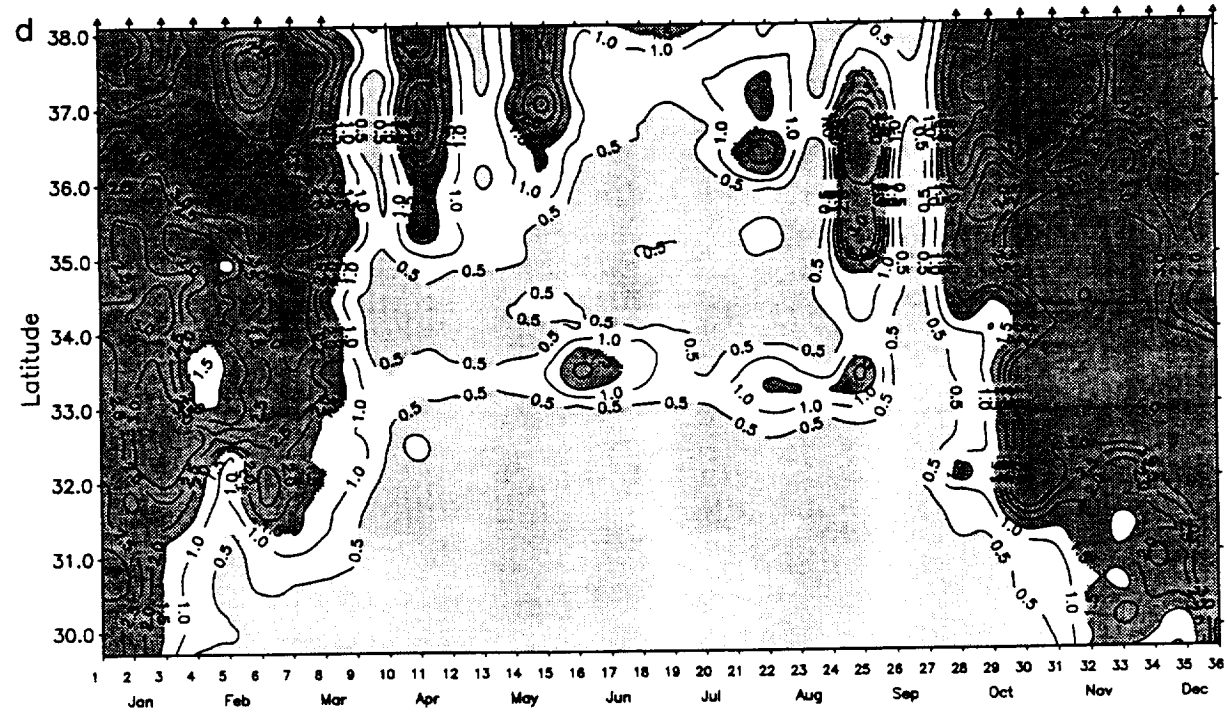

Fig. 2. (continued)

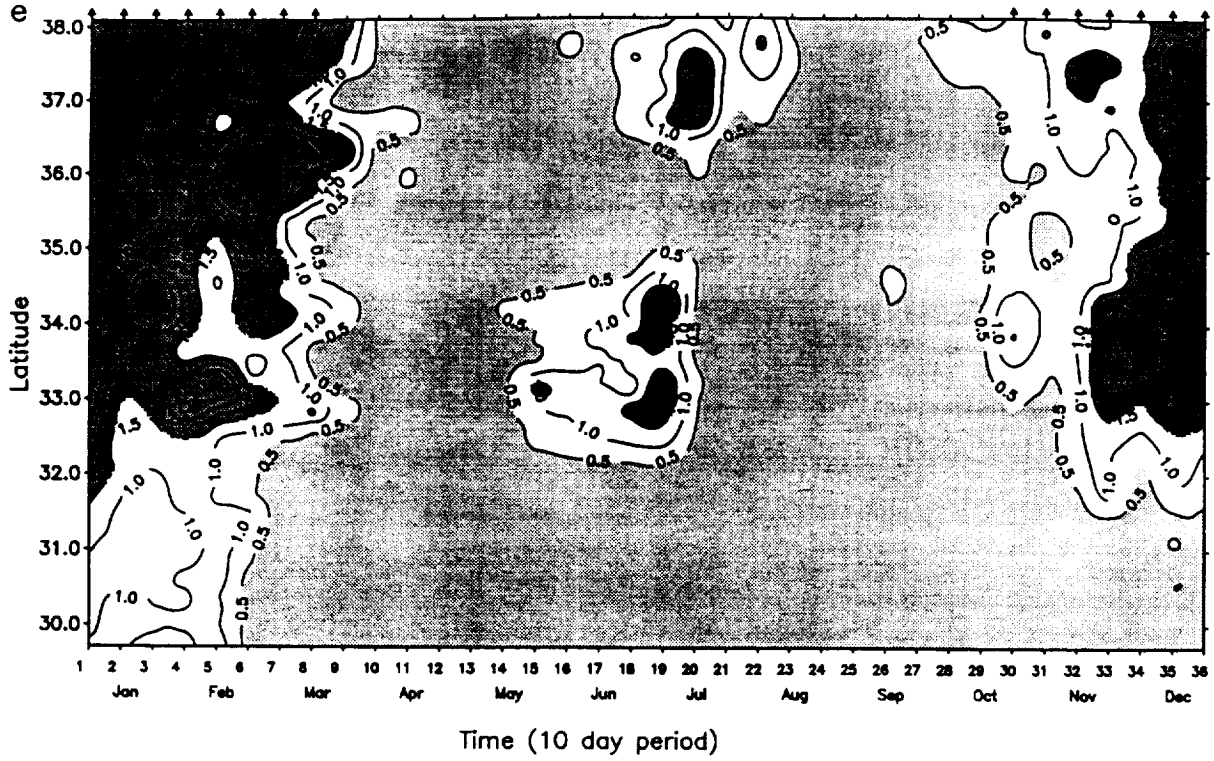

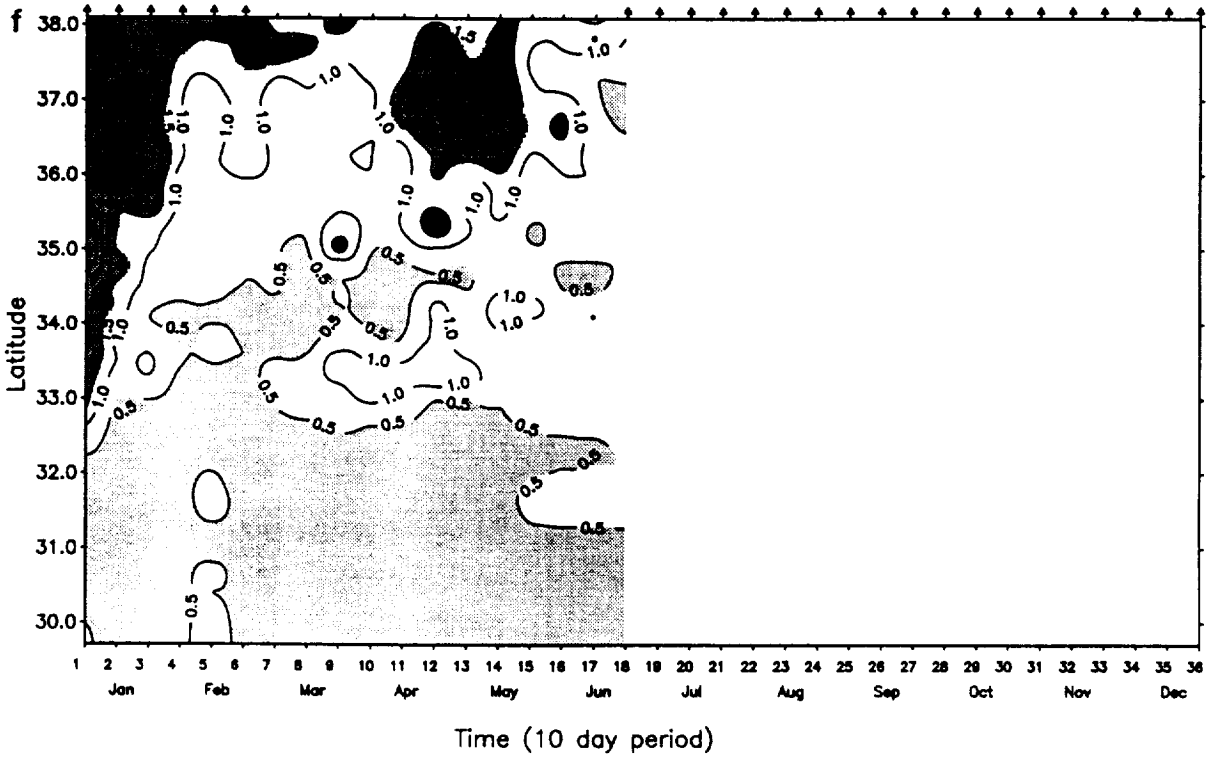

Fig. 2. (continued)

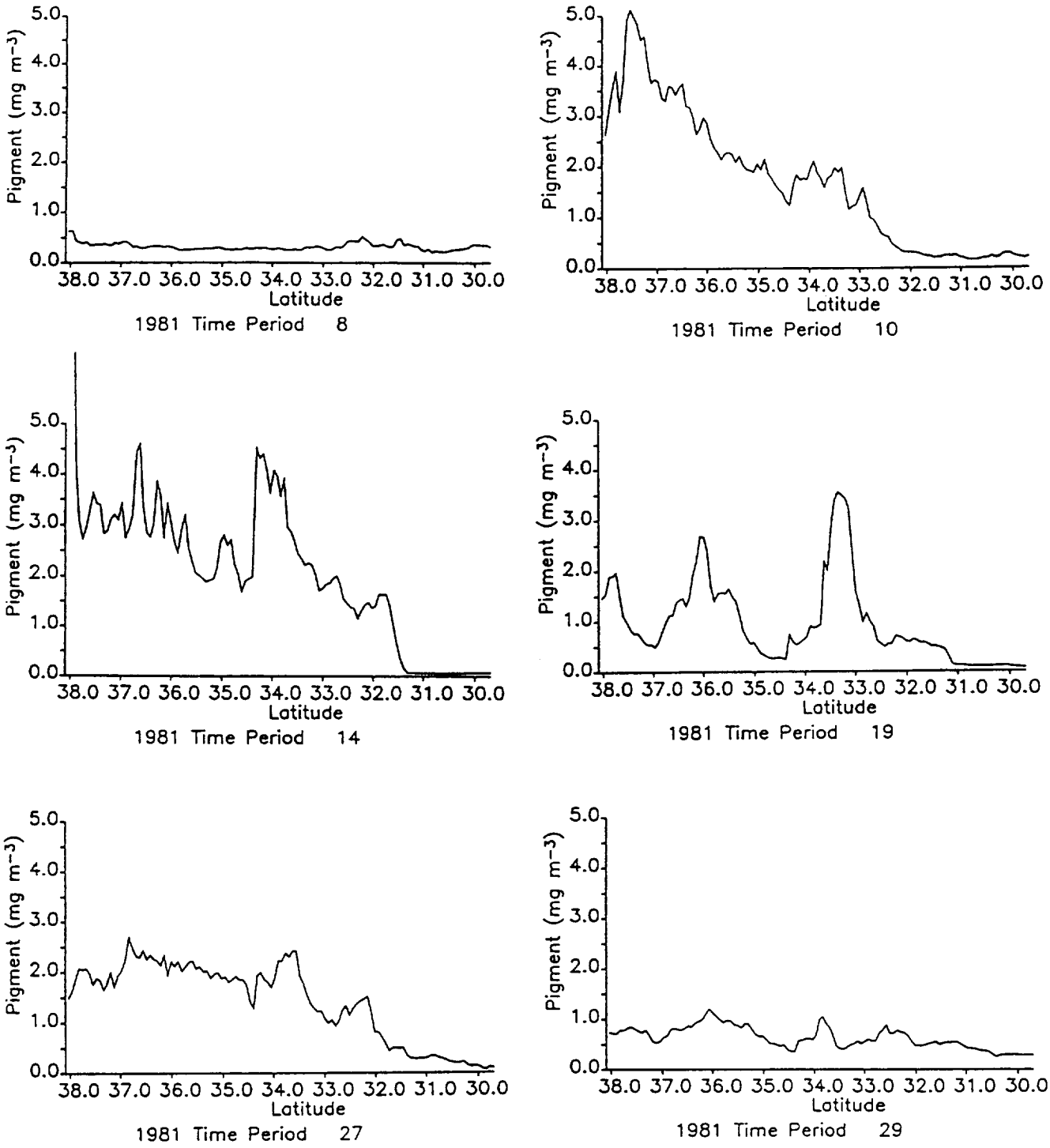

Fig. 3. Individual transects from periods in 1981 illustrating specific features of the seasonal cycle which reoccur in different years (see text): (*a*) period 8 (Julian days 71–80, March 12– 21), (*b*) period 10 (Julian days 91–100, April 1–10), (*c*) period 14 (Julian days 131–140, May 11–20), (*d*) period 19 (Julian days 181–190, June 30–July 9), (*e*) period 27 (Julian days 261–270, September 18–27), and (*f*) period 29 (Julian days 281–290, October 8–17).

4. Concentrations north of the frontal zone decrease to between 0.5 and 1.5 mg m^{-3} in mid to late summer. Although this reduction is often less or delayed at latitudes centered at ≈33°N, the signature of the frontal zone weakens and periodically disappears.

5. The frontal zone is reestablished between ≈32°N and 33°N for a brief period in the late summer (late August–September) by short time scale (20–40 days) increases in pigment concentration north of these latitudes.

6. This increase is followed by a sudden decrease (within 10 days) in concentrations at all latitudes north of ≈33°N. For this period in the fall (September or October), low

concentrations (often <0.5 mg m^{-3}) are again present over the entire latitudinal range of the study area, and the frontal zone disappears.

Time period 8 (Julian days 71–80, March 12–21) in 1981 (Figure 3*a*) is an example of the low concentrations present over the entire transect in the early spring. They are never greater than 0.5 mg m^{-3} and there is no evidence of a frontal zone. Dramatic increases in pigment concentration take place in most years in the northern portions of the study area following this early spring period. The data from period 10 (Figure 3*b*) (Julian days 91–100, April 1–10) show concentrations greater than 3.0 mg m^{-3} at latitudes north of 36°N and concentrations greater than 1.5 mg m^{-3} extending south to ≈33°N. A strongly developed frontal zone is evident between 32°N and 33°N, separating these higher concentrations from concentrations less than 0.5 mg m^{-3} south of 32°N. Similar high concentrations are present in the north at period 14 (Julian days 131–140, May 11–20) (Figure 3*c*). The frontal zone is farther south (≈31.5°N) and has a stronger gradient than at period 10. In addition (and not evident in the contour plot), pigment concentrations south of the front are lower than at previous times. Period 19 (Julian days 181–190, June 30 to July 9) (Figure 3*d*) illustrates the midsummer decline in pigment concentration seen in most years in northern portions of the transect. While concentrations south of the front remain low, concentrations north of ≈31°N are less than 1.5 mg m^{-3} over most of the transect. The frontal zone, while still present, is considerably weaker and is farther south (just north of 31°N). Increases in concentration in the late summer in the northern portion of the transect reestablish the strong frontal zone at ≈32°N. This feature is illustrated in Figure 3*e* showing period 27 (Julian days 261–270, September 18–27). Data from this period also show that concentrations south of the frontal zone are slightly higher than the very low values seen in midsummer (Figures 3*c* and 3*d*). The fall decrease in concentrations over northern portions of the transect is illustrated in Figure 3*f* (period 29, Julian days 281–290, October 8–17). During this period the frontal zone is not evident in the satellite pigment data.

Although the purpose of this study is to examine latitudinal and temporal variability within the study region, the transects presented in Figures 2 and 3 obviously miss any longitudinal variability which would bias both the position and gradient of the front presented in Figures 2 and 3. *Peláez and McGowan* [1986] show that the two-dimensional attitude of the frontal zone can be quite variable. Ten-day composite images from 1981 are presented in Plate 1 to illustrate the two-dimensional structure of features in the study area common to most years. (Plate 1 is shown here in black and white. The color version can be found in the separate color section in this issue.) These images are from the same periods shown in Figure 3 to allow a comparison with both the individual transects and the temporal contours. Superimposed on the images in Plate 1 is the meridional spatial region within which the data were longitudinally averaged to produce the transects shown in Figures 2 and 3.

Plate 1*a* (period 8) shows that the low concentrations present in early spring in the study area are present over most of the CCS. In general, only regions within ≈20 km of the coast have concentrations greater than 1.0 mg m^{-3}. The image composite in Plates 1*b* and 1*c* (periods 10 and 14) shows the spatial extent of pigment concentration increases characteristic of the late spring and early summer. This latter image does, however, show lower concentrations of pigment in the southern portion of the study area. The orientation of the frontal zone during both time periods is strongly east-west. Plate 1*d* (period 19) indicates that lower pigment concentrations in the northern portion of the transect in midsummer are due to spatial changes in the offshore distribution of pigment. The region influenced by higher concentrations has contracted eastward to within ≈100 km of the coast except in specific areas where filaments of higher pigment concentration extend offshore. In the fall (period 27, Plate 1*e*), a diffuse region of increased concentration has expanded offshore in the northern portion of the study area with filaments evident only seaward of the study area and no intrusions of offshore, oligotrophic water apparent within the transect. The image for period 29 (Plate 1*f*) shows generally lower concentrations along the entire transect during this fall period and the reappearance of filaments with higher pigment concentration extending offshore through the sampled transect producing the strong latitudinal variability seen in Figure 3*f*. Higher concentrations in the southern portion of the study area, compared with those in midsummer, are evident. A tongue of higher pigment concentration extending down the western edge of the transect between ≈32°N and 30°N alters the orientation of the frontal zone away from east-west and reduces the gradient of pigment concentration in the transects shown in Figures 2 and 3 for this time period.

3.2. *Interannual Variability*

Interannual variability of pigment concentrations in the transect is summarized by decomposing the time and space series into empirical orthogonal functions (EOFs). Suspect winter data in each year (marked in Figure 2) were not included in the calculation. Each mode of an EOF decomposition has a spatial pattern whose amplitude in time is represented by a time series. Original pigment concentrations associated with any one mode can be reconstructed by multiplication of the spatial value and the amplitude value at the time of interest. The original total pigment concentrations can be reconstructed by summation over all modes of this product. The first EOF mode, which accounts for 62.4% of the total variance, is presented in Figure 4. The second EOF mode accounts for less than 10% of the variance. This and higher modes are probably not statistically significant and are not presented here. The spatial pattern of the first mode shows relatively high values north of ≈32°N, a strong latitudinal gradient between ≈32.3°N and 31.5°N, and low values south of 31.5°N. The temporal variability of this dominant pattern is shown by the amplitude time series (Figure 4). The seasonal cycle described previously is readily apparent, as is the interannual variability of these features.

Temporal development of this pigment pattern for the period in 1979 when data are available and throughout 1980 and 1981 closely follow the general seasonality described above. Most characteristics of the general seasonal cycle are present in 1982, but the magnitude and timing of specific features are different. The early spring period of low pigment concentrations occurs ≈20 days later in

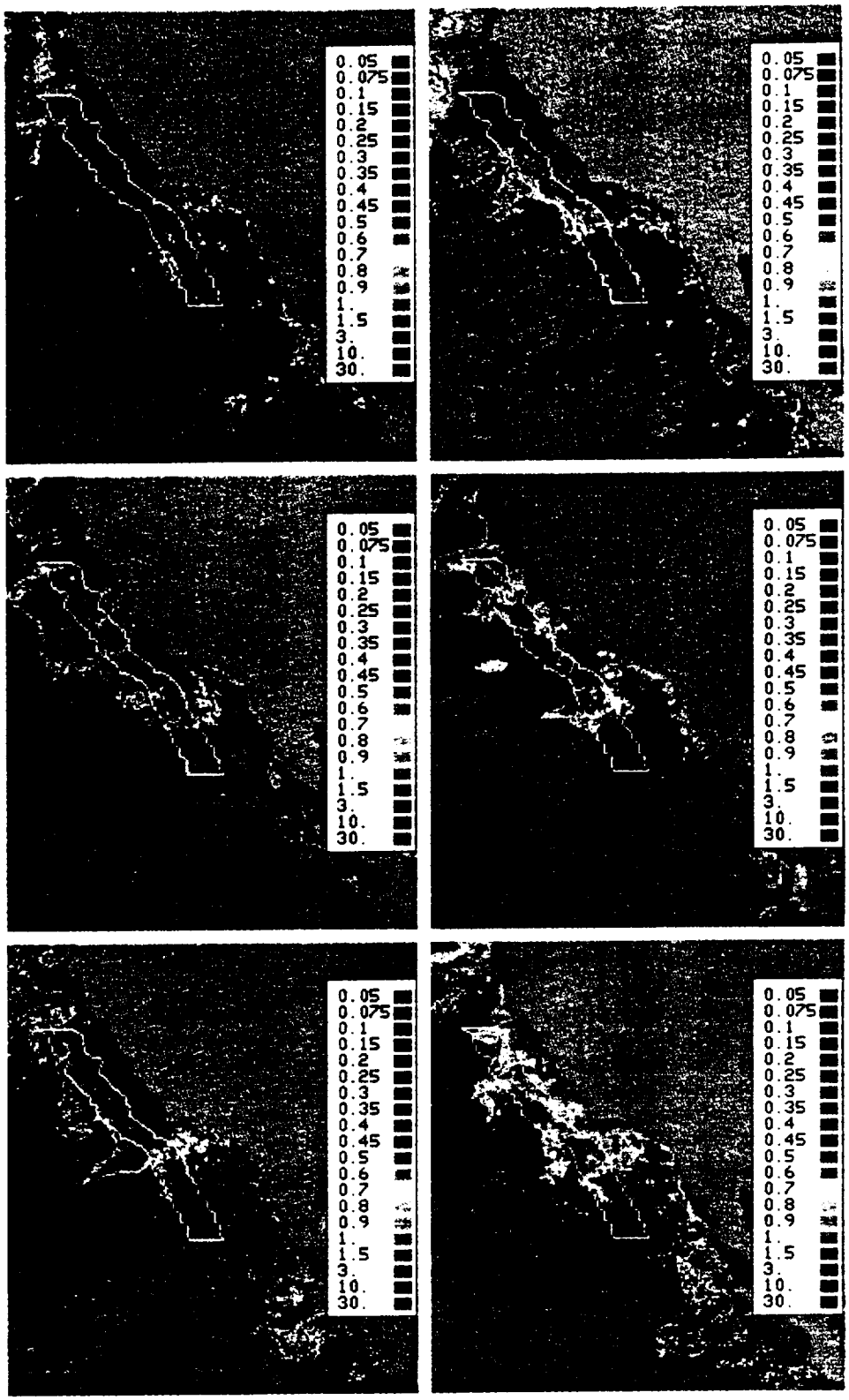

Plate 1. Ten-day composite CZCS images of the periods in 1981 shown in Figure 3. (The color version and a complete description of this figure can be found in the separate color section in this issue.)

the year than in 1980 and 1981 (compare also these time series in Figure 2). The spring increase in concentration at latitudes north of ≈32°N following this period is considerably smaller in both latitudinal and temporal extent than in previous years and appears as a series of episodic increases. Examination of Figure 2*d* shows that these increases take place north of ≈36°N from the beginning of April until June. In the summer and fall.

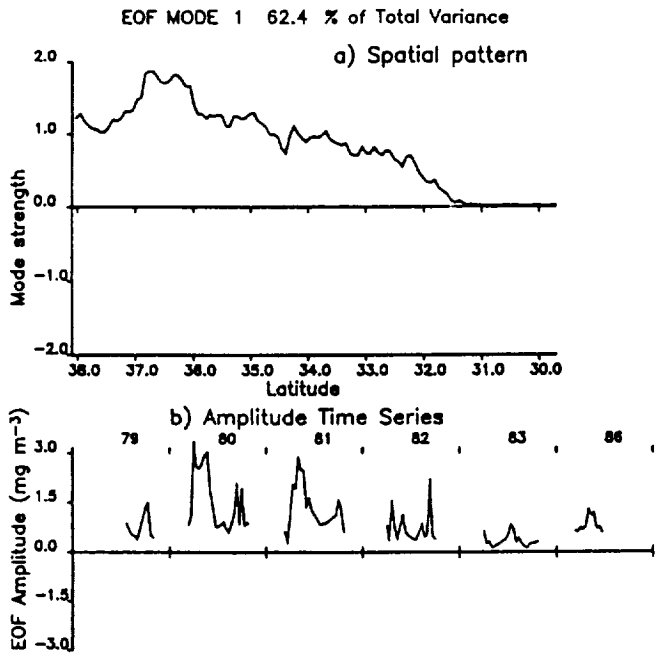

Fig. 4. The first EOF mode (*a*) spatial pattern and (*b*) amplitude time series of the meridional transect in Figure 1 over the 6 years of WCTS data presented in Figure 2. Note that winter data from the periods assumed to be affected by the atmospheric correction error (marked in Figure 2) are not included in the decomposition.

the 1982 time series in Figure 4 is similar to the general seasonal pattern but the fall increase begins in mid-August, 20–30 days earlier than previous years. Figure 2*d* shows that oligotrophic conditions extend farther north than in previously examined years, with the frontal zone remaining at ≈33°N throughout the summer. In 1982 the frontal zone is weak throughout the summer except for a period in early June and again in the period leading up to the fall increase. Summer concentrations in the northern portion of the transect are lower than those of previous years (generally <0.5 mg m^{-3}).

The time series in 1983 (Figure 4) is very different from the general seasonal pattern. While concentrations along the entire transect are low in the earliest part of the year, no subsequent spring or fall increase in concentration takes place. The largest amplitudes of the spatial pattern occur in midsummer but are still lower than those of other years. Figure 2*e* shows that oligotrophic conditions dominate the study area throughout the spring, summer, and fall. The increase in concentration between 32°N and 35°N in early June briefly establishes a frontal zone which lasts until mid-July, although for most of this time the gradient is weak. A short time scale increase takes place north of 36°N in July with concentrations of >2.0 mg m^{-3}. With these episodic exceptions, pigment concentrations remain less than 0.5 mg m^{-3} from mid-March until mid-October (the entire period for which 1983 data are considered valid) over the whole study area.

The time series from 1986 (Figure 4) indicates that the spring increase is relatively weak and occurs relatively late in the spring. Figure 2*f* indicates that the spring increase in pigment concentration occurs primarily north of ≈36°N and that the frontal zone between 32°and 33°N is weaker than that evident in 1980 and 1981.

4. Discussion

4.1. *Comparison With Previous Work*

The reduction in pigment gradient across the front in late summer pointed out by *Peláez and McGowan* [1986] using individual images is evident in our analysis of the entire data set of CZCS images. The temporal progression of the frontal zone described in the preceding section (see Figure 2), however, differs from that described by these authors. They describe a continual southward movement of the front, starting in spring, and reaching its southern most position in August or September. In Figure 2 the frontal zone moves southward in the spring (in 1980 and 1981) but reaches its most southerly position in May–June. Thereafter, the frontal gradient is weaker and moves northward until the brief fall pigment increase. *Peláez and McGowan* also describe interannual variability in different seasons from an analysis of an individual image from each of 3 years. They describe similar summer (July) patterns in each year (1979, 1980, 1981). This similarity is also evident in our data (Figure 2) and appears to be true of 1982 as well. However, they describe spring (April) conditions in 1980, 1981, and 1982 as being remarkably similar. This is not true of patterns evident in Figures 2 and 5. Both the actual concentrations and the spatial–temporal extent of higher pigment concentrations in the spring of 1982 are less than those of 1980 and 1981. This agrees with the interannual variability of pigment patterns during the spring discussed by *Thomas and Strub* [1989]. Differences between the seasonality and interannual variability described here and those discussed by Peláez and McGowan may be due to a number of factors. These authors use only 21 images, selected on the basis of being extensively cloud free, and base their discussion on these individual images. They interpret color patterns rather than the actual pigment concentrations contoured here. Their visual interpretation also might differ in location, including patterns extending into the bight, whereas our transect is restricted to the same geographic region throughout the year. Although our spatial temporal averaging eliminates smaller scale features, we argue that use of the entire data set resolves the large-scale patterns and seasonal variability better than a small group of hand-selected images, which may alias episodic or short–term changes into an apparent seasonal evolution.

4.2. *Comparisons With in Situ Data*

Unfortunately, few in situ biological data from the CalCOFI program coincide with the CZCS data presented here, and other sampling programs do not have the spatial and/or temporal coverage necessary for a meaningful comparison. A cruise from 1981 and a comprehensive series of cruises in 1984, however, provide an illustration of surface and subsurface hydrographic and biological characteristics in the study area. The extent to which these data reflect patterns in the years covered by the WCTS is unknown, although subsurface hydrographic data collected on cruises in February and April 1980 [*SIO*, 1985*a*] (not shown) indicate patterns similar to those described below.

The extent to which the patterns shown in Figures 2–4 are influenced by changes in the vertical distribution of chlorophyll is difficult to assess, owing both to the lack of concurrent in situ data and to the fact that spatial and temporal patterns are hard to separate and often

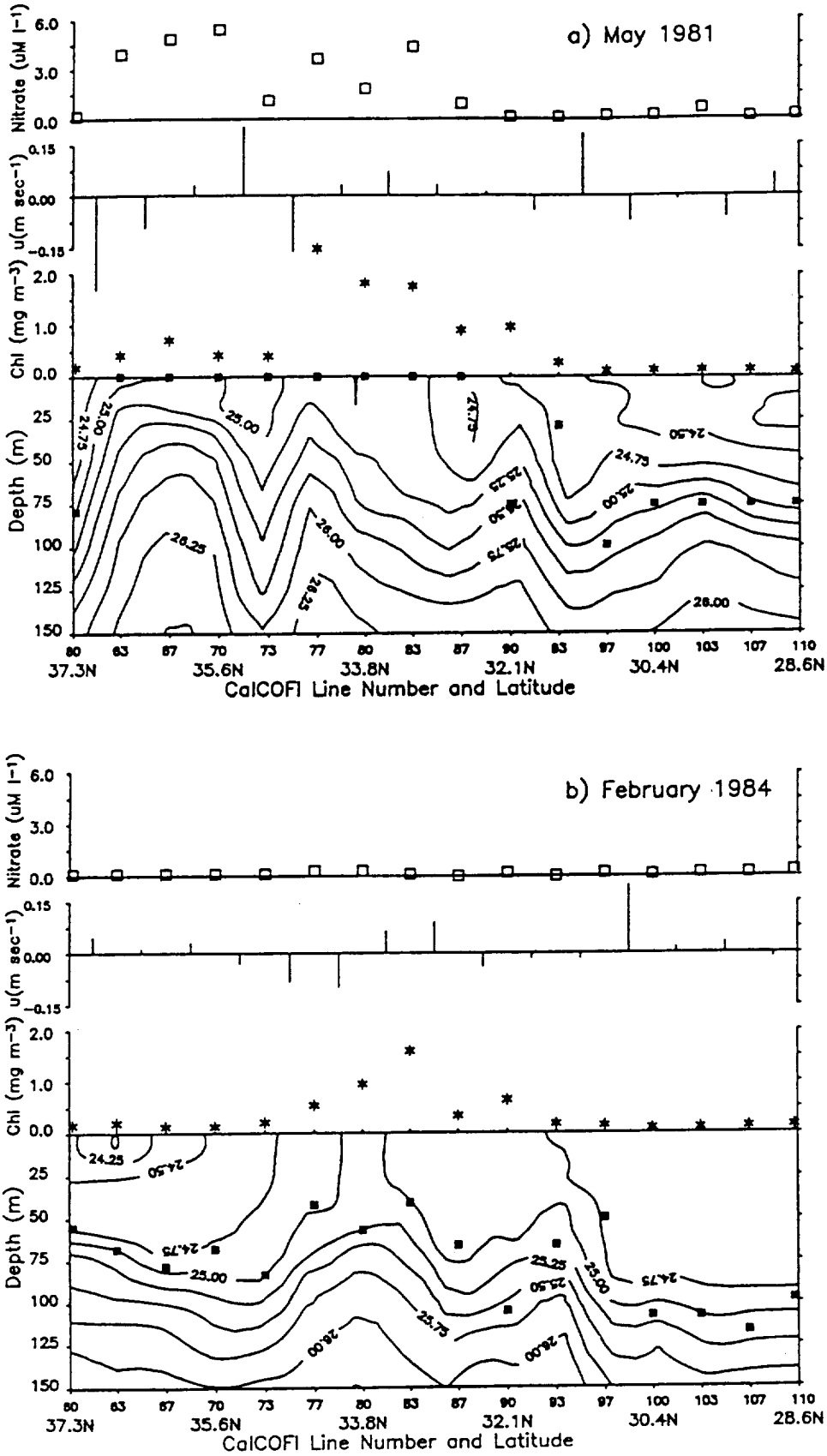

Fig. 5. Vertical contours of density structure through station 70 (see Figure 1) on each CalCOFI line from CalCOFI cruises (*a*) 8105, (*b*) 8402, (*c*) 8404, (*d*) 8405–06, (*e*) 8407, and (*f*) 8407. The first two digits indicate the year, and the last two, the month of the cruise. Shown as solid squares on the contour plot is the depth of the nitracline (defined as the shallowest depth at which nitrate concentrations are $> 0.5\ \mu M$). Also shown are pigment concentrations (chlorophyll plus phaeopigments) at the surface (usually 1–3 m), cross-shelf geostrophic velocities (0/500m) and surface nitrate concentrations (arrows indicate concentrations $> 7.0\ \mu M$).

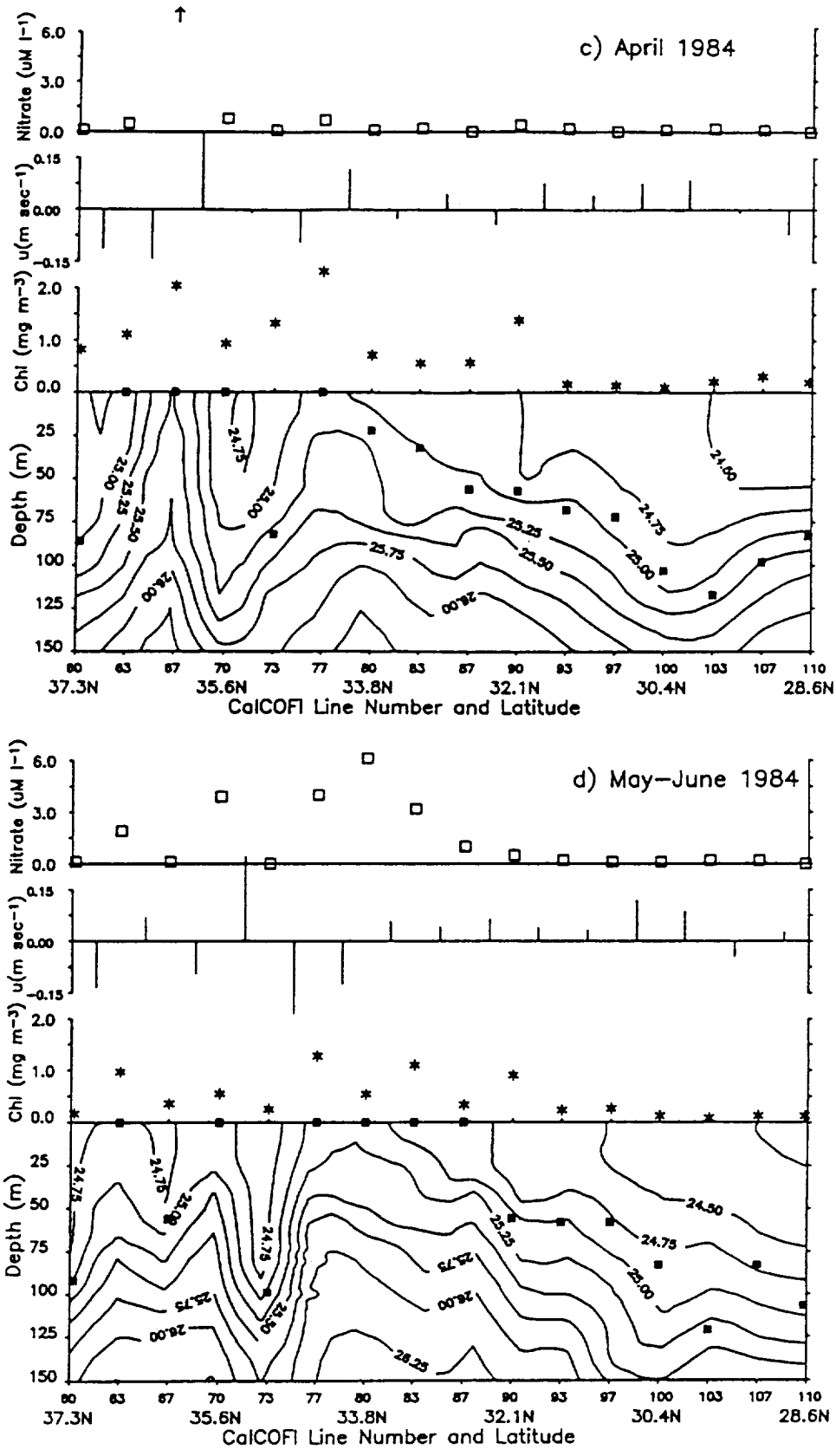

Fig. 5. (continued)

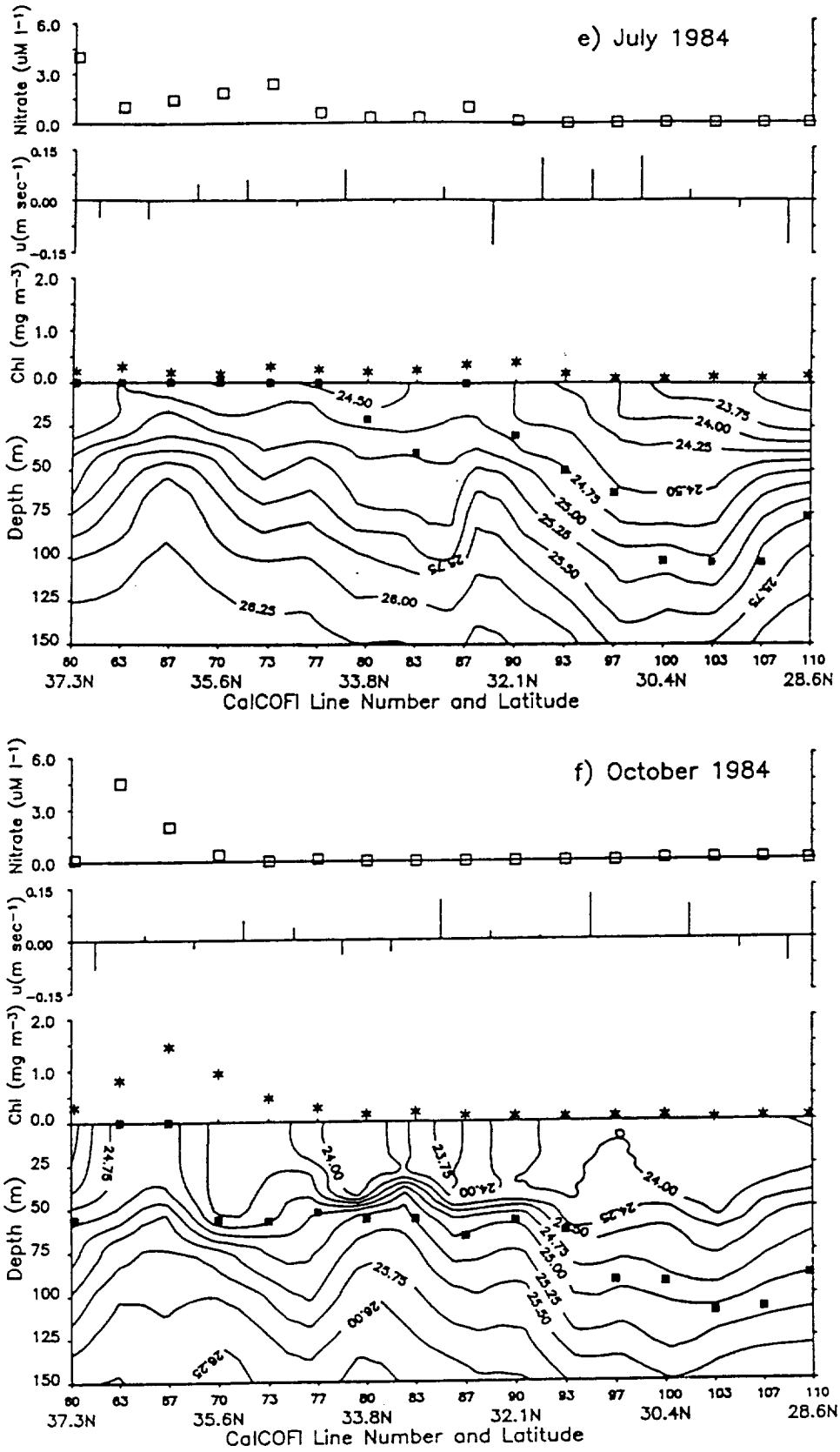

Fig. 5. (continued)

not resolved in the CalCOFI data. For regions south of the frontal zone, in which surface concentrations are always low (Figure 2), and the nitracline (defined here as the shallowest depth at which nitrate concentrations were ≥ 0.50 μM) and pycnocline are relatively deep all year (Figure 5), the presence of a subsurface chlorophyll maximum at depths deeper than ≈60 m (1984 CalCOFI data; not shown) probably has little influence on the pigment concentrations measured by the satellite. This argument is less valid in regions north of the front where high pigment concentrations are present in the spring and the pycnocline, nitracline, and subsurface chlorophyll maximum (not shown) are often relatively shallow (Figure 5). Temporal changes in the vertical distribution of chlorophyll, such as sinking in the late spring or vertical mixing in the fall, could induce spatial pattern in the upper attenuation depth integrated by the CZCS. *Hayward and Venrick* [1982] show that total water column chlorophyll concentrations are strongly correlated with surface concentrations in the CCS. The 1984 CalCOFI data indicate that in general, the subsurface chlorophyll maximum north of the front is deeper than 20 m over the whole year and probably is not seen by the CZCS. The position of the frontal zone evident in the CZCS data is closely related to that in hydrographic and other biological data, as is discussed in the introduction. These factors argue that surface pigment patterns seen by the CZCS are not strongly biased by temporal changes in vertical distribution. The fact remains, however, that the CZCS measures only those pigments in the upper water column, and these need not reflect total water column concentrations. Spatial and temporal patterns evident in Figures 2–4 should not be interpreted as those of total water column biomass.

4.2.1. *Spatial structure.* Contours of subsurface density along a transect similar to that used to sample the CZCS image composites (station 70 from CalCOFI lines 60 to 110) from the 1981 cruise and the five cruises in 1984 are plotted in Figure 5 along with the depth of the nitracline and surface "pigment concentration" (chlorophyll plus phaeopigment concentration). The location of these stations is shown in Figure 1.

The contours of subsurface density in Figure 5 indicate the presence of a hydrographic frontal zone at latitudes similar to those where pigment gradients are strongest in the satellite data, a relationship supported by the previous observations of *Peláez and McGowan* [1986] and *Niiler et al.* [1989] and long-term averages of density structure [*Lynn et al.*, 1982]. In each of the months presented, dense water is relatively deep in the southern portion of the transect, shelves at a frontal zone located between lines 100 and 93 (≈31.5°N) and is relatively shallow north of ≈32°N. In both February and October (Figures 5*b* and 5*f*), the frontal zone is primarily a subsurface feature, and a well-mixed surface layer eliminates any latitudinal gradient at depths shallower than ≈50 m. The data from these cruises suggest that a hydrographic expression of the frontal zone is present throughout the year, at least in 1984. Analysis of dynamic height over longer time scales [*Lynn et al.*, 1982; *Roesler and Chelton*, 1987] indicate that this is a recurring feature of the CCS in this region. Data from May 1981 show a pattern similar to that of May–June 1984, as do data from February and April 1980 (not shown). We thus take the features evident in the 1984 data to be representative of normal conditions.

Profiles of cross-shelf geostrophic velocity (relative to 500 m) included in Figure 5 indicate the surface flow associated with the subsurface density field. Strong (> 10 cm s^{-1}) onshore flow usually occurs between 29°N and 32°N, over the main frontal zone, in agreement with the previously mentioned studies. Especially in April and May–June (Figures 5*c* and 5*d*), strong horizontal density gradients in the northern portion of the transect are evidence of intense cross-shelf flows characteristic of the CCS during the summer [*Mooers and Robinson*, 1984; *Kosro*, 1987] and similar to the filaments visible in Figure 4. Although the CalCOFI grid spacing does not adequately resolve these features, the data indicate that north of 32°N, higher pigment and nutrient concentrations and a shallower nitracline are often bracketed by offshore flow to the north and onshore flow to the south (especially in February, April, and May–June). This is consistent with the conceptual model of a meandering southward jet within the CCS, with eutrophic water inshore and more oligotrophic water offshore of the jet.

The biological implications of this subsurface density structure are seen in the depth of the nitracline and surface in situ pigment and nitrate concentrations at each station along the transect (Figure 5). In a nutrient-limited system, the relationship between the depth of the nutricline and the depth of the euphotic zone is evidence of the extent of physical forcing and nutrient availability for phytoplankton growth in the upper part of the water column. Oligotrophic regions are generally characterized by reduced physical forcing with upper water column primary production in approximate equilibrium with nutrient regeneration. The flux of new nutrients into the upper water column is relatively low. In these regions the nutricline and euphotic zone depth will be similar and are usually relatively deep. Regions where the nutricline is relatively shallow compared with the depth of the euphotic zone have been disturbed from this equilibrium. These are regions where recent physical forcing has introduced new nutrients into the euphotic zone and are generally more eutrophic, conditions characteristic of eastern boundary currents. Wind forcing resulting in coastal upwelling [*Huyer*, 1983; *Traganza et al.*, 1987; *Jones et al.*, 1983], Ekman pumping [*Chelton*, 1982; *Strub et al.*, 1990], and vertical mixing [*Husby and Nelson*, 1982; *Thomas and Strub*, 1989] have all been shown to influence the productivity in the CCS. During summer, coastal upwelling is characteristic of the entire region.

In each of the months presented, the depth of the nitracline becomes shallower at the frontal zone coincident with the shoaling isopycnals. During the spring and summer cruises, the nitracline and surface pigment and nitrate concentrations are higher in the northern portions of the transect. The February and October cruises (winter and fall) do not show increased pigment concentrations at the frontal zone. In May 1981 and in May–June and July 1984, the nitracline actually outcrops the surface at line 87 and stations farther north. South of the frontal zone, the nitracline is typically at or below 100 m. Surface pigment concentrations are always less than 0.5 mg m^{-3} and often less than 0.25 mg m^{-3} south of the

frontal zone, indicative of an oligotrophic water column and consistent with the patterns of satellite-measured pigment concentration presented in Figure 2.

Changes in pigment concentration along the transect shown in Figure 2 are a close approximation of changes within what *Lynn and Simpson* [1987] describe as a transition zone in the CCS. This transition zone is in the high-speed core of the CCS which the authors characterize as being dominated by mesoscale eddies and meanders. The images shown in Plate 1 indicate that most of the latitudinal variability illustrated in Figures 2 and 3 is due to such mesoscale features oriented in a cross-shelf direction and associated with strong cross-shelf flow [*Mooers and Robinson*, 1984; *Kosro*, 1987] described above. The WCTS CZCS data presented in Figure 2 suggest that the most temporally stable feature in this transition zone is a tongue of higher pigment concentration located more than 200 km offshore of the SCB between ≈32.5°N and 34°N. This is immediately "downstream" of Point Conception, a region of strong and persistent upwelling [*Brink et al.*, 1984; *Atkinson et al.*, 1986] suggesting that advection of nutrients and biomass from this upwelling region might play a role in the patterns evident in Figure 2, as was implied by *Haury et al.* [1986].

4.2.2. *Temporal structure.* The seasonal pattern evident in Figures 2 and 4 cannot be compared directly to the in situ data on account of the mismatch in years, spatial resolution and synopticity of sampling; obviously, these in situ data will not allow an examination of interannual variability. The in situ data from 1984 do, however, illustrate two features of the seasonal pattern seen in the satellite data. In addition, previously published hydrographic and biological data from 1983 allow explanations of the highly anomalous pigment concentrations and patterns in this year.

The mid–late summer decrease in surface pigment concentrations north of ≈33°N evident in the satellite data in 1979–1982 (Figure 2) is supported by the July in situ measurements from 1984 (Figure 5*e*) in which concentrations are lower north of the front (< 0.5 mg m^{-3}) than those of either May–June or April. Spatial patterns in the satellite imagery of 1981 suggest that reduced pigment concentrations within the transect in mid–late summer are due to a retreat of higher biomass toward the coast (contrast Plates 1*c* and 1*d*). Comparisons of the mean cross-shelf distribution of pigment in a zonal transect (see Figure 1) in spring and summer (Figure 6) show that this onshore redistribution is a recurring feature of the CCS at this latitude (≈35°N to 38°N). Regions of higher pigment concentration extend ≈500 km offshore in the spring (April–May) of 1980 and 1981 and ≈300 km offshore in the spring of 1982 and 1986. In contrast, higher concentrations in summer (June–July) are restricted to within 100–200 km of the coast. The exception to this trend is 1983, when regions of higher pigment concentration do not extend farther than 200 km offshore during either spring or summer. Subsurface density structure suggests that this contraction of pigment concentration toward the coast as the summer progresses is accompanied by an increase in vertical stratification in the region of the sampled transect (contrast the stratification in the upper 50 m in Figure 5*c* and 5*d* with 5*e*) which would reduce the vertical flux of nutrients into the upper water column. A comparison of the buoyancy frequency N of the upper 50 m over three of the 1984 cruises, averaged within each cruise over each station where the nitracline outcrops the surface (see Figure 5), is 0.045, 0.064, and 0.086 rad s^{-1} for April, May–June, and July, respectively. The density difference over the top 50 m is almost twice as strong in July as it is in May–June. Reduced vertical flux is also implied by the surface nutrient concentrations at these stations. Although the nitracline outcrops the surface (by our definition) at seven northern stations in July (Figure 5*e*), mean surface nitrate concentrations are only 1.7 μM compared to 3.5 μM during May–June. If other factors are assumed constant, the July nutrient concentrations would support approximately half the phytoplankton biomass that concentrations in May–June would. Reduced biomass in midsummer is also supported by phytoplankton growth rates. A comparison of the depth averaged vertically integrated primary productivity in the euphotic zone (approximately the 1% light level) at stations north of the frontal zone over the same CalCOFI cruises shows that rates are considerably lower in July (a mean of 1.2 mgC m^{-3} h^{-1}) than in either April or May–June (means of 5.2 and 3.7 mgC m^{-3} h^{-1} respectively). The high productivity in April might explain the presence of high chlorophyll concentrations in association with relatively low nitrate concentrations present in the spring. While this discussion is internally consistent, the data do not explain why the productivity in May–June is less than that in April despite relatively high nutrient concentrations at the surface.

The mechanisms responsible for this summer onshore redistribution of pigment concentration are not clear. Preliminary results from the Coastal Transition Zone (CTZ) experiment indicate that high phytoplankton biomass, originating nearshore in upwelling regions, is usually associated with the inside or nearshore region of the meandering velocity structure making up the mesoscale filaments observed in satellite imagery [*A. Huyer and T. Cowles, personal communication*, 1989]. This suggests that the offshore extent of high pigment derived from coastal upwelling would be controlled by the cross-shelf location of the high velocity core of the CCS. This is supported by data in Figure 5 and by the similarities of dynamic height and chlorophyll concentration shown in the CalCOFI data reports. The seasonality of the cross-shelf position of velocity structure in the CCS [*Lynn and Simpson*, 1987], however, shows an opposite trend to that seen in the CZCS data over most of the latitudinal range of our mean cross-shelf transect (see Figure 1). Their data (a long-term average of geostrophic velocities perpendicular to CalCOFI lines) show the main core of the CCS farther offshore in June–July than in April–May. Only in the most northern portion of the study area does the core of the CCS shift onshore during the May–July period. It is possible that in such a dynamic system the long-term average presented by these authors smoothes the actual cross-shelf current structure beyond the point where a meaningful comparison can be made. Although these data are not concurrent, they do suggest that control of the cross-shelf extent of high pigment concentrations might not be due to current structure at all times of the year.

The data presented above are consistent in suggesting that current structure might be important in mid–late

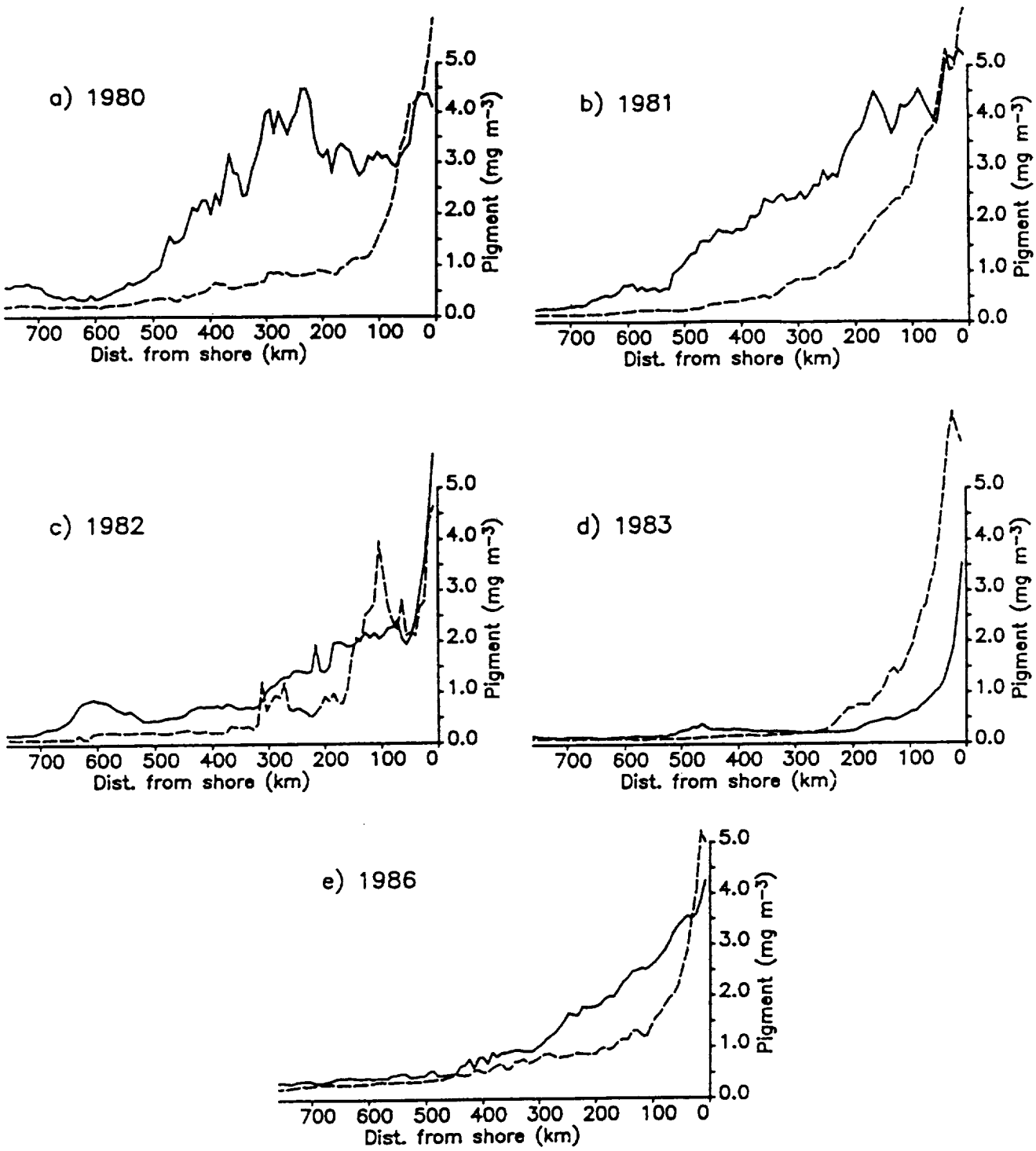

Fig. 6. The mean cross-shelf distribution of pigment concentration over the latitudinal range shown in Figure 1. Shown for each year is a mean for three 10-day periods in the spring (beginning April 11) as a solid line and a mean for three 10-day periods in the summer (beginning June 10, except 1986 May 21), as a dashed line.

summer when stratification in the central and offshore CCS is the strongest and coastal upwelling is the primary source of nutrients and resultant higher phytoplankton biomass. *Thomas and Strub* [1989] show that in the winter and spring, vertical mixing by wind events can lead to increases in pigment concentration over large portions of the CCS, extending up to 700 km offshore in a diffuse spatial pattern very different than the filaments and eddies seen in the later summer. It is possible, then, that in the early portion of the year, vertical nutrient fluxes by other mechanisms, in addition to upwelling, are important. At this time, resultant biological distributions do not have a strong resemblance to the current structure. As the summer progresses, the offshore water column becomes

increasingly stratified, nutrients are depleted, regeneration cannot support the biomass, and cells sink out of the upper water column. Nutrient flux in the upper water column and spatial patterns of phytoplankton biomass become increasingly dominated by coastal upwelling and the current structure of the CCS. This hypothesis cannot be tested with the data presently available and awaits a more detailed sampling of both biological and physical variables over seasonal time scales.

The in situ data from October 1984 (Figure 5*f*) appear to illustrate conditions during a fall period of relatively low pigment concentration in northern portions of the transect similar to those evident at the end of each year in Figure 2. Surface in situ pigment concentrations are < 0.5 mg m^{-3} at all stations south of $\approx 35°$N, and no surface chlorophyll gradient is present in the vicinity of $\approx 32°$N. Mean concentrations are slightly less than those evident in Figure 3*f* (period 29, 1981); however, maxima in both data sets are similar (≈ 1.5 mg m^{-3}). Plate 1 shows that spatial patterns of pigment at this time (period 29) are similar to those of mid–late summer (period 19) but that concentrations are 2–3 times lower. In this early fall period, the upper 50 m of the water column is well mixed (Figure 5*f*) and the pycnocline both relatively strong and deep compared to previous cruises (except at two northern stations where cross-shelf flow is evident). The nitracline is also relatively deep and often below the pycnocline, isolating surface water from nutrient enrichment. Mean depth-averaged vertically integrated primary productivity for stations north of the (subsurface) front in October 1984 is 1.0 mgC m^{-3} h^{-1}, similar to that of July but less than those of April and May–June (see above). During this period the frontal zone is a subsurface feature, and oligotrophic conditions characteristic of the southern portion of the study area are present in the upper water column as far north as 35°N.

Changes in pigment concentration within the northern portion of the meridional transect during this latter portion of the year (period 29 in Figure 3 and Plate 1) appear to result from both a change in cross-shelf distribution of biomass and a change in actual concentration (contrast periods 27 and 29 in Plate 1). Changes in the cross-shelf distribution of biomass both during the fall increase and during the late-fall decrease are difficult to compare to climatologies of geostrophic current structure due to the short time scale of these pigment features (10–20 days, see Figure 2). Published presentations of the cross-shelf current structure [*Lynn and Simpson*, 1987; *Roesler and Chelton*, 1987] use monthly means which do not resolve such short-term changes. Furthermore, such spatial structure might be lost in these long-term averages. The late-fall periods of low pigment concentration appear to occur at the same time as a change in nearshore current direction. *Chelton* [1984] shows that surface currents within ≈ 75 km of the coast change from southward (throughout spring and summer) to northward in October (and throughout winter). Again, Chelton's data are long-term averages and not directly comparable. It does suggest, however, that in October, surface water near the coast has its source to the south rather than the north and might have different chemical and biological characteristics. *Roemmich* [1989] highlights the importance of horizontal nutrient advection in this region, especially close to the coast.

The El Niño of 1983 is associated with anomalous biological and hydrographic conditions all along the west coast of North America [*McGowan*, 1985; *Norton et al.*, 1985; *Huyer and Smith*, 1985]. *Thomas and Strub* [1989] show that the changes in spatial pattern and concentration of pigment in 1983 at the time of the spring transition are the smallest of the 5 years of CZCS data they examine. A comparison of a spring image of the SCB from 1982 with one from 1983 by *Fiedler* [1984] shows that pigment concentrations are both lower and more closely associated with the coast in 1983. The time series shown in Figures 2*e* and 4 show that anomalously low concentrations were characteristic of the study region over the whole year. Published in situ data suggest that these lower concentrations are due to stronger stratification and anomalously deep pycnocline and nutricline associated with the 1982–1983 El Niño [*Rienecker and Mooers*, 1986; *Simpson*, 1983; *McGowan*, 1985]. The low pigment concentrations are probably not due to reduced wind forcing. *Rienecker and Mooers* [1986] show that the monthly averaged Bakun upwelling index at 36°N in 1983 does not differ significantly from long-term means. *Simpson* [1984*b*] argues that these anomalies are a result of increased onshore transport of subarctic water from the offshore portions of the CCS. These conditions within the water column are consistent in suggesting that a reduced vertical nutrient flux into the euphotic zone in 1983 resulted in reduced primary productivity and biomass over large regions of the CCS.

4.3. *Relationships to Wind Forcing*

Three indices of wind forcing (wind stress curl, alongshore wind stress, and wind mixing ($u*^3$)) at two locations representing the northern and southern portions of the meridional transect (see Figure 1) were calculated for each of the years of the WCTS. Examination of the time series in each year, however, indicated that most features of the interannual variability evident in the pigment data (Figures 2 and 4) could not be explained by these wind products. This is consistent with the statistical analysis of monthly anomalies in CZCS pigment concentrations by *Strub et al.* [1990], who found that only 25% of the pigment variance could be explained by wind forcing. Some features of the seasonal and spatial variability did appear to be more closely coupled to wind forcing, and in Figure 7 we present the 6-year mean [1979–1983, 1986] of these wind products.

The dominant feature of these data is the lower wind forcing and reduced seasonality over the southern portions of the transect compared with the northern portions. This supports the previously discussed relationship between nutricline depths (Figure 4) and the influence of physical forcing and reflects the relative seasonality of pigment concentrations in these portions of the study area.

Alongshore wind stress in the north of the transect (Figure 7) is generally less in July and August than in April and May. *Strub et al.* [1987*a*] show this to be characteristic of the entire California coast. Reduced upwelling in the mid–late summer might explain the reduced offshore extent of higher biomass shown in Figure 6.

The coincidence of the date of the spring transition in current and wind structure along the west coast (Table 1) and the timing of the spring increase in pigment

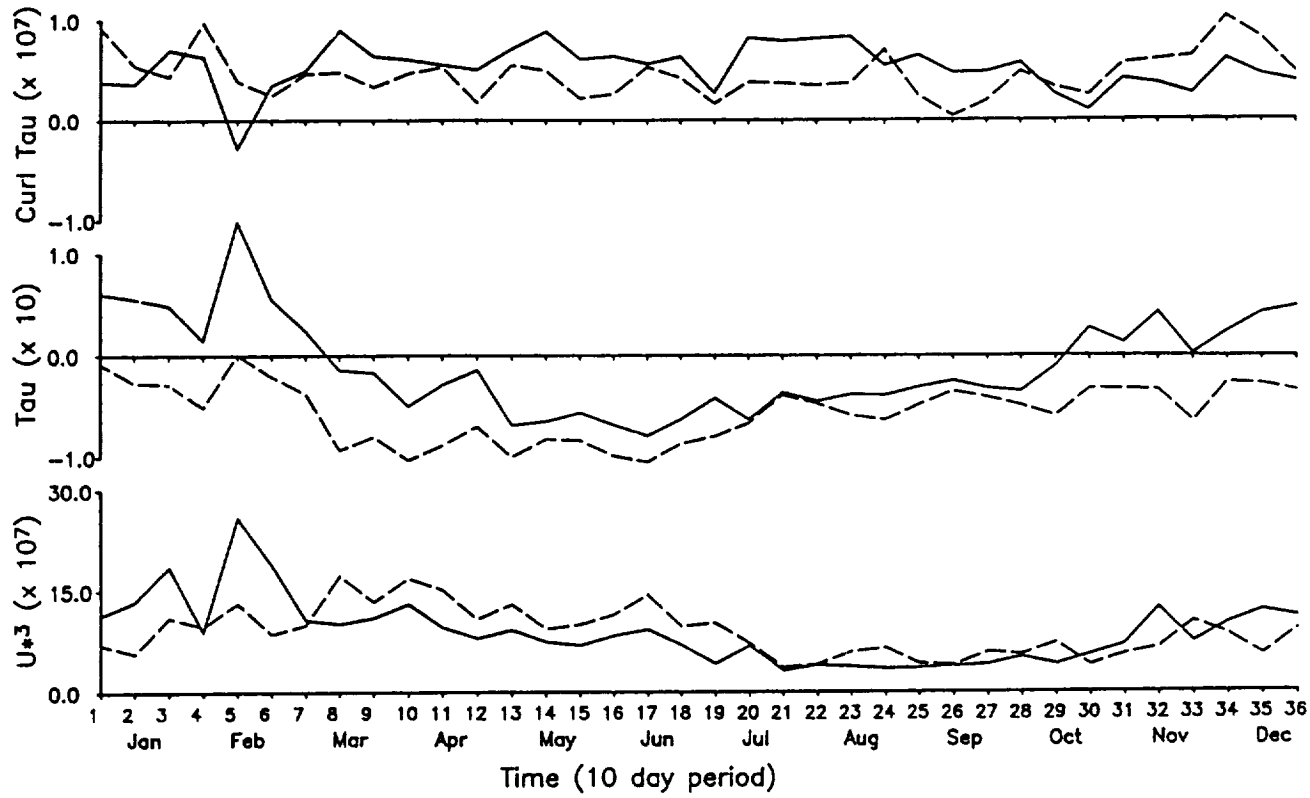

Fig. 7. Wind forcing from LFM data, characterized as $u*^3$, alongshore wind stress and wind stress curl averaged from daily values to 10 day means, and then averaged over 6 years (1979–1983, 1986), at a station representing the northern (solid line) and the southern (dashed line) portions of the meridional transect (see Figure 1).

TABLE 1. The Spring and Fall Transition Dates With Julian Days and the 10-Day Period in Which They Occur

	Spring			Fall		
Year	Date	Julian Day	Period	Date	Julian Day	Period
1980	March 22	82	9	Oct. 25	298	30
1981	March 26	85	9	Oct. 27	300	30
1982	April 18	108	11	Oct. 13	287	29
1983	April 4	94	10	Oct. 30	303	31
1986	March 17	77	8			

concentrations north of ≈33°N (Figure 2) indicates a strong relationship between phytoplankton growth rates and wind forcing during this period in most years. The spring transition marks the seasonal change from northward mean wind stress and downwelling at the coast to southward mean wind stress and upwelling [*Huyer et al.*, 1979], seasonality evident only north of ≈34°N [*Strub et al.*, 1987*b*]. A more detailed explanation of the dates chosen for the spring and fall transitions are given by *Strub and James* [1988] and *Thomas and Strub* [1989]. *Thomas and Strub* show that large spatial scale changes in pigment concentration can be associated with this physical event, but they emphasize the interannual variability of both spatial and temporal patterns in the CZCS imagery. This variability is evident in March–April data shown in Figure 2. These authors argue that because the water column in offshore regions south of ≈40°N is vertically stratified and nutrient depleted in late winter, interannual variability is due not only to differences in alongshore wind stress (upwelling) but also to the strength and timing of wind mixing events.

The wind data do not provide an explanation for the increase in pigment concentrations in the fall in the northern portion of the transect. This increase appears to occur at a time of reduced wind mixing and alongshore stress. Furthermore, no consistent relationship is evident between the date of the fall transition in wind and current structure (Table 1) (the switch from mean southward alongshore wind stress to northward) and the fall decrease in pigment concentrations or elimination of the frontal gradient seen in Figure 2. A detailed analysis of pigment temporal patterns and large-scale forcing in the fall is beyond the scope of this study and probably requires a

more complete time series of in situ biological and chemical measurements concurrent with hydrographic data than are available to us.

5. SUMMARY

Analysis of the complete CZCS data set from 6 years (1979–1983, 1986) illustrates the seasonal and interannual variability of near-surface phytoplankton pigment concentrations along an offshore meridional transect in the CCS from ≈38°N to ≈30°N. Concentrations in winter were not analyzed on account of errors in the atmospheric correction algorithm used to process the satellite data. The transect crosses a semipermanent frontal zone which is also evident in in situ hydrographic data, illustrating the variability in the latitudinal position and relative gradient of pigment concentrations across the front. Seasonality is strongly developed in the region north of the front (≈32°N) but virtually absent in water to the south. The seasonal development of higher concentrations in the northern portion of the transect determines the strength and latitudinal position of the frontal zone as expressed in pigment concentration.

A number of features in the time series of pigment concentrations recur in different years, and a generalized seasonal cycle is apparent, superimposed on interannual variability. This seasonal cycle shows low early spring concentrations throughout the latitudinal range of the transect and a late spring increase in concentration north of ≈32°N which forms a zonally oriented frontal gradient. Concentrations south of the frontal zone remain low throughout the spring, summer, and fall. Concentrations north of the frontal zone decrease in midsummer, reducing or eliminating the frontal gradient, but increase for a brief period in early fall, reestablishing the strong frontal gradient. In the late fall, concentrations decrease north of the front, eliminating the frontal gradient, and low concentrations are again present throughout the study area.

Three principal features of interannual variability are evident in the data. In 1982 the frontal gradient is less and is displaced ≈150 km north of its position in other years. Also in 1982 the spring increase in concentration north of the front occurs ≈20 days later in the year and the fall features of the seasonal cycle occur 20–30 days earlier than previous years resulting in a "summer period" which is 40–50 days shorter than that of other years. No increase in pigment concentration takes place in the spring of 1983, and pigment concentrations throughout the transect remain low throughout this El Niño year. The frontal zone is evident for only a brief period in June.

Analysis of two-dimensional spatial patterns in the images and cross-shelf transects of the data in regions north of the front indicate that the midsummer decrease in concentration within the sampled transect is the result of changes in the cross-shelf distribution of pigment. Regions of higher pigment concentration extend 150–300 km farther offshore in spring and early summer than in mid and late summer in each year (except 1983, when higher concentrations remain closely associated with the coast throughout the year).

The time series of CZCS data is long enough to show extensive interannual variability and to identify some specific features which appear to reoccur on a regular basis. Suggestions are made regarding mechanisms responsible for these features. Verification, however, awaits a detailed analysis of concurrent hydrographic, chemical and biological in situ measurements over seasonal time scales.

Acknowledgments. We thank those responsible for the collection and publication of the CalCOFI data, Mark Abbott for access to the CZCS West Coast Time Series, and NCAR for the meteorological data. Tim Cowles and Adriana Huyer provided helpful comments on various aspects of this work. This work was supported by NASA grant NAGW-1251 and by a Killam Postdoctoral Fellowship (A.C.T.).

REFERENCES

Abbott, M. R., and P. M. Zion, Spatial and temporal variability of phytoplankton pigment off northern California during Coastal Ocean Dynamics Experiment 1, *J. Geophys. Res.*, *92*, 1745–1756, 1987.

Atkinson, L. P., K. H. Brink, R. E. Davis, B. H. Jones, T. Paluszkiewicz, and D. W. Stuart, Mesoscale hydrographic variability in the vicinity of points Conception and Arguello during April–May 1983: The OPUS 1983 experiment, *J. Geophys. Res.*, *91*, 12,899–12,918, 1986.

Brink, K. H., D. W. Stuart, and J. C. VanLeer, Observation of the coastal upwelling region near 34°30'N off California: Spring 1981, *J. Phys. Oceanogr.*, *14*, 378–391, 1984.

Brinton, E., Distributional atlas of Euphausiacea (Crustacea) in the California Current region, *CalCOFI Atlas 5*, Calif. Coop. Oceanic Fish. Invest., Univ. of Calif., San Diego, La Jolla, 1967.

Chelton, D. B., Large-scale response of the California Current to forcing by wind stress curl, *CalCOFI Rep. 23*, pp. 130–148, Calif. Coop. Oceanic Fish. Invest., Univ. of Calif., San Diego, La Jolla, 1982.

Chelton, D. B., Seasonal variability of alongshore geostrophic velocity off central California, *J. Geophys. Res.*, *89*, 3473–3486, 1984.

Chelton, D. B., A. W. Bratkovitch, R. L. Bernstein, and P. M. Kosro, Poleward flow off central California during the spring and summer of 1981 and 1984, *J. Geophys. Res.*, *93*, 10,604–10,620, 1988.

Denman, K. L., and M. R. Abbott, Time evolution of surface chlorophyll patterns from cross-spectrum analysis of satellite color images, *J. Geophys. Res.*, *93*, 6789–6798, 1988.

Fiedler, P. C., Satellite observations of the 1982–1983 El Niño along the U.S. Pacific coast, *Science*, *224*, 1251–1254, 1984.

Gordon, H. R., D. K. Clark, J. L. Mueller, and W. A. Hovis, Phytoplankton pigments from the Nimbus-7 coastal zone color scanner: Comparisons with surface measurements, *Science*, *210*, 63–66, 1980.

Gordon, H. R., D. K. Clark, J. W. Brown, O. B. Brown, R. H. Evans, and W. W. Broenkow, Phytoplankton pigment concentrations in the Middle Atlantic Bight: Comparison of ship determinations and CZCS estimates, *Appl. Opt.*, *22*, 20–36, 1983.

Hayward, T. L., and E. L. Venrick, Relation between surface chlorophyll, integrated chlorophyll and integrated primary production, *Mar. Biol.*, *69*, 247–252, 1982.

Haury, L. R., An offshore eddy in the California Current system, IV, Plankton distributions, *Prog. Oceanogr.*, *13*, 95–111, 1984.

Haury, L. R., J. J. Simpson, J. Peláez, C. J. Koblinsky, and D. Wiesenhahn, Biological consequences of a recurrent eddy off Point Conception, California, *J. Geophys. Res.*, *91*, 12,937–12,956, 1986.

Hickey, B. M., The California Current system—Hypotheses and facts, *Prog. Oceanogr.*, *8*, 191–279, 1979.

Husby, D. M., and C. S. Nelson, Turbulence and vertical stability in the California Current, *CalCOFI Rep. 23*, pp. 113–129, Calif. Coop. Oceanic Fish. Invest., Univ of Calif., San Diego, La Jolla, 1982.

Huyer, A. E., Coastal upwelling in the California Current system, *Prog. Oceanogr.*, *12*, 259–284, 1983.

Huyer, A. E., and R. L. Smith, The signature of El Niño off

Oregon, 1982–1983, *J. Geophys. Res.*, *90*, 7133–7142, 1985.
Huyer, A. E., E. J. Sobey, and R. L. Smith, The spring transition in currents over the Oregon continental shelf, *J. Geophys. Res.*, *84*, 6995–7011, 1979.
Jones, B. H., K. H. Brink, R. C. Dugdale, D. W. Stuart, J. C. VanLeer, D. Blasco, and J. C. Kelley, Observations of a persistent upwelling center off Point Conception, California, in *Coastal Upwelling*, edited by E. Suess and J. Thiede, pp. 37–60, Plenum, New York, 1983.
Kelly, K. A., Swirls and plumes or application of statistical methods to satellite-derived sea surface temperatures, Ph.D. thesis, *S.I.O. Ref. 83-15*, *CODE Tech. Rep. 18*, 210 pp., Scripps Inst. of Oceanogr., La Jolla, Calif., 1983.
Kosro, P. M., Structure of the coastal current field off northern California during the Coastal Ocean Dynamics Experiment, *J. Geophys. Res.*, *92*, 1637–1654, 1987.
Lynn, R. J., and J. J. Simpson, The California Current system: The seasonal variability of its physical characteristics, *J. Geophys. Res.*, *92*, 12,947–12,966, 1987.
Lynn, R. J., K. A. Bliss, and L. E. Eber, Vertical and horizontal distributions of seasonal mean temperature, salinity, sigma-*t*, stability, dynamic height, oxygen, and oxygen saturation in the California Current, 1950–1978, *CalCOFI Atlas 30*, Calif. Coop. Oceanic Fish. Invest., Univ. of Calif., San Diego, La Jolla, 1982.
McGowan, J. A., El Niño 1983 in the Southern California Bight, in *El Niño North*, edited by W. S. Wooster and D. L. Fluharty, Washington Sea Grant Program, University of Washington, Seattle, 1985.
Mooers, C. N. K., and A. R. Robinson, Turbulent jets and eddies in the California Current and inferred cross-shore transports, *Science*, *223*, 51–53, 1984.
Niiler, P. P., P-M. Poulain, and L. R. Haury, Synoptic three-dimensional circulation in an onshore-flowing filament of the California Current, *Deep Sea Res.*, *36*, 385–405, 1989.
Norton, J., D. McLain, R. Brainard, and D. Husby, The 1982–83 El Niño off Baja and Alta California and its ocean climate context, in *El Niño North*, edited by W. S. Wooster and D. L. Fluharty, Washington Sea Grant Program, University of Washington, Seattle, 1985.
Pares-Sierra, A., and J. J. O'Brien, The seasonal and interannual variability of the California Current system: A numerical model, *J. Geophys. Res.*, *94*, 3159–3180, 1989.
Peláez, J., and F. Guan, California Current chlorophyll measurements from satellite data, *CalCOFI Rep. 29*, pp. 212–225, Calif. Coop. Oceanic Fish. Invest., Univ. of Calif., San Diego, La Jolla, 1982.
Peláez, J., and J. A. McGowan, Phytoplankton pigment patterns in the California Current as determined by satellite, *Limnol. Oceanogr.*, *31*, 927–950, 1986.
Reid, J. L., Jr., R. A. Schwartzlose, and D. M. Brown, Direct measurements of a small surface eddy off northern Baja California, *J. Mar. Res.*, *21*, 205–218, 1963.
Rienecker, M. M., and C. N. K. Mooers, The 1982–1983 El Niño signal off northern California, *J. Geophys. Res.*, *91*, 6597–6608, 1986.
Roemmich, D., Mean transport of mass, heat, salt and nutrients in southern California coastal waters: Implications for primary production and nutrient cycling, *Deep Sea Res.*, *36*, 1359–1378, 1989.
Roesler, C. R., and D. B. Chelton, Zooplankton variability in the California Current, 1951–1982, *CalCOFI Rep. 28*, pp. 59–96, Calif. Coop. Oceanic Fish. Invest., Univ. of Calif., San Diego, La Jolla, 1987.
Scripps Institution of Oceanography (SIO), Physical, chemical and biological data report, *S.I.O. Ref. 84-18*, Univ. of Calif., San Diego, La Jolla, 1984*a*.
Scripps Institution of Oceanography (SIO), Physical, chemical and biological data report, *S.I.O. Ref. 84-23*, Univ. of Calif., San Diego, La Jolla, 1984*b*.
Scripps Institution of Oceanography (SIO), Physical, chemical and biological data report, *S.I.O. Ref. 85-9*, Univ. of Calif., San Diego, La Jolla, 1985*a*.
Scripps Institution of Oceanography (SIO), Physical, chemical and biological data report, *S.I.O. Ref. 85-14*, Univ. of Calif., San Diego, La Jolla, 1985*b*.
Simpson, J. J., Large-scale thermal anomalies in the California Current during the 1982–1983 El Niño, *Geophys. Res. Lett.*, *10*, 937–940, 1983.
Simpson, J. J., El Niño–induced onshore transport in the California Current during 1982–1983, *Geophys. Res. Lett.*, *11*, 241–242, 1984*a*.
Simpson, J. J., An offshore eddy in the California Current system, III, Chemical structure, *Prog. Oceanogr.*, *13*, 71–93, 1984*b*.
Simpson, J. J., C. J. Koblinsky, J. Peláez, L. R. Haury, and D. Wiesenhahn, Temperature–plant pigment–optical relations in a recurrent offshore mesoscale eddy near Point Conception, California, *J. Geophys. Res.*, *91*, 12,919–12,936, 1987.
Smith, R. C., X. Zhang, and J. Michaelsen, Variability of pigment biomass in the California Current system as determined by satellite imagery, 1, Spatial variability, *J. Geophys. Res.*, *93*, 10,863–10,882, 1988.
Strub, P. T., and C. James, Atmospheric conditions during the spring and fall transitions in the coastal ocean off western United States, *J. Geophys. Res.*, *93*, 15,561–15,584, 1988.
Strub, P. T., J. S. Allen, A. Huyer, R. L. Smith, and R. C. Beardsley, Seasonal cycles of currents, temperatures, winds, and sea level over the northeast Pacific continental shelf: 35°N to 48°N, *J. Geophys. Res.*, *92*, 1507–1526, 1987*a*.
Strub, P. T., J. S. Allen, A. Huyer, and R. L. Smith, Large-scale structure of the spring transition in the coastal ocean off western North America, *J. Geophys. Res.*, *92*, 1527–1544, 1987*b*.
Strub, P. T., C. James, A. C. Thomas, and M. R. Abbott, Seasonal and nonseasonal variability of satellite-derived surface pigment concentration in the California Current, *J. Geophys. Res.*, *95*, 11,501–11,530, 1990.
Thomas, A. C., and W. J. Emery, Relationships between near-surface plankton concentrations, hydrography, and satellite-measured sea surface temperature, *J. Geophys. Res.*, *93*, 15,733–15,748, 1988.
Thomas, A. C., and P. T. Strub, Interannual variability in phytoplankton pigment distribution during the spring transition along the west coast of North America, *J. Geophys. Res.*, *94*, 18,095–18,117, 1989.
Traganza, E. D., D. G. Redalje, and R. W. Garwood, Chemical flux, mixed layer entrainment and phytoplankton blooms at upwelling fronts in the California coastal zone, *Cont. Shelf Res.*, *7*, 89–105, 1987.
Wickham, J. B., A. A. Bird, and C. N. K. Mooers, Mean and variable flow over the central California continental margin, 1978–1980, *Cont. Shelf Res.*, *7*, 827–849, 1987.
Wyllie, J. G., Geostrophic flow of the California Current at the surface and at 20 m, *CalCOFI Atlas 4*, Calif. Coop. Oceanic Fish. Invest., Univ. of Calif., San Diego, La Jolla, 1966.

A. C. Thomas and P. T. Strub, College of Oceanography, Oregon State University, Corvallis, OR 97331.

(Received January 15, 1990;
accepted May 9, 1990.)

APPENDIX G

SEASONAL AND NONSEASONAL VARIABILITY OF SATELLITE- DERIVED SURFACE PIGMENT CONCENTRATION IN THE CALIFORNIA CURRENT

P. Ted Strub, Corinne James, Andrew C. Thomas
and Mark R. Abbott

JOURNAL OF GEOPHYSICAL RESEARCH, VOL. 95, NO. C7, PAGES 11,501–11,530, JULY 15, 1990

Seasonal and Nonseasonal Variability of Satellite-Derived Surface Pigment Concentration in the California Current

P. Ted Strub, Corinne James, Andrew C. Thomas, and Mark R. Abbott

College of Oceanography, Oregon State University, Corvallis

Satellite-derived pigment concentrations from the west coast time series (WCTS) are averaged into monthly mean fields over the California Current system (CCS) for the period July 1979 to June 1986. Errors caused by the scattering algorithm used in the WCTS are reduced by an empirical correction function, although winter values (November–February) remain unreliable. For the March–October period we look at both the mean seasonal development and the nonseasonal monthly anomalies of pigment concentration. These are compared with fields of alongshore wind stress, mixing power of the wind (u_*^3) and wind stress curl. Outside of the Southern California Bight there is a strong seasonal cycle with a spring–summer maximum, a northward progression of high pigment concentrations from California to Oregon and a double maximum off Washington (spring and summer, with a lull in between). Within the Southern California Bight, seasonality is low, with a relative minimum in late summer. Off Baja California the pattern is similar to that off northern California. In regions where previous work has been done, there is general agreement with the seasonal cycles found here. Nonseasonal variability in pigment concentration over the large-scale CCS (400 km wide) is most closely related statistically to synoptic fields of wind stress curl. Within 100 km of the coast, the strongest relations are between pigment concentration and both u_*^3 and alongshore wind stress. Correlations with these wind variables account for only 25% of the monthly variance in anomalous satellite-derived pigment concentrations. This is partly due to the noise in both wind and pigment data sets but also demonstrates the fact that much of the anomalous pigment variability is not a response to anomalous wind forcing on these time scales. Correlations are also low between anomalous pigment concentrations and anomalous sea level heights, which serve as a crude proxy for the strength of the alongshore current over the shelf. The largest nonseasonal anomaly in the data occurred during the 1982–1983 El Niño, which caused a large-scale decrease in pigment concentration, stronger and longer lasting in the south than in the north.

1. Introduction

The large-scale patterns of satellite-derived surface pigment concentration off the west coast of North America are presented and their statistical relation to surface wind forcing are examined. Spatial patterns in the California Current system (CCS) between approximately 25°N and 50°N, and between 105°W and 140°W are discussed in terms of both seasonal and nonseasonal variability over the period July 1979 to June 1986.

Although previous studies have utilized satellite data from the coastal zone color scanner (CZCS) to show spatial and temporal patterns of surface pigment concentration within the CCS, most have treated restricted time periods and/or relatively small spatial regions [*Abbott and Zion*, 1985, 1987; *Barale and Fay*, 1986; *Peláez and McGowan*, 1986; *Michaelsen et al.*, 1988; *Smith et al.*, 1988]. Our approach is to examine the large-scale variability by averaging data into monthly means within 1° spatial blocks. Although this temporal and spatial averaging eliminates much of the mesoscale variability that has been the focus of the CZCS analyses cited above [*Denman and Abbott*, 1988], it does produce a more regular time series than that provided by the temporally and spatially patchy individual images and makes quantitative use of the entire west coast time series (WCTS) of CZCS data.

The satellite time series provides a unique opportunity to test connections between wind forcing and biological response in the upper ocean over a seven year period in an eastern boundary current system. An increasing number of studies have looked for correlations between monthly (or shorter) averages of alongshore wind stress (as an upwelling index) and indicators of biological productivity at higher trophic levels [*Bakun*, 1973; *Botsford*, 1986; *Botsford et al.*, 1989; *Landry et al.*, 1989]. It is therefore appropriate to test the connection between wind forcing and pigment concentration, a variable approximating the time integral of previous primary productivity in the upper ocean.

In section 2 we summarize the large-scale seasonal characteristics of the California Current; this section can be skipped by those familiar with this region. Section 3 describes the data and methods used here and discusses problems known to affect the satellite-derived pigment concentrations and the wind data used in this study. In section 4 we present the results of the statistical analysis, and in section 5 these results are discussed in light of past observations and theory. Section 6 summarizes the main conclusions of the study with reference to the pertinent figures. Sections 3–6 are divided into subsections which consider the seasonal and nonseasonal variability separately. Appendix A describes details of the CZCS data processing. Appendix B gives the details of the principal estimator pattern methodology.

Paper number 89JC03739.
0148-0227/90/89JC-03739$05.00

2. The California Current System

The CCS is the equatorward eastern boundary current (EBC) of the North Pacific, connecting the eastward flowing west wind drift in the north (approximately 45°–50°N) to the westward flowing North Equatorial Current in the south (approximately 20°N). The CCS has a fairly regular geometry and narrow shelf. Previous work has shown regional differences in both the physical and biological oceanography within the CCS. Although no single work provides a detailed comparison of regions within the CCS, the literature suggests differences in the forcing and response between the Washington–Oregon coasts, the northern–central California coasts, the Southern California Bight, and the Baja California coast.

2.1. *Physical Overview*

Water entering the CCS from the north is relatively cold, fresh and rich in nutrients. Water to the west of the current is warmer and lower in nutrients. In the south and away from the coast off Baja California, water is warm, salty and low in nutrients [*Hickey*, 1979; *Freeland et al.*, 1984; *Martin and Gordon*, 1988; *Scripps Institution of Oceanography*, 1984*a*, 1984*b*, 1984*c*, 1984*d*]. During spring and summer upwelling, water close to the coast is cold, salty, and high in nutrients, except where it is influenced by the fresh water from rivers such as the Fraser and Columbia and from San Francisco Bay [*Huyer*, 1983; *Traganza et al.*, 1983]. North of ≈ 34°N, shelf regions experience episodic upwelling events even in winter; in the southern portions of the CCS, winds are upwelling favorable throughout the year [*Strub et al.*, 1987*a*]. Coastal upwelling, increased mixing over the shelf and topographic effects combine to produce a nearshore band of higher nutrient levels and pigment concentrations all year [*Barale and Fay*, 1986].

The climatological picture of the CCS current regime in summer consists of southward meandering surface flow, with a maximum velocity over the shelf off Oregon and Washington, ≈ 150 km offshore off central California and close to the coast again off Baja California. Off southern California (≈ 32°N) the current has a strong onshore component and flows eastward. Part of this flow turns south along the Baja California coast and part flows northward into the Southern California Bight [*Pavlova*, 1966; *Hickey*, 1979, 1989; *Pares-Sierra and O'Brien*, 1989; *Niiler et al.*, 1989]. The historical hydrographic data [*Hickey*, 1979; *Roesler and Chelton*, 1987] and the model of *Pares-Sierra and O'Brien* [1989] suggest that the flow into the bight is strongest in summer. Within the bight itself, the circulation often consists of a cyclonic gyre. In winter, southward flow is weaker and farther offshore, and the northward flowing Davidson Current is found next to the coast [*Hickey*, 1979].

Off central Oregon and Washington, alongshore currents over the shelf are quite regular, flowing southward for most of the spring and summer and fluctuating with storm winds in fall and winter [*Huyer et al.*, 1979]. The Columbia River plume is advected to the south in summer, influencing the coast of Oregon, and to the north in winter, influencing the coast of Washington [*Hickey*, 1989]. Between Cape Blanco and Point Conception (43°–35°N) the currents over the shelf exhibit large fluctuations with periods of 20–40 days [*Strub et al.*, 1987*a*]. These may be associated with jets, meanders, and eddies, seen to extend 100–400 km offshore in sea surface temperature images (from advanced very high resolution radiometer, or AVHRR) during spring through fall [*Ikeda and Emery*, 1984; *Flament et al.*, 1985; *Kosro and Huyer*, 1986; *Moum et al.*, 1988].

Both local wind stress and remote forcing affect the variability of the California Current. Sources of remote forcing include the inflow from the west wind drift at the north [*Chelton and Davis*, 1982], onshore transport of central Pacific water from the west [*Simpson*, 1984], Kelvin and coastally trapped waves propagating into the region from the south [*Spillane et al.*, 1987; *Pares-Sierra and O'Brien*, 1989; *Davis and Bogden*, 1989], and the oceanic component of the El Niño, also entering from the south [*Enfield and Allen*, 1980; *Chelton and Davis*, 1982]. Local winds over the California Current in the north (48°N) are primarily northward and are maximum in winter; in the south (25°–35°N) they are southward, on average, and maximum in late spring [*Nelson*, 1977; *Strub et al.*, 1987*a*]. At mid-latitudes (40°N), however, winds have a strong seasonal cycle consisting of relatively persistent southward winds in summer (with periods of relaxation) and intermittent northward (storm) winds in winter. *Strub et al.* [1987*b*] show the large spatial scale and short time scale of the spring transition in wind, sea level, water temperature and currents which separates the winter and summer regimes of the CCS. The spring transition was previously documented for the Oregon coast by *Huyer et al.* [1979]. This seasonality decreases at lower latitudes such that south of ≈ 34°N, winds are southward in both winter and summer. The average curl of the wind stress is positive in a narrow (100–200 km) band next to the coast and negative farther offshore [*Nelson*, 1977; *Rienecker and Ehret*, 1988]. The sign of the curl is consistent (through Sverdrup dynamics) with the general southward flow of the current and with the poleward undercurrent found over the continental slope *Hickey*, 1979; *Chelton*, 1984; *Pares-Sierra and O'Brien*, 1989].

2.2. *Biological Overview*

Temporal and spatial characteristics of chlorophyll concentration over the full extent of the CCS have not been documented. Numerous authors, however, have treated specific regions and/or time periods which are briefly reviewed here.

North of 48°N, *Thomas and Emery* [1986] show a strong relationship between winter (November–December) surface chlorophyll concentrations and hydrographic variables. Concentrations along the middle and outer shelf, in the northward flowing Davidson Current water, were < 0.2 mg m^{-3}. In summer, concentrations were > 5.0 mg m^{-3} in colder shelf water and < 1.0 mg m^{-3} in warmer, more stratified water over the shelf break and offshore [*Mackas et al.*, 1980; *Thomas and Emery*, 1988]. *Pan et al.* [1988] use CZCS data from 1979 to show the onset of a spring bloom in April, with elevated concentrations (≈ 1.0 mg m^{-3}) extending 100–200 km offshore. These offshore concentrations decreased in May. Maximum concentrations over the shelf were noted in August. These authors show that average monthly concentrations in regions $\geq$ 350 km offshore remain between 0.2 and 0.3 mg m^{-3} over the period March to September.

Off Oregon and Washington, *Landry et al.* [1989] review seasonal variation in chlorophyll concentrations using spatial averages from historical in situ data. Winter (November–February) surface concentrations are $\approx$ 1.0 mg m^{-3} in a region extending 90 km offshore. They report a spring bloom in March–April off Washington, with concentrations reaching 3.0 mg m^{-3}. They had insufficient data to document a bloom off Oregon. They do, however, show winter surface nitrate concentrations of $\approx$ 5.0 μM off both Oregon and Washington, indicating that light is probably limiting phytoplankton growth before March. Surface chlorophyll concentrations in areas greater than $\approx$ 70 km offshore have a midsummer minimum of $\approx$ 0.3 mg m^{-3}. Inshore of $\approx$ 40 km, concentrations are maximum (> 3.0 mg m^{-3} off Oregon and > 6.0 mg m^{-3} off Washington) in summer months (May, June, and July) because of wind-driven coastal upwelling.

Spring and summer patterns of pigment concentration off central–northern California (38°–40°N) are strongly influenced by wind forcing, coastal features such as capes and possibly bottom topography in a region extending several hundred kilometers offshore [*Abbott and Zion*, 1987]. These authors show that both concentrations and variance are lower offshore and that there is a zone 50–70 km wide nearshore with concentrations greater than 2.0 mg m^{-3}. A close association exists between satellite-measured pigment concentrations, satellite measured sea surface temperature, and surface nutrient distributions in this region of strong summer upwelling [*Traganza et al.*, 1983; *Abbott and Zion*, 1985]. The seaward edge of high pigment concentrations off central–northern California is highly scalloped in summer and numerous mesoscale features are visible in individual satellite images, suggesting a dynamic interaction between the recently upwelled water next to the coast, the southward jet of the CCS and more oligotrophic waters of the central Pacific [*Abbott and Zion*, 1985; *Peláez and McGowan*, 1986; *Haury et al.*, 1986; *Simpson et al.*, 1986].

Both spatial and temporal variability of pigment concentration off southern and central California have been studied using CZCS data by *Smith et al.* [1988], *Michaelsen et al.* [1988], and *Peláez and McGowan* [1986]. A gradient from high concentrations nearshore to low concentrations offshore persists throughout the year. These data are supported by zonal transects of in situ measured surface chlorophyll concentration reported by *Mullin* [1986] and *Haury et al.* [1986]. In general, concentrations are greater than 2.0 mg m^{-3} within 25 to 50 km of the coast and decrease to < 0.5 mg m^{-3} at distances greater than 200 km. A distinct latitudinal difference in nearshore pigment concentrations off southern California is noted by *Smith et al.* [1988]. Concentrations north of Point Conception have a higher mean and lower temporal variance than concentrations in the Southern California Bight. The eastward intrusion of water into the bight described in section 2.1 is very low in nutrients and chlorophyll, as was documented by *Peláez and McGowan* [1986]. These authors also show a seasonally varying tongue of high pigment concentration which extends south of Point Conception offshore of the bight. From individual CZCS images in 1981 and 1982 they show that this tongue extends farthest south in August or September and is less well defined and farther north in fall and winter. Data from *Haury et al.* [1986] suggest that offshore regions of higher biomass southwest of Point Conception might be the result of advection from coastal areas of high productivity. An alternate explanation for the position of this tongue is given by *Chelton et al.* [1982], who show this region to be coincident with an offshore maximum in zooplankton biomass where upwelling by Ekman pumping is suggested by positive wind stress curl.

Eppley et al. [1985] use in situ measurements to show that the annual cycle in total water column primary production is weak in the Southern California Bight but that chlorophyll concentrations in the upper attenuation depth are maximum in winter. In winter, phytoplankton are evenly distributed within the mixed layer, but during spring and summer a subsurface maximum develops [*Cullen and Eppley*, 1981] below the depth where the satellite can measure. While chlorophyll integrated over the euphotic zone has a maximum in spring and is higher in summer than winter, chlorophyll concentrations in the upper attenuation depth (that measured by the CZCS) have a winter maximum and a summer minimum [*Michaelsen et al.*, 1988]. Winter maxima in satellite color data will be due to this artifact of the depth of sampling [*Campbell and O'Reilly*, 1988] as well as to an error in the atmospheric correction algorithm at large solar zenith angles. This error is discussed in detail in the next section and in Appendix A.

3. Data and Methods

3.1. *Satellite-Derived Chlorophyll*

Coastal zone color scanner data of the region 20°–55°N, 105°–140°W were recorded at the Scripps Satellite Oceanography Facility (SSOF) for the period July 1979 to June 1986 and processed at the Jet Propulsion Laboratory (JPL) to form the west coast time series [*Abbott and Zion*, 1985]. Details of the processing can be found in Appendix A, along with a discussion of the sources of error. In the present analyses, the mosaic fields (7-km resolution) were used to form monthly means of surface pigment concentration in 1° blocks (Figure 1). Higher cross-shelf resolution was obtained in the 100-km region next to the coast, where monthly means were also formed for blocks 1° in latitude and 25 km wide in the east-west direction.

The approach taken here is to assume that the data set contains the signals of interest along with both systematic and random errors. After screening the images visually for obvious errors, we first identify a systematic bias in the data, which we believe is due to an incomplete removal of atmospheric scattering effects (see below and Appendix A). After removing this bias, random and undetected systematic errors remain in the data. The effects of random errors are reduced by the temporal and spatial averaging. The methods of empirical orthogonal function (EOF) analysis and principal estimator pattern (PEP) analysis are used to extract the biological signal from the noise and to relate the anomalous pigment concentrations to surface wind forcing (Appendix B).

3.1.1. *Effects of errors in the data.* Although the statistical methods used should separate the large-scale signal from the random noise, they may not remove the effects of undetected systematic errors. Thus before proceeding, we discuss ways in which the sources of error (described in Appendix A) might appear in the results.

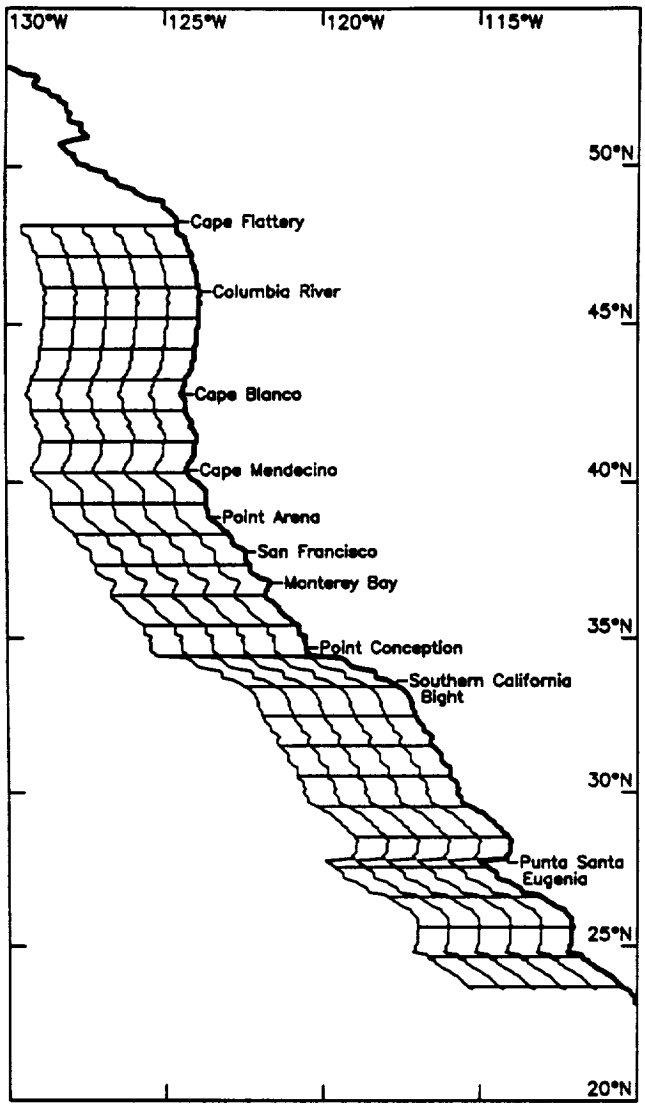

Fig. 1. Coastal outline, derived from the satellite imagery, showing the geographic points referenced in the text. Also shown are the 1° × 1° bins used to average pigment data over the large-scale CCS. Using Point Conception as the starting point, the coast was divided into 1° latitude sections. The offshore boundaries of the bins are multiples of 1° in longitude from the coast in the E–W direction.

Sensor degradation: An overall decrease in the sensitivity of the sensor occurred over the course of the mission, and a correction function is included in the Miami processing software to account for this. This change in sensor sensitivity happened at specific times, rather than gradually. Thus although the correction for the long-term trend in sensor degradation is believed to be good, short-term changes may not be well accounted for. If an incorrect long-term correction remains in the data, we expect to see a trend over the whole data set that would be evident, for instance, in the time series of the EOFs. Short-term shifts in the sensitivity would not be obvious and the suggestion has been made that absolute pigment concentrations in individual images should be considered good to a factor of 2 [*R. Evans*, personal communication, 1989]. Temporal averaging may help reduce the size of abrupt changes and also reduce any effect of alternating bias in the sensor. The change in sensitivity would affect whole images and would not change spatial relationships within the image. It would also not be correlated with other physical variables, such as wind, and would thus tend to be eliminated by the PEP analysis, which brings out the spatial patterns of pigment concentration that vary in concert with spatial patterns of the wind variables.

Cloud screening: As is described in Appendix A, clouds may not have been correctly identified in some cases. Temporal averaging will reduce this effect for cirrus and cumulus, which have an approximately random distribution along the west coast. In summer, however, a bank of stratus clouds often lies offshore, with a band of clear water next to the coast. Undetected subpixel-sized clouds next to this stratus bank would systematically affect a north-south strip some distance offshore. Since the position of the cloud bank changes in time, temporal averaging will both reduce this effect and smear it over a wider region. The orientation of this error, however, should still be in a north-south band.

Cloud ringing: The failure of the sensor to recover immediately from saturation after viewing bright clouds causes incorrect chlorophyll values to the east of clouds for distances of up to 70 km [*Mueller*, 1988]. *Eckstein and Simpson* [1990] estimate errors of $\geq$40% from this source. The algorithm of Mueller was used in the WCTS processing to produce a cloud mask to indicate where data might be affected. In the present study this mask was examined for a number of images but was not used in the final analysis, since it was found to eliminate more data than was necessary. Thus effects of cloud ringing remain in the data. Temporal averaging will reduce the effects of random clouds (cirrus and cumulus), but the presence of the stratus bank offshore in summer will again provide a source of systematic error which should have a north-south banded nature. Regions to the east of islands may also be affected, although no emphasis is placed on the few such regions in our area.

Atmospheric scattering: Both Rayleigh and aerosol (Mie) scattering increase the radiances seen by the satellite. The problem is most severe when the angle formed by the satellite, the sun, and the viewing point beneath the satellite is large (a value of 50° is often used as a rough limit). This occurs in winter at high latitudes. The single-scattering Rayleigh algorithm used in the WCTS processing produces winter values of chlorophyll known to be too high. The multiple-scattering Rayleigh algorithm used in processing the global CZCS data is better [*Gordon et al.*, 1988*a*], but may still create systematic biases in winter at high latitudes (see below). If only Rayleigh (molecular) scattering were involved, the symptoms of this error would be fairly simple, i.e., uniformly increasing chlorophyll with latitude and with a seasonal maximum in winter. These properties are used to form a crude empirical correction function for the scattering errors below. Errors in the aerosol scattering are not as easily accounted for.

Uniform aerosols: The WCTS was processed using the clear water procedure with uniform values of $\epsilon = 1$, on the assumption that all aerosols are identical marine aerosols (Appendix A). Errors occur where winds blow continental type aerosols over the ocean. If these winds have synoptic (3–5 days) time scales, monthly averaging will reduce these errors. North of 35°N, winds are usually from

the southwest or the northwest during the passage of synoptic weather systems from fall through spring. During clear periods in spring through fall, a diurnal sea breeze develops which includes onshore winds at midday and in the afternoon [*Beardsley et al.*, 1987] at the time of the CZCS image. Thus, during much of the year, the wind flow off the west coast is onshore and the assumption of uniform marine aerosols is reasonably valid. Regions where this may not be true include the Southern California Bight during extended periods of Santa Ana (offshore) winds. At present, there is no consistent solution to this problem using the WCTS. Individual investigators interested in specific regions may be able to tune the values of ϵ used to process raw images for specific regions and times. Use of this approach in the WCTS processing, however, would have introduced an unacceptable level of subjectivity into the final product. Consistency of processing was one of the goals of the processing. Attempts to adjust the values of ϵ on a scene-by-scene basis during tests of the global CZCS processing resulted in greater errors than assuming uniform marine aerosols, which was the final procedure adopted in that processing as well [*G. Feldman*, personal communication, 1989].

An estimate of the cumulative effect of these errors in our region comes from *Abbott and Zion* [1985], who find that WCTS estimates of surface pigment concentration from individual images off northern California are roughly within a factor of 2 of in situ values. This is the same level of error found in other regions [*Gordon et al.*, 1983*a*, 1988*b*; *Denman and Abbott*, 1988; *Balch et al.*, 1989*b*] and suggested for the global CZCS data set [*R. Evans*, personal communication, 1989]. The temporal and spatial averaging used in the present study should reduce some (not all) of the effects of errors described above.

3.1.2. *An empirical correction function.* The most serious systematically identifiable problem in the WCTS comes from the single-scattering Rayleigh algorithm. We have attempted to reduce this error by forming a correction function based on the assumption that true chlorophyll levels are low some distance from the coast for most of the year [*Thomas and Emery*, 1986; *Landry et al.*, 1989; *Haury et al.*, 1986]. A 2.5° wide band of the CZCS data separated from the coast by 2.5° longitude and extending from 25°N to 50°N is used to define a region where we expect the true annual cycle of surface pigment concentration to be low and the apparent annual cycle in the WCTS to be dominated by the Rayleigh scattering error. This region consists of the western half of the domain shown in Figure 1. We expect the error to increase to the north and to be maximum in December. The first EOF of the data in this band accounts for 70% of the variance and has the temporal and spatial characteristics expected of the Rayleigh scattering error (Figure 2*a*). The product of the temporal and spatial functions is used as a first-order correction function (dependent on month and latitude). In the analyses presented below, we will always note when this empirical correction function has been used.

The general effect of subtracting this correction function from the monthly CZCS data is shown by performing an EOF analysis on the raw, monthly 1° mean WCTS pigment data (no empirical correction or seasonal cycle removed). Figure 2*b* shows the spatial pattern and mean monthly time series of the first EOF of the uncorrected data. It is dominated by the north-south gradient seen most clearly at the offshore edge and by a cross-shelf gradient, with higher values offshore. The time series peaks in December–January. Figure 2*c* shows the first EOF calculated from the same data after removing the latitude and time dependent function shown in Figure 2*a*. What appears now is the development of the band of high pigment near the coast in summer. This is one view of the annual cycle in surface pigment. It represents that part of the seasonal cycle that can be represented by one spatial pattern and accounts for 36% of the variance in the monthly, corrected, 1° averaged WCTS data.

The WCTS will eventually be reprocessed with the multiple-scattering Rayleigh model, which has been used in the global CZCS processing. To determine whether this new version of the WCTS will produce results different from those derived below for the empirically corrected WCTS data used here, we obtained the monthly composites of the global data set (processed with the multiple-scattering algorithm) for the period November 1978 to June 1981. This is the period for which the sensor was most stable [*R. Evans*, personal communication, 1989]. Thus we have WCTS and global data for a common period of 2 years, July 1979 to June 1981. Comparisons of the annual cycles derived from these 2 years from the corrected WCTS and the global CZCS data are presented in section 4.1 in support of the argument that the major conclusions about the seasonal development for the March–October period based on the corrected WCTS will not be changed when the

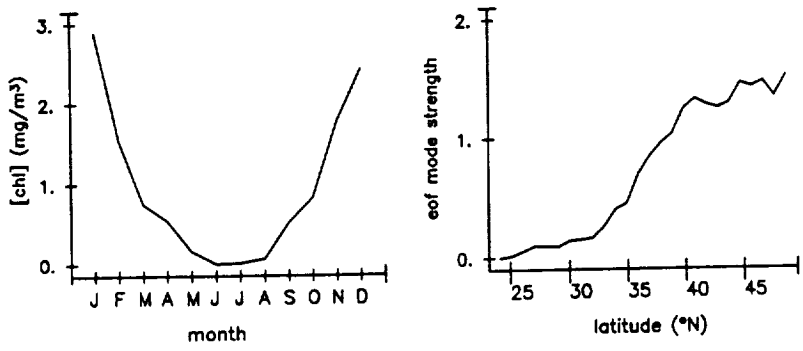

Fig. 2*a*. The first EOF of an offshore band of pigment concentration, accounting for 70.6% of the variance. The time series has been averaged by calendar month. This EOF is used as the correction function to reduce effects of errors in the scattering algorithm.

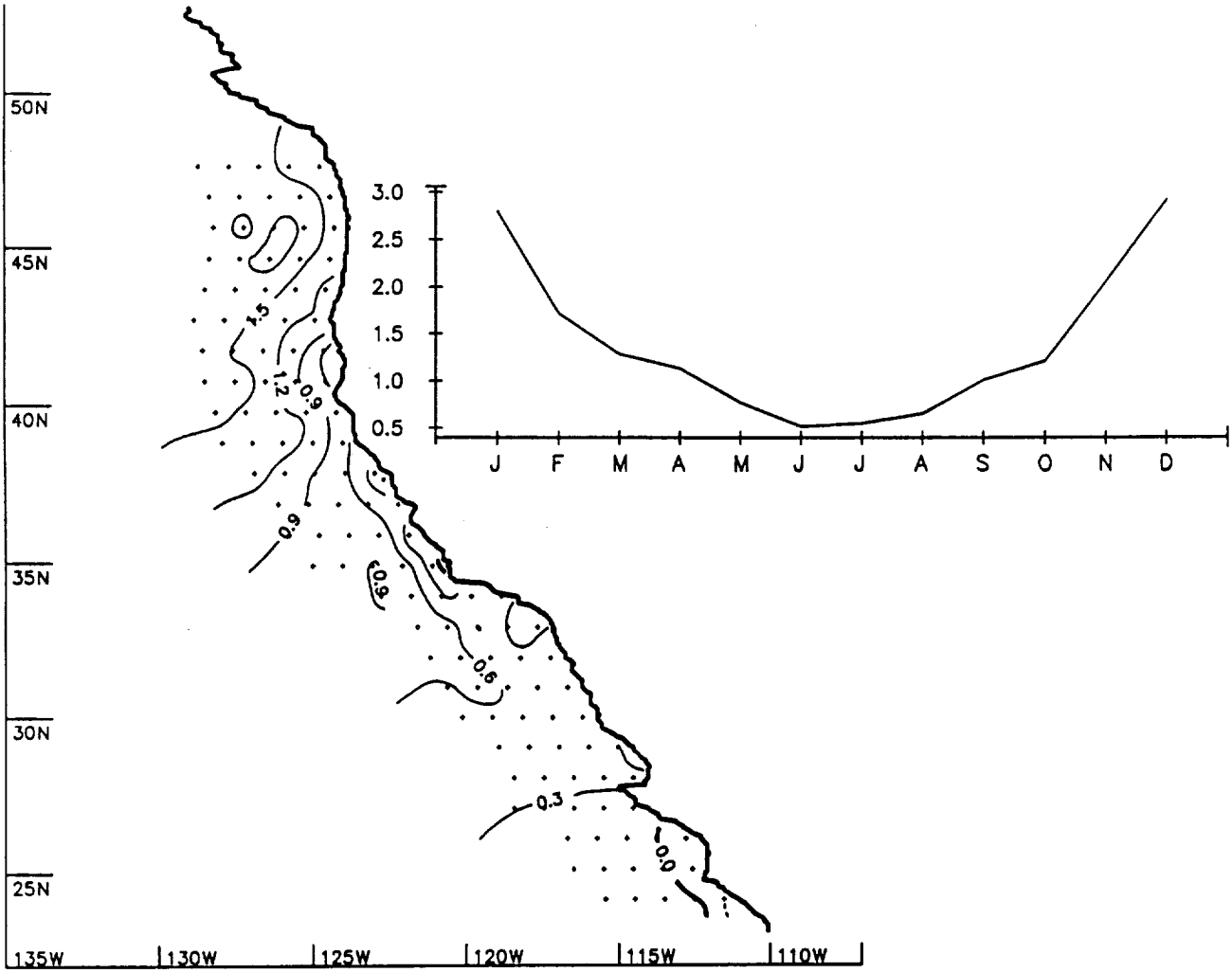

Fig. 2*b*. The first EOF of the monthly pigment data, with no correction applied and no seasonal cycle removed, accounting for 85.4% of the variance. The time series has been averaged by calendar month.

data are eventually reprocessed with the multiple-scattering algorithm.

If the error in the scattering algorithm were only a function of latitude and season, it would be part of the monthly seasonal cycle at each location and would not affect the monthly anomalies, which are formed by removing the seasonal cycle at each location. The initial EOF analysis of the CZCS anomalies, however, was dominated by spatial modes concentrated in the north, with temporal peaks in one or two winters. We cannot determine whether this is caused by actual winter phytoplankton dynamics or interannual differences in atmospheric properties. For this reason we exclude the 4-month winter period November–February in each year from the final data set used in the statistical analyses of anomalous CZCS. With the additional exclusion of 1984 due to lack of data (see below), the monthly pigment time series consists of a total of 48 time points from July 1979 through June 1986.

3.2. *Wind Data*

The surface wind data come from National Meteorological Center's Limited-Area Fine Mesh (LFM) 6-hour forecasts, archived at the National Center for Atmospheric Research. These fields are formed at 12 hour intervals on a polar stereographic grid with 190-km spacing at 60°N. Since sampling by merchant ships is insufficient to calculate reliable curl fields and buoy coverage is neither continuous nor spatially suited to curl calculation, products such as the LFM fields must be relied on, with attention to the degree to which they represent the true variability in the wind.

We consider three wind variables: wind stress ($\overline{\tau}$), curl of the wind stress, and u_*^3, where $u_*^2 = |\overline{\tau}| / \rho_a$. The alongshore wind stress (τ_a) at the coast represents an index of coastal upwelling [*Bakun*, 1973]. The curl of the wind stress represents an index of offshore upwelling due to Ekman pumping. The variable u_*^3 represents the wind energy available for vertical mixing. Windstress is formed from winds using a standard bulk formula, with a constant drag coefficient of $c_D = 1.3 \times 10^{-3}$ and a constant air density of $\rho_a = 1.3$ kg m^{-3}. The analyses consider two-dimensional fields of the wind variables and a one-dimensional coastal strip of wind variables, interpolated to points 0.5° from the coast and separated by 1° in the alongshore direction (the centers of the 1° × 1° CZCS blocks next to the coast in Figure 1). In the coastal strip, the alongshore component of the wind stress (defined

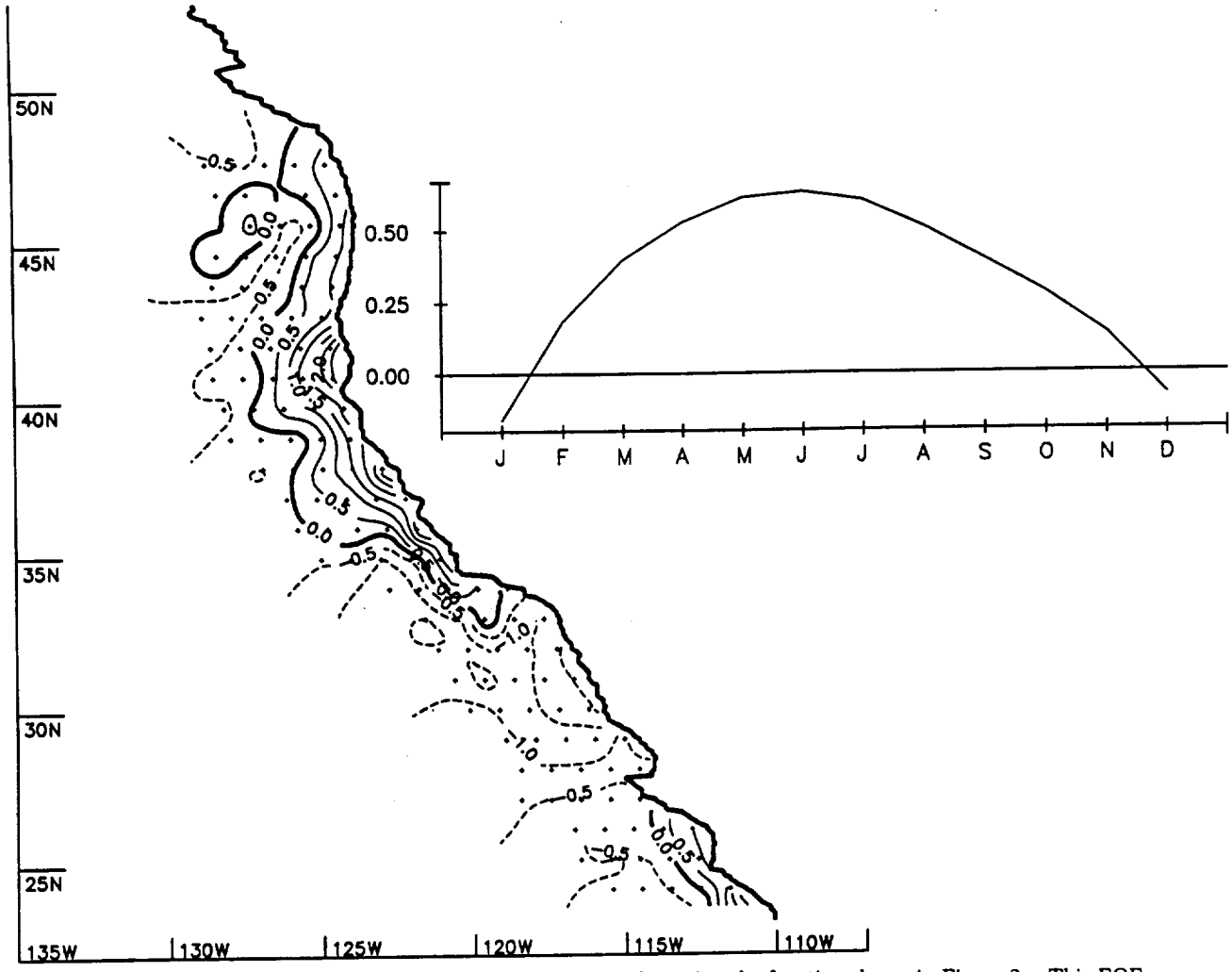

Fig. 2c. As in Figure 2b for the same data corrected by subtracting the function shown in Figure 2a. This EOF accounts for 36.2% of the corrected monthly variance and describes the mean seasonal cycle.

by the coastal orientation) is used as the indicator of upwelling.

An evaluation of the 12-hour LFM winds was made by correlating them with winds observed at eight National Data Buoy Center (NDBC) buoys in 1981–1983. The average correlation coefficients for (u, v) components were (0.60, 0.80) in spring, (0.55, 0.73) in summer, (0.70, 0.87) in fall, and (0.70, 0.83) in winter. These winds thus explain 50%–70% of the variance in twice-daily winds in the N–S direction and 30%–50% of the variance in the E–W direction. The variability of the monthly average fields is much less, increasing the correlations.

Fields of wind stress curl calculated from the LFM data were evaluated by comparing them to similar fields calculated from ship winds by *Nelson* [1977] and *Rienecker and Ehret* [1988]. These were qualitatively similar, except for the absence (in the LFM fields) of a band of positive curl off Oregon and Washington in summer. This is thought to be a failure in the LFM winds and the same failure is found in the Navy's Fleet Numerical Oceanographic Center (FNOC) wind fields. Values of the wind stress curl are also lower (by roughly a factor of 5–10) than those calculated from ship and buoy winds separated by 25–150 km, reflecting the relative smoothness of the LFM winds on scales of 100–200 km.

There may also be a displacement of the large-scale features in the LFM wind fields. This was noted in considering the winds calculated from FNOC operational surface pressure fields by *Bakun* [1973]. The summer maximum in southward winds was found to occur too far to the south in the operational FNOC wind product because of an overestimate of the effect of the thermal low over southern California and Mexico, producing the correct temporal development but an error in the spatial placement of the maximum. In comparing wind variables to satellite pigment concentrations using either point correlations or the PEP patterns, we must keep in mind the possible displacement or distortion of the spatial features of the wind fields. This could cause an apparent correlation of the LFM winds in one region with the pigment response in a separate region, whereas the real winds and pigment response may have been coincident in space.

3.3. *Statistical Methods*

Time series of CZCS and wind data cover the period July 1979 to June 1986. Monthly means of CZCS pigment were formed on the original mosaic grid (0.07° × 0.07°). These were then averaged over the 1° × 1° blocks shown in Figure 1 extending 5° offshore; data in the region

next to the coast were also averaged into four 1° latitude by 0.28° (25 km) longitude blocks. Even with this spatial and temporal averaging, gaps comprising 10% of the total data occur in the CZCS time series, usually covering only 1–2 months at a time. For each location, gaps were filled by optimal interpolation in time, using an exponentially damped cosine fit to the autocovariance function determined from the data at that location. Very few images were recorded during 1984 and we exclude this year from the time series analyses. Excluding 1984, only 7% of the data set was filled by interpolation. A monthly seasonal cycle was formed from 6-year means of the calendar months at each location and subtracted from the monthly means to form monthly anomalies.

Wind variables were calculated for each 12-hour period on the original LFM grid and averaged into monthly means. The wind variables for each 12-hour period were also interpolated to the centers of the CZCS 1° × 1° blocks closest to the coast and averaged into monthly means. The seasonal cycles and monthly anomalies of the wind variables were formed in the same manner as for pigment concentrations.

Empirical orthogonal functions (EOFs) were formed for all variables, using the covariance matrices of the monthly anomalies [*Richman*, 1986]. The method of principal estimator patterns (PEPs), also known as canonical correlation analysis, was used to test the statistical connection between each wind variable and the CZCS pigment field [*Hotelling*, 1936; *Davis*, 1977, 1978], using lags of 0 and 1 month between wind variables and pigment concentration. This method calculates the skill of the wind variables in predicting the pigment concentration, as the percent of variance explained. Use of the 1-month lag between wind and pigment did not improve the statistics and is not discussed further. To assess whether this skill was greater than that expected for random variables, the calculation was repeated for lags greater than 6 months, for which any statistical relation between monthly anomalies is assumed random. The average percent of variance explained for these long lags is referred to as the artificial skill. Further details of the PEP method are described in Appendix B.

4. Results

4.1. *Seasonal Cycle*

The 6-year means of pigment concentration for the calendar months March–October on the mosaic grid are shown in Plate 1. The time and latitude dependent correction function (Figure 2*a*) has been subtracted from these data. Locations where the correction produces pigment concentrations less than or equal to 0 are shown in white. Figure 3 shows the number of years of data used to form the mean at each grid point for each calendar month. Data availability is generally good (4–6 realizations) near the coast for March through May and August through November. Winter is poorly represented in the north due to cloud cover; relatively poor sampling in June and July is due to a midsummer annual minimum in power supply aboard the satellite.

The seasonal progression in Plate 1 shows that in March a diffuse region of higher pigment concentration (1–2 $mg\,m^{-3}$) extends several hundred kilometers offshore from southern Oregon to Point Conception. The width of this region is reduced between May and June. In June the narrow pigment maximum develops a strongly meandering offshore edge which continues into July. The nature of the June and July means may reflect the fact that most of the data available in these month came from just 2 years, 1980 and 1981. The width of the high pigment concentration region expands in August and September as the very high nearshore values decrease. Smaller-scale features are also evident in Plate 1. A narrow band of high pigment concentration is present north of the Columbia River (46°N) in April–May, decreasing in June and reappearing in July–October. A region of apparently high pigment is present in all months around the San Francisco Bay (37.5°N). A band of high pigment concentration extends southeast of Point Conception. Low pigment concentrations are seen within the Southern California Bight during most months. Note the general similarity between the spatial structure of the first EOF of corrected WCTS data in Figure 2*c* and the summer pattern in Plate 1.

Figure 4*a* presents the mean annual evolution of the latitudinal structure of pigments in alongshore bands of 25 km and 100 km width next to the coast and 50 km and 200 km width farther offshore. (Note that for this discussion, distance "offshore" is defined as distance in an east-west direction. This definition may be misleading in the Southern California Bight, where points identified as 100–300 km offshore are closer than that to the shore in a northward direction.) The correction function (Figure 2*a*) has been subtracted from the data (reducing winter values in the north), and the full WCTS period (excluding 1984) has been used to form the mean calendar months at each location. Because of errors in the atmospheric correction, data from November to February should be disregarded in favor of the center portion of each year between the vertical lines.

The 25 km closest to the coast (Figure 4*a*, bottom right) is the region most influenced by coastal upwelling, mixing associated with bottom topography and river input, which may create case II water conditions (see Appendix A). In this region there is an increase in pigment concentration north of approximately (46°N) in April–May, a decrease in June and another increase in July (also apparent in Plate 1). The early increase is delayed and lower off Oregon (42°–46°N). Off northern California, pigment concentrations increase first off San Francisco (37°–38°N) in March, then everywhere from Point Conception to Cape Mendocino (35°–42°N) in April–May. The increased pigment values move north and appear off Oregon in June–August. Lower pigment values are found in the Southern California Bight (32°–34°N) with a relative maximum in March–April and a minimum in late summer and fall. Off Baja California, there is a region of higher pigment concentration south of 32°N with peaks around the two major capes (25°N and 28°N) in late spring and early summer, followed by a minimum in late summer and fall, similar to that in the bight to the north.

Most of the above features are found in the 25 to 75-km band (Figure 4*a*, bottom left) with lower concentrations in this area farther from the coast. This band is mostly offshore of the continental shelf, in deep water. This region clearly shows the low values found most of the year off southern California and northern Baja (30°N to 33°N), with a relative minimum in August. A late

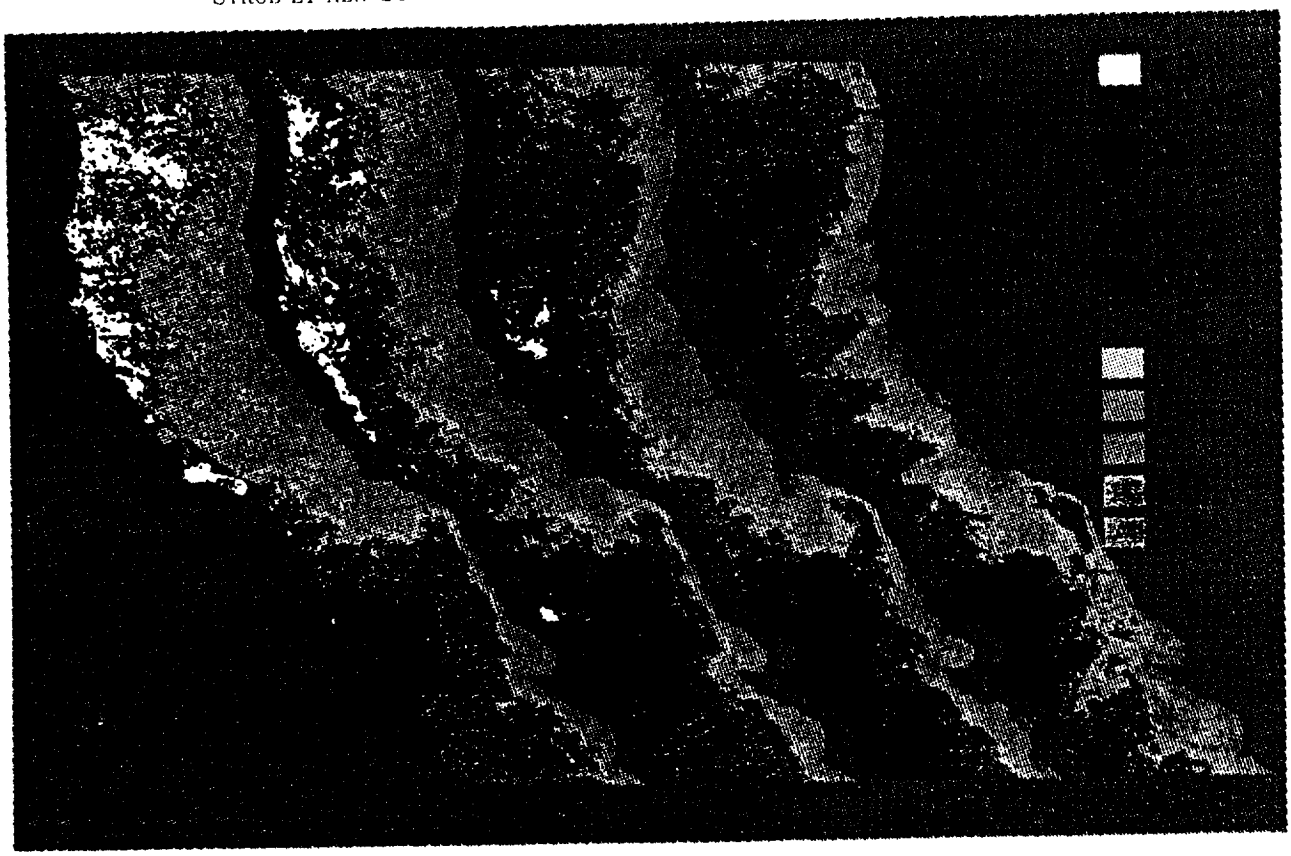

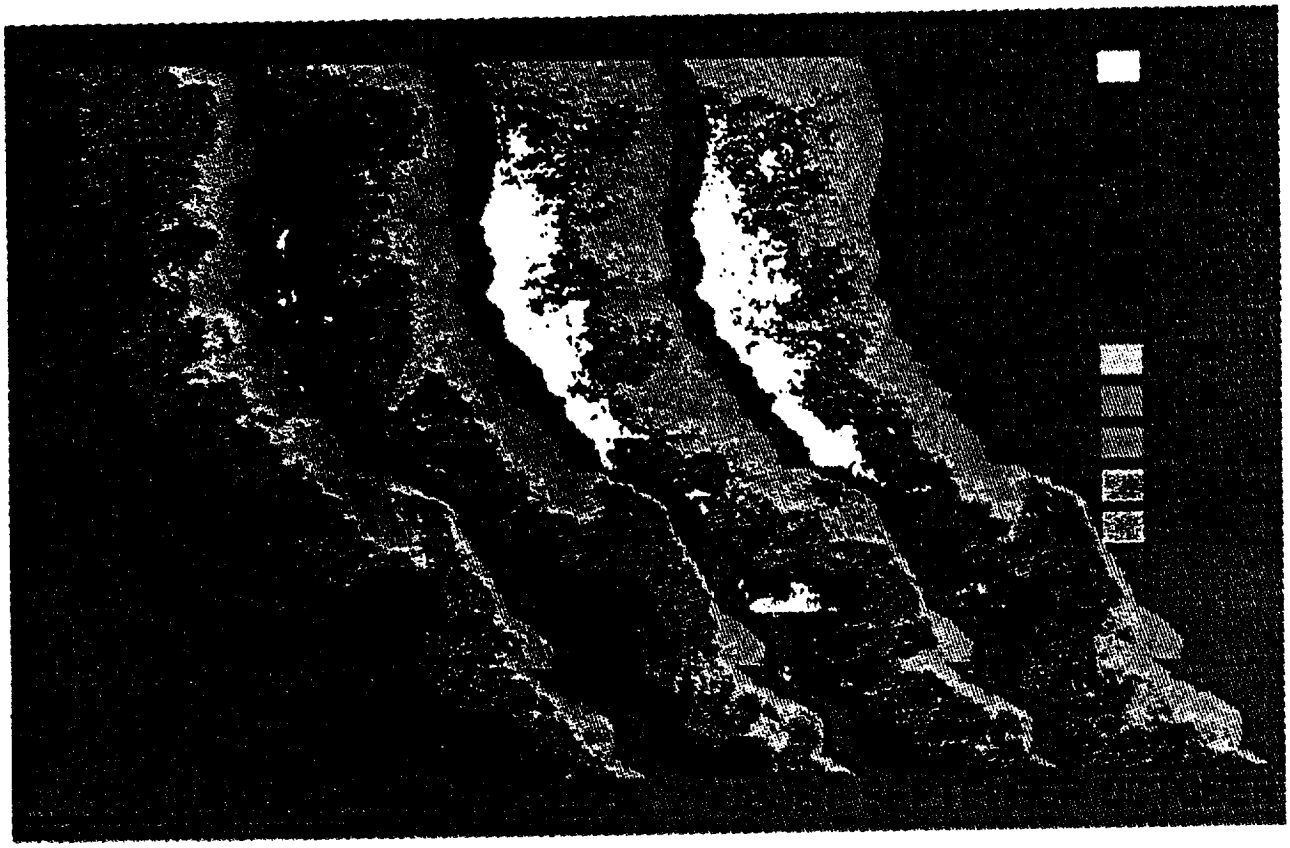

Plate 1. Six-year monthly mean pigment concentrations for March–October (July 1979 to June 1986, excluding 1984). Resolution is 0.07° × 0.07° (WCTS mosaic grid). The correction function (Figure 2a) has been used, reducing values in the north in winter. Values reduced to less than 0 are colored white (values in the color bar are in milligrams per cubic meter).

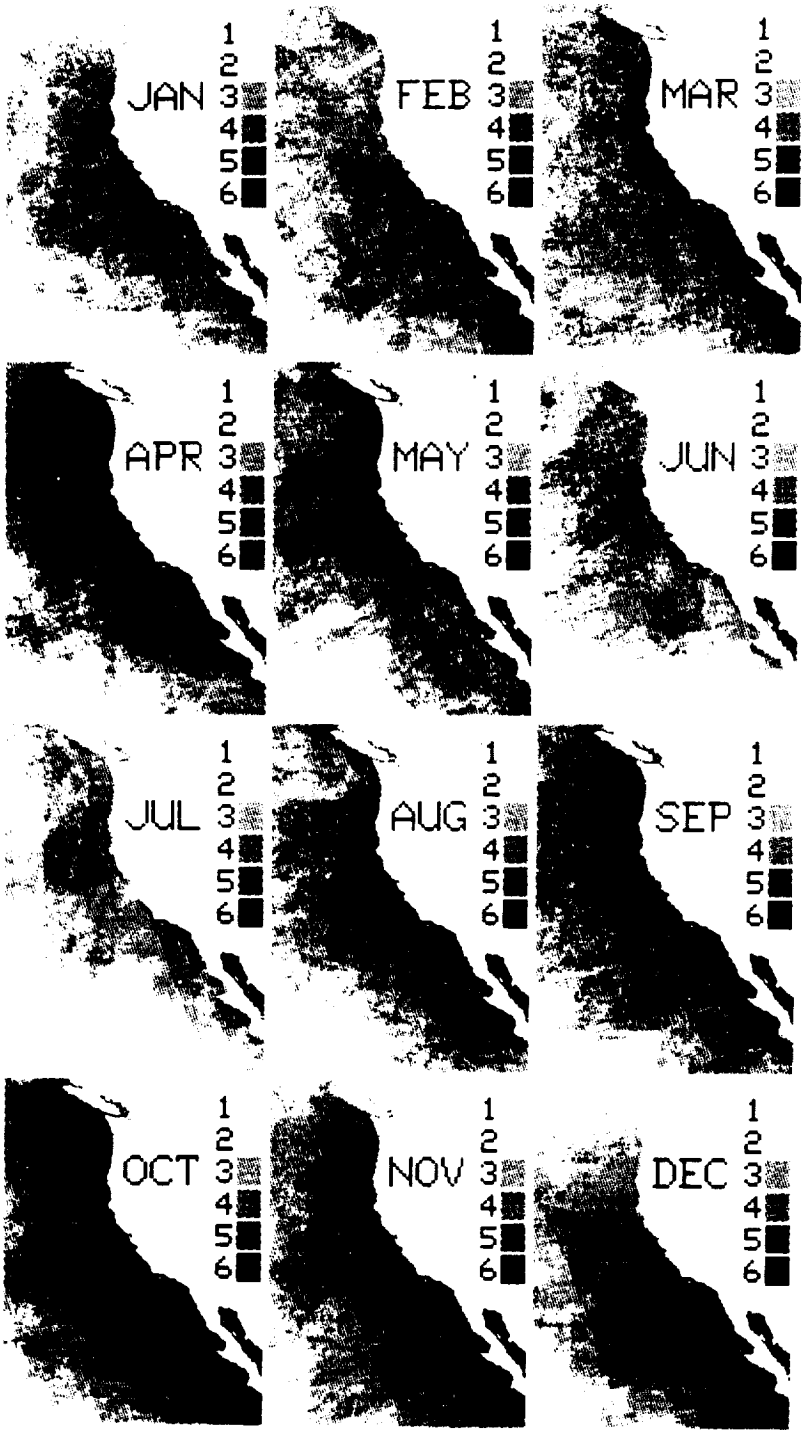

Fig. 3. Number of months of data used to form the monthly means in Plate 1.

summer maximum appears off Washington in August. The wider coastal band from 0–100 km offshore (top right) provides a smoother picture of seasonally varying pigment concentration in the large-scale coastal ocean next to North America. Farther from the coast, in the band between 100–300 km offshore (top left), there is a small increase in pigment everywhere north of 33°N in early spring, maximum and longest lasting at 34°N and 37°N–38°N. Between 300–500 km offshore (not shown) the only feature is a brief and weak (<0.5 $mg\,m^{-3}$) spring bloom off California, lasting longest between 32°N and 35°N where advection from north of the Southern California Bight brings coastal water into this band.

To assess whether use of the multiple-scattering Rayleigh correction would change the picture derived from the corrected WCTS data, similar annual cycles are formed from the available global CZCS data for the period July 1979 through June 1981 and presented in Figure 4*b*;

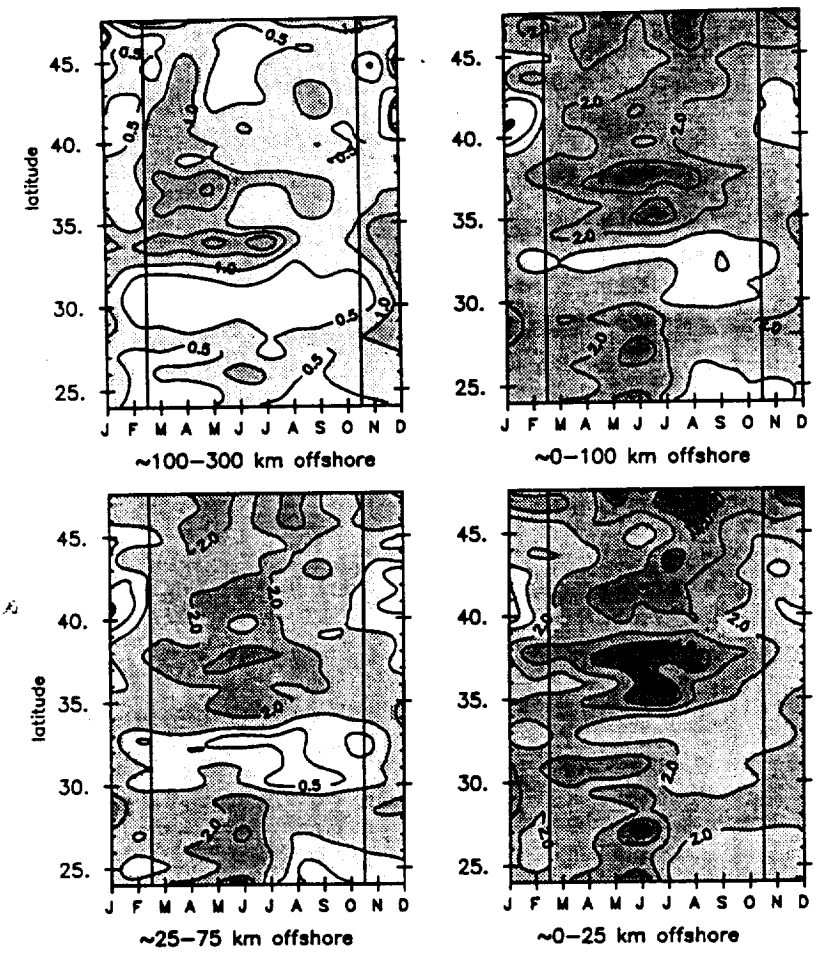

Fig. 4*a*. Seasonal cycles of surface pigment concentration (mg m^{-3}) in different offshore bands, contoured as a function of latitude and month. The band from ≈ 0–100 km offshore (top right) is the 1° band closest to the coast in Figure 1; the band from ≈ 0–25 km offshore is a similar coastal band 0.28°wide, etc. These seasonal cycles are formed from the full WCTS data set (excluding 1984). The empirical correction function (Figure 2*a*) has been subtracted from this data.

these can be compared in general with Figure 4*a*. To provide a direct comparison, the corrected WCTS data from the same 2-year period used in Figure 4*b* are shown in Figure 4*c*. When comparing Figure 4*a* with either 4*b* or 4*c*, it should be kept in mind that the complete time period used in Figure 4*a* includes a major El Niño, during which pigment values were lower than usual, especially south of the Columbia River. The years 1980 and 1981 also had stronger spring transitions than the other years, with high pigment concentrations far offshore [*Thomas and Strub*, 1989].

Many of the prominent features in Figure 4*a* are found in Figures 4*b* and 4*c*, with a few exceptions. In the 0- to 25-km and 0- to 100-km bands (bottom and top right), the early spring bloom and subsequent decrease in pigment concentration is seen off Washington and northern Oregon, but the second summer increase off Washington is weaker in the global data than in the corrected WCTS. Details of the summer maxima also differ between Figures 4*b* and 4*c*, but both show the progression of increased pigment concentration from northern California to Oregon in the 100 km next to the coast in the second half of summer. Data from the global data set show maxima more localized in Figure 4*b* than the corrected WCTS in Figure 4*c*, which seems to miss the maximum between Capes Mendocino and Blanco (41°N) in spring of these 2 years, especially over the shelf (bottom right). These differences may reflect the fact that the WCTS and the global data sets were constructed from different sets of images, in addition to the use of the multiple-scattering algorithm and a more detailed sensor degradation correction function. Data from this 2 year period between 0–25 and 25–75 km offshore show the maximum off Oregon in late summer to be more localized around Cape Blanco (most clearly seen in Figure 4*b*). Pigment concentrations are lower south of 33° in the global data set than in the WCTS, reflecting the apparent failure of the empirical correction function in the south. The global data in Figure 4*b* are more like the corrected WCTS from the full period in Figure 4*a* and clearly show the low seasonality and low concentrations in the Southern California Bight. In the global data within 100 km of the coast, the minimum in late summer appears more as a spring increase south of 32°N and north of 33°N, followed by a decrease in late summer between 28°and 33°N. The late summer minimum is not as evident in the corrected WCTS from this 2-year period, indicating that this feature of the 6-year mean (Figure 4*a*) comes mostly from the 1981–1983 and 1985 period. It is of interest

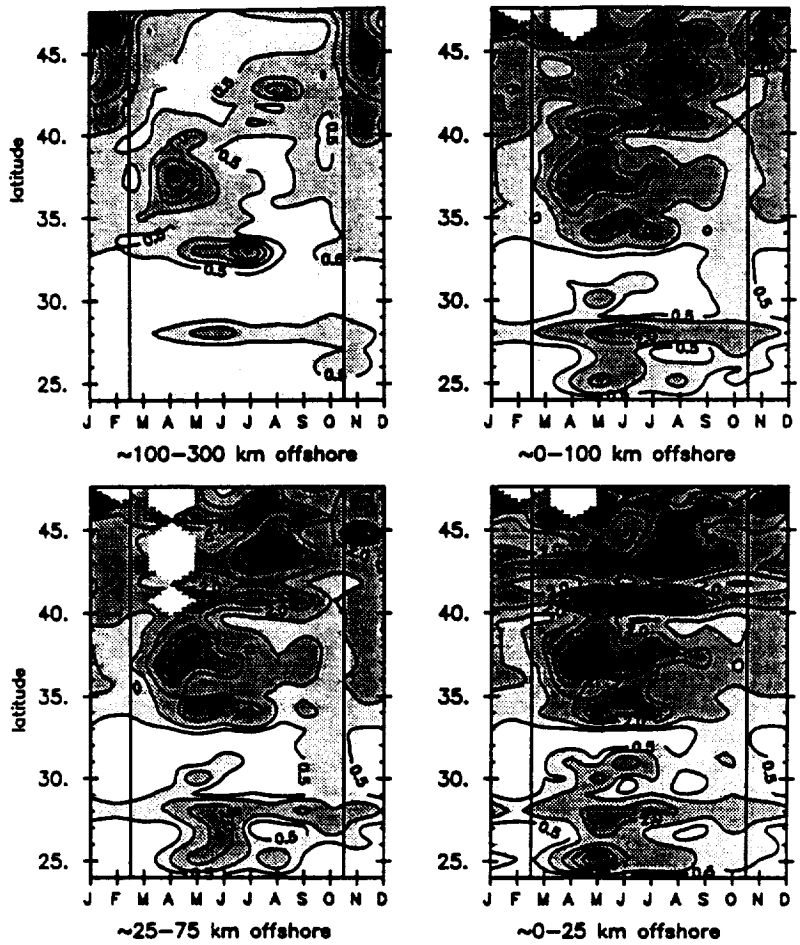

Fig. 4*b*. Seasonal cycles, as in Figure 4*a*, except formed from monthly composites from the global CZCS data set for the two-year period July 1979 through June 1981. No correction function has been applied.

that the global data show a systematic increase in pigment concentration in November through February in the region from 100 to 300 km offshore (Figure 4*b*, top left) and increasing north of approximately 33°N, suggesting that the improved scattering algorithm has not solved all of the problems with winter data at high latitudes.

An alternate method of looking at annual cycles is to fit annual and semiannual harmonics to the time series at each point [*Chelton*, 1984; *Strub et al.*, 1987*a*]. The disadvantage of this method is its inability to represent abrupt seasonal changes. The advantage, however, is that it allows one to calculate the significance of the seasonal cycle using bootstrap statistics, i.e., the probability that a random data set would fit the harmonics as well [*Strub et al.*, 1987*a*; *Michaelsen et al.*, 1988]. We have fit annual and semiannual harmonics to the corrected WCTS data used to form Figure 4*a* and reconstructed plots of the annual cycles similar to those presented in Figure 4*a*. In general, the annual cycles look very much like Figure 4*a*, except for the lack of short or closely spaced features, such as the double maximum off Washington in summer. In Figure 4*d* we present the latitudinal distribution of the coefficient of determination (fraction of variance explained) for the multiple regression of annual and semiannual harmonics in the four bands shown in Figure 4*a*. Also presented are the bootstrap estimates of the 95% significance level, averaging around 0.1. For the regions within 100 km of the coast, the results show the fits to be significant for latitudes south of 28°N and between 34° and 43°N, where the fits account for 30–50% of the monthly variability. The failure of the fits north of 43° may reflect shorter period fluctuations such as the double summer maxima there. The failure of the fits in the region between 28° and 33°N reflects the very low degree of seasonality in the Southern California Bight and off Baja California north of Punta Eugenia.

4.2. *Nonseasonal Variability*

4.2.1. *Point correlations.* The simplest test of the relation between anomalies of monthly wind variables and pigment concentrations consists of point correlations of the time series. The general result of these tests is that monthly anomalies of pigment concentration are very marginally correlated with local alongshore wind stress in a few nearshore locations and are significantly correlated with local u_*^3 in some offshore regions and wind stress curl in some nearshore regions. Only 16–24% of the variance in these limited regions is accounted for. More specifically, positive correlations between southward wind stress and increased pigment concentration occur in the 25 km next to the coast between 35°N and 47°N, but correlation coefficients are less than or equal to 0.3, accounting for

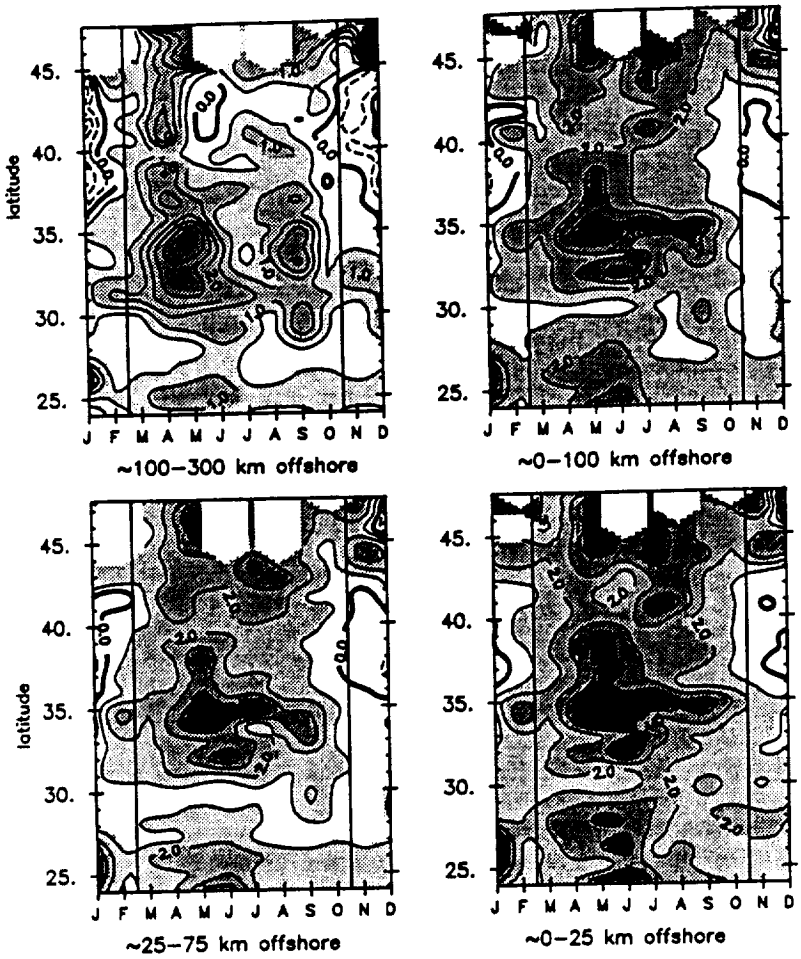

Fig. 4c. Seasonal cycles, as in Figure 4*a*, except formed from the corrected WCTS data set for the same 2-year period shown in Figure 4*b*.

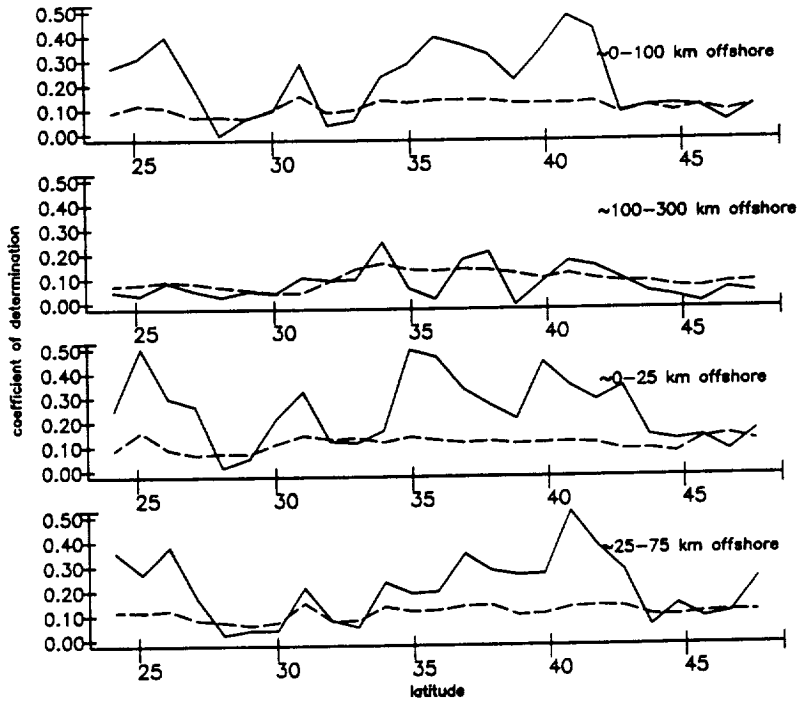

Fig. 4d. Coefficient of determination (fraction of variance explained) for fits of annual and semiannual harmonics to the data in the same bands as shown in Figure 4*a*. The dashed line gives the 95% significance level.

only 1–10% of the variance at a few locations. For the other wind variables, the highest point correlations are between pigment concentration and u_*^3 between 35°N and 46°N in the region 200–400 km from the coast, where the maximum value of r is 0.49 at 44°N (explaining 24% of the variance). Pigment concentrations are also correlated with wind stress curl between 34°N and 40°N in the 200 km region next to the coast (maximum $r = 0.40$, explaining 16% of the variance). Bootstrap estimates of the 95% confidence level for these correlations show that values of $r \approx 0.25$ are significant at the 95% level.

4.2.2. *EOFs of anomalous chlorophyll pigment concentration.* Figure 5 shows the first three EOFs of the monthly pigment concentration anomalies on the 1° blocks. Most of the variance occurs north of approximately 31°N, and comparisons with wind forcing in the next section are restricted to that region. The full EOFs are shown here for completeness. These three functions account for 34.5%, 11.3%, and 7.6% of the total pigment variance. The spatial functions resemble the typical geometric patterns described by *Richman* [1986], with no zero crossing in the first, a north-south separation in the second, and an east-west separation in the third. When the functions are recalculated using only data north of 31°N (these are the functions used in the subsequent PEP analysis) they explain more of the variance (39.0%, 12.4%, and 8.8%), and the only change is a shrinking of the regions where the first spatial function exceeds values of 1.5.

These three functions account for 60% of the interannual variability north of 31°N. The first function appears to be dominated by a low-frequency change from low values in 1979 to higher pigment concentrations in 1980–1982, followed by extremely low values beginning in April 1983, returning in 1985–1986 to moderately low values similar to 1979. Although relatively low concentrations continue to be found over the large-scale California Current in 1985 and 1986, values in the north (function 2) and in the narrower coastal region (function 3) are high again in spring 1986. This extends and quantifies the picture of low values of pigment concentration derived from CZCS data during the 1982–1983 El Niño previously described by *Fiedler* [1984] off southern California. The high values in the spring of 1986 and the similarity of values for the first function in 1979 and 1985–1986 provides support for the contention

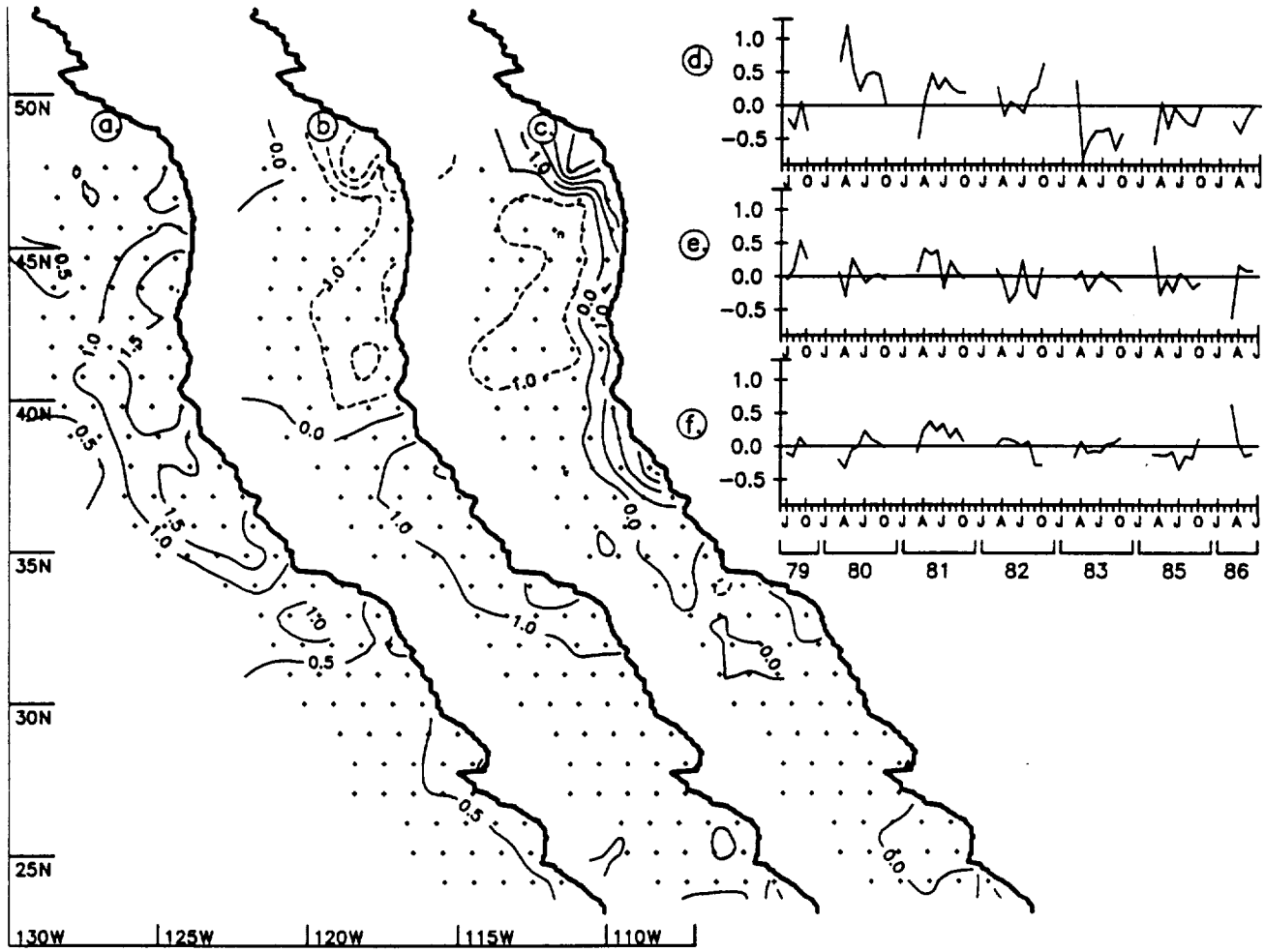

Fig. 5. The first three EOFs of monthly anomalous pigment variance from the data averaged to the grid in Figure 1. The product of space and time functions give anomalies in milligrams per cubic meter. The first three EOFs account for 34.7%, 11.3%, and 7.6% of the anomaly variance (respectively) over the domain shown here. Space functions for *(a)* EOF 1, *(b)* EOF 2, and *(c)* EOF 3; time series for *(d)* EOF 1, *(e)* EOF 2, and *(f)* EOF 3. Note that 1984 is omitted from the time series.

that the long-term trend in the decrease in sensitivity of the sensor has been adequately accounted for.

Changing spatial patterns of pigment concentration are described by combinations of these three functions. In the second half of 1979, the only strong function is the second, showing an increase in pigment concentration in the south in fall. In 1980 the dominant feature is the large-scale bloom (function 1) in spring, followed by the decrease in offshore concentrations and increasing coastal concentration (function 3) in midsummer. The third function is strong for most of 1981 and the first function is weaker than in 1980, reflecting the stronger confinement of the spring bloom and summer pigment concentrations to the coastal region. The second function indicates greater concentrations in the south in 1981 and greater concentrations in the north in 1982. This is consistent with previous observations of winds, currents and sea level in 1981–1982, which showed the spring transition and general upwelling region to be more confined to the north in 1982 than in 1981 [*Strub et al.*, 1987*b*]. The situation in 1982 is otherwise more confused until the end of summer, when pigment concentrations rise in the large-scale region (function 1). Beginning in April 1983 the dominant feature is the large-scale reduction of surface pigment concentration noted earlier. The only positive anomalies thereafter occur in the south in March 1985 (function 2) and in a northern, coastal band in March 1986 (functions 2 and 3).

4.2.3. *PEP analysis.* Table 1 shows the percent of total chlorophyll and wind variance accounted for by each PEP, the skill in predicting the first pigment EOF, and the chi-square significance level resulting from the PEP analyses, assuming 10 degrees of freedom (see Appendix B). Two domains are used for the pigment analysis. The wider region (Figure 1) composed of five 1° bands next to the coast from 31°N to 50°N is called the large-scale CCS region (left four columns in Table 1). A narrow region composed of four 0.28° bands (still 1° in latitude) from 31°N to 50°N is called the coastal band (right four columns in Table 1). Subdivision of the narrow nearshore region into these four bands of 0.28° (25 km) width is motivated by the assumption that the physical and biological response to wind-driven coastal upwelling should be strongest over the shelf, which has scales of 20–40 km in our region. Two domains are also used for the wind analysis. Wind fields on the original LFM grid, covering the large-scale two-dimensional CCS region, are referred to as "synoptic" (top three rows of Table 1). The area covered by these synoptic fields extends farther offshore than the 5°covered by the pigment data (Figure 6 shows the location of data variables). Wind variables interpolated to just the centers of the one-dimensional north-south band closest (0.5°) to shore in Figure 1 are referred to as "coastal" (bottom three rows of Table 1).

Over the large-scale CCS region, (Table 1, left), the synoptic wind variable that explains the most variance in the first PEP is the wind stress curl. The spatial functions for each variable and the common time series function are shown in Figure 6. The spatial functions show both offshore and coastal regions of maximum positive wind stress curl which correspond to positive coastal pigment concentration anomalies of up to 1.0 mg m^{-3}. This mode accounts for 62% of the first pigment EOF, $\approx$ 25% of total chlorophyll variance, and 8.5% of the large-scale curl variance. Both spatial functions have greater values in the southern region (35°N to 38°N). The overall pattern of the time series shows a long-term fluctuation, similar to that seen in the time series of the first pigment EOF (Figure 5*d*): high values in 1980–1981, a sudden drop in April 1983, and low values thereafter. The significance level based on 10 degrees of freedom is 95%. The higher PEP modes based on synoptic wind stress curl are much less significant. The first PEPs of the other two synoptic wind variables (u_*^3 and τ_y) explain less pigment variance and are less statistically significant (Table 1). The spatial fields of these wind variables (not shown) describe an offshore maximum in southward wind stress and u_*^3 over the location of the zero curl contour in Figure 6, rather than maxima over the chlorophyll maxima. These are the patterns which create the positive curl between the maximum southward stress and the coast. Thus they support the interpretation that wind stress curl is the synoptic field most closely correlated to large-scale anomalous chlorophyll.

Results of the PEP statistics comparing the large-scale pigment concentrations with wind variables confined to a coastal strip 0.5° from shore are shown in Table 1 (bottom left). The motivation is to see whether wind forcing adjacent to the coast (for instance, upwelling favorable winds) might result in higher concentrations, which are then advected offshore. The test was primarily designed for τ_a, which would cause both upwelling and offshore Ekman advection, rather than for wind stress curl or u_*^3, which should work in a local fashion. For all three wind variables, the skill (amount of large-scale pigment variance explained) goes down, although the statistical significance increases for u_*^3 and τ_a. The increase in significance is partly because the artificial skill is greater for the synoptic

TABLE 1. Principal Estimator Statistics

	5° Wide Band				Coastal Band			
	Pigment Variance, %	Wind Variance, %	Skill	χ^2 Significance	Pigment Variance, %	Wind Variance, %	Skill	χ^2 Significance
				Synoptic				
Curl τ	24.7	8.5	0.62	0.95	24.3	10.1	0.63	0.93
u_*^3	18.5	3.8	0.46	0.82	20.8	4.0	0.54	0.94
τ_y	15.7	7.0	0.37	0.73	19.7	5.9	0.50	0.90
				Coastal				
Curl τ	9.0	33.5	0.20	0.73	7.9	45.5	0.19	0.80
u_*^3	18.1	17.8	0.41	0.99+	22.8	16.6	0.56	0.99+
τ_a	13.7	12.5	0.29	0.92	19.3	11.5	0.47	0.99+

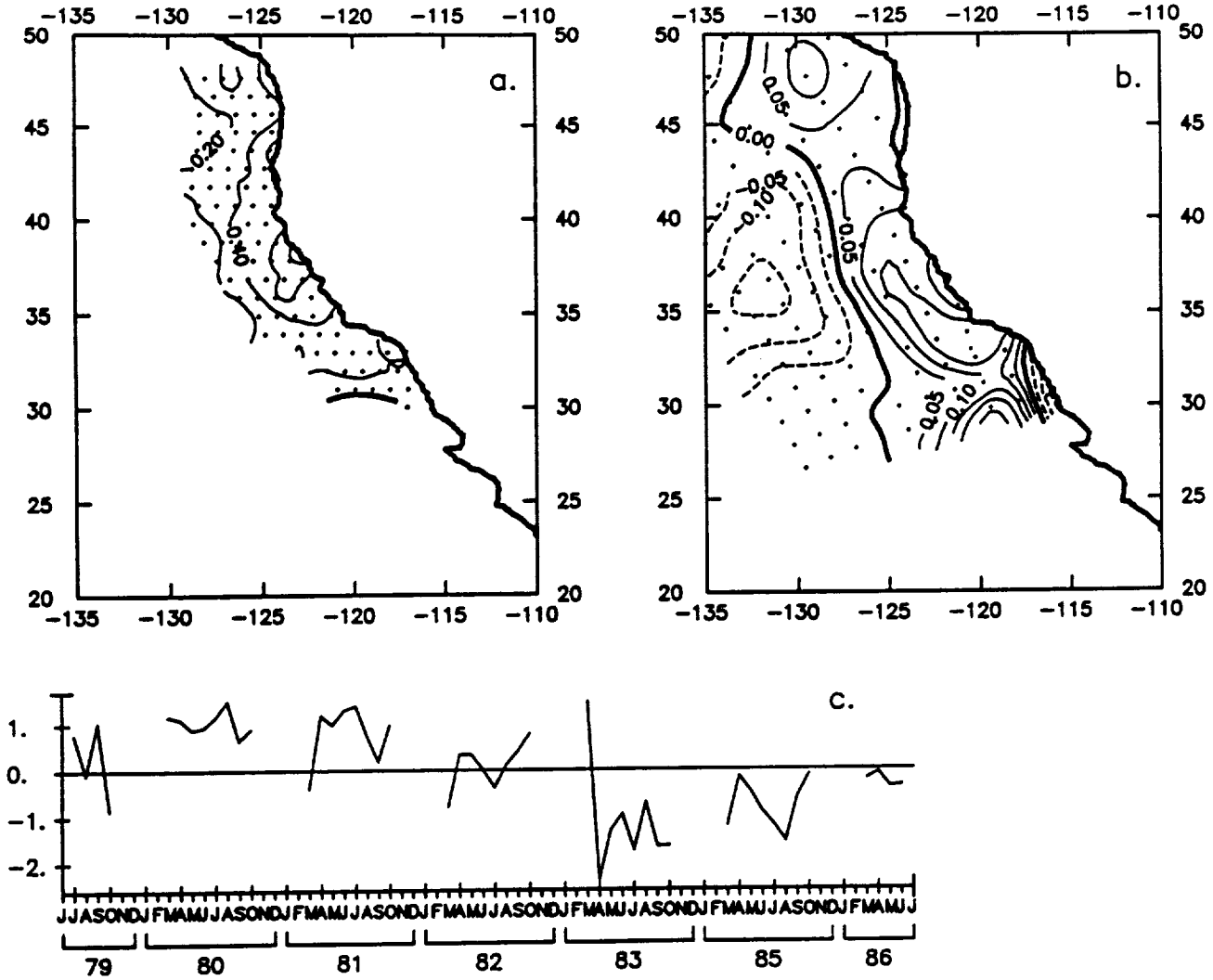

Fig. 6. The first spatial PEPs for *(a)* pigment in the large-scale CCS and *(b)* synoptic curl τ, and *(c)* the common time series for both. Units for the product of space and time functions are milligrams per cubic meter and (10^{-7} N m^{-3}). The grid for each variable is indicated by dots.

wind fields than for the coastal strip (you can explain more chlorophyll variance by regressing against random winds at many points than at fewer points). Thus the chi-square statistics (ratios of variance explained to artificial skill) are larger for the coastal wind than for the synoptic wind fields. One can argue that the high significance level for u_*^3 in the coastal band is physically reasonable, since increased mixing power would be more effective in enriching the surface layer in the 100 km next to the coast, where the nutricline is closer to the surface owing to upwelling.

The greater importance of u_*^3 and τ_a next to the coast is supported by the fact that these become the wind variables most closely related to pigment concentration when wind variables and pigment concentrations are all restricted to the 100 km next to the coast. Results of the PEP analysis confined to this coastal band are presented in Table 1 (bottom right). The relation between pigment and wind stress curl is not significant, and only u_*^3 and τ_a explain a significant amount of variance (23% and 19%, respectively). The first PEP spatial and temporal patterns for this coastal analysis are shown for u_*^3 and τ_a in Figures 7 and 8, respectively. The spatial patterns for pigment concentration are similar, with greater values next to the coast, although the pigment maxima are located in different regions. Pigment maxima associated with u_*^3 occur between Point Arena and Cape Mendocino and north of Cape Blanco, while those associated with higher τ_a are located around Monterey Bay and between capes Mendocino and Blanco. The spatial function of u_*^3 is positive north of 37°N and becomes very negative to the south (Figure 7). The spatial function for alongshore wind stress is northward south of 37°N, southward between 37°N and 43°N, and northward north of 43°N (Figure 8). Since winds are southward (on average) in the south and the absolute magnitude of u_*^3 cannot be negative, we interpret positive values of the time series to indicate anomalously weak southward winds (or northward winds) south of 37°N and stronger southward winds between 37°N and 43°N, caused by a shift in the position and/or strength of the high pressure system next to the coast. The region of stronger winds between 35°N and 43°N coincides with the region of greatest increase in pigment concentration.

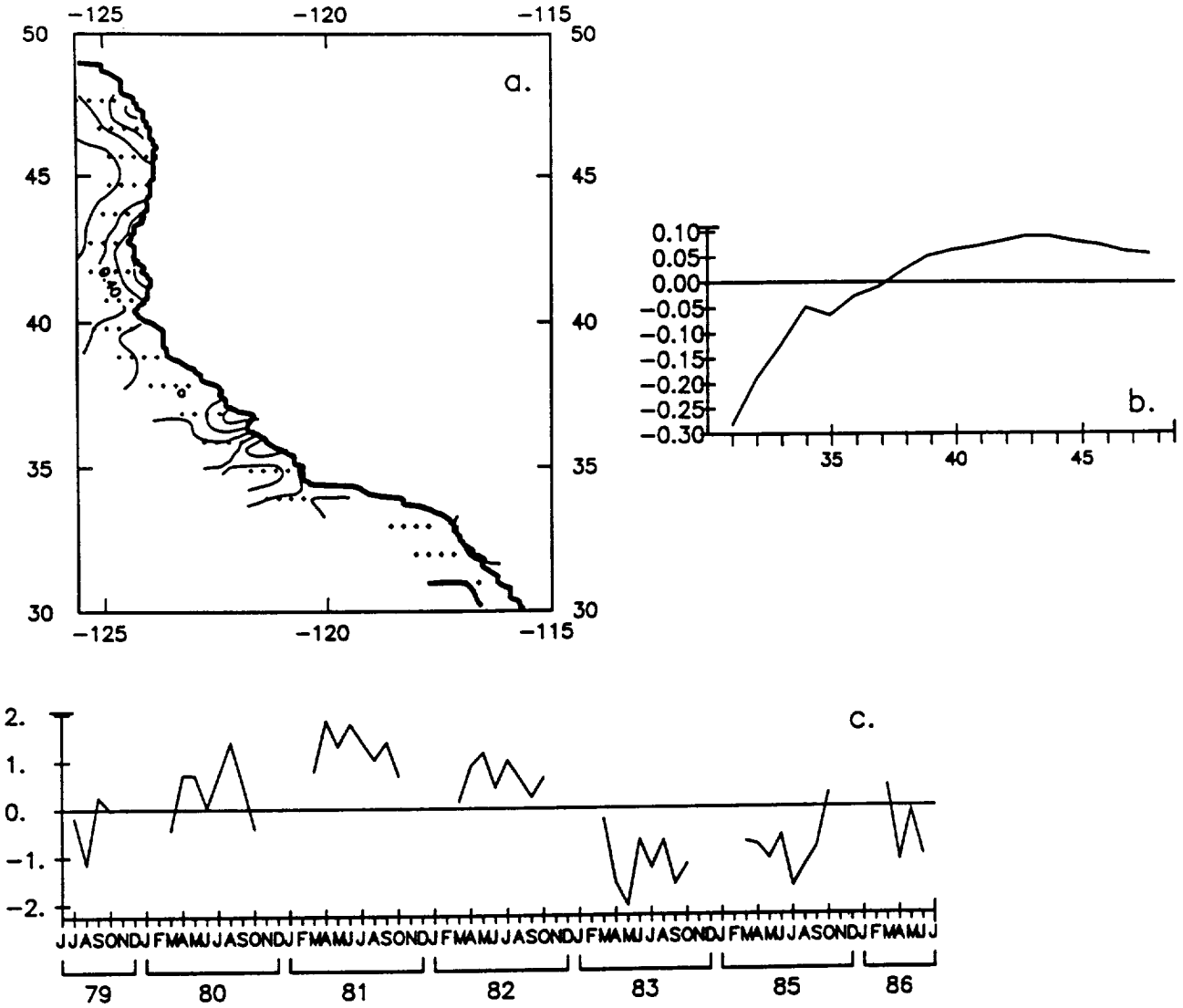

Fig. 7. As in Figure 6 for *(a)* pigment in the narrow coastal strip (four 0.28° wide bands) and *(b)* u_*^3 at locations 0.5° from the coast centered on the pigment grid, and *(c)* the common time series for both. Units for u_*^3 are (10^{-6} m^3 s^{-3}). Note the expansion of the horizontal scale in Figure 7*a*.

When the narrow band of coastal pigment is compared with the large-scale synoptic wind fields, all are significant at the 90–94% level and account for ≈ 20–24% of the anomalous coastal pigment variance (Table 1, top right). The spatial functions are very similar to those found before, with maximum u_*^3 and southward wind stress in a region ≈ 400 km offshore over the line of zero wind stress curl. The curl is positive in the 400 km next to the coast with maximum values both ≈ 200 km offshore and next to the coast as in Figure 7. Thus as before, all three fields argue for the importance of synoptic wind stress curl. In this case, however, the lack of correlation between pigment in the coastal band and wind stress curl immediately over it (Table 1, bottom right) weakens the argument for the importance of wind stress curl in the 100 km next to the coast, unless its spatial distribution near the coast is poorly represented by the LFM fields (a distinct possibility).

The process of identifying the most important of the wind variables is complicated by the high correlation that exists between τ_a, u_*^3, and large-scale curl, making the separation of their effects difficult. There is also a close tie between the physical effects of the three wind variables, since higher levels of surface mixing (u_*^3) will be more effective in bringing nutrients into the surface layer in the presence of upwelling (caused by either τ_a or wind stress curl). Our interpretation of these statistics is that anomalous synoptic wind stress curl is the important variable for the large-scale changes in anomalous pigment; in the region closer to the coast, the evidence is less supportive of wind stress curl and favors u_*^3 and τ_a, but cannot differentiate between them.

5. Discussion

5.1. *The Seasonal Cycle*

Due to the use of the correction function, the seasonal cycles presented in Figure 4*a* must be viewed as the signal that remains after removing the component of the north-south gradient with an annual peak in winter (Figure 2*a*). The temporal amplitude of the correction is ≤ 0.1 in June–

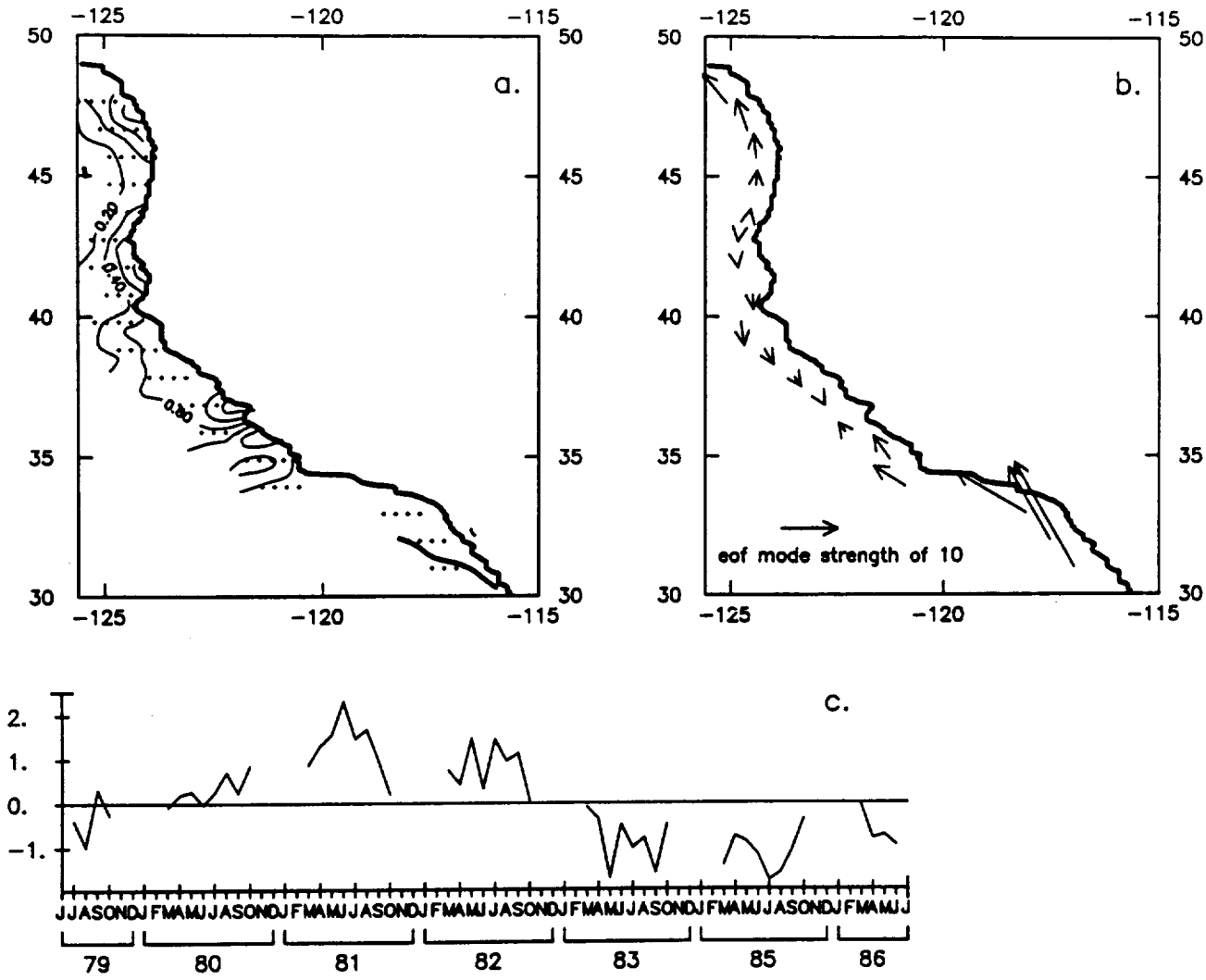

Fig. 8. As in Figure 7 for (*a*) pigment in the narrow coastal strip, and (*b*) alongshore wind stress 0.5° from the coast, and *(c)* the common time series. Units for wind stress are (10^{-3} N m^{-2}).

August (virtually nothing is subtracted at any latitude in those months) and ≈ 2.7 in January. The spatial amplitude is zero at 24°N (nothing is subtracted in any month at that latitude) and is ≈ 1.5 at 48°N. In the March–October period the maximum correction is at 48°N in October, with a value of ≈ 1.2 mg m^{-3}.

In the Southern California Bight between 29°N and 33°N, the primary conclusion from the analysis presented here is that seasonality is very low. The primary seasonal feature identifiable in the March–October period is the late summer minimum in the region 25–100 km from the coast in Figure 4*a* (most clearly seen in the bottom left and top right panels). Since the correction function removes less than 0.3 mg m^{-3} south of 33°N, we would argue that this summer minimum is not caused by our correction function. The low seasonality and the summer minimum are qualitatively in agreement with results from *Eppley et al.* [1985] from in situ data. Thus the March–October seasonal cycle in the corrected surface pigment concentration appears qualitatively in agreement with in situ studies of the southern region. In the northern portion of the study area, the CZCS climatology is in good agreement with that of *Landry et al.* [1989], even though the correction function is large in winter. In particular the double peak (spring and summer) reported off Washington by Landry et al. is present within 25 km of the coast in Figure 4*a* (bottom right). This degree of agreement between seasonal cycles derived from the corrected WCTS CZCS and historical in situ pigment concentrations in a southern and a northern region gives us some confidence in the patterns presented in Figures 2*c* and 4*a* and in Plate 1. The spatially locked pattern in Figure 2*c* accounts for 36% of the variance in the corrected data; fits of annual and semiannual harmonics result in seasonal cycles similar to Figure 4*a* that account for a similar amount of variance (30%–50%) in the region between 33°N and 43°N within 100 km of the coast.

Plate 1 and Figure 4*a* show that the lack of a spring bloom off Oregon suggested by the few data available to Landry et al. appears to be real, at least for the 1979–1986 mean. It should be noted, however, that there is a large degree of interannual variability in the satellite-derived pigment concentration at the time of spring transition [*Thomas and Strub*, 1989] and a spring bloom does appear

off Oregon in some years, in particular, 1980 and 1982 of the present data set. Thus Figures 4*b* and 4*c* show higher spring values in the region within 25 km of the coast off Oregon in these 2-year means.

The northward migration of high pigment values from northern California to Oregon between May and August, evident in Figures 4*a* to 4*c*, is consistent with the appearance of offshore filaments of pigment in the northern part of the CCS in individual CZCS images from late summer and fall and with the seasonal northward migration of maximum southward wind stress [*Strub et al.*, 1987*a*]. The narrow meandering region of high pigment concentration off northern California in summer (Plate 1) has been investigated in detail during summer 1987 and 1988 during the Coastal Transition Zone experiment (CTZ) [*CTZ Group*, 1988]. Results indicate that a meandering surface jet forms the offshore boundary of the high pigment concentration region, causing its scalloped appearance. The maximum seen west of San Francisco may be exaggerated by the presence of case II water from San Francisco Bay; this is also a region where filaments originating at Cape Mendocino and Point Arena carry both pigment and gelbstoffe offshore, making the interpretation of the CZCS signal more difficult.

The low seasonality and low surface pigment concentrations in the Southern California Bight have been well documented and attributed to the onshore flow of oligotrophic offshore water [*Peláez and McGowan*, 1986]. The same authors note the higher productivity around the Channel Islands, as do *Smith et al.* [1988]. As was described above, *Michaelsen et al.* [1988] present seasonal cycles from $\approx$ 31°N to 36°N that have an inverted seasonal cycle (winter maximum, summer minimum). They attribute the summer minimum to the sensor's inability to see the deep chlorophyll maximum which develops under the highly stratified and nutrient depleted surface layer. Although we would suggest that much of the winter maximum in their cycle omes from errors in the atmospheric scattering algorithm, we are in agreement with the finding of a late summer minimum between 31°N and 34°N, although this is a minor effect. The summer minimum is consistent with the climatological monthly geostrophic velocity fields derived from California Cooperative Oceanic Fisheries Investigations (CalCOFI) data [*Roesler and Chelton*, 1987], which show stronger onshore flow into the bight in summer, pushing this oligotrophic water both southward and northward. The same monthly fields show that in September an alongshore northward current develops next to the coast north of Punta Eugenia that may bring more eutrophic water into the bight from the upwelling region off Baja California, ending the summer minimum. Off Baja California, higher pigment concentrations in summer are similar in magnitude and timing to those off central and northern California. This clarifies the fact that the low concentrations in the eastward flowing current entering the bight are more of an intrusion over the California Current rather than the southern end of the productive region, especially in the 100 km next to the coast (Figure 4*a*).

An alternate suggestion concerning the summer minimum in the bight is that it is an artifact of a seasonal change in the aerosols over the bight, caused by the incorrect assumption of uniform marine aerosols in the image processing. Only a detailed reprocessing of the data can determine whether a systematic error is caused by the assumption of uniform aerosols. Given the consistency of the summer minimum with previous in situ measurements [*Eppley et al.*, 1985] and with the seasonal changes in the geostrophic currents noted above, we favor the view that it is a real, although minor, phenomenon. We emphasize, however, that the primary conclusion concerning the Southern California Bight is that it is a region of very low seasonality in comparison to the rest of the California Current. Conclusions based on data from this anomalous region should not be used to characterize the CCS.

Seasonal cycles of the wind variables in the coastal band (0.5° from the coast), calculated for the same period as the pigment data, are presented in Figure 9 for comparison with Figure 4*a*. There is a good visual correspondence between the seasonal cycles of pigment concentration in the coastal bands of Figure 4*a* and both upwelling favorable wind stress and wind stress curl in Figure 9 north of 35°N. The slope of the northward progression of higher pigment concentrations in March to July at these latitudes is similar to that of negative (southward) alongshore wind stress. Correspondence is especially strong between the summer maxima of pigment concentration, southward wind stress, and positive curl between 35°N and 40°N and between spring and fall minima in pigment concentration and negative wind stress curl between 40°N and 45°N. Comparison of these curl data to climatological curl fields [*Nelson*, 1977] leads us to question the lack of a positive curl in the coastal region off Oregon in the summer in Figure 9. If one connects the regions of positive curl south

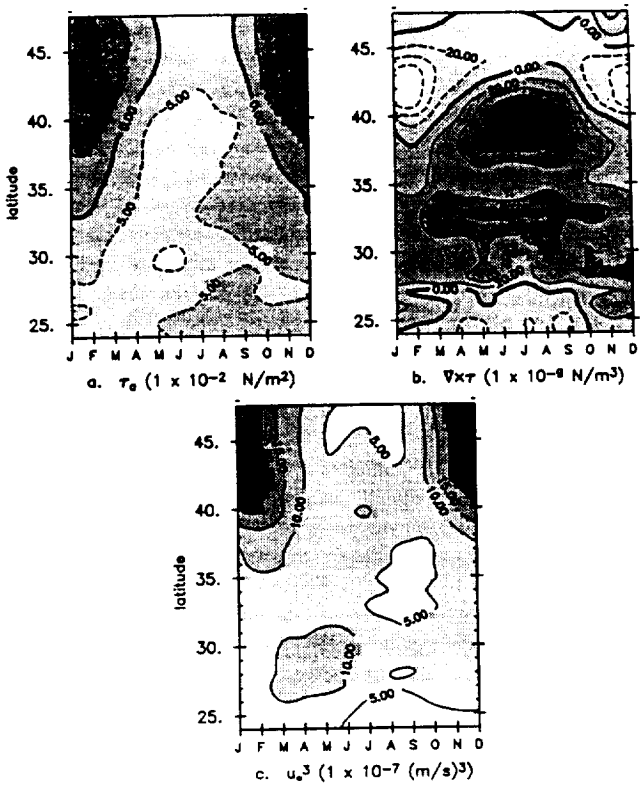

Fig. 9. Seasonal cycles of *(a)* alongshore wind stress (10^{-2} N m^{-2}), *(b)* curl τ (10^{-9} N m^{-3}), and *(c)* u_*^3 (10^{-7} m^3 s^{-3}), in the coastal band, contoured as in Figure 4*a*.

of 43°N and north of 46°N, a northward progression in time is seen, similar to those of pigment maxima and southward windstress. There is also a strong seasonal pattern in u_*^3 north of 35°N, reaching a minimum in mid to late summer. Between 26°N and 31°N this pattern is reversed and has a much lower amplitude, with a maximum in spring. The region where this seasonal pattern may influence pigment concentrations most is in the north, where one expects winter mixed layer depths and surface nutrient levels to be greater. The onset of a spring bloom at these latitudes may take place under conditions similar to those of the North Atlantic, where net positive phytoplankton productivity begins as the mixing power of the wind decreases and light and stratification increase [*Sverdrup*, 1953; *Riley*, 1957]. A North Atlantic type spring bloom does not usually occur off northern and central California [*Thomas and Strub*, 1989], where the upper water column appears nutrient limited even in late winter. Calculation of correlations between the seasonal cycles of pigment and wind result in high values in the regions where the variables covary most strongly, but no statistical certainty can be calculated for these correlations owing to the low number of degrees of freedom in the seasonal cycles and the tendency for all seasonal cycles to correlate artificially well [*Chelton*, 1982*b*].

5.2. *Nonseasonal Variability*

Much of the large-scale nonseasonal variance of anomalous pigment concentration appears as a single long-period oscillation centered around the 1982–1983 El Niño (EOF 1 in Figure 5). Wind variables would need to have much of their nonseasonal variance in a similar oscillation to yield significant correlations between the raw time series at a given location, which is usually not the case. The PEP method finds that part of the variance of the anomalous wind that covaries with the pigment anomalies.

5.2.1. *Relation to wind variables.* Over the 5° wide CCS region, the wind variable that covaries with the anomalous pigment concentration most strongly is the wind stress curl. The first PEP describes a band of positive curl 400 km wide with a maximum located ≈ 200 km offshore and anomalously high pigment concentrations over the entire CCS, with maximum values at 38°N near the coast (Figure 6). Approximately 25% of the total variance of anomalous pigment concentration and 8.5% of anomalous curl variance are contained in this function. Although this may seem like a small amount of pigment variance (corresponding to an equivalent correlation coefficient of $r = 0.5$), much of the total pigment variance in the satellite data may be noise, caused by the various sources of error described in section 3 and Appendix A, and actual small-scale variance related to local biological and physical factors, which are not adequately resolved in space and time in our analysis. The LFM winds also fail to accurately represent wind variance with spatial scales less than approximately 600 km. Assuming that the first pigment EOF is the important large-scale signal, the ability to explain 62% of its variance (Table 1) is the significant result. The other synoptic wind fields examined explain lower amounts of the pigment and wind variance in the large-scale CCS. More importantly, they have the spatial functions consistent with positive wind stress curl.

Values of the spatial and temporal functions result in peak pigment anomalies of ± 1.5 mg m^{-3} and peak curl anomalies of 4×10^{-8} N m^{-3}. Our comparisons of the LFM winds used here with buoy winds show that while spatial differences (such as those used in the curl calculation) are coherent, the LFM fields underestimate the magnitudes of the measured horizontal differences by a factor of approximately 5–10 [*Strub and James*, 1990]. Maximum curl anomalies are therefore likely to be of the order of 2–4 $\times 10^{-7}$ N m^{-3}. These values would lead, through Ekman pumping, to vertical displacements of ≈ 5–10 m per month, enough to have an effect on the normally shallow (20–40 m) pycnoclines found in summer and potentially contribute to nutrient flux into the euphotic zone.

When the wind variables and pigment concentrations are confined to the 100-km-wide coastal strip, the significant correlations explaining the greatest amount of pigment variance are found for u_*^3 and alongshore wind stress, accounting for 56% and 47% of the first pigment EOF, respectively. It is difficult to separate the effects of wind mixing (u_*^3) from upwelling (τ_a) in the present data. The spatial functions of wind variables suggest shifts in strength and position of the atmospheric high pressure system off northern California, leading to both greater upwelling and wind mixing. Our analysis cannot differentiate between the two processes, which are highly correlated with each other.

The correspondence between anomalous large-scale pigment concentration and wind stress curl over the CCS is similar to the relation between anomalous curl, southward transport, and zooplankton volume found by *Chelton* [1982*a*] and *Chelton et al.* [1982] from CalCOFI data off central and southern California. In the narrower region within 100 km of the coast, the correspondence between anomalous pigment concentration and alongshore wind stress and/or u_*^3 is more like the expected relation between an upwelling index (alongshore wind stress divided by Coriolis parameter) and biological response [*Bakun*, 1973]. Off Oregon and Washington, *Landry et al.* [1989] find correlations of ≈ 0.35 between the upwelling index and surface chlorophyll based on limited field data and correlations of 0.3–0.5 between the upwelling index and in situ nutrient data. These values are similar to the highest point correlations found here between alongshore wind stress and pigment ($r \leq 0.3$) and the amount of pigment variance explained in the coastal band by the PEP of alongshore wind stress (≈ 20%, which would correspond to an equivalent $r = 0.45$). As in the wider, 5° region, the fact that the wind variables explain ≈ 50% of the first pigment EOF is the significant finding.

5.2.2. *Relation to the El Niño.* Previous studies show the physical manifestations of the 1982–1983 El Niño in the CCS to cover the period between November 1982 and mid-1984. High SST and sea level appeared in November 1982 and were maximum by 2 standard deviations over most of the CCS in winter 1982–1983 [*Norton et al.*, 1985; *Strub et al.*, 1987*a*]. High temperatures and low salinities were seen over most of the CCS in 1983, but by the end of 1984, *Rienecker and Mooers* [1986] show the subsurface water characteristics off central and northern California to be only slightly warm (1 standard deviation) and salty, rather than fresh. Off central California, *Chelton et al.* [1988] document warm, salty water flowing northward in July

1984, as opposed to the warm, fresh water found in August 1983 by *Simpson* [1984]. By January 1985, temperature and salinity off central California were more or less normal in a strongly northward flowing Davidson Current [*Chelton and Kosro*, 1987]. Off central Oregon, sea level and SST returned to normal values by the end of 1984 [*Huyer and Smith*, 1985].

Biologically, a northward displacement of a large number of species was observed in 1983 [*Miller et al.*, 1985; *Pearcy and Schoener*, 1987]. Both satellite [*Fiedler*, 1984] and in situ data [*McGowan*, 1985] show that phytoplankton pigment concentrations off southern California were anomalously low by March 1983. McGowan found the nutricline in the Southern California Bight to have deepened from its normal depth of 50 m to 80 m in March 1983. Phytoplankton response to the El Niño was maximum in late summer and fall, lagging behind the physical anomalies but then responding rapidly. McGowan states that one of the most distinct features of the phytoplankton distribution during this period was the disappearance of the region of maximum surface biomass in the offshore area of the Southern California Bight, south of Point Conception. Off Oregon, surface chlorophyll values in June 1983 were below 1.0 mg m^{-3} in the 25 km next to the coast, in comparison to normal values greater than 3 mg m^{-3}; concentrations were higher off Washington but still below normal [*Pearcy et al.*, 1985]. In September 1983, chlorophyll concentrations of 3–8 mg m^{-3} were found north of 45°N, but concentrations dropped to less than 1 mg m^{-3} south of 44°N [*Fisher et al.*, 1984]. Similar patterns of low values off southern Oregon and higher values off northern Oregon and Washington were found in September 1984 and June 1985 [*Fisher and Pearcy*, 1985*a*, *b*].

The time series of the first EOF of pigment concentrations (Figure 5*d*) gives the appearance of relatively low values extending into 1985 and 1986. Time-latitude contours of the monthly anomaly data from the same longitudinal bands used in Figure 4*a* (not shown) give a similar impression but show that the pigment values were not as low after August 1983 north of the Columbia River and that slightly positive anomalies reappear in a patchy pattern over most of the domain in 1985 and 1986.

The clearest presentation of the nature of the differences in the fields before and after the El Niño comes from a comparison of selected spring and fall individual monthly composites from fall 1979 to spring 1986 (Plate 2). Neither the mean seasonal cycle nor the empirical correction function has been subtracted from these monthly means, since the purpose of the figure is to allow a comparison of similar months on different years. These may be placed in the context of the time series in Figure 5*d*. The monthly mean from October 1979 shows the fall pattern during the period of relatively low pigment concentration early in the time series. April and September 1981 present spring and fall patterns in a year with moderately high pigment concentrations. Similar pictures can be found in 1980 and 1982 (not shown). These can be compared with the very low values following the El Niño in April and September 1983, where high pigment concentrations are restricted to very narrow coastal regions south of some latitude. Higher values existed farther from shore north of 43°N in April 1983 and north of 40°N in September 1983. October 1983 (not shown) was similar to September 1983. Higher pigment concentrations are present in September 1984 north of 36°N (Plate 2), although this northern region is still narrower and lower in concentration than September 1981. In September 1985, the broad pigment front has moved back north to ≈ 40°N. In August of 1984 and 1985 (not shown), the broad front was lacking and the pattern consisted of a narrow coastal band of high pigment concentration stretching north from Point Conception (35°N), similar to the pattern south of 40°N in September 1985. In October 1985 (not shown) the pattern is similar to September 1985 except that the front has moved south to 36°N. Pigment concentrations in April 1986 are similar in pattern to 1981, but remain lower in concentration. Thus the patterns found from April 1983 to sometime in 1986 are characterized by a narrow coastal band of high pigment concentration south of some latitude, as described off southern California during the El Niño by *Fiedler* [1984] and (during some months) by a wider region of high pigment concentration north of that latitude. The broad north-south gradient of pigment concentration separating these regions is similar to the pigment front found in the Southern California Bight in 1979–1982 [*Peláez and McGowan*, 1986]. By spring 1986, the front has return to its normal location, but values are still low in comparison to 1980–1982.

The low concentrations during 1983 and the north-south gradient off Oregon and Washington in 1984–1985, evident in the satellite data, agree with the few in situ data available, as reviewed above. This pattern may be related to the northward flow found off Oregon in 1983 [*Huyer and Smith*, 1985] and off central California in July 1984 and January 1985 [*Chelton et al.*, 1988; *Chelton and Kosro*, 1987]. Replacement of the warm, fresh water observed in 1983 with warm, salty and nutrient-poor water from the south would result in continued low primary productivity south of the northward extent of the advection, as seen in September 1984 and 1985 (Plate 2).

If the alongshore transport associated with the 1982–1983 El Niño were the dominant cause of interannual variability in the large-scale pigment concentration of the CCS, a strong relation should exist between pigment concentration and the strength of the transport in the California Current. Although no regular time series of the large-scale transport exists, coastal sea level serves as a proxy for the alongshore current over the shelf. Monthly mean sea levels from Newport and Coos Bay, Oregon (45°N and 43°N), have been obtained and adjusted for atmospheric pressure to form a time series of adjusted sea level (ASL). Correlations of nonseasonal anomalies of these time series to the time series from the first EOF of anomalous pigment concentration in both the 5° and 1.12° bands result in correlation coefficients of the right sign (negative) but marginally significant at best ($r \approx -0.25$). Correlations of the ASL anomalies to the anomalous pigment concentrations located immediately offshore of the sea level stations yield identical results. Thus the hypothesis that alongshore transport over the shelf, as represented by ASL, controls more of the variance in pigment concentration than local or large-scale wind forcing is not supported by this data. We do not argue, however, that the fields of pigment concentration in Plate 2

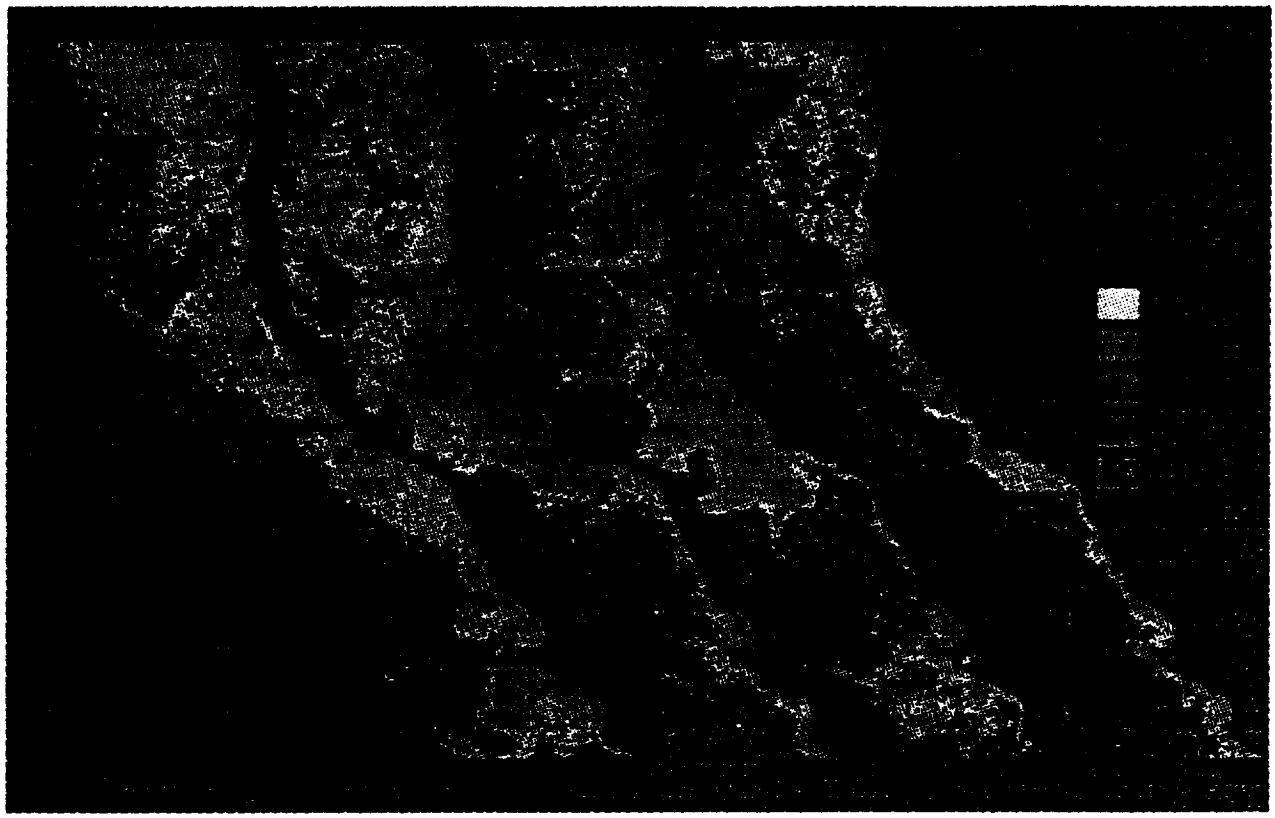

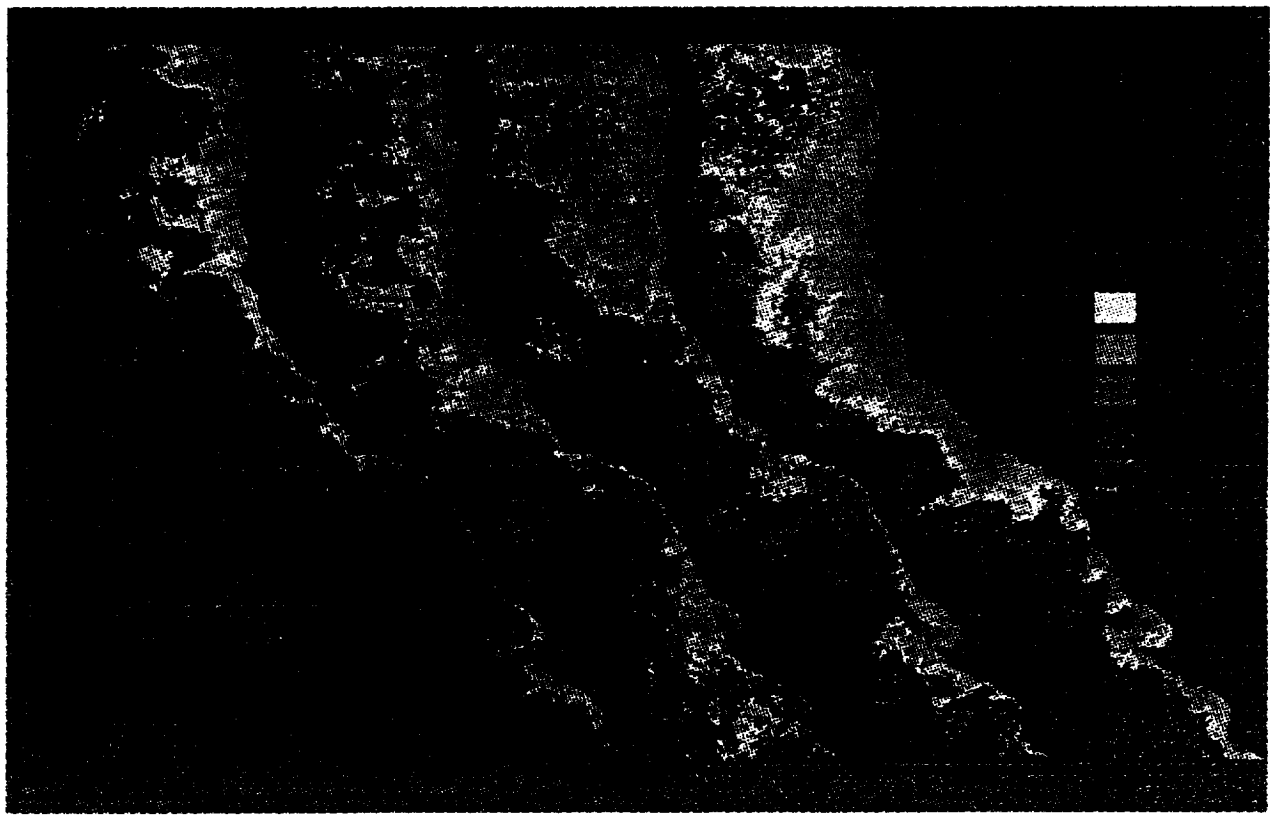

Plate 2. Monthly mean pigment concentrations for selected individual months, identified in each image. Neither the seasonal cycle nor the empirical correction function has been subtracted. Units are milligrams per cubic meter.

are unrelated to the true large-scale circulation of the CCS. On the contrary, the fluctuating alongshore displacement of the broad north-south gradient of pigment from its usual position off southern California suggests that the large-scale circulation was directly involved in creating this pattern, since the location of this pigment front is thought to be directly related to the onshore transport in the CCS [*Peláez and McGowan*, 1986]. Only when satellites yield quasi-coincident fields of satellite-derived surface pigment concentration and currents will we be able to investigate the direct connection between the two.

One is left with the picture of a slow oscillation in anomalous pigment concentration in the large-scale CCS that is related most strongly to a specific pattern of wind stress curl over the CCS. Only a small part of the variance of the curl field is represented by this pattern. There is also a relation to changes in water mass coincident with the El Niño, but the biological response appears more complex than indicators of coastal alongshore advection in the CCS such as ASL. The relation between fields of pigment concentration and the true large-scale circulation in the CCS remains unknown. Relatively long period variability has been found in the CCS by others in both physical variables such as surface temperature [*Norton et al.*, 1985] and biological variables such as crab catch [*Botsford*, 1986]. Although some of this variability can be explained statistically by wind stress curl or alongshore wind stress, a significant portion remains unexplained. Biological variability is inherently greater than the variability of any single physical factor in the surrounding environment, and responses are usually nonlinear, further increasing the difficulty of finding linear statistical relationships. The existence of long-period fluctuations such as seen here in anomalous pigment concentrations underscores the need for time series long enough to define the true variability of both the biological data and the physical environment.

6. Summary and Conclusions

6.1. *The Seasonal Cycle*

1. Use of the WCTS, corrected empirically for errors in the atmospheric algorithm, yields a reasonable March-October seasonal cycle of pigment concentration (Figures 2*c* and 4*a* and Plate 1): there is a spring bloom off Washington in April–May, with decreasing concentrations in June and increasing concentrations again in July; there is a seasonal increase off northern California in March–April, progressing northward to appear off Oregon in July; in the Southern California Bight, seasonality is low, with a relative minimum in late summer; off Baja California there is generally a maximum in summer, as off northern California, and a minimum in late summer, as in the bight. The most robust of these features are the low seasonality of the bight, the high degree of seasonality elsewhere, and the early maximum off Washington and central and northern California, progressing to the north off Oregon. There is more year-to-year variability in the appearance of the double maximum off Washington, the lack of the spring bloom off Oregon, and the late summer minimum in the bight.

2. Between 35°N and 45°N, summer patterns (Plate 1 and Figure 4*a*) show a relatively narrow region of high pigment concentration, with a scalloped nature. The region of pigment concentration may lie inshore of the southward jet in the CCS; in spring and fall the pattern is wider and more diffuse.

3. North of 35°N there is a good visual correspondence between the seasonal patterns of upwelling favorable winds, wind stress curl and pigment concentration (Figures 4*a* and 9).

6.2. *Nonseasonal Local Variability*

4. Point correlations between anomalous alongshore (upwelling favorable) wind stress and pigment concentration are only marginally significant ($r \leq 0.3$) in the 25 km next to the coast between 35°N and 45°N and insignificant elsewhere. Higher point correlations are found between anomalous pigment concentration and wind stress curl ($r \approx 0.4$) in the 200 km next to the coast from 35°N to 40°N and 300 km offshore at 46°N. The highest point correlations are found between anomalous pigment concentrations and u_*^3 in the region 200–400 km offshore between 35°N to 45°N ($r \approx 0.5$).

6.3. *Nonseasonal Large-Scale Variability*

5. The first EOF of anomalous pigment concentration (Figure 5) describes a coherent rise and fall of pigment concentrations in the CCS (accounting for 40% of the total pigment variance). The large-scale decrease in pigment concentration is centered on the 1982–1983 El Niño, but the overall time series (Figure 5*d*) has a longer period than the El Niño, approximately covering the 7 years of data.

6. PEP analysis reveals that this first pigment EOF is significantly correlated with the wind stress curl in a 400-km band next to the coast which has a maximum 200 km offshore between 35°N and 40°N; this PEP accounts for 62% of this pigment EOF (25% of the total variance of the anomalous pigment concentration) but only 8.5% of the total variance of the anomalous wind stress curl (Figure 6).

6.4. *Nonseasonal Coastal Variability*

7. In the 100 km next to the coast, the first pigment EOF is most closely related to u_*^3 (the first PEP explains 56% of the pigment EOF and 17% of the wind variance (Figure 7)) and alongshore wind stress (explaining 47% of the pigment EOF and 12% of the wind stress (Figure 8)). Both processes may act together to increase nutrients in the mixed layer.

6.5. *Interannual Variability and El Niño*

8. Although the 1982–1983 El Niño had a strong effect on the large-scale pigment values, the fluctuations in pigment concentration in some regions had a longer period than the El Niño. Correlation of pigment concentrations with proxies of coastal circulation such as sea level are usually less significant than those with local alongshore wind stress. A relation between the pigment concentration and the larger-scale circulation in the CCS is hinted at by individual monthly fields (Plate 2) but details remain unknown because of a lack of knowledge of monthly fields of transport. The long-period fluctuation described by the first EOF of anomalous pigment concentration (Figure 5*d*) is similar in nature to other long-period biological fluctuations in the CCS documented in the literature.

APPENDIX A: WEST COAST TIME SERIES

A1. *Methods of CZCS Processing*

The purpose of producing the west coast time series of CZCS data was to provide users with a consistently processed series of satellite-derived surface pigment fields in a timely fashion. The bulk of the level 1 (raw, sensor unit data) tapes were obtained from the Scripps Satellite Oceanography Facility along with a few calibrated radiance temperature (CRT) tapes from NOAA National Environmental Satellite Data and Information Service (NESDIS). Eight hundred thirteen tapes were copies from SSOF and 46 were acquired from NESDIS. These 813 tapes represented the entire holdings of level 1 CZCS data from the west coast at SSOF. Of the total 859 tapes, 22 were essentially duplicates between the SSOF and CRT tapes, 4 tapes had fatal tape recorder errors (extra lines, etc.), and 13 tapes had unreadable pass times. Of the remaining 820 tapes, 43 had no landmarks and thus could not be navigated and 5 had severe noise in the radiance data. This left 772 passes of which 38 could not be navigated properly because the mirror was moving during data acquisition. This latter problem occurs as the satellite passes northward across the equator. Depending on the season, the mirror might still have been moving when the satellite was as far north as 35°N, as the satellite operators attempted to avoid glint contamination. A total of 734 tapes were thus available for final processing, of which 701 were SSOF tapes and 33 were CRT tapes.

The basic data processing and display package used to process the WCTS was developed at the University of Miami by O. Brown, R. Evans, J. Brown, and A. Li. This package has been used by a number of researchers and forms the basis of the global CZCS processing at the NASA Goddard Space Flight Center [*Feldman et al.*, 1989].

The first step is ingestion of the raw, level 1 data. The individual passes were navigated to correct for errors in the satellite ephemeris. This process uses the world data base II coastlines to match up with clear portions of the coast and allows the manipulation of the apparent pitch, roll, yaw, and tilt of the sensor as well as the satellite time. This method can usually register images to within one pixel. After navigation, the data were then screened before further processing. This consisted of overlaying a grid of 5° latitude by 5° longitude "tiles" on the complete pass. This grid covered the entire WCTS domain from 15°N to 50°N and from 105°W to 140°W. Each tile was screened visually to determine which tiles had sufficient clear ocean pixels to warrant further processing. In addition to clear tiles, those tiles that had clear regions that were a continuation of clear areas in adjacent tiles were also flagged acceptable for further processing. This screening step was done to reduce the total processing time. Browse images were also created from the complete passes. The full swath was then trimmed by 100 pixels at either edge in order to eliminate spurious data that appear under the very large view angles present at the edges of the pass.

The voltages measured by the CZCS are converted into radiance using a calibration function for each wavelength. This has been the focus of considerable research, as the calibration system on board the satellite did not test the complete optical path of the sensor [*Gordon et al.*, 1983*b*]. A complete discussion of CZCS calibration is given by *Gordon* [1987]. As was discussed by *Gordon et al.* [1983*b*] and *Mueller* [1985], the CZCS degradation was particularly apparent in the 443 nm (channel 1) band. Initial models by *Gordon et al.* [1983*b*] used a parabolic decay function that had an inflection point at approximately orbit 24,400, which occurred in 1984. An improved model which eliminated this problem of "increasing" sensitivity after orbit 24,400 was developed by H. Gordon and embedded in the Miami software used in the WCTS processing. A further refinement of the calibration function [*R. Evans*, personal communication, 1989] indicates that the degradation of the CZCS was not a smooth process, but rather occurred as a series of discrete events and also significantly affected the other channels. Given the sensitivity of the sensor to changes in chlorophyll concentration, errors in calibration affect the quality of the chlorophyll estimates and results in a factor of 2 uncertainty in individual images [*R. Evans*, personal communication, 1989].

The raw data files were screened for cloud and land effects with a two-step process. First, a fixed threshold was used for channel 5 (750-nm band) to separate ocean pixels from land and cloud pixels. An albedo of 22 sensor counts was used as the threshold. Then non-ocean pixels were flagged and not considered for further processing. Second, as the CZCS scans from west to east, the data are occasionally corrupted as the scanner moves from bright targets to dark targets, such as from cloud to ocean. Because of the sensor design, this sometimes results in "ringing," as the sensor amplifiers recover from saturating radiance. This effect has been described by *Mueller* [1988], who also gives a method for flagging such corrupted pixels. A version of this routine was implemented that creates another image that consists of a flag identifying pixels that may be affected by this ringing. The horizontal extent of the ringing can extend anywhere from 0 to 150 pixels, depending on the viewing geometry and the albedo of the bright target. These possible corrupted pixels remain in the data set for further processing, unlike the non-ocean pixels. Ringing can also occur to the east of land under certain conditions, but very little of the WCTS domain is affected (perhaps the region in the NE Southern California Bight to the east of the Channel Islands).

The remaining ocean pixels were then used to estimate pigment concentration. The first step in this process is atmospheric correction, which has been described by *Gordon et al.* [1983*a*] in some detail. Since scattering by the atmosphere contributes 80–90% of the total satellite-sensed signal, it must be accurately estimated. The basic assumption is that the effects of Rayleigh (molecular) and Mie (particulate) scattering can be separated unambiguously and that the radiance measured in the 670 nm band originates entirely in the atmosphere (i.e., the water-leaving radiance, $L_w \approx 0$). Correction for Rayleigh scattering was based on a single-scattering model which may not be appropriate for low sun angles [*Gordon and Castaño*, 1987; *Gordon et al.*, 1988*a*]. The aerosol correction method relies on the "clear water radiance" approach to estimating the aerosol scattering contribution to the total satellite-sensed signal. That is, at low pigment concentrations, the water-leaving radiances are well known at 520, 550, and 670 nm, so that the aerosol component can be estimated for such pixels. Such information is then used to estimate a set of epsilons that describes the scattering characteristics

of the aerosol as a function of wavelength (the function at 443 nm is estimated by extrapolation from the other wavelengths). On the basis of discussions with R. Evans (University of Miami) it was decided to use a fixed set of epsilons ($\epsilon = 1.0$ for all wavelengths). This set is appropriate for marine-type aerosols such as those that dominate the west coast where the wavelength dependence of the scattering is weak. However, it should be noted that this will not produce optimal results in all locations at all times. There are situations where the atmosphere is dominated by continental-type aerosols or where there is considerable spatial variability in aerosol type, and the "standard" epsilons are not appropriate. Processing of the global CZCS data at NASA Goddard Space Flight Center (GSFC) has also assumed a constant set of epsilons for all images [*Feldman et al.*, 1989]. Recent work by *Gordon et al.* [1988*b*] attempts to estimate the set of epsilons on a pixel by pixel basis, thus eliminating the problem of spatial variation in aerosol type. This method is still under development.

After atmospheric correction, the in-water algorithms were applied to the water-leaving radiances. These algorithms are based on in situ measurements of upwelling radiance and pigment concentrations [*Clark*, 1981]. The present algorithms are based on a pair of algorithms that use the ratio of 443 nm to 550 nm and 520 nm to 550 nm, depending on whether the pigment estimate is "high" (> 1.5 mg m^{-3}) or "low" (< 1.5 mg m^{-3}).

The pigment images were then remapped to a fixed grid. Each pixel was set to be 0.01° of latitude and longitude. Thus these images do not preserve area as one moves latitudinally. Instead, the images become distorted as the east-west dimension is a function of latitude. The individual tiles were then resampled at reduced resolution to create a mosaic image which was used in the present analysis and covered the entire study area (20°–55°N, 105°–140°W). These pixels were created by averaging blocks of 7×7 pixels. If fewer than 25 pixels were cloud-free, then an average value was not formed and the reduced-resolution pixel was flagged as cloud. Only valid (i.e., ocean) pixels were used in the average.

A2. *Sources of Error in the WCTS CZCS Data*

There are several sources of error in the final CZCS data set which consists of 734 mosaics and 9114 tiles. These can be broken down roughly into processing errors and algorithm errors. Similar to the GSFC global CZCS processing [*Feldman et al.*, 1989], the purpose of the WCTS was to deliver reasonable quality data to any interested researcher; thus a balance had to be struck between in-depth, image-by-image processing and bulk, rapid delivery of a consistently processed data set.

Processing errors are those that result from operator errors in the CZCS processing stream. These include navigation errors, undetected gain errors on the sensor, and undetected sunglint in the data. First, navigation errors are generally small; for the majority of the passes, the pixel location is good to approximately 1 km. However, there are some scenes that may have been contaminated by a moving mirror and were not flagged as such. Other errors, such as improper yaw corrections, can also occur. In general, these errors can be identified as shifts in the relative location of features in the coastline. Second, the gain on the CZCS channels was improperly identified in the original level 1 data or was set incorrectly and was not detected in the initial data screening. This results in complete algorithm failure. Usually, such scenes have all ocean values set to 0 or 1. Third, the mirror was set the wrong way to avoid glint. This type of error usually looks like a "haze" of high chlorophyll values in a region where they are not expected. In general, this is a minor problem as it is a simple matter to identify and eliminate such scenes during the navigation process.

Algorithm errors result either from the assumptions made during processing or from the basic assumptions of the CZCS algorithms. These errors include incorrect cloud masking, incorrect assumptions concerning low sun angles, aerosol removal, effects of terrestrial input, contamination by case II waters, and "switching" between the low-pigment and high-pigment in-water algorithms.

As was noted by *Eckstein and Simpson* [1990], the use of a fixed threshold based on the channel 5 albedo may result in incomplete cloud and land masking. This results in part from errors in the ground processing system which results in regularly spaced scans of apparently low radiance. This problem manifests itself as a series of scan lines across clouds and land consisting of apparent pigment retrievals. Although the spacing is usually regular (every sixteenth line [*Eckstein and Simpson*, 1990]), the spacing occasionally deviates from this pattern. Also, this noise problem is present in only a fraction of the CZCS images, primarily early in the mission of Nimbus 7. The other problem in the area of cloud and land masking relates to low albedos present in images with low sun angles and large clouds. At low sun angles, radiance is so low that it is difficult to distinguish ocean from land and cloud. Also, tall clouds can cast shadows that have a radiance low enough that the fixed threshold mask assumes that the shadow area is ocean. For land areas this is easy to detect, as there are apparent pigment retrievals over known land masses; for ocean areas, there is no easy way to detect shadows. *Eckstein and Simpson* [1990] also describe a method for a variable threshold mask for CZCS data.

As noted earlier, assumptions concerning atmospheric correction are crucial in obtaining good quality pigment estimates. The first assumption is that we can separate Rayleigh and aerosol scattering into two distinct effects. *Gordon et al.* [1983*a*] state that in general this should not be a problem, but we cannot provide a quantitative assessment of the effects of a violation of this assumption. The second assumption is that a uniform set of epsilons will work for every image. This assumption is fairly robust, but it will fail under conditions of strong temporal and spatial variability in atmospheric conditions. For instance, the assumption of uniform aerosol type will not work during strong continental input (such as during Santa Ana conditions off southern California) or very clear atmospheres, as occasionally occur off British Columbia. However, for most images off the west coast, we expect that our basic assumption of uniform epsilons will work reasonably well. *Gordon et al.* [1988*b*] present a method for making aerosol corrections on a pixel by pixel basis, which may improve the processing when the method is fully developed.

The other potential source of error in the atmospheric correction process is in the Rayleigh correction. The

algorithm used in the WCTS assumes single scattering, which may be invalid at low sun angles, for which one must account for multiple Rayleigh scattering [*Gordon and Castaño*, 1987; *Gordon et al.*, 1988*a*]. If this is not done, the radiances in the blue wavelengths are lower than they should be, resulting in apparently high chlorophyll concentrations. This is most pronounced at sun/sensor angles greater than 50°. Thus, in December, measurements north of about 35° are suspect; by the same measure, data south of 50°N should be valid between the spring and fall equinoxes. The degree of this error depends in part on the type of atmosphere that is present in the scene so one cannot give a fixed sun/sensor angle cutoff for all passes. That is, the effect may be important at smaller sun/sensor angles under certain atmospheric conditions. The present global CZCS processing uses a multiple-scattering Rayleigh model [*Feldman et al.*, 1989].

The next source of error arises in the in-water algorithms. The basic assumption is that the optical properties are those of case I water [*Morel and Prieur*, 1977]; the primary determinant of variability in the optical properties is phytoplankton pigment and covarying detritus. There are several conditions that may occur that would cause this assumption to be violated. It has been suggested that areas of high wind (and hence large areas of whitecaps on the sea surface) may result in incorrect estimates of water-leaving radiance [e.g., *Tassan*, 1981]. Terrestrial input of materials can result in incorrect phytoplankton pigment estimates. In particular, the Fraser River (British Columbia), the Columbia River (Oregon), and San Francisco Bay (California) occasionally appear as regions of spurious pigment concentrations. Coccolithophore concentrations can be high, resulting in poor pigment estimates [*Balch et al.*, 1989*a*; *Gordon et al.*, 1988*b*]. However, coccolith blooms are thought to be generally rare off the west coast, compared with the Atlantic Ocean [*Balch et al.*, 1989*a*]. Pigment degradation products, such as gelbstoffe, have different optical properties than chlorophyll, resulting in poor pigment retrievals. Although gelbstoffe is generally associated with nearshore and terrigenous sources, *K. Carder* [personal communication, 1989] has measured high gelbstoffe concentrations in filaments several hundred kilometers offshore in the California Current. High pigment concentrations are often associated with high concentrations of suspended particulates, such as detritus. These particulates can strongly affect the optical properties of the water such that L_w (670 nm) $\neq 0$. The result of this latter type of error is that oceanographic features appear in the field of L_w (670 nm) radiances, which was earlier assumed to consist only of atmospheric effects. Clearly, this will result in incorrect pigment estimates. Finally, the use of a two-part in-water algorithm (for low and high pigment) can result in discontinuities in the pigment distribution. This can be observed in the histogram of pigment values [e.g., *Denman and Abbott*, 1988] or as a "speckling" on 1-km scales in the image as the algorithm switches between the high- and the low-pigment algorithms.

The final source of errors in CZCS processing is in the area of sampling, which cannot be improved either by reducing operator error or changing the fundamental algorithms. First, the CZCS responds to a weighted average of the vertical distribution of phytoplankton pigment [*Smith*, 1981; *Gordon and Clark*, 1980]. In general, this is assumed to be over the first two optical depths. However, on occasion the distribution at depth is effectively uncorrelated with the near-surface concentration so that one cannot accurately estimate integrated water column pigment from near-surface estimates [e.g., *Hayward and Venrick*, 1982]. This problem is even more severe in estimates of water column production from CZCS data [*Balch et al.*, 1989*b*]. The second problem involves subpixel-sized clouds. This may be a serious problem, particularly on the fringes of fog and cloud banks, where small clouds may not be detected. This will result in spurious pigment estimates. The third problem is in the area of data collection. The CZCS in general was turned on over U.S. coastal waters, but not every pass was collected. SSOF relied on specific requests for data for many years before they began routine collection. Also, passes were often not collected during vacation and holiday periods, and NASA would not collect data during manned missions. The sensor began to fail in spring 1984, so collections were sporadic, especially in summer, until the final shutdown of the sensor in 1986. In addition to these gaps, there are gaps due to clouds, which are by far more troublesome. As clouds and wind patterns are closely related on the west coast of the U.S., the CZCS data are biased in time and space (see *Abbott and Zion* [1987] for a description). There is no simple solution to this problem.

A3. *Summary*

Previous work with CZCS data indicates the pigment estimates are generally within a factor of 2 of simultaneous ship estimates [e.g., *Gordon et al.*, 1983*a*, 1988*b*; *Balch et al.*, 1989*b*; *Denman and Abbott*, 1988]. The degree of scatter is usually higher at high pigment levels. As the above discussion indicates, there are clearly instances when estimates from individual images are worse than this.

The purpose of providing large sets of consistently processed CZCS data to a number of investigators is twofold: to make possible both (1) the evaluation of systematic biases in the data set and (2) the extraction of the important surface pigment signal, after accounting for the systematic biases and random noise. The present paper serves as an example of both types of analysis, which are necessary to look at the seasonal and nonseasonal variability in the WCTS. Although an improved (multiple-scattering) Rayleigh model has been used in the global CZCS processing [*Feldman et al.*, 1989], questions remain concerning other possible sources of systematic errors (uniform aerosols, etc.). Even with further improvements in the algorithms, it seems likely that analyses of these CZCS data sets will continue to require the examination of systematic bias and the extraction of the signal of interest in the presence of a fairly high level of noise. In this respect, the CZCS data are no different from other satellite data (for instance, altimeter data) and other large oceanic data sets (for instance, CalCOFI or merchant ship observations). The information is there, awaiting to be revealed by the proper combination of statistics and insight.

APPENDIX B: THE PEP METHOD

The method of principal estimator patterns [*Davis*, 1977, 1978] constructs a linear combination of a set of predictors (in this case, the EOFs of the wind variables) that explains

the largest possible fraction of the variance of another set of data (in this case, the EOFs of the pigment concentration). Formally, the time series of T measurements of the wind variables (the predictor) at X spatial locations, $v(x,t)$, and the time series of T measurements of the pigment concentrations (the predictand) at Y spatial locations, $p(y,t)$, are represented by their EOFs:

$$v(x,t) = \sum_{m=1}^{X} w_m(t) W_m(x) \qquad (B1a)$$

$$p(y,t) = \sum_{n=1}^{Y} p_n(t) P_n(y) \qquad (B1b)$$

where $w_m(t), p_n(t)$ are the orthogonal EOF time series for wind and pigment concentrations and $W_m(x), P_n(y)$ are the EOF space functions. Here x and y are generalized space coordinates, i.e., they may represent 1, 2, or 3 dimensions (even a fourth, lags in time). A subset, $\hat{v}(x,t)$ of $M(\leq X)$ of the predictor variables is chosen,

$$\hat{v}(x,t) = \sum_{m=1}^{M} w_m(t) W_m(x) \qquad (B2a)$$

and used to estimate a subset of $N(\leq Y)$ pigment EOFs,

$$\hat{p}(y,t) = \sum_{n=1}^{N} p_n(t) P_n(y) \qquad (B2b)$$

A linear estimator can be formed which gives the predictand EOFs in terms of the M predictor variables,

$$\hat{p}_n(t) = \sum_{m=1}^{M} \alpha_{nm} w_m(t) \qquad (B3a)$$

where

$$\alpha_{nm} = \frac{\langle p_n w_m \rangle}{\langle w_m^2 \rangle} \qquad (B3b)$$

Temporal averaging is denoted by angle brackets. The PEPs are formed as linear combinations of the spatial patterns of the EOFs of each variable ($W_m(x)$, $P_n(y)$), resulting in a spatial function for each, related by a single time series. The goal is to maximize the amount of predictand variance explained by the PEPs, defined as

$$E = \sum_{n=1}^{N} \langle \hat{p}_n^2 \rangle \qquad (B4a)$$

subject to the constraint that the new time series, $z_n(t)$, be orthonormal, $\langle z_n(t) z_m(t) \rangle = \delta_{mn}$. The mean square predictand, E, may be written as

$$E = \sum_{k=1}^{M} \sum_{n=1}^{N} \sum_{m=1}^{M} A_{nm} \mu_{nk} \mu_{mk} \langle z_k^2 \rangle \qquad (B4b)$$

If $\sigma_n^2 = \langle w_n^2 \rangle$, α_{nm} is given above, and matrix $\mathbf{A}$ is defined by the elements

$$A_{ij} = \sum_{n=1}^{N} \alpha_{ni} \alpha_{nj} \sigma_i \sigma_j \qquad (B5a)$$

the method of Lagrange multipliers yields the eigenvalue problem

$$\sum_j A_{nj} \mu_{jm} - \lambda_m \mu_{nm} = 0 \qquad (B5b)$$

The eigenvectors, μ_{nm}, are used to form the new spatial functions,

$$W_n'(x) = \sum_{m=1}^{M} \sigma_n \mu_{nm} W_m(x) \qquad (B6a)$$

$$P_n'(y) = \sum_{m=1}^{N} \sum_{k=1}^{M} \alpha_{mk} \sigma_k \mu_{kn} P_m(y) \qquad (B6b)$$

and the time series corresponding to each pair of spatial functions,

$$z_n(t) = \sum_{m=1}^{M} \mu_{mn} \frac{w_m(t)}{\sigma_m} \qquad (B6c)$$

The time series for the original predictor and predictand can be reconstructed as

$$\hat{v}(x,t) = \sum_{m=1}^{M} w_m(t) W_m(x) = \sum_{m=1}^{M} z_m(t) W_m'(x) \qquad (B7a)$$

$$\hat{p}(y,t) = \sum_{n=1}^{N} p_n(t) P_n(y) = \sum_{m=1}^{M} z_m(t) P_m'(y) \qquad (B7b)$$

The fraction of the variance of the original predictand EOF, $p_n(t)P_n(x)$, represented by the PEPs, is referred to as the skill in predicting the variance in that EOF S_n (Table 1), calculated from

$$S_n = \frac{\langle \hat{p}_n^2 \rangle}{\langle p_n^2 \rangle} = \sum_{m=1}^{N} \frac{\alpha_{nm}^2 \sigma_m^2}{\langle p_n^2 \rangle} \qquad (B8)$$

The percent of total pigment or wind variance accounted for by the mth PEP is also reported in Table 1, calculated for pigment as

$$100 \times \frac{\lambda_m}{\sum_k^Y \langle p_k^2(t) \rangle} \qquad (B9a)$$

where the divisor is the total variance of the original pigment concentration data set, and calculated for wind as:

$$100 \times \frac{\sum_x^X W_m'^2(x)/X}{\sum_k^X \langle w_k^2(t) \rangle} \qquad (B9b)$$

The proportion of pigment variance represented by the PEPs, S_n, may not be significantly greater than that obtained from two uncorrelated sets of data. To test this, the PEP analysis is carried out for the same sets of data but displaced in time relative to each other sufficiently to assure that any correlation between the two is fortuitous. In our case, the available wind time series is longer than that of the pigment concentrations, allowing the formation of these long lags. These time series are used to estimate S_A, the artificial skill, which is the skill expected from the PEP method if the time series are uncorrelated. The ratio of the skill to artificial skill should have a chi-square distribution, which can be used to test the significance

of the amount of variance explained by the predictor, if the number of degrees of freedom is known [*Davis*, 1977]. Following *Davis* [1978], the values of the ratio S/S_A are fit to chi-square distributions with varying numbers of degrees of freedom. The best fit in our case is found for 10 degrees of freedom, and this is used to calculate the significance level in Table 1. The significance is interpreted as the probability that a random variable will explain less of the original variance than is explained by the PEP.

Acknowledgments. This work was supported by NASA Grants NAGW-869 and NAGW-1251 and by a Killam Postdoctoral Fellowship (A.C.T.). The CZCS west coast time series was supplied by NODS at JPL. The LFM winds were obtained from NCAR and tide gauge data were obtained from Jane Huyer and Bob Smith. Gene Feldman supplied the global CZCS monthly composites. We benefitted from discussions with Dudley Chelton, Tim Cowles, Bill Pearcy, and Pat Wheeler during the data analysis. Critical comments from two anonymous reviewers resulted in a stronger, longer paper.

REFERENCES

Abbott, M. R., and P. M. Zion, Satellite observations of phytoplankton variability during an upwelling event, *Cont. Shelf Res.*, *4*, 661–680, 1985.

Abbott, M. R., and P. M. Zion, Spatial and temporal variability of phytoplankton pigment off northern California during Coastal Ocean Dynamics Experiment 1, *J. Geophys. Res.*, *92*, 1745–1756, 1987.

Bakun, A., Coastal upwelling indices, west coast of North America, 1946–71, *Tech. Rep. NNFS SSRF-671*, 103 pp., Nat. Oceanic and Atmos. Admin., Seattle, Wash., 1973.

Balch, W. M., R. W. Eppley, M. R. Abbott, and F. M. H. Reid, Bias in satellite-derived pigment measurements due to coccolithophores and dinoflagellates, *J. Plankton Res.*, *11*, 575–581, 1989*a*.

Balch, W. M., M. R. Abbott, and R. W. Eppley, Remote sensing of primary production, I, A comparison of empirical and semi-empirical algorithms, *Deep Sea Res.*, *36*, 281–295, 1989*b*.

Barale, V., and R. W. Fay, Variability of the ocean surface color field in central California near-coastal waters as observed in a seasonal analysis of CZCS imagery, *J. Mar. Res.*, *44*, 291–316, 1986.

Beardsley, R. C., C. E. Dorman, C. A. Friehe, L. K. Rosenfeld, and C. D. Winant, Local atmospheric forcing during the Coastal Ocean Dynamics Experiment, 1, A description of the marine boundary layer and atmospheric conditions over a northern California upwelling region, *J. Geophys. Res.*, *92*, 1467–1488, 1987.

Botsford, L. W., Effects of environmental forcing on age-structured populations: Northern California Dungeness crab (*Cancer magister*) as an example, *Can. J. Fish. Aquat. Sci.*, *43*, 2435–2352, 1986.

Botsford, L. W., D. A. Armstrong, and J. M. Shenker, Oceanographic influences on the dynamics of commercially fished populations, in *Coastal Oceanography of Washington and Oregon*, edited by M. R. Landry and B. M. Hickey, pp. 511–565, Elsevier, New York, 1989.

Campbell, J. W., and J. E. O'Reilly, Role of satellites in estimating primary productivity on the northwest Atlantic continental shelf, *Cont. Shelf Res.*, *8*, 179–204, 1988.

Chelton, D. B., Large-scale response of the California Current to forcing by wind stress curl, *CalCOFI Rep. 23*, pp. 130–148, Calif. Coop. Oceanic Fish. Invest., Univ. of Calif., San Diego, La Jolla, 1982*a*.

Chelton, D. B., Statistical reliability and the seasonal cycle: Comments on "Bottom pressure measurements across the Antarctic Circumpolar Current and their relation to the wind," *Deep Sea Res.*, *29*, 1381–1388, 1982*b*.

Chelton, D. B., Seasonal variability of alongshore geostrophic velocity off central California, *J. Geophys. Res.*, *89*, 3473–3486, 1984.

Chelton, D. B., and R. E. Davis, Monthly mean sea level variability along the west coast of North America, *J. Phys. Oceanogr.*, *12*, 757–784, 1982.

Chelton, D. B., P. A. Bernal, and J. A. McGowan, Large-scale interannual physical and biological interaction in the California Current, *J. Mar. Res.*, *40*, 1095–1125, 1982.

Chelton, D. B., and P. M. Kosro, Central California Coastal Circulation Study CTD observations – Cruise 8501, January 1985, *Data Rep. 129, Ref. 87-05*, Coll. of Oceanogr., Oreg. State Univ., Corvallis, 1987.

Chelton, D. B., A. W. Bratkovich, R. L. Bernstein, and P. M. Kosro, Poleward flow off central California during the spring and summer of 1981 and 1984, *J. Geophys. Res.*, *93*, 10,604–10,620, 1988.

Clark, D. K., Phytoplankton algorithms for the Nimbus-7 CZCS, in *Oceanography From Space*, edited by J. F. R. Gower, pp. 227–238, Plenum, New York, 1981.

Coastal Transition Zone Group, The Coastal Transition Zone Program, *Eos Trans. AGU*, *69*, 697–707, 1988.

Cullen, J. J., and R. W. Eppley, Chlorophyll maximum layers of the southern California Bight and possible mechanisms of their formation and maintenance, *Oceanol. Acta*, *4*, 23–32, 1981.

Davis, R. E., Techniques for statistical analysis and prediction of geophysical fluid systems, *Geophys. Astrophys. Fluid Dyn.*, *8*, 245–277, 1977.

Davis, R. E., Predictability of sea level pressure anomalies over the North Pacific Ocean, *J. Phys. Oceanogr.*, *8*, 233–246, 1978.

Davis, R. E., and P. S. Bogden, Variability on the California shelf forced by local and remote winds during the Coastal Ocean Dynamics Experiment, *J. Geophys. Res.*, *94*, 4763–4784, 1989.

Denman, K. L., and M. R. Abbott, Time evolution of surface chlorophyll patterns from cross-spectrum analysis of satellite color images, *J. Geophys. Res.*, *93*, 6789–6798, 1988.

Eckstein, B. A., and J. J. Simpson, Cloud screening coastal zone color scanner images using channel 5, *Int. J. Remote Sens.*, in press, 1990.

Enfield, D. B., and J. S. Allen, On the structure and dynamics of monthly mean sea level anomalies along the Pacific coast of North and South America, *J. Phys. Oceanogr.*, *10*, 557–578, 1980.

Eppley, R. W., E. Stewart, M. R. Abbott, and U. Heyman, Estimating ocean primary production from satellite chlorophyll, Introduction to regional differences and statistics for the Southern California Bight, *J. Plankton Res.*, *7*, 57–70, 1985.

Feldman, G., N. Kuring, C. Ng, W. Esaias, C. McClain, J. Elrod, N. Maynard, D. Endres, R. Evans, J. Brown, S. Walsh, M. Carle and G. Podesta, Ocean color: Availability of the global data set, *Eos Trans. AGU*, *70*, 634–641, 1989.

Fiedler, P. C., Satellite observations of the 1982–1983 El Niño along the U.S. Pacific coast, *Science*, *224*, 1251–1254, 1984.

Fisher, J. P., and W. G. Pearcy, Studies of juvenile salmonids off northern California, Oregon, Washington and Vancouver Island, 1984, Data report, *Ref. 85-2*, Coll. of Oceanogr., Oreg. State Univ., Corvallis, 1985*a*.

Fisher, J. P., and W. G. Pearcy, Studies of juvenile salmonids off the Oregon and Washington Coast, 1985, Data report, *Ref. 85-14*, Coll. of Oceanogr., Oreg. State Univ., Corvallis, 1985*b*.

Fisher, J. P., W. G. Pearcy, and A. W. Chung, Studies of juvenile salmonids off the Oregon and Washington coast, 1983, Data report, *Ref. 84-2*, Coll. of Oceanogr., Oreg. State Univ., Corvallis, 1984.

Flament, P., L. Armi, and L. Washburn, The evolving structure of an upwelling element, *J. Geophys. Res.*, *40*, 11,765–11,778, 1985.

Freeland, H. J., W. R. Crawford, and R. E. Thomson, Currents along the Pacific coast of Canada, *Atmos. Ocean*, *22(2)*, 151–172, 1984.

Gordon, H. R., Calibration requirements and methodology for remote sensors viewing the ocean in the visible, *Remote Sens. Environ.*, *22*, 103–126, 1987.

Gordon, H. R., and D. J. Castaño, The coastal zone color scanner atmospheric correction algorithm: Multiple scattering effects, *Appl. Opt.*, *26*, 2111-2122, 1987.

Gordon, H. R., and D. K. Clark, Remote sensing optical properties of a stratified ocean: an improved interpretation, *Appl. Opt.*, *19*, 3428–3430, 1980.

Gordon, H. R., D. K. Clark, J. W. Brown, O. B. Brown, R. H.

Evans, and W. W. Broenkow, Phytoplankton pigment concentrations in the Middle Atlantic Bight: Comparison of ship determinations and CZCS estimates, *Appl. Opt.*, *22*, 20–36, 1983*a*.

Gordon, H. R., J. W. Brown, O. B. Brown, R. H. Evans, and D. K. Clark, Nimbus 7 CZCS: Reduction of its radiometric sensitivity with time, *Appl. Opt.*, *22*, 3929–3931, 1983*b*.

Gordon, H. R., J. W. Brown, and R. H. Evans, Exact Rayleigh scattering calculations for use with the Nimbus-7 coastal zone color scanner, *Appl. Opt.*, *27*, 862–871, 1988*a*.

Gordon, H. R., O. B. Brown, R. H. Evans, J. W. Brown, R. C. Smith, K. S. Baker, and D. K. Clark, A semi-analytic radiance model of ocean color, *J. Geophys. Res.*, *93*, 10,909–10,924, 1988*b*.

Haury, L. R., J. J. Simpson, J. Peláez, C. J. Koblinsky, and D. Wiesenhahn, Biological consequences of a recurrent eddy off Point Conception, California, *J. Geophys. Res.*, *91*, 12,937–12,956, 1986.

Hayward, T. L., and E. L. Venrick, Relation between surface chlorophyll, integrated chlorophyll, and integrated primary production, *Mar. Biol.*, *69*, 247–252, 1982.

Hickey, B. M., The California current system—Hypotheses and facts, *Prog. Oceanogr.*, *8*, 191–279, 1979.

Hickey, B. M., Patterns and processes of circulation over the continental shelf off Washington, in *Coastal Oceanography of Washington and Oregon*, edited by M. R. Landry and B. M. Hickey, pp. 41–115, Elsevier, New York, 1989.

Hotelling, H., Relations between two sets of variates, *Biometrika*, *28*, 321–377, 1936.

Huyer, A. E., Coastal upwelling in the California current system, *Progr. Oceanogr.*, *12*, 259–284, 1983.

Huyer, A. E., and R. L. Smith, The signature of El Niño off Oregon, 1982–1983, *J. Geophys. Res.*, *90*, 7133–7142, 1985.

Huyer, A. E., E. J. Sobey, and R. L. Smith, The spring transition in currents over the Oregon continental shelf, *J. Geophys. Res.*, *84*, 6995–7011, 1979.

Ikeda, M., and W. J. Emery, Satellite observations and modeling of meanders in the California Current system off Oregon and northern California, *J. Phys. Oceanogr.*, *14*, 1434–1450, 1984.

Kosro, P. M., and A. Huyer, CTD and velocity surveys of seaward jets off northern California, July 1981 and 1982, *J. Geophys. Res.*, *91*, 7680–7690, 1986.

Landry, M. R., J. R. Postel, W. K. Peterson, and J. Newman, Broad-scale distributional patterns of hydrographic variables on the Washington/Oregon shelf, in *Coastal Oceanography of Washington and Oregon*, edited by M. R. Landry and B. M. Hickey, pp. 1–40, Elsevier, New York, 1989.

McGowan, J. A., El Niño 1983 in the Southern California Bight, in *El Niño North*, edited by W. S. Wooster and D. L. Fluharty, pp. 166–184, Washington Sea Grant Program, University of Washington, Seattle, 1985.

Mackas, D. C., G. C. Louttit, and M. J. Austin, Spatial distribution of zooplankton and phytoplankton in British Columbia coastal waters, *Can. J. Fish. Aquatic Sci.*, *37*, 1476–1487, 1980.

Martin, J. H., and R. M. Gordon, Northeast Pacific iron distribution in relation to phytoplankton productivity, *Deep Sea Res.*, *35*, 177–196, 1988.

Michaelsen, J., X. Zhang, and R. C. Smith, Variability of pigment biomass in the California Current system as determined by satellite imagery, 2, Temporal variability, *J. Geophys. Res.*, *93*, 10,883–10,896, 1988.

Miller, C. B., H. P. Batchelder, R. D. Brodeur, and W. G. Pearcy, Response of the zooplankton and ichthyoplankton off Oregon to the El Niño event of 1983, in *El Niño North*, edited by W. S. Wooster and A. L. Fluharty, pp. 185–187, Washington Sea Grant Program, University of Washington, Seattle, 1985.

Morel, A., and L. Prieur, Analysis of variations in ocean color, *Limnol. Oceanogr.*, *22*, 709–722, 1977.

Moum, J. N., D. R. Caldwell, and P. J. Stabeno, Mixing and intrusions in a rotating cold-core feature off Cape Blanco, Oregon, *J. Phys. Oceanogr.*, *18*, 823–833, 1988.

Mueller, J. L., Numbus-7 CZCS: Confirmations of its radiometric sensitivity decay rate through 1982, *Appl. Opt.*, *24*, 1043–1047, 1985.

Mueller, J. L., Nimbus-7 CZCS: Electronic overshoot due to cloud reflectance, *Appl. Opt.*, *27*, 438–440, 1988.

Mullin, M. M., Spatial and temporal scales and patterns, in *Plankton Dynamics of the Southern California Bight*, edited by R. W. Eppley, pp. 216–273, Springer-Verlag, New York, 1986.

Nelson, C. S., Wind stress and wind stress curl over the California Current, *Rep. NMFS SSRF-714*, 87 pp., Nat. Oceanic and Atmos. Admin., Monterey, Calif., 1977.

Niiler, P. P., P.-M. Poulain, and L. R. Haury, Synoptic three-dimensional circulation in an onshore-flowing filament of the California Current, *Deep Sea Res.*, *36*, 385–405, 1989.

Norton, J., D. McLain, R. Brainard, and D. Husby, The 1982–83 El Niño event off Baja and Alta California and its ocean climate context, in *El Niño North*, edited by W. S. Wooster and D. L. Fluharty, pp. 44–72, Washington Sea Grant Program, University of Washington, Seattle, 1985.

Pan, D., J. F. R. Gower, and G. A. Barstad, Seasonal variation of the surface chlorophyll distribution along the British Columbia coast as shown by CZCS satellite imagery, *Limnol. Oceanogr.*, *33*, 227–244, 1988.

Pares-Sierra, A., and J. J. O'Brien, The seasonal and interannual variability of the California Current System: A numerical model, *J. Geophys. Res.*, *94*, 3159–3180, 1989.

Pavlova, Y. V., Seasonal variations of the California current, *Oceanology Engl. Transl.*, *6*, 806–814, 1966.

Pearcy, W. J., and A. Schoener, Changes in the marine biota coincident with the 1982–1983 El Niño in the northeastern subarctic Pacific Ocean, *J. Geophys. Res.*, *92*, 14,417–14,428, 1987.

Pearcy, W., J. Fisher, R. Brodeur, and S. Johnson, Effects of the 1983 El Niño on coastal nekton off Oregon and Washington, in *El Niño North*, edited by W. S. Wooster and D. L. Fluharty, pp. 188–204, Washington Sea Grant Program, University of Washington, Seattle, 1985.

Peláez, J., and J. A. McGowan, Phytoplankton pigment patterns in the California Current as determined by satellite, *Limnol. Oceanogr.*, *31*, 927–950, 1986.

Rienecker, M. M., and L. L. Ehret, Wind stress curl variability over the North Pacific from the Comprehensive Ocean-Atmosphere Data Set, *J. Geophys. Res.*, *93*, 5069–5077, 1988.

Rienecker, M. M., and C. N. K. Mooers, The 1982–1983 El Niño signal off northern California, *J. Geophys. Res.*, *91*, 6597–6608, 1986.

Richman, M. B., Rotation of principal components, *J. Climatol.*, *6*, 293–335, 1986.

Riley, G. A., Phytoplankton in the north central Sargasso Sea 1950–52, *Limnol. Oceanogr.*, *2*, 252–270, 1957.

Roesler, C. S., and D. B. Chelton, Zooplankton variability in the California Current, 1951–1982, *Rep. 20*, pp. 89–101, Calif. Coop. Oceanic Fish. Invest., Univ. of Calif., San Diego, La Jolla, 1987.

Scripps Institution of Oceanography, Physical, chemical and biological data report, *S.I.O. Ref. 84-18*, Univ. of Calif., San Diego, La Jolla, 1984*a*.

Scripps Institution of Oceanography, Physical, chemical and biological data report, *S.I.O. Ref. 84-23*, Univ. of Calif., San Diego, La Jolla, 1984*b*.

Scripps Institution of Oceanography, Physical, chemical and biological data report, *S.I.O. Ref. 84-25*, Univ. of Calif., San Diego, La Jolla, 1984*c*.

Scripps Institution of Oceanography, Physical, chemical and biological data report, *S.I.O. Ref. 84-30*, Univ. of Calif., San Diego, La Jolla, 1984*d*.

Simpson, J. J., El Niño-induced onshore transport in the California Current during 1982–1983, *Geophys. Res. Lett.*, *11*, 233–236, 1984.

Simpson, J. J., C. J. Koblinsky, J. Peláez, L. R. Haury, and D. Wiesenhahn, Temperature–plant pigment–optical relations in a recurrent offshore mesoscale eddy near Point Conception, California, *J. Geophys. Res.*, *91*, 12,919–12,936, 1986.

Smith, R. C., Remote sensing and the depth distribution of ocean chlorophyll, *Mar. Ecol.*, *5*, 359–361, 1981.

Smith, R. C., X. Zhang, and J. Michaelsen, Variability of pigment biomass in the California current system as determined by satellite imagery, 1, Spatial variability, *J. Geophys. Res.*, *93*, 10,863–10,882, 1988.

Spillane, M. C., D. B. Enfield, and J. S. Allen, Intraseasonal oscillations in sea level along the west coast of the Americas, *J. Phys. Oceanogr.*, *17*, 313–325, 1987.

Strub, P. T., and C. James, Evaluation of surface wind fields over the coastal ocean off western U.S., in *Coastal Ocean Prediction Systems*, Report of planning workshop held 31 October to 2 November 1989, Univ. of New Orleans, vol. II, edited by C. N. K. Mooers, JOI Rep., in press, 1990.

Strub, P. T., J. S. Allen, A. Huyer, R. L. Smith, and R. C. Beardsley, Seasonal cycles of currents, temperatures, winds, and sea level over the northeast Pacific continental shelf: 35°N to 48°N, *J. Geophys. Res.*, *92*, 1507–1526, 1987*a*.

Strub, P. T., J. S. Allen, A. Huyer, and R. L. Smith, Large-scale structure of the spring transition in the coastal ocean off western North America, *J. Geophys. Res.*, *92*, 1527–1544, 1987*b*.

Sverdrup, H. U., On conditions for the vernal blooming of phytoplankton, *J. Cons. Explor. Mer.*, *18*, 287–295, 1953.

Tassan, S., A global sensitivity analysis for the retrieval of chlorophyll concentrations from remotely sensed radiances—The influence of the wind, in *Oceanography From Space*, edited by J. F. R. Gower, pp. 371–376, Plenum, New York, 1981.

Thomas, A. C., and W. J. Emery, Winter hydrography and plankton distributions on the southern British Columbia shelf, *Can. J. Fish. Aquat. Sci.*, *43*, 1249–1258, 1986.

Thomas, A. C., and W. J. Emery, Relationships between near-surface plankton concentrations, hydrography, and satellite-measured sea surface temperature, *J. Geophys. Res.*, *93*, 15,733–15,748, 1988.

Thomas, A. C., and P. T. Strub, Interannual variability in phytoplankton pigment distribution during the spring transition along the west coast of North America, *J. Geophys. Res.*, *94*, 18,095–18,117, 1989.

Traganza, E. D., V. M. Silva, D. M. Austin, W. E. Hanson, and S. H. Bronsink, Nutrient mapping and recurrence of coastal upwelling centers by satellite remote sensing: Its implication to primary production and the sediment record, in *Coastal Upwelling: Its Sediment Record*, edited by E. Suess and J. Thiede, pp. 61–83, Plenum, New York, 1983.

M.R. Abbott, C. James, P.T. Strub, and A.C. Thomas, College of Oceanography, Oregon State University, Oceanography Admin. Bldg. 104, Corvallis, OR 97331.

(Received June 27, 1989;
revised November 20, 1989;
accepted November 28, 1989.

APPENDIX H

RELATIONSHIPS BETWEEN NEAR-SURFACE PLANKTON CONCENTRATIONS HYDROGRAPHY, AND SATELLITE-MEASURED SEA SURFACE TEMPERATURE

A. C. Thomas and W. J. Emery

JOURNAL OF GEOPHYSICAL RESEARCH, VOL. 93, NO. C12, PAGES 15,733–15,748, DECEMBER 15, 1988

Relationships Between Near-Surface Plankton Concentrations, Hydrography, and Satellite-Measured Sea Surface Temperature

A. C. THOMAS[1] AND W. J. EMERY[2]

Department of Oceanography, University of British Columbia, Vancouver, Canada

In situ measurements of surface chlorophyll and zooplankton concentration are compared with in situ hydrographic measurements and infrared satellite images of the west coast of British Columbia for early winter and midsummer study periods. Maximum winter concentrations of chlorophyll (1.0 mg m^{-3}) and zooplankton (2900 counts m^{-3}) were found in colder, more stratified nearshore water. Warmer water over the middle and outer shelf consistently had the lowest chlorophyll and zooplankton concentrations (<0.2 mg m^{-3} and <1700 counts m^{-3}, respectively). Correlations between winter $\log_e$ transformed zooplankton concentrations and surface temperature demonstrated that infrared satellite imagery explained 49% of the sampled zooplankton concentration variance. The winter association of specific chlorophyll concentrations with identifyable hydrographic regimes enabled the satellite imagery, in conjunction with an image-derived salinity model, to explain 55% of the sampled chlorophyll variance. Maximum summer chlorophyll concentrations (>20.0 mg m^{-3}) coincided with intermediate temperatures around the edge of an upwelling frontal zone with lower concentrations (≈ 5.0 mg m^{-3}) in the coldest, most recently upwelled water. Lowest concentrations (<1.0 mg m^{-3}) were present in vertically stratified regions of the shelf. A least squares fit nonlinear equation showed that satellite-measured surface temperature patterns explained 72% of the $\log_e$ transformed chlorophyll variance. In contrast with the above relationships, summer zooplankton concentrations were not consistently related to satellite temperature patterns. While peaks showed a qualitative association with higher chlorophyll concentrations at the outer edge of the upwelling area, surface temperature was a poor predictor of zooplankton concentration over the study area as a whole.

INTRODUCTION

In the past, the mapping of plankton distributions and the development of models relating them to physical oceanographic processes, especially in complex and dynamic continental shelf regions, have suffered from the unavoidable nonsynoptic nature of ship sampling. It is extremely difficult, especially with nonconservative biological variables, to separate spatial variability from temporal variability. Satellite infrared images of sea surface temperature (SST) provide a means of synoptically mapping and monitoring the surface signature of many of the physical processes which potentially have important biological implications. To the extent that plankton spatial patchiness is a response to physical processes, surface distributions of phytoplankton and zooplankton may be correlated with surface thermal features visible in satellite imagery. Satellite images of sea surface temperature may thus contain valuable information about the spatial and temporal distribution of surface plankton. In this paper we examine the extent to which satellite images of sea surface temperature reflect distributions of near-surface phytoplankton and zooplankton. Our purpose is not only to examine relationships between hydrographic properties and plankton concentrations but also to show simple, quantitative relationships between the cheap and readily available synoptic coverage of infrared satellite imagery and more expensive and, at best, quasi-synoptic surface plankton measurements.

The importance of physical processes in determining the patterns and dominant spatial scales of biological variability was reviewed by *Denman and Powell* [1984], *Legendre and Demers* [1984], and *Mackas et al.* [1985]. Temperature has often been used as an indicator of the physical regime for comparison with plankton distributions [e.g., *Denman and Platt*, 1975; *Denman*, 1976; *Fasham and Pugh*, 1976; *Fournier et al.*, 1979; *Simpson et al.*, 1986], demonstrating that significant correlations exist between the thermal regime of the ocean and plankton distributions. These correlations can result from a direct biological response to temperature per se [e.g., *Eppley*, 1972], or more commonly from either direct interaction with mixing and advective processes or indirect interaction through trophic relationships [e.g., *Lekan and Wilson*, 1978; *Steele and Henderson*, 1979; *Smith and Vidal*, 1984].

Especially in dynamic areas, the synoptic perspective of infrared remote sensing has proved valuable in showing the spatial relationships between physical features and plankton distributions [*Traganza et al.*, 1983; *Abbott and Zion*, 1985; *Campbell and Esaias*, 1985; *Simpson et al.*, 1986]. These relationships have been shown to apply not only to chlorophyll distributions but also to zooplankton distributions [*Wiebe et al.*, 1985; *Haury et al.*, 1986; *Boyd et al.*, 1986] and fish distributions [*Breaker*, 1981; *Lasker et al.*, 1981; *Laurs et al.*, 1984].

An early winter sampling period and a midsummer sampling period were used to investigate relationships between satellite-measured surface thermal patterns, hydrography, and in situ plankton distributions over the southern continental shelf off Vancouver Island, British Columbia. The study area and relevant bathymetry are shown in Figure 1. *Thomas and Emery* [1986] showed that patterns of winter chlorophyll and zooplankton concentration in this region were closely related to in situ hydrographic properties. The cross-shelf position of the northward flowing Davidson Current was correlated with regions of lower chlorophyll and zooplankton concentrations.

[1]Now at College of Oceanography, Oregon State University, Corvallis.

[2]Now at Colorado Center for Atmospheric Research, University of Colorado, Boulder.

Paper number 88JC03322.
0148-0227/88/88JC-03322$05.00

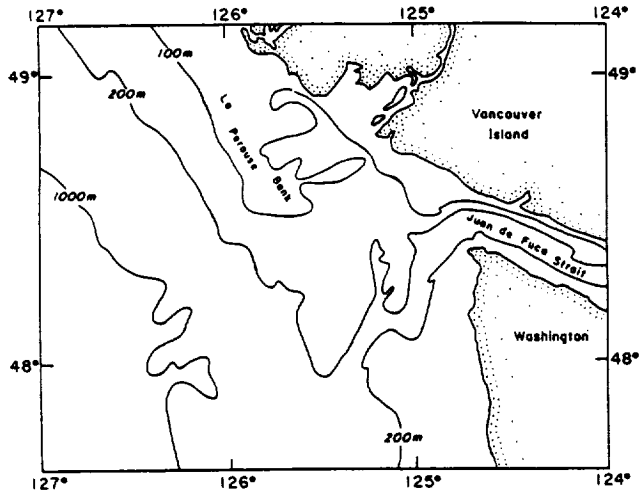

Fig. 1. The study area on the southern British Columbia continental shelf, showing bathymetry and relevant geographic features.

Colder and more stratified nearshore water was associated with higher plankton concentrations.

The summer southern British Columbia shelf is dominated by intense spatial and temporal patchiness of both phytoplankton and zooplankton biomass [*Mackas et al.*, 1980; *Denman et al.*, 1981; *Mackas*, 1984]. Dissimilarity correlograms calculated by *Mackas* [1984] showed that summer plankton patchiness patterns are stretched parallel to the bathymetry with cross-shelf correlation scales one-third shorter than the alongshore scales. Satellite images of ocean color along the shelf edge demonstrate the patchy nature of the chlorophyll distribution and its general relationship to flow patterns [*Thomson and Gower*, 1985]. *Mackas et al.* [1980] and *Denman et al.* [1981] showed that summer zooplankton and phytoplankton concentrations were relatively high inshore of an alongshore salinity front, but lower seaward of this front, over the middle shelf. Localized peaks in phytoplankton and zooplankton biomass were present over both shallow banks and the outer shelf edge. Wind-driven upwelling is known to occur during the summer [*Ikeda and Emery*, 1984]. *Freeland and Denman* [1982], however, showed that the arrival of deep, nutrient rich water on the shelf is often uncoupled from the wind forcing. They argued that localized upwelling off the mouth of Juan de Fuca Strait is most likely associated with a topographically induced cyclonic eddy.

These previous studies have shown the southern British Columbia shelf to be physically dynamic and likely to have strong surface thermal gradients. Many of these processes and features are visible to infrared satellite imagery [e.g., *Ikeda and Emery*, 1984; *Thomas and Emery*, 1986; *Emery et al.*, 1986]. The shelf also has a productive and heterogeneous plankton regime which these studies have shown to be closely coupled to the physical regime. This continental shelf region therefore provides a suitable location to examine relationships between infrared satellite imagery and plankton distributions.

Data Collection and Processing

Advanced very high resolution radiometer (AVHRR) satellite images of the west coast of British Columbia were received and processed at the University of British Columbia Satellite Oceanography Laboratory during two in situ sampling periods representing an early winter situation (November 28 to December 3, 1983) and a mid summer situation (July 10–18, 1984). Cloud-free weather along the British Columbia coast during both periods resulted in sequences of 10 infrared images of the study area for the winter sampling period and 15 infrared images for the summer sampling period. Raw satellite data were processed into navigated images of maximum spatial resolution (1 pixel = 1.1 km) according to the procedure described by *Emery and Ikeda* [1983] using high-quality satellite ephemeris data supplied by the U.S. Navy. Final navigational accuracy was usually within one pixel over the entire image. Land- and cloud-contaminated pixels in each image were manually flagged. Attempts to use a split-window atmospheric correction [*McClain*, 1981] for these images resulted in an unacceptable increase in the spatial variance of the resultant temperature signal. This variance was most likely due to uncorrelated noise in channels 4 and 5. Although spatial filters would reduce this noise, they would also blur small-scale thermal patterns and gradients. In situ near-surface temperature measurements were used as ground truth data to provide the equivalent of an atmospheric correction for channel 4 of each satellite image. This assumes a horizontally homogeneous atmospheric attenuation which is likely to be valid over the relatively small study area, provided that pixels contaminated with cloud or fog are avoided. Ship measurements of surface temperature from cross-shelf transects were compared with satellite measurements from the same geographic locations and the least possible temporal separation (always less than 12 hours). A mean bias was calculated for each satellite image based on these transects and subtracted from the entire image to produce two temperature data sets of minimum root-mean-square difference. These mean biases (t_{ship}-$t_{channel4}$) ranged between 2.3° and 3.8°C. Correlations between satellite- and ship-measured temperature along the transects used to make these corrections ranged between 0.901 and 0.992 (the number of observations ranged from 72 to 108).

Near-surface measurements of temperature, salinity, fluorescence, and zooplankton-sized particle abundance were made once per minute along a series of cross-shelf transects using a continuous flow, high-resolution, automated sampling system. The transects sampled during each cruise are shown in the next section, superimposed on concurrent satellite imagery. A detailed description of the apparatus and its use is given by *Mackas et al.* [1980] and will not be repeated here. Sampling depth was 1.5 m during the winter cruise, when the automated sampling system was linked to the ship's water intake and sea chest. Different plumbing aboard the summer research vessel did not allow a similar linkup, and water was sampled from ≈0.5 m through a towed hose (≈8 cm internal diameter) attached to a worm-gear pump. Flow rates through the automated sampler were ≈16 L min^{-1} and ≈13 L min^{-1} during the winter and summer, repectively. Logistics necessitated the use of a different prototype of the automated sampling system for the two sampling periods. Discrete samples were withdrawn from the sampling apparatus at half-hourly intervals and used for instrument calibration and later nutrient analysis. Fluorescence was converted to chlorophyll concentration by regression and was used as a measure of phytoplankton biomass. Particle counts were used as an estimation of zooplankton abundance. The instrument counts particles in the water presented to it in the size range 0.3–3.0 mm. Although this is the smaller end of the zooplankton size spectrum, it does represent the numerically dominant portion of the population [*Mackas et al.*, 1980]. The counts thus give a

biased representation of total biomass distribution but a realistic estimate of the relative numbers of small zooplankton. Surface temperatures recorded during the winter cruise included a small but significant ($\approx 0.5°C$) positive offset caused by warming in the ship's plumbing system [see *Mackas et al.*, 1980]. This bias was constant; as emphasis in this study is on relative temperatures and spatial patterns, no attempt was made to correct for this offset.

At a cruising speed of approximately 18.5 km h^{-1}, the spatial resolution of the near-surface in situ data was ≈ 300 m. Obviously bad data points were first removed, and then the data record was averaged into 1-km bins. This smoothing procedure eliminated small-scale structure but reduced the noise level, producing an in situ data set with a spatial resolution similar to that of the AVHRR data.

To reduce apparent spatial patchiness in the zooplankton data caused by diurnal vertical migrations, each of the winter transects, and each of the summer transects except part of leg 4, were sampled during daylight. Although night might have been a more effective time to sample, this portion of the cruises was utilized by other biological sampling.

Vertical temperature-salinity (T-S) profiles were obtained with a Guildline conductivity-temperature-depth probe (CTD) at stations 18.5 km apart along each of the winter transects. Summer vertical temperature profiles were collected using an expendable bathythermograph (XBT). Summer station spacing was 9.25 and 18.5 km across shelf and 18.5 km along shelf. The geographic locations of these stations are given in the next section in relation to the concurrent satellite-measured surface thermal patterns.

Two approaches were used to quantify similarities between satellite-measured thermal patterns and plankton distributions. The first approach used a least squares approximation to define regression equations relating plankton concentrations with satellite surface temperature. The regression coeficients were then used to create a "plankton" image from the mean satellite temperature image and the relationship between image (modeled) concentrations and ship-measured concentrations used as a measure of similarity. The second approach expanded on relationships between specific plankton concentrations and hydrographic zones identified in temperature-salinity-plankton plots. Specific zones within each image were isolated by density slicing the thermal image at subjectively chosen thresholds. Each zone was then assigned the mean plankton concentration calculated from the in situ data points within the threshold boundaries and a "plankton" image created from these regions. The statistical relationship between modeled and measured concentrations was then calculated and used as a measure of similarity.

Three statistics were used to quantify the relationship between modeled and measured plankton concentrations. A root-mean-square (rms) difference between the two quantities provided a dimensional estimate of the model success in the same units as the treated data. The rms difference was defined as

$$\text{rmsdif} = \left[\frac{1}{N}\sum_{i=1}^{N}(x_i - \hat{x}_i)^2\right]^{1/2}$$

where x_i are the actual measured concentrations, $\hat{x}_i$ are the modeled values from the same locations in the "plankton" image, and N is the number of data points. This statistic is equal to the standard deviation when the modeled value is the mean of the measured values (as it was within specific hydrographic regimes following the second modeling approach). Comparisons of model successes between the different units of chlorophyll and zooplankton concentration, and also between various normalizing transformations of the plankton data, were made with a dimensionless "error" term defined by normalizing the mean square difference by the original variance. Total model error was defined as

$$\varepsilon^2 = \frac{\sum (x_i - \hat{x}_i)^2}{\sum (x_i - \bar{x})^2}$$

where $\bar{x}$ is the mean of the measured plankton values and other terms are as previously defined. This term is the proportion of the original variance unexplained by the model, and the term

$$r^2 = \frac{\sum (\hat{x}_i - \bar{x})^2}{\sum (x_i - \bar{x})^2}$$

is the proportion of the variance explained by the model. Both of these terms are nondimensional, and it can be seen that

$$\varepsilon^2 + r^2 = 1$$

The number of degrees of freedom in these calculations is not easily defined. The statistics just defined incorporate both the large-scale field of variability (gradients larger than the length of the transects), which will not have been sampled in a statistically adequate manner, and smaller-scale variability (gradients shorter than the transects), which will have been sampled adequately. The number of data points used in these calculations was 461 and 453 respectively, for the winter and summer cruises. Each of these data points, however, cannot be considered independent [*Mackas*, 1984; *Millard et al.*, 1985] owing to the short distance between them (high rate of sampling) relative to the length scales of oceanographic processes. The separation of the data points was 1 km, considerably less than the ≈ 30 km length scales observed to dominate this region of the continental shelf by *Denman and Freeland* [1985]. For temperature and salinity, this spatial autocorrelation is a result of mixing associated with eddies, tidal advection, and other processes with length scales larger than 1 km. The autocorrelation of chlorophyll and zooplankton is a result of interaction with these physical processes as well as biological processes, all of which induce well-known spatial patchiness.

The statistics utilize the total variability within the data. In the absence of a precise method of calculating the degrees of freedom associated with them, we first separate the larger- and smaller-scale variability and then present arguments for the degrees of freedom and/or significance of each.

WINTER AND SUMMER HYDROGRAPHIC ZONATION

Satellite-Measured Surface Thermal Patterns

The sea surface temperature in each region of the winter shelf remained approximately constant over the period of in situ sampling. Furthermore, visual analysis of the winter satellite image series showed that the overall pattern of sea surface temperature remained nearly constant over the sampling period and that most of the interimage variability was at smaller scales (of the order of 5–10 km). The correlation of surface thermal patterns in the winter satellite image sequence

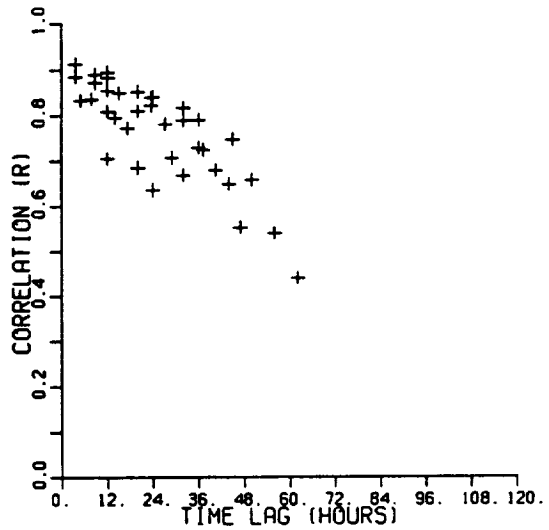

Fig. 2. Temporal correlation of winter surface thermal patterns in the study area calculated from correlations between all possible pairs of detrended satellite images.

over the sampling period is shown in Figure 2. Correlations were calculated between all possible pairs of images using image subsamples ($\approx 150 \times 150$ km) centered on the shelf study area and plotted as a function of their temporal separation. A large component of a simple correlation between images would be due to the dominant cross-shelf gradient in temperature which was present in each image. To isolate and examine underlying thermal patterns, this gradient was removed from each image subsample by calculating and subtracting the least squares fit plane (in x, y, t°C space) of each image from itself. Correlation calculations shown in Figure 2 were then made on the residual thermal pattern.

The high correlation of thermal patterns over the winter study period permitted the nine image sequence to be reduced to a single mean image representing the surface thermal regime present during the winter cruise. This decision is supported by *Denman and Freeland* [1985], who concluded that surface thermal patterns on the British Columbia shelf over time periods of a single cruise (≈ 10 days) can be considered synoptic. Plate 1 shows the winter mean image calculated as the arithmetic mean of the nine most cloud-free images, with surface sampling transects and vertical stations superimposed. (Plate 1 can be found in the separate color section in this issue.) Only pixels which were cloud free in five or more images were used to calculate a mean temperature; pixels failing this criterion were classified as cloud.

The mean image shows the winter shelf could be divided into three major surface thermal zones. The dominant feature of this image is a region of warmest water over the middle and outer shelf, with temperatures above 12.2°C (warm zone). Maximum cross-shelf penetration of this warm water was in the southern portion of the study area, immediately south of La Perouse Bank. At La Perouse Bank the warm water curved offshore, away from the shelf. Coldest surface water was present as a continuous zone closest to shore, with temperatures below 11.5°C (cold zone). A distinct feature of this cold coastal zone was a tongue extending away from shore in a southward direction in the vicinity of La Perouse Bank. A frontal zone created by the strong surface thermal gradient separating cold coastal water from warmer water over the middle and outer shelf is visible in the image. Surface water seaward of the warmest band, over the outer shelf, formed a third thermal zone with intermediate temperatures of 11.6°C (offshore zone). Water seaward of this zone was colder (11.0°C in the satellite image) but was never sampled by the ship (see Plate 1). Although this water clearly formed another surface thermal zone, it will not be treated in this study, as no in situ data were available for comparison.

Visual analysis of the summer image series revealed significant changes in the overall surface thermal pattern in the study area over the period of in situ sampling. A mean image for the entire summer image series was therefore not meaningful, and all in situ data could not be considered synoptic. The correlation of summer surface thermal patterns in the study area over time (Figure 3) was calculated from detrended images in the same manner as the winter sequence.

Over time periods of less than 36 hours, surface patterns remained highly correlated. At separations starting at 24 hours, however, the range in correlation values began to increase. At 48 hours separation, correlations ranged from 0.72 to 0.38. This reflects a short time scale "event" which rapidly

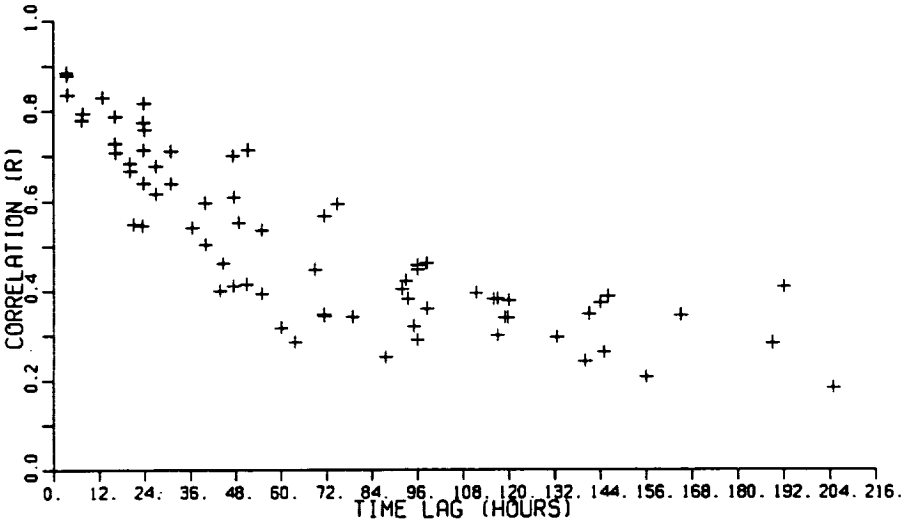

Fig. 3. Temporal correlation of summer surface thermal patterns in the study area calculated from correlations between all possible pairs of detrended satellite images.

changed surface temperatures and patterns on July 16–17. Prior to this event, image patterns remained similar, and high correlations in Figure 3 extend to separations as long as 72 hours. Extrapolated structure functions from data averaged over 25 cruises [*Denman and Freeland*, 1985] show that near-surface thermal patterns might be considered synoptic for time scales of less than 10 days. Although the satellite-measured surface skin temperature is probably less conservative than the integrated upper layers measured by these authors, data presented here suggest that specific events during the summer can make time scales of synopticity considerably shorter than this 10-day mean.

The summer image sequence was condensed into two representations for comparison with in situ plankton data. A mean image (Plate 2*a*) represents the arithmetic mean of the nine highly correlated images recorded prior to the cooling event on July 16–17. (Plate 2 can be found in the separate color section in this issue.) This image shows that the shelf area south of La Perouse Bank and over Juan de Fuca Canyon remained relatively cold throughout the study period, with thermal patterns retaining a generally circular shape (a cold zone). Mean surface temperatures in this region ranged from 11.5° to 12.6°C. The shelf areas seaward and also north of this region, over La Perouse Bank, were relatively warm during this early portion of the study period, with mean surface temperatures ranging from 13.5° to 15.5°C (warm zone). The region over La Perouse Bank, however, cooled rapidly during the study period. The strong similarity of surface thermal patterns during the latter portion of the study period and those presented by *Ikeda and Emery* [1984] suggests that this cooling event was a wind-driven upwelling event. This is supported by unquantified observations from the ship of winds exceeding 10 m s^{-2} out of the northwest starting on July 15. Bakum wind data for this period (B. M. Hickey et al., manuscript in preparation, 1988) show an increase in upwelling favorable winds during this period. In situ sampling during this cooling event was restricted to a single transect (leg 6). A single concurrent image (Plate 2*b*) is used to represent surface thermal patterns during this latter portion of the summer sampling period. This image shows the continued presence of the cold region off the mouth of Juan de Fuca Strait. North of this zone, however, the shelf is now dominated by colder surface water. A tongue of warmer water extends northward across the shelf, isolated by this colder water. This tongue was presumably a residual of the stratified warm water which had previously occupied this portion of the shelf (see Plate 2*a*).

Surface and Subsurface Hydrography

Contour plots of the spatial distribution of winter surface temperature and salinity presented by *Thomas and Emery* [1986] indicated the association of low temperatures with low salinities; they also showed this water to be restricted to the inner shelf and most pronounced off the mouth of Juan de Fuca Strait. Surface salinity distribution over the shelf increased from less than 30 in nearshore areas, to 32 over the outer shelf. A steep salinity gradient (1.0 in 4 km) was coincident with the thermal front evident in the mean satellite image separating colder coastal regions from warmer regions over the middle shelf (Plate 1). The surface expression of the 31.5 isohaline extended furthest from shore in the La Perouse Bank area forming a low-salinity, low-temperature tongue. The thermal expression of this can be seen in the vicinity of the northern three transects (Plate 1).

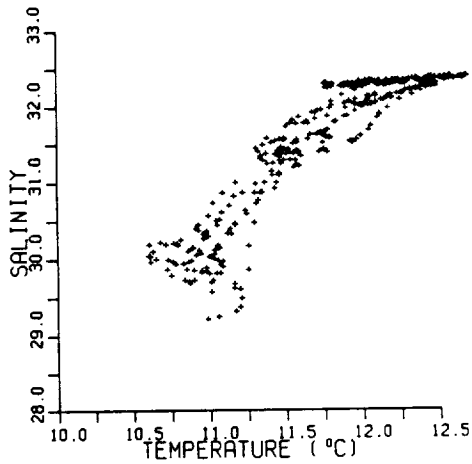

Fig. 4. Winter surface *T-S* relationships from in situ sampled data (all transects).

Temperature-salinity plots of surface data from the water study period (Figure 4) show the hydrographic relationship of surface waters and support the surface zonation inferred from the satellite imagery. Nearshore water had the lowest temperatures (< 11.5°C) and salinities (< 31.5). Two types of surface water with higher salinities (> 32.0) can also be differentiated by temperature in the plots. Warmest temperatures in the study area were above 12.2°C. A second high-salinity water type had temperatures between 11.5°C and 12.2°C. Other T-S pairs form a line between coastal water characteristics and the warmest, high-salinity water, indicating that mixing and interaction between colder coastal water and the warmest water formed a major portion of sampled surface water over the winter shelf. Contours of subsurface temperature and salinity from legs 1 and 4 (Figure 5) show the inner-shelf colder, low salinity water was a near-surface feature. The warmest surface water visible in the satellite image was a distinct core of warm water (< 11.5°C) over the middle and outer shelf.

Thomas and Emery [1986] identified the zone of relatively warm water over the outer shelf visible in both satellite imagery and in vertical profiles of temperature as the northward flowing Davidson Current which *Ikeda et al.* [1984] identified in winter infrared imagery of the same area. The shallow, cold, and relatively fresh water near shore is indicative of estuarine influence from Juan de Fuca Strait and/or coastal rivers. The colder regions visible in the satellite imagery therefore represent the buoyancy-driven Vancouver Island Coastal Current [*Freeland et al.*, 1984; also, B. M. Hickey et al., manuscript in preparation, 1988]. Vertical profiles identify these regions as the most strongly stratified areas of the shelf during the winter. The satellite imagery documents the extension and isolation of coastal current water out over the shelf in the vicinity of La Perouse Bank.

Regions of large surface temperature gradient, identified in the imagery (Plate 1), were coincident with large salinity gradients [*Thomas and Emery*, 1986] and formed a frontal zone separating Vancouver Island Coastal Current water from Davidson Current water. Water seaward of the Davidson Current had a similar high salinity but lower temperatures and is termed offshore water in this study. This water represents the most oceanic of the water types sampled during the winter study period.

The summer *T-S* plot (Figure 6*a*) of surface characteristics prior to the cooling event shows a general trend of colder

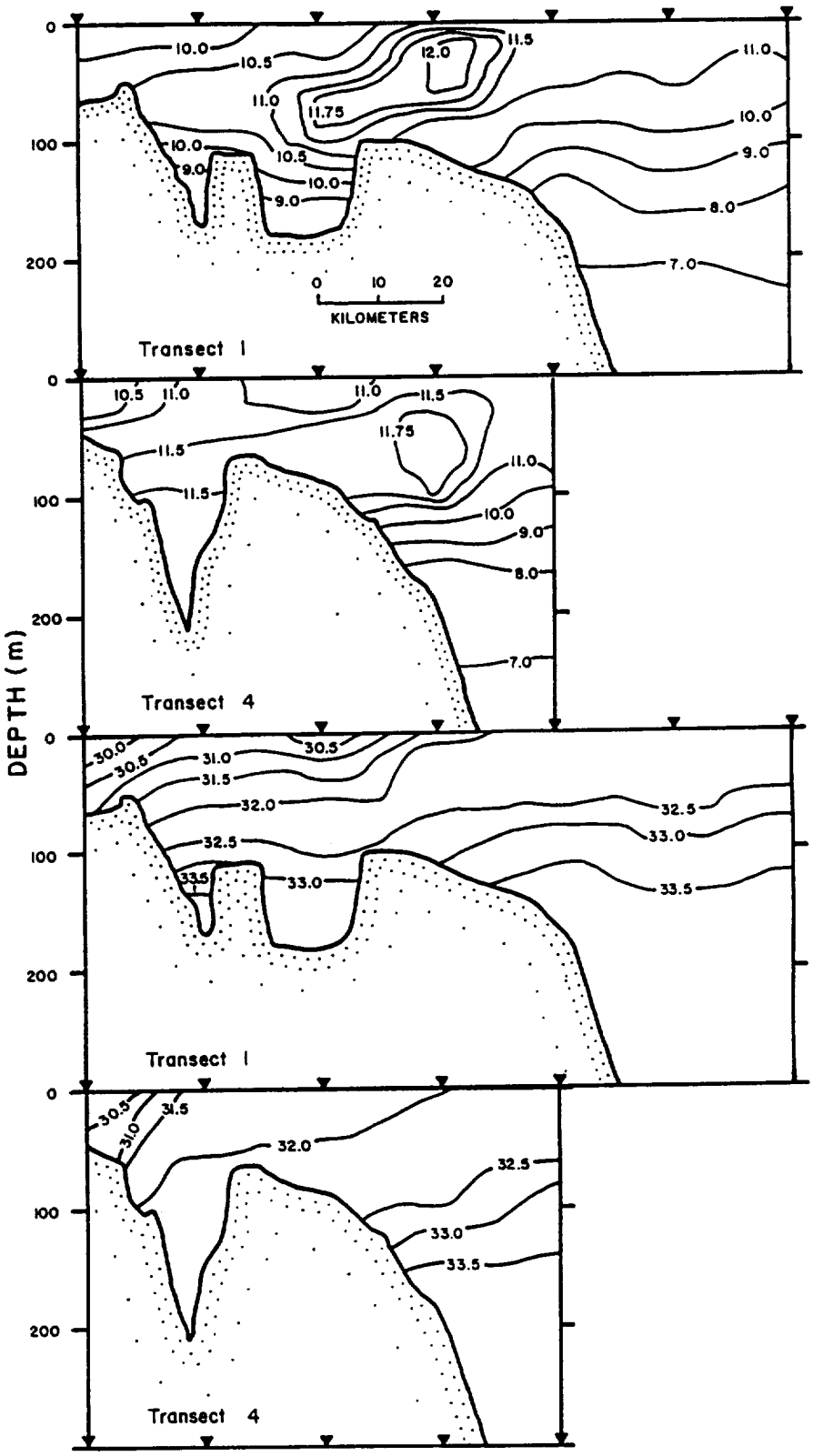

Fig. 5. Cross-shelf contours of winter subsurface temperature and salinity from stations along transects 1 and 4. Triangles represent station locations, also shown in Plate 1. Depth is in meters.

temperatures associated with higher salinities but does not give a clear definition of water masses and mixing trends. This is most likely due to strong summer solar heating of surface water, which would change the relationship between surface temperature and salinity over relatively short time periods. Surface temperatures in this region are likely to be more variable in the summer than in winter, when air-sea temperature differences are small and solar heating is minimal. *T-S* characteristics of surface water during the cooling event (Figure 6*b*) indicate that although surface temperature patterns have

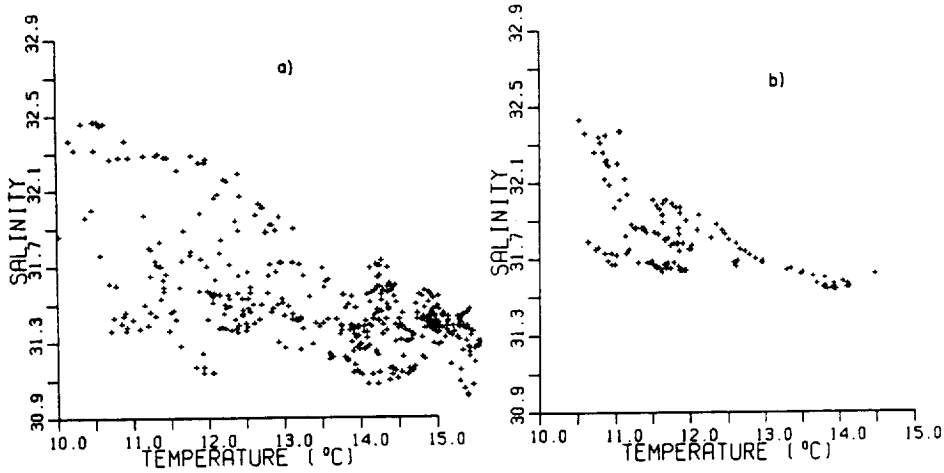

Fig. 6. Summer surface T-S relationships of in situ data from (*a*) precooling event data (transects 1–4) and (*b*) data during the cooling event (transect 6).

changed, temperature and salinity properties of surface water have not. This figure shows that the warm tongue of water visible in Plate 2*b* has the same T-S characteristics as surface water which previously occupied the entire shelf in the northern portion of the study area. This argues that the warm tongue is a residual of the previous stratified conditions.

Summer subsurface isotherms (Figure 7) sloped upward towards the shore. The location of sampling stations is given in Plate 2*a* in relation to surface thermal patterns. Stratification was weakest in the region of colder surface water (leg 2) centered over Juan de Fuca Canyon, where temperatures in the top 5 m were below 11.0°C. A frontal zone separated this vertically mixed water from offshore more stratified water with near-surface temperatures above 13.0°C. In the northern part of the study area (leg 4), over La Perouse Bank, no frontal zone existed during the initial portion of the sampling period, and stratified, offshore conditions extended across the entire shelf.

The summer association of colder surface temperatures with higher salinities is opposite to that found in winter and indicates a subsurface origin of nearshore colder surface water typical of upwelling systems and characteristic of the Pacific west coast during summer [*Pietrafesa*, 1983]. The persistent cold feature in the Juan de Fuca Canyon region identified in the image sequence is most likely the surface expression of upwelling induced by the cyclonic eddy described by *Freeland and Denman* [1982] and analyzed in infrared imagery by *Emery et al.* [1986].

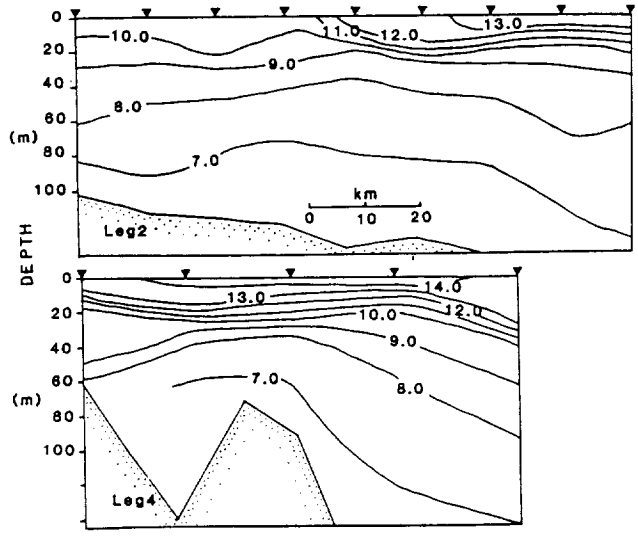

Fig. 7. Cross-shelf contours of summer subsurface temperature from stations through the eddy (leg 2) and north of the eddy (leg 4). Triangles represent station locations, also shown in Plate 2*a*, and depth is in meters.

PLANKTON CONCENTRATIONS AND SURFACE HYDROGRAPHY

Thomas and Emery [1986] showed that winter regions of low temperature and salinity were areas of highest chlorophyll and zooplankton concentration. Maximum biomass was in nearshore regions, associated with Vancouver Island Coastal Current water. In southern portions of the study area (legs 1, 2, and 3), the frontal zone separating this water from warmer and more saline outer shelf water was coincident with localized peaks in both chlorophyll and zooplankton concentration. This peak in concentration, however, did not extend north of the La Perouse Bank area. In warmer water seaward of the frontal zones (Davidson Current and offshore water), zooplankton concentrations were consistently low. Chlorophyll concentrations were lowest in the warmest water over the middle shelf (Davidson Current), and increased again coincident with cooler offshore water over the outer shelf.

Figures 8*a* and 8*b* illustrate this quantitative relationship between winter plankton concentrations and the surface hydrographic zones distinguishable on T-S plots. Water from the Davidson Current, Vancouver Island Coastal Current, and offshore zone were each associated with characteristic chlorophyll and zooplankton concentrations. Vancouver Island Coastal Current water and offshore water generally supported chlorophyll concentrations above 0.51 mg m^{-3}. Offshore water was never associated with concentrations below 0.25 mg m^{-3}. Davidson Current water, however, was associated with concentrations below 0.25 mg m^{-3} and never supported concentrations above 0.51 mg m^{-3}. Zooplankton concentrations above 1900 counts m^{-3} were associated with Vancouver Island Coastal Current water. Both Davidson Current water and offshore water were characterized by zooplankton concentrations below 1500 counts m^{-3}.

While the hydrographic separation of zooplankton con-

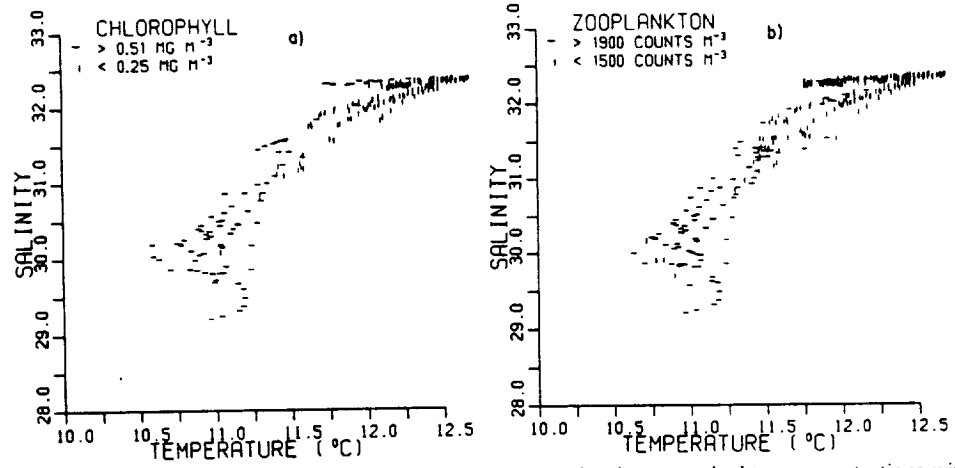

Fig. 8. The association of (*a*) winter chlorophyll concentrations and (*b*) winter zooplankton concentrations with surface *T-S* properties.

centrations in Figure 8*b* is not as robust as that for chlorophyll concentrations (Figure 8*a*), a trend is seen in the sampled points suggesting mixing between Davidson Current water and Vancouver Island Coastal Current water. Values most similar to Davidson Current hydrographic characteristics often had lower chlorophyll and zooplankton concentrations.

Quantitative comparisons of summer plankton concentrations with surface temperature and salinity characteristics indicated a similar association of specific concentrations with shelf hydrography. Data collected prior to the cooling event, during legs 1–4 (Figures 9*a* and 9*b*) showed that shelf regions with surface temperatures above 13.5°C (indicative of the stratified portions of the shelf) never supported chlorophyll concentrations above 5.1 mg m^{-3}. This water was generally

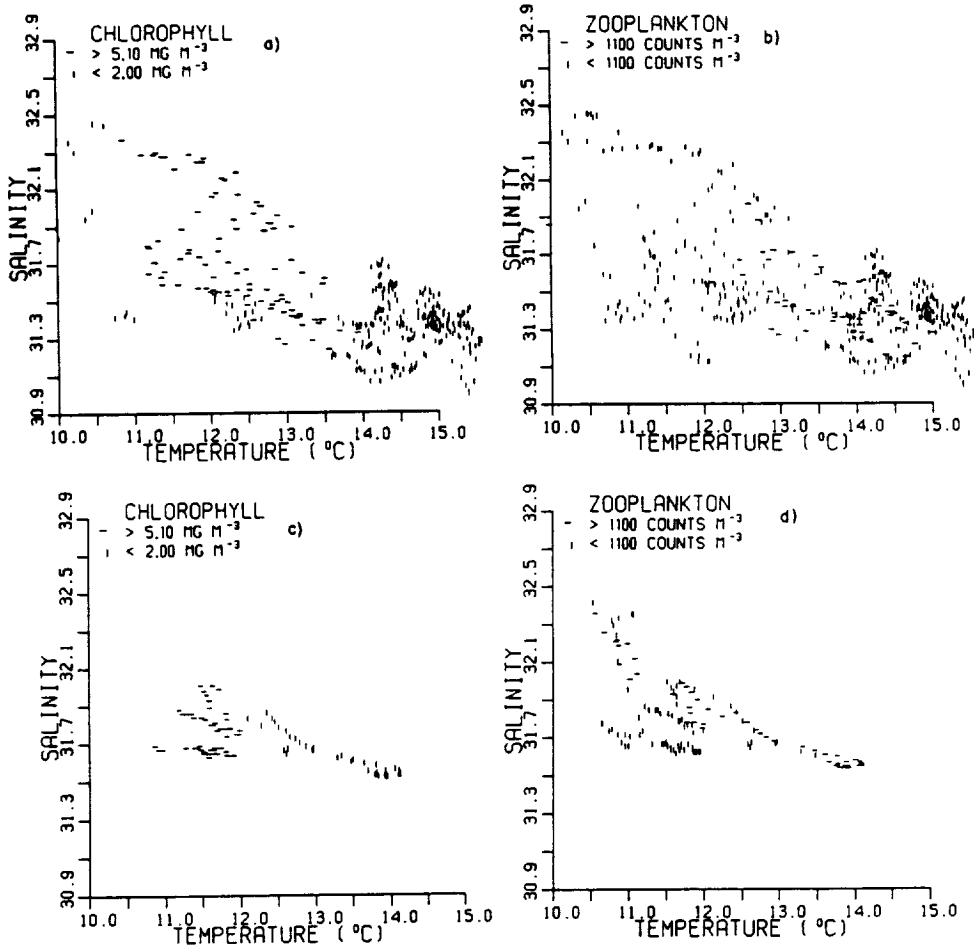

Fig. 9. The association of summer surface plankton concentrations with surface *T-S* properties: (*a*) chlorophyll and (*b*) zooplankton concentrations prior to the cooling event (legs 1–4), and (*c*) chlorophyll and (*d*) zooplankton concentrations during the cooling event (leg 6).

associated with concentrations of less than 2.0 mg m^{-3}. In contrast, hydrographic properties indicative of upwelling, with surface temperatures colder than 13.5°C, rarely had concentrations below 5.1 mg m^{-3}. Exceptions to this pattern occurred at individual sample points with the lowest temperatures (<11.0°C).

Summer zooplankton concentrations prior to the cooling event did not show a consistent association with specific surface hydrographic characteristics (Figure 9*b*). Concentrations above and below the 1100 counts m^{-3} threshold occurred in both the warmer and cooler hydrographic regimes. Although highest concentrations (>1100 counts m^{-3}) showed a general association with intermediate temperatures, this relationship was not consistent. Numerous sample locations with characteristics in this region of *T-S* space had lower zooplankton concentrations. Efforts to divide the zooplankton concentrations at different and more numerous thresholds did not simplify their distributional relationship with surface hydrography.

Zooplankton counts measured during the summer were generally lower than those from the winter, a situation inconsistent with normal seasonal trends. Whether this is real or an artifact of sampling is unknown. As mentioned previously, different automated samplers were used for the two sampling periods. Differences in instrument sensitivity, the actual zooplankton size spectrum present, damage to organisms by the two plumbing systems, and zooplankton avoidance would all contribute to the observed difference. As absolute abundances do not affect the results presented here, no effort has been made to cross correlate the two samplers.

Data sampled during the cooling event along leg 6 (Figures 9*c* and 9*d*) indicate that relationships between chlorophyll concentration and hydrography established previously, were maintained despite the dramatic changes in sea surface temperature pattern evident in Plates 2*a* and 2*b*. Figure 9*c* shows that chlorophyll concentrations greater than 5.1 mg m^{-3} were restricted to colder surface water (<12.1°C). Water warmer than this threshold never supported concentrations greater than 2.0 mg m^{-3}. These data provide biological support for the suggestion based on hydrographic data that this warm tongue was a residual of the warm, stratified water previously occupying this portion of the shelf. Figure 9*d* again shows an ambiguous association between zooplankton concentrations and hydrography but suggests that the warm water tongue was generally associated with higher concentrations (>1100 counts m^{-3}).

PLANKTON CONCENTRATIONS AND SATELLITE TEMPERATURE

Winter plankton concentration thresholds used to examine relationships between concentration and surface hydrography are superimposed on the mean winter satellite image (Plates 3*a* and 3*b*) to show their spatial relationship with satellite-measured sea surface temperature patterns. (Plate 3 can be found in the separate color section in this issue.) These data illustrate the association of thermally defined regions with specific plankton concentrations and show that surface thermal fronts visible in the imagery are coincident with boundaries in the plankton regime. Winter chlorophyll concentrations greater than 0.51 mg m^{-3} are restricted to the cold nearshore zone of the Vancouver Island Coastal Current and the thermal zone seaward of the Davidson Current (offshore water). Increased chlorophyll concentrations are associated with the tongue of coastal current water isolated over the La Perouse Bank area. High concentrations within the coastal current water extend completely into the frontal region in the southern portion of the study area but not at the northern transects on the seaward side of the cold water tongue, indicating a change in biomass associated with the surface frontal zone across the study area. Chlorophyll concentrations of less than 0.25 mg m^{-3} are primarily restricted to surface water warmer than 12.0°C. The spatial distribution of this water and its associated chlorophyll concentration in the image show a penetration into the shelf region south of La Perouse Bank and into surface regions on the nearshore side of the bank. *Thomas and Emery* [1986] discuss the isolation of this water on the shelf in more detail.

Spatial distributions of winter zooplankton concentration in relation to satellite themal patterns (Plate 3*b*) reveal the more simplistic division of plankton and hydrographic zones evident in the zooplankton *T-S*-plankton plot. Higher concentrations are generally restricted to the nearshore portion of the shelf, in coastal current water, including high concentrations within the Coastal Current water in the tongue over La Perouse Bank. In warmer water over the middle and outer shelf, winter zooplankton concentrations remained low. Exceptions to this pattern occurred primarily along the northern two transects, where some higher concentrations were seen in Davidson Current water. It is possible that a lack of synopticity contributes to this anomaly. The satellite images making up the mean image were recorded between 24 and 80 hours prior to this in situ sampling of these two transects. The position of the frontal zone and zooplankton concentrations in the in situ data in this region might not be well represented by the mean satellite image.

Summer chlorophyll concentrations superimposed on the mean satellite image (Plate 4*a*) show a consistent relationship between their distribution and satellite-measured sea surface temperature. (Plate 4 can be found in the separate color section in this issue.) Plate 4*a* shows that highest concentrations were associated with cold water, especially around the outer edge of the cyclonic eddy off the mouth of Juan de Fuca Strait. Lowest concentrations were present both in the coldest water in the center of the eddy and also throughout the warmest water. This demonstrates that the relationship shown in the *T-S*-plankton plots was maintained spatially over the entire study area. Chlorophyll concentrations sampled later in the study period along leg 6 (Plate 4*c*) showed that despite dramatic changes in the sea surface temperature pattern associated with the cooling event, this relationship between temperature and chlorophyll concentration was maintained. While higher concentrations were present throughout the cooler water now occupying most of the shelf, a decrease in concentration was coincident with the tongue of warm water isolated over the shelf, north of the cyclonic eddy.

Patterns of zooplankton concentration during the early portion of the summer study period (Plate 4*b* were less consistently related to features visible in the mean image. Increased concentrations in the southern portion of the study area were generally associated with the surface frontal zone at the outer edge of the eddy. Although these increases were not consistent along the frontal region, they do suggest that higher zooplankton biomass was generally coincident with the regions of higher phytoplankton concentration seen in Plate 4*a*. A localized peak in zooplankton concentration was also present along the northern transect in warm, strongly stratified surface

TABLE 1. Covariance Matrix of Surface Temperature, Chlorophyll, and Zooplankton During the Winter and Summer

	Data			Detrended Data			Covariance Remaining, %		
	Temperature	Chlorophyll	Zooplankton	Temperature	Chlorophyll	Zooplankton	Temperature	Chlorophyll	Zooplankton
				Winter					
Temperature	0.275			0.155			56.4		
Chlorophyll	−0.070	0.041		−0.054	0.039		77.1	95.1	
Zooplankton	−228.1	83.9	429376.5	−85.3	64.7	257285.3	37.4	77.1	59.9
				Summer					
Temperature	2.048			0.429			20.6		
Chlorophyll	−2.798	15.507		−0.375	11.543		13.4	74.4	
Zooplankton	53.1	271.1	1380587.6	32.6	528.3	1227080.5	61.4	194.9	88.9

Values are given for before and after detrending by removal of the least squares fit plane from each of the variables and for the percentage of covariance remaining after detrending.

water. High concentrations in this portion of the study area did not appear to be associated with any identifiable surface hydrographic feature. The highest concentrations seen by *Mackas et al.* [1980] over the outer shelf in the southern portion of the study area are similar to those seen in Plate 4*b*, although these authors did not observe an associated peak in chlorophyll concentration. The peak in zooplankton concentration evident along the northern transect in the vicinity of La Perouse Bank was also not observed by *Mackas et al.* [1980]. The image recorded after the cooling event (Plate 4*d*) shows that this higher zooplankton concentration was maintained within the warmer water, now isolated as a narrow tongue on the shelf.

Image-Derived Plankton Distributions

Plates 3 and 4 indicate that relationships between plankton concentrations and surface hydrography not only were maintained when compared with satellite-measured sea surface temperature but also formed coherent and relatively unambiguous spatial patterns similar to those in the satellite imagery. This suggests that major features of the surface distribution of both phytoplankton and zooplankton concentration might be represented by satellite images of surface thermal patterns. Both winter chlorophyll and zooplankton data and summer chlorophyll data collected prior to the cooling event were used to form statistical estimates of the ability of the infrared images to represent plankton distributional patterns. Spatial relationships between summer zooplankton concentrations and the mean image were not consistent enough to allow meaningful statistical estimates of their similarity, and the single transect of both chlorophyll and zooplankton data from the later time period were considered too sparse to attempt a quantitative estimate of similarity.

During both winter and summer, the large-scale structure was a general cross-shelf gradient from colder temperatures and higher plankton concentrations nearer shore to higher temperatures and lower plankton concentrations offshore. The dependence of chlorophyll and zooplankton variance on the large-scale structure was estimated by first examining the covariance matrix of the variables for the entire study area. The dominant trend of each variable was then removed by subtracting a least squares fit plane in x, y, z space, where z was the value of the variable being detrended, and a second covariance matrix calculated from the residuals. Approximately 76% of the chlorophyll and 37% of the zooplankton winter covariance with temperature (Table 1) remained after detrending, providing an estimate of the proportions of the winter covariance associated with large-scale features and with smaller-scale features. The summer covariance matrices (Table 1) show that although 74% of the chlorophyll variance is associated with small-scale features, only ≈13% of the chlorophyll-temperature covariance is associated with features smaller than the length scale of the transects.

Although the larger-scale structure has not been statistically resolved in this study, the cross-shelf gradient making up this structure is a commonly observed feature along the North American west coast [e.g., *Mackas et al.*, 1980; *Traganza et al.*, 1983; *Ikeda and Emery*, 1984; *Abbott and Zion*, 1985; *Emery et al.*, 1986]. Although very few degrees of freedom can be associated with it in this study, it seems reasonable to assume it to be a real and recurring feature.

The small-scale temperature-plankton variability is both more variable in time and space, and less well studied. The high-resolution sampler and the satellite data are especially suited for studying these smaller-scale features. The number of independent realizations associated with the smaller-scale structure can be estimated by calculating a dominant length scale of variability. It can be assumed that on average, data points separated by more than this length scale will be independent, and those closer than this separation are spatially autocorrelated and dependent. Previous authors have used the spatial structure function to investigate length scales in the marine environment [*Lutjeharms*, 1981; *Deschamps et al.*, 1981; *Denman and Freeland*, 1985]. The spatial structure function,

$$D^2(h) = \frac{1}{n}\sum_{i=1}^{n}(f_{(i)} - f_{(i+h)})^2$$

for the variable f at a spatial distance or lag h, represents as a mean square difference the statistical influence of a point upon other points at distance h. Dominant features of a specific spatial scale will produce a peak in the function at that spatial lag. Scales at which little spatial structure exists will be represented by flat portions of the function [*Lutjeharms*, 1981].

Structure functions of surface temperature, salinity, chlorophyll, and zooplankton from each leg of each cruise were calculated from the data detrended by a least squares fit straight line to estimate a cross-shelf length scale. Summer chlorophyll and zooplankton data were first $\log_e$ transformed as was recommended by *Denman and Freeland* [1985] to increase the normality of their distributions. This transformation was not applied to the winter biological data because rates of biological processes which tend to cause these variables to depart from a normal distribution, such as grazing and

growth, are minimal during winter. Structure functions from each cross-shelf transect within a season were averaged to produce a mean function for each variable for the winter and summer sampling periods. The magnitude of the structure function for each variable was then scaled to fit between 0 and 1, to facilitate comparison.

The structure functions (Figure 10) show that during both winter and summer, a length scale is apparent in the hydrographic and the planktonic data. The winter functions show that chlorophyll and zooplankton reach a distinct peak in dissimilarity at a separation of ≈ 10 km. Both temperature and salinity functions show a change in slope at ≈ 18 km. The summer functions show that chlorophyll, temperature, and salinity reach a broad peak in dissimilarity at ≈ 19 km. The zooplankton structure function shows a much shorter length scale of dissimilarity, suggesting a dissociation from the other variables and shorter length scale patchiness. An alongshore length scale is difficult to calculate from the transects sampled in this study. *Denman and Freeland* [1985], however, show that temperature, salinity, and chlorophyll all reach a peak of dissimilarity at ≈ 30 km in this region of the shelf. *Mackas* [1984] shows that zooplankton biomass has an alongshore length scale of ≈ 25 km. These values suggest that adjacent transects were not independent but that transects separated by more than this distance were.

Using an average cross-shelf length scale for each season and assuming transects separated by more than 30 km to be independent, the winter data set yields $(461/14)/2 \approx 16.5$ independent realizations and the summer data set yields $(453/19)/2 \approx 12$ independent realizations. These are applicable to that portion of the covariance associated with smaller-scale structure.

The interpretation of the statistics is that while they are an effective representation of the relationship between the satellite data and the plankton concentrations presented here, their statistical applicability outside the time and space scales of the data themselves is unsure.

Winter

Winter surface chlorophyll and zooplankton concentrations were regressed against mean satellite temperatures using both untransformed and $\log_e$ transformed values. The success of these four regressions is presented in Table 2. Biological processes within plankton communities result in an "overdispersed" or patchy distribution of both organisms and other nonconservative properties such as nutrients. Relationships between population variables primarily controlled by these biological processes and any more conservative variable are therefore likely to be most closely described by some form of logarithmic function [e.g., *Denman and Freeland*, 1985, *Abbott and Zion*, 1985]. A linear relationship between a relatively conservative tracer of the physical regime (temperature) and a biological variable such as chlorophyll implies that the phytoplankton cells are acting as Lagrangian tracers of the physical regime and their distribution is more likely a result of linear mixing of biomass than active growth.

The error ϵ^2 associated with the winter regression of chlorophyll concentration [chl] and satellite temperature was approximately 22% less than that associated with the regression of $\log_e$ [chl]. This supports the previously presented argument that the biological component of processes controlling distribution are reduced in winter. The magnitude of the errors associated with the regression of $\log_e$ [zoop] and [zoop] was similar. "Plankton" images of [chl] and $\log_e$ [zoop] constructed from the regression equations (Plates 5*a* and 5*b*) reproduce the general patterns of distribution indicated by the biomass overlays in Plates 3*a* and 3*b*, including mesoscale patterns associated with the tongue of coastal water over La Perouse Bank. (Plate 5 can be found in the separate color section in this issue.) These patterns are similar to those shown in the contour plots of *Thomas and Emery* [1986]. They obviously fail to show smaller-scale peaks in concentration associated with the hydrographic frontal zone in the southern portion of the study area. In this region, peaks in both chlorophyll and zooplankton concentration were more closely associated with surface thermal gradients than surface temperature and will only contribute to the error of a simple regression. The strong surface thermal gradient in the northern portion of the study area (see Plate 1) was not associated with a peak in chlorophyll or zooplankton concentration. This inconsistency prevented a regression of concentration with surface temperature gradient being used to model concentrations along the frontal zone.

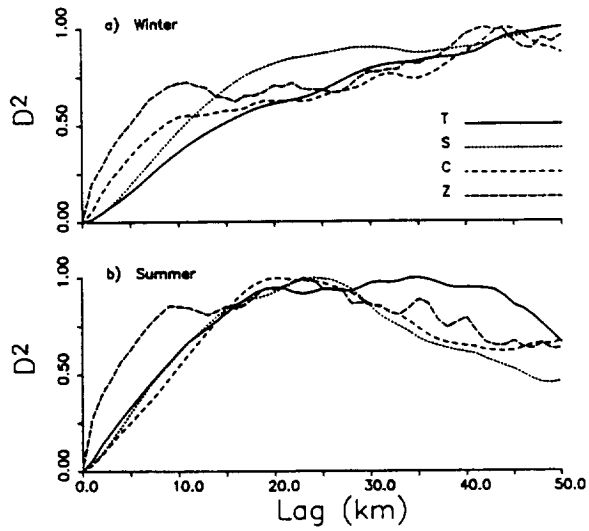

Fig. 10. Mean cross-shelf structure functions of temperature, salinity, chlorophyll concentration, and zooplankton counts for (*a*) winter and (*b*) summer, scaled between 0 and 1. Mean functions for each variable were formed by averaging function values at each lag from the winter and summer transects.

Superimposed on each image are the sampled transects, coded to show regions where major departures from the overall regression equation occur (see Plate 5 caption). Consistent patterns in this error indicate regions where failure might be due to systematic changes in the functional relationship between hydrography and plankton concentration. Both images

TABLE 2. Winter Regression Model Statistics for Chlorophyll and Zooplankton Concentration and Mean Satellite Temperature

Variable	ϵ^2	rmsdif	r^2	α	β
[chl]	0.635	0.16	0.366	−0.290	3.782
$\log_e$ [chl]	0.808	1.50	0.192	−1.727	18.879
[zoop]	0.560	490.3	0.441	−1028.5	13700.2
$\log_e$ [zoop]	0.516	0.30	0.485	−0.679	15.29

Least squares regression coefficients of the slope and intercept are α and β; rmsdif is root-mean-square difference in the same units as the variable. $N = 461$ for each regression.

TABLE 3. Winter Density Slice Model Statistics for Chlorophyll and Zooplankton Concentration Using Image-Derived Hydrographic Thresholds

Variable	Zone	T	S	$\bar{x}$	rmsdif	r^2	ϵ^2
Chlorophyll (Plate 6*a*)	total				0.137	0.534	0.454
	VICC	<11.75		0.47	0.175		
	DC	>12.06	<32.0				
		>12.30	=32.25	0.14	0.119		
	offshore	>12.30	>32.0	0.46	0.059		
	transition	11.75–12.06	<32.0	0.27	0.131		
Chlorophyll (redefined thresholds; not shown)	total				0.139	0.526	0.471
	VICC	<11.60		0.48	0.182		
	DC	>12.20	<32.25				
		>12.30	=32.25	0.13	0.113		
	offshore	>12.30	>32.0	0.46	0.059		
	transition 1	11.60–11.90	<32.0	0.20	0.146		
	transition 2	11.90–12.20	<32.0	0.36	0.139		
Zooplankton (Plate 6*b*)	total				481.5	0.459	0.540
	VICC	<11.80		2088.7	634.6		
	transition	>11.80	<31.85	1495.3	431.4		
	offshore		>31.85	1070.7	333.5		

T and S are the mean image temperature and the modeled salinity thresholds used to separate each zone. "Total" refers to all data points in the study area (statistics for the total image), VICC refers to points in the image classified as Vancouver Island Coastal Current water, DC refers to Davidson Current water, and "transition" refers to transition zones between hydrographic regimes. The rms difference rmsdif is in the same units as the original variable, and $\bar{x}$ is the mean concentration within the zone.

show an expected lack of fit in frontal regions, especially in the southern portion of the study area. The chlorophyll image shows that regions occupied by offshore water tend to depart from the overall regression, indicating an inconsistent relationship between temperature and chlorophyll across the shelf. The regression equation is most likely dominated by the gradient from high to low chlorophyll concentrations from colder Vancouver Island Coastal Current water to warmer Davidson Current water. The zooplankton image indicates larger errors at the seaward portions of legs 5 and 6. It is possible that the previously mentioned lack of synopticity is contributing to the error in these regions. The chlorophyll regression in this region, however, did not seem to be affected.

The T-S-plankton plots showed that regions of specific plankton concentration on the winter shelf could be separated in terms of temperature and salinity. A simple mixing model was used to predict surface salinity distribution from the satellite temperature image. Using these two image products, each pixel of the study area could be assigned coordinates in T-S space to mimic the T-S-plankton diagrams. Surface water was assumed to be a result of mixing between the three previously described water regimes (Figure 4). Salinity variations within both the Davidson Current and offshore regimes were small, and a mean salinity of 32.35 was calculated from all points within the region. The separation between this region and less saline regimes could be unambiguously identified in the satellite imagery by the distinct surface thermal signature of Davidson Current water. All pixels in the image seaward of the main (warmest) core of this water were assigned this mean salinity.

Salinity variations between this core and coastal current water were modeled as a line of mixing between the warmest Davidson Current water present in the study area (12.65°C, 32.25) and the center of the cluster of points defining coastal current water (10.88°C, 30.00) (see Figure 4). All pixels shoreward of the main core of Davidson Current water were then assigned the salinity predicted by temperature, assuming mixing along the straight line joining these two water types in T-S space.

The "salinity" image produced from this model showed the same features as contours of measured surface salinity presented by *Thomas and Emery* [1986]. Redrawn T-S-plankton plots using modeled salinity, mean satellite temperatures, and sampled plankton concentrations showed that this model allowed the same separation of water types and plankton concentrations as that seen in the original T-S-plankton plots (Figures 8*a* and 8*b*).

Hydrographic thresholds used to define regions of similar plankton concentration in satellite derived T-S space are given in Table 3 along with mean concentrations calculated for the resultant regions. "Plankton" images constructed from these means are given in Plates 6*a* and 6*b*. (Plate 6 can be found in the separate color section in this issue.) Statistics of these images (Table 3) show that Plate 6*a* reduced the error of the chlorophyll estimation to 0.454, considerably less than the simple temperature regression model. This model explained approximately 55% of the sampled chlorophyll variance with an overall rms difference of 0.137 mg m^{-3}. The majority of the unexplained variance was associated with colder coastal current water. Chlorophyll concentrations in both Davidson Current and offshore water were more effectively modeled with rms differences of 0.119 and 0.059 mg m^{-3}, respectively. The error associated with the zooplankton image (Plate 6*b*) was higher than the error associated with the $\log_e$ regression model. Table 3 shows that the offshore water had the lowest rms difference, indicating that concentrations within this hydrographic regime were the most precisely modeled. Zooplankton concentrations in coastal current water had the greatest rms difference and were the least precisely modeled.

The transects overlayed on these "plankton" images give a spatial representation of the model errors. Consistent errors at the boundaries of hydrographic zones are indicative of slight mismatches in synopticity. While the mean image provides the best reduction of the satellite image series to represent surface

thermal patterns over the study period, it obviously loses the more precise coregistering of individual in situ transects with concurrent satellite imagery. Errors in both the chlorophyll and zooplankton models within the coastal current regime reflect the inability of this simple modeling approach to reproduce the increased spatial patchiness of this zone. The remarkably effective representation of surface plankton concentrations within the Davidson Current and offshore zones indicates a strong dominance of plankton distributional patterns by large-length-scale physical mixing processes.

A further effort was made to reduce the error of the threshold chlorophyll model by subdividing the image into another T-S region, and narrowing the threshold limits of previously defined hydrographic regions. Redefined thresholds for these five regions are given in Table 3. No attempt was made to improve the extremely low rms difference in offshore water. Statistics of this model (Table 3) show a slight improvement in the modeling of Davidson Current water concentrations, but both coastal current and unlabeled mixed water retain similar rms differences. The image overall had a slightly greater rms difference (0.139 mg m^{-3}) than that of the four-zone model (Plate 6*a*), indicating a limit to the amount of plankton variance directly associated with T-S properties.

Summer

Summer T-S-plankton plots (Figure 9*a*) showed that (unlike in winter) the majority of chlorophyll variation was associated with temperature and that salinity need not be considered. These figures also show no consistent relationship between zooplankton concentration and surface hydrography. Attempts to derive quantitative models of surface zooplankton distribution from surface temperature were not successful.

Regressions of chlorophyll concentration on mean satellite temperature (Table 4) showed that $\log_e$ transformed concentrations produced 40% less error than untransformed concentrations and explained approximately 60% of the sampled variance. The "plankton" image produced by the $\log_e$ [chl] regression equation is shown in Plate 7. (Plate 7 can be found in the separate color section in this issue.) The increased success of the $\log_e$ transformed regression is indicative of a significant biological control of patterns of chlorophyll concentration over the summer shelf. It implies a linear mixing of exponentially changing population variables such as growth rate rather than a simple linear mixing of biomass as was observed in winter. Plate 7 shows the location of highest chlorophyll concentrations in zones of colder water within the upwelling regions and lower concentrations within zones of warmer, vertically stratified water. Departures from the overall regression were maximum in the colder zone, especially around its outer edge, where maximum biomass was observed.

TABLE 4. Summer Regression Model Statistics for Chlorophyll and Zooplankton Concentration and Satellite Temperature (Legs 1 – 4)

Variable	rmsdif	r^2	ϵ^2	α	β
[chl]	3.238	0.324	0.676	−2.587	37.965
$\log_e$ [chl]	0.747	0.607	0.392	−1.070	14.883
[zoop]	1174.8	0.0003	0.9997	23.2	335.3
$\log_e$ [zoop]	0.994	0.022	0.978	−0.231	8.764

Least squares regression coefficients for slope and intercept are given as α and β; rmsdif is in the same units as the variable (N = 453).

TABLE 5. Summer Density Slice Model Statistics for Chlorophyll Concentration Using Temperature Thresholds

Zone	T	$\bar{x}$	rmsdif	r^2	ϵ^2
Total			3.112	0.391	0.625
Stratified	>13.8	0.57	0.689		
Coldest	<12.0	2.24	0.594		
Frontal	12.0–13.8	5.53	4.470		

T is temperature from the mean satellite image. "Total" refers to all sampled data points, "stratified" refers to offshore warmest water, "coldest" refers to most recently upwelled water, and "frontal" refers to upwelled water of intermediate temperature around the edge of the upwelling zone.

The lack of correlation between zooplankton concentration and satellite temperature is evident in Table 4.

A significant failure of the regression equation was the prediction of highest chlorophyll concentrations in the coldest and most recently upwelled water in the center of the eddy. This does not follow the established association of chlorophyll and surface temperature in an upwelling region. Lower concentrations are expected in most recently upwelled water, with maximum values at some intermediate temperature on the outer edge of the upwelling zone in "older" upwelled water [e.g., *MacIsaac et al.*, 1985].

Temperature thresholds which would partition the shelf into three zones of chlorophyll concentration representing warm regions (stratified water) with low concentrations, cold regions (most recently upwelled water) also with low concentrations, and intermediate temperatures (older upwelled water) with highest concentrations were identified from the T-S-plankton plot. The mean summer image was then sliced at these thresholds, and a "plankton" image was created by assigning the mean chlorophyll concentrations (calculated from in situ data) to each zone. These temperature thresholds, the mean chlorophyll concentrations, and the rms differences for each region (Table 5) show that the warm stratified region and the newly upwelled, coldest water were most effectively modeled. The greatest error was, not surprisingly, associated with the frontal zone around the outer edge of the eddy where the highest concentrations were observed. Although the density slice model reproduced the three major regions of chlorophyll concentration expected from theoretical considerations, the total error associated with the resultant "plankton" image was larger than that of the regression model (Table 4), explaining only $\approx$40% of the sampled variance.

The association of lower chlorophyll concentrations with both the coldest water and the warmest water and the association of maximum concentrations with an intermediate temperature suggested that the data might best be modeled by a nonlinear equation. A Gaussian equation would reproduce this relationship, predicting decreasing concentrations with both increasing and decreasing temperatures away from a chlorophyll maximum. A Gaussian curve of the form

$$\log_e [\text{chl}] = a \exp [-b(T - c)^2] + d$$

where T is the satellite temperature in degrees celsius was fitted to the data using a least squares approximation. These data and the resultant curve are shown in Figure 11. The least squares approximation of the regression coefficients was

$$a = 3.5645 \quad b = 0.3379 \quad c = 12.5992 \quad d = -1.8949$$

C-3

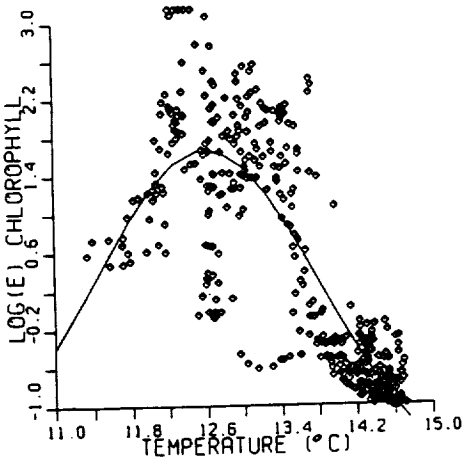

Fig. 11. Relationship between $\log_e$ transformed summer chlorophyll concentrations and satellite temperatures, showing the least squares fit nonlinear equation.

with c representing the temperature at which maximum chlorophyll concentrations were present. The "plankton" image created from this regression equation is shown in Plate 8, and the statistics of its relationship with sampled data are given in Table 6. This model reduced the $\log_e$ rms difference between actual and modeled data to 0.628 mg m^{-3} and explained approximately 72% of the sampled chlorophyll variance. The error associated with this model is approximately 30% less than that of the linear regression.

Plate 8 shows a circular zone of maximum chlorophyll concentration around the edge of the cold upwelling region (see Plate 2*a*). (Plate 8 can be found in the separate color section in this issue.) Lower concentrations are in the center of this region. A relatively sharp gradient coinciding with the thermal front (Plate 2*a*) separates the zone of high concentrations from low concentrations found in warmer, stratified water outside the upwelling region over the rest of the shelf and shelf break.

The spatial pattern of error associated with this model reflects primarily the increased variance within the region of maximum biomass (Plate 4*a*). A region of increased error along the southern transects is coincident with the transition from maximum biomass to minimum biomass at the thermal frontal zone. In this region, slight differences in synopticity contribute to the error. At frontal zones, minimal spatial and/or temporal changes in the thermal gradient position or magnitude would create maximum departures from the regression equation. A comparison with Plate 4*b* shows that this region is also a zone of maximum zooplankton concentration. Increased grazing rates along this portion of this transect probably also contribute to the observed departures from the overall regression equation.

The spatial relationship between summer temperature and chlorophyll measured in this study resembles that reported by *Abbott and Zion* [1985] for data from an upwelling region off California. These authors reported similar correlation coefficients for linear regressions relating satellite-measured $\log_e$ chlorophyll concentrations to satellite temperature and showed that a nonlinear model improves the predictive capability of the regression (they do not give the mathematical form of their equation). Although higher concentrations are expected to coincide with cooler surface temperatures in upwelling systems, maximum concentrations occur downstream of the most recently upwelled water [e.g., *Jones et al.*, 1983; *Brink et al.*, 1981] Upwelling reported by these authors was induced by episodic wind events. Data reported here indicate that similar spatial relationships between surface chlorophyll concentration and surface temperature occur in the topographically induced upwelling zone on the southern British Columbia coast.

Summer chlorophyll distributions shown in Plate 8 differ from those reported by *Mackas et al.* [1980] and *Denman et al.* [1981]. These authors showed high concentrations over the outer edge of La Perouse bank, immediately seaward of a region of mixing over the shallow banks. Plates 4*a* and 8 show that this region has low chlorophyll concentrations, and Figure 7 shows it to be stratified. In addition, neither surface temperature nor chlorophyll distributions shown by these authors indicated the presence of an upwelling eddy. Highest surface salinities shown by *Mackas et al.* [1980] were associated with offshore zones of maximum temperature. This is not indicative of active upwelling. Physical processes during these studies seem to be quite different from those reported here and are probably largely responsible for the observed differences in plankton distribution. These differences emphasize the variable nature of the oceanography in this region of the shelf and highlight the importance of frequent and synoptic sampling by remote sensing techniques.

SUMMARY

Both winter and summer surface hydrographic zones on the southern British Columbia continental shelf were associated with specific plankton concentrations. Comparisons of these plankton concentrations with surface temperatures mapped by infrared satellite images showed that associations demonstrated in T-S space were coherent in space over the study area. These associations, as well as least squares regression equations, were used to build satellite image derived models of surface plankton distribution. The similarity of winter plankton and hydrographic distributions as well as the general positive correlation of phytoplankton and zooplankton concentrations indicate either a large degree of physical control over biological distributions or a rapid biological response to physical forcing. During winter, low incident light and low-temperature regimes in temperate latitudes will slow biological processes, reducing the biological component of any response. Winter plankton will act more as Lagrangian tracers of the physical regime. This implies that the similarity in distributions of hydrographic and biological variables on the winter shelf was primarily a function of physical advective processes. Distributions of summer plankton concentrations indicated an interaction between physical processes and biological response. A nonlinear regression equation relating summer surface chlorophyll concentrations and temperature showed a frontal zone of maximum biomass associated with the thermal

TABLE 6. Summer Nonlinear Regression Model Statistics for $\log_e$ Chlorophyll Concentration and Satellite Temperature (Legs 1–4)

	Value
Variable	$\log_e$ [chl]
rmsdif	0.628
r^2	0.719
ε^2	0.277

Regression coefficients and the form of the nonlinear equation are given in the text (N = 453).

frontal zone separating the upwelling area from stratified regions of the shelf. In contrast to the relatively good relationship between surface temperature and winter zooplankton and with both winter and summer chlorophyll, no consistent quantitative relationship existed between summer zooplankton concentrations and satellite temperature. Qualitative associations, however, suggested that maximum biomass was located around the outer edge of an upwelling area, in regions of higher chlorophyll concentration.

Data presented here illustrate that the ability of infrared satellite images to monitor physical processes has important implications for the monitoring and mapping of resultant biological distributions. These plankton distributions have both a physical (mixing and advective) component and a biological (nutrient uptake, cell division, and grazing) component. In situations where the biological component is either reduced or strongly correlated with the physical component, the relationship between concentration and surface temperature can often be exploited, allowing satellite images of sea surface temperature to reproduce the general spatial characteristics of surface plankton distributions. Statistical relationships between these spatial distributions, measured and quantified here for the southern British Columbia continental shelf, demonstrate both an interpolatory and a predictive role for infrared imagery when used in conjunction with concurrent in situ sampling.

Acknowledgments. We are grateful to D. L. Mackas, M. R. Abbott, G. A. Borstad, and T. R. Parsons for useful discussions and comments on various aspects of the work presented here. Bill Meyers, Denis LaPlante, and Paul Nowlan provided technical assistance with the image processing and Broccoli Oceanographic Inc. of Sidney, British Columbia, provided support at sea. This work was supported by the Canadian Natural Sciences and Engineering Council and the Science Council of British Columbia for collaborative work between the authors and G. A. Borstad Ltd. of Sidney on biological applications of infrared imagery. Support during the preparation of this manuscript for one of the authors (A.C.T.) was by NASA grant NAGW-1251.

REFERENCES

Abbott, M. R., and P. M. Zion, Satellite observations of phytoplankton variability during an upwelling event, *Cont. Shelf Res.*, *4*, 661–680, 1985.

Boyd, S. H., P. H. Wiebe, R. H. Backus, J. E. Craddock, and M. A. Daher, Biomass in the micronekton in Gulf Stream ring 82-B and environs: Changes with time, *Deep Sea Res.*, *33*, 1885–1905, 1986.

Breaker, L. C., The application of satellite remote sensing to west coast fisheries, *Mar. Technol. Soc. J.*, *15*, 32–40, 1981.

Brink, K. H., B. H. Jones, J. C. Van Leer, C. N. K. Mooers, D. W. Stuart, M. R. Stevenson, R. C. Dugdale, and G. W. Heburn, Physical and biological structure and variability in an upwelling center off Peru near 15°S during March 1977, in *Coastal Upwelling, Coastal and Estuarine Sci.*, vol. 1, edited by F. A. Richards, pp. 473–495, AGU, Washington, D. C., 1981.

Campbell, J. W., and W. E. Esaias, Spatial patterns in temperature and chlorophyll on Nantucket Shoals from airborne remote sensing data, May 7–9, 1981, *J. Mar. Res.*, *43*, 139–161, 1985.

Denman, K. L., Covariability of chlorophyll and temperature in the sea, *Deep Sea Res.*, *23*, 539–550, 1976.

Denman, K. L., and H. J. Freeland, Correlation scales, objective mapping, and a statistical test of geostrophy over the continental shelf, *J. Mar. Res.*, *43*, 517–539, 1985.

Denman, K. L., and T. Platt, Coherences in the horizontal distribution of phytoplankton and temperature in the upper ocean, *Mem. Soc. R. Sci. Liege*, *7*, 19–30, 1975.

Denman, K. L., and T. M. Powell, Effects of physical processes on planktonic ecosystems in the coastal ocean, *Oceanogr. Mar. Biol.*, *22*, 125–168, 1984.

Denman, K. L., D. L. Mackas, H. J. Freeland, M. J. Austin, and S. H. Hill, Persistent upwelling and mesoscale zones of high productivity off the west coast of Vancouver Island, Canada, in *Coastal Upwelling, Coastal and Estuarine Sci.*, vol. 1, edited by F. A. Richards, pp. 514–521, AGU, Washington, D. C., 1981.

Deschamps, P. Y., R. Frouin, and L. Wald, Satellite determination of the mesoscale variability of the sea surface temperature, *J. Phys. Oceanogr.*, *11*, 961–970, 1981.

Emery, W. J., and M. Ikeda, A comparison of geometric correction methods for AVHRR imagery, *Can. J. Remote Sens.*, *10*, 46–56, 1983.

Emery, W. J., A. C. Thomas, M. J. Collins, W. R. Crawford, and D. L. Mackas, An objective method for computing advective surface velocities from sequential infrared satellite images, *J. Geophys. Res.*, *91*, 12,865–12,878, 1986.

Eppley, R. W., Temperature and phytoplankton growth in the sea, *Fish. Bull.*, *90*, 1063–1085, 1972.

Fasham, M. J. R., and P. R. Pugh, Observations on the horizontal coherence of chlorophyll and temperature, *Deep Sea Res.*, *23*, 527–538, 1976.

Fournier, R. O., M. Van Det, J. S. Wilson, and N. B. Hargreaves, Influence of the shelf break front off Nova Scotia on phytoplankton standing stock in winter, *J. Fish. Res. Board Can.*, *36*, 1228–1237, 1979.

Freeland, H. J., and K. L. Denman, A topographically controlled upwelling center off southern Vancouver Island, *J. Mar. Res.*, *40*, 1069–1093, 1982.

Freeland, H. J., W. R. Crawford, and R. E. Thomson, Currents along the Pacific coast of Canada, *Atmos. Ocean*, *22*, 151–172, 1984.

Haury, L. R., J. J. Simpson, J. Peláez, C. J. Koblinsky, and D. Wiesenhahn, Biological consequences of a recurrent eddy off Point Conception, California, *J. Geophys. Res.*, *91*, 12,937–12,956, 1986.

Ikeda, M., and W. J. Emery, A continental shelf upwelling event off Vancouver Island as revealed by satellite infrared imagery, *J. Mar. Res.*, *42*, 303–317, 1984.

Ikeda, M., W. J. Emery, and L. A. Mysak, Seasonal variability in meanders of the California Current System off Vancouver Island, *J. Geophys. Res.*, *89*, 3487–3505, 1984.

Jones, B. H., K. H. Brink, R. C. Dugdale, D. W. Stuart, J. C. Van Leer, D. Blasco, and J. C. Kelley, Observations of a persistent upwelling center off Point Conception, California, in *Coastal Upwelling: Its Sediment Record*, edited by E. Suess and J. Thiede, pp. 37–60, Plenum, New York, 1983.

Lasker, R., J. Peláez, and R. M. Laurs, The use of satellite infrared imagery for describing ocean processes in relation to spawning of the northern anchovy, *Remote Sens. Environ.*, *11*, 439–453, 1981.

Laurs, R. M., P. C. Fiedler, and D. R. Montgomery, Albacore tuna catch distributions relative to environmental features observed from satellites, *Deep Sea Res.*, *31*, 1085–1099, 1984.

Legendre, L., and S. Demers, Towards dynamic biological oceanography and limnology, *Can. J. Fish. Aquat. Sci.*, 41, 2–19, 1984.

Lekan J. F., and R. E. Wilson, Spatial variability of phytoplankton biomass in the surface waters of Long Island, *Estuarine Coastal Shelf Sci.*, *6*, 239–251, 1978.

Lutjeharms, J. R., Spatial scales and intensities of circulation in the ocean areas adjacent to South Africa, *Deep Sea Res.*, *28*, 1289–1302, 1981.

MacIsaac, J. J., R. C. Dugdale, R. T. Barber, D. Blasco, and T. T. Packard, Primary production cycle in an upwelling center, *Deep Sea Res.*, *32*, 503–529, 1985.

Mackas, D. L., Spatial autocorrelation of plankton community composition in a continental shelf ecosystem, *Limnol. Oceanogr.*, *29*, 451–471, 1984.

Mackas, D. L., G. C. Louttit, and M. J. Austin, Spatial distribution of zooplankton and phytoplankton in British Columbia coastal waters, *Can. J. Fish. Aquat. Sci.*, *37*, 1476–1487, 1980.

Mackas, D. L., K. L. Denman, and M. R. Abbott, Plankton patchiness: Biology in the physical vernacular, *Bull. of Mar. Sci.*, *37*, 652–674, 1985.

McClain, E. P., Split window and triple window sea surface temperature determination from satellite measurements, paper presented at Mini-Symposium on Application of Aerospace Remote Sensing in Marine Research, ICES Statutory Meeting, Int. Counc. for the Explor. of the Sea, 1981.

Millard, S. P., J. R. Yearsley, and D. P. Lettenmaier, Space-time correlation and its effects on methods for detecting aquatic ecological change, *Can. J. Fish. Aquat. Sci.*, *42*, 1391–1400, 1985.

Pietrafesa, L. J., Shelfbreak circulation, fronts and physical oceanography: East and west coast perspectives, *Spec. Publ. Soc. Econ. Paleontol. and Mineral.*, *33*, 233–250, 1983.

Simpson, J. J., C. J. Koblinsky, J. Peláez, L. R. Haury, and D. Wiesenhahn, Temperature–plant pigment–optical relations in a recurrent offshore mesoscale eddy near Point Conception, California, *J. Geophys. Res.*, *91*, 12,919–12,936, 1986.

Smith, S. L., and J. J. Vidal, Spatial and temporal effects of salinity, temperature and chlorophyll on the communities of zooplankton in the southeastern Bering Sea, *J. Mar. Res.*, *42*, 221–257, 1984.

Steele, J. H., and E. W. Henderson, Spatial patterns in North Sea plankton, *Deep Sea Res.*, *26*, 955–963, 1979.

Thomas, A. C., and W. J. Emery, Winter hydrography and plankton distributions on the southern British Columbia shelf, *Can. J. Fish. Aquat. Sci.*, *43*, 1249–1258, 1986.

Thomson, R. E., and J. F. R. Gower, A wind-induced mesoscale eddy over the Vancouver Island continental slope, *J. Geophys. Res.*, *90*, 8981–8993, 1985.

Traganza, E. D., V. M. Silva, D. M. Austin, W. L. Hanson, and S. H. Bronsink, Nutrient mapping and recurrence of coastal upwelling centers by satellite remote sensing: Its implication to primary production and the sediment record, in *Coastal Upwelling: Its Sediment Record*, edited by E. Suess and J. Thiede, pp. 61–83, Plenum, New York, 1983.

Wiebe, P. H., G. R. Flierl, C. S. Davis, V. Barber, and S. H. Boyd, Macrozooplankton biomass in Gulf Stream warm core rings: Spatial distribution and temporal changes, *J. Geophys. Res.*, *90*, 8885–8901, 1985.

W. J. Emery, Colorado Center for Atmospheric Research, University of Colorado, Boulder, CO 80309.

A. C. Thomas, College of Oceanography, Oceanography Administration Building 104, Oregon State University, Corvallis, OR 97331.

(Received June 30, 1988;
revised July 19, 1988;
accepted July 22, 1988.)

APPENDIX I

SPATIAL PATTERNS OF ZOOPLANKTON COMMUNITY COMPOSITION AND SATELLITE MEASURED SURFACE TEMPERATURE

A. C. Thomas

Continental Shelf Research, Vol. 12, No. 5/6, pp. 753–777, 1992.
Printed in Great Britain.

0278–4343/92 $5.00 + 0.00

Spatial patterns of zooplankton community composition and satellite measured surface temperature

A. C. THOMAS*

(*Received* 20 *August* 1990; *accepted* 13 *November* 1990)

Abstract—Data from the continental shelf off southern British Columbia, Canada, are used to test the hypothesis that patterns of surface temperature evident in infrared satellite images reflect spatial patterns of zooplankton community composition. During both a winter and a summer sampling period, multivariate analysis of a relatively small number of taxonomic categories shows that stations close in multidimensional taxonomic space are also close in geographic space. Stations grouped into near-shore, mid-shelf, and outer-shelf clusters which could be contoured in geographic space. These contours are similar to surface thermal gradients separating hydrographic regimes visible in both *in situ* hydrographic data and satellite images over the middle and inner shelf, supporting previous work which suggests a strong physical control over zooplankton community distribution in this region. Station groups over the outer shelf are not closely related to surface thermal patterns, but suggest an association with bathymetry. The distribution of species included in the taxonomic enumeration and previously published accounts of their biogeography are consistent with the association of specific communities with specific hydrographic regimes on the shelf.

INTRODUCTION

IT IS well known that changes in the biological properties of a planktonic ecosystem occur in response to gradients and boundaries in the physical regime. While these changes are often manifested as changes in total biomass (e.g. ROMAN *et al.*, 1985; WIEBE *et al.*, 1985; ALLISON and WISHNER, 1986; YAMAMOTO and NISHIZAWA, 1986) they can include, or are sometimes even restricted to, changes in species composition (e.g. TREMBLAY and ROFF, 1983; MACKAS and ANDERSON, 1986; WISHNER and ALLISON, 1986; BOUCHER *et al.*, 1987). In the ocean, changes in both phytoplankton and zooplankton biomass coincident with physical features such as frontal zones, upwelling regions and eddy structures are well documented. This is largely due to the relative ease of measuring plankton biomass, making it possible to quantitatively analyse enough samples to resolve patchiness associated with localized physical processes. While large, basin-scale changes in species composition (e.g. FAGER and MCGOWAN, 1963; FASHAM and ANGEL, 1975) have been the subject of investigation from the earliest oceanographic expeditions, the expensive and

*Department of Oceanography, University of British Columbia, Vancouver, B.C., Canada.
Present address: Atlantic Centre for Remote Sensing of the Oceans, Suite 301, 6155 North St., Halifax, Nova Scotia, Canada B3K 5R3.

time consuming nature of taxonomic enumeration of samples has made the analysis of the large number of samples necessary to resolve smaller scale changes in species composition less popular. At these smaller scales, the biological response to many physical gradients or boundaries may be manifested only as subtle changes in species composition, and sometimes only as changes in the relative dominance hierarchy within a regionally ubiquitous community list (Haury, 1976; McGowan and Walker, 1979; Mackas and Sefton, 1982; Haury *et al.*, 1986; Boucher *et al.*, 1987).

Compounding the difficulty of examining mesoscale and smaller scale variability in plankton community structure is the unavoidable non-synoptic nature of ship sampling over the necessary spatial scales. This problem is most extreme in complex and dynamic coastal regions. Satellite images of sea surface temperature, however, give a synoptic realization of the surface physical regime and allow a previously unattainable estimate of the synopticity of *in situ* sampling programs.

Infrared satellite images might provide both spatial and temporal information about these community patterns and/or boundaries if associations between hydrography and the spatial pattern of zooplankton communities exist. This study is a preliminary test of the hypothesis that in a region where biological processes are dominated by physical forcing, relationships between the spatial patterns of zooplankton community composition and the physical regime are such that satellite images of sea surface temperature reflect spatial patterns of zooplankton community structure. This hypothesis is tested using zooplankton samples, hydrographic data and infrared satellite imagery from the southern British Columbia continental shelf (Fig. 1). Data are from both a winter study period, when physical processes are expected to strongly dominate factors determining plankton distributions, and a summer study period, during which the potential for a strong biological contribution to these factors is greater.

Previous studies of this region have shown both the spatial and the temporal heterogeneity of zooplankton biomass (Mackas *et al.*, 1980; Mackas, 1984; Thomas and Emery, 1986; 1988). These studies, including Denman *et al.* (1981), emphasize the close relationship between shelf hydrography and biomass distribution. Mackas and Sefton (1982) extend this work to show the spatial and temporal variability of the summer zooplankton community structure when examined at spatial scales of 5–200 km. The location and shapes of spatial patterns were stable over time during summer sampling periods. Dissimilarity correlograms calculated by Mackas (1984) show that zooplankton community patterns have positive spatial autocorrelation with cross-shelf length scales of approximately 1/3 those in the along-shelf direction. Mackas and Sefton (1982) suggest that the summer spatial distribution of zooplankton community composition reflects the general physical circulation and bathymetry of the shelf. Changes in the species composition within the patterns, and the lack of any consistent association of a particular species assemblage with specific geographic locations suggested that the summer British Columbia continental shelf plankton community was primarily controlled by physical advection and allochthonous biological processes.

As a test of the stated hypothesis, a limited number of taxonomic characteristics (as a surrogate for an actual zooplankton community study) from each station are identified and enumerated to (1) determine if stations with similar zooplankton community characteristics are adjacent in geographic space forming spatial patterns, and (2) compare these spatial patterns with both *in situ* hydrographic data and satellite measured surface thermal patterns.

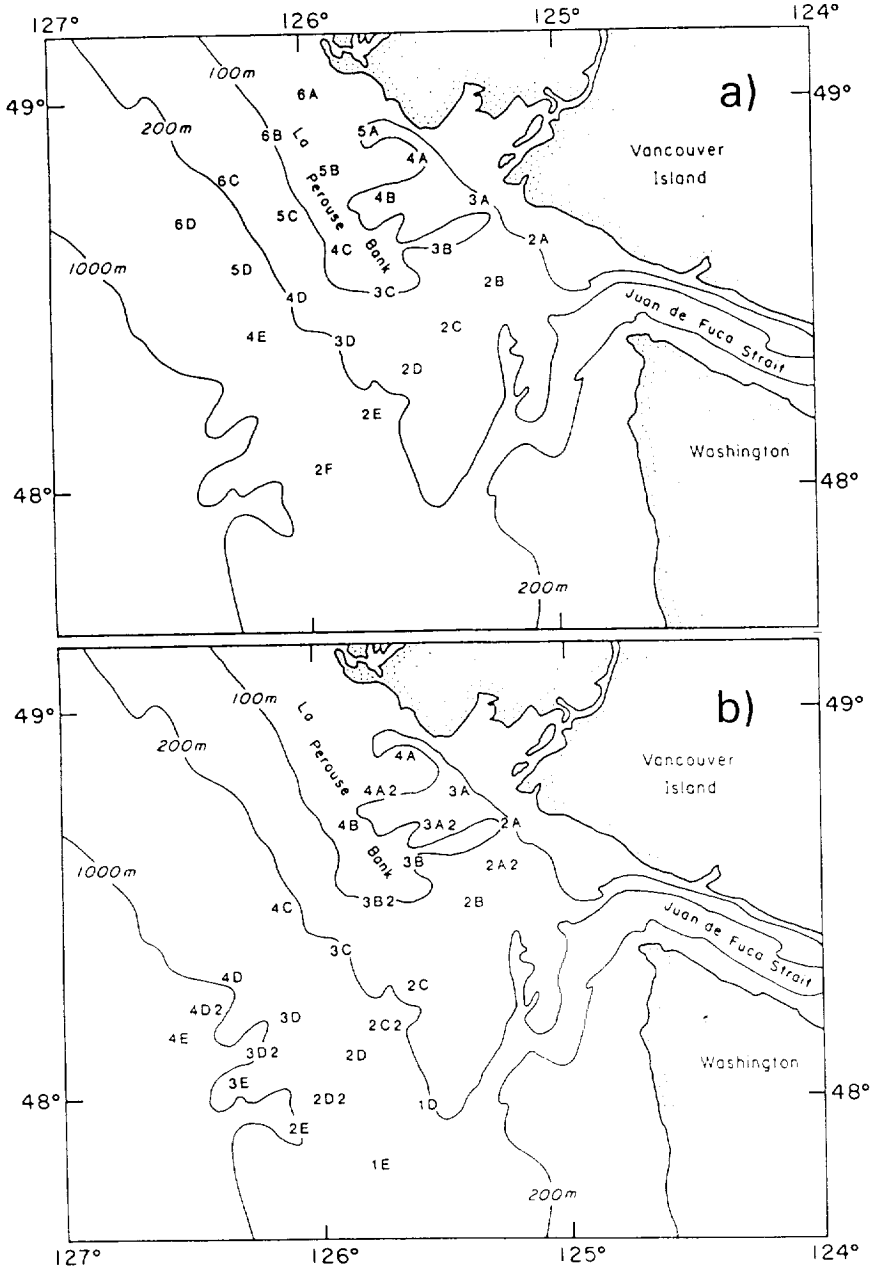

Fig. 1. The study area on the southern British Columbia (Canada) continental shelf showing relevant bathymetry. Locations and names of winter (a) and summer (b) zooplankton sampling stations are shown.

METHODS

Data collection

Advanced Very High Resolution Radiometer (AVHRR) satellite images of the west coast of British Columbia were received and processed at the University of British Columbia Satellite Oceanography Laboratory during two *in situ* sampling periods; one in early winter (28 November–3 December 1983) and the second in mid-summer (10–18 July 1984). Cloud-free weather along the British Columbia coast during both periods enabled the collection of 10 and 15 infrared images of the study area for the winter and summer sampling periods, respectively. The satellite data were processed into navigated images of maximum spatial resolution (1.1 km) according to the procedure described by EMERY and IKEDA (1983) using high quality satellite ephemeris data supplied by the U.S. Navy. Land and cloud contaminated pixels in each image were then flagged. Satellite radiance measurements from Band 4 were converted to temperature fields by regression against *in situ* measurements of near-surface temperature from a series of cross-shelf transects made in the same geographic locations and with the least possible temporal separation (always less than 12 h). A mean bias was calculated from each regression and subtracted from the entire image providing the equivalent of an atmospheric correction for each satellite image. This assumes a horizontally homogenous atmospheric attenuation which is likely to be valid over the relatively small study area provided pixels contaminated with cloud or fog are avoided. Correlations between satellite and ship measured temperature along the transects used to make these corrections ranged between 0.901 and 0.992 (n ranged from 72 to 108).

Zooplankton samples were collected at the stations shown in Fig. 1a and b using a vertically hauled, black nylon bongo net of 0.5 m diameter and 0.233 mm mesh size. The nets were hauled at a constant rate of ≈ 1 m s^{-1} from 200 m or within 5 m of the bottom, whichever was shallower. Sampling was conducted at varying times of the day due to constraints on ship time. At stations with depths less than 200 m, vertical integration of the water column will reduce sample to sample variability caused by diel vertical migrations. At stations deeper than 200 m, diel vertical migration across the 200 m isobath will contribute to the error in the analysis. This vertical integration also minimizes apparent spatial patchiness which might be induced by the vertical displacement of the zooplankton community by internal waves. All samples were preserved in 5% buffered formalin for later analysis.

Vertical profiles of hydrographic properties were taken at each of the zooplankton sampling stations. During the winter cruise, profiles of temperature and salinity were obtained with a CTD. Summer vertical temperature profiles were collected using expendable bathythermographs (XBTs).

Data preparation

Visual inspection of both the winter and summer satellite image series showed that both sea surface temperatures and the overall patterns of surface temperature distribution within the study area on the shelf remained approximately constant over the period of *in situ* sampling. Spatial variability was restricted to small scales (5–10 km) and the temporal

correlations of sea surface temperature patterns remained high over the sampling period (THOMAS and EMERY, 1988) implying that *in situ* samples within each cruise can be considered a synoptic representation of the spatial variability.

Satellite data concurrent with zooplankton sample collection during each cruise were reduced to a single mean image representing the temporal mean of the sea surface temperature field over the period of sampling. Winter sampling took place over a 72 h period during which eight images were recorded. Summer sampling took place over a 48 h period. The mean summer image presented here was calculated from four images spanning a 56 h interval about this sampling period. In each mean image, pixels occupied by cloud in more than 50% of the images making up the mean were flagged as cloud.

Previous statistical analysis of the summer zooplankton community in the study area using a detailed taxonomic enumeration (38 taxonomic categories; MACKAS and SEFTON 1982) showed that approximately 95% of the between station covariance structure would be preserved using only 10–12 categories. STONE (1980) and GARDNER (1982) identify specific copepod taxa which are indicative of the large scale circulation off the British Columbia west coast and MACKAS and SEFTON (1982) identify those taxa which form dominant members of the plankton community. Taxonomic categories for this study were chosen on the basis of their numerical dominance within the sample, ease and accuracy of identification, suspected importance to the overall plankton ecology of the shelf and to include some of the species identified by Stone and Gardner as being indicative of large-scale circulation patterns. For the winter samples, a set of 15 taxonomic categories were chosen, identified and enumerated (Table 1). A set of 17 taxonomic categories were enumerated from the summer samples (Table 1). The level of taxonomic identification varied among categories. Copepods were both identified to species (the last three developmental stages were summed) and also grouped into more general headings. Other less numerous invertebrates were also combined under general headings. No attempt was made to provide a complete analysis of the zooplankton community composition. The goal was to enumerate enough characteristics of the community to resolve geographic pattern. For the numerically rare taxonomic categories (<50 individuals in a sample), the entire sample was counted. To enumerate the more abundant categories, samples were sequentially split with a Folsom plankton splitter until the number of individuals was less than 300.

During both winter and summer, a proportion of the enumerated categories were completely absent at some stations. A second data matrix for each cruise was created using those taxonomic categories which were missing entirely from any of the stations during a cruise. These categories were recombined into a presence/absence format and the resultant binary data matrices also used in the analysis. Taxonomic categories missing from more that 40% of the stations within a cruise were deleted from the original data matrices. This provided two data sets with which to test the hypothesis; one, biased toward more the ubiquitous shelf taxa from the enumerated list, and a second, biased towards the spatially rarer or more patchy taxa. There is a distinction here between rarity of occurrence, which has no numerical connotations but implies patterns of distribution (presence and absence) and numerical rarity (biomass differences), which will be discussed below.

Relationships between stations were determined by multivariate cluster analysis of the taxonomic characteristics of stations sampled during each cruise. This classification technique groups stations into clusters based on some measure of between-site correlation or similarity measured as a distance in multi-dimensional taxonomic space. Spatial

Table 1. Taxonomic categories enumerated from the winter and summer samples

Taxonomic category	Abbreviation
Winter	
Total chaetognaths	CH
Total Small Copepods (<2 mm)	SC
Total Large Copepods (>2 mm)	LC
Total euphausiids	EUP
Tomopteris spp.	TOM
Metridia pacifica	Mp
Corycaeus anglicus	Ca
Euchaeta elongata	Ee
Eucalanus bungii	Eb
Heterorhabdus tanneri	Ht
Candacia bipinnata	Cb
Rhincalanus nasutus	Rn
Gaetanus intermedius	Gi
Euchirella curticauda	Ec
Epilabidocera longipeda	El
Summer	
Total chaetognaths	CH
Total Small Copepods (<2 mm)	SC
Total Large Copepods (>2 mm)	LC
Total euphausiids	EUP
Total amphipods	AMP
Tomopteris spp.	TOM
Medtridia pacifica	Mp
Euchaeta elongata	Ee
Eucalanus bungii	Eb
Heterorhabdus tanneri	Ht
Gaidius minutus	Gm
Calanus pacificus	Cp
Epilabidocera longipeda	El
Candacia bipinnata	Cb
Lucicutia ovalis	Lo
Neocalanus cristatus	Nc
Neocalanus plumchrus	Np

patterns were then identified as the patterns formed in geographic space by stations classified as being close in taxonomic space.

Matrices defining between-station resemblances based on presence/absence characteristics for both cruises were calculated directly from the binary data. Resemblance was measured as a distance defined as

$$c(i, j) = (2(1 - \cos \alpha_{i,j}))^{1/2}$$

where $\cos \alpha_{i,j}$ is the cosine separation of the two binary element station vectors i and j given by

$$\cos \alpha_{i,j} = \frac{a}{((a+b)(a+c))^{1/2}}$$

where a, b, and c are the first three elements of a 2×2 contingency table defining the two stations (ORLOCI, 1978) (a = number of groups present at both stations, b = number present at station i but not j, c = number present at j but not i).

Classification of stations using the more ubiquitous taxonomic categories was based on between-station resemblance measured as a Euclidean distance in multi-dimensional species space. To prevent domination of the station separations by the numerically more abundant taxonomic categories, numbers per sample in the original data matrices were first normalized to relative frequency. The necessity of this normalization was exacerbated by the use of such wide taxonomic categories as 'Total Small Copepods' in the same matrix as actual species counts (see Table 1). The number of each taxonomic category at each station was redefined as a relative frequency by

$$F(h,k) = \frac{x_{h,k}}{\sum_{k=1}^{N} x_h}$$

where x is the abundance of taxonomic category h at station k and summation is over all stations N.

Each station vector has both a directional component, determined by the ratios of the taxonomic frequencies, and a length component, determined (after the previously given normalization) by the magnitude of frequencies among those taxonomic categories present. Stations with identical taxonomic compositional ratios will actually be separated in multi-dimensional species space by differing magnitudes of relative frequency. In order to classify stations solely on the basis of relative taxonomic composition, the effect of differing magnitudes of relative frequency can be removed from each station vector by normalizing such that

$$\sum_{h=1}^{S} F_k^2 = 1.0$$

where summation is over all species at station k and separation becomes a chord length. In practice, this second normalization and the matrix of between-station chord lengths was calculated from the frequency-normalized matrix in a single step as

$$c(j,k) = [2(1 - q_{jk}/(q_{jj}q_{kk})^{1/2})]^{1/2}$$

where $q_{jk} = \Sigma F_{hj}F_{hk}$, $q_{jj} = \Sigma F_{hj}^2$, $q_{kk} = \Sigma F_{hk}^2$ and summation is over all species h for two stations j and k (ORLOCI, 1978).

It is useful to discuss the effects of these data transformations to the raw data counts in geometric terms. The frequency normalization gives each axis defining a multi-dimensional hypervolume in taxonomic space an equal length (=1.0). This normalization weights each taxonomic category equally in its potential contribution to the angular separation of station vectors in this space. This places increased weight or emphasis on the numerically less abundant categories and also on those categories with a more patchy distribution. The exclusion of spatially rate categories from this data matrix minimized this effect. The second transformation maps each station vector onto the surface of a

hyperspherical volume of unit radius, and the Euclidean distance between any two stations becomes a chord length between two points on this surface. This transformation also obviates the need to normalize the raw counts by the volume of water filtered in each sample. Stations with similar taxonomic frequency compositional ratios will be interpreted as being close in taxonomic space, regardless of the actual magnitude of their relative frequencies.

The matrices of between-station resemblance calculated from the binary data and the frequency normalized data for each season were used as input to a complete linkage, agglomerative, hierarchic clustering algorithm. This algorithm forms groups or clusters by sequentially joining stations which are closest in species space. Distances between multi-station clusters are defined by the maximum of all possible pair-wise distances between members of one cluster and the other. While other, more complex algorithms exist, this one was chosen for its ease of implementation and its ability to form tight and separate initial clusters of most closely related stations. A potential disadvantage of the algorithm is the possibility of forming loose clusters, late in the hierarchy, with members whose main resemblance to one another is their non-association with the initial tighter clusters (PIELOU, 1977).

A different clustering algorithm was used to test the stability of cluster membership and the relative effects of the above disadvantage. The winter and summer frequency normalized data matrices of between-station similarity were clustered again using a single linkage, agglomerative, hierarchic algorithm. Resultant cluster membership was compared to those formed by complete linkage. This second algorithm redefines distances between already-formed clusters and other stations or clusters as the *minimum* of all possible pair-wise distances between members of the first cluster and the new station or cluster. This algorithm has the opposite tendency of the complete linkage algorithm. It tends to accrete stations onto previously formed clusters rather than form new and distinct clusters. Strong similarities between station groups formed by the two algorithms will indicate that membership within a cluster is not unduly biased by the choice of algorithm.

RESULTS

Station groupings

Multivariate classifications of the stations sampled during winter and summer are presented as dendograms showing between-cluster distance and interpreted dominant station clusters (Figs 2a, b and 3a, b). These clusters were chosen subjectively in an attempt to maximize the similarity between the two data sets within each season and to keep the number of interpreted clusters similar to the number of thermal regions evident in the satellite imagery. For both the winter and summer data, the dendrograms show that at the very closest separations, relationships between stations differ between the binary and frequency normalized data matrices. Later in the hierarchy, however, a level is reached where the relationships appear to stabilize and the station composition of clusters formed by both matrices becomes quite similar. These differences at the closest separations of the heirarchy are not surprising, given the different nature and emphasis of the two data sets. It is encouraging, however, that when the number of stations in the clusters becomes large enough to form meaningful contours in geographic space, cluster membership between the two matrices is remarkably similar. This suggests that similar processes determine

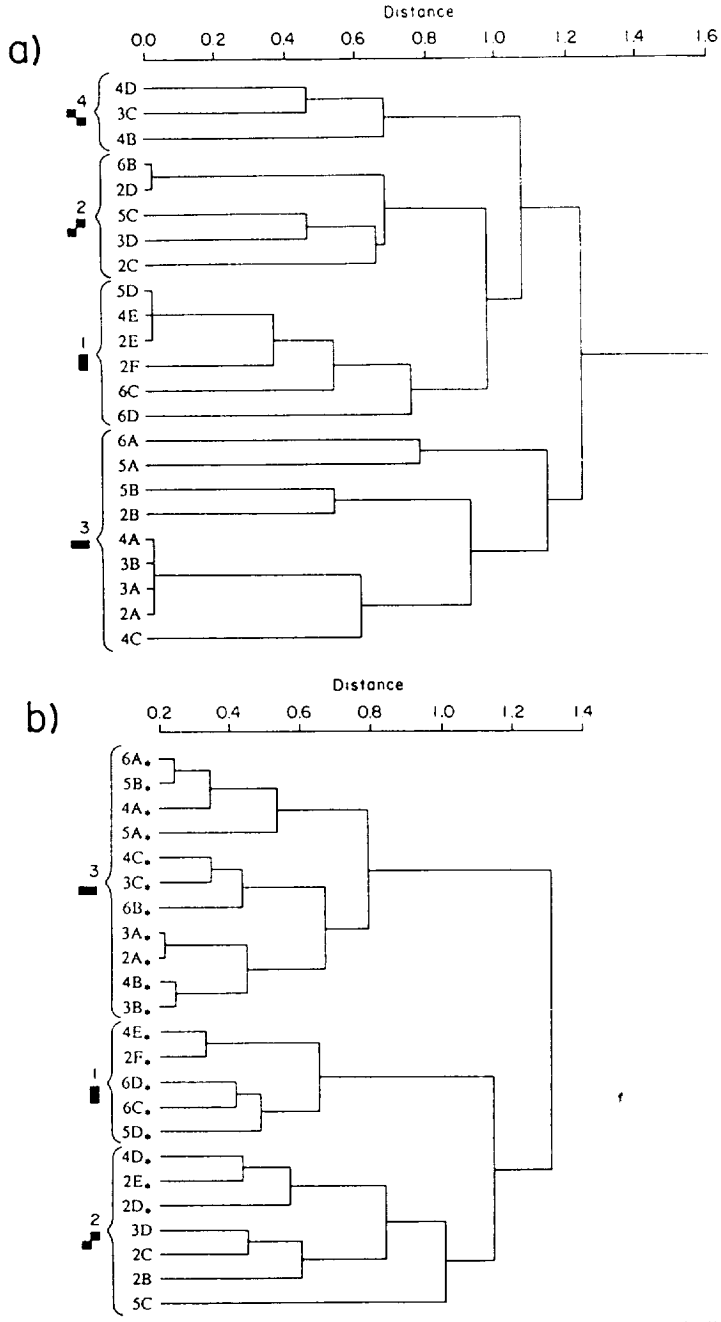

Fig. 2. Dendrograms of winter station classification showing between station similarity for the binary data (a) and the frequency normalized data (b). Brackets show the interpreted major station groups, with a number and symbol used to refer to them within the text and on other figures. The frequency normalized data dendrogram (b) indicates the overlap between cluster membership formed by the complete linkage algorithm illustrated here and the single linkage cluster algorithm used to test for algorithm bias. Stations marked by a * belonged to the same cluster in both algorithms.

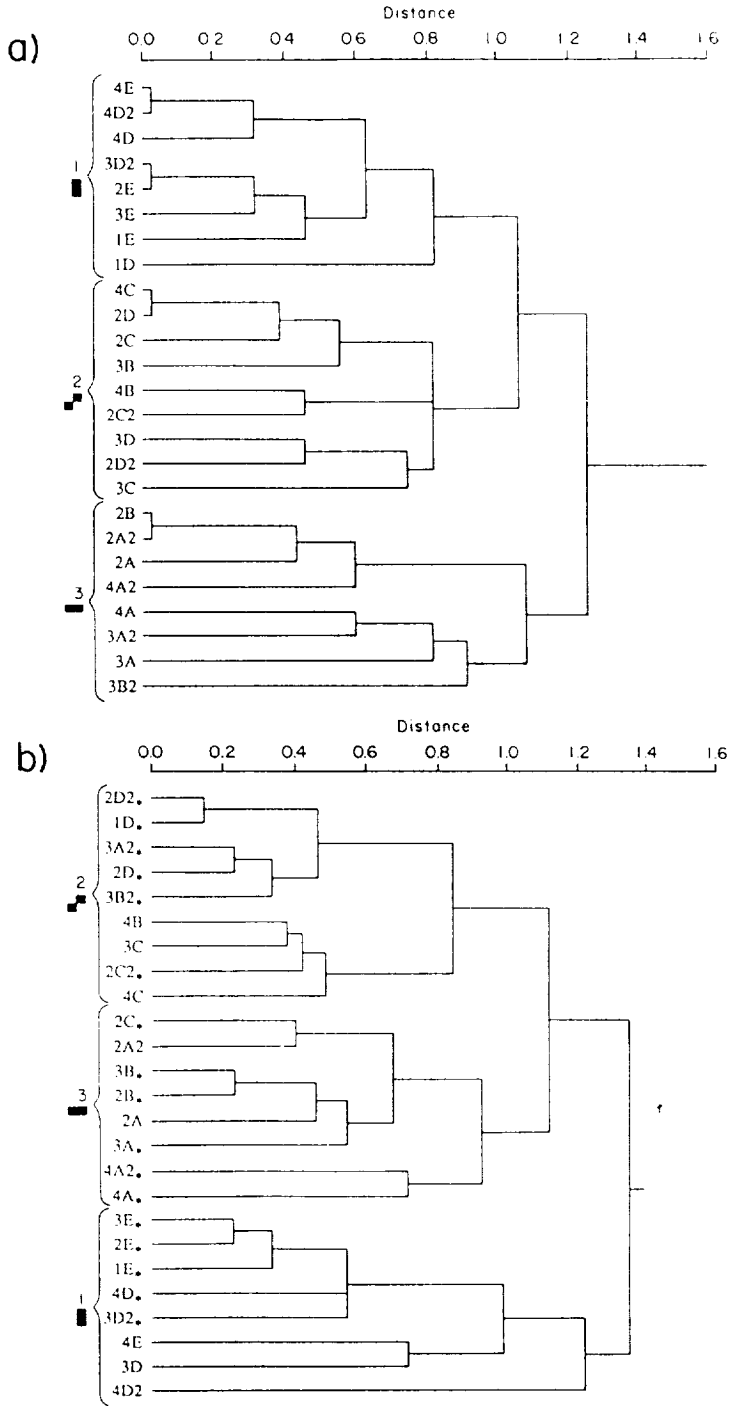

Fig. 3. Dendrograms of summer station classification showing between station similarity for the binary data (a) and the frequency normalized data (b). Brackets indicate the interpreted dominant station groups. Overlap between frequency normalized cluster membership and those formed by the single linkage algorithm is shown the same way as in Fig. 2.

zooplankton distributions on the southern British Columbia shelf with regard to both the relative dominance among more ubiquitous taxonomic groups and the occurrence of spatially rarer groups.

Stations which were classified into the same cluster by both the complete linkage and the single linkage algorithms are indicated on the frequency normalized dendograms (Figs 2b and 3b). During the winter (Fig. 2b), single linkage station membership in both Cluster 1 and Cluster 3 was identical to that of the complete linkage. Three of the seven stations making up Cluster 2 were also placed in this cluster by the single linkage. Three of the remaining four stations are from the middle shelf and were accreted to the already formed inner-shelf group (Cluster 3). The similarity between clusters formed by the single and complete linkage of the summer frequency normalized data (Fig. 3b) also suggests that algorithm bias is minimal. Five of the eight stations in Cluster 1, six of the nine stations making up Cluster 2 and six of the eight stations making up Cluster 3 were common to both algorithms. Four of the remaining stations were accreted late in the hierarchy to the entire cluster of all stations. In total, none of the winter stations actually changed cluster membership, and four of the 25 summer stations changed membership. The similarity of the results of these two algorithms implies that clusters identified by the complete linkage dendrograms in Figs 2 and 3 are realistic interpretations of station relationships and that station membership in these groups was not unduly biased by artifacts of the complete linkage clustering algorithm.

The spatial distribution of stations making up these clusters (Figs 4a, b and 5a, b) shows that stations closely related by taxonomic characteristics are generally close in geographic space. Stations within the same cluster are not scattered randomly in the study area. This indicates first, that the number of taxonomic categories used in the cluster analysis was sufficient to identify spatial patterns of the stations and second that the spatial separation of sampling sites was small enough to resolve horizontal patchiness in the distribution of the taxonomic characteristics in both winter and summer sampling periods. This second result is consistent with the results of MACKAS (1984) who calculated a roughly 30 km cross-shelf and 100 km along-shelf length scale of autocorrelation in zooplankton community structure.

Geographic positioning of the winter stations (Fig. 4a, b) shows that Cluster 1 from both the binary and frequency normalized data matrices represents outer-shelf stations having similar zooplankton taxonomic characteristics. These characteristics, based on the binary data, are shown in Table 2. This cluster has the least number of missing taxonomic groups among those enumerated. Taxonomic characteristics of this cluster formed from frequency normalized data are summarized in Table 3 as the mean relative frequency vector of each taxonomic group for each cluster. These characteristics are necessarily qualitative as the normalization procedures allow the clustering algorithm to classify only by the relative proportions of each taxonomic group. These data show that stations in Cluster 1 from the outer-shelf had the highest proportion of *Tomopteris* spp., *Metridia pacifica* and *E. bungii* but the lowest proportion of *Candacia bipinnata*, *Corycaeus anglicus* and Large Copepods.

Cluster 3 from both winter analyses is made up of stations from the inner shelf (Fig. 4). The frequency data dendrogram (Fig. 2b) includes more stations in this cluster than the binary data dendrogram (Fig. 2a). This cluster is represented by the fewest number of taxonomic groups (Table 2) with *E. elongata*, *Tomopteris* spp., and *Gaetanus intermedius* absent at all stations. With the exception of *E. bungii*, which is present at most stations in

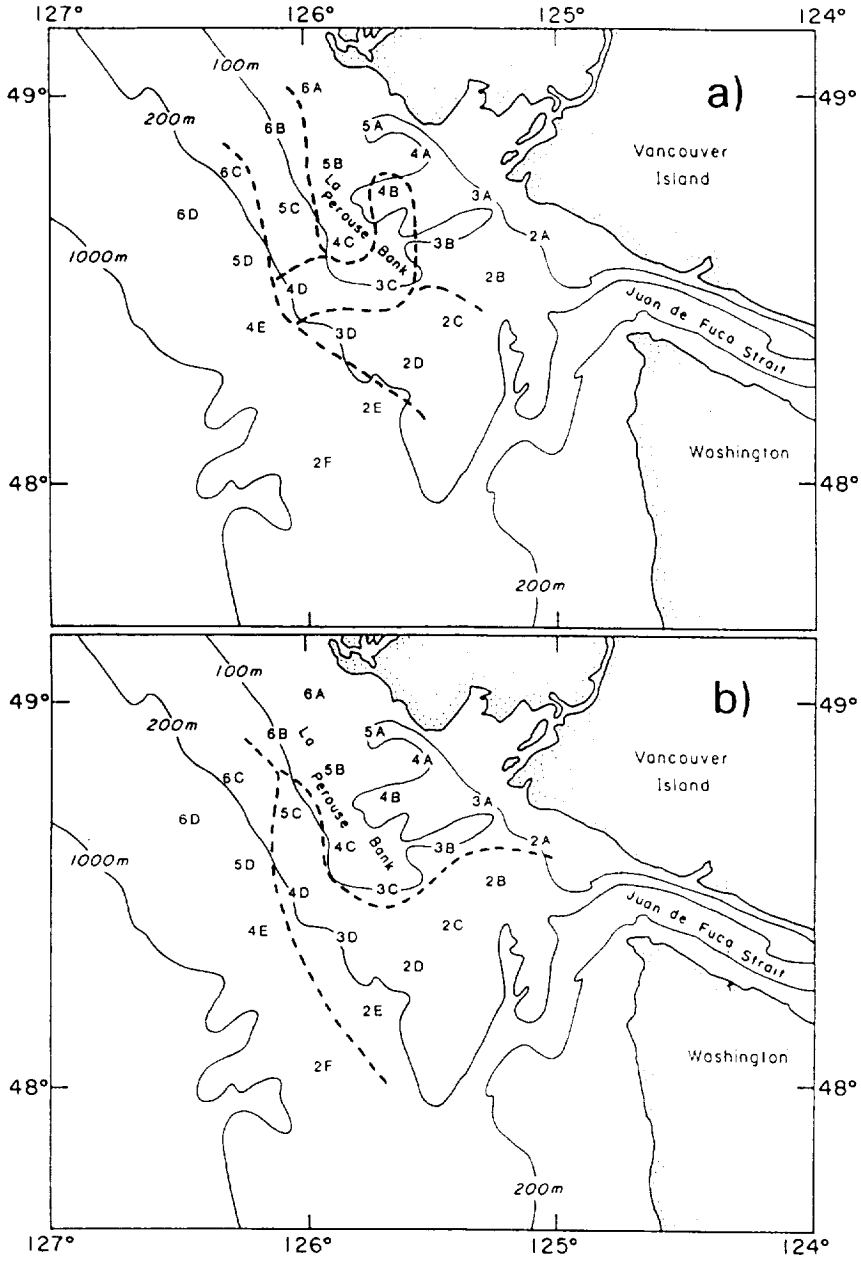

Fig. 4. Study area map of the winter stations showing the spatial grouping of stations according to (a) the binary dendrogram and (b) the frequency normalized dendrogram of Fig. 2.

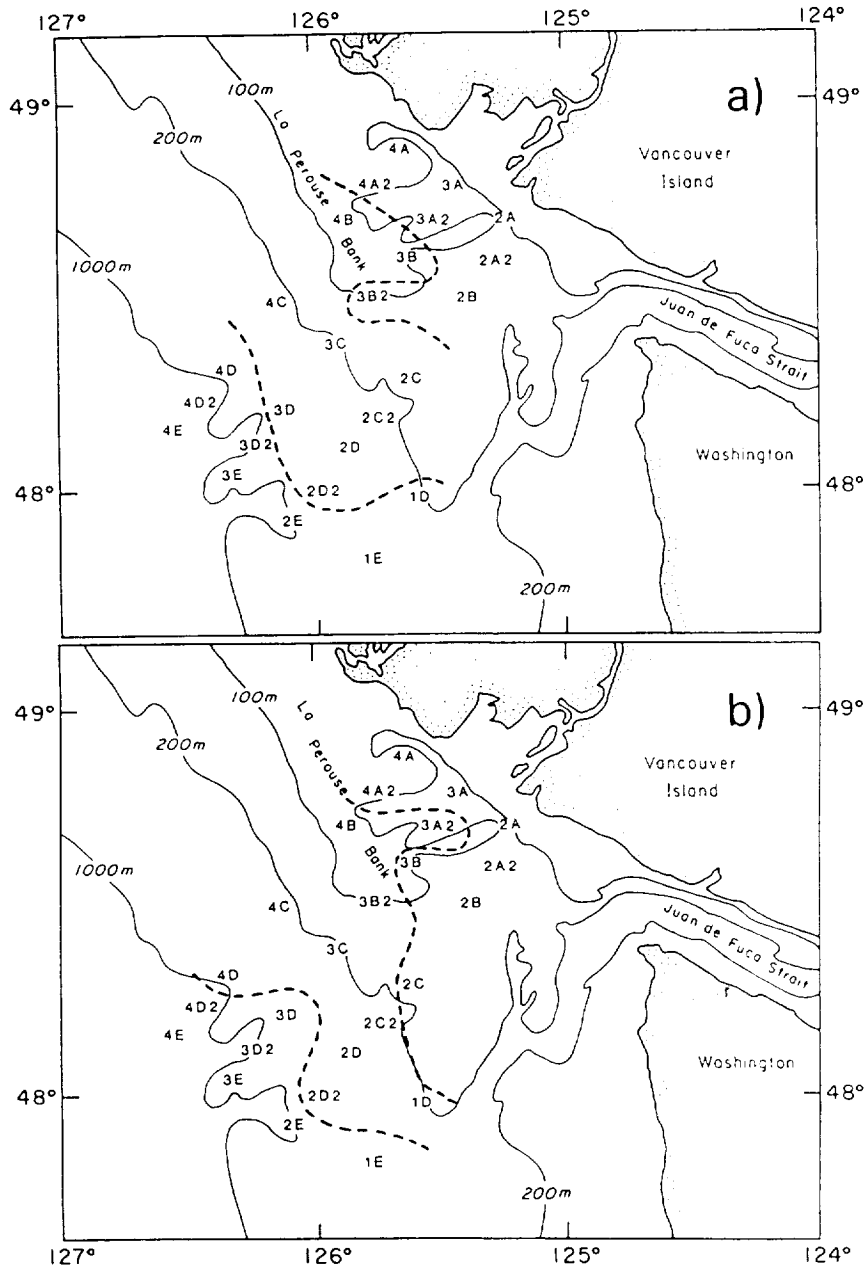

Fig. 5. Study area map of the summer stations showing the spatial grouping of stations according to (a) the binary dendrogram and (b) the frequency normalized dendrogram of Fig. 3.

Table 2. Winter station binary data showing presence and absence, grouped by cluster membership indicated on Fig. 2a

		Taxonomic category							
	Station	Ee	Eb	TOM	Ec	Ht	Gi	Rn	El
	2E	1	1	1	1	1	1	0	0
	2F	1	1	1	1	1	1	1	0
	4E	1	1	1	1	1	1	0	0
Cluster 1	5D	1	1	1	1	1	1	0	0
	6C	1	1	1	1	1	0	0	0
	6D	1	1	1	1	0	1	1	1
	2C	0	1	1	0	1	0	1	0
	2D	0	1	1	0	0	0	0	0
Cluster 2	3D	0	1	1	0	1	0	0	1
	5C	0	1	1	0	1	0	0	0
	6B	0	1	1	0	0	0	0	0
	2A	0	1	0	0	0	0	0	0
	2B	0	1	0	1	0	0	0	1
	3A	0	1	0	0	0	0	0	0
	3B	0	1	0	0	0	0	0	0
Cluster 3	4A	0	1	0	0	0	0	0	0
	4C	0	1	0	0	0	0	1	0
	5A	0	0	0	0	1	0	0	0
	5B	0	1	0	0	0	0	0	1
	6A	0	0	0	0	0	0	0	0
	3C	0	1	1	0	0	0	1	0
Cluster 4	4B	0	0	1	0	0	0	1	0
	4D	1	1	1	0	0	0	1	0

all clusters, the rest of the taxonomic groups are present in Cluster 3 at only one station each. The mean frequency vector (Table 3) shows Cluster 3 stations have the highest proportions of chaetognaths, large and small copepods and *C. anglicus*, but the lowest proportions of *Tomopteris* spp. and *E. bungii*.

Geographic positions of the remaining winter stations indicate a mid-shelf group separating the inner-shelf and the outer-shelf station groups (Fig. 4). The binary data dendrogram (Fig. 2a) separates these stations into two clusters (Clusters 2 and 4). Table 2 shows that Clusters 2 and 4 have *E. curticauda* and *G. intermedius* missing entirely. The frequency dendrogram (Fig. 2b) classifies the mid-shelf stations as a single cluster (Cluster

Table 3. Winter mean frequency vector for each cluster identified in Fig. 2b

	CH	SC	LC	Mp	Ca	EUP	Eb	TOM	Cb
Cluster 1	0.167	0.218	0.194	0.366	0.048	0.216	0.345	0.691	0.090
Cluster 2	0.266	0.296	0.231	0.207	0.121	0.417	0.305	0.159	0.479
Cluster 3	0.413	0.349	0.314	0.151	0.590	0.166	0.128	0.024	0.283

Values indicate the magnitude of the relative frequency component along each species axis.

2). The final linkage of this cluster, however, occurs late in the hierarchy where the algorithm might be biased. The mean frequency vector of these stations (Table 3) shows Cluster 2 to have the highest proportion of *C. bipinnata* and euphausiids but in general to have characteristics intermediate between that of Cluster 1 and Cluster 3 (the outer and inner shelf groups).

The summer distribution of station cluster membership (Fig. 5a, b) shows a similar cross-shelf trend to that seen during the winter. Both the binary and the frequency dendrograms identify an outer-shelf group of stations (Cluster 1). All taxonomic categories are represented in this cluster (Table 4). The mean frequency vector (Table 5) for stations in Cluster 1 shows a low relative proportion of euphausiids, chaetognaths, *Calanus pacificus*, and total Small Copepods but the highest relative proportion of amphipods, *E. bungii*, and *M. pacifica*.

Cluster 2 of both summer dendrograms is a mid-shelf station group (Fig. 5) in which four of the enumerated taxonomic categories are missing entirely (Table 4). The mean frequency vector for this cluster (Table 5) shows these stations to have the highest proportions of euphausiids, chaetognaths, *C. pacificus* and total Large Copepods and the lowest proportions of *E. bungii*.

Table 4. Summer station binary data showing presence and absence, grouped by cluster membership indicated in Fig. 3a

		Taxonomic category										
	Station	TOM	Nc	Np	Ee	Mp	El	Ht	Gm	Cb	Lo	AMP
	1D	0	1	0	0	1	0	1	0	0	0	1
	1E	0	1	1	1	1	1	1	0	0	1	1
	2E	1	1	1	1	1	1	1	0	0	1	1
Cluster 1	3D2	1	1	1	1	1	1	1	0	0	1	1
	3E	1	1	1	1	1	1	1	0	1	1	1
	4D	1	1	1	1	1	0	1	0	1	1	1
	4D2	1	1	1	1	1	0	1	1	1	1	1
	4E	1	1	1	1	1	0	1	1	1	1	1
	2C	0	1	1	1	1	1	0	0	0	0	1
	2C2	0	1	0	0	1	1	0	0	0	0	1
	2D	0	1	1	0	1	1	0	0	0	0	1
	2D2	0	1	1	0	1	0	0	0	0	0	1
Cluster 2	3B	0	1	1	0	0	1	0	0	0	0	1
	3C	1	0	1	0	1	1	0	0	0	0	1
	3D	0	0	1	0	1	0	0	0	0	0	1
	4B	0	0	0	0	1	1	0	0	0	0	1
	4C	0	1	1	0	1	1	0	0	0	0	1
	2A	0	0	1	1	1	1	0	0	0	0	0
	2A2	0	1	1	1	1	1	0	0	0	0	0
	2B	0	1	1	1	1	1	0	0	0	0	0
	3A	0	1	0	0	0	1	0	0	0	0	0
Cluster 3	3A2	0	0	1	0	0	1	0	0	0	0	0
	3B2	0	0	0	0	1	0	0	0	0	0	0
	4A	0	0	0	0	1	1	0	0	0	0	0
	4A2	0	0	0	1	1	1	0	0	0	0	0

Table 5. Summer mean frequency vector for each cluster identified in Fig. 3b

	EUP	AMP	CH	LC	SC	Eb	Cp	Mp
Cluster 1	0.015	0.095	0.030	0.030	0.023	0.093	0.015	0.110
Cluster 2	0.064	0.021	0.058	0.070	0.048	0.011	0.083	0.007
Cluster 3	0.038	0.006	0.030	0.017	0.048	0.020	0.017	0.008

Values indicate the magnitude of the component along each species axis.

The remaining summer stations (Cluster 3) form a cluster representing an inner-shelf coastal group (Fig. 5a, b) extending furthest offshore in the southern portion of the study area. The binary data matrix shows these stations to have the fewest representatives (Table 4) with six of the 11 enumerated groups absent entirely. The mean frequency vector (Table 5) for this cluster indicates stations characterized by the lowest proportion of total Large Copepods and amphipods and the highest proportion of total Small Copepods.

Surface thermal patterns, in situ *hydrography and station patterns*

The mean satellite image representing surface thermal patterns during the winter cruise is shown in Fig. 6. A comparison of this image with Fig. 1a indicates sampling occurred in three major surface thermal zones on the shelf. The dominant feature of the image is the along-shore zone of warmest water (temperatures above 12.2°C) over the middle and outer shelf area. The inner shelf is occupied by the coldest surface water (temperatures less than 11.5°C) which is separated from the warmer water to seaward by a frontal zone with maximum surface thermal gradient in the northern and southern portions of the study area. A tongue of cold coastal water can be seen extending south over shallow portions of the shelf in the vicinity of La Perouse Bank (see Fig. 1a). Seaward of the warmest water zone is a region of cooler surface temperature (<12.0°C). Still further to seaward, at the bottom left of the image, surface temperatures are again less than 11.5°C but sampling did not extend into this regime.

Contours of the winter subsurface vertical temperature structure across the shelf (Fig. 7) show that the satellite measured surface thermal patterns are representative of the general water column structure in the study area. The location of the transect in relation to surface temperature patterns is shown in Fig. 6. The warmest zone identified in the satellite image is visible as a distinct core of warm, isothermal water occupying the middle and outer shelf. Previous winter studies (IKEDA *et al.*, 1984; THOMAS and EMERY, 1986) have identified this water as the northern extension of the poleward flowing Davidson Current. The subsurface coutours show the coldest water along the inner shelf to be a near-surface feature with this portion of the shelf more strongly stratified than others. This water is the Vancouver Island Coastal Current, a buoyancy driven surface flow of lower salinity, driven primarily by estuarine outflow from Juan de Fuca Strait and coastal rivers (FREELAND *et al.*, 1984; THOMAS and EMERY, 1986; HICKEY *et al.*, 1990). The sampled region of slightly increased stratification and cooler surface temperatures seaward of the main core of the Davidson Current (Fig. 7) is termed North Pacific water in this paper.

The mean satellite image of the summer sampling period (Fig. 8) shows that colder surface temperatures (<13.0°C) are again associated with near-shore regions of the British Columbia shelf, but are now concentrated off the mouth of Juan de Fuca Strait. Warmer

surface temperatures (>13.0°C) extend across the rest of the shelf and are continuous with warm surface water far beyong the continental shelf. The cold surface region at the mouth of the strait is most likely the surface expression of a cyclonic eddy seen in previous studies (FREELAND and DENMAN, 1982; EMERY *et al.*, 1986). The upwelling of cold water within the eddy is induced by its interactions with bottom topography and outer-shelf undercurrents (FREELAND and DENMAN, 1982). Subsurface profiles of the vertical temperature structure (Fig. 9) confirm this interpretation of the satellite imagery. The location of this cross-shelf transect is shown in Fig. 8. The colder region closest to shore is less stratified, with cold water present at the surface over the inner shelf. A surface frontal zone, with isotherms indicative of upwelling, separates this region from warmer, more stratified water over the middle and outer shelf. Subsurface profiles from the northern portion of the study area (THOMAS and EMERY, 1988) confirm that warm regions north of the cold eddy visible in the satellite image represent stratified conditions extending across the entire shelf.

A similarity between the spatial distribution of the station clusters and satellite measured patterns of sea surface temperature is evident in both the winter and summer data over middle and inner regions of the British Columbia continental shelf (Figs 10a, b and 11a, b). In both seasons, a separate station cluster is associated with colder water over the inner shelf with different clusters present in warmer water over the middle and outer portions of the shelf. This suggests a relationship between the zooplankton composition of the water column and the hydrography of the shelf. These data indicate that station clusters over the outer shelf are not well correlated with any single or identifiable thermal feature during either season.

The winter satellite image (Fig. 10a, b) shows the inner-shelf stations (Cluster 3) to be associated with colder Vancouver Island Coastal Current water and implies that the frontal zone separating this water from warmer Davidson Current water over the middle and outer shelf (Fig. 7) acts as a faunal boundary. Satellite images monitoring the position of this front therefore identify the boundary between stations having different zooplankton compositions. Station spatial patterns derived from both winter data matrices show that the zooplankton composition of the colder water extending offshore over La Perouse Bank is most similar to that of stations nearest shore, suggesting that this region retains a coastal type zooplankton community (Fig. 10a, b).

These figures also show that stations in warmer Davidson Current water extending offshore immediately south of La Perouse Bank are more closely associated with stations from the mid-shelf. The binary data (Fig. 10a) divides these mid-shelf stations into two groups. Members of Cluster 4 are located around the outside edge of the cold tongue overlying La Perouse Bank. Those of Cluster 2 are associated with the main body of the Davidson Current in the southern portion of the study area but also with colder water at two stations further north. A partial explanation of this ambiguity is the temporal variability in the cross-shelf position of the frontal zone in this region which is masked by the mean image. The original image sequence shows these two stations to be within a region of maximum variability associated with small-scale displacements of the frontal zone.

Patterns formed by winter station clusters on the outer shelf do not correspond to surface thermal patterns in a consistent manner. Outer-shelf stations (Cluster 1) occur in both the main core of Davidson Current water and in cooler, more stratified North Pacific water to seaward (Fig. 10a, b). These stations are generally located seaward of the 200 m depth contour (Fig. 4a, b) and appear to show a stronger association with bathymetry.

Comparison of summer sea surface temperature patterns and station clusters (Fig. 11a, b) shows a group of stations (Cluster 3) associated with colder surface water of the inner shelf identified as an upwelling zone and two groups (Clusters 1 and 2) associated with warmer more stratified water over the middle and outer shelf. Stations between the upwelling region and the outer-shelf area are grouped together (Cluster 2) over the middle shelf. These stations are located in the region of shear between southward moving California Current System water along the outer shelf and northward moving Vancouver Island Coastal Current water along the inner shelf (FREELAND *et al.*, 1984; HICKEY *et al.*, 1990).

The separation between stations making up the summer outer-shelf cluster (Cluster 3) and the mid-shelf cluster (Cluster 2) does not appear to be associated with any visible thermal feature in the satellite imagery (Fig. 11a, b). Similarly, the subsurface temperature contours (Fig. 9) do not show any discontinuity in this region. Surface currents in the outer portion of the shelf are dominated by advection from the northwest (FREELAND *et al.*, 1984). The cluster boundary is coincident with the outer edge of the shelf, showing an association with the 1000 m contour (Fig. 5a, b) and a general relationship to bottom topography as seen in the winter data.

DISCUSSION

The association between patterns of summer sea surface temperature and spatial patterns formed by the station clusters are consistent with MACKAS and SEFTON'S (1982) contention that advection is primarily responsible for determining summer patterns of shelf zooplankton distribution. Figures 10a and b suggest that this conclusion is also applicable to the winter shelf. Reduced physiological rates in the winter zooplankton community would increase the tendency of plankton to behave as lagrangian tracers of the physical regime; distributional patterns resulting from biological interactions, responses and/or processes would be suppressed. A similar effect is seen in the distribution of winter

Fig. 6. Infrared satellite image representing the mean sea surface temperature over the period of winter sampling (see text for details of image processing). Land is colored brown and clouds flagged as grey. The temperature scale is shown on the right of the image. The black line indicates the ship track along which the subsurface temperature transect in Fig. 7 was sampled.

Fig. 8. Infrared satellite image representing the mean sea surface temperature over the period of summer sampling. The temperature scale is shown at the right of the image. The location of the subsurface temperature transect (Fig. 9) is shown.

Fig. 10. A detail of the winter mean satellite image showing the location and classification of winter stations according to (a) the binary data and (b) the frequency normalized data in relation to surface temperature. Cluster symbols are those given in Fig. 2a and b and the station names and positions are as shown in Fig. 4a and b. The temperature scale is the same as that in Fig. 6.

Fig. 11. A detail of the summer mean satellite image showing the location and classification of summer stations according to (a) the binary data and (b) the frequency normalized data in relation to surface temperature. Cluster symbols are those given in Fig. 3a and b and the station names and positions are as shown in Fig. 5a and b. The temperature scale is the same as that in Fig. 8.

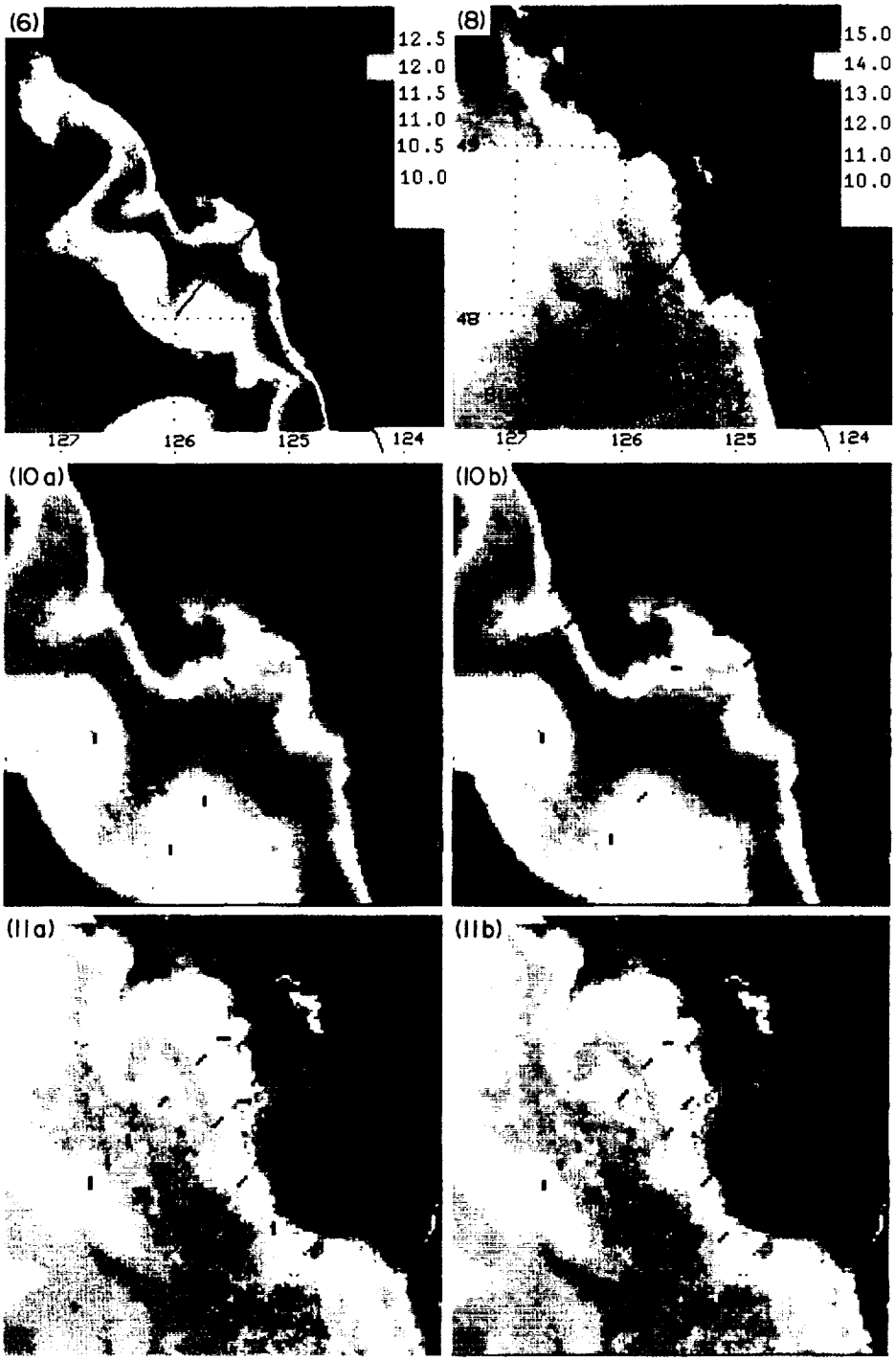

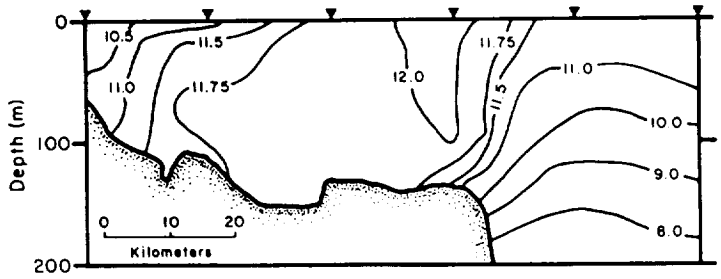

Fig. 7. Cross-shelf contours of winter subsurface temperature in the southern portion of the study area. Colder near-surface water is seen at the coast and a core of warmest water is present over the middle and outer shelf. Station locations are shown by triangles. The transect location is shown in Fig. 6.

surface zooplankton biomass. THOMAS and EMERY (1986) and THOMAS and EMERY (1988) show a stronger relationship between surface hydrography and zooplankton biomass distribution in winter than in summer. The correlation of zooplankton community composition with temperature and salinity gradients normal to the coastline on the Scotia Shelf (TREMBLAY and ROFF, 1983) indicated a similar functional link between hydrographic processes and species distributions in this Atlantic subartic shelf region. The interaction of behavioral characteristics and dynamic processes in the water column can also result in associations between species or groups of species and hydrography. PETERSON *et al.* (1979) show how the behavioral characteristics of zooplankton in the Oregon coastal upwelling zone act to maintain their cross-shelf position. Similar interactions between vertical migration, temperature preference and hydrographic properties across the Gulf Stream produce distinct species groups associated with specific hydrographic features (WISHNER and ALLISON, 1986).

BOUCHER *et al.* (1987) use principal component analysis to show an association of surface zooplankton community composition with shelf and shelfbreak physical structure in the northern Mediterranean Sea. Although there is a contrast in the spatial scales of community variability resolved by BOUCHER *et al.* (1987) (≈4 km after smoothing) and scales in this study (≈20 km), the detailed vertical hydrographic data presented by these authors illustrating the relationship between subsurface physical processes, surface

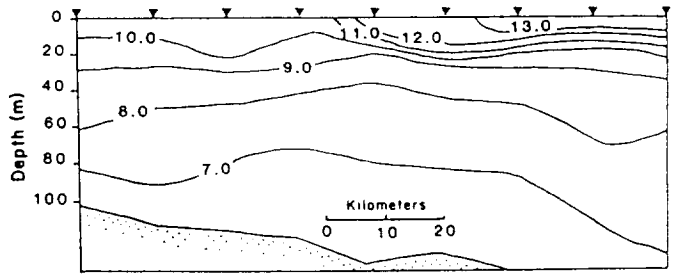

Fig. 9. Cross-shelf contours of summer subsurface temperature through the northern portion of the region of upwelling. Cold water is seen at the surface closest to shore, separated by a surface frontal zone from warmer, more stratified water offshore. Station locations are shown by triangles. The transect location is shown in Fig. 8.

structure and the resultant zooplankton community patterns, is consistent with relationships presented here. Data in Figs 10 and 11 contrast with the results reported by STAR and MULLIN (1981) which indicate that patchiness of individual taxa in the North Pacific and California Current were not correlated with temperature and were probably a result of intrinsic biological processes. This inconsistency most likely illustrates the difference between a shelf ecosystem more dominantly influenced by physical processes (advection and mixing), and a more stable offshore ecosystem where biological processes become more important.

Some of the deeper living species used in the cluster analysis are probably not closely associated with near-surface physical processes (e.g. *L. ovalis*, *H. tanneri*), although their exact vertical distributions are unknown. Implied relationships between their horizontal distribution and satellite images of surface temperatures are therefore not straightforward. At least two factors might influence the results shown here. In shallower regions of the study area, advection and/or vertical mixing often result in either an almost isothermal water column, or regions where surface thermal boundaries reflect subsurface hydrographic boundaries. Both Figs 7 and 9 illustrate this. In these regions, it is not unreasonable to observe an association between non-surface dwelling zooplankton species and surface thermal patterns. In deeper regions over the outer shelf and shelfbreak, subsurface advection will be more dissociated from surface advection and hydrographic characteristics. This factor probably contributed to the lack of a relationship between station cluster patterns and surface thermal patterns during both sampling periods over the outer shelf.

Taxonomic characteristics of the station clusters provide biological clues to the origin of the principal hydrographic regimes in the study region inferred from satellite and *in situ* hydrographic data. *C. anglicus* is a common neritic species in British Columbian waters reaching high densities in estuarine conditions (LEWIS and THOMAS, 1986; LEGERE, 1957). In the winter, the highest relative proportion of this species (Table 3) was in the near-shore station cluster (Cluster 2), associated with colder water (Fig. 10b) in a shelf region of strong estuarine influence (Fig. 7 and THOMAS and EMERY 1986). Other winter station clusters were associated with warmer water of presumably more oceanic origin and had a lower proportion of this species. Shallow regions of the shelf might also be less suitable for species requiring deeper water during a portion of their life history. For the winter data Table 3 shows Cluster 3 has the lowest proportions of euphausiids and *M. pacifica*, both known to be strong diel migrators. These stations also have the lowest proportion of *E. bungii*, an ontogenetic migrator, which KRAUSE and LEWIS (1979) and LEWIS and THOMAS (1986) have shown to overwinter at depths greater than 100 m in British Columbia coastal waters. STONE (1980) and GARDNER (1982) show that the copepod *C. bipinnata* is primarily associated with subtropical water and is evidence of equatorial water being advected north and onto the British Columbian shelf. The winter data (Table 3) show this species to have the highest relative frequency in Cluster 2. Stations in this cluster are associated with the warm core of Davidson Current water in the satellite image (Fig. 10b). Summer data (Table 4) show that this species is present only at stations on the outer shelf in warmer water (Fig. 11a), and is not present at cooler, inner-shelf stations. Similarly, *E. curticauda* is an oceanic, southerly species associated with northward intrusions of subtropical water (STONE, 1980). Winter data (Table 2) shows this species to be present only at stations associated with warmer Davidson Current water. It is not present at stations in the Vancouver Island Coastal Current water.

CONCLUSIONS

Multivariate analysis of zooplankton taxonomic characteristics on the southern British Columbia shelf groups stations into spatial patterns similar to those of surface temperature identified in concurrent infrared satellite imagery for both a winter and a summer sampling period. Spatial patterns generated by samples from stations on the outer shelf and shelf break are not associated with any identifiable hydrographic feature, but appear more closely related to bathymetry. Subsurface temperature profiles show that the surface thermal frontal zones visible in the imagery reflect boundaries in the overall hydrography of the shelf water column. This preliminary test indicates that satellite detected hydrographic boundaries are also boundaries between regions of differing zooplankton community characteristics. These data suggest that in regions where biological spatial patterns are strongly controlled by physical processes, infrared satellite images contain valuable information about the spatial distribution of zooplankton communities. This has obvious connotations in both the interpolation of sampled stations to produce maps of species and/or community distribution, resource management, and in the planning of research cruises. Readily available infrared satellite images allow planning of the necessary station locations to meet specific experimental criteria, as well as an indication of the synopticity of spatially and temporally separated stations. Previous work (MACKAS, 1984) indicates that distributional patterns on the British Columbia shelf are stable in time, at least during the summer, and that it is the species makeup of the patterns which changes. The similarity of these patterns with the shelf hydrography shown in this study suggests that shorter time scale (days) mesoscale changes in the shelf hydrography, such as those discussed by THOMSON (1984), IKEDA and EMERY (1984), THOMSON and GOWER (1985) and THOMAS AND EMERY 1988) are likely to be associated with changes in both distributional pattern and composition. The temporal continuity of the associations between zooplankton distributional pattern and specific hydrographic characteristics demonstrated here is a subject for future work.

Acknowledgements—I thank D. L. Mackas for many helpful discussions and comments on this work and W. J. Emery for his guidance, support and encouragement. An anonymous reviewer provided a thorough and insightful critique of an earlier version of this manuscript. This research was supported by an NSERC postgraduate fellowship and a British Columbia GREAT award for cooperative work between the author, W. J. Emery and G. A. Borstad and Associates Ltd., of Sidney, British Columbia, on biological applications of remote sensing. Support during final preparation of this manuscript was provided by NASA grant NAGW-1251 and the Atlantic Centre for Remote Sensing of the Oceans.

REFERENCES

ALLISON S. K. and K. F. WISHNER (1986) Spatial and temporal patterns of zooplankton biomass across the Gulf Stream. *Marine Ecology Progress Series*, **31**, 233–244.

BOUCHER J., F. IBANEZ and L. PRIEUR (1987) Daily and seasonal variations in the spatial distribution of zooplankton populations in relation to the physical structure in the Ligurian Sea Front. *Journal of Marine Research*, **45**, 133–173.

DENMAN K. L., D. L. MACKAS, H. J. FREELAND, M. J. AUSTIN and S. H. HILL (1981) Persistent upwelling and mesoscale zones of high productivity off the west coast of Vancouver Island, Canada. In: *Coastal upwelling*, F. A. RICHARDS, editor, American Geophysical Union, Washington D.C.

EMERY W. J. and M. IKEDA (1983) A comparison of geometric correction methods for AVHRR imagery. *Canadian Journal of Remote Sensing*, **10**, 46–56.

EMERY W. J., A. C. THOMAS, M. J. COLLINS, W. R. CRAWFORD and D. L. MACKAS (1986) An objective method for computing advective surface velocities from sequential infrared satellite images. *Journal of Geophysical Research*, **91**, 12856–12878.

FAGER E. W. and J. A. MCGOWAN (1963) Zooplankton species groups in the North Pacific. *Science*, **140**(3566), 453–460.

FASHAM M. J. R. and M. V. ANGEL, (1975) The relationship of the zoogeographic distributions of the planktonic ostracods in the north-east Atlantic to the water masses. *Journal of the Marine Biological Association of the U.K*, **55**, 739–757.

FREELAND H. J. and K. L. DENMAN (1982) A topographically controlled upwelling center off southern Vancouver Island. *Journal of Marine Research*, **40**, 1069–1093.

FREELAND H. J., W. R. CRAWFORD and R. E. THOMSON (1984) Currents along the Pacific coast of Canada. *Atmosphere–Ocean*, **22**, 151–172.

GARDNER G. A (1982) Biological and hydrographical evidence for Pacific equatorial water on the continental shelf north of Vancouver Island, British Columbia. *Canadian Journal of Fisheries and Aquatic Sciences*, **39**, 660–667.

HAURY L. R (1976) Small-scale pattern of a California Current zooplankton assemblage. *Marine Biology*, **37**, 137–157.

HAURY L. R., J. J. SIMPSON, J. PELAEZ, C. J. KOBLINSKY and D. WIESENHAHN (1986) Biological consequences of a recurrent eddy off Point Conception, California. *Journal of Geophysical Research*, **91**, 12,937–12,956.

HICKEY B. M., R. THOMSON, H. YIH and P. LEBLOND (1990) A buoyancy driven coastal current. *Journal of Geophysical Research*, in review.

IKEDA M. and W. J. EMERY (1984) A continental shelf upwelling event off Vancouver Island as revealed by satellite infrared imagery. *Journal of Marine Research*, **42**, 303–317.

IKEDA M., W. J. EMERY and L. A. MYSAK (1984) Seasonal variability in meanders of the California Current System off Vancouver Island. *Journal of Geophysical Research*, **89**, 3487–3505.

KRAUSE E. P. and A. G. LEWIS (1979) Ontogenetic migration and distribution of *Eucalanus bungii* (Copepoda: Calanoida) in British Columbia waters. *Canadian Journal of Zoology*, **57**, 2211–2222.

LEGERE J. E. H. (1957) The qualitative and quantitative distribution of plankton in the Strait of Georgia in relation to certain environmental factors. *Journal of the Fisheries Research Board of Canada*, **14**, 521–552.

LEWIS A. G. and A. C. THOMAS (1986) Tidal transport of planktonic copepods across the sill of a British Columbia fjord. *Journal of Plankton Research*, **8**, 1079–1089.

MACKAS D. L. (1984) Spatial autocorrelation of plankton community composition in a continental-shelf ecosystem. *Limnology and Oceanography*, **29**, 451–471.

MACKAS D. L. and H. A. SEFTON (1982) Plankton species assemblages off southern Vancouver Island: geographic pattern and temporal variability. *Journal of Marine Research*, **40**, 1173–1200.

MACKAS D. L. and E. P. ANDERSON (1986) Small-scale zooplankton community variability in a northern British Columbia fjord system. *Estuarine and Coastal Shelf Science*, **22**, 115–142.

MACKAS D. L., G. C. LOUTTIT and M. J. AUSTIN (1980) Spatial distribution of zooplankton and phytoplankton in British Columbia coastal waters. *Canadian Journal of Fisheries and Aquatic Sciences*, **37**, 1476–1487.

MCGOWAN J. A. and P. W. WALKER (1979) Structure in the copepod community of the North Pacific Central Gyre. *Ecological Monographs*, **49**, 195–226.

ORLOCI L. (1978) *Multivariate analysis in vegetation research*. W. Junk, The Hague.

PETERSON W. T., C. B. MILLER and A. HUTCHINSON (1979) Zonation and maintenance of copepod populations in the Oregon upwelling zone. *Deep-Sea Research*, **26**, 467–494.

PIELOU E. C. (1977) *Mathematical ecology*. J. Wiley and Sons, New York.

ROMAN M. R., A. L. GAUZENS and T. J. COWLES (1985) Temporal and spatial changes in epipelagic microzooplankton and mesozooplankton biomass in warm-core Gulf Stream ring 82-B. *Deep-Sea Research*, **32**, 1007–1022.

STAR J. L. and M. M. MULLIN (1981) Zooplanktonic assemblages in three areas of the North Pacific as revealed by continuous horizontal transects. *Deep-Sea Research*, **28**, 1303–1322.

STONE D. P. (1980) The distribution of zooplankton communities in a glacial runoff fjord and exchanges with the open sea. In: *Fjord oceanography*, H. J. FREELAND, D. M. FARMER and C. D. LEVINGS, editors, NATO Conference Series IV: Marine Sciences, Vol. 4. Plenum Press, New York.

THOMAS A. C. and W. J. EMERY (1986) Winter hydrography and plankton distribution on the southern British Columbia continental shelf. *Canadian Journal of Fisheries and Aquatic Sciences*, **43**, 1249–1258.

THOMAS A. C. and W. J. EMERY (1988) Relationships between near-surface plankton distributions, hydrography, and satellite measured sea surface temperature patterns. *Journal of Geophysical Research*, **93**, 15,733–15,748.

THOMPSON R. E. (1984) A cyclonic eddy over the continental margin of Vancouver Island: Evidence for baroclinic instability. *Journal of Physical Oceanography*, **14**, 1326–1348.

THOMSON R. E. and J. F. R. GOWER (1985) A wind induced mesoscale eddy over the Vancouver Island continental slope. *Journal of Geophysical Research*, **90**, 8981–8993.

TREMBLAY M. J. and J. C. ROFF (1983) Community gradients in the Scotian Shelf zooplankton. *Canadian Journal of Fisheries and Aquatic Sciences*, **40**, 598–611.

WIEBE P. H., G. R. FLIERL, C. S. DAVIS, V. BARBER and S. H. BOYD (1985) Macrozooplankton biomass in Gulf Stream warm-core rings: spatial distribution and temporal changes. *Journal of Geophysical Research*, **90**, 8885–8901.

WISHNER K. F. and S. K. ALLISON (1986) The distribution and abundance of copepods in relation to the physical structure of the Gulf Stream. *Deep-Sea Research*, **33**, 705–731.

YAMAMOTO T. and S. NISHIZAWA (1986) Small-scale zooplankton aggregations at the front of a Kuroshio warm-core ring. *Deep-Sea Research*, **33**, 1729–1740.

APPENDIX J

THE INFLUENCE OF HYDROGRAPHIC CONDITIONS AND WIND FORCING ON THE DISTRIBUTION AND ABUNDANCE OF DUNGENESS CRAB LARVAE

R. C. Hobbs, L. W. Botsford, and A. C. Thomas

Influence of Hydrographic Conditions and Wind Forcing on the Distribution and Abundance of Dungeness crab, Cancer magister, Larvae

Roderick C. Hobbs, Louis W. Botsford
Department of Wildlife and Fisheries Biology
and
Center for Population Biology
University of California
Davis, CA 95616

and

Andrew Thomas
College of Oceanography
Oregon State University
Corvallis, OR 97331-5503

Abstract

Hobbs, R. C., L. W. Botsford, and A. Thomas. 1991. Influence of hydrographic conditions and wind forcing on the distribution and abundance of Dungeness crab, Cancer magister, larvae. Can. J. Fish. Aquat. Sci. 00:000-000.

The distribution of the late larval phases of the Dungeness crab (Cancer magister) was sampled by joint U.S.A. / U.S.S.R. plankton surveys off the coasts of Washington, Oregon and northern California involving more than 120 stations from 5 km to 360 km offshore and between 40°N and 48°N latitudes in each of the five years 1981 to 1985. The observed cross-shelf distribution of megalopae was consistent with a mechanism by which diel vertical migratory behavior of the late stage megalopae in the presence of wind induced currents results in onshore transport to favorable settlement areas. Total onshore transport for 45 days prior to sampling, estimated as the effects of wind on a passive particle at the surface at night and in the Ekman layer during the day, is correlated with the nearshore abundance of megalopae. Mean larval densities for each of the 5 cruises declined exponentially with time of year of the cruise. This implied: (1) an instantaneous mortality rate of 0.066 d^{-1} and (2) that survival is independent of variation in environment from year to year. Also, abundance of megalopae was not correlated with station hydrographic data (salinity, temperature and dissolved oxygen) or chlorophyll levels (satellite data from the Coastal Zone Color Scanner). Cross-shelf distributions were, with one exception, consistent with earlier observations by others, in that later stage zoeae were found progressively further offshore with time of year, and megalopae occurred progressively nearer shore with time of year.

Introduction

Commercial harvest of the Dungeness crab (Cancer magister) along the west coast of the U.S. from central California to Washington (Figure 1) generates from 15 to 20 million dollars per year in exvessel value alone. Landings by state fluctuate by as much as an order of magnitude in apparent 10 year cycles, which are synchronous from northern California to Washington (reviewed in Botsford 1986, Botsford, et al. 1989). Although considerable research has focused on determining the cause of these cycles, their dynamic basis is still not understood. In past research, three general hypotheses have been considered: (1) density-dependent recruitment, (2) environmental forcing, and (3) a predator-prey interaction. The last one has been discounted for both salmon and humans as predators (Botsford, et al. 1982, Botsford, et al. 1983), but the first two are still under consideration. Possible mechanisms of density-dependent recruitment include cannibalism (Botsford and Wickham 1978), density-dependent egg production or larval survival (McKelvey, et al. 1980) and an egg-predator nemertean worm which acts in a density-dependent manner (Botsford and Wickham 1978, Wickham 1979a, Hobbs and Botsford 1989). The stages most likely to be affected by environmental forcing are the egg and larval stages. Population levels (using catch as a proxy) are correlated with wind stress during the late larval period (Johnson, et al. 1986), and sea surface temperature during the hatching period (Wild 1980). Mechanisms proposed are wind driven transport to a suitable settlement environment and poor egg clutch survival due to high temperatures, respectively.

Because variation in larval survival, transport and successful settlement could determine the cycles in Dungeness crab abundance, a broad-scale survey of the distribution and abundance of larval crabs would be useful in understanding the population dynamics of the Dungeness crab. The joint U.S.A. / U.S.S.R. ichthyoplankton surveys off the coasts of Washington, Oregon and northern California during the years 1981 to 1985 coincided with the larval phase of the Dungeness crab. More than 120 stations from 5 km to 360 km offshore and between 40°N and 48°N latitudes were sampled in each of the five years. The data from these cruises provided a unique opportunity for comparison of larval abundance and distribution to environmental conditions over a broad spatial range. We present here analysis of the distribution of larval abundance with regard to hydrographic conditions and wind.

Larval life history and development

Dungeness crab larvae hatch near January each year from eggs carried on the female's abdomen, then progress through five zoeal stages during the next three to four months. They then metamorphose into a megalopal stage and settle to the bottom about one to two months later (Lough, 1976, Reilly 1983, Hatfield 1983, Stevens and Armstrong 1985).

The timing of metamorphosis may vary with latitude and from year to year. In two consecutive years (1970, 71) of sampling off Newport, Oregon Lough (1976) first collected megalopae in mid-April and observed that most of the larvae were megalopae by early May. Megalopae were found to first appear somewhat earlier in central California, around mid-March (Reilly 1983). Hobbs and Botsford (unpubl.(a)) found metamorphosis had occurred

three weeks earlier off Newport, Oregon in 1984 than Lough reported for 1970 and 1971. They concluded from five years of samples that most metamorphosis from zoeae to megalopae off Washington, Oregon and northern California occurred over a span of two to three weeks at a given latitude and that this peak of metamorphosis occurs either nearly simultaneously at all latitudes or in a manner that proceeds from south to north over a span of less than a month.

The extended larval period provides a substantial opportunity for transport. For example, during the first three months of the year, moving at average surface current speeds (9 km/d), passive drifting larvae could be transported as much as 800 miles north by the Davidson Current (Johnson, et al. 1986). After the spring transition, larvae could then be transported south a considerable distance by the California Current.

Larval survival and development

The local physical and biological environment of the larvae may affect timely larval development and survival rates. Laboratory studies indicate that the development rate and survival of larvae are sensitive to temperature and salinity concentration (Reed 1969, Gaumer 1971, Sulkin and McKeen, 1989). Fitting a response surface to the survival data of Reed (1969), Lough (1976) found that optimal survival of early instar zoeae occurred at salinities above 25‰ and temperatures between 9° and 15°C. Survival of zoeae declined rapidly after 14 days of starvation as well (Reed 1969). Sulkin and McKeen (1989) found that the survival rate of larvae through the first 4 zoeal instars were nearly the same at 10°C and 15°C but survival to megalopae stage at 15°C was about half of the survival rate at 10°C. No larvae survived to

megalopae at 20°C. Development rates increased with temperature in their laboratory reared larvae which completed the five zoeal stages in 70 days at 10°C but only in 39 days at 15°C (Sulkin and McKeen 1989). Lough (1976), however, observed megalopae appearing at about the same time in two years, although the mean sea surface temperature differed by almost 2°C between the two years.

Larval transport

The California Current System in the ocean off Washington, Oregon and northern California consists of the southward flowing California Current and the northward flowing California Undercurrent which surfaces as the Davidson Current in the fall and winter (Hickey 1979, 1989). Flows during the winter are typically southward in the upper layer offshore and northward inshore and beneath the upper layers offshore. After the spring transition the California Current moves inshore and flows are typically southward at the surface and northward below. Wind driven variations in the alongshore flow are significant (Hickey 1979, 1989, Strub et al. 1987b). Cross-shelf transport at the surface is almost entirely wind driven, being typically onshore during the fall and winter months and offshore during the spring and summer months. Cross-shelf transport beneath the surface is generally opposite to that at the surface (Hickey 1979, 1989, Strub et al. 1987b). The winds are typically onshore between 35°N and 39° N latitude in the winter diverging to the north and south. Above 42°N latitude the winds generally are northward. At some time during March or April the divergence zone below 39°N shifts northward to around 48°N so that the winds are typically onshore and southward above 45°N latitude and increasingly southward below this latitude during the spring and summer. This shift in the

divergence zone is referred to as the spring transition and drives the reversal in cross-shelf transport that occurs at this time (Strub et al. 1987a, b). Vertical migratory behavior of larvae could interact with this wind driven transport system to move them offshore or onshore, or maintain a relatively fixed cross-shelf position in addition to the north-south transport afforded by the California and Davidson Currents.

The few available observations of horizontal distribution of larvae have not yielded a consistent explanation of larval transport. There is some evidence that larvae occur progressively farther offshore during successive zoeal stages (Lough 1976, Reilly 1983). Megalopae have been found concentrated offshore in British Columbian waters (Jamieson and Phillips 1988, Jamieson et al. 1989). Later megalopal stages are typically found closer to shore than earlier ones (Hatfield 1983, Jamieson and Phillips 1988). Most researchers believe that successful larvae (i.e., those that survive into the juvenile population) must settle near shore. Megalopae are known to settle nearshore in shallow coastal regions and estuaries (Reilly 1983, Stevens and Armstrong 1984, 1985), and few Dungeness crab are found at depths greater than 60 m (e.g., Carrasco, et al. 1985). McConnaughey, et al. (unpubl. University of Washington, School of Fisheries, Seattle, WA 98195) have recently demonstrated a relationship between rotation-corrected Bakun winds and the density of age zero benthic juveniles from six years of trawl surveys off the Washington coast.

Wind forced transport of the larvae would depend on their vertical distribution, for which some observations exist. Researchers have typically found the megalopal stage associated with the surface more than the zoeal stages (Reilly 1983, Booth et al. 1985, Hobbs and Botsford unpubl.(a)).

Megalopae have been seen during the day clinging to the pleustonic hydroid, Velella velella (Wickham 1979b, Reilly 1983, Shenker 1988) and other flotsam, and aggregating in windrows at the surface (Shenker 1988) on cloudy days. There is evidence for diel vertical migration of megalopae with most in the neuston at night (Booth et al. 1985, Jamieson and Phillips 1988, Jamieson et al. 1989), but as deep as 60 m on bright days (Botsford and Shenker unpublished plankton data). From the analyses of diel variation in vertical distribution for five years of data from the USA/USSR Ichthyoplankton cruises Hobbs and Botsford (unpubl.(a)) concluded that vertical migratory behavior varies with development stage. The late stage megalopae were found to exhibit a diel vertical migration being in the neuston at night and below during the day. The fraction of late stage megalopae in the neuston was found to be constant at .62 ± .09 from the hours of 1900 PST to 0800 PST and .08 ± .02 between the hours of 0800 PST and 1900 PST(cf., Jamieson and Phillips 1988, Jamieson, et al 1989). These results are consistent with those obtained by Booth, et al. (1985) (see Hobbs and Botsford unpubl.(a) for discussion.) . The early stage megalopae were rarely found in the neuston and were generally below the neuston at all hours in the one year that the ichthyoplankton cruise coincided with the time of metamorphosis from zoeae to megalopae. In all five ichthyoplankton cruises zoeae were generally found below the neuston at all hours of the day except for two or three hours in the evening (Hobbs and Botsford unpubl.(a)).

Metapopulation dynamics

Knowledge of the impact of environmental factors on larval survival and transport is critical to an understanding of the dynamics of the coastwide "metapopulation" of Dungeness crabs. Recent investigations of models

which explicitly include the metapopulation distributed along the coast have shown that behavior depends critically on the nature of transport between subpopulations. The different types of behavior have important practical consequences. For example, because the coastwide cycles are synchronous (PMFC 1965) has implied that the cycles must be caused by a coastwide environmental factor . However this has been countered by the proposal that a metapopulation consisting of density-dependent individually cyclic populations that are independent except for alongshore transport of larvae between them, can also become synchronized. In modeling studies of the latter hypothesis, the tendency of a spatially distributed meroplanktonic population to become synchronized depends critically on the nature of alongshore transport (Hobbs and Botsford,unpubl.(b)). We here address the question of environmental influence on larval survival and transport through analysis of the distribution of larval abundance estimates from the five joint U.S.A. / U.S.S.R. ichthyoplankton cruises with regard to shipboard hydrographic and meteorological observations and auxiliary chlorophyll and wind data.

Data and methods

Cruise data

The dates of the five cruises and other associated information are given in Table 1. Note that the 1984 cruise occurred approximately five weeks earlier than the 1983 and 1985 cruises, which were about two weeks earlier than the 1981 and 1982 cruises. We pair the 1983 and 1985 cruises, and the 1981 and 1982 cruises, as replicates, to separate patterns of distribution resulting from intra-annual larval ontogeny from patterns resulting from

inter-annual environmental variation. Each cruise took about a month and sampled 124 stations from 5 km to 360 km offshore and between 40°N and 48°N latitudes. A typical plot of station locations is shown in Figure 2. Note that the cruise proceeded from north to south. Samples at most stations consist of a neuston tow and an oblique bongo tow, but at some stations only a neuston sample was taken. Neuston tows using a 0.3 m high by 0.5 m wide Sameoto sampler (Sameoto and Jaroszynski, 1969) with a 0.505 mm mesh net were made at 2.0 knots (1.03 m/sec) for ten minutes. Bongo tows were a standard MARMAP bongo tow (Smith and Richardson, 1977) with a 60 cm diameter, 0.505 mm mesh nets with either 300 m or 570 m of wire out. Flow meters in the mouths of the nets were used to determine the volume of water filtered. A cruise report is available for each cruise (Table 1) which includes the date, time and location of each sample station and haul factors for converting raw counts to numbers per 10 m^2 surface area. Hydrographic data and information on sea state and cloud cover were also taken at each station. The salinity and temperature data have been analyzed by Savage (1989b).

The ichthyoplankton samples from each cruise were sorted for fish larvae in Poland and brachyuran larvae were set aside for our use. Samples containing greater than about 60 zoeae were divided using a plankton splitter to generate a subsample of approximately 25 to 50 zoeae. These zoeae were examined under a binocular dissecting microscope, and identified as either C. magister , other brachyura, or unidentifiable (damaged). All megalopae were examined and identified as C. magister or other brachyura (Lough 1975).

The 1981-3 and 85 cruises occurred at a time of year when most (95%) of the crab larvae had progressed to the megalopal stage with a few still in late

zoeal stages. The 1984 cruise occurred at the time of metamorphosis with most larvae in north being zoeae and in south megalopae.

Abundance estimates

We estimated local larval abundance and the fraction of larvae in the neuston from the paired neuston and bongo samples using a bias-corrected maximum likelihood method (Hobbs and Botsford unpubl.(a)). The abundance of megalopae, in the 1981-3 and 85 cruises, were estimated assuming a diel pattern of migration with a constant fraction of megalopae in the neuston during the day and at night. To estimate abundance at stations where only neuston samples were taken (75 stations, all in the 1982 cruise) we used the maximum likelihood estimates (derived in Hobbs and Botsford unpubl.(a)) of 62 percent of megalopae in the neuston at night (hours of 1900 PST to 0800 PST) and 8 percent of megalopae in the neuston during the day (0800 PST to 1900 PST) as "correction factors" (cf., Jamieson and Phillips 1988, Jamieson, et al 1989) to estimate the abundance in the entire water column from the neuston sample. We used the same methods to calculate the abundance of zoeae found in the 1981-3 and 85 cruises but because of the limited number of zoeae found in these cruises and low numbers found in the neuston samples at most hours of the day and night, we use a three hour moving average estimate of the fraction of zoeae in the neuston as the "correction factors" (Hobbs and Botsford unpubl.(a)). In the 1984 cruise samples nearly all of the larvae were found in the bongo samples, and the average abundances of both zoeae and megalopae were sufficiently large that we used only the bongo samples as measures of local abundance for this cruise.

Chlorophyll data

Chlorophyll abundance data at the sample stations and for each year were compiled from Coastal Zone Color Scanner (CZCS) digital images. The CZCS, an instrument on the NIMBUS-7 satellite, measures intensity of light reflected from the ocean surface at specific bands in the visible spectrum, from these readings chlorophyll abundance can be estimated. Both cloud cover and the low sun angle at higher latitudes early in the year obscure the surface reflectance making the chlorophyll readings at those points unreliable or nonexistent. We were able to obtain useable chlorophyll readings for approximately one third of the stations. These stations are predominantly within 100 km of the shore and later in the year due to the extensive cloud cover earlier in the year.

Wind data

We used the U. S. Navy's Fleet Numerical Oceanographic Center (FNOC) meteorological wind fields to study wind driven transport of larvae. This wind product provides twice daily u and v (eastward and northward respectively) components of surface wind velocity on a grid with 380 kilometer spatial resolution over the entire study period. These winds are based on ship and buoy measurements of wind velocity and pressure, converted into pressure fields. These pressure fields are combined with model derived pressure fields in a statistically optimal sense to produce geostrophic winds. Surface components of these winds are then produced by a reduction in velocity and a rotation to simulate boundary layer conditions based on an estimate of boundary layer stability.

Estimation of wind driven transport of larvae

Wind driven transport of zoeae and early megalopae was modeled as mass transport in the upper Ekman layer. This assumes that these larvae are distributed throughout the upper Ekman layer and do not migrate vertically.

Because the late stage megalopae show a distinct pattern of vertical migration, being primarily at the surface at night and below during the day wind driven transport of megalopae was modeled in three ways. The first assumes the megalopae are distributed throughout the upper Ekman layer and does not take into account vertical migration. The latter two attempt to account for vertical migration by assuming that the megalopae are distributed throughout the upper Ekman layer during half of each day and are in the neuston for the remaining half. Transport of the megalopae in the neuston is considered to be much closer to the actual wind direction.

Ekman transport is 90° to the right of the wind velocity. The components of Ekman transport, T_{EK}, are calculated as

$$T_{EKx} = \frac{\tau_y}{f} \quad \text{and} \quad T_{EKy} = \frac{-\tau_x}{f}$$

where x and y are eastward and northward respectively, f is the Coriolis parameter at the appropriate latitude and τ_x and τ_y are components of surface wind stress. The surface wind stress components are given by

$$\tau = \rho_{air} C_D W^2$$

where ρ_{air} is the air density, C_D is a dimensionless drag coefficient and W is the corresponding component of the wind velocity. Ekman transport, T_{EK}, is

actually a volume transport integrated over a surface wind driven layer. Ekman velocities were estimated by assuming an Ekman wind driven layer of depth D_{EK} given by

$$D_{EK} = \frac{4.3\ W}{\sqrt{\sin \phi}}$$

where W is now the wind speed in the direction of the wind and ø is the latitude. The Ekman velocity components are the calculated as

$$V_{EK} = \frac{T_{EK}}{D_{EK}\ \rho_{water}}$$

where ρ_{water} is the density of sea water.

Advection of megalopae in the neuston was assumed to be 3% of the wind speed and then calculated as first, in the direction of the wind and second , 15° to the right of the wind to simulate some influence of Coriolis at the air/water interface.

Transports were calculated for each of the forty-five days prior to and including the median sample day at each latitude for each of the late cruises (1981-3, 85) as follows. The u and v (eastward and northward respectively) components of the FNOC wind fields were interpolated to 11 points at the coast at even latitudes from 39°N to 49°N. The three transport vectors for each of the forty-five days were then calculated as: (1) Ekman transport, (2) Ekman transport for 12 hours per day and 3% of the wind vector for the remaining 12 hours, and (3) Ekman transport 12 hours per day and 3% of the wind speed, 15° to the right of the wind direction for the remaining 12 hours.

Analysis and Results

Intra-annual Temporal Patterns

Because each of the cruises spanned about one month and began on a different date during the spring with nearly three months separating the beginning of the earliest cruise and the end of the latest cruise (Table 1), the larval populations would be expected to change dramatically over this time due to mortality, metamorphosis and settlement. Estimates of the rates of these phenomena could be used to adjust or account for differences between years that were due only to differences in intra-annual timing of the sampling.

To estimate intra-annual mortality rate from our inter-annual data we regressed the logarithm of average larval density (per 10 m^2) over each cruise divided by estimated egg production (approximated by total [male] catch in the following year c.f. Hobbs and Botsford 1989) on time of year at the midpoint of the cruise (Figure 3). We divided by estimated adult female abundance to remove the effect of variation in egg production between years, but because of low variability in estimated female abundance (coefficient of variation = 0.2), dividing by this factor had little effect on the result. The estimated overall decline for total larvae is 0.066 d^{-1}, or a half life of about 10.5 days. This rate includes losses due to mortality of zoeae and megalopae and settlement of megalopae. The slope of regression of adjusted megalopal density (-0.054 d^{-1}) is not as steep as the rate of decline for total larvae, because it includes not just losses due to mortality and settlement, but also additions due to metamorphosis from zoeae to megalopae (Figure 3). The rate of decline of adjusted zoeal density (-0.089 d^{-1}) includes both losses due to mortality and

losses due to metamorphosis. The fact that the zoeal and the megalopae rates are close to the rate of decline for total larvae suggests that both settlement and metamorphosis rates are less than the mortality rate. Because we have information on only two stages, it is not possible to estimate rates of metamorphosis and settlement. In addition, metamorphosis is most likely not constant with time, but occurs over a small time period so that much of the difference between the rate for zoeae and the rate for megalopae may be due to the fact that the 1984 cruise preceded the time of metamorphosis in the northern latitudes.

Quasi-synoptic abundance estimates (QSAEs)

To remove the intra-annual variation in the abundance data so that we could evaluate effects of inter-annual environmental differences we constructed a quasi-synoptic data set using the the larval mortality rate estimated above. Because the last larval stage is probably the most important one for final settlement, we focus primarily on the megalopae in the late cruises (1981-3, 85). The quasi-synoptic data set is constructed from the day-night corrected abundance estimates by removing the effects of larval decline within each year, using the rate of larval decline (-0.066 per day, Figure 3) estimated above so that,

$$A(t_0) = A(t)\, e^{-m(t_0-t)}$$

where $A(t_0)$ is quasi-synoptic abundance on day t_0 (May 10), A(t) is the abundance observed on day t and m is the instantaneous larval mortality rate (-0.066 per day). We chose May 10 because it is a date common to all four of the late cruises (Table 1). For the 1984 cruise we use the average sample date

for the cruise (Julian day 83) for t_0 and the bongo tow abundance since a very small fraction of the larvae were found in the neuston.

Distribution of larvae

To analyze the influence of inter-annual variability in the physical environment on spatial distribution of larvae, we constructed two dimensional distributions of the quasi-synoptic abundance estimates for the 1981-3 and 85 cruises. For the megalopae (Figures 4a, b, c and d) although the abundances are corrected for day-night differences, the daytime samples have a greater variance and a higher probability of a zero estimate when larvae are present. To indicate differences in precision and the probability of false zeros, we differentiated between day and night samples on the plots. The distributions shown for each year are the estimated total number of megalopae throughout the water column present at each station adjusted to May 10.

The distributions for the two cruises during late April and early May differ substantially from each other, 1985 has more offshore samples through all latitudes than 1983 (Figures 4c, d). The distribution for 1983 is skewed toward the north with a single large sample offshore in the south. The megalopae in the two later cruises are predominantly nearshore and to the north (Figures 4a, b). The offshore megalopae are also concentrated in the north in 1981 but distributed over all latitudes in 1982.

The QSAEs of megalopae in the 1981-3 and 85 cruises, when lumped by degree of latitude, had no apparent regular pattern in the distribution of megalopae. The years 1981 and 1983 had high densities of megalopae at intermediate latitudes and at the lowest latitude, while 1982 had peaks in the

north latitudes, and 1985 had peaks in the southern latitudes. Although 1981 did have single peak of high abundance in the lowest latitudes over 90% of the larvae in 1981 and 1982 were north of 44°N latitude. The 1981 and 82 cruises sampled the southern stations near the first of June, about 6 weeks after the peak of metamorphosis from zoeae to megalopae at these latitudes, the majority of megalopae would have settled out prior to sampling.

The cross-shelf distributions are more regular (Figure 5). The averaged distribution for all four years shows two peaks, at 10 km and 200 km offshore, and very few Dungeness crab megalopae beyond 250 km offshore. The 1983 cruise has peaks at 75 km and 200 km offshore and the 1985 cruise has peaks both nearshore and at 200 km offshore. The offshore peak in 1983 results from a single large sample in the south (Figure 4c). The cruises later in the year (1981 and 1982) show only a single peak nearshore with very few megalopae beyond 150 km offshore.

Zoeal QSAEs are highest at the extreme latitudes in the earlier cruises (83, 85) and at intermediate latitudes in the later cruises (81, 82). The cross-shelf distribution of zoeae (Figure 6) is dominated by the single large peak in 1983 at 200 km offshore. In the remaining years the zoeae are fairly evenly distributed with lower abundances in the nearest onshore and stations furthest offshore. Significant zoeal abundances are found beyond 250 km in all years except 1983.

Because the March-April cruise (1984) coincided with the timing of metamorphosis from zoeae to megalopae (Hobbs and Botsford in prep(a)) the larvae were predominantly zoeae at the begining of the cruise in the north, and megalopae at the end of the cruise in the south (Figure 7a). Peak

densities for megalopae and zoeae are less than 100 kilometers offshore in 1984 with few larvae found beyond 250 kilometers (Figure 7b).

Megalopal abundance and local conditions

We compared the QSAEs to the hydrographic and chlorophyll data at each station. There was no significant statistical relationship between log transformed QSAEs (natural log of (1 + abundance)) and the local hydrographic conditions. However, megalopae abundance appeared to decline at the extremes of both sea surface temperature (Figure 8) and dissolved oxygen concentration. There is no apparent visual relationship between megalopae abundance and salinity or chlorophyll abundance. Chlorophyll abundance declined exponentially with distance offshore (Figure 9) and did not depend on latitude or Julian date. There was no significant relationship between the QSAEs and chlorophyll abundance.

Sea surface temperature (SST) is the only one of the these hydrographic factors that varied significantly from year to year in our data. SST generally increased with Julian date and decreased with latitude in all years with the exception of 1982 in which several nearshore stations in the south had low temperatures due to seasonal upwelling (Savage 1989b). The cruises can be classified by the mean sea surface temperatures at the hydrographic stations as warm (1981, 12.1° C. and 1983, 12.0° C.) and cool (1982, 10.4° C. and 1985, 10.3° C.).

To compare these average station temperatures to the average temperatures experienced by larvae we calculated a mean temperature for each cruise as a mean of the temperature values weighted by the QSAEs. The earlier cruises have mean larval temperatures nearly identical to the mean

temperature in those years (1983, 12.2° C. and 1985, 10.6° C.). The later cruises have mean larval temperatures nearly identical to each other and intermediate between the mean temperatures in those years (1981, 11.1° C. and 1982, 10.8° C.). The similarity between the mean larval temperatures in the two later cruises results from the low abundance in the southern latitudes on both of these cruises where the greatest inter-annual differences in SST occurred. The low abundance at these stations is probably due to settlement rather than extremes of SST. Variation of SST over the range observed in these cruises apparently does not determine the abundance of larvae.

Wind fields and north-south larval transport

Larval transport is dependent on alongshore currents and wind driven cross-shelf transport. The distribution of egg production (when estimated from landing statistics) per kilometer of coast (Figure 10) is fairly constant north to south and year to year. If significant alongshore transport of larvae occurred within the predominant currents (i.e., the Davidson current in winter, and the California Current in spring), we would expect to see higher densities of the population collected in the north in the 1984 cruise (late March-early April) and larvae distributed back toward the south in the later (May-June) cruises. The QSAEs for the four late cruises are fairly evenly distributed over the range of sample stations (Figures 4a, b, c, d), however, the distributions in the 1984 samples show a peak of abundances both in the north and in the south (Figure 7a).

Wind fields and cross-shelf larval transport

Early larval period - Zoeae and early instar megalopae spend little time in the neuston so that transport of these larvae is probably related to wind driven

mass transport of the Ekman layer. To determine the effect of cross-shelf Ekman transport on the cross-shelf distributions of these early larval stages we have used FNOC wind data to calculate the shoreward mass transport (perpendicular to the shore line at each latitude) for each year (Figures 11a, b, c, d and e). If we assume that the Ekman layer is 100 meters deep then a value of 100 metric tonnes per second per 100 meters of coastline (0.01 t s^{-1} m^{-1}) is a mean shoreward velocity of approximately one kilometer per day. The estimated velocity is less important than the duration of onshore transport, because shoreward surface flow is deflected by the continental barrier into vertical mixing and subsurface offshore transport. The general pattern in these plots is onshore transport at one to two kilometers per day during the winter months with a fairly quiescent period of one to two months then offshore transport at one to two kilometers per day in late spring and summer. Onshore transport is stronger in the north and offshore transport begins earlier and is stronger in the south. 1983 shows the greatest estimated onshore transport with values greater than 50 (0.01 t s^{-1} m^{-1}) continuing to the first of April, Julian day 91, at most latitudes (Figure 11c). The period of onshore transport ends near Julian day 75 in 1984 (Figure 11d), day 60 in 1981 (Figure 11a) and 1982 (Figure 11b) and day 50 in 1985 (Figure 11e).

Observed zoeal distributions bear some relationship to these inter-annual differences. Of the four later cruises, the 1981 and 1982 samples had similar onshore transport regimes and have somewhat similar cross-shelf distributions with peaks of zoeae density at 210 kilometers, except that 1981 also has a peak nearshore. The zoeae in the 1983 samples are distributed on average 100 kilometers further offshore than the zoeae in the 1985 samples and these two years represent the extremes of onshore transport in our

samples, with onshore transport terminating latest in 1983 and earliest in 1985 (Figures 11c, d). These observations suggest that longer duration of the onshore transport period may result in increased offshore transport in the early larval stages but differential maturation rates could also account for the observed differences.

Late larval period - The distribution of late stage megalopae may also be influenced by transport prior to the time of sampling. We noted above that megalopae were distributed closer to shore in the later cruises (1981 and 1982). This is consistent with the hypothesis that wind forcing during the late larval period transports larvae toward the favorable settlement habitat near shore.

We compared the estimated effects of wind forcing to larval distributions. The late instar megalopae spend about half of their time in the neuston, so Ekman transport of the whole mixed layer is probably not a complete model of passive transport of these larval stages. For the purpose of comparison, we calculated larval transport for the forty-five day period prior to sampling for the late cruises (1981-3, 85) in three ways: (1) Ekman transport, (2) Ekman transport for 12 hours per day and 3% of the wind speed in the direction of the wind for the remaining 12 hours, and (3) Ekman transport 12 hours per day and 3% of the wind speed with the direction rotated 15° to the right for the remaining 12 hours. The first assumes the megalopae are distributed throughout the upper Ekman layer and does not take into account vertical migration. The latter two attempt to account for vertical migration by assuming that the megalopae are distributed throughout the upper Ekman layer during the day but are in the neuston at night. Transport of the megalopae in the neuston is considered to be much closer to the wind direction at the sea surface than Ekman mass transport, but the actual

direction in relation to the calculated wind direction is not well known. We consider two different methods of calculation in an attempt to bracket this uncertainty.

Transport for the 45 days prior to the sample date for the even latitudes is displayed as drift tracks which end at the longitude of the nearshore sample station (Figures 12a, b, c and d). These show a consistent latitudinal pattern that varies in magnitude from year-to-year. Typically the onshore component increases with latitude, and the southward component decreases with latitude for methods 2 and 3. Ekman transport only, method 1, is generally southward in the northern latitudes and offshore in the south. Both 1981 and 1982 have almost no north-south transport in the north and transport of three to four degrees of latitude in the south. Years 1983 and 1985 show a pattern similar to later cruises except that the rapid southward transport in methods 2 and 3 is preceded by a period of onshore transport. The sample dates in these earlier cruises occur about three weeks prior to the same latitudes in the 1981 and 1982 cruises, so that an onshore phase at the same time of year would not show up in plots for later cruises.

To evaluate the effect on transport of larvae to nearshore habitat, we examined the onshore component of transport by each of the three methods for each year (Figures 13a, b, c, d). The latitudinal pattern of onshore transport remains the same from year to year (with the exception of the far north in 1983), but the magnitude varies. Onshore transport calculated by methods 2 and 3 is generally strong in the north and weak or reversed in the south (Figures 13a, b, c, d). Ekman transport only (method 1) is much smaller in magnitude and generally offshore in the south. In the May-June cruises (1981

and 1982), method 2 was the only method of calculation that resulted in net onshore transport at all latitudes.

There is some correspondence between these patterns and the QSAEs (Figures 4a, b, c, d). For example, onshore transport in the north calculated by both the second and third methods in 1981 is more than twice the 1982 values (Figures 12a, b). This difference is consistent with the greater offshore densities in the north in 1982 than in 1981 (Figures 4a, b). The year 1985 has greater onshore transport (calculated by methods 2 and 3) at all latitudes than 1983 (Figures 13 c, d). Although 1985 has many more offshore stations with megalopae than 1983, the greatest abundance is found inshore in 1985 and offshore in 1983 (Figures 4c, d and 5).

To summarize the broadscale patterns, we compared the onshore transport calculated by method 2 averaged over the coast with the average quasi-synoptic densities of megalopae nearshore (< 50 km offshore). Onshore transport is greatest in 1981, slightly less in 1985, intermediate in 1982 and low in 1983 (Figure 14a). The nearshore density of megalopae corrected for time of sampling and relative egg production repeats this pattern almost exactly (Figure 14b).

Discussion

Mortality rate and hydrographic conditions

The smooth decline in annual samples of abundance with time of year lends support to the estimate of larval mortality rate and also suggests that the highly variable environment from year to year has no impact on survival through the year. The latter is important because it implies that if the

physical environment does have an effect on recruitment, it occurs late in the year, and probably involves transport to favorable settling sites (i.e., nearshore) or survival during or after settlement. This conclusion must be accompanied by the caveat that we have only 5 data points, which probably do not span the entire range of possible oceanic conditions in the study area. In addition, we note that the catch record does not indicate a large fluctuation in recruitment (i.e., large change in abundance four years later) resulting from at least the 1981-3 years. If an environmental signal is important in recruitment it did not vary significantly during these years.

Sea surface temperature did vary significantly from year to year in particular 1983 has been identified as an El Niño year and had high water temperatures in our hydrographic data. Temperature has also been linked to variation in egg and larval survival in laboratory studies (Reed 1969, Wild 1980, Sulkin and McKeen, 1989). Specifically, temperatures of 15°C or greater (Lough, 1976, Sulkin and McKeen, 1989) or less than 9°C (Lough, 1976) have been linked to higher mortality in the late instar zoeae. Although the megalopae in our samples had recently completed this stage at temperatures near those measured, no resulting inter-annual variation in larval abundance seems to have occurred in our samples. This suggests several possibilities: (1) ocean temperatures rarely exceed the tolerance range of the larvae (i.e. in our samples only one station recorded a temperature above 15°C and ten stations were below 9°C, Figure 8), (2) the larvae are sufficiently tolerant of transient temperature fluctuations that these adverse conditions have little impact on cumulative survival, and (3) the larvae are able through vertical migration to lessen the impact of more damaging conditions. In any

case, inter-annual temperature variations do not appear to be important in determining year class strength.

Spatial distributions

There is not an obvious north-south pattern in the larval distributions. However, the two May-June (1981, 1982) cruises do show lower numbers of megalopae in the south relative to the northern samples in those years suggesting that a significant settlement of megalopae may have occurred in the south prior to the sampling time.

The cross-shelf distributions show a more distinct pattern largely consistent with the observation in earlier studies that later stage zoeae are found progressively further offshore (Lough 1976, Reilly 1983) and megalopae first appear offshore then move rapidly onshore (Hatfield 1983, Jamieson and Phillips 1988, Jamieson et al. 1989). Applying this scenario to the megalopae data the 1983 cruise occurs at a time when the megalopae were accumulating offshore, in 1985 the megalopae were moving onshore, and in 1981 and 1982 the majority of megalopae had been transported to the nearshore environment. Although the stations were sampled on average five days later in the year in 1983 than in 1985 the larval population in 1985 appears to have progressed a bit further in the hypothetical larval development scenario. The peak of megalopae abundance in the 1984 sample, however, was nearer to shore than the offshore peaks in the 1983 and 1985 samples that were taken 6 weeks later in the year. This discrepancy may be due two factors: (1) the megalopae were only in the southern part of the cruise area where the larvae tended to be closer to shore in general and (2) the early stage megalopae follow a diel migration pattern similar to the zoeae which have a similar

cross-shelf distribution (Figure 7b) so they would be likely to continue to move offshore with the zoeae.

Wind driven transport of larvae

During the early larval period, zoeae and early stage megalopae were rarely found in the neuston, hence standard Ekman transport is a reasonable model for passive transport of these stages. Wind driven Ekman transport during January through March is predominantly onshore, and peak larval densities for the cruise at the end of this period (1984) are near shore (i.e., within 50 km). In later cruises, zoeae are distributed further offshore. These observations are generally consistent with a scenario that differs slightly from earlier proposals that the zoeal stages moved continuously offshore (cf. Lough 1976, Reilly 1983). A scenario in which zoeae and early stage megalopae remain largely near shore until after the spring transition is more consistent with typical intra-annual patterns of wind-forced currents. However, the peak densities of zoeae in the 1983 sample which experienced 40 more days of onshore transport than the zoeae in the 1985 sample are 100 km further offshore than those in the 1985 samples. This suggests that the zoeae are beneath the Ekman layer and subject to cross-shelf counter flows which move them progressively offshore. These cross-shelf counter flows can be as shallow as 40 m (Hickey 1989). A more precise understanding of the vertical distribution of zoeae and the cross-shelf currents is necessary to resolve this issue.

During the late larval period, the distinctive diel vertical migratory behavior of late stage megalopae coupled with onshore winds provides a mechanism for rapid onshore transport of larvae as much as 300 kilometers

offshore in the north and to lesser extent in the south (assuming that they are transported at 3 percent of the wind speed). Thus larvae further offshore may return to the nearshore environment in years with strong onshore winds but be stranded in years with weaker winds. The strong relationship between the mean coast-wide onshore transport and the mean larval densities nearshore in each year support this idea. In the southern part of the cruise area the relatively weak onshore transport in late April followed by a period of rapid southward transport suggests that the timing of the period of onshore transport may also be important.

Johnson et al. (1986) found a significant correlation between southward (135 degrees to 202.5 degrees) component of wind stress averaged over the months of April, May and June and landings four and five years later. That their analysis did not detect a correlation between landings and an eastward component of the winds may be due to two causes. First, our results indicate that the majority of the larvae have moved into the nearshore by the end of May. By including the June winds, which are predominantly southward in direction and stronger than the April and May winds, Johnson et al. (1986) may have biased their results toward a more southerly direction. Second, their analysis was based on winds computed from pressure fields. Halliwell and Allen (1987) have shown that the rotation correction used in these computations is not as great as it should be, and that they should be rotated further anticlockwise. This rotational correction varies from 15 to 50 degrees at the latitudes of interest here. A recalculation of the correlations of Johnson et al., (1986) in light of the improved understanding both of larval phenology and of wind driven currents a could result in useful insights on the impact of wind forcing on the population dynamics of Dungeness crab.

Although based on only 4 years of data our conclusions are plausible when considered in the context of the correlation between Dungeness crab landings and winds (Johnson et al., 1986), the results recently obtained by McConnaughey, et al. (unpubl. data) relating winds to Dungeness crab settlement success, and observations of the importance of transport during critical early life stages of other marine crustaceans. Annual variations in wind fields have been statistically associated with abundance of several spiny lobster species (Jasus spp.) in the Tasmanian Sea (Harris et al. 1988), the pink shrimp, Pandalus jordani, off the coast of the north-western U. S. (Rothlisberg and Miller, 1983) and blue crab, Callinectes sapidus, in Chesapeake Bay on the east coast of the U. S. (Johnson et al., 1984). ENSO events which affect both the wind field and circulation on the west coast of Australia are correlated with western rock lobster, Panulirus cygnis, settlement and catch records (Pearce and Phillips, 1988, Phillips and Pearce, 1989). Larvae of both the blue crab and fiddler crab (Uca spp.) in Delaware Bay, U.S.A. leave and return to the parent estuary by means of the current system in the mid-Atlantic Bight (Epifanio et al. 1988, Epifanio et al. 1989), and active vertical migration to regulate passive transport of during storm surges has been suggested as an important mechanism for return of blue crab larvae into Chesapeake Bay by both field observations (Goodrich et al. 1989) and modeling studies (Johnson and Hess, 1990). In a review of transport of the larvae of three coastal crustacea P. cygnis, and the banana prawn, Penaeus merguiensis, both off Australia and P.jordani, off the north-western U. S., Rothlisberg (1988) concludes that active control of transport through vertical migration is important both for retention of larvae in rearing grounds and transport to and from the adult habitat.

Our results have implications for the larger question of the mechanisms determining the cycles in abundance in the Dungeness crab fishery. Of the several environmental factors we considered, the timing and strength of onshore winds in the spring appears to be most important in the successful settlement of a larval year class. Equally important is the fact that variations in SST, salinity, dissolved oxygen, and chlorophyll abundance do not affect larval success. These observations allow us to narrow our focus to larval transport as the form of environmental forcing in the population dynamics of the crab, but do not resolve the question of the relative importance of environmental forcing and density-dependent effects such as post-settlement cannibalism. If post-settlement survival rates are highly variable or depend on adult densities then the initial size of the post-settlement juvenile population may have little bearing on resulting adult year class strength (cf., Connell 1985). For example, McConnaughey and Armstrong (pers. com.) found little correspondence between the abundance of age zero benthic juveniles and subsequent adult abundance from their six years of sampling data.

Acknowledgments

We thank Art Kendall of the Northwest and Alaska Fisheries Center of the National Marine Fisheries Service for his assistance and advice in obtaining the larvae and various data. We thank Richard D. Methot, Jr. for originating our access to these data, and he, David F. Johnson, and Jonathan M. Shenker for their assistance in obtaining data, sorting and preliminary analysis of the data. We thank Gary Brewer and U. S. Minerals Management Service for support in the most recent phase of this project. We thank the members of T.I.N.R.O. (Pacific Research Institute of Fisheries and Oceanography, U.S.S.R.) who collected these samples, and members of the Polish Plankton Sorting Center who initially sorted them. Finally we thank Glenn Jamieson, Art Kendall, Robert McConnaughey, and Thomas Wainwright for thoughtful reviews of an earlier form of this manuscript.

References

Booth, J., A. Phillips, and G. S. Jamieson. 1985. Fine scale spatial distribution of Cancer magister megalopae and its relevance to sampling methodology. Pp. 273-286. In: Melteff, B. (ed.), Proceedings of the symposium on Dungeness Crab Biology and Management. Oct. 1984. Univ. Alaska Sea Grant Rpt. No. 85-3.

Botsford, L. W. 1986. Population dynamics of the Dungeness crab (Cancer magister). Pp 140-153. In: G. S. Jamieson and N. Bourne [ed.] North Pacific Workshop on stock assessment and management of invertebrates. Can. Spec. Publ. Fish. Aquat. Sci. 92.

Botsford, L. W. and D. E. Wickham. 1978. Behavior of age-specific, density-dependent models and the northern California Dungeness crab (Cancer magister) fishery. J. Fish. Res Board Can. 35:833-943

Botsford, L. W., R. D. Methot and J. E. Wilen. 1982. Cyclic covariation in the California king salmon, Oncorhynchus tshawytscha, silver salmon, O. kisutch, and Dungeness crab, Cancer magister, fisheries. Fish. Bull. U. S. 80(4): 791-801.

Botsford, L. W., R. D. Methot Jr. and W. E. Johnston. 1983. Effort dynamics of the northern California Dungeness crab (Cancer magister) fishery. Can. J. Fish. Aquat. Sci. 40: 337-346.

Botsford, L. W., Armstrong D. A. and Shenker, J. M. 1989. Oceanographic Influences on the Dynamics of Commercially Fished Populations. Pp 511-566. In: M. R. Landry and B. M. Hickey [eds.] Coastal Oceanography of Washington and Oregon. Elsevier, Amsterdam & New York. 607p.

Carrasco, K. R., D. A. Armstrong, D. R. Gunderson, and C. Rogers. 1985. Abundance and growth of Cancer magister young-of-the-year in the near shore environment. Proceedings of the Symposium on Dungeness Crab Biology and Management. Oct. 1984. Alaska Sea Grant Rept No. 85-3:171-184.

Clark, J. B. 1984. Ichthyoplankton off Washington, Oregon, and northern California, May-June 1981. NWAFC Proc. Rep. 84-11, 45 p.

Clark, J. B. 1986. Ichthyoplankton off Washington, Oregon, and northern California, May-June 1982. NWAFC Proc. Rep. 87-01, 44 p.

Clark, J. B., and A. W. Kendall, Jr. 1985. Ichthyoplankton off Washington, Oregon, and northern California, April-May 1983. NWAFC Proc. Rep. 85-10, 48 p.

Clark, J. B., and D. S. Savage. 1988. Ichthyoplankton off Washington, Oregon, and northern California, March-April 1984. NWAFC Proc. Rep. 88-09, 57 p.

Connell, J. H. 1985. The consequences of variation in initial settlement vs. post-settlement mortality in rocky intertidal communities. J. Exp. Mar. Biol. Ecol. 93:11-45.

Epifanio, C. E., K. T. Little, and P. M. Rowe. 1988. Dispersal and recruitment of fiddler crab larvae in the Delaware River Estuary. Mar. Ecol. Prog. Ser. 43 : 181-188.

Epifanio, C. E., A. K. Masse, and R. W. Garvine. 1989. Transport of blue crab larvae by surface currents off Delaware Bay, USA. Mar. Ecol. Prog. Ser. 54 : 35-41.

Gaumer, T. F. 1971. Controlled rearing of Dungeness Crab larvae and the influence of environmental conditions on their survival. Commer. Fish. Res. Dev. Act Prog. Rep., Nov. 16, 1965 to June 30, 1970. Fish. Comm. Ore., Closing Rep., 43 p.

Goodrich, D. M., J. van Montfrans, and R. J. Orth. 1989. Blue crab megalopal influx to Chesapeake Bay: evidence for a wind driven mechanism. Est. Coast. and Shelf Sci. 29 : 247-260.

Halliwell, J. R, Jr., and J. S. Allen. 1987. The large-scale coastal wind field along the west coast of North America 1981-1982. J. Geophys. Res. 92 (C2) : 1861-1884.

Harris, G. P., P. Davies, M. Nunez, and G. Meyers. 1988. Interannual variability in climate and fisheries in Tasmania. Nature 333 : 754-757.

Hatfield, S. E. 1983. Distribution of zooplankton in association with Dungeness crab, Cancer magister, larvae. In: P. W. Wild and R. N. Tasto (eds.) Life History, Environment, and Mariculture Studies of the Dungeness crab, Cancer magister, with Emphasis on the Central California Fishery Resource. CDFG Fish Bull. 172.

Hickey, B. M. 1979. The California Current System - hypotheses and facts. Prog. Oceanogr., 8: 191-279.

Hickey, B. M. 1989. Patterns and processes of circulation over the Washington continental shelf and slope. Pp 41-116. In: M. R. Landry and B. M. Hickey [eds.] Coastal Oceanography of Washington and Oregon. Elsevier, Amsterdam & New York. 607p.

Hobbs, R. C. and L. W. Botsford. 1989. Dynamics of an Age-Structured Prey with Density- and Predation-Dependent Recruitment: The Dungeness Crab and a Nemertean Egg Predator Worm. Theor. Pop. Biol. 36:1-22.

Jacoby, C. 1982. Behavior responses of the larvae of Cancer magister Dana (1852) to light, pressure, and gravity. Mar. Behav. Physiol. 8:267-283.

Jamieson, G. S. and A. C. Phillips. 1988. Occurrence of Cancer crab (C. magister and C. oregonensis) megalopae off the west coast of Vancouver Island, British Columbia. U. S. Fish. Bull. 86(3): 525-542.

Jamieson, G. S., Phillips, A. C., & Hugget., W. S. (1989). Effects of ocean variability on the abundance of Dungeness crab larvae. pp. 305-325. In: R. J. Beamish, & G. A. McFarlane (Ed.), Effects of Ocean Variability on Recruitment and an Evaluation of Parameters Used in Stock Assessment Models.

Johnson, D. R., B. S. Hester, and J. R. McConangha. 1984. Studies of a wind mechanism influencing the recruitment of blue crabs in the Middle Atlantic Bight. Continental Shelf Res. 3 : 425-437.

Johnson, D. F., L. W. Botsford, R. D. Methot, Jr., and T. C. Wainwright. 1986. Wind stress and cycles in Dungeness crab (Cancer magister) catch off California, Oregon, and Washington. Can. J. Fish. Aquat. Sci. 43:838-845.

Johnson, D. F., and K. W. Hess. 1990. Numerical simulations of blue crab larval dispersal and recruitment. Bull. of Mar. Sci. 46 (1) : 195-213.

Lough, R. G. 1975. Dynamics of crab larvae (Anomura, Brachyura) off the Central Oregon Coast, 1969-1971. Ph.D. thesis, Oregon State University. 299 pp.

Lough, R. G. 1976. Larval dynamics of the Dungeness crab, Cancer magister, off the Oregon coast, 1970-1971. U. S. Natl. Mar. Fish. Serv., Fish Bull. 74(2):353-376.

McKelvey, R., D. Hankin, K. Yanosko, and C. Snygg. 1980. Stable cycles in multistage recruitment models: an application to the northern California Dungeness crab (Cancer magister) fishery. Can. J. Fish. Aquat. Sci. 37:2323-2345.

Pearce, A. F., and B. F. Philips. 1988. ENSO events, the Leeuwin Current, and larval recruitment of the western rock lobster. J. Cons. Int. Explor. Mer. 45 : 13-21.

Phillips, B. F., and A. F. Pearce. 1989. Inter-annual variability in ocean circulation and rock lobster recruitment in the southeastern Indian Ocean. In: Long-term Variability of Pelagic Fish Populations and their

Environment (Proceedings of the International Symposium). Sendai, Japan

PMFC. 1965. Discussion following report on Dungeness crab. 16th and 17th Annual Report Pacific Marine Fishery Commission. pp. 38-39. Portland, Oregon: PMFC.

Reed, P. H. 1969. Culture methods and effects of temperature and salinity on survival and growth of the Dungeness crab (Cancer magister) larvae in the laboratory. J. Fish Res. Board Can. 26 (2) : 389-397.

Reilly, P. N. 1983. Dynamics of Dungeness crab, Cancer magister, larvae off central and northern California. In: P. W. Wild and R. N. Tasto (eds.) Life History, Environment, and Mariculture Studies of the Dungeness crab, Cancer magister, with Emphasis on the Central California Fishery Resource. CDFG Fish Bull. 172, pp. 57-84.

Rothlisberg, P. C. 1988. Larval transport in coastal crustacea: three case histories. In: B.-O. Jansson (Ed.) Coastal-Offshore Ecosystem Interactions. Berlin, Heidelberg: Springer-Verlag. 367p.

Rothlisberg, P. C., and C. B. Miller. 1983. Factors affecting the distribution, abundance, and survival of Pandalus jordani (decapoda, pandalidae) larvae off the Oregon coast. Fish. Bull., U. S. 81 : 455-472.

Sameoto, D. D. and Jaroszynski, L. O. 1969. Otter surface sampler: a new neuston net. J. Res. Board Canada. 25:2240-2244.

Savage, D. S. 1989a. Ichthyoplankton off Washington, Oregon, and northern California, April-May 1985. NWAFC Proc. Rep. 89-06, 54 p.

Savage, D. S. 1989b. Salinity and Temperature Data Comparisons for 1980-1987 Cruises off the Coasts of Washington, Oregon, and California. NWAFC Proc. Rep. 89-16, 169 p.

Shenker, J.M. 1988. Oceanographic associations of neustonic larval and juvenile fishes and Dungeness crab megalopae off Oregon. Fish. Bull., U. S. 86: 299-319.

Smith, P. E. and Richardson, S. L. (eds.) 1977. Standard techniques for pelagic fish egg and larvae surveys. FAO Fish. Tech. Pap. 175, 100p.

Stevens, B. and D. A. Armstrong. 1984. Distribution, abundance and growth of juvenile Dungeness crabs, (Cancer magister), in Grays Harbor estuary Washington U. S. A. Fish. Bull. 82(3) pp. 469-483.

Stevens, B. G. and D. A. Armstrong. 1985. Ecology, growth and population dynamics of juvenile Dungeness crab, Cancer magister Dana, in Grays Harbor estuary Washington. Pp. 119-134. In: Melteff, B. (ed.), Proceedings of the symposium on Dungeness Crab Biology and Management. Oct. 1984. Univ. Alaska Sea Grant Rpt. No. 85-3.

Strub, P. T., J. S. Allen, A. Huyer, and R. L. Smith. 1987a. Large-Scale Structure of the Spring Transition in the Coastal Ocean off Western North America. J. Geophys. Res. 92 (c2) : 1527-1544.

Strub, P. T., J. S. Allen, A. Huyer, R. L. Smith, and R. C. Beardsley. 1987b. Seasonal Cycles of Currents, Temperatures, Winds and Sea Level Over the Northeast Pacific Continental Shelf: 35°N to 48°N. J. Geophys. Res. 92 (C2) : 1507-1526.

Sulkin, S. D., and G. L. McKeen. 1989. Laboratory study of survival and duration of individual zoeal stages as a function of temperature in the brachyuran crab, Cancer magister. Mar. Biol. 103:31-37.

Wickham, D. E. 1979a. Predation by the nemertean Carcinonemertes errans on eggs of the Dungeness crab Cancer magister. Mar. Biol. 55:45-53.

Wickham, D. E. 1979b. The relationship between megalopae of the Dungeness crab, Cancer magister, and the hydroid,Velella velella, and its influence on abundance estimates of C. magister megalopae. Cal. Fish and Game. 65:184-186.

Wild, P. W. 1980. Effects of seawater temperature on spawning, egg development, hatching success and population fluctuations of the Dungeness crab, Cancer magister. CalCOFI Rpt. 21:115-120.

Table 1. Cruise information for the five years of sampling.

Year	1981	1982	1983	1984	1985
Start Date	9-May	3-May	23-April	11-March	19-April
End Date	2-June	1-June	15-May	4-April	10-May
Cruise I.D.	1PO81	1PO82	1EQ83	1PO84	1BA85
Chief Scientist	I. Zhuteyov	A. Artemov	M. Stepanenko	Y. Pashenko	M. Stepanenko
Research Vessel	Poseydon	Poseydon	Equator	Poseydon	Mys Babyshkina
Cruise Report Authors	Clark 1984	Clark 1986	Clark and Kendall 1985	Clark and Savage 1988	Savage 1989a
NWAFC Proc. Rep.	84-11	87-01	85-10	88-09	89-06

Figures

Figure 1. Annual Dungeness crab landings by state (kg x 10^6). Catch is a good index of legal abundance in most years. Because of high harvest rates it also approximates recruitment.

Figure 2. A typical cruise track. This is the 1981 cruise which began at 48°N latitude in mid May and ended at 40°N latitude in early June (from Clark 1984). The tracks of the other cruises vary from this one only in the order of sampling of nearshore stations at each latitude.

Figure 3. Larval densities averaged over all locations for each cruise, divided by relative egg production in each year, and plotted against the mean sample date for each cruise. Slopes are: total larvae = -0.066 d^{-1}, zoeae = -0.089 d^{-1}, and megalopae = -0.054 d^{-1}.

Figures 4a, b, c, d. Quasi-synoptic plots of the corrected megalopal abundances in each of the later cruises with the estimated abundance represented by the size of the square. Day and night samples are indicated by the open and closed squares respectively. (a) 1981, (b) 1982, (c) 1983, (d) 1985.

Figure 5. Average of the corrected megalopae abundances lumped by distance offshore for each of the cruises 1981-3, 5 and all four years together.

Figure 6. Average of the corrected zoeae abundances lumped by distance offshore for each of the cruises 1981-3, 5 and all four years together.

Figure 7a, b. Average of the bongo tow megalopae and zoeae abundances for the 1984 cruise (a) lumped by latitude (b) lumped by distance offshore.

Figure 8. Natural log of (1 + abundance per 10 m^2) for stations of the 1981-3, 5 cruises. Abundance appears to decline at the extremes of temperature.

Figure 9. Chlorophyll abundance as measured by the CZCS satellite compared to distance offshore for the sample stations for which we could obtain readings for the 1981-3, 5 cruises. Chlorophyll abundance declines exponentially with distance offshore.

Figure 10. Estimated female abundance by latitude for the five cruise years. Estimated from the crab landings [males] in the following year.

Figure 11a, b, c, d, e. Ten day averaged onshore Ekman mass transport by latitude calculated from the FNOC wind field data for the first half of each of the five years (a) 1981, (b) 1982, (c) 1983, (d) 1984, (e) 1985.

Figure 12a, b, c, d. Wind drift tracks for the 45 days prior to sampling in each of the later cruises ending at the sample point at four latitudes. These were calculated from the FNOC wind field data as:(1) Ekman mass transport, (2) Ekman transport for 12 hours per day and 3% of the wind velocity for the remaining 12 hours, and (3) Ekman transport 12 hours per day and 3% of the wind speed, 15° to the right of the wind direction for the remaining 12 hours. (a) 1981, (b) 1982, (c) 1983, (d) 1985.

Figure 13a, b, c, d. Total onshore transport for the 45 days prior to sampling in each of the later cruises by latitude calculated from the FNOC wind field data as:(1) Ekman mass transport, (2) Ekman transport for 12 hours per day and 3% of the onshore component of the wind for the remaining 12 hours, and (3) Ekman transport 12 hours per day and 3% of the onshore component of the rotated wind vector (15° to the right) for the remaining 12 hours. (a) 1981, (b) 1982, (c) 1983, (d) 1985.

Figure 14a, b. (a) Total onshore transport for the 45 days prior to sampling in the 1981-3, 5 cruises calculated from the FNOC wind field data as Ekman transport for 12 hours per day and 3% of the onshore component of the wind for the remaining 12 hours. (b) Mean corrected megalopae densities nearshore (< 50 kilometers) in the 1981-3, 5 cruises.

Figure 1.

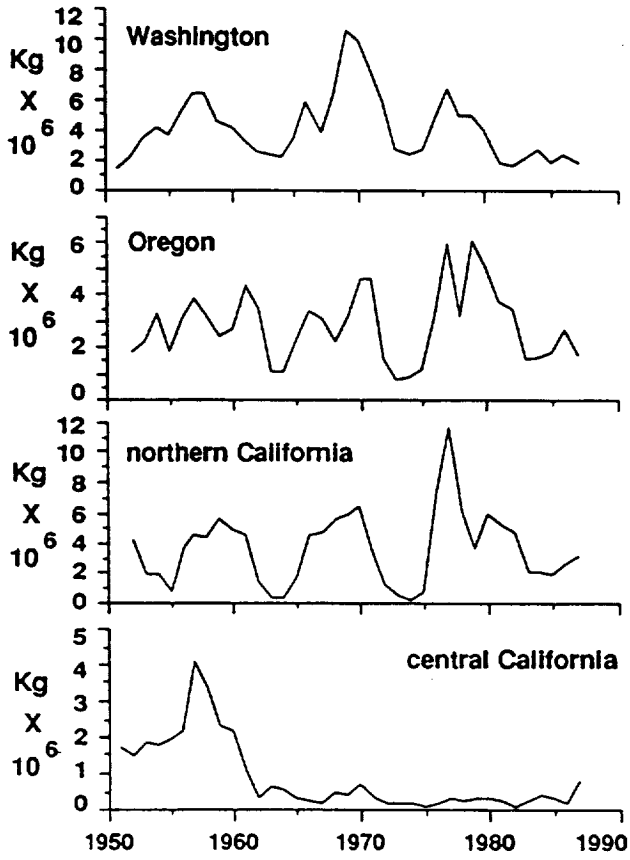
Washington
Oregon
northern California
central California
Kg X 10^6
0
2
4
6
8
10
12
1
3
5
1950
1960
1970
1980
1990

fig 2

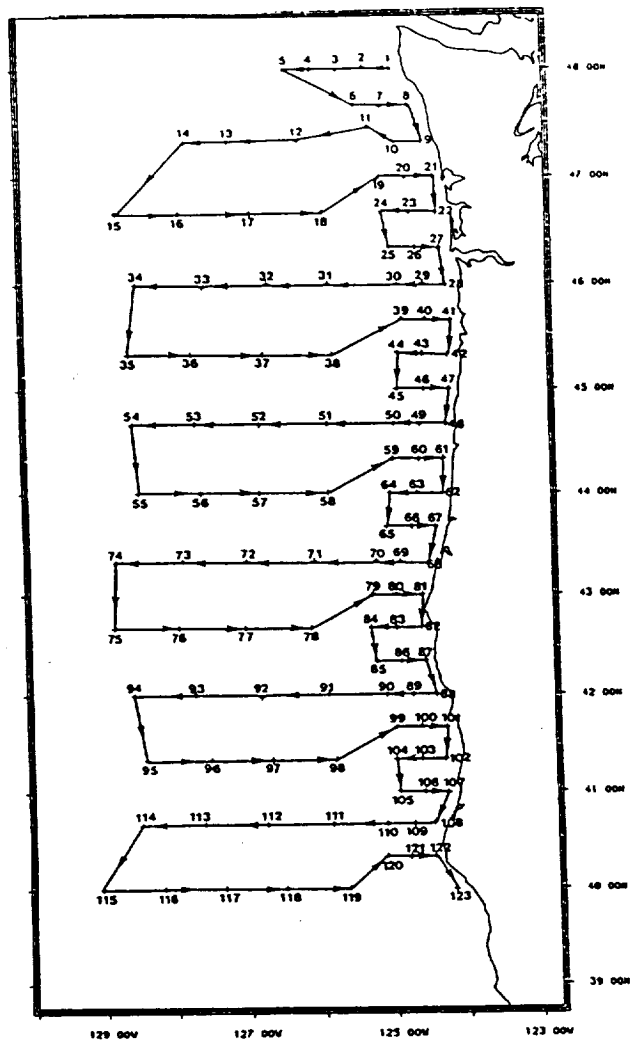
48 00N
47 00N
46 00N
45 00N
44 00N
43 00N
42 00N
41 00N
40 00N
39 00N
129 00W
127 00W
125 00W
123 00W

Figure 3

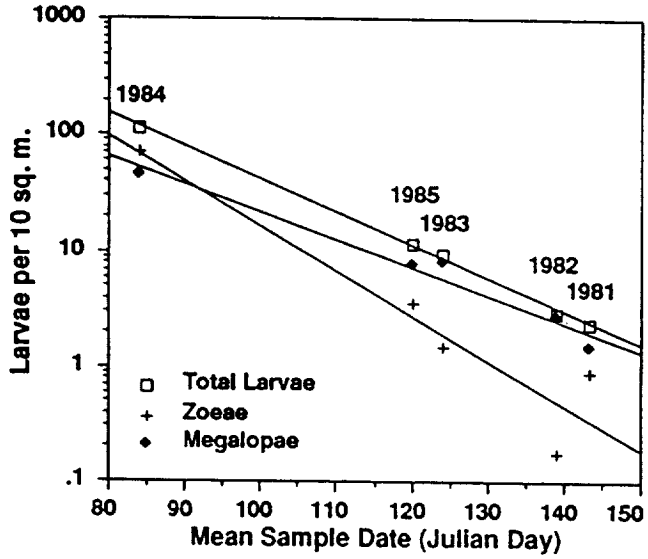
1000
100
10
1
.1
Larvae per 10 sq. m.
1984
1985
1983
1982
1981
Total Larvae
Zoeae
Megalopae
80
90
100
110
120
130
140
150
Mean Sample Date (Julian Day)

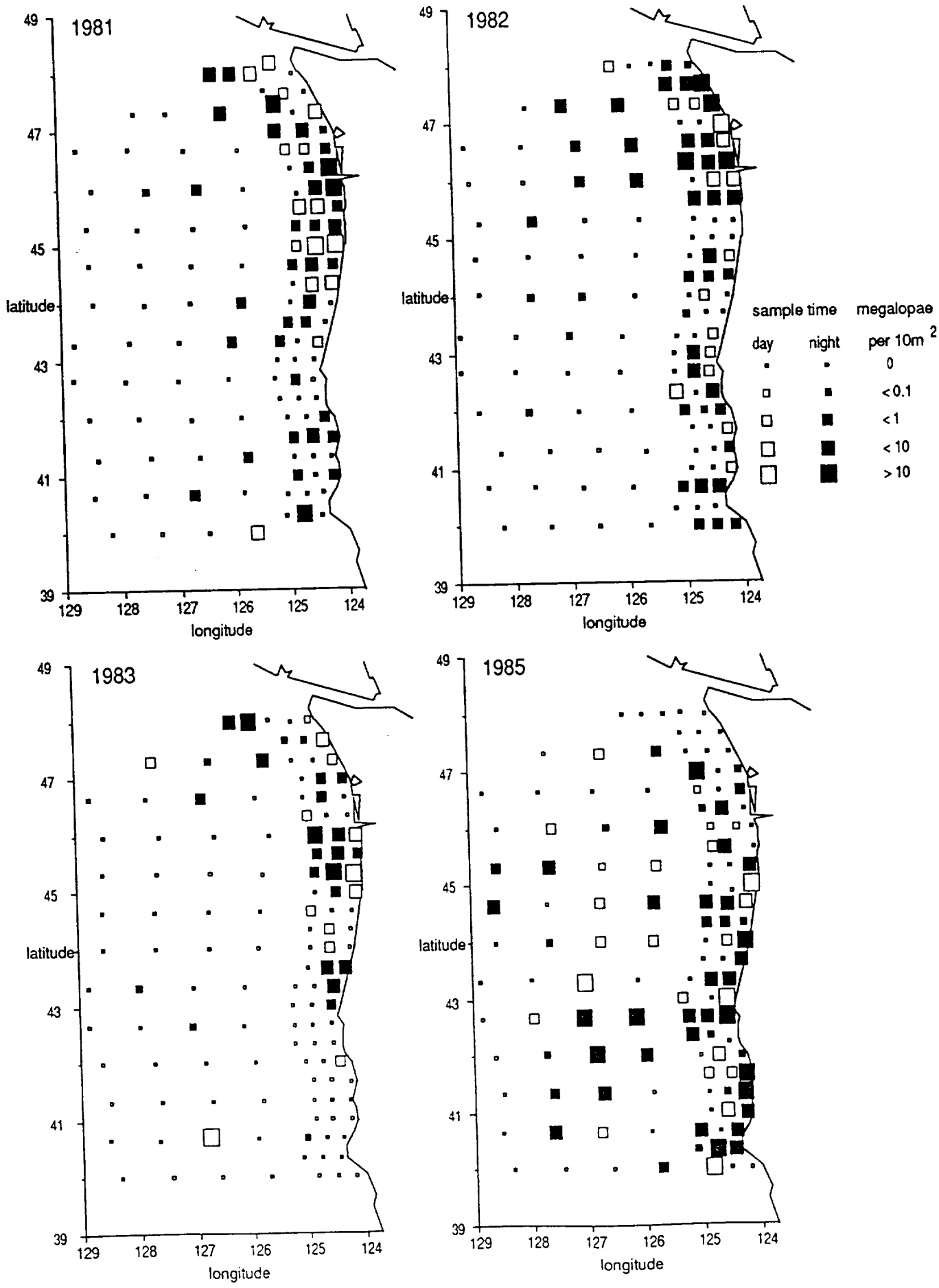
1981
1982
1983
1985
49
47
45
43
41
39
latitude
129
128
127
126
125
124
longitude
sample time
day
night
megalopae
per 10m 2
0
< 0.1
< 1
< 10
> 10

Figure 5

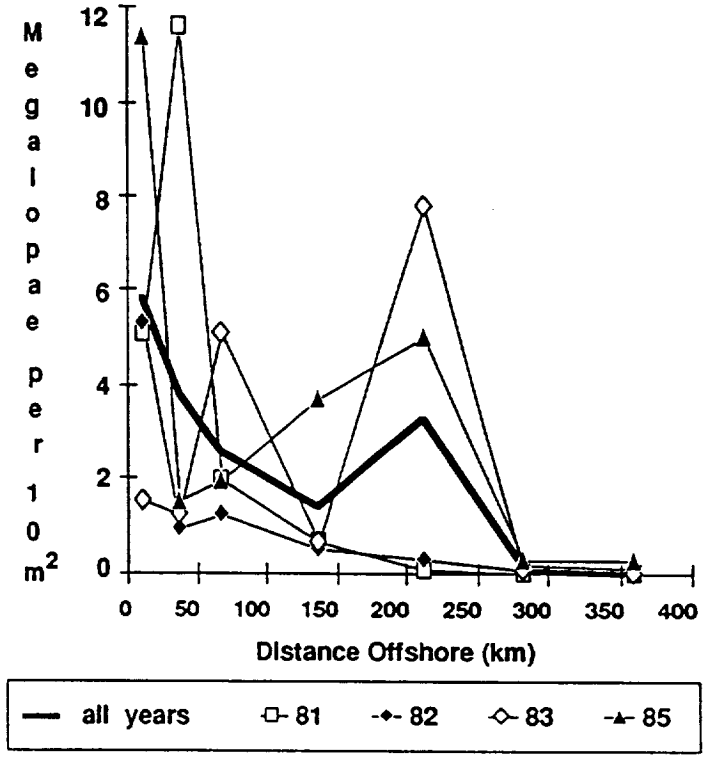
Megalopae per 10 m2
12
10
8
6
4
2
0
0
50
100
150
200
250
300
350
400
Distance Offshore (km)
all years
81
82
83
85

Figure 6

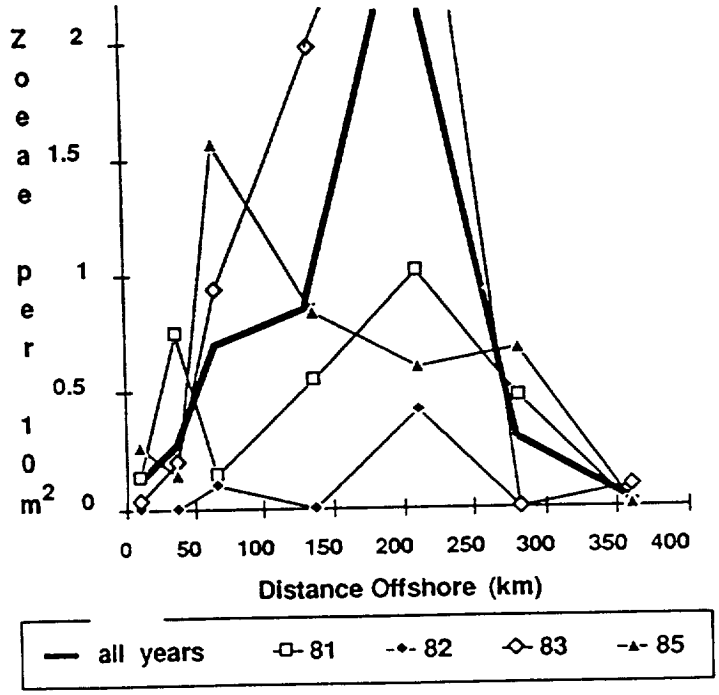
Z
o
e
a
e
p
e
r
1
0
m2
2
1.5
1
0.5
0
0
50
100
150
200
250
300
350
400
Distance Offshore (km)
all years
81
82
83
85

Figures 7a,b

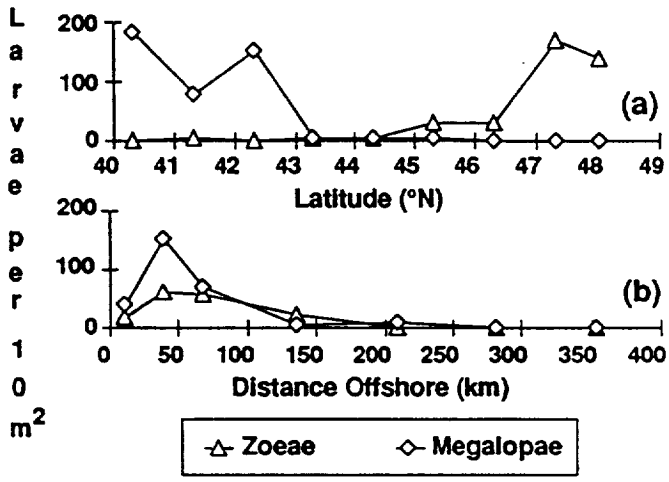
Larvae per 10 m2
200
100
0
40
41
42
43
44
45
46
47
48
49
(a)
Latitude (°N)
200
100
0
0
50
100
150
200
250
300
350
400
(b)
Distance Offshore (km)
Zoeae
Megalopae

Fig 8 log meg vs sst

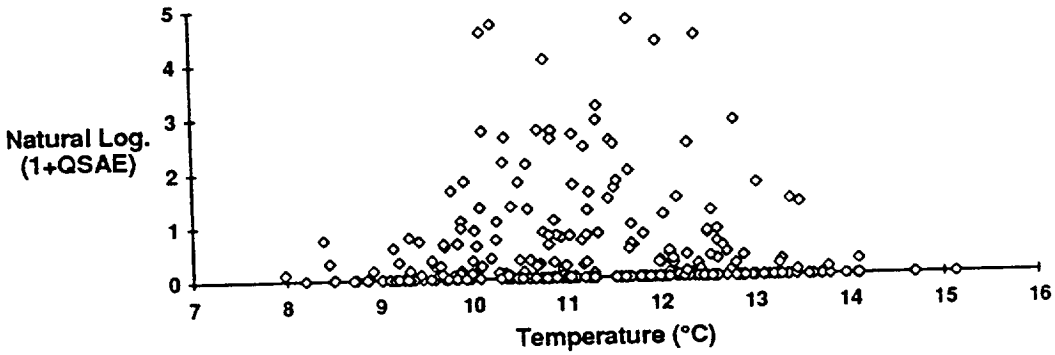

9

Fig 8 chlor vs dist ofs

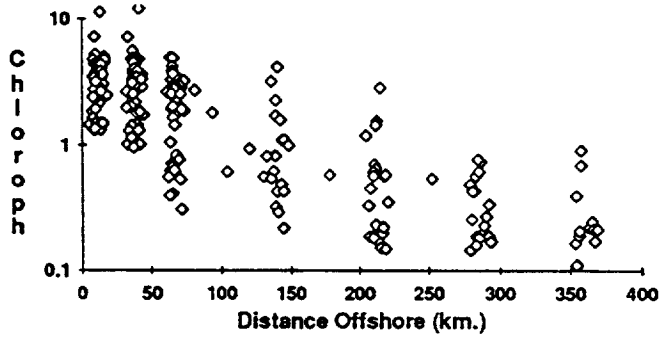

Fig 9 EstFemAbunCrYrs

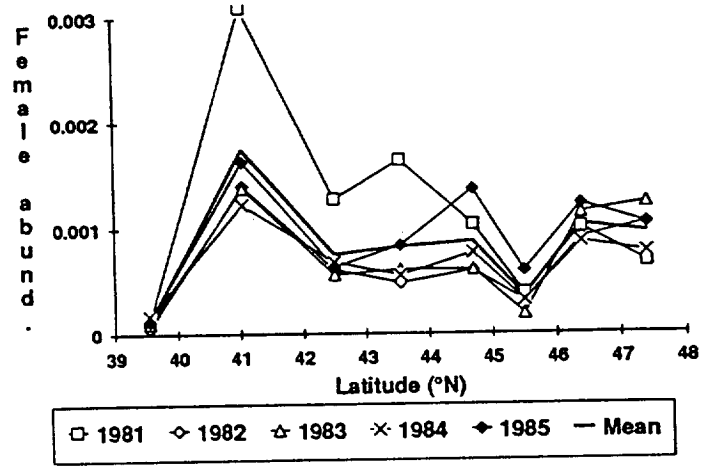

figure 11

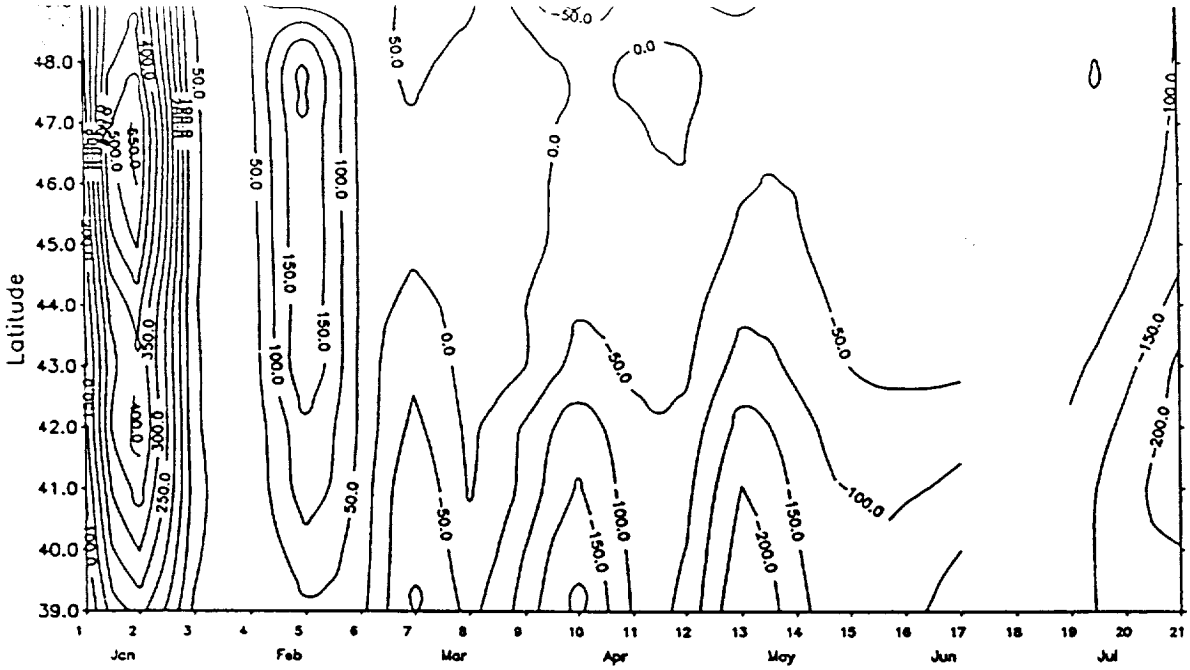

(a) 1981

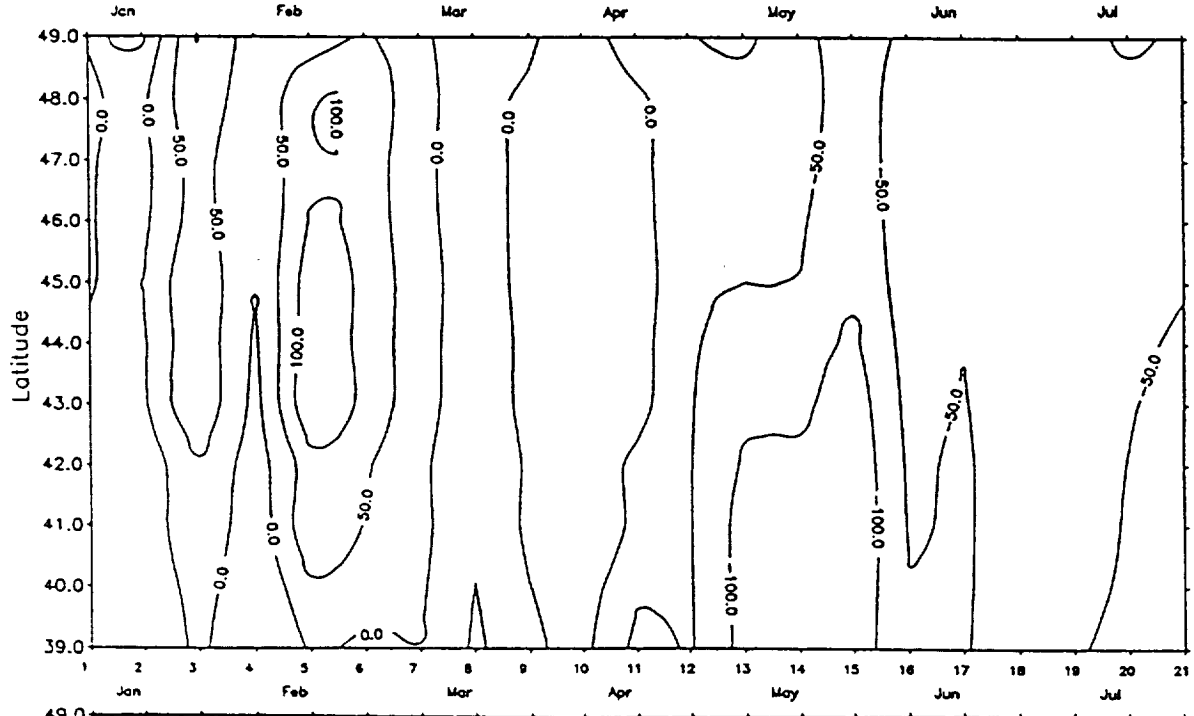

(b) 1982

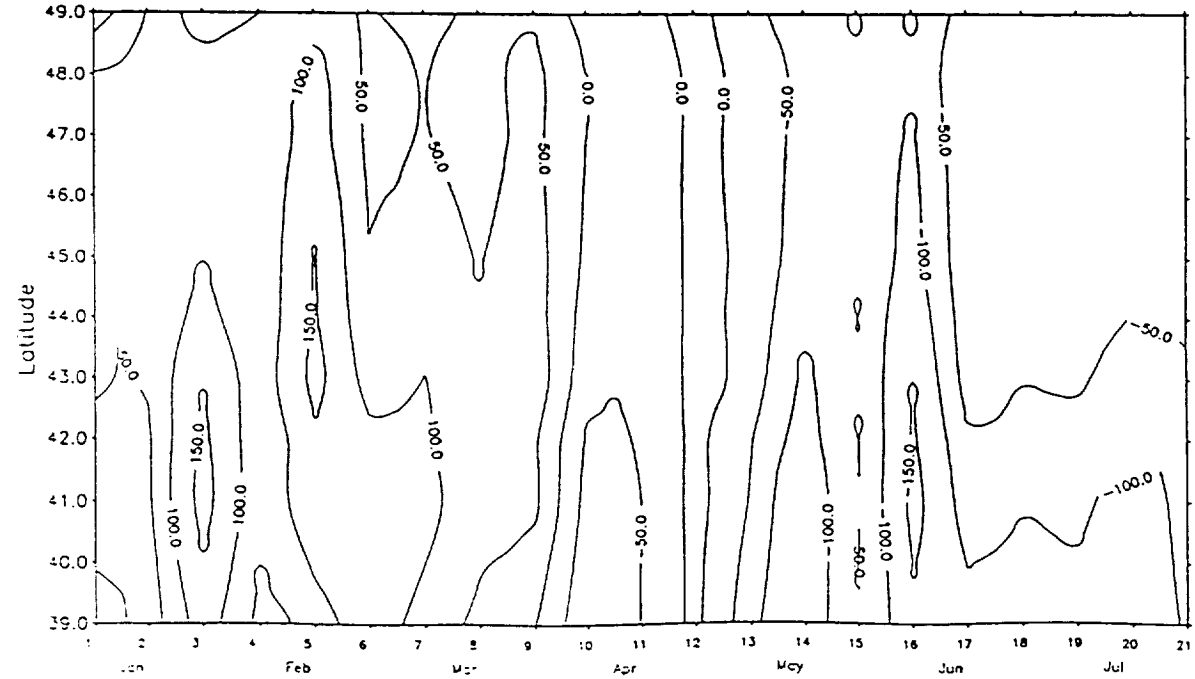

(c) 1983

Figure 11

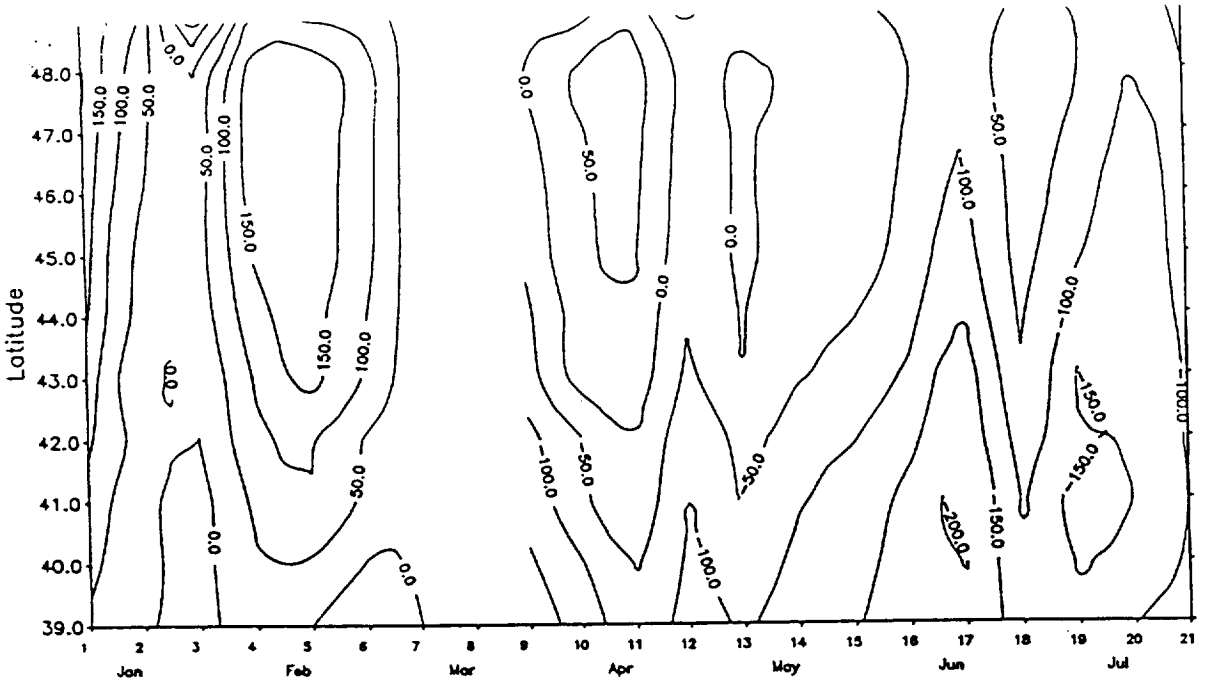

(a) 1984

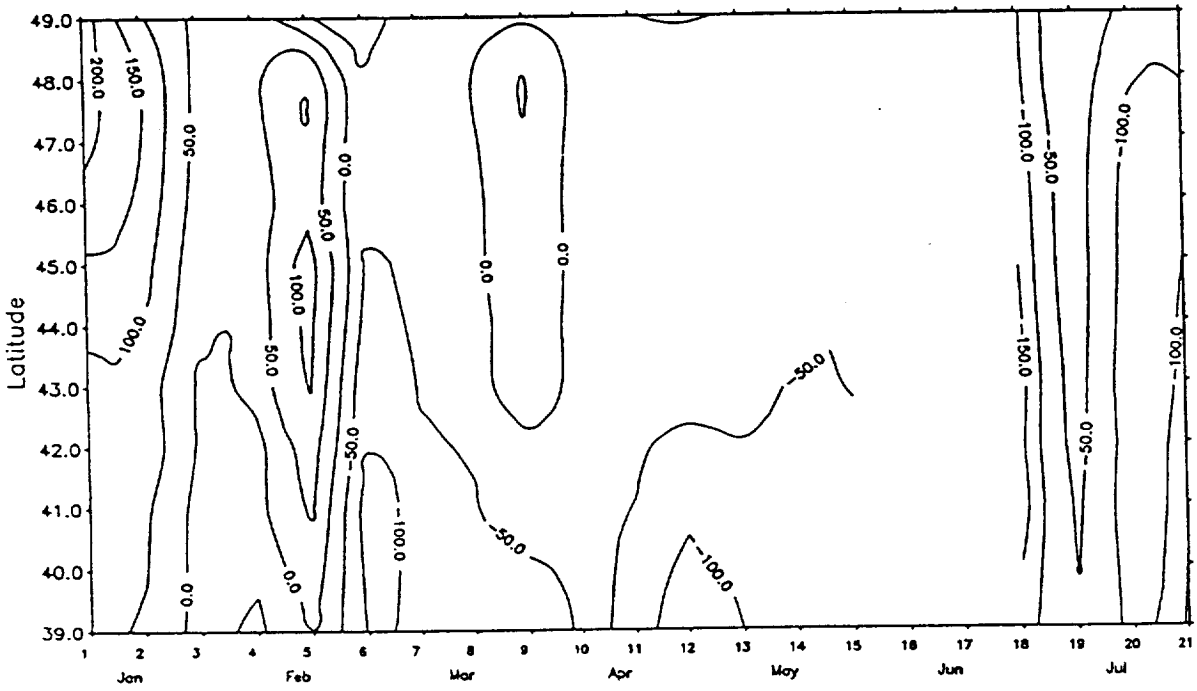

(b) 1985

Figures ~~11~~ 12a,b,c,d

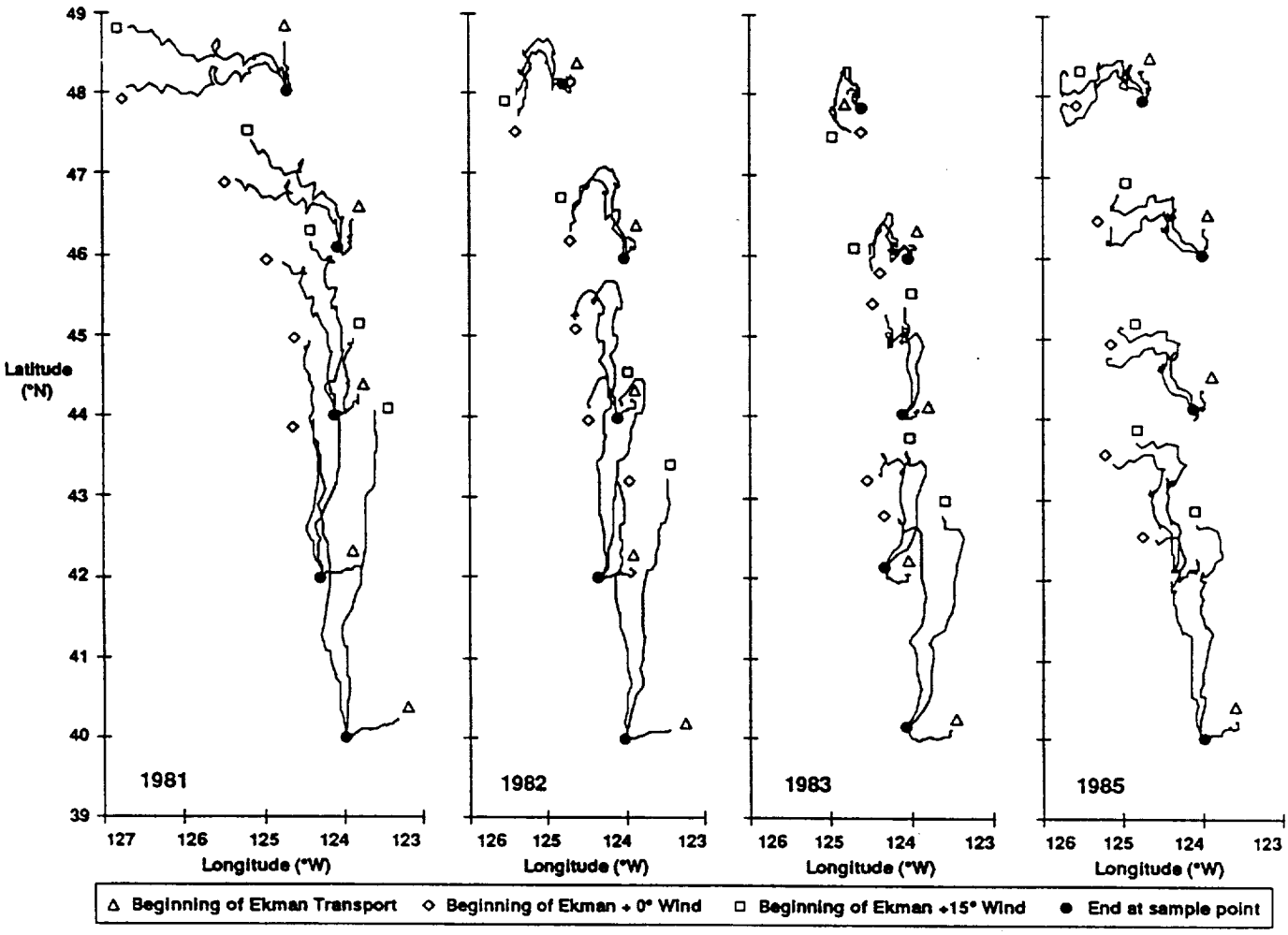

13

Figure ~~12~~a,b,c,d Onshore Transport

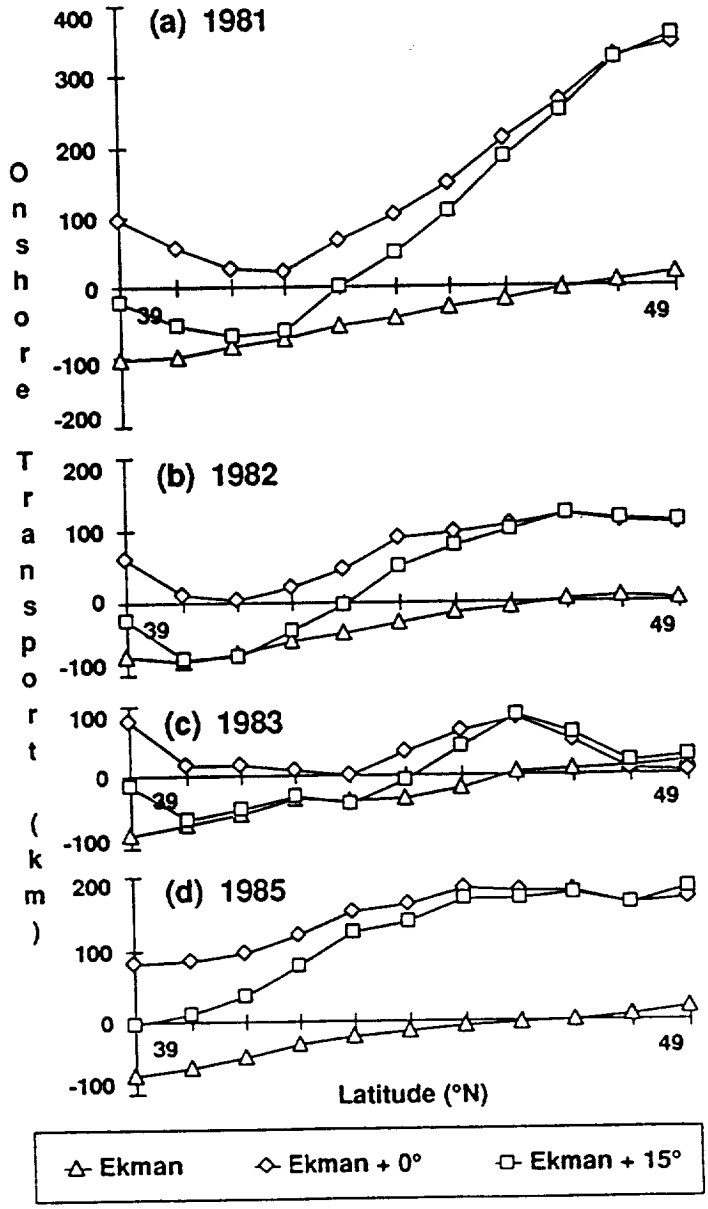

Figure 13a,b Onshore Transport and Meg. Dens

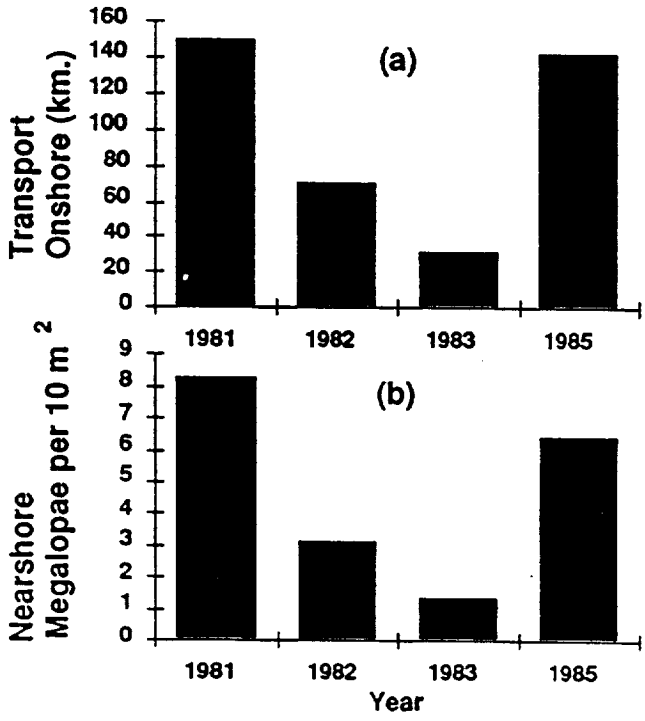

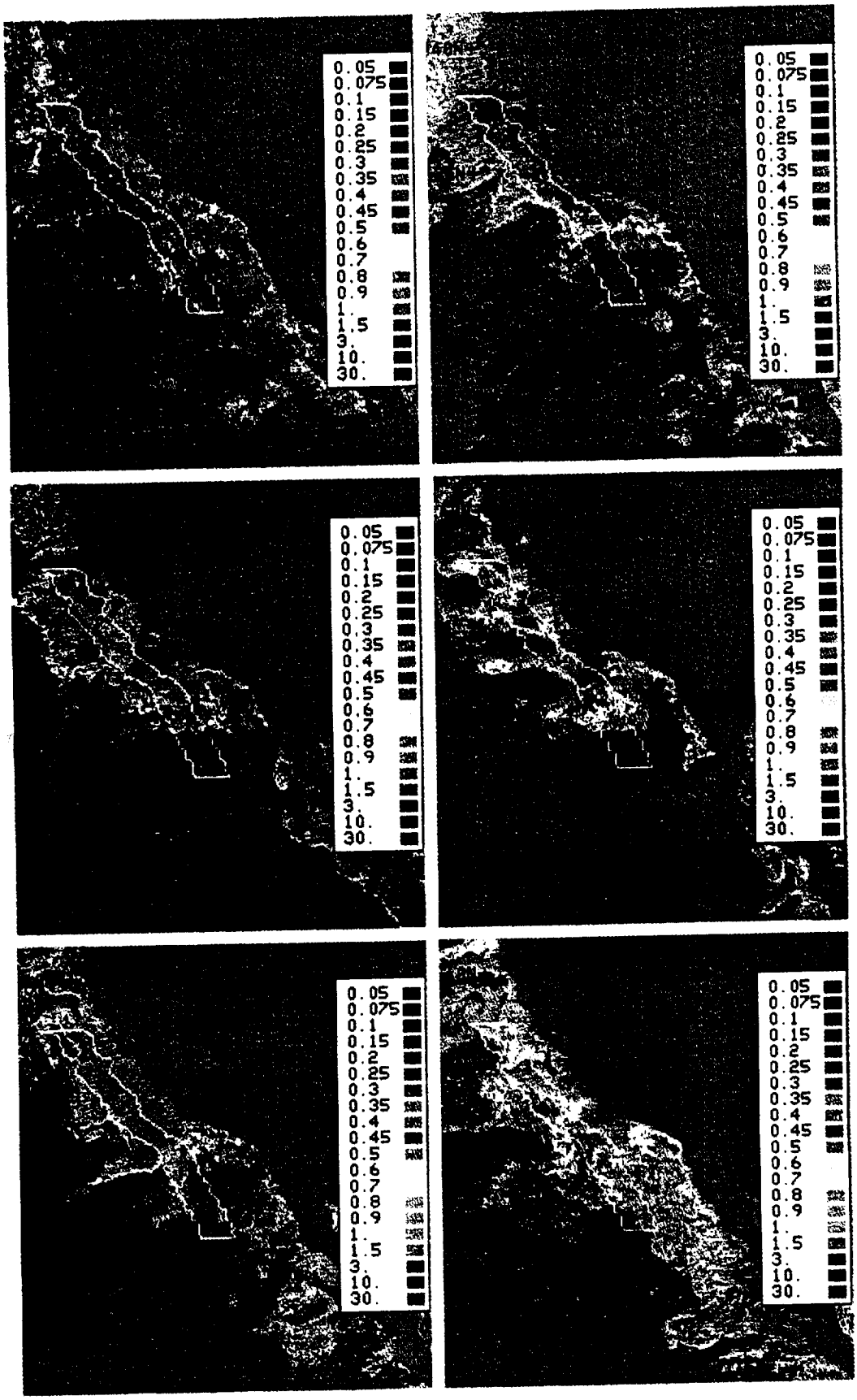

Plate 1 [*Thomas and Strub*]. Ten-day composite CZCS images of the periods in 1981 shown in Figure 3. Pigment concentrations are color coded as is shown in each image. Clouds, land, and missing data in each composite are masked as grey tones, and the meridional transect over which the data are zonally averaged to form a mean transect is shown.